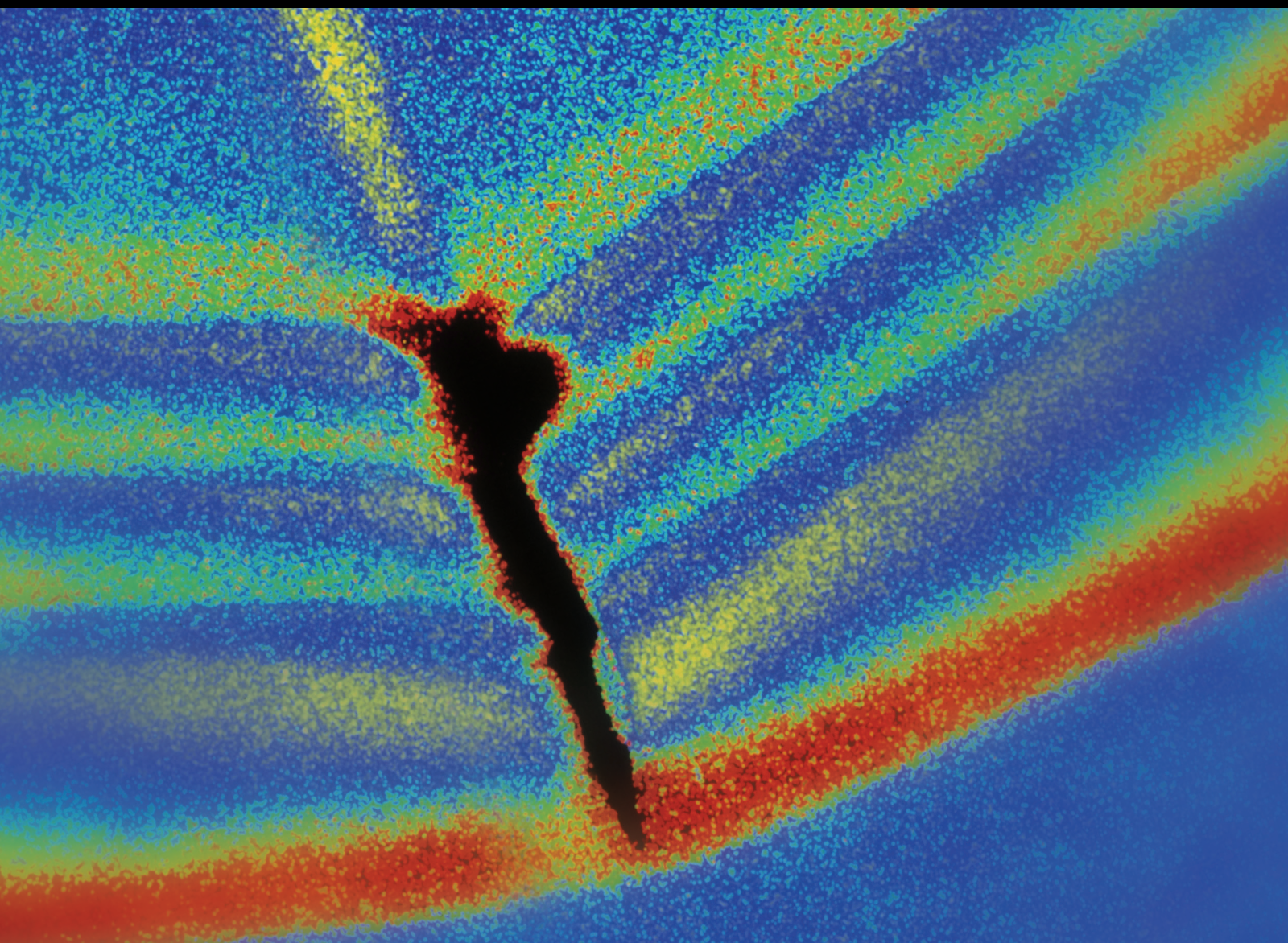


# Vibration-Based Damage Identification and Condition Monitoring in Mechanical Structures and Components

Special Issue Editor in Chief: Rafał Burdzik

Guest Editors: Maosen Cao, Andrzej Katunin, and Sandris Ručevskis





---

# **Vibration-Based Damage Identification and Condition Monitoring in Mechanical Structures and Components**

Shock and Vibration

---

**Vibration-Based Damage Identification  
and Condition Monitoring in Mechanical  
Structures and Components**

Special Issue Editor in Chief: Rafal Burdzik  
Guest Editors: Maosen Cao, Andrzej Katunin,  
and Sandris Rucevskis



---

Copyright © 2018 Hindawi. All rights reserved.

This is a special issue published in "Shock and Vibration." All articles are open access articles distributed under the Creative Commons Attribution License, which permits unrestricted use, distribution, and reproduction in any medium, provided the original work is properly cited.

## Editorial Board

- Brij N. Agrawal, USA  
Felix Albu, Romania  
Marco Alfano, Italy  
Sumeet S. Aphale, UK  
Hassan Askari, Canada  
Lutz Auersch, Germany  
Matteo Aureli, USA  
Mahmoud Bayat, USA  
Marco Belloli, Italy  
Giosuè Boscato, Italy  
Francesco Braghin, Italy  
Rafał Burdzik, Poland  
Salvatore Caddemi, Italy  
Ivo Caliò, Italy  
Antonio Carcaterra, Italy  
Dumitru I. Caruntu, USA  
Cristina Castejón, Spain  
Nicola Caterino, Italy  
Gabriele Cazzulani, Italy  
Noel Challamel, France  
Athanasios Chasalevris, UK  
Xavier Chimentin, France  
Nawawi Chouw, New Zealand  
Simone Cinquemani, Italy  
Pedro A. Costa, Portugal  
Alvaro Cunha, Portugal  
Giorgio Dalpiaz, Italy  
Farhang Daneshmand, Canada  
Silvio L.T. de Souza, Brazil  
Dario Di Maio, UK  
Luigi Di Sarno, Italy  
Longjun Dong, China  
Lorenzo Dozio, Italy  
Mohamed El Badaoui, France  
Mohammad Elahinia, USA  
Fiorenzo A. Fazzolari, UK  
Matteo Filippi, Italy  
Piotr Folega, Poland  
Paola Forte, Italy  
Francesco Franco, Italy  
Juan C. G. Prada, Spain  
Pedro Galvín, Spain  
Gianluca Gatti, Italy  
Marco Gherlone, Italy
- Anindya Ghoshal, USA  
Gilbert R. Gillich, Romania  
Nere Gil-Negrete, Spain  
Adam Glowacz, Poland  
Itzhak Green, USA  
Hassan Haddadpour, Iran  
M.I. Herreros, Spain  
Hamid Hosano, Japan  
Reza Jazar, Australia  
Sakdirat Kaewunruen, UK  
Yuri S. Karinski, Israel  
Jeong-Hoi Koo, USA  
Georges Kouroussis, Belgium  
Mickaël Lallart, France  
Luca Landi, Italy  
Marco Lepidi, Italy  
Zhixiong Li, China  
Manuel Lopez Aenlle, Spain  
Nuno M. Maia, Portugal  
Stefano Manzoni, Italy  
Giuseppe Carlo Marano, Italy  
Stefano Marchesiello, Italy  
Francesco S. Marulo, Italy  
Jean-Mathieu Mencik, France  
Laurent Mevel, France  
Fabio Minghini, Italy  
Mahdi Mohammadpour, UK  
Rui Moreira, Portugal  
Emiliano Mucchi, Italy  
Peter Múčka, Slovakia  
Sara Muggiasca, Italy  
Tony Murmu, UK  
Pedro Museros, Spain  
Roberto Nascimbene, Italy  
Sundararajan Natarajan, India  
Toshiaki Natsuki, Japan  
Miguel Neves, Portugal  
Nicola Nisticò, Italy  
Roberto Palma, Spain  
A. Papageorgiou, Greece  
Francesco Pellicano, Italy  
Paolo Pennacchi, Italy  
Giuseppe Petrone, Italy  
Evgeny Petrov, UK
- Giuseppe Piccardo, Italy  
Antonina Pirrotta, Italy  
Franck Poisson, France  
Luca Pugi, Italy  
Mohammad Rafiee, Canada  
Carlo Rainieri, Italy  
José J. Rangel-Magdaleno, Mexico  
Didier Rémond, France  
Francesco Ripamonti, Italy  
Riccardo Rubini, Italy  
Salvatore Russo, Italy  
Giuseppe Ruta, Italy  
Edoardo Sabbioni, Italy  
Filippo Santucci de Magistris, Italy  
Onome E. Scott-Emuakpor, USA  
Roger Serra, France  
Chengzhi Shi, USA  
Vadim V. Silberschmidt, UK  
Kumar V. Singh, USA  
Jean-Jacques Sinou, France  
Isabelle Sochet, France  
Alba Sofi, Italy  
Jussi Sopanen, Finland  
Stefano Sorace, Italy  
Andrea Spaggiari, Italy  
Shuaishuai Sun, Australia  
Chao Tao, China  
Marco Tarabini, Italy  
Gloria Terenzi, Italy  
Mario Terzo, Italy  
Tai Thai, Australia  
Marc Thomas, Canada  
Hamid Toopchi-Nezhad, Iran  
Carlo Trigona, Italy  
Federica Tubino, Italy  
Nerio Tullini, Italy  
Angelo Marcelo Tusset, Brazil  
Jens Twiefel, Germany  
Filippo Ubertini, Italy  
Marcello Vanali, Italy  
F. Viadero, Spain  
M. Ahmer Wadee, UK  
Jörg Wallaschek, Germany  
Matthew J. Whelan, USA



---

Agnieszka Wylomanska, Poland  
Davood Younesian, Iran

Enrico Zappino, Italy  
Radoslaw Zimroz, Poland

# Contents

## **Vibration-Based Damage Identification and Condition Monitoring in Mechanical Structures and Components**

Rafał Burdzik , Maosen Cao , Andrzej Katunin, and Sandris Ručevskis 

Editorial (2 pages), Article ID 6750937, Volume 2018 (2018)

## **Vibration-Based Damage Identification and Condition Monitoring of Metro Trains: Warsaw Metro Case Study**

Alicja Kowalska-Koczwara , Filip Pachla , Piotr Stecz, Krzysztof Stypuła, Tadeusz Tatara, Jerzy Lejk, and Marek Sokołowski

Research Article (14 pages), Article ID 8475684, Volume 2018 (2018)

## **A Study on Coupling Faults' Characteristics of Fixed-Axis Gear Crack and Planetary Gear Wear**

Xin Wang 

Research Article (13 pages), Article ID 4692796, Volume 2018 (2018)

## **Forward Analysis of Love-Wave Scattering due to a Cavity-Like Defect**

Chen Yang , Bin Wang, and Zhenghua Qian 

Research Article (11 pages), Article ID 3456270, Volume 2018 (2018)

## **Dynamic Characteristic and Fatigue Accumulative Damage of a Cross Shield Tunnel Structure under Vibration Load**

Qixiang Yan, Hang Chen , Wenyu Chen, Junchen Zhang, Shuqi Ma , and Xi Huang

Research Article (14 pages), Article ID 9525680, Volume 2018 (2018)

## **Detection of Delamination in Laminate Wind Turbine Blades Using One-Dimensional Wavelet Analysis of Modal Responses**

Łukasz Doliński , Marek Krawczuk, and Arkadiusz Żak

Research Article (15 pages), Article ID 4507879, Volume 2018 (2018)

## **An Integrated Cumulative Transformation and Feature Fusion Approach for Bearing Degradation Prognostics**

Lixiang Duan , Fei Zhao, Jinjiang Wang, Ning Wang, and Jiwang Zhang

Research Article (15 pages), Article ID 9067184, Volume 2018 (2018)

## **Optimal Sensor Placement for Spatial Structure Based on Importance Coefficient and Randomness**

Haoxiang He , Honggang Xu, Xiaobing Wang, Xiaofu Zhang, and Shaoyong Fan

Research Article (14 pages), Article ID 7540129, Volume 2018 (2018)

## **The Time-Space Joint Response Characteristics of AE-UT under Step Loading and Its Application**

Xiaoran Wang, Xiaofei Liu , Enyuan Wang , Chong Zhang, Haishan Jia, and Dexing Li

Research Article (11 pages), Article ID 6210594, Volume 2018 (2018)

## **A Novel Faults Diagnosis Method for Rolling Element Bearings Based on ELCD and Extreme Learning Machine**

Mingliang Liang, Dongmin Su, Daidi Hu, and Mingtao Ge 

Research Article (10 pages), Article ID 1891453, Volume 2018 (2018)

**A SVDD and  $K$ -Means Based Early Warning Method for Dual-Rotor Equipment under Time-Varying Operating Conditions**

Zhinong Jiang , Minghui Hu, Kun Feng , and Hao Wang  
Research Article (14 pages), Article ID 5382398, Volume 2018 (2018)

**A New Method for Weak Fault Feature Extraction Based on Improved MED**

Junlin Li, Jingsheng Jiang, Xiaohong Fan, Huaqing Wang , Liuyang Song , Wenbin Liu, Jianfeng Yang, and Liangchao Chen  
Research Article (11 pages), Article ID 9432394, Volume 2018 (2018)

**Acoustic Emission Monitoring and Failure Precursors of Sandstone Samples under Various Loading and Unloading Paths**

Jie Xu, Jingdong Jiang, Lingling Zuo, and Yufeng Gao  
Research Article (11 pages), Article ID 9760940, Volume 2017 (2018)

**Analysis of the Impacts of Bearing on Vibration Characteristics of Rotor**

Peiji Yang, Qi Yuan, Chao Huang, Yafeng Zhou, Hongliang Li, and Yu Zhou  
Research Article (7 pages), Article ID 8098591, Volume 2017 (2018)

**Planetary Gearbox Fault Diagnosis via Torsional Vibration Signal Analysis in Resonance Region**

Kangqiang Li, Zhipeng Feng, and Xihui Liang  
Research Article (18 pages), Article ID 6565237, Volume 2017 (2018)

**Nonpenetrating Damage Identification Using Hybrid Lamb Wave Modes from Hilbert-Huang Spectrum in Thin-Walled Structures**

Zijian Wang, Pizhong Qiao, and Binkai Shi  
Research Article (11 pages), Article ID 5164594, Volume 2017 (2018)

**Information-Based Construction of High-Speed Railway Tunnel**

Qian Yang and Zhaoling Wang  
Research Article (11 pages), Article ID 5318785, Volume 2017 (2018)

**Diagnosis of Localized Faults in Multistage Gearboxes: A Vibrational Approach by Means of Automatic EMD-Based Algorithm**

M. Buzzoni, E. Mucchi, G. D'Elia, and G. Dalpiaz  
Research Article (22 pages), Article ID 8345704, Volume 2017 (2018)

**Data-Driven Iterative Vibration Signal Enhancement Strategy Using Alpha Stable Distribution**

Grzegorz Żak, Agnieszka Wyłomańska, and Radosław Zimroz  
Research Article (11 pages), Article ID 3698370, Volume 2017 (2018)

**Measures of Dependence for  $\alpha$ -Stable Distributed Processes and Its Application to Diagnostics of Local Damage in Presence of Impulsive Noise**

Grzegorz Żak, Marek Teuerle, Agnieszka Wyłomańska, and Radosław Zimroz  
Research Article (9 pages), Article ID 1963769, Volume 2017 (2018)

## Editorial

# Vibration-Based Damage Identification and Condition Monitoring in Mechanical Structures and Components

Rafał Burdzik <sup>1</sup>, Maosen Cao <sup>2</sup>, Andrzej Katunin,<sup>3</sup> and Sandris Ručevskis <sup>4</sup>

<sup>1</sup>Silesian University of Technology, Katowice, Poland

<sup>2</sup>Hohai University, Nanjing, China

<sup>3</sup>Silesian University of Technology, Gliwice, Poland

<sup>4</sup>Riga Technical University, Riga, Latvia

Correspondence should be addressed to Rafał Burdzik; [rafal.burdzik@polsl.pl](mailto:rafal.burdzik@polsl.pl)

Received 28 August 2018; Accepted 28 August 2018; Published 1 November 2018

Copyright © 2018 Rafał Burdzik et al. This is an open access article distributed under the Creative Commons Attribution License, which permits unrestricted use, distribution, and reproduction in any medium, provided the original work is properly cited.

Damage detection and identification as well as continuous condition monitoring are one of the most important issues related to proper operation of machines and structural parts in order to ensure their structural integrity, safety, and desirable operational properties. In recent years, an exponential development of vibration-based methods for damage detection and identification as well as condition monitoring used for machines and structures has been observed. This development was possible for two main reasons: the advance of apparatus and measurement techniques in vibration engineering and the development of advanced mathematical tools for signal conditioning and postprocessing. Both of these reasons influence modern trends related to vibration-based damage identification and condition monitoring in mechanical structures and components. This special issue is focused on recent attempts in development of vibration-based damage identification in mechanical structures and also homogeneous and inhomogeneous structures, especially stressing the latter such as advanced composites, and related issues connected with modal analysis and structural dynamic analysis. Moreover, the special issue covers damage identification and monitoring topics related to theoretical studies and numerical simulations as well as practical solutions, in particular in rotary machinery and vibration-generating devices, structural elements of heavy machinery and vehicles, etc. Thus, this special issue collects interdisciplinary approaches on vibration-based damage identification and condition monitoring, and it can be good motivation to consider and develop some innovative directions of research.

All the trends and innovations in vibration-based damage identification and condition monitoring have attracted the attention to this special issue from the international researchers and scientists. This special issue has attracted 40 submissions from authors from all around the world; only 19 papers have been selected and included in this special issue on shock and vibration and vibration-based damage identification and condition monitoring in mechanical structures and components. The selection of the high-level papers was conducted as a rigorous peer-review process by the international, well-recognized experts in the appropriate fields presented in each paper. Thus, each manuscript has been evaluated as single, original work with the comparison with current state of art. The editors of the special issue would like to thank all authors of all submitted articles. More of the submitted papers were interesting and present original research. The first selection consisted in assessing compliance with the topic of special issue. The second stage of evaluation was based on originality and quality of the paper. The last editorial stage selected best papers to present wide range of research on vibration-based damage identification and condition monitoring in mechanical structures and components. Thus, even good papers could be rejected to ensure presentation of different areas.

The papers collected in this special issue focus on such topics as incident Love wave propagation, which interacts with the cavity-generating forward-scattered and back-scattered surface wave, vibration-based damage identification and condition monitoring of metro trains, detection of delamination in laminate wind turbine blades using

one-dimensional wavelet analysis of modal responses, study on coupling faults characteristics of fixed-axis gear crack and planetary gear wear, planetary gearbox fault diagnosis via torsional vibration signal, diagnosis of localized faults in multistage gearboxes, weak fault feature extraction method, fatigue accumulative damage of a cross shield tunnel structure under vibration load, novel faults diagnosis method for rolling element, integrated cumulative transformation and feature fusion approach for bearing degradation prognostics, early warning method for dual-rotor equipment under time-varying operating conditions, acoustic emission monitoring and failure precursors of sandstone samples, optimal sensor placement for spatial structure based on importance coefficient and randomness, alpha-stable distributed processes and its application to diagnostics of local damage, and non-penetrating damage identification using hybrid lamb wave modes from the Hilbert–Huang spectrum in thin-walled structures. Selected papers present application of vibration (and acoustics)-based diagnostic and monitoring methods for different mechanical structures and materials. Other criteria of selection were to present novel approach and possibilities in signal processing and original research on application of new mathematical methods for the purpose of damage identification or structural health monitoring. Therefore, this special issue presents different approaches in vibration-based diagnostics, and it can indicate new areas or new application for further research.

### **Conflicts of Interest**

The editors declare that they have no conflicts of interest.

*Rafał Burdzik*  
*Maosen Cao*  
*Andrzej Katunin*  
*Sandris Ručevskis*

## Research Article

# Vibration-Based Damage Identification and Condition Monitoring of Metro Trains: Warsaw Metro Case Study

Alicja Kowalska-Koczwara <sup>1</sup>, Filip Pachla <sup>1</sup>, Piotr Stecz,<sup>1</sup>  
Krzysztof Stypuła,<sup>1</sup> Tadeusz Tatara,<sup>1</sup> Jerzy Lejk,<sup>2</sup> and Marek Sokołowski<sup>2</sup>

<sup>1</sup>Cracow University of Technology, Warszawska 24 St., 31-155 Cracow, Poland

<sup>2</sup>Metro Warszawskie Sp. z o. o., Wilczy Dół 5 St., 02-798 Warsaw, Poland

Correspondence should be addressed to Filip Pachla; [fpachla@pk.edu.pl](mailto:fpachla@pk.edu.pl)

Received 18 December 2017; Accepted 31 March 2018; Published 10 May 2018

Academic Editor: Rafał Burdzik

Copyright © 2018 Alicja Kowalska-Koczwara et al. This is an open access article distributed under the Creative Commons Attribution License, which permits unrestricted use, distribution, and reproduction in any medium, provided the original work is properly cited.

The work concerns the monitoring of the technical condition of metro trains. For this purpose, a vibration monitoring system installed in buildings in the vicinity of the underground is used. Based on measured vibrations buildings, the identification of technical condition in metro trains is conducted. The results of measurements from the system are also used to assess the impact of vibrations on people staying in buildings through the WODL ratio. Exceeding the assumed levels of the WODL ratio is the basis for repairing trains by turning wheels. Statistical analysis of the data was implemented and trends for particular time periods of measurements were shown. With the entered monitoring system and the introduced WODL index thresholds, it is possible to better plan the costs associated with the repair and replacement of wheels of rolling stock, where there are large values of radial runout. According to the introduced monitoring procedure, the number of complaints from residents decreased and the comfort of their lives improved.

## 1. Introduction

The vibration monitoring system in civil engineering mainly concerns two aspects: structural health monitoring [1–4] and ambient or seismic vibration monitoring [5–7]. There are relatively few articles that address the issue of monitoring vibrations in buildings from existing road, rail, or metro infrastructure. Investigators are concerned about short-term monitoring [8] or vibrations, which are measured on the ground [9] or in the tunnel [10] and eventually the building model is excited by recorded signals [11]. It is worth noting that the building structure exposed to vibrations is investigated by researches, while human perception of vibrations is a decisive parameter of evaluation. People are more sensitive to vibrations than building structures are, especially when these vibrations occur often, although they are not very strong. These kinds of situations occur in buildings located close to the road, railway, tramway, or subway. Often, during the

designing or the building of these urban infrastructures, human perception of vibrations throughout these buildings located is not taken into account [12, 13]. Furthermore, the exploitation of this parameter of evaluation is not monitored. Meanwhile, this existing infrastructure has become older, sometimes infrastructures conditions change (due to traffic increases or changing of train or tram types), and some of its elements become slightly damaged, all of which can influence human perception of vibrations. It is impossible to change the location of an existing urban infrastructure. The vibration monitoring system can provide solutions to the necessary infrastructure design (i.e., by introducing additional vibroinsulation [14, 15]). Some small repairs in the existing infrastructure system are sufficient to ensure vibrational comfort in buildings located nearby.

A few years after the opening of its first metro line, Warsaw Metro owners observed a growing number of complaints from the residents of neighbouring buildings. This prompted

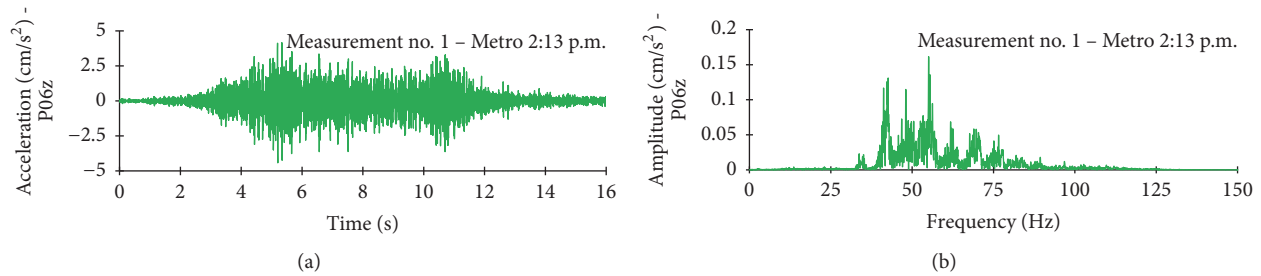


FIGURE 1: Exemplary record of vertical component of the floor apartment vibrations and its FFT analysis.

scientists and engineers from the Cracow University of Technology to design and build the vibration monitoring system. The basis for building the monitoring system was to understand the phenomenon related to the propagation of vibration for shallow subways. The vibrations generated when the wheel comes into contact with the rail are propagated through the subway tunnel and ground, which are then transmitted to buildings located near the metro line. Some numerical and analytical solutions of the contact problem between the rail and wheel can be found in literature, for example, [16–19]. In these paper authors focused on experimental solution of the problem. A point of focus for the Warsaw Metro is the human perception of vibrations, but it is worth noting that for these shallow subways, vibrations are perceived to be larger on lower floors. This was the most critical observation which has contributed towards building the system. Human sensitivity to the vertical vibrations of floors, in some buildings located near metro line, was particularly evident in the preconstruction measurements. The sensitivity of individual floors depends on their dynamic characteristics, which is contingent on their floor structure, stiffness, and dimensions. These three factors made it necessary to select representative measurements points within buildings that are not always located close to the metro tunnel. Monitoring the human perception of vibrations of each metro train helps Warsaw Metro owners to determine which trains should continue operating and those that should not. This paper describes the observations and analysis of this monitoring system between 2003 and 2011.

After proper verification of the system developed by the authors, other proposals of systems appeared [20]. Another way for evaluation of the vibration impacts in the transport infrastructure environment was presented in [21].

## 2. System Description

The monitoring system was developed at the Institute of Structural Mechanics at Cracow University of Technology. This system allows for constant monitoring of vibrations. Based on the measured vibrations in three selected buildings, the identification of the technical condition of metro trains is performed. The vibrations generated when the wheel comes into contact with the rail are transferred through the tunnel structure and the ground, around the building, and close to the metro line. Previous experience shows that the

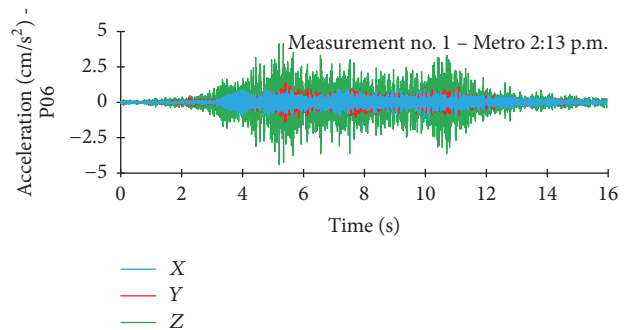


FIGURE 2: Relations between horizontal and vertical components of vibrations recorded at the ceiling of the building M22A.

wheel's profile has a significant influence on the level of vibrations. Therefore, these vibrations are a source of discomfort for the people in buildings close to the metro lines. The perception of vibrations by humans in the buildings is a complex problem, and it depends on, for example, the ceiling structure, its stiffness, and dimensions. Therefore, it is important to select the accurate, representative position of sensors in the buildings.

In the presented system, developed for the Warsaw metro line, the results of analysis, in relation to the comfort limits required for the people, constitute the criterion for evaluating the admissibility of the train for further operation [22]. Continuous monitoring of the vibration caused by each of the passing trains allows the individual trains to be eliminated before the vibration limit is reached. Moreover, these trains can be removed from operation before any complaint from the residents of the buildings near the subway line occurs. The accelerometer is mounted on the floor of the room in the building and is used to measure the vertical vibrations of the ceiling. Exemplary record of vertical component of the floor apartment vibrations and corresponding FFT are presented in Figure 1. Horizontal components were also measured but the level of maximum values of vibrations is smaller compared with the vertical component (see Figure 2). The results of analyses concerning these components are therefore not presented at work. It can be found in the [22], where data not presented in the paper was showed.

Signal vibration is triggered by the signal transmitted (wireless) from the measuring point located in the tunnel, triggering the registration with a photocell when passing a

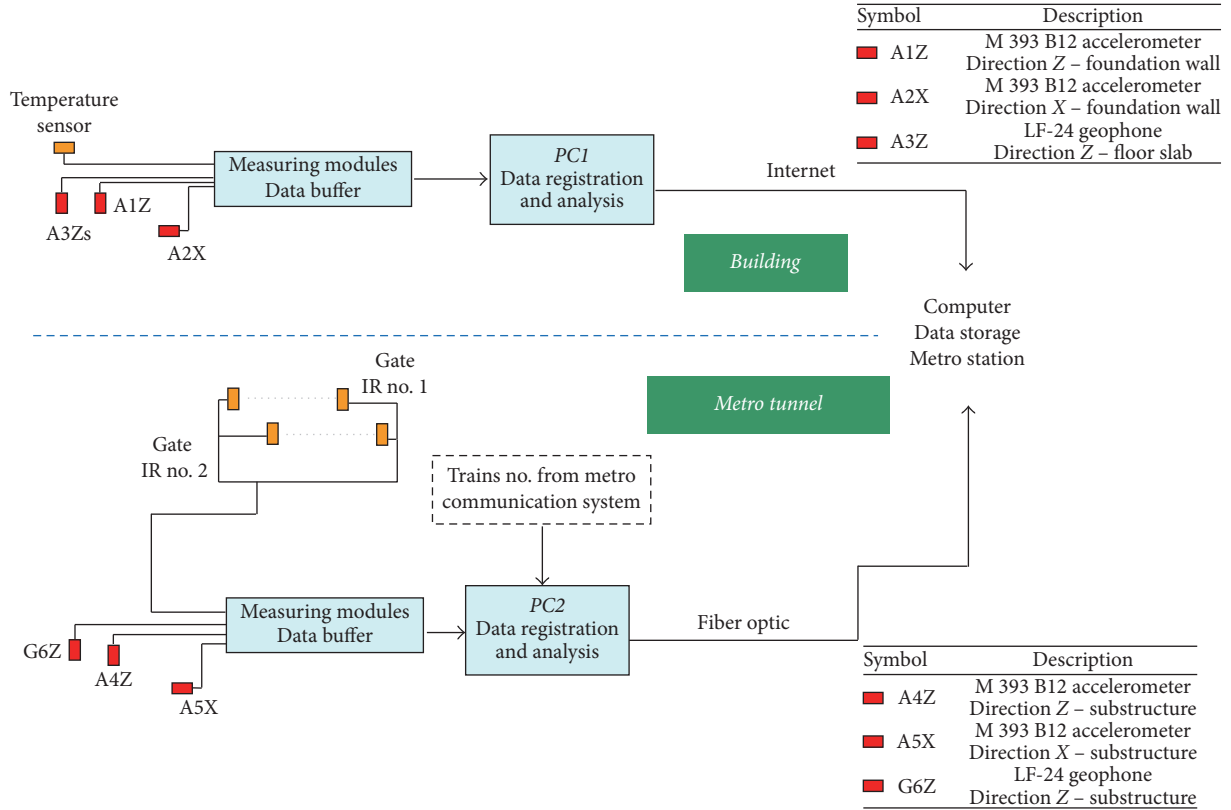


FIGURE 3: General plan of the system.

subway train. The system also records the speed of train. The vibration monitoring system consists of two independent measuring sys, each of which consists of two measuring stations. One station is located in a residential building and the other in the underground tunnel under the building. Every single passage of metro train was registered and considered in the analysis. Metro passages were identified by photocell monitoring in metro tunnels. Figure 3 shows the block diagram of complete monitoring system with all the sensors. In this paper we consider only human vibration comfort inside buildings. The sensor which is responsible for this parameter is only A3Zs mounted in the middle of the ceiling of the cellar. As in the system and during our measurement activities, we use the same reference system: X direction is always horizontal and perpendicular to the source of vibrations, Y is horizontal and parallel to the source of vibrations, and Z direction is vertical. From the beginning the assumption in the monitoring system was to get data from X direction with respect to the building vibration influence (A2X sensor) corresponding to the data from the tunnel (A5X). Another assumption was to get data of vertical vibrations from the building (A1Z) and tunnel (A4Z). These calculations are not presented in this paper.

In the system high sensitivity seismic accelerometers type PCB 393B12 are used, with the sensitivity on the level of 10 V/g ( $\pm 0,5$  g range) and frequency range from 0,15 Hz till 1 kHz ( $\pm 5\%$ ). Sampling rate is set on 400 Hz which is adequate for studied problem and it fulfils the Nyquist's condition. Noise

level is much lower than signal from metro train (compare Figures 1(a) and 2)

Registered data is transferred to the central unit. Then, the following analyses are performed:

- (i) calculation of RMS (root means square) values in one-third bands and comparing them with assumed thresholds,
- (ii) determining peaks in one-third bands octave and comparing them with assumed thresholds,
- (iii) determining the maximum value from the entire time sequence,
- (iv) generating a report.

The results are presented as WODL ratios. The WODL ratio (in English, the human vibration perceptivity ratio), proposed in [23] and in Polish code [24], is the measure of vibration perception by people. It is the maximum ratio of the acceleration RMS value, obtained from the analysis of the acceleration RMS value, equivalent to the threshold for the perception of vibration by humans (in the same 1/3 octave band), chosen from each 1/3 octave band, comp. equation (1).

The advantage of such a coefficient is that the result of the analysis from the frequency band is not independent, since the WODL indicates directly how many times the threshold for human vibration has been exceeded.

$$\text{WODL} = \max \left( \frac{a_{\text{RMS}}}{a_z} \right), \quad (1)$$



FIGURE 4: General view of the buildings: (a) N118 and (b) M22.

where  $a_{\text{RMS}}$  is acceleration RMS value obtained from analysis;  $a_z$  is acceleration RMS value equivalent to the threshold for the perception of vibration in a  $z$  direction in the same 1/3 octave band as in  $a_{\text{RMS}}$ .

Frequency values corresponding to 1/3 octave bands used in analysis are equal to 1.25, 1.6, 2, 3.16, . . . , 63, 80, 100 and listed also in Table 3 of ISO standard [25].

WODL ratios are coefficients calculated according to (1) using RMS basic procedure described in Polish standards [24, 26] and in ISO standard [27]. Recorded signals are filtered using Butterworth low-pass filter with cut-off frequency of 120 Hz according to requirements described in Polish standard [24].

RMS method averages acceleration values in duration:

$$a_W = \left[ \frac{1}{T} \int_0^T a_W^2(T) dt \right]^{1/2}, \quad (2)$$

where  $a_W(T)$  is weighted acceleration as a function of time [ $\text{m/s}^2$ ];  $T$  is the duration of measurement [s].

RMS is basic method of evaluation according to ISO standard [25]. For signals with high crest factor (greater than 9), occasional shocks and transient vibration additional evaluation method like VDV analysis or MTVV analysis are required. Vibrations recorded in metro monitoring system are signals without shocks and with crest factor below 9 that is why RMS method was chosen for analysis and WODL ratio illustrated in most friendly way the percentage of exceedance of perception threshold of vibration.

Measurements in metro system last 24 hours and about 350 dynamical events are registered per day (concerning the tracks closer to the building). Metro managements care about good relations with residents of the buildings located in zone of metro dynamic influences. Because of many complaints of residents, researchers decided to use duration time of single event according to Polish standard [24] in which duration of vibration is defined as time in which amplitudes are greater than 0.2 of maximum value of vibrations. Adoption of such procedure is more rigorous than using of the whole record of vibrations for analysis and results of analyses are more independent from arbitral decision where to start and stop analyses.

### 3. Influence of Wheels Reprofileing on Human Vibrations in the Buildings

In the case of determining the vibration comfort of people in buildings, the decision parameter is the maximum RMS values obtained in each one-third octave band from the analysis of the perceived human horizontal and vertical vibrations of the floors. The influence on the vertical vibration of the ceilings has been assumed, since the vibration measurements generated by the metro in Warsaw have indicated that people are more sensitive to vertical vibrations of the ceilings [22]. The distribution of these values in time can be important for drawing practical conclusions.

Exemplary results of the analysis are given in this section. The data presented below relates to the selected measurement point installed in building N118, as well as building M22 (see Figure 4). The N118 building is a masonry residential building built in the 1950s. The building has 7 storeys above ground level and a basement. The bearing walls are arranged in the longitudinal direction. In the horizontal plan the building is L-shaped. The dimensions of the building in plan are 25.4 m by 72.8 m. The distance to the metro tunnel wall is 14.0 m.

The M22 building was built in 1936 and survived World War II. It is a masonry residential building. The building has four storeys above ground level and a basement. The bearing walls are arranged in longitudinal direction. The ceiling above the basement is dense-ribbed, while those in the upper levels are Klein type. The dimensions of the building in plan are 18.9 m by 12.6 m. The distance to the metro tunnel wall is 19.5 m.

Currently, both buildings are being operated. Due to the function they perform they are subject to regular reviews. Their technical condition is maintained in proper condition. The sensor installed in the building is also regularly monitored and calibrated. The results of our experimental investigations show that despite many years of influence of dynamic loads originating from metro line, there is no significant degradation of the buildings stiffness and their natural frequencies. Referring to the results of previous experiments [14, 19, 22, 23] the condition of the wheels is responsible for increasing vibrations in the buildings in the neighbourhood of metro line.

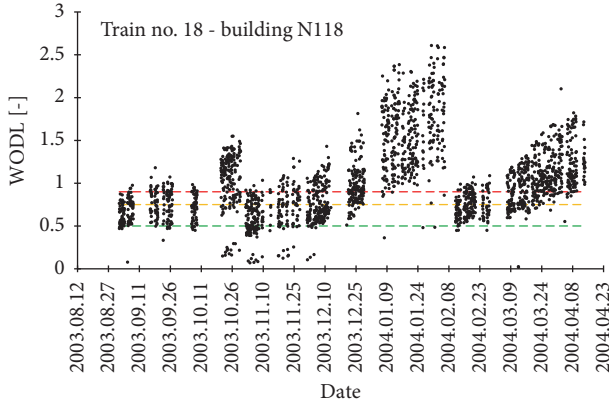


FIGURE 5: Distribution of WODL values for train number 18 in building N118.

We established that technical condition of the building, ground properties, and the metro tunnel itself are unchangeable in contrary to wheels' condition.

WODL indicator shows the real influence of vibrations on people inside buildings without calculating floors parameters; the results come from real measurements. The main idea of this parameter is to measure vibration comfort inside buildings. It is not necessary to calculate floors parameters; it is just diagnostics indicator. When measuring hundreds of floors, it is impossible to calculate all of their constructions, but using WODL indicator we can in a relative short time qualify if the human vibration comfort is exceeded or it is normative according to the standard.

Each of the recorded vertical vibrations of the ceiling is automatically analyzed, according to the Polish code [24], based on the experienced vibration by people. In this section, a more detailed analysis is presented on the daily distribution for the sensor located on the ceiling. Each passing of the train is represented by a single point. Within one day, the same train may pass by a sensor many times. There are also days (or weeks) when a train is not in use; therefore, there is no sensor registration for this train. The individual coloured lines in the graphs indicate the threshold values defined in the system:

- (i) green, 50% limit value of the defined threshold,
- (ii) yellow, 75% limit value of the defined threshold,
- (iii) red, 90% limit value of the defined threshold.

The selected train (number 18) was analyzed from 2003 to 2011. Figures 5 and 6 present exemplary results from the continuous Warsaw Metro vibration monitoring system for the chosen Metropolis trains. The results presented in Figure 5 were recorded for 8 months (from September 2003 to April 2004).

More recent results from 2008 (excluding 2009, no data for continuous monitoring of vibration) until February 2011 are presented in Figure 6. The longer the train is in operation, the greater the difference is in WODL value for each day (see Figure 5). This indicates an increase in radial defects of the wheels. If the train's wheels reprofile, the daily values of the WODL coefficient are more consolidated in the chart.

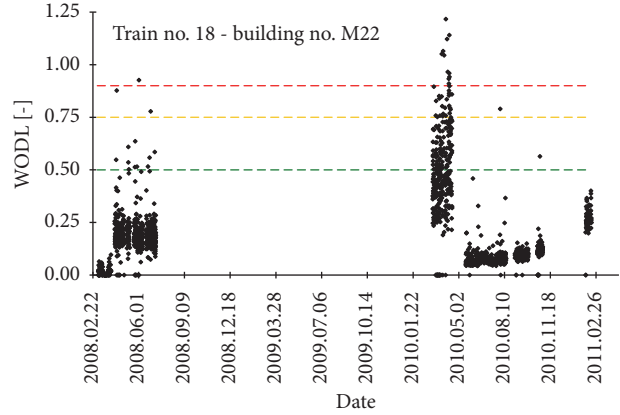


FIGURE 6: Distribution of WODL values for train number 18 in building M22A.

TABLE 1: Equations of trend function for the examined train compositions.

Train number	Trend equation
18	<u><math>y = 0.0074x - 281.09</math></u>
	<u><math>y = 0.0143x - 540.70</math></u>
	<u><math>y = 0.0102x - 387.20</math></u>
	$y = 0.0014x - 55.053$
	$y = 0.0007x - 26.928$

This was observed for all analyzed trains. It can be assumed that when the values of WODL are scattered and high, usually followed by a sudden decrease in value, it indicates a reprofiling of the wheels. Another characteristic of this reprofiling is manifested when the train presents high WODL values, with an increased quantity over a short period. As shown in Figure 5, the WODL value can change by more than one. Figure 6 shows the results for the M22A building for the previously presented subway train number 18, between March 2008 and April 2011. Based on the available data, the trend function values for the periods between wheel reprofiling were calculated. This data is presented in Table 1. In the table, the underlined equations indicate the trends from the 2003 to 2004 service life, while the remaining equations display the trends from 2008 to 2011. This data was analyzed by calculating the mean value, standard deviation of mean value, and maximum and minimum values for the obtained trend equation coefficients (see Table 2). Linear functions were used to describe trends in specific time periods because of good fit, in most cases  $R^2$  values are higher than 0.9, and in other cases they are close to this value. This system is dedicated to use for engineers in their everyday tasks not only for scientific purposes. Linear trend was used in case to maximum simplify diagnostic conclusions and characterised good fit with values of the adjustment coefficients  $R^2$  (in most cases higher than 0.9).

Based on the data collected from 2003 to 2004, the average value of  $A$  was almost three times larger than in the period spanning from 2008 to 2011 (comp. Table 2). This

TABLE 2: Statistical analysis of functions of all trends for particular time periods.

Observation period	2003-2004		2008-2011	
Equation coefficients	A	B	A	B
Average value	0.0088	341.58	0.0031	122.29
Standard deviation	0.0038	155.71	0.0039	155.11
Maximum value	0.0151	664.81	0.0159	626.52
Minimum value	0.0003	10.71	0.0002	9.41

shows that vibrations increased about three times faster in the first period, with a similar standard deviation in both periods and a similar range of values (from 0.0003 to 0.0151 in the first period and from 0.0002 to 0.0159 in the second). The lower value of  $B$ , for the period 2008–2011, reflects the average level of vibration measured on the ceiling, comp. Table 2. The average level of vibration for the analyzed period was lower than in the 2003-2004 period. The continuous monitoring system of the Warsaw metro has been operating since 2003. The data from 2009 illustrates a significant change in the use of monitoring systems. From the information obtained from the operators of the system, it has also changed the procedure of reprofiling the wheels in trains. At present, if the train is retracted for reprofiling, all the wheels are corrected in shape, not only those on the axle where the greatest deviations are found in the radial run measurements (e.g., in the first years of use of monitoring system). Such a procedure has contributed to a significant improvement in the protection against human perceived vibration in buildings. This is presented in the drawings from 2008 to 2011. The data from 2008 shows significant levels of WODL. The nature of the presented data in the following years differs from this trend and has been converted into visuals, for clarity and ease of use. This change was the result of closer monitoring of changes in trends in operating warehouses. This computer visualization was analyzed positively by the operators in the Warsaw Metropolis. Currently, the visual trend analysis is implemented in the latest version of the monitoring system (GUI version) and allows the system operator to create such charts for proper operation. Trend monitoring is very important in terms of operating costs, as it allows the user to schedule the necessary repairs in advance, while saving unnecessary overhaul costs.

In the next part of this chapter, the WODL coefficients were calculated as a function of time over the following eight months (for selected trains). The selection of trains for analysis was dictated by the long-time period between reprofiling. When this period was relatively short, the train was not suitable for long-term analysis (since the trend was difficult to estimate). The Metropolis trains are numbered 17, 18, 19, 20, 24, 25, and 28 for detailed analysis. For each of the trains, the chart presents the analyzed time period, followed by a trend analysis for maximum and average WODL. To get a ratio to the design due to the estimation of dynamic influences, it was necessary to specify the envelope values of the WODL. This is the maximum achievable (experimental, not computationally) value that determines the real dynamic impact limit on the roof of the building to be

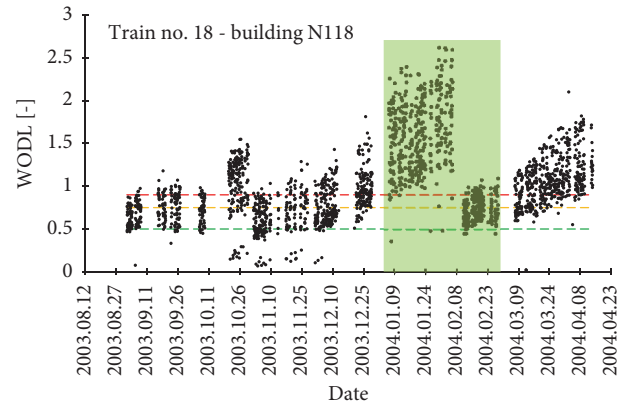


FIGURE 7: Time period for analysis of trends occurring during the crossings of selected subway train compositions.

measured. It can be used in the future as an indicator that has been determined based on measurements and can be used to determine the maximum possible dynamic impacts on building ceilings, which corresponds to human perceptions in buildings. Identifying the indicator is important, as there is a design trend that aims to estimate future adverse dynamic influences from individual sources of vibration, in the case of the design of buildings in the dynamic impact zone. This data is the result of experiential measurements, not from approximate calculations. In Figure 7, there are the time periods for the individual trains, from which data are selected for further analysis. These are the periods between the wheel's reprofiling, when the WODL ratio increases. In the next step, the maximum value of the WODL and the average value are calculated for each day; the single point represents the max WODL for the day or the average WODL for the day. The results for train number 18 are presented in Figure 8, while the aggregate results for selected metro trains and the value of determination factor  $R^2$  are presented in Table 3.

The increase in WODL over the week ranges from about 0.9% to 1.8% and  $R^2$  determines a range between 69.5% and 93.7%. The conclusion is that adjusting the trend lines is not very advantageous especially for trains numbers 18, 25, 17, and 19. To determine diagnostic indicators that could be used in building calculations in neighbourhoods of the metro line, an attempt should be made to narrow the dataset so as not to lose the most relevant value.

Due to the large spread of data and the desire to set a limit value for the most unfavorable, calculating the envelope of the maximum value of WODL seems intentional and

TABLE 3: Aggregate results for envelope max WODL, for selected trains metro and value of determination factor  $R^2$ .

Number	Train number	Trend equation	$R^2$	Increase WODL/week [%]
1	17	$y = 0.0128x$	0.8310	1.3
2	18	$y = 0.0173x$	0.6953	1.7
3	19	$y = 0.012x$	0.8308	1.2
4	20	$y = 0.0154x$	0.8834	1.5
5	24	$y = 0.0154x$	0.9181	1.5
6	25	$y = 0.0095x$	0.7989	0.9
7	28	$y = 0.0177x$	0.9367	1.8

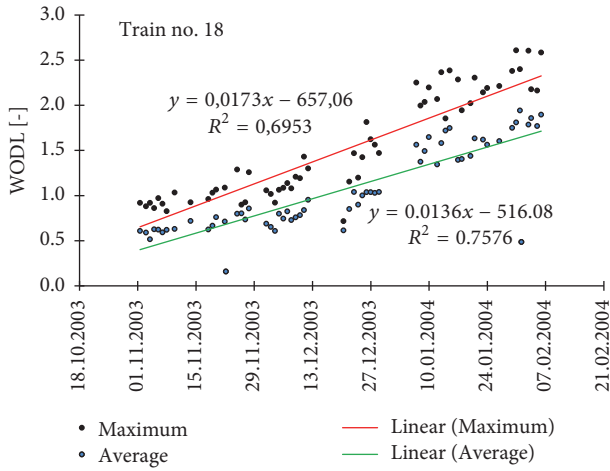


FIGURE 8: Trend line charts for envelope value max WODL together with function value.

appropriate. This analysis may be used in the future to predict the maximum possible dynamic impacts on people living in buildings close to the metro line. Figure 9 presents the WODL ratio envelope but in the uptrend.

Therefore, even in the following days, the WODL values were lower; they were omitted from the trend chart and only the next value if it was higher than the previous one. In conclusion, the WODL ratios do not exceed 3 (maximum for train number 18, ratio 2.6). Figure 10 presents the trend for the envelopes of increasing MAX WODL values from Figure 9.

The coefficient shows how much of the variation of the explanatory variable approximates the modeled phenomenon. It is a measure of the degree to which a model explains the development of an explanatory variable. It can also be said that the deterministic factor describes the part of the explanatory variable that results from its dependence on the explanatory variables included in the model. The coefficient of determination takes values from the range  $[0; 1]$  if the model is free, and the least squares method is used to estimate the parameters. Its values are expressed in percentages. Model matching is the better, and the  $R^2$  value is closer to unity. It is expressed as

$$R^2 = \frac{\sum_{t=1}^n (\hat{y}_t - \bar{y}_t)^2}{\sum_{t=1}^n (y_t - \bar{y}_t)^2}, \quad (3)$$

where  $y_t$  is the actual value of variable  $y$  at time  $t$ ,  $\hat{y}_t$  is theoretical value of the explanatory variable  $y$  (based on the model);  $\bar{y}_t$  is the arithmetic mean of the empirical values of the explanatory variable.

Weekly WODL increments range from 1% to 2% and the  $R^2$  determinate range is from 92.3% to 98.1% (see Table 3). In summary, it is possible to assume for the most unfavorable situation which may occur in the future during the operation of subway trains in Warsaw, the increase of WODL is 2% (see Figure 10, for train number 18, and Table 4) and the WODL value 2.6 (see Figure 9, train number 18). Figure 3 shows the trend line for the WODL max envelope value with the value of the function, as well as the value of the determinant  $R^2$ . Percentages show the WODL of the calculated trend line per week (delta WAT/week). The data presented are summarized in Table 5 for all tested trains with a comparison for the WODL max envelope and WODL max in the table.

As can be seen the values of WODL increments are quite similar, while the value of the determinant ( $R^2$ ) varies considerably (see Table 5). This is caused by a large spread of data. By analyzing the envelope value of the maximum WODL value, it can be concluded that the fit of the model is much closer to value 1.0 (100%).

#### 4. Rush Hours Effect

First step in this kind of analysis was to define time of day in which rush hours in Warsaw Metro occur. Number of tickets that were bought on two metro stations, Raclawicka and Pola Mokotowskie, was used to estimate rush hours for first line of Warsaw metro. Analysis was made during working days and on Saturdays on data covering years 2003 and 2004. Based on these data rush hours on the test measuring profile are as follows:

- (i) from Monday to Friday, morning rush hours from 7.00 till 8.00 a.m. and afternoon rush hours from 2.00 till 6.00 p.m.,
- (ii) on Saturday, morning rush hours from 11.00 a.m. till 3.00 p.m. and afternoon rush hours from 5.00 p.m. till 6.00 p.m.

Because of differences between working days and weekends and because of smaller number of passengers during weekends, working days rush hours were chosen for monitoring as decisive. Exemplary results of daily distribution of

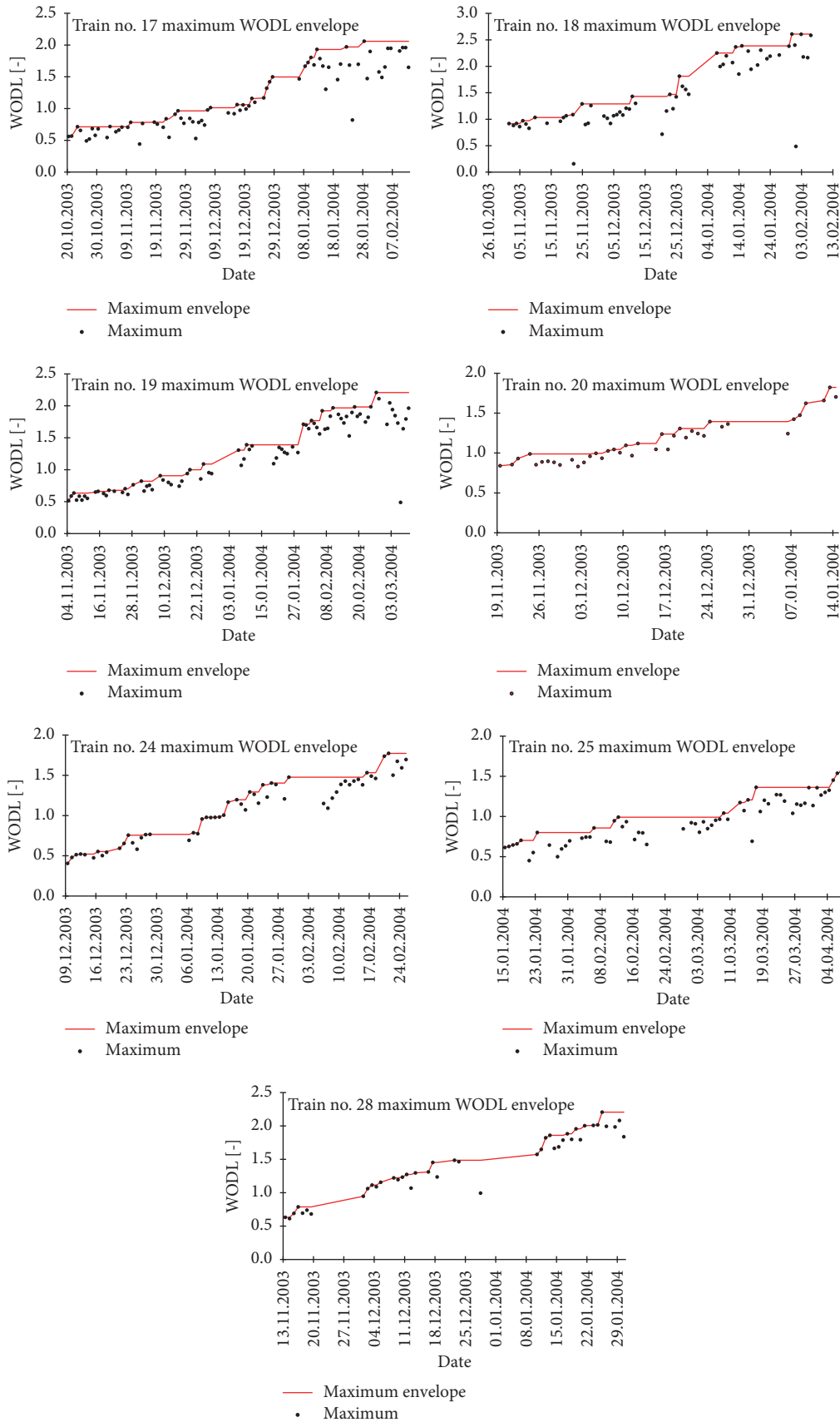


FIGURE 9: Envelope of maximum values of WODL in the upward trend.

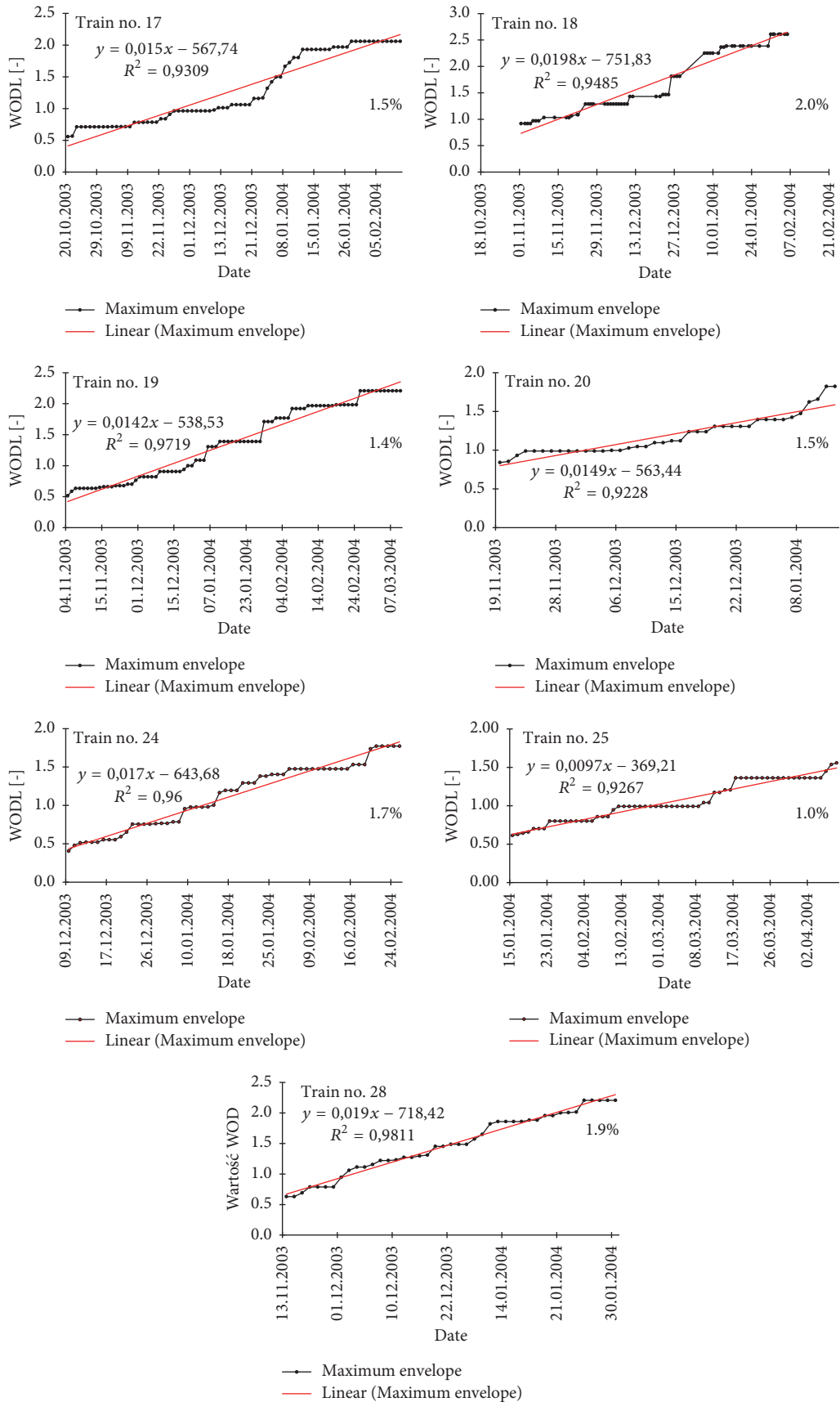


FIGURE 10: Envelope of the maximum values of WODL in the upward trend with the trend line.

TABLE 4: Results for envelope max WODL, for selected trains metro.

Number	Train number	Trend equation	$R^2$	Increase WODL/week [%]
1	17	$y = 0.0150x$	0.9309	1.5
2	18	$y = 0.0198x$	0.9485	2.0
3	19	$y = 0.0142x$	0.9719	1.4
4	20	$y = 0.0149x$	0.9228	1.5
5	24	$y = 0.0170x$	0.9600	1.7
6	25	$y = 0.0097x$	0.9267	1.0
7	28	$y = 0.0190x$	0.9811	1.9

TABLE 5: Results for envelope max WODL, for selected subway train compositions.

Number	Train number	Maximum WODL			Maximum WODL envelope		
		Trend equation	$R^2$	Increase WODL/week [%]	Trend equation	$R^2$	Increase WODL/week [%]
1	17	$y = 0.0128x$	0.8310	1.3	$y = 0.0150x$	0.9309	1.5
2	18	$y = 0.0173x$	0.6953	1.7	$y = 0.0198x$	0.9485	2.0
3	19	$y = 0.012x$	0.8308	1.2	$y = 0.0142x$	0.9719	1.4
4	20	$y = 0.0154x$	0.8834	1.5	$y = 0.0149x$	0.9228	1.5
5	24	$y = 0.0154x$	0.9181	1.5	$y = 0.0170x$	0.9600	1.7
6	25	$y = 0.0095x$	0.7989	0.9	$y = 0.0097x$	0.9267	1.0
7	28	$y = 0.0177x$	0.9367	1.8	$y = 0.0190x$	0.9811	1.9

maximum value of WODL coefficient for train number 18 recorded in January 2004 on building N118 are shown in Figure 11.

Average values of WODL coefficient for train number 18 for different time of day: morning, rush hours and evening are listed in Table 6. In this table date of measurement and number of trains passing during the day is also listed.

In thirteen days from working days during January 2004 average value of WODL is higher during rush hours than in the morning, and in twelve days average WODL values were higher during rush hours than in the evening. The total average value calculated for whole month also shows that WODL coefficient is higher for rush hour than beyond them. What is interesting this difference between average value of WODL is higher comprising rush hours to the evening than to the morning, but the highest value of WODL occurs in the evening not in the rush hours.

Between 6 and 10 of February wheels of train number 18 were rolled which of course effect on WODL results. Daily distribution after this renovation is shown in Figure 12 and average values of WODL are listed in Table 7.

The main observation is that renovation of wheels has much higher influence on WODL values than rush hours effect. Which is proper for diagnosis of wheel train condition, and which was assumption of monitoring system in Warsaw Metro.

Total average value calculated for whole February is higher for rush hours but differences between rush hours and the other time of day are not as significant as it was before wheels were rolled. Comparing days in which during rush hours average value of WODL was higher than in other time of the day it can be seen that

- (i) only during 5 days WODL is higher during rush hours than in the morning, during two days this value is the same, and during 5 days WODL is lower during rush hours than in the morning,
- (ii) during 7 days WODL is higher during rush hours than in the evening and during two days this value is the same,
- (iii) difference between the total average value of WODL during rush hours and in the evening is again higher than difference between rush hours and morning.

Before and after renovation of train wheels average values of WODL are higher (but not very significant) during the rush hours than for other time of day. These differences are in both cases higher when rush hours are compared with the evening. Standard deviation for rush hours is higher than for the other daytime. This all suggest that train filled with passengers can give higher human perception of vibration residing in buildings located close to metro line.

Rush hours in Warsaw Metro are not estimated precisely which could be a reason of relatively small differences

TABLE 6: Average values of WODL for different time of day, train number 18.

Number	Date	Number of drives	Average WODL		
			Morning	Rush hour	Evening
1	2004-01-06	12	1.83	1.65	1.34
2	2004-01-07	19	1.36	1.19	1.52
3	2004-01-08	19	1.48	1.76	1.33
4	2004-01-09	19	1.70	1.76	1.50
5	2004-01-11	18	1.52	1.08	1.20
6	2004-01-12	34	1.70	1.15	1.57
7	2004-01-13	13	1.73	1.68	1.74
8	2004-01-14	18	1.49	1.90	2.08
9	2004-01-16	18	1.26	1.38	1.65
10	2004-01-17	14	1.63	1.23	1.11
11	2004-01-19	19	1.49	1.54	1.29
12	2004-01-20	19	1.60	1.68	1.65
13	2004-01-21	18	1.47	1.73	1.66
14	2004-01-22	18	1.69	1.78	1.42
15	2004-01-23	19	1.56	1.75	1.51
16	2004-01-26	15	1.43	1.68	1.84
17	2004-01-29	19	1.79	1.96	1.55
18	2004-01-30	18	1.72	1.93	1.78
19	2004-01-31	14	1.96	1.97	1.88
Average value			1.60	1.62	1.56
Standard deviation			0.1739	0.2820	0.2463
Maximum value			1.96	1.97	2.08
Minimum value			1.26	1.08	1.11

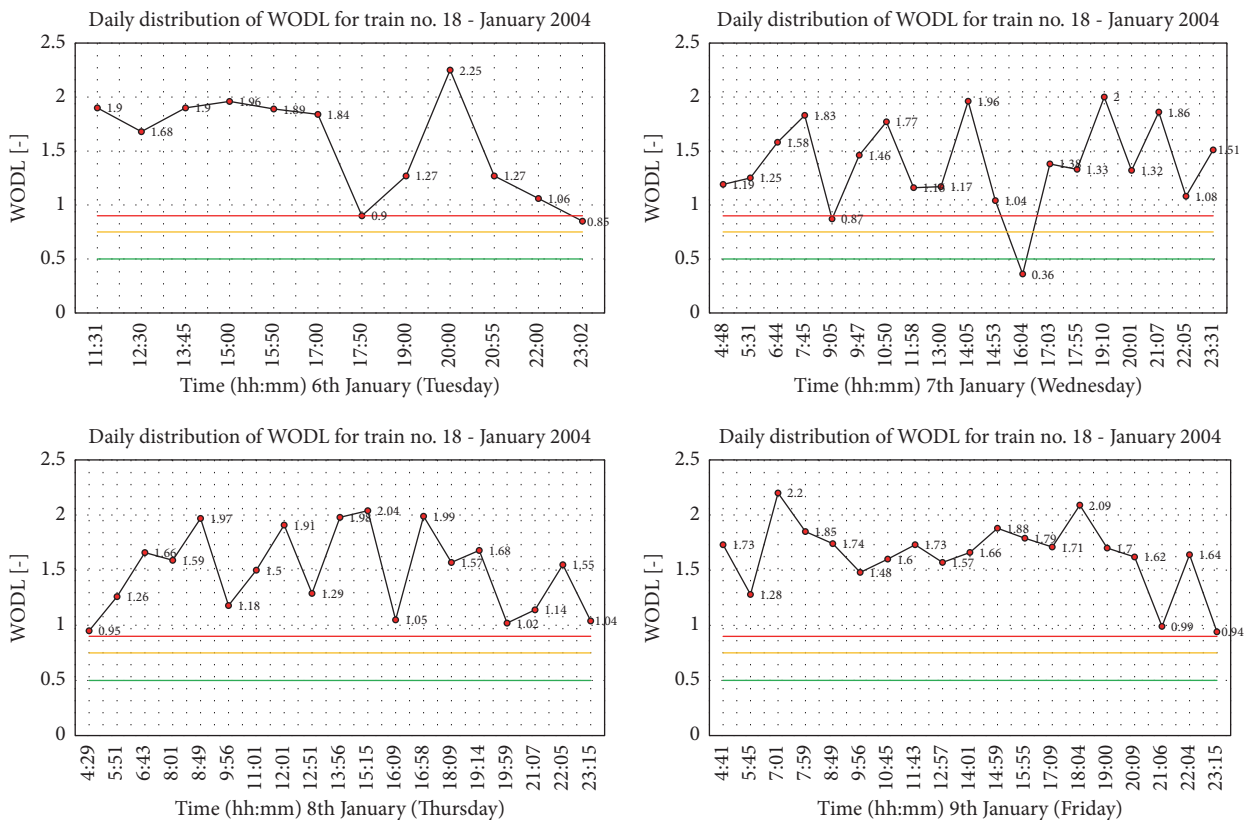


FIGURE 11: Daily distribution of maximum WODL value for train number 18.



FIGURE 12: Continued.

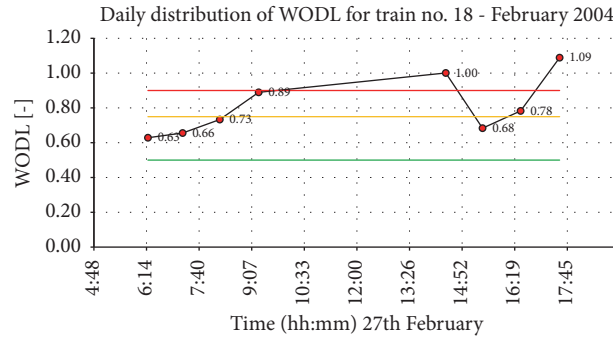


FIGURE 12: Daily distribution of maximum WODL value for train number 18 after wheel renovation.

TABLE 7: Average values of WODL for different time of day after wheels renovation, train number 18.

Number	Date	Number of drives	Average WODL		
			Morning	Rush hour	Evening
5	2004-02-11	19	0.65	0.57	0.68
6	2004-02-12	18	0.70	0.64	0.64
7	2004-02-13	11	0.71	0.71	0.64
8	2004-02-15	18	0.73	0.68	0.74
9	2004-02-16	18	0.81	0.65	0.77
10	2004-02-17	18	0.75	0.73	0.73
11	2004-02-18	18	0.77	0.85	0.76
12	2004-02-19	18	0.81	0.89	0.81
13	2004-02-20	13	0.78	0.81	0.79
14	2004-02-24	15	0.78	0.78	0.58
15	2004-02-26	18	0.78	0.86	0.78
16	2004-01-27	8	0.73	0.89	0.78
Average value			0.75	0.76	0.73
Standard deviation			0.0479	0.1074	0.0729
Maximum value			0.81	0.89	0.81
Minimum value			0.65	0.67	0.58

between morning and rush hours. This indicates that morning rush hours should be specified during more precise measurements.

## 5. Conclusions

In the paper the monitoring system in Warsaw metro was presented. Since 2003, when the system was installed, many changes have been made in the operation and management of the metro.

Many advantages can be distinguished after the system was introduced. First of all, the number of complaints related to the negative impact of vibrations on people in nearby buildings has decreased. The main reason for these complaints was problems with wheel profiling. The level of these impacts and the rate of change were observed only after the system was installed. This significantly contributed

to improving the comfort of use of buildings near the metro line.

The method of repairing wheels on trains has also been fundamentally changed. During the first period of system operation, only the wheels with the largest damage were repaired, which did not give good results. The system introduced the principle of repairing all wheels on the train, which improved comfort and contributed to the extension of the period between subsequent repairs.

The system also allowed better planning of repairs. Thanks to the introduced alarm levels in the system, it is possible to plan repairs for individual trains. It also allows for better planning of costs and organization of costs. The measurement system together with the software allows you to make decisions that affect the image of the metro manager in an easy and quick way and enables the rationalization of costs.

The vibration monitoring system introduced on the first metro line in Warsaw has fulfilled its role so well that it is currently being expanded on subsequent sections of the second metro line in Warsaw.

## Conflicts of Interest

The authors declare that there are no conflicts of interest regarding the publication of the paper.

## References

- [1] B. Chen, Y. L. Xu, and X. Zhao, "Integrated vibration control and health monitoring of building structures: a time-domain approach," *Smart Structures and Systems*, vol. 6, no. 7, pp. 811–833, 2010.
- [2] A. Deraemaeker, E. Reynders, G. De Roeck, and J. Kullaa, "Vibration-based structural health monitoring using output-only measurements under changing environment," *Mechanical Systems and Signal Processing*, vol. 22, no. 1, pp. 34–56, 2008.
- [3] J. M. W. Brownjohn, A. de Stefano, Y.-L. Xu, H. Wenzel, and A. E. Aktan, "Vibration-based monitoring of civil infrastructure: Challenges and successes," *Journal of Civil Structural Health Monitoring*, vol. 1, no. 3-4, pp. 79–95, 2011.
- [4] A. Mita and S. Takhira, "A smart sensor using a mechanical memory for structural health monitoring of a damage-controlled building," *Smart Materials and Structures*, vol. 12, no. 2, pp. 204–209, 2003.
- [5] M. D. Kohler, P. M. Davis, and E. Safak, "Earthquake and ambient vibration monitoring of the steel-frame UCLA factor building," *Earthquake Spectra*, vol. 21, no. 3, pp. 715–736, 2005.
- [6] R. D. Nayeri, S. F. Masri, R. G. Ghanem, and R. L. Nigbor, "A novel approach for the structural identification and monitoring of a full-scale 17-story building based on ambient vibration measurements," *Smart Materials and Structures*, vol. 17, no. 2, Article ID 025006, 2008.
- [7] M. R. Kaloop, J. W. Hu, M. A. Sayed, and J. Seong, "Structural performance assessment based on statistical and wavelet analysis of acceleration measurements of a building during an earthquake," *Shock and Vibration*, vol. 2016, Article ID 8902727, 13 pages, 2016.
- [8] H. Xia, J. Chen, P. Wei, C. Xia, G. De Roeck, and G. Degrande, "Experimental investigation of railway train-induced vibrations of surrounding ground and a nearby multi-story building," *Earthquake Engineering and Engineering Vibration*, vol. 8, no. 1, pp. 137–148, 2009.
- [9] D. P. Connolly, G. Kouroussis, P. K. Woodward, P. A. Costa, O. Verlinden, and M. C. Forde, "Field testing and analysis of high speed rail vibrations," *Soil Dynamics and Earthquake Engineering*, vol. 67, pp. 102–118, 2014.
- [10] H.-c. Guo, "Blasting Vibration Monitoring and Control Technology Applied in Construction of Huaishuping Tunnel," *Tunnel Construction*, 2006.
- [11] M. Nefovska-Danilovic, M. Petronijevic, and B. Savija, "Traffic-induced vibrations of frame structures," *Canadian Journal of Civil Engineering*, vol. 40, no. 2, pp. 158–171, 2013.
- [12] M. F. M. Hussein, *Vibration from underground railways [Ph.D. Thesis]*, University of Cambridge, 2004.
- [13] F. Pachla, B. R. Pawlik, K. Stypula, and T. Tatara, "Vibration induced by railway traffic-zones of influence on buildings and humans," in *Proceedings of the 27th International Conference on Vibroengineering*, vol. 13, pp. 188–192, September 2017.
- [14] J. Kawecki, K. Koziol, and K. Stypula, "The Design of Rail Tracks including the Influence of Vibration on People in Buildings," in *Proceedings of the Eleventh International Conference on Computational Structures Technology*, B. H. V. Topping, Ed., vol. 176, pp. 1–9, Dubrovnik, Croatia, September 2012.
- [15] D. Makovicka, D. Makovicka Jr, and D. Makovička, "Analysis of Vibro-Isolated Building Excited by the Technical Seismicity of Traffic Effects," in *Proceedings of the D. MakovičkaJr*, vol. 2, pp. 64–69, 2016.
- [16] A. Chudzikiewicz and J. Korzeb, "Simulation study of wheels wear in low-floor tram with independently rotating wheels," *Archive of Applied Mechanics*, vol. 88, no. 1-2, pp. 175–192, 2018.
- [17] F. P. Bowden and D. Tabor, "The Area of Contact between Stationary and between Moving Surfaces," *Proceedings of the Royal Society A Mathematical, Physical and Engineering Sciences*, vol. 169, no. 938, pp. 391–413, 1939.
- [18] R. Enblom and M. Berg, "Simulation of railway wheel profile development due to wear influence of disc braking and contact environment," *Wear*, vol. 258, no. 7-8, pp. 1055–1063, 2005.
- [19] R. Ciesielski and K. Stypula, "Influence of shape change of carriage wheels in consequence of exploitation wear on the level of building vibration caused by shallow underground train passages – case history," in *Proceedings of Conference Structural Dynamics EURO-DYN 2002*, Grundmann and Schuëller, Eds., pp. 313–316, Swets & Zeitlinger, 2002.
- [20] M. Nader and J. Korzeb, "Concept of a monitoring system for evaluation vibration, sound and another physical factors on construction and operation stages of metro line," in *Proceedings of 4th International Conference on Experiments/Process/System/Modelling/Simulation/Optimization*, vol. 1, pp. 158–164, 2011.
- [21] J. Korzeb and A. Chudzikiewicz, "Evaluation of the vibration impacts in the transport infrastructure environment," *Archive of Applied Mechanics*, vol. 85, no. 9-10, pp. 1331–1342, 2015.
- [22] P. Stecz, *Effect of long-term dynamic loads generated by subway trains passes by [Ph.D. thesis]*, Cracow University of Technology, 2014.
- [23] J. Kawecki and J. K. Stypula, "Providing vibration comfort for people in buildings exposed to impact of communication influences, Wydawnictwo PK," *Wydawnictwo PK, Kraków*, 2013.
- [24] Standard PN-B-02171:2017-06, Evaluation of the impact of vibrations on people in buildings, (in Polish).
- [25] ISO 2631-1, Mechanical vibration and shock – Evaluation of human exposure to whole-body vibration – Part 1: General requirements, 1997.
- [26] Standard PN-B-02171:1988, Evaluation of the impact of vibrations on people in buildings, (in Polish).
- [27] Standard ISO 2631-2, Guide to the evaluation of human exposure to whole body vibration. Part 2- Vibration in buildings, 2003.

## Research Article

# A Study on Coupling Faults' Characteristics of Fixed-Axis Gear Crack and Planetary Gear Wear

Xin Wang 

*School of Mechanical Engineering, Baoji University of Arts and Sciences, Baoji 721016, China*

Correspondence should be addressed to Xin Wang; 46607190@qq.com

Received 15 October 2017; Accepted 1 April 2018; Published 8 May 2018

Academic Editor: Rafał Burdzik

Copyright © 2018 Xin Wang. This is an open access article distributed under the Creative Commons Attribution License, which permits unrestricted use, distribution, and reproduction in any medium, provided the original work is properly cited.

To identify the fault frequency characteristics of the gear transmission system under coupling fault of fixed-axis gear crack and planetary gear wear, dimensionless dynamical equations of gear transmission system were established. Bifurcations in normal condition and coupling fault condition were contrasted. The affected excitation frequency range was found. Fault frequency characteristics in sensitive interval caused by the coupling fault of fixed-axis gear crack and planetary gear wear were analyzed. Simulation analysis shows that the crack fault in fixed-axis gear brings up peaks in doubling of 1~10 for fault frequency, the wear fault in planetary gear increases the amplitude of meshing frequency and its double and triple, and the coupling of both shows two kinds of fault features around the planetary gear meshing frequency.

## 1. Introduction

The wind turbine gearbox is the core component of the wind turbine; its transmission system is a multistage gear transmission system with a two-stage fixed-axis gear and a one-stage planetary gear. The wind turbine gearbox has a high failure rate by the disorder, variable load, and strong impact wind load. The vibration mechanism and fault mechanism of multistage gear transmission system are not clear, so the online monitoring and fault diagnosis of the wind turbine gearbox are not perfect. A lot of fault were not discovered early, resulting in a chain reaction. It makes the whole transmission system downtime, resulting in huge economic loss and bad social impact. Only by studying the vibration mechanism and fault mechanism of the multistage gear transmission system and finding out the complex signal correlation characteristics caused by the fault, can the early fault of the gear be identified by the signal processing method.

There is a large difference between the local fault vibration signal of the planetary gearbox and the fixed-axis gearbox. The dynamic model of the single pair cannot describe the modulation effect of the dynamic signal in the coupling state, and the fault side band of the coupling state cannot be properly extracted. Therefore, it is necessary to delve into the

spectral characteristics of the vibration signal of the planetary gearbox (especially in the case of coupling faults), so as to achieve the purpose of fault diagnosis of the planetary gearbox through the fault feature frequency component.

For the study of coupling faults, Li et al. [1, 2] used the combined intelligent signal analysis method based on wavelet packet, empirical mode decomposition, Wigner distribution, and AR model to identify five single faults and three coupling faults. Then he proposed a new method [3], using the independent component analysis (ICA - R) as the fault frequency tracking tool to simplify the coupling fault to a single fault. Luo et al. [4] proposed a sparse representation method based on wavelet based compound fault feature extraction, which can separate and extract different transient characteristics of bearings and gears. Xiao-yu et al. [5] differentiated single fault and coupling faults through the correlation dimension and the largest Lyapunov exponent. The research on coupling failure is based on the experimental signal analysis, and its accuracy depends on the large data accuracy. Data of different test rig may contain its unique characteristic and do not have generality for fault diagnosis of other devices. Experimental method cannot distinguish which feature is common feature which is a unique feature and the mechanism of various features. So with research on the nonlinear characteristics

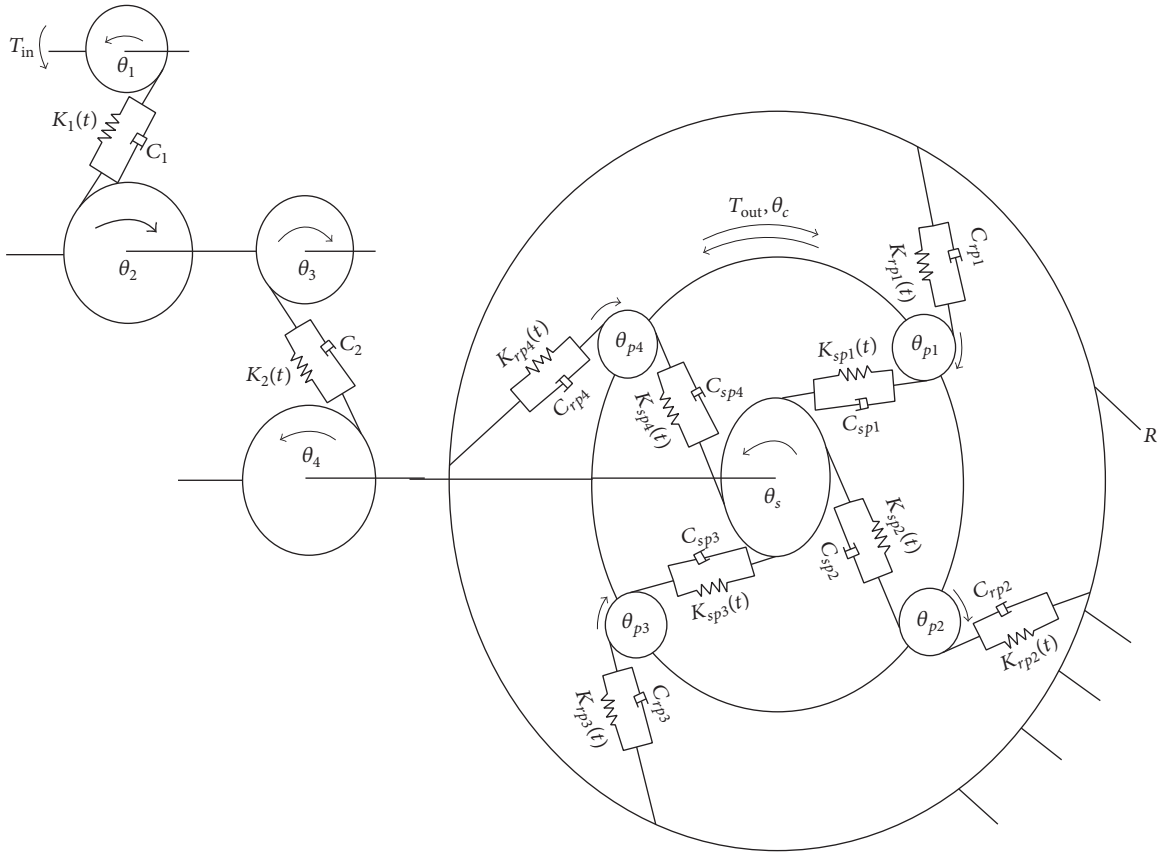


FIGURE 1: Torsional dynamic model of gear transmission system.

and fault mechanism of coupling faults from the angle of bifurcation and chaos characteristics, we can distinguish the changes caused by the coupling effect and find the general characteristics of coupling.

In the article [6], the coupling fault of fixed-axis crack and planetary gear chipping was studied from the nonlinear angle, and the fault frequency characteristics of the coupling fault were analyzed. However, wear fault occurs more frequently and is more difficult to identify than chipping fault. When the system has wear fault, it will affect the clearance between the gears. The clearance is the main cause of the collision movement within the system, which will change the motion state of the system. Therefore, it is of great significance to study the influence of wear fault on the bifurcation characteristics of the system compared with chipping fault. On the basis of article [6], this paper studies the coupling fault of fixed-axis crack and planetary gear wear. The nonlinear dynamic model with the coupling fault of the fixed-axis crack fault and the planetary wear fault is established, and the bifurcation characteristics and coupling fault characteristics of the fixed-axis gear in the system are analyzed by the simulation method in normal state, fixed-axis crack fault state, planetary wear fault state, and coupling fault state. Characteristics and frequency bands of the fault frequency are discussed for different excitation frequencies. According to the numerical simulation results, the fault frequency of the measured signal is identified.

## 2. Torsional Dynamic Model of Gear Transmission System

The system studied in this paper is a test rig of gear transmission system which contains a two-stage fixed-axis gear and a one-stage planetary gear, where spur gears 1 and 2 compose the 1st-stage fixed-axis gear for the input, spur gears 3 and 4 compose the 2nd-stage fixed-axis gear, and the planet carrier is for the output. The torsional dynamic model is established by using the lumped mass method (Figure 1).

When gear system, the drive shaft, bearing, and box bearing stiffness are relatively large, then regardless of their flexibility the gear system turns into pure torsional vibration model. If the gear system input and output shaft stiffness is relatively small, the gear system can be isolated from the prime mover and the load, and a separate vibration model of the gear system can be established. Due to the nonconsideration of the specific vibration form of the transmission shaft, the support stiffness and damping of the transmission shaft, bearing, and box can be expressed as the combined equivalent values. The model does not consider the transverse vibration displacement of gears. Gear parameters are simulated with a spring and a damper.

See Figure 1, where,  $\theta_s, \theta_c, \theta_{pn}, \theta_1, \theta_2, \theta_3,$  and  $\theta_4$  represent the angular displacement of sun gear, planet carrier, planetary gear  $n$  ( $n = 1, 2, 3, 4$ ), and spur gears 1, 2, 3, and 4, respectively. Throughout this paper, the subscripts  $s, c, pn, r, 1, 2, 3,$  and  $4$

denote sun gear, planet carrier, planetary, ring gear, and spur gears 1, 2, 3, and 4. Quantities  $r_s$ ,  $r_c$ ,  $r_{pn}$ ,  $r_1$ ,  $r_2$ ,  $r_3$ , and  $r_4$  are the base circle radius of gears. Quantities  $K_{spn}(t)$ ,  $K_{rpn}(t)$ ,  $K_1(t)$ , and  $K_2(t)$  denote the meshing stiffness of sun gear with planetary gear  $n$ , ring gear with planetary gear  $n$ , 1st-stage fixed gear, and 2nd-stage fixed gear. Quantities  $C_{spn}$ ,  $C_{rpn}$ ,  $C_1$ , and  $C_2$  denote the damping of sun gear with planetary gear  $n$ , ring gear with planetary gear  $n$ , 1st-stage fixed gear, and 2nd-stage fixed gear.  $T_{in}$  is the input and  $T_{out}$  is the output.

**2.1. Motion Differential Equations of the System.** Based on the Lagrangian equation, the motion differential equations of the system are established on the basis of the clearance, the time-varying meshing stiffness, and the comprehensive meshing error [7, 8]:

$$\begin{aligned} J_1 \ddot{\theta}_1 + r_1 F_1 &= T_{in} \\ J_{23} \ddot{\theta}_2 - r_2 F_1 + r_3 F_2 &= 0 \\ J_{4s} \ddot{\theta}_{4s} + \sum_{n=1}^4 r_s F_{spn} - r_4 F_2 &= 0 \\ J_{pn} \ddot{\theta}_{pn} - r_{pn} F_{spn} + r_{pn} F_{rpn} &= 0 \\ J_c \ddot{\theta}_c - \sum_{n=1}^4 r_c F_{spn} - \sum_{n=1}^4 r_c F_{rpn} &= -T_{out}, \end{aligned} \quad (1)$$

where  $J_{23} = J_2 + J_3$ ,  $J_{4s} = J_4 + J_s$ ;  $J_1, J_2, J_3, J_4, J_s, J_{pn}$ , and  $J_c$  are the moment of inertia of each gear on the shaft;  $F_1, F_2, F_{spn}$ , and  $F_{rpn}$  are the meshing force of each stage on the meshing line,  $F_i = C_i \dot{x}_i + K_i(t) f(x_i)$  ( $i = 1, 2, spn, rpn$ );  $x_i$  is the relative displacement of each stage meshing line ( $i = 1, 2, spn, rpn$ ):

$$\begin{aligned} x_1 &= r_1 \theta_1 - r_2 \theta_2 - e_1(t), \\ x_2 &= r_3 \theta_3 - r_4 \theta_4 - e_2(t), \\ x_{spn} &= r_s \theta_s - r_{pn} \theta_{pn} - r_c \theta_c - e_{spn}(t), \\ x_{rpn} &= r_{pn} \theta_{pn} - r_c \theta_c - e_{rpn}(t); \end{aligned} \quad (2)$$

$f(x_i)$  is the clearance nonlinear function ( $i = 1, 2, spn, rpn$ ), written as

$$f(\bar{x}_i) = \begin{cases} \bar{x}_i - b_i, & \bar{x}_i > b_i \\ 0, & |\bar{x}_i| \leq b_i \\ \bar{x}_{rpi} + b_i, & \bar{x}_i < -b_i, \end{cases} \quad (3)$$

where  $b_i$  is half of the clearance ( $i = 1, 2, spn, rpn$ ).

The time-varying meshing stiffness of the gear pair  $K_i(t)$  will be specified in Section 2.2.

The damping coefficient forms

$$\begin{aligned} C_1 &= 2\xi_1 \sqrt{\frac{K_{m1}}{(1/m_1 + 1/m_2)}} \\ C_2 &= 2\xi_2 \sqrt{\frac{K_{m2}}{(1/m_3 + 1/m_4)}} \end{aligned}$$

$$\begin{aligned} C_{spn} &= 2\xi_{spn} \sqrt{\frac{K_{mspn}}{(1/m_s + 1/m_{pn})}} \\ C_{rpn} &= 2\xi_{rpn} \sqrt{\frac{K_{mrpn}}{(1/m_r + 1/m_{pn})}}, \end{aligned} \quad (4)$$

where  $\xi_1, \xi_2, \xi_{spn}$ , and  $\xi_{rpn}$  are damping ratios and  $m_1, m_2, m_3, m_4, m_s, m_{pn}$ , and  $m_r$  are the mass of each gear.

The comprehensive meshing error of gear pair using the 1st harmonic form of meshing function is

$$e_i(t) = e_{ai} \sin(w_{mi}t + \varphi_i), \quad (5)$$

where  $e_{ai}$  is the comprehensive meshing error amplitude of each gear ( $i = 1, 2, spn, rpn$ ).  $\varphi_i$  is the comprehensive meshing error initial phase of each gear ( $i = 1, 2, spn, rpn$ );  $w_{mi}$  is the meshing frequency of each gear ( $i = 1, 2, spn, rpn$ ).

Define time nominal scale  $w_h$ , order  $\tau = w_h t$ , where  $w_h = \sqrt{K_{m1} \times m_{e1}}$ ;  $\bar{x}_i$  is dimensionless displacement,  $\bar{x}_i = x_i/b_1$ ,  $i = 1, 2, spn, rpn$ ;  $\Omega_i$  is dimensionless excitation frequency,  $\Omega_i = w_{mi}/w_h$ ,  $i = 1, 2, spn, rpn$ ;  $\bar{e}_{ai}$  is dimensionless comprehensive meshing error amplitude,  $\bar{e}_{ai} = e_{ai}/b_1$ ,  $i = 1, 2, spn, rpn$ . Dimensionless nonlinear function is

$$f(\bar{x}_i) = \begin{cases} \bar{x}_i - \frac{b_i}{b_1}, & \bar{x}_i > \frac{b_i}{b_1} \\ 0, & |\bar{x}_i| \leq \frac{b_i}{b_1} \\ \bar{x}_{rpi} + \frac{b_i}{b_1}, & \bar{x}_i < -\frac{b_i}{b_1}. \end{cases} \quad (6)$$

The equations are normalized, and the system dimensionless motion differential equations can be got:

$$\begin{aligned} \ddot{\bar{x}}_1 + \frac{C_1}{m_{e1} w_h} \dot{\bar{x}}_1 + \frac{K_1(\tau)}{m_{e1} w_h^2} f(\bar{x}_1) - \frac{C_2}{m_{e2} w_h} \dot{\bar{x}}_2 \\ - \frac{K_2(\tau)}{m_{e2} w_h^2} f(\bar{x}_2) &= \frac{T_{in} r_1}{J_1 w_h^2 b_1} + \frac{e_{a1}}{b_1} \Omega_1^2 \sin(\Omega_1 \tau + \varphi_1) \\ \ddot{\bar{x}}_2 - \frac{C_1}{m_{e1} w_h} \dot{\bar{x}}_1 - \frac{K_1(\tau)}{m_{e2} w_h^2} f(\bar{x}_1) + \frac{C_2}{m_{e3} w_h} \dot{\bar{x}}_2 \\ + \frac{K_2(\tau)}{m_{e3} w_h^2} f(\bar{x}_2) - \sum_{n=1}^4 \frac{C_{spn}}{m_{4s} w_h} \dot{\bar{x}}_{spn} \\ - \sum_{n=1}^4 \frac{K_{spn}(\tau)}{m_{4s} w_h^2} f(\bar{x}_{spn}) &= \frac{e_{a2}}{b_1} \Omega_2^2 \sin(\Omega_2 \tau + \varphi_2) \\ \ddot{\bar{x}}_{spn} + \frac{1}{m_{4s} w_h} \sum_{n=1}^4 C_{spn} \dot{\bar{x}}_{spn} + \frac{1}{m_c w_h} \sum_{n=1}^4 C_{spn} \dot{\bar{x}}_{spn} \\ + \frac{1}{m_{pn} w_h} C_{spn} \dot{\bar{x}}_{spn} + \frac{1}{m_{4s} w_h^2} \sum_{n=1}^4 K_{spn}(\tau) f(\bar{x}_{spn}) \\ + \frac{1}{m_c w_h^2} \sum_{n=1}^4 K_{spn}(\tau) f(\bar{x}_{spn}) \end{aligned}$$

$$\begin{aligned}
& + \frac{1}{m_{pn}w_h^2} K_{spn}(\tau) f(\bar{x}_{spn}) - \frac{1}{m_{pn}w_h} C_{rpn} \dot{\bar{x}}_{rpn} \\
& + \frac{1}{m_c w_h} \sum_{n=1}^4 C_{rpn} \dot{\bar{x}}_{rpn} - \frac{1}{m_{pn}w_h^2} K_{rpn}(\tau) f(\bar{x}_{rpn}) \\
& + \frac{1}{m_c w_h^2} \sum_{n=1}^4 K_{rpn}(\tau) f(\bar{x}_{rpn}) - \frac{r_4 C_2}{m_{4s} r_s w_h} \dot{\bar{x}}_2 \\
& - \frac{r_4 K_2(\tau)}{m_{4s} r_s w_h^2} f(\bar{x}_2) = \frac{r_c T_{out}}{J_{ce} w_h^2 b_1} \\
& + \frac{e_{aspn}}{b_1} \Omega_{spn}^2 \sin(\Omega_{spn} \tau + \varphi_{spn}) \\
\ddot{\bar{x}}_{rpn} & - \frac{1}{m_{pn}w_h} C_{spn} \dot{\bar{x}}_{spn} + \frac{1}{m_c w_h} \sum_{n=1}^4 C_{spn} \dot{\bar{x}}_{spn} \\
& - \frac{1}{m_{pn}w_h^2} K_{spn}(\tau) (\bar{x}_{spn}) \\
& + \frac{1}{m_c w_h^2} \sum_{n=1}^4 K_{spn}(\tau) f(\bar{x}_{spn}) + \frac{1}{m_{pn}w_h} C_{rpn} \dot{\bar{x}}_{rpn} \\
& - \frac{1}{m_c w_h} \sum_{n=1}^4 C_{rpn} \dot{\bar{x}}_{rpn} + \frac{1}{m_{pn}w_h^2} K_{rpn}(\tau) f(\bar{x}_{rpn}) \\
& - \frac{1}{m_c w_h^2} \sum_{n=1}^4 K_{rpn}(\tau) f(\bar{x}_{rpn}) = \frac{r_c T_{out}}{J_{ce} w_h^2 b_1} \\
& + \frac{e_{arpn}}{b_1} \Omega_{rpn}^2 \sin(\Omega_{rpn} \tau + \varphi_{rpn}),
\end{aligned} \tag{7}$$

where  $m_{e1}, m_{e2}, m_{e3}, m_{4s}$  are the equivalent masses of gear;  $J_{ce}$  is the equivalent moment of inertia of gear:

$$\begin{aligned}
m_{e1} &= \frac{J_1 J_{23}}{J_{23} r_1^2 + J_1 r_2^2}, \\
m_{e2} &= \frac{J_{23}}{r_2 r_3}, \\
m_{e3} &= \frac{J_4 J_{23}}{J_{23} r_4^2 + J_4 r_3^2}, \\
m_{4s} &= \frac{J_{4s}}{r_s^2}, \\
J_{ce} &= J_c + N m_{pn} r_c^2.
\end{aligned} \tag{8}$$

**2.2. Mesh Stiffness.** The potential energy method [9] is used to evaluate the mesh stiffness with the consideration of Hertzian energy  $k_h$ , bending energy  $k_b$ , shear energy  $k_s$ , and axial compressive energy  $k_a$ . The beam model of a gear tooth is shown in Figure 2(a). The stiffness expressions are

$$\begin{aligned}
\frac{1}{k_b} &= \frac{[1 - (N - 2.5) \cos \alpha_1 \cos \alpha_3 / N \cos \alpha_0]^3 - (1 - \cos \alpha_1 \cos \alpha_2)^3}{2EL \cos \alpha_1 \sin^3 \alpha_2} \\
&+ \int_{-\alpha_1}^{\alpha_2} \frac{3 \{1 + \cos \alpha_1 [(\alpha_2 - \alpha) \sin \alpha - \cos \alpha]\}^2 (\alpha_2 - \alpha) \cos \alpha}{2EL [\sin \alpha + (\alpha_2 - \alpha) \cos \alpha]^3} d\alpha \\
\frac{1}{k_s} &= \frac{1.2(1 + \nu) \cos^2 \alpha_1 (\cos \alpha_2 - ((N - 2.5) / N \cos \alpha_0) \cos \alpha_3)}{EL \sin \alpha_2} \\
&+ \int_{-\alpha_1}^{\alpha_2} \frac{1.2(1 + \nu) (\alpha_2 - \alpha) \cos \alpha \cos^2 \alpha_1}{EL [\sin \alpha + (\alpha_2 - \alpha) \cos \alpha]} d\alpha \\
\frac{1}{k_a} &= \frac{\sin^2 \alpha_1 (\cos \alpha_2 - ((N - 2.5) / N \cos \alpha_0) \cos \alpha_3)}{2EL \sin \alpha_2} \\
&+ \int_{-\alpha_1}^{\alpha_2} \frac{(\alpha_2 - \alpha) \cos \alpha \sin^2 \alpha_1}{2EL [\sin \alpha + (\alpha_2 - \alpha) \cos \alpha]} d\alpha \\
k_h &= \frac{\pi EL}{4(1 - \nu^2)},
\end{aligned} \tag{9}$$

where  $E$  represents the elastic modulus;  $L$  is tooth width;  $N$  is tooth number;  $\alpha_0$  is the pressure angle;  $\nu$  is Poisson's ratio.

**2.2.1. Overall Mesh Stiffness.** Gear tooth profile follows an involute curve up to the base circle as shown in Figure 2(a). The tooth profile between the base circle and the root circle is not an involute curve and hard to describe analytically [10]. Therefore, straight lines  $NN'$  and  $DD'$  are used to simplify the curve. For the single-tooth-pair meshing duration, the total effective mesh stiffness can be calculated as [11]

$$\begin{aligned}
K_t &= \frac{1}{1/k_h + 1/k_{b1} + 1/k_{s1} + 1/k_{a1} + 1/k_{b2} + 1/k_{s2} + 1/k_{a2}},
\end{aligned} \tag{10}$$

where subscripts 1 and 2 represent the driving gear and the driven gear, respectively.

For the double-tooth-pair meshing duration, there are two pairs of gears meshing at the same time. Total effective mesh stiffness can be obtained as [11]

$$K_t = K_{t1} + K_{t2} = \sum_{j=1}^2 \frac{1}{1/k_{h,j} + 1/k_{b1,j} + 1/k_{s1,j} + 1/k_{a1,j} + 1/k_{b2,j} + 1/k_{s2,j} + 1/k_{a2,j}}, \tag{11}$$

where  $j = 1$  for the 1st pair and  $j = 2$  for the 2nd pair of meshing teeth.

**2.2.2. Crack Modeling.** The crack is modeled as a straight line from the gear tooth danger area (Figure 2(b)). The crack

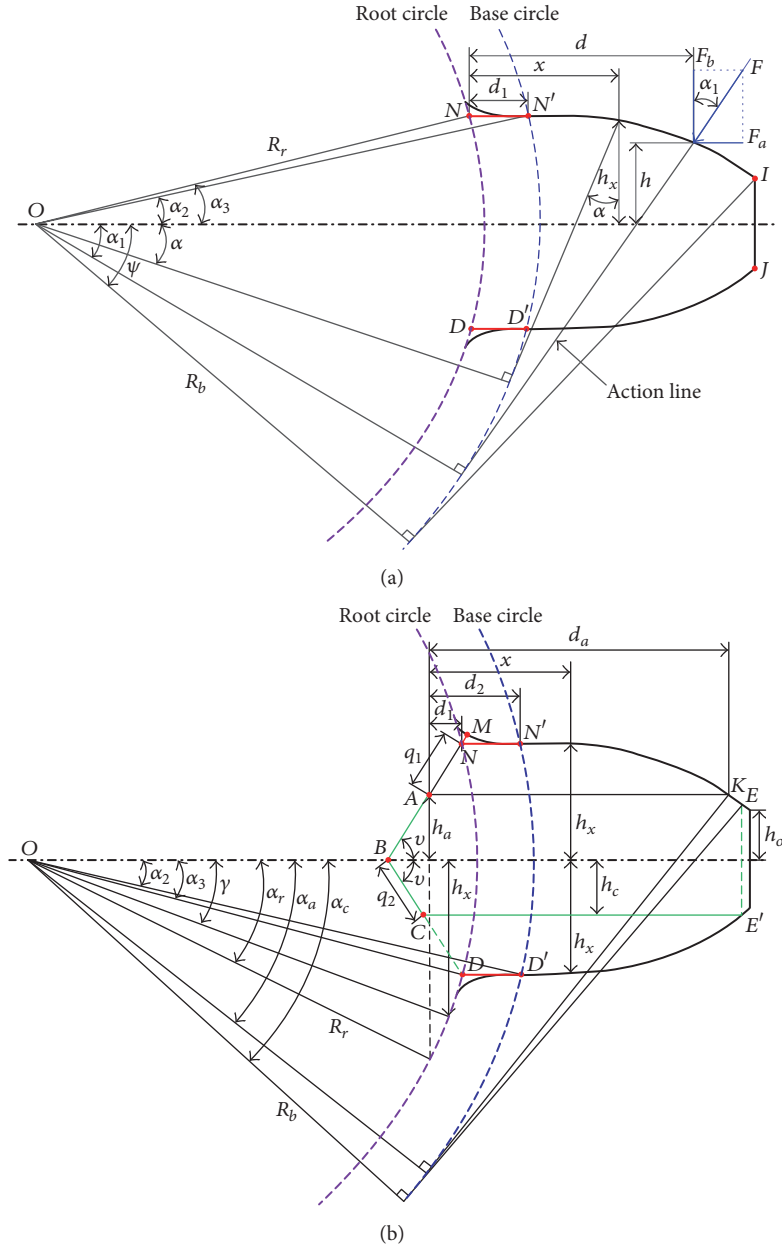


FIGURE 2: Beam model of an external gear tooth: (a) beam model and (b) cracked tooth model [9].

propagates along the straight line until reaching the tooth central line at point *B*. Then, it changes the propagation direction towards point *D* where the tooth breaks. According to the state of the crack in the test rig, only the state when the crack does not reach the centerline is studied, where  $q_1$  is the crack length and the angle between the crack line and the tooth center line is defined as  $v$ .

The Hertzian stiffness and axial compressive stiffness will not be affected by the crack propagation [10]. Only the bending stiffness and the shear stiffness will be affected due to the change in the tooth length and the tooth height caused by the crack. The bending stiffness and the shear stiffness with the crack fault are

$$\frac{1}{k_b} = \int_{\alpha_3}^{\alpha_r} \frac{12 \sin \alpha [N \cos \alpha_0 / (N - 2.5) - (\cos \alpha + \cos \alpha_3 - \cos \alpha_r - (q_1/R_r) \cos v) \cos \alpha_1]^2}{EL (\sin \alpha_3 + \sin \alpha - (q_1/R_r) \sin v)^3} d\alpha + \frac{4 [1 - (N - 2.5) \cos \alpha_1 \cos \alpha_3 / N \cos \alpha_0]^3 - 4 (1 - \cos \alpha_1 \cos \alpha_2)^3}{EL \cos \alpha_1 (2 \sin \alpha_2 - (q_1/R_b) \sin v)^3}$$

TABLE 1: Gear parameters.

Gear	Number of teeth	$R_{ri}/\text{mm}$	$R_{bi}/\text{mm}$	Mass $m_i/\text{g}$	$J_i/(\text{g}\cdot\text{m}^2)$	Face width/mm	Module/mm	Wheel axle distance/mm
1	29	19.2	20.4	125	0.05	30	1.5	91.318
2	100	68.9	70.5	1224.5	6	30	1.5	
3	36	23.9	25.3	224	0.14	30	1.5	
4	90	61.5	63.4	1111	4	20	1.5	90.8304
s	28	12.3	13	41	0.007	20	1.0	
pn	36	16	17	34.6	0.01	20	1.0	
c			30	848.7	0.76	20	1.0	
r	100	45.6	47			20	1.0	

$$+ \int_{-\alpha_1}^{\alpha_2} \frac{12 \{1 + \cos \alpha_1 [(\alpha_2 - \alpha) \sin \alpha - \cos \alpha]\}^2 (\alpha_2 - \alpha) \cos \alpha}{EL [\sin \alpha_2 - (q_1/R_b) \sin \nu + \sin \alpha + (\alpha_2 - \alpha) \cos \alpha]^3} d\alpha \quad (12)$$

$$\frac{1}{k_s} = \int_{\alpha_3}^{\alpha_r} \frac{2.4 (1 + \nu) \cos^2 \alpha_1 \sin \alpha}{EL (\sin \alpha_3 - (q_1/R_r) \sin \nu + \sin \alpha)^3} d\alpha + \frac{2.4 (1 + \nu) \cos^2 \alpha_1 (\cos \alpha_2 - ((N - 2.5)/N \cos \alpha_0) \cos \alpha_3)}{EL (2 \sin \alpha_2 - (q_1/R_b) \sin \nu)} \quad (13)$$

$$+ \int_{-\alpha_1}^{\alpha_2} \frac{2.4 (1 + \nu) (\alpha_2 - \alpha) \cos \alpha \cos^2 \alpha_1}{EL [\sin \alpha_2 - (q_1/R_b) \sin \nu + \sin \alpha + (\alpha_2 - \alpha) \cos \alpha]} d\alpha.$$

Calculate the bending and shear stiffness of the cracked tooth, and then calculate the overall mesh stiffness of the cracked tooth by (11). In this study, we assume that the 1st-stage fixed-axis small gear (spur gear 1) has a crack fault. The crack gear in test rig is shown in Figure 3 (crack length  $q_1 = 1$  mm, crack angle  $\nu = 70^\circ$ ). The time-varying meshing stiffness is calculated when the speed is 1 Hz (Figure 4). The gear parameters of gear transmission system are shown in Table 1.

**2.2.3. Wear Model.** The gap between the teeth is altered when the wear occurs. When the gears are evenly worn, the gap between the teeth of the faulted gears will be increased. Therefore all tooth wear fault can be expressed in terms of constants. The function is

$$f(\bar{x}_i) = \begin{cases} \bar{x}_i - (1 + a), & \bar{x}_i > (1 + a) \\ 0, & |\bar{x}_i| \leq 1 \\ \bar{x}_i + (1 + a), & \bar{x}_i < -(1 + a), \end{cases} \quad (14)$$

where parameter  $a$  is the size of all tooth wear. Assuming that there is all tooth wear fault in the planetary gear 1, the gear shown in Figure 5 is a planetary gear with all tooth wear fault in the test rig of this paper, and its fault feature is set to  $a = 0.1$ .

### 3. Analysis of Nonlinear Dynamic Behavior of Coupling Fault

**3.1. System Bifurcation Diagrams.** The bifurcation diagrams with the excitation frequency changed are calculated, respectively, when the system is in normal state, planetary gear wear fault state, and the fixed-axis crack fault state, and two faults

coexist. The structure parameters of the system are shown in Tables 1 and 2, pressure angle  $\alpha_0 = 20^\circ$ ,  $T_{\text{in}} = 6.5 \text{ N}\cdot\text{m}$ , and  $T_{\text{out}} = 8.5 \text{ N}\cdot\text{m}$ . The values in Table 2 are equal on the meshing line of gear, so the subscript  $i$  is omitted.

Due to the fact that there are a lot of side frequencies at the meshing point of the 1st-stage fixed-axis gear, so as to study the bifurcation of this point, the nonlinear differential equations (7) are numerically solved using the variable step Runge-Kutta method to obtain the bifurcation diagram of the relative displacement of the 1st-stage fixed-axis gear in four states with the dimensionless excitation frequency  $\Omega_1$  changed (Figure 6).

In (7), it can be seen that all stages of gears are affected not only by their own vibration characteristics, but also by the influence of adjacent teeth on the vibration characteristics. Therefore, when using variable step Runge-Kutta method for iterative calculation of coupling faults, the fault features of the planetary gear wear fault are transmitted to the 2nd-stage fixed-axis gear through the velocity and displacement of the planetary gear and the sun gear meshing point and then transmitted to the 1st-stage fixed-axis gear which has two kinds of faults (the planetary gear wear fault and the 1st-stage fixed-axis crack). The two faults can interact and then show the coupling effect.

When the excitation frequency is small in normal state, the motion state of the 1st-stage fixed-axis gear is periodic (Figure 6(a)). When the excitation frequency increases to 0.5, the system becomes with quasiperiodic motion by periodic motion. When the excitation frequency increases to 1 (critical rotational speed), the system resonates and the motion becomes chaotic. Then the system is divided into three times periodic motion and finally into the quasiperiodic motion.

TABLE 2: Parameters of calculation.

Parameters of calculation	Value
Gear clearance $b$ ( $\mu\text{m}$ )	5
Comprehensive meshing error amplitude $e_a$ ( $\mu\text{m}$ )	5
Meshing pair damping ratio $\xi$	0.07
Gear contact ratio	1.68



FIGURE 3: Fixed-axis gear with crack.

Figure 6 shows that when the system only has a fixed-axis crack fault, it has an effect on the period, the quasi-period, and the 3 times periodic motion when the excitation frequency is less than 3. That is, fault periodic motion is increased in the original periodic motion, indicating that the fixed-axis crack fault is sensitive to low speed. In actual operation, the motor speed is usually a low speed. This creates the fixed-axis fault which is easy to identify, and the planetary gear fault is difficult to identify.

When the system only has the planetary gear wear fault, the quasiperiodic motion with excitation frequency greater than 3 (3 times critical speed) becomes the intermittent periodic motion, indicating that the planetary gear wear fault is sensitive to the high speed.

When the system has the coupling fault, the fault characteristics are similar to single fixed-axis crack fault when the excitation frequency is less than 3, and the fault characteristics are similar to single planetary gear wear fault when the excitation frequency is greater than 3. Planetary fault and fixed-axis fault affect different speed, so the vibration coupling phenomenon of the two on the bifurcation diagram is not obvious. Since the mutual influence of the coupling fault cannot be found from the bifurcation diagram, it is necessary to further study the fault frequency characteristics caused by the coupling fault.

**3.2. Coupling Fault Frequency Characteristics.** The fault characteristics of the fixed-axis crack fault in low excitation frequency have been described in the literature [6]. This paper will study the planetary wear fault at high excitation frequency. The vibration is obvious in the interval of  $\Omega_1 = [3.5, 5]$ . So this part will be studied. The time domain, frequency domain, phase diagram, and Poincaré section of the 1st-stage fixed-axis gear are shown in Figure 7 in the

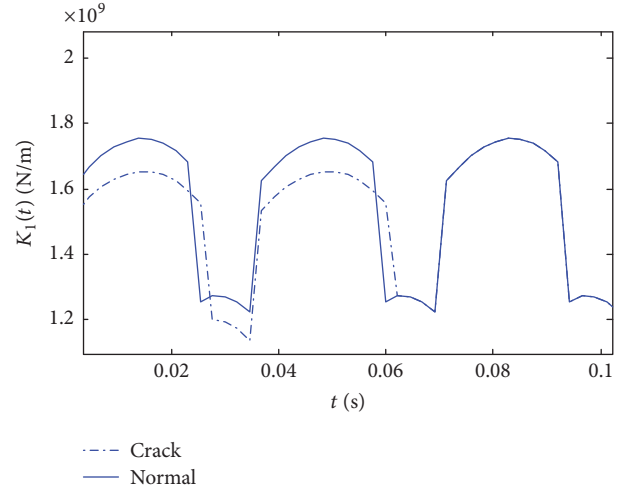


FIGURE 4: The meshing stiffness of the fixed-axis gear with crack.

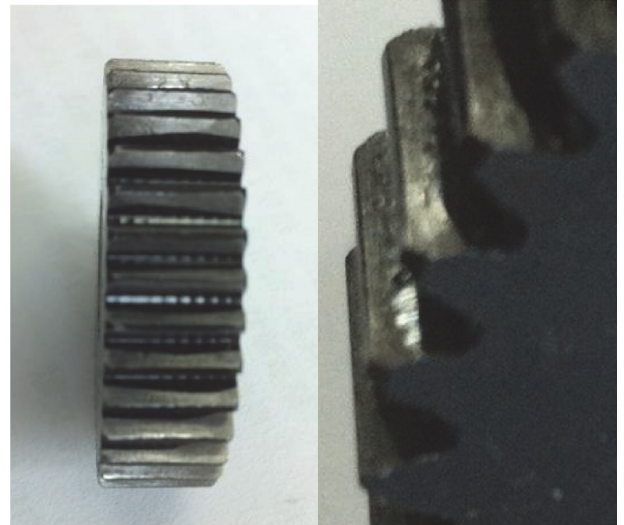


FIGURE 5: Planetary gear with wear fault.

normal state, the fixed-axis crack state, and the coupling fault state of fixed-axis crack + planetary wear, when the excitation frequency is 3.5. Dimensionless characteristic frequencies of gear transmission system at all stages are shown in Table 3.

There is an increase in the impact of fault in the time domain (Figures 7(a), 8(a), and 9(a)) as the number of faults increases. The phase diagram behaves as quasiperiodic motion bands in the normal state (Figure 7(b)), and the band becomes wider in crack fault state (Figure 8(b)). When a coupling fault occurs, the fault cycle makes the band full (Figure 9(b)). The point group of the Poincaré section (Figures 7(c), 8(c), and 9(c)) also increases with the increase of fault. The amplitude of the coupling fault in frequency domain (Figures 7(d), 8(d), and 9(d)) increases significantly.

Figures 7(e), 8(e), and 9(e) are the spectral refinement of Figures 7(d), 8(d), and 9(d), at low frequencies. It can be seen from Figure 7(e) that the main peak of the system is the meshing frequency of 1st-stage fixed-axis gear  $f_1$ , the

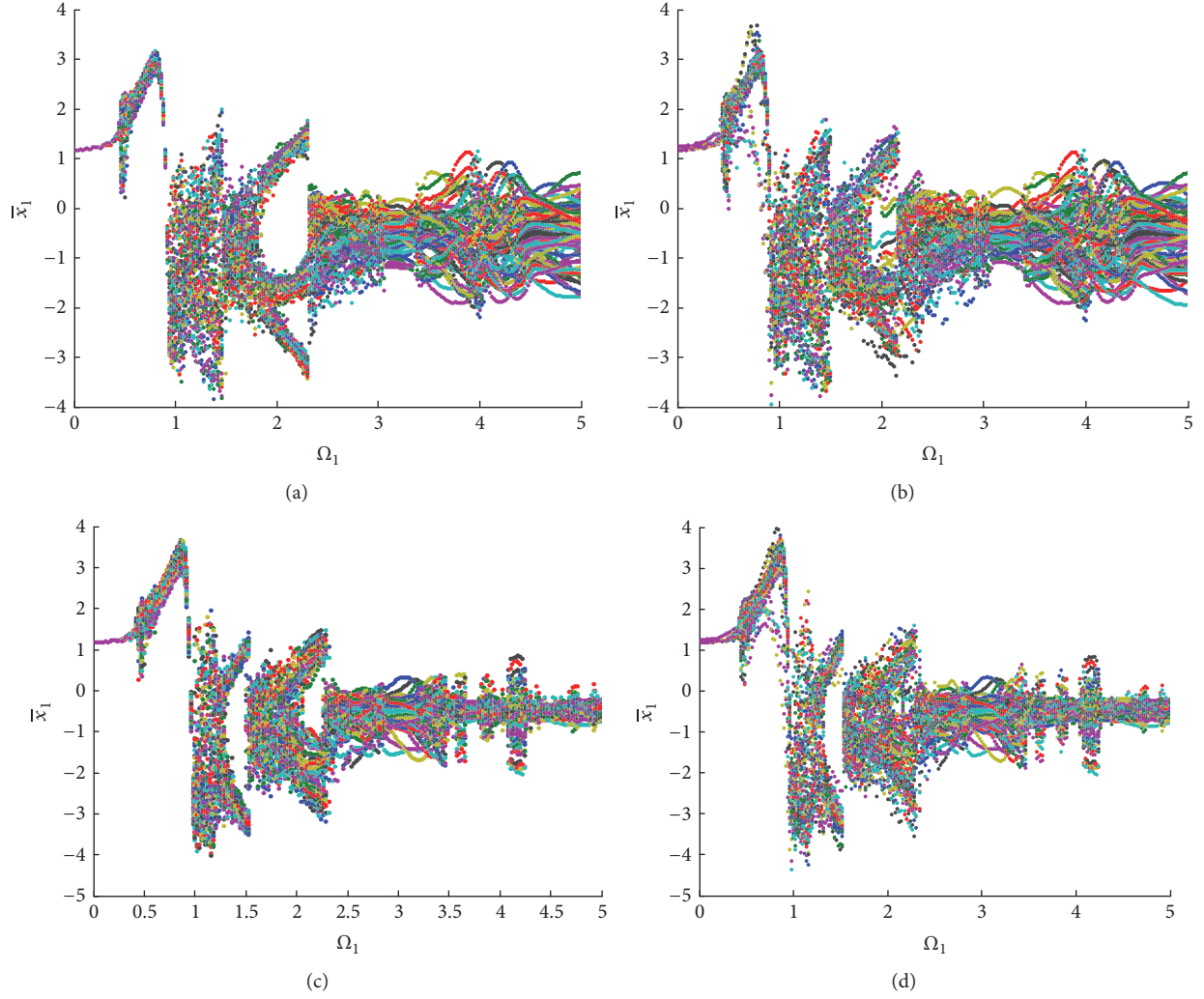


FIGURE 6: Displacement bifurcation diagram of the first fixed gear: (a) normal state, (b) fixed-axis crack, (c) planetary wear, and (d) two-fault coupling.

TABLE 3: Dimensionless characteristic frequencies of gear transmission system (Hz).

Characteristic frequency	Dimensionless frequency
Meshing frequency of 1st-stage fixed-axis gear $f_1$	1
Meshing frequency of 2nd-stage fixed-axis gear $f_2$	0.3599
Meshing frequency of planetary $f_3$	0.0877
Fault frequency of 1st-stage fixed-axis gear $f_d$	0.0345
Planetary fault frequency $f_r$	0.0024

meshing frequency of 2nd-stage fixed-axis gear  $f_2$ , the meshing frequency of the planetary gear  $f_3$ , and its double and triple ( $2f_3, 3f_3$ ) in normal state. There are a large number of regular side frequencies around the meshing frequency of the planetary gear and its double and triple. The side frequency is the rotation frequency of the 2nd-stage rotating shaft  $f_d$ . It can be seen from Figure 8(e) that the fault frequency of the fixed-axis crack  $f_d$  occurs at a peak value of 1~10 times, and the amplitude gradually decreases. Figure 9(e) shows that the increase of planetary gear wear fault makes the amplitude of the planetary gear meshing frequency and its double and

triple increased. So two kinds of fault characteristics occur at the same time in coupling faults state, all around the planet gear meshing frequency.

#### 4. Experimental Failure Analysis

The test rig of gear transmission system which contains a two-stage fixed-axis gear and a one-stage planetary is shown in Figure 10. The parameters are shown in Tables 1 and 3. Test and analyze the signal of the test rig in normal state and coupling faults state, in which the crack failure occurs on

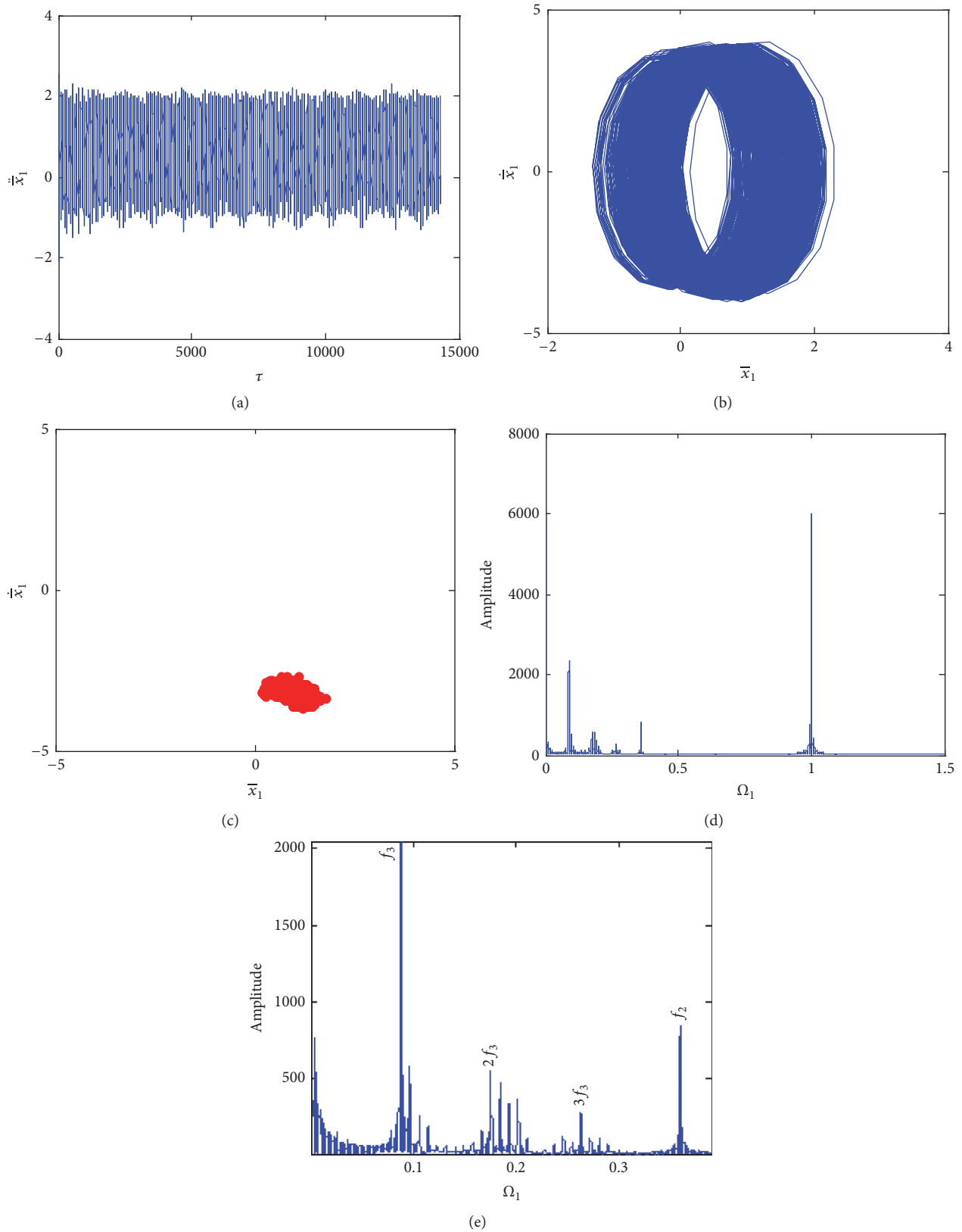


FIGURE 7: Vibration characteristics when the excitation frequency is 3.5 in normal state: (a) time domain, (b) phase diagram, (c) Poincaré section, (d) frequency domain, and (e) frequency refinement spectrum.

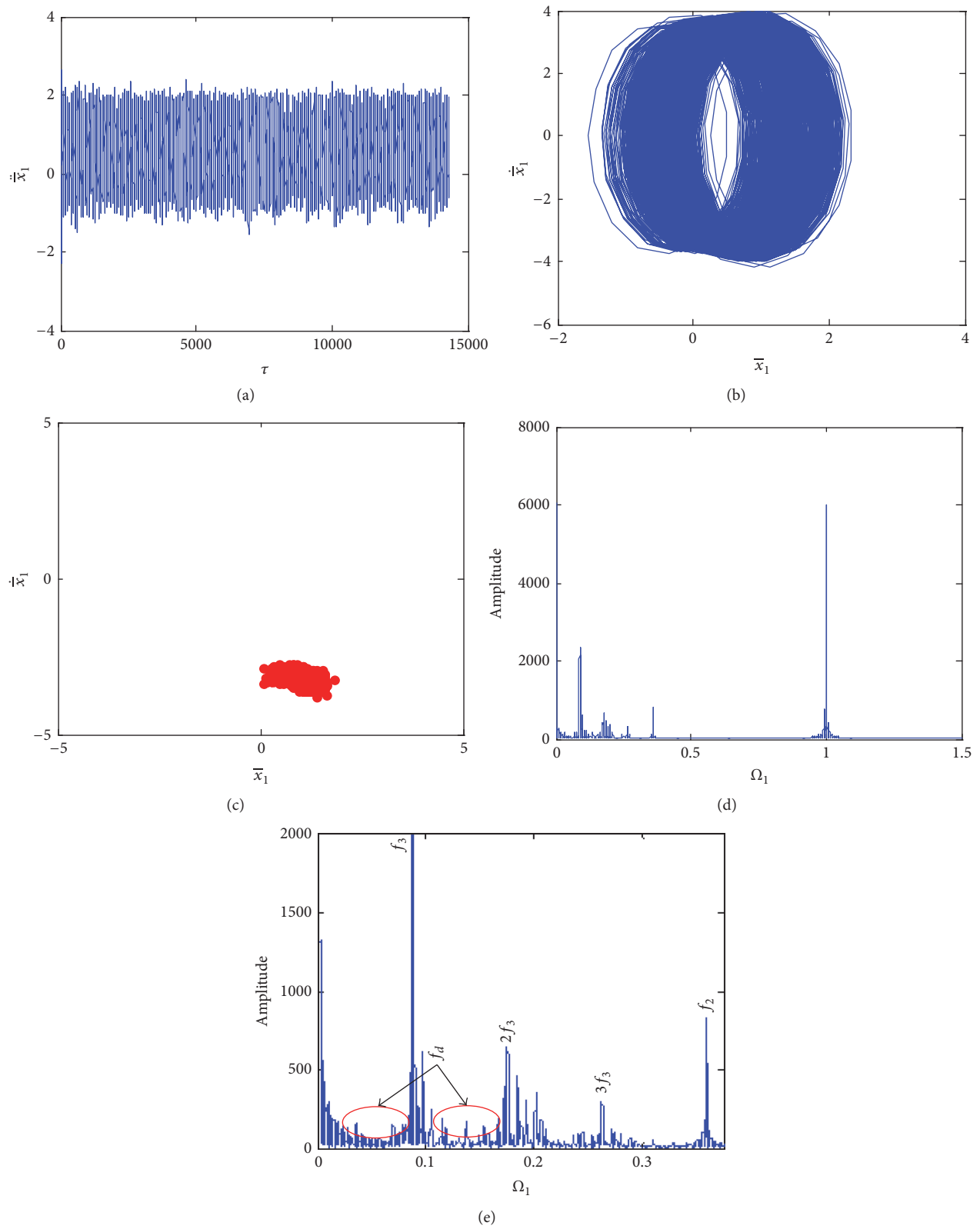


FIGURE 8: Vibration characteristics when the excitation frequency is 3.5 in fixed-axis crack state: (a) time domain, (b) phase diagram, (c) Poincaré section, (d) frequency domain, and (e) frequency refinement spectrum.

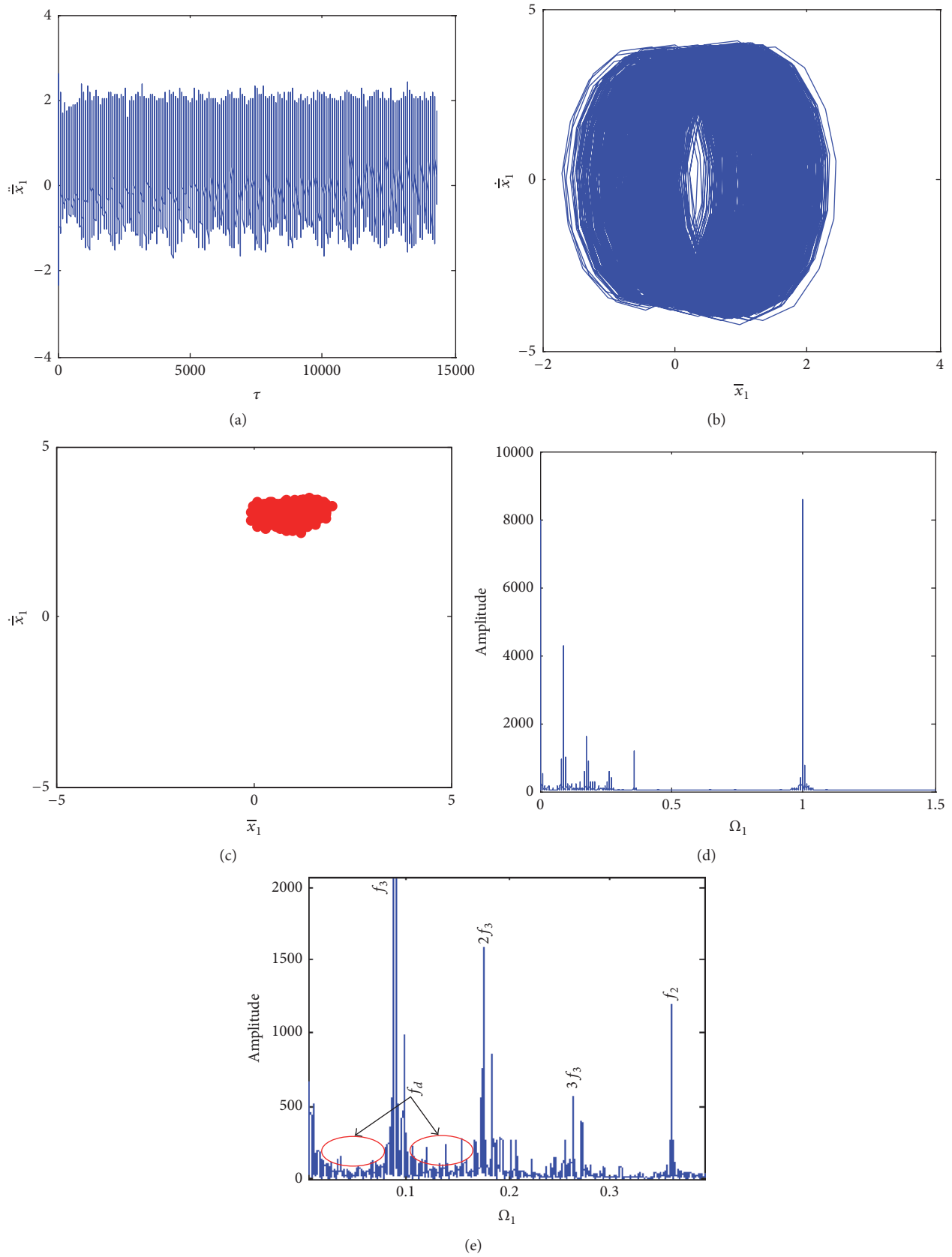


FIGURE 9: Vibration characteristics when the excitation frequency is 3.5 in coupling faults state: (a) time domain, (b) phase diagram, (c) Poincaré section, (d) frequency domain, and (e) frequency refinement spectrum.



FIGURE 10: The test rig of gear transmission system: 1: motor; 2: torque sensor and encoder; 3: two-stage fixed-axis gearbox; 4: radial load of bearing; 5: one-stage planetary gearbox; 6: brake.

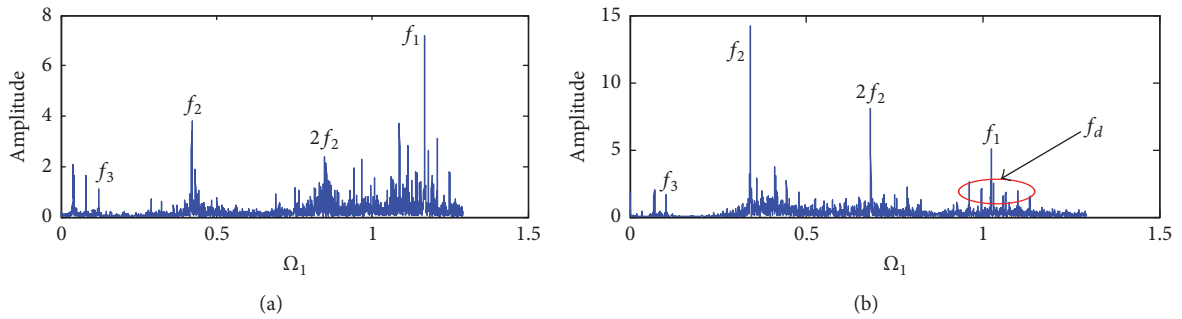


FIGURE 11: Spectrum of the fixed-axis gearbox: (a) normal state and (b) coupling faults of fixed-axis gear crack and planetary wear.

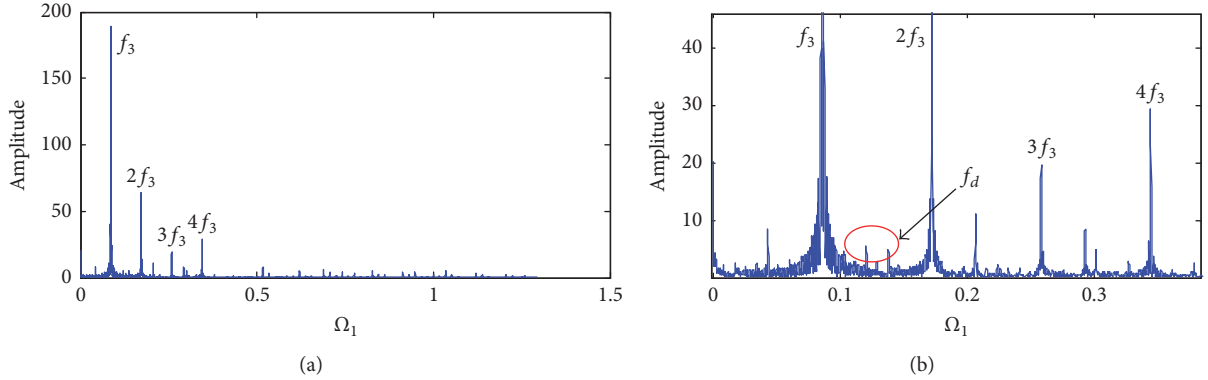


FIGURE 12: Spectrum of the planetary gearbox with the coupling faults of fixed-axis gear crack and planetary gear wear: (a) frequency domain and (b) frequency refinement spectrum.

the 1st-stage pinion (spur gear 1 in Figure 1) with the crack length  $q_1 = 1$  mm and the crack angle  $\nu = 70^\circ$ , as shown in Figure 3. Planetary wear fault occurs in the first planetary gear  $p1$  in Figure 1, and the planetary gear wear parameter is  $a = 0.1$  (Figure 5). Sampling frequency is 3000 Hz, the number of sampling points is 2048, and the axial measurement points of the fixed-axis gearbox drive side are selected for testing. In order to facilitate the comparison, the spectrums are normalized to get the dimensionless spectrum in normal state and coupling faults state (Figure 11).

The amplitude of the 2nd-stage fixed-axis meshing frequency  $f_2$  and its doubling  $2f_2$  increased in the coupling

faults state (Figures 11(a) and 11(b)). Around the fixed-axis gear meshing frequency  $f_1$  appears a large amount of fixed-axis fault characteristic frequency  $f_d$ . But the amplitude of the planetary gear meshing frequency  $f_3$  is relatively weak, and the surrounding frequency is not easy to identify. So the dimensionless radial spectrum of the planetary gearbox under the coupling faults state is investigated, as shown in Figure 12.

The amplitude of planetary gear meshing frequency  $f_3$  and its frequency-doubling ( $2f_3$ ,  $3f_3$ , and  $4f_3$ ) in vibration signals of the planetary gearbox greatly increased (Figures 12 and 11). As can be seen in the frequency refinement diagram

near the frequency of the planetary gear, the fault frequency of the fixed axis  $f_d$  is found around  $f_3$ , which is consistent with the numerical simulation results. By observing the vibration signal of the fixed-axis gearbox and the planetary gearbox, the fixed-axis crack fault and the planetary gear wear fault were identified.

## 5. Conclusion

In this study, dimensionless dynamical equations of gear transmission system which contains a two-stage fixed-axis gear with crack fault and a one-stage planetary gear with wear fault were established. With contrasted bifurcation and frequency spectrum characteristics of system in normal condition and coupling faults condition, it found that when the system has the coupling fault, the fault characteristics are similar to single fixed-axis crack fault when the excitation frequency is less than 3, and the fault characteristics are similar to single planetary gear wear fault when the excitation frequency is greater than 3. This paper studied the planetary wear fault at high excitation frequency. Fault frequency characteristics caused by the coupling faults of the fixed-axis crack fault and the planetary gear wear fault were analyzed. Simulation analysis shows that the crack fault in fixed-axis gear brings up peaks in doubling of 1~10 for fault frequency, the wear fault in planetary gear increases the amplitude of meshing frequency and its double and triple, and the coupling of both shows two kinds of fault features around the planetary gear meshing frequency. For the test rig, by observing the vibration signal of the fixed-axis gearbox and the planetary gearbox, it is found that the experimental characteristics are consistent with the numerical simulation results. Through numerical simulation results the fixed-axis crack fault and the planetary gear wear fault are accurately identified. This study explored the complex fault features in multistage gear transmission system and cognized fault dynamic behaviors of multistage gear transmission system comprehensively to diagnose the complex fault of multistage gear accurately.

## Conflicts of Interest

The author declares that there are no conflicts of interest regarding the publication of this paper.

## Acknowledgments

The author gratefully acknowledges the financial support from the Key Project of Baoji University of Arts and Sciences (no. 209010861).

## References

- [1] Z. Li, X. Yan, Z. Tian, C. Yuan, Z. Peng, and L. Li, "Blind vibration component separation and nonlinear feature extraction applied to the nonstationary vibration signals for the gearbox multi-fault diagnosis," *Measurement*, vol. 46, no. 1, pp. 259–271, 2013.
- [2] Z. Li, X. Yan, C. Yuan, J. Zhao, and Z. Peng, "The fault diagnosis approach for gears using multidimensional features and intelligent classifier," *Noise & Vibration Worldwide*, vol. 41, no. 10, pp. 76–86, 2010.
- [3] Z. Li, "A novel solution for the coupled faults isolation in gear pairs using the conception of frequency tracking," *Elektronika ir Elektrotechnika*, vol. 20, no. 3, pp. 69–72, 2014.
- [4] C. Luo, C. Shen, W. Fan, G. Cai, W. Huang, and Z. Zhu, "Research on the sparse representation for gearbox compound fault features using wavelet bases," *Shock and Vibration*, vol. 2015, Article ID 560171, 2015.
- [5] L. Xiao-yu, X. Yu-xiu, and X. Gang, "Nonlinear characteristics of complex and weak faults of planetary gear transmission system," *Mechanical Science and Technology for Aerospace Engineering*, vol. 34, no. 4, pp. 538–543, 2013.
- [6] X. Wang, X. Y. Xu, and B. L. Wu, "Study on failure characteristics of gearbox transmission system with coupling faults," *Journal of Vibration*, vol. 36, no. 12, pp. 217–223, 2017.
- [7] D. Qin, W. Long, J. Yang, and H. Zhou, "Dynamic characteristics of wind turbine transmission system under varying wind speed and operation control conditions," *Jixie Gongcheng Xuebao/Journal of Mechanical Engineering*, vol. 48, no. 7, pp. 1–8, 2012.
- [8] D. Qin, M. Tian, and J. Yang, "Study on dynamic characteristics of gear transmission system of wind generator under varying wind load," *Acta Energetica Solaris Sinica*, vol. 33, no. 2, pp. 190–196, 2012.
- [9] X. H. Liang, M. J. Zuo, and M. Pandey, "Analytically evaluating the influence of crack on the mesh stiffness of a planetary gear set," *Mechanism and Machine Theory*, vol. 76, pp. 20–38, 2014.
- [10] A. Kapelevich and Y. Shekhtman, "Tooth fillet profile optimization for gears with symmetric and asymmetric teeth," in *Proceedings of the American Gear Manufacturers Association Fall Technical Meeting 2008*, pp. 73–83, USA, October 2008.
- [11] X. Tian, M. J. Zuo, and K. R. Fyfe, "Analysis of the vibration response of a gearbox with gear tooth faults," in *Proceedings of the 2004 ASME International Mechanical Engineering Congress and Exposition*, pp. 785–793, Calif, USA, November 2004.

## Research Article

# Forward Analysis of Love-Wave Scattering due to a Cavity-Like Defect

Chen Yang , Bin Wang, and Zhenghua Qian 

State Key Laboratory of Mechanics and Control of Mechanical Structures, Nanjing University of Aeronautics and Astronautics, 29 Yudao Jie, Nanjing 210016, China

Correspondence should be addressed to Zhenghua Qian; qianzh@nuaa.edu.cn

Received 27 December 2017; Accepted 31 January 2018; Published 22 April 2018

Academic Editor: Maosen Cao

Copyright © 2018 Chen Yang et al. This is an open access article distributed under the Creative Commons Attribution License, which permits unrestricted use, distribution, and reproduction in any medium, provided the original work is properly cited.

This paper presents a modified boundary element method (BEM) to solve the scattering problem of Love surface wave from a two-dimensional cavity defect. Because of the truncation of BEM models at a far distance from the cavity, spurious reflected waves are generated. In order to eliminate the unwanted reflections, the guided Love-wave displacement patterns are assumed on the far-field infinite boundaries previously omitted by model truncation, and they are incorporated into the BEM equation set as modified items. The numerical results are verified by theoretical solutions of far-field Green's functions. Additional parametric studies are performed to find out the influence of truncation distance and defects' geometric characters on the accuracy of scattered wave solutions.

## 1. Introduction

The ultrasonic nondestructive testing (NDT) techniques have wide applications for quantitative characterizations of mechanical properties and detection and characterization of cracks and defects. Traditional ultrasonic testing techniques using bulk waves are very time-consuming, since these techniques need an overall inspection of the structure. However, ultrasonic guided waves are attractive for inspection of long-range or wide area structures because they can travel considerable distances and therefore scan large regions for defects in shorter testing time [1, 2].

The current NDT applications of guided waves include pitch-catch [3] or pulse-echo [4], flaw detection method, phased array configuration [5], and diffraction tomography [6]. Generally, these methods make use of time-of-flight (TOF) of the reflected waves from inner defects to locate their approximate positions.

However, further information (e.g., defect shapes or depths) cannot be further utilized because of the complexity of guided waves. Hence, the quantitative nondestructive testing requires a thorough understanding of surface wave scattering in forward and inverse aspects. For the forward problem, we need to solve the near- and far-fields accurately

and obtain the scattering coefficients for following inverse reconstruction [7–9].

The Love-wave is a special kind of guided waves that travels along the surface of elastic layer covered on top of an elastic half-plane. The scattered Love-waves are relied on to investigate underground information in geotechnique engineering, earthquake engineering [10], or detecting flaws and cracks at the bounding interface in nondestructive testing applications [11]. An effective utilization of the Love-wave requires a thorough understanding of its scattering phenomenon.

For the calculation of scattered wave field over a finite domain, various technologies can be implied, like finite element method (FEM) [12], BEM [13], mode-exciting method [14], matrix theory [15], and so on. However, for the forward analysis of a half-plane, the BEM is especially effective, since only the interfaces and flaw boundaries need to be meshed. There are BEM approaches using two kinds of Green's functions: half-space and full-space. Using the former one, only the flawed portion needs to be meshed; however, Green's function cannot be written in a closed form. Conversely, using the latter one, the whole interface should be meshed; however, Green's function is much simpler. Thus, for the forward analysis of Love-wave, we adopt the latter one.

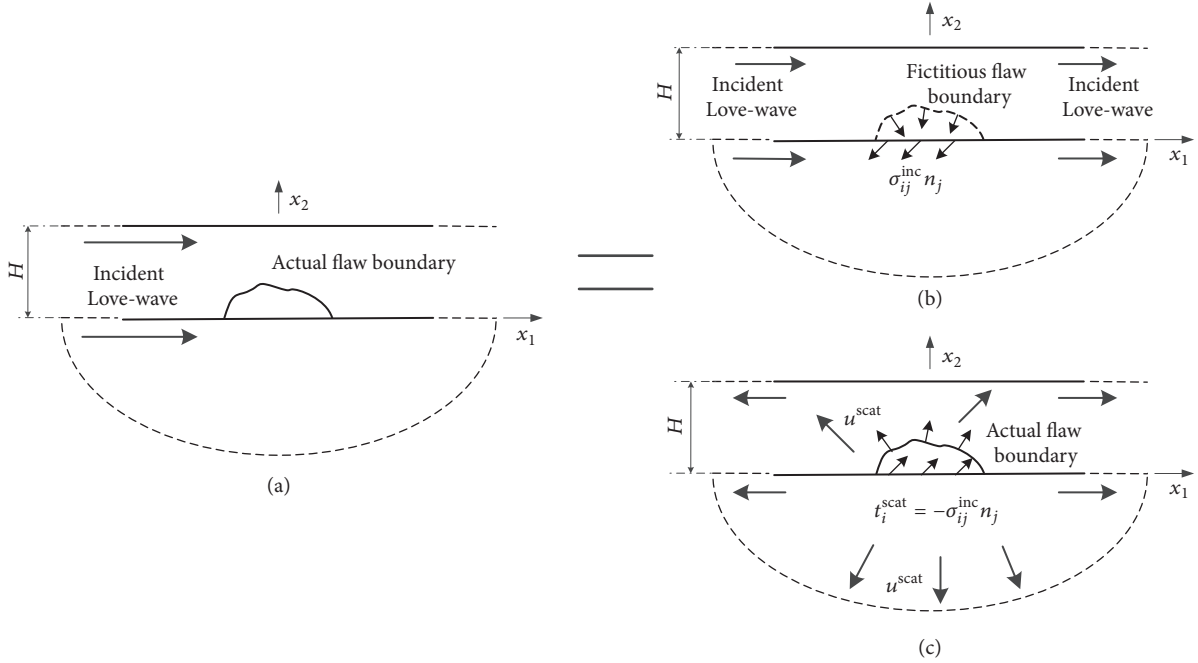


FIGURE 1: Linear superposition principle: (a) the total field; (b) the incident field; (c) the scattered field.

However, in traditional BEM approaches, due to the inevitable artificial truncation of BEM model, spurious reflected waves are introduced in the final results of scattered wave field, which causes considerable error. Another big challenge to solve the scattering problem is the existence of multiple dispersive modes of Love-waves at a certain frequency along with the modal conversion, due to the interaction at the damage location.

Here, a modified BEM for calculating scattered Love-waves is introduced. In this paper, the guided Love-wave displacement patterns are assumed on the far-field infinite boundaries previously omitted, and they are incorporated into BEM equation sets as the modified items. With this improvement, the spurious reflected waves are eliminated. The numerical results are verified by theoretical far-field Green's functions [16, 17]. Furthermore, various parametric studies of the influence of defect locations and geometrical shapes and size on the calculations of Love-wave scattered fields are carried out in the later sections, which have potential values for investigating forward problem or inverse problem of flaw reconstruction based on surface waves.

## 2. Statement of the Problem

The Love surface wave propagates along the surface of elastic layer of thickness  $H$  covered on top of a homogeneous, elastic half-plane, containing a cavity of arbitrary shape on the bonding interface of the  $x_1$ - $x_2$  plane (see Figure 1(a)). Here, we consider an incident Love-wave propagating in the  $x_1$ -direction, which interacts with the cavity generating forward-scattered and back-scattered surface wave.

By virtue of linear superposition principle, the total field in the flawed structure defined by Figure 1(a) can be

considered as the superposition of the incident and the scattered waves. The incident wave can be treated in the intact (or reference) structure without cavity, as shown by Figure 1(b), and the scattered field is analyzed in the flawed configuration in Figure 1(c). The scattered field is equivalent to the field generated by the contribution of the tractions exerted on the actual surface of the cavity. Furthermore, these tractions are equal in magnitude but opposite in sign to the corresponding tractions produced by the incident Love-wave field on the surface of the fictitious cavity as shown by Figure 1(b). Thus, these tractions can be obtained by calculating the stress components and the outward normal vectors along the fictitious cavity surface using the Cauchy's formula from the incident field. The dynamic reciprocal theorem is then applied to calculate the scattered wave field equivalent to the radiated field generated by these tractions.

## 3. Equations

**3.1. The Elastodynamic Reciprocal Theorem.** The dynamic reciprocal theorem relates two elastodynamic states 1 and 2 of the same bounded or unbounded body, which can be stated as

$$\begin{aligned}
 & \int_V [f_k^1(\mathbf{x}, \omega) u_k^2(\mathbf{x}, \omega) - f_k^2(\mathbf{x}, \omega) u_k^1(\mathbf{x}, \omega)] dV(\mathbf{x}) \\
 &= \int_A [\tau_{kl}^2(\mathbf{x}, \omega) n_k u_l^1(\mathbf{x}, \omega) \\
 & \quad - \tau_{kl}^1(\mathbf{x}, \omega) n_k u_l^2(\mathbf{x}, \omega)] dA(\mathbf{x}),
 \end{aligned} \tag{1}$$

where  $f_k^{1,2}$ ,  $u_k^{1,2}$ , and  $\tau_{kl}^{1,2}$  represent body forces, displacements, and stresses, respectively, and  $n_k$  is the  $k$ th component of unit vector outward surface normal to  $A$ .

Let us consider two-dimensional elastodynamic problems in an isotropic half-plane with a different homogeneous and isotropic layer covered with boundary  $L$ . The boundary integral equation of antiplane motion for a source point  $\xi$  taken on  $L$ , in the absence of body forces, is developed from (1) and derived as

$$\begin{aligned} & \frac{1}{2}u(\xi, \omega) \\ &= \int_L [u^*(\xi, \mathbf{x}, \omega)t(\mathbf{x}, \omega) - t^*(\xi, \mathbf{x}, \omega)u(\mathbf{x}, \omega)] dL(\mathbf{x}), \end{aligned} \quad (2)$$

where the factor 1/2 is valid only if the boundary  $L$  is smooth at point  $\xi$  and  $u^*$  and  $t^*$  are the full-space frequency domain elastodynamic antiplane fundamental solution displacement and traction tensors, respectively, which are derived [18] as

$$\begin{aligned} u^*(\xi, \mathbf{x}, \omega) &= \frac{i}{4\mu_I} H_0^{(1)}(k_T^B r) \quad (0 \leq \xi_2 \leq H) \\ &\text{or } \frac{i}{4\mu_{II}} H_0^{(1)}(k_T^A r) \quad (\xi_2 \leq 0) \\ t^*(\xi, \mathbf{x}, \omega) &= -\frac{ik_T^B}{4} H_1^{(1)}(k_T^B r) \frac{\partial r}{\partial n} \quad (0 \leq \xi_2 \leq H) \\ &\text{or } -\frac{ik_T^A}{4} H_1^{(1)}(k_T^A r) \frac{\partial r}{\partial n} \quad (\xi_2 \leq 0), \end{aligned} \quad (3)$$

where  $H_n^{(1)}(\cdot)$  is the Hankel function of the  $n$ th order of the first kind;  $\mu_A$ ,  $\mu_B$ ,  $k_T^A$ , and  $k_T^B$  stand for the elastic constants and the wave-numbers of the shear wave at current frequency, for the upper and lower materials, respectively, where  $k_T^J = \omega/\sqrt{\mu_J/\rho_J}$  ( $J = A, B$ ), in which  $\rho_A$  and  $\rho_B$  are material densities;  $r$  represents the distance between  $\xi$  and  $\mathbf{x}$ ;  $u^*$  and  $t^*$  are the displacement and boundary traction, respectively, at the point  $\mathbf{x}$ , respectively, due to a unit line force exerted at  $\xi$ . For current antiplane problem, both the line force and Green's function --  $u^*$  and  $t^*$  only have the  $x_3$  component.

Let us assume that, except the flaw region  $L_1$  and  $L_5$ , both the free-traction surface and the interface are flat. Let  $L_0$  and  $L_3$  be the free upper surface and the interface between upper-layer and half-plane, respectively, and  $L_\infty^a$  and  $L_\infty^b$  represent the remaining infinite part of upper and lower boundary, respectively, which will be omitted by truncation in traditional BEM (see Figure 1).

By substituting all boundaries divided in Figure 2 into (2), the BIE of the layered media and half-plane are derived as

$$\begin{aligned} & \frac{1}{2}u(\xi, \omega) + \int_{L_0 \cap L_3 \cap L_1} t^B(\xi, \mathbf{x}, \omega)u(\mathbf{x}, \omega) dL(\mathbf{x}) \\ &+ \left( \int_{L_\infty^a \cup L_\infty^b} t^B(\xi, \mathbf{x}, \omega)u(\mathbf{x}, \omega) dL(\mathbf{x}) \right. \end{aligned}$$

$$\begin{aligned} & \left. - \int_{L_\infty^a} u^B(\xi, \mathbf{x}, \omega)t(\mathbf{x}, \omega) dL(\mathbf{x}) \right) \\ &= \int_{L_3 \cap L_1} u^B(\xi, \mathbf{x}, \omega)t(\mathbf{x}, \omega) dL(\mathbf{x}), \end{aligned} \quad (4)$$

$$\begin{aligned} & \frac{1}{2}u(\xi, \omega) + \int_{L_3 \cap L_5} t^A(\xi, \mathbf{x}, \omega)u(\mathbf{x}, \omega) dL(\mathbf{x}) \\ &+ \int_{L_\infty^a} (t^A(\xi, \mathbf{x}, \omega)u(\mathbf{x}, \omega) \\ &- u^A(\xi, \mathbf{x}, \omega)t(\mathbf{x}, \omega)) dL(\mathbf{x}) \\ &= \int_{L_3 \cap L_5} u^A(\xi, \mathbf{x}, \omega)t(\mathbf{x}, \omega) dL(\mathbf{x}), \end{aligned} \quad (5)$$

respectively, where the superscripts  $A$  and  $B$  indicate the Green functions of half-plane and the layer, respectively.

**3.2. Far-Field Assumption.** Since body waves geometrically attenuate in the propagating direction, the far-field displacement solution can be approximated by a series of Love surface waves, neglecting the contribution of body waves.

Therefore, we assume that if the truncated points are located far enough from the source regions, the displacement solutions of the infinite boundary at each side can be expressed as

$$\begin{aligned} u(\mathbf{x}, \omega) &\approx R_1^-(\omega)u^{1-}(\mathbf{x}, \omega) + R_2^-(\omega)u^{2-}(\mathbf{x}, \omega) + \dots \\ &+ R_n^-(\omega)u^{n-}(\mathbf{x}, \omega) \end{aligned} \quad \text{For } \mathbf{x} \in L_{-\infty}^a \cup L_{-\infty}^b, \quad (6)$$

$$\begin{aligned} u(\mathbf{x}, \omega) &\approx R_1^+(\omega)u^{1+}(\mathbf{x}, \omega) + R_2^+(\omega)u^{2+}(\mathbf{x}, \omega) + \dots \\ &+ R_n^+(\omega)u^{n+}(\mathbf{x}, \omega) \end{aligned}$$

$$\text{For } \mathbf{x} \in L_{+\infty}^a \cup L_{+\infty}^b,$$

where the coordinate vector  $\mathbf{x}$  is in the form of  $(x_1, x_2)$ ,  $R_i^\pm(\omega)$  are defined as the unknown complex amplitudes of the far-field solutions of the  $i$ th order mode Love-wave. Here,  $n$  is the number of modes, and  $u^{i\pm}(\mathbf{x}, \omega)$  represent the  $i$ th order mode displacement of unit amplitude Love-wave propagating in the positive and negative direction of axis  $x_1$ . (Note that Love surface waves are dispersive.)

By virtue of assumptions in (6), (4) and (5) can be rewritten as

$$\begin{aligned}
& \frac{1}{2}u(\xi, \omega) + \int_{L_0 \cap L_3 \cap L_1} t^B(\xi, \mathbf{x}, \omega) u(\mathbf{x}, \omega) dL(\mathbf{x}) - \int_{L_3 \cap L_1} u^B(\xi, \mathbf{x}, \omega) t(\mathbf{x}, \omega) dL(\mathbf{x}) \\
&= \sum_i R_i^- \left[ \int_{L_{-\infty}^a \cup L_{-\infty}^b} t^B(\xi, \mathbf{x}, \omega) u^{i-}(\mathbf{x}, \omega) dL(\mathbf{x}) - \int_{L_{-\infty}^a} u^B(\xi, \mathbf{x}, \omega) t^{i-}(\mathbf{x}, \omega) dL(\mathbf{x}) \right] \\
& \quad + R_i^+ \left[ \int_{L_{+\infty}^a \cup L_{+\infty}^b} t^B(\xi, \mathbf{x}, \omega) u^{i+}(\mathbf{x}, \omega) dL(\mathbf{x}) - \int_{L_{+\infty}^a} u^B(\xi, \mathbf{x}, \omega) t^{i+}(\mathbf{x}, \omega) dL(\mathbf{x}) \right] \quad (i = 1, 2, \dots, n), \\
& \frac{1}{2}u(\xi, \omega) + \int_{L_3 \cap L_1} t^A(\xi, \mathbf{x}, \omega) u(\mathbf{x}, \omega) dL(\mathbf{x}) - \int_{L_3 \cap L_1} u^A(\xi, \mathbf{x}, \omega) t(\mathbf{x}, \omega) dL(\mathbf{x}) \\
&= -\sum_i R_i^- \left[ \int_{L_{-\infty}^a} t^A(\xi, \mathbf{x}, \omega) u^{i-}(\mathbf{x}, \omega) dL(\mathbf{x}) - \int_{L_{-\infty}^a} u^A(\xi, \mathbf{x}, \omega) t^{i-}(\mathbf{x}, \omega) dL(\mathbf{x}) \right] \\
& \quad + R_i^+ \left[ \int_{L_{+\infty}^a} t^A(\xi, \mathbf{x}, \omega) u^{i+}(\mathbf{x}, \omega) dL(\mathbf{x}) - \int_{L_{+\infty}^a} u^A(\xi, \mathbf{x}, \omega) t^{i+}(\mathbf{x}, \omega) dL(\mathbf{x}) \right] \quad (i = 1, 2, \dots, n),
\end{aligned} \tag{7}$$

respectively. From (7), we define

$$\begin{aligned}
A_i^{B\pm}(\xi) &= \int_{L_{\pm\infty}^a \cup L_{\pm\infty}^b} t^B(\xi, \mathbf{x}, \omega) u^{i\pm}(\mathbf{x}, \omega) dL(\mathbf{x}) \\
& \quad - \int_{L_{\pm\infty}^a} u^B(\xi, \mathbf{x}, \omega) t^{i\pm}(\mathbf{x}, \omega) dL(\mathbf{x}), \\
A_i^{A\pm}(\xi) &= \int_{L_{\pm\infty}^a} t^A(\xi, \mathbf{x}, \omega) u^{i\pm}(\mathbf{x}, \omega) dL(\mathbf{x}) \\
& \quad - \int_{L_{\pm\infty}^a} u^A(\xi, \mathbf{x}, \omega) t^{i\pm}(\mathbf{x}, \omega) dL(\mathbf{x})
\end{aligned} \tag{8}$$

which represent the corrected items accounting for the contribution of the omitted boundary. Thus, (7) are simplified as

$$\begin{aligned}
& \frac{1}{2}u(\xi, \omega) + \int_{L_0 \cap L_3 \cap L_1} t^B(\xi, \mathbf{x}, \omega) u(\mathbf{x}, \omega) dL(\mathbf{x}) \\
& \quad - \int_{L_3 \cap L_1} u^B(\xi, \mathbf{x}, \omega) t(\mathbf{x}, \omega) dL(\mathbf{x}) \\
&= \sum_i (R_i^- A_i^{B-} + R_i^+ A_i^{B+}) \quad (i = 1, 2, \dots, n). \\
& \frac{1}{2}u(\xi, \omega) + \int_{L_3 \cap L_1} t^A(\xi, \mathbf{x}, \omega) u(\mathbf{x}, \omega) dL(\mathbf{x}) \\
& \quad - \int_{L_3 \cap L_1} u^A(\xi, \mathbf{x}, \omega) t(\mathbf{x}, \omega) dL(\mathbf{x}) \\
& \quad + \sum_i (R_i^- A_i^{A-} + R_i^+ A_i^{A+}) \\
&= \int_{L_3} u^A(\xi, \mathbf{x}, \omega) t(\mathbf{x}, \omega) dL(\mathbf{x}) \quad (i = 1, 2, \dots, n)
\end{aligned} \tag{9}$$

Note that  $2n$  unknown parameters  $R_i^\pm(\omega)$  are introduced into the BIEs, which will add degrees of freedom to the final BEM system of the BIEs.

**3.3. Correction over the Omitted Part of the Infinite Boundary.** In traditional BEM approaches, the contribution of integral

terms on the infinite boundary, that is, the fourth term on the right-hand side of (4) and the third term on the right-hand side of (5), is omitted, which introduces considerable error. In order to separately determine the integral terms over infinite boundaries such as  $L_{\pm\infty}^a$  and  $L_{\pm\infty}^b$ , a multidomain approach is applied, which involves the division of the whole interfaces and boundaries into four regions by introducing two fictitious boundaries  $L_2$  and  $L_4$ , as shown in Figure 2. Here, an incident Love-wave mode with unit amplitude is introduced propagating along the upper free surface in the positive or negative direction of  $x_1$ , respectively (see Figure 3).

Let us choose the Love surface wave of unit amplitude as elastodynamic state 1 and the full-space fundamental solution as elastodynamic state 2. For instance, by virtue of reciprocal theorem seen from (2), the BIE for region 1 is given as

$$\begin{aligned}
\frac{1}{2}u^{i\pm}(\xi, \omega) &= \int_L \left[ u^*(\xi, \mathbf{x}, \omega) t^{i\pm}(\mathbf{x}, \omega) \right. \\
& \quad \left. - t^*(\xi, \mathbf{x}, \omega) u^{i\pm}(\mathbf{x}, \omega) \right] dL(\mathbf{x}).
\end{aligned} \tag{10}$$

By simplifying (10), we arrive at

$$\begin{aligned}
A_i^{B+}(\xi) &= -\frac{1}{2}u^{i+}(\xi, \omega) \\
& \quad - \int_{L_0^+ \cup L_1^+ \cup L_3^+ \cup L_2} t^B(\xi, \mathbf{x}, \omega) u^{i+}(\mathbf{x}, \omega) dL(\mathbf{x}) \\
& \quad + \int_{L_1^+ \cup L_3^+ \cup L_2} u^B(\xi, \mathbf{x}, \omega) t^{i+}(\mathbf{x}, \omega) dL(\mathbf{x}).
\end{aligned} \tag{11}$$

By implying an analogous approach for other regions, we can get  $A_i^{B-}(\xi)$ ,  $A_i^{A-}(\xi)$  and  $A_i^{A+}(\xi)$ , which are expressed as

$$\begin{aligned}
A_i^{B-}(\xi) &= -\frac{1}{2}u^{i-}(\xi, \omega) \\
& \quad - \int_{L_0^- \cup L_1^- \cup L_3^- \cup L_2} t^B(\xi, \mathbf{x}, \omega) u^{i-}(\mathbf{x}, \omega) dL(\mathbf{x}) \\
& \quad + \int_{L_1^- \cup L_3^- \cup L_2} u^B(\xi, \mathbf{x}, \omega) t^{i-}(\mathbf{x}, \omega) dL(\mathbf{x})
\end{aligned} \tag{12}$$



$$\begin{aligned}
& \frac{1}{2}u(\mathbf{v}_j, \omega) + \sum_{e \in L_3} \sum_{k=1}^{N_e} \left\{ \int_{L_e} t^A(\mathbf{v}_j, \eta, \omega) \phi_k(\eta) dL(\eta) \right\} \\
& \cdot u(\mathbf{v}_k, \omega) + \sum_{i=1}^n A_i^{A-}(\xi_j) R_i^-(\omega) \\
& + \sum_{i=1}^n A_i^{A+}(\xi_j) R_i^+(\omega) \\
& = \sum_{e \in L_3} \sum_{k=1}^{N_e} \left\{ \int_{L_e} u^A(\mathbf{v}_j, \eta, \omega) \phi_k(\eta) dL(\eta) \right\} t(\xi_k, \omega) \\
& \qquad \qquad \qquad j = 1, 2, \dots, N_2,
\end{aligned} \tag{15}$$

where  $N_1, N_2$  are the total number of nodes for the layer and half-plane, respectively,  $N_e$  is the number of nodes per element,  $\phi_k$  is the same shape function for each element, and  $\eta \in [-1, 1]$  represents the intrinsic coordinate of the parent element. It is noted that the calculation of corrected coefficients  $A_i^{B\pm}(\xi)$  and  $A_i^{A\pm}(\xi)$  is performed in the previous section.

Equations (15) can be expressed in a more concise manner by defining

$$T_{jk}^B = \begin{cases} \int_{L_e} t^B(\xi_j, \eta, \omega) \phi_k(\eta) dL(\eta) & j \neq k \\ \int_{L_e} t^B(\xi_j, \eta, \omega) \phi_k(\eta) dL(\eta) + \frac{1}{2} & j = k \end{cases} \tag{16}$$

$$G_{jk}^B = \int_{L_e} u^B(\xi_j, \eta, \omega) \phi_k(\eta) dL(\eta),$$

$$T_{jk}^A = \begin{cases} \int_{L_e} t^A(\mathbf{v}_j, \eta, \omega) \phi_k(\eta) dL(\eta) & j \neq k \\ \int_{L_e} t^A(\mathbf{v}_j, \eta, \omega) \phi_k(\eta) dL(\eta) + \frac{1}{2} & j = k \end{cases} \tag{17}$$

$$G_{jk}^A = \int_{L_e} u^A(\mathbf{v}_j, \eta, \omega) \phi_k(\eta) dL(\eta),$$

where the subscripts represent the collocation points  $\xi_j$  and  $\mathbf{v}_j$  with the node  $k$  of element  $e$ . Then the above equations are rewritten as

$$\begin{aligned}
& \sum_{e \in L_0 \cup L_1 \cup L_3} \sum_{k=1}^{N_e} T_{jk}^B u(\xi_j, \omega) + \sum_{i=1}^n A_i^{B-}(\xi_j) R_i^-(\omega) \\
& + \sum_{i=1}^n A_i^{B+}(\xi_j) R_i^+(\omega) = \sum_{e \in L_1 \cup L_3} \sum_{k=1}^{N_e} G_{jk}^B t(\xi_j, \omega) \\
& \qquad \qquad \qquad j = 1, 2, \dots, N_1,
\end{aligned} \tag{18}$$

$$\begin{aligned}
& \sum_{e \in L_3} \sum_{k=1}^{N_e} T_{jk}^A u(\mathbf{v}_k, \omega) + \sum_{i=1}^n A_i^{A-}(\mathbf{v}_j) R_i^-(\omega) \\
& + \sum_{i=1}^n A_i^{A+}(\mathbf{v}_j) R_i^+(\omega) = \sum_{e \in L_3} \sum_{k=1}^{N_e} G_{jk}^A t(\mathbf{v}_k, \omega) \\
& \qquad \qquad \qquad j = 1, 2, \dots, N_2.
\end{aligned} \tag{19}$$

Then, let us assemble the local elements  $T_{jk}^B, G_{jk}^B$  into global matrices  $\mathbf{H}^B, \mathbf{G}^B$ , the node displacement  $u(\xi_j, \omega)$  and node traction  $t(\xi_j, \omega)$  into global matrices  $\mathbf{U}^B, \mathbf{T}^B$ , and the correction  $A_i^{B\pm}(\xi_j)$  and the unknown amplitudes  $R_i^\pm(\omega)$  into the correction matrices  $\mathbf{A}^{B\pm}$  and the amplitude matrices  $\mathbf{R}^\pm$ . Equation (18) can be written as

$$\mathbf{H}^B \mathbf{U}^B + \mathbf{A}^{B\pm} \mathbf{R}^\pm = \mathbf{G}^B \mathbf{T}^B, \tag{20}$$

where

$$\mathbf{U}^B = [u(\xi_1, \omega) \ u(\xi_2, \omega) \ \dots \ u(\xi_{N_1}, \omega)]^T$$

$$\mathbf{T}^B = [t(\xi_1, \omega) \ t(\xi_2, \omega) \ \dots \ t(\xi_{N_1}, \omega)]^T$$

$$\mathbf{A}^{B\pm} = \begin{bmatrix} A_1^{B\pm}(\xi_1) & A_2^{B\pm}(\xi_1) & \dots & A_n^{B\pm}(\xi_1) \\ A_1^{B\pm}(\xi_2) & A_2^{B\pm}(\xi_2) & \dots & A_n^{B\pm}(\xi_2) \\ \vdots & \vdots & \ddots & \vdots \\ A_1^{B\pm}(\xi_{N_1}) & A_2^{B\pm}(\xi_{N_1}) & \dots & A_n^{B\pm}(\xi_{N_1}) \end{bmatrix} \tag{21}$$

$$\mathbf{R}^\pm = [R_1^\pm(\omega) \ R_2^\pm(\omega) \ \dots \ R_n^\pm(\omega)]^T.$$

Conveniently, the corrected BEM system can be rewritten as

$$\begin{aligned}
& \begin{bmatrix} \mathbf{T}_{11}^B & \mathbf{T}_{12}^B & \mathbf{T}_{13}^B & \mathbf{T}_{14}^B \\ \mathbf{T}_{21}^B & \mathbf{T}_{22}^B & \mathbf{T}_{23}^B & \mathbf{T}_{24}^B \\ \mathbf{T}_{31}^B & \mathbf{T}_{32}^B & \mathbf{T}_{33}^B & \mathbf{T}_{34}^B \\ \mathbf{T}_{41}^B & \mathbf{T}_{42}^B & \mathbf{T}_{43}^B & \mathbf{T}_{44}^B \end{bmatrix} \begin{bmatrix} \mathbf{U}_0 \\ \mathbf{U}_3 \\ \mathbf{U}_1 \\ \mathbf{U}_3^+ \end{bmatrix} + \mathbf{A}^{B\pm} \mathbf{R}^\pm \\
& = \begin{bmatrix} \mathbf{G}_{11}^B & \mathbf{G}_{12}^B & \mathbf{G}_{13}^B & \mathbf{G}_{14}^B \\ \mathbf{G}_{21}^B & \mathbf{G}_{22}^B & \mathbf{G}_{23}^B & \mathbf{G}_{24}^B \\ \mathbf{G}_{31}^B & \mathbf{G}_{32}^B & \mathbf{G}_{33}^B & \mathbf{G}_{34}^B \\ \mathbf{G}_{41}^B & \mathbf{G}_{42}^B & \mathbf{G}_{43}^B & \mathbf{G}_{44}^B \end{bmatrix} \begin{bmatrix} \mathbf{T}_0 \\ \mathbf{T}_3^- \\ \mathbf{T}_1 \\ \mathbf{T}_3^+ \end{bmatrix},
\end{aligned} \tag{22}$$

where  $\mathbf{T}_{ij}^B, \mathbf{G}_{ij}^B$  are block matrices of  $\mathbf{T}^B, \mathbf{G}^B$  and  $\mathbf{U}_\alpha^\pm, \mathbf{T}_\alpha^\pm$  are the node displacement vectors and node traction vectors corresponding to  $L_\alpha^\pm$ , respectively.

Analogously, (19) can be expressed in matrix form:

$$\mathbf{H}^A \mathbf{U}^A + \mathbf{A}^{A\pm} \mathbf{R}^\pm = \mathbf{G}^A \mathbf{T}^A, \tag{23}$$

where

$$\mathbf{U}^A = [u(\mathbf{v}_1, \omega) \quad u(\mathbf{v}_2, \omega) \quad \cdots \quad u(\mathbf{v}_{N_2}, \omega)]^T \quad (24)$$

$$\mathbf{T}^A = [t(\mathbf{v}_1, \omega) \quad t(\mathbf{v}_2, \omega) \quad \cdots \quad t(\mathbf{v}_{N_2}, \omega)]^T$$

$$\mathbf{A}^{A\pm} = \begin{bmatrix} A_1^{A\pm}(\mathbf{v}_1) & A_2^{A\pm}(\mathbf{v}_1) & \cdots & A_n^{A\pm}(\mathbf{v}_1) \\ A_1^{A\pm}(\mathbf{v}_2) & A_2^{A\pm}(\mathbf{v}_2) & \cdots & A_n^{A\pm}(\mathbf{v}_2) \\ \vdots & \vdots & \vdots & \vdots \\ A_1^{A\pm}(\mathbf{v}_{N_1}) & A_2^{A\pm}(\mathbf{v}_{N_1}) & \cdots & A_n^{A\pm}(\mathbf{v}_{N_1}) \end{bmatrix}, \quad (25)$$

$$\begin{bmatrix} \mathbf{T}_{11}^A & \mathbf{T}_{12}^A & \mathbf{T}_{13}^A \\ \mathbf{T}_{21}^A & \mathbf{T}_{22}^A & \mathbf{T}_{23}^A \\ \mathbf{T}_{31}^A & \mathbf{T}_{32}^A & \mathbf{T}_{33}^A \end{bmatrix} \begin{bmatrix} \mathbf{U}_3^- \\ \mathbf{U}_5 \\ \mathbf{U}_3^+ \end{bmatrix} + \mathbf{A}^{A\pm} \mathbf{R}^\pm$$

$$= \begin{bmatrix} \mathbf{G}_{11}^A & \mathbf{G}_{12}^A & \mathbf{G}_{13}^A \\ \mathbf{G}_{21}^A & \mathbf{G}_{22}^A & \mathbf{G}_{23}^A \\ \mathbf{G}_{31}^A & \mathbf{G}_{32}^A & \mathbf{G}_{33}^A \end{bmatrix} \begin{bmatrix} \mathbf{T}_3^- \\ \mathbf{T}_5 \\ \mathbf{T}_3^+ \end{bmatrix}, \quad (26)$$

where  $\mathbf{T}_{ij}^B$ ,  $\mathbf{G}_{ij}^B$  are block matrices of  $\mathbf{T}^B$ ,  $\mathbf{G}^B$  and  $\mathbf{U}_\alpha^\pm$ ,  $\mathbf{T}_\alpha^\pm$  are the node displacement vectors and node traction vectors corresponding to  $L_\alpha^\pm$ , respectively.

It should be pointed out that the unknown coefficient matrices  $\mathbf{R}^\pm$  which are assembled into the modified BEM system ((20) and (23)), will add  $2n$  degrees of freedom into the final BEM system of equations. Here, we propose a modified method for Love-wave multimode by introducing finite sequence truncated points on far-field regions. Based on the far-field assumption (see (6)), far-field displacements of  $2n$  sequence points  $\xi_{m+i}$  ( $i = 1, 2, \dots, n$ ) and  $\xi_{N+i-1}$  ( $i = 1, 2, \dots, n$ ) (see Figure 1) are written as

$$u(\xi_{m+i}, \omega) = \sum_{j=1}^n u^{j-}(\xi_{m+i}, \omega) R_j^-(\omega)$$

$$u(\xi_{N+i-1}, \omega) = \sum_{j=1}^n u^{j+}(\xi_{N+i-1}, \omega) R_j^+(\omega) \quad (27)$$

( $i = 1, 2, \dots, n$ ),

which can also be expressed as the form of matrix

$$\mathbf{I}_R^- \mathbf{U}_3^- = \mathbf{U}_R^- \mathbf{R}^-, \quad (28)$$

where

$$\mathbf{I}_R^- = \begin{bmatrix} -\mathbf{I}_n & \mathbf{0} \\ \mathbf{0} & \mathbf{0} \end{bmatrix} \quad (29)$$

$\mathbf{U}_R^-$

$$= \begin{bmatrix} u^{1-}(\xi_{m+1}, \omega) & u^{2-}(\xi_{m+1}, \omega) & \cdots & u^{n-}(\xi_{m+1}, \omega) \\ u^{1-}(\xi_{m+2}, \omega) & u^{2-}(\xi_{m+2}, \omega) & \cdots & u^{n-}(\xi_{m+2}, \omega) \\ \vdots & \vdots & \vdots & \vdots \\ u^{1-}(\xi_{m+n}, \omega) & u^{2-}(\xi_{m+n}, \omega) & \cdots & u^{n-}(\xi_{m+n}, \omega) \end{bmatrix} \quad (30)$$

$$\mathbf{I}_R^+ \mathbf{U}_3^+ = \mathbf{U}_R^+ \mathbf{R}^+, \quad (31)$$

where

$$\mathbf{I}_R^+ = \begin{bmatrix} \mathbf{0} & \mathbf{0} \\ \mathbf{0} & -\mathbf{I}_n \end{bmatrix}$$

$\mathbf{U}_R^+$

$$= \begin{bmatrix} u^{1+}(\xi_{N-n+1}, \omega) & u^{2+}(\xi_{N-n+1}, \omega) & \cdots & u^{n+}(\xi_{N-n+1}, \omega) \\ u^{1+}(\xi_{N-n+2}, \omega) & u^{2+}(\xi_{N-n+2}, \omega) & \cdots & u^{n+}(\xi_{N-n+2}, \omega) \\ \vdots & \vdots & \vdots & \vdots \\ u^{1+}(\xi_N, \omega) & u^{2+}(\xi_N, \omega) & \cdots & u^{n+}(\xi_N, \omega) \end{bmatrix}. \quad (32)$$

Then, by virtue of boundary conditions of two kinds, continuity of displacements and stresses, among the boundary  $L_3$ , (22) and (26) and (28) and (31) are finally assembled into global BEM system, to obtain the scattering coefficients and displacements directly; thus

$$\begin{bmatrix} \mathbf{T}_{11}^B & \mathbf{T}_{12}^B & \mathbf{T}_{13}^B & \mathbf{T}_{14}^B & -\mathbf{G}_{12}^B & \mathbf{0} & -\mathbf{G}_{14}^B & \mathbf{A}_0^B & \mathbf{A}_0^{B+} \\ \mathbf{T}_{21}^B & \mathbf{T}_{22}^B & \mathbf{T}_{23}^B & \mathbf{T}_{24}^B & -\mathbf{G}_{22}^B & \mathbf{0} & -\mathbf{G}_{24}^B & \mathbf{A}_{3-}^B & \mathbf{A}_{3-}^{B+} \\ \mathbf{T}_{31}^B & \mathbf{T}_{32}^B & \mathbf{T}_{33}^B & \mathbf{T}_{34}^B & -\mathbf{G}_{32}^B & \mathbf{0} & -\mathbf{G}_{34}^B & \mathbf{A}_1^B & \mathbf{A}_1^{B+} \\ \mathbf{T}_{41}^B & \mathbf{T}_{42}^B & \mathbf{T}_{43}^B & \mathbf{T}_{44}^B & -\mathbf{G}_{42}^B & \mathbf{0} & -\mathbf{G}_{44}^B & \mathbf{A}_{3+}^B & \mathbf{A}_{3+}^{B+} \\ \mathbf{0} & \mathbf{T}_{11}^A & \mathbf{0} & \mathbf{T}_{13}^A & \mathbf{G}_{11}^A & \mathbf{T}_{12}^A & \mathbf{G}_{13}^A & \mathbf{A}_{3-}^A & \mathbf{A}_{3-}^{A+} \\ \mathbf{0} & \mathbf{T}_{21}^A & \mathbf{0} & \mathbf{T}_{23}^A & \mathbf{G}_{21}^A & \mathbf{T}_{22}^A & \mathbf{G}_{23}^A & \mathbf{A}_5^A & \mathbf{A}_5^{A+} \\ \mathbf{0} & \mathbf{T}_{31}^A & \mathbf{0} & \mathbf{T}_{33}^A & \mathbf{G}_{31}^A & \mathbf{T}_{32}^A & \mathbf{G}_{33}^A & \mathbf{A}_{3+}^A & \mathbf{A}_{3+}^{A+} \\ \mathbf{0} & \mathbf{I}_R^- & \mathbf{0} & \mathbf{0} & \mathbf{0} & \mathbf{0} & \mathbf{0} & \mathbf{U}_R^- & \mathbf{0} \\ \mathbf{0} & \mathbf{0} & \mathbf{0} & \mathbf{I}_R^+ & \mathbf{0} & \mathbf{0} & \mathbf{0} & \mathbf{0} & \mathbf{U}_R^+ \end{bmatrix} \begin{bmatrix} \mathbf{U}_0 \\ \mathbf{U}_{3-} \\ \mathbf{U}_1 \\ \mathbf{U}_{3+} \\ \mathbf{T}_{3-} \\ \mathbf{U}_5 \\ \mathbf{T}_{3+} \\ \mathbf{R}^- \\ \mathbf{R}^+ \end{bmatrix} \quad (33)$$

$$= \begin{bmatrix} \mathbf{G}_{11}^B & \mathbf{G}_{12}^B & \mathbf{G}_{13}^B & \mathbf{G}_{14}^B & \mathbf{0} & \mathbf{0} & \mathbf{0} & \mathbf{0} & \mathbf{0} \\ \mathbf{G}_{21}^B & \mathbf{G}_{22}^B & \mathbf{G}_{23}^B & \mathbf{G}_{24}^B & \mathbf{0} & \mathbf{0} & \mathbf{0} & \mathbf{0} & \mathbf{0} \\ \mathbf{G}_{31}^B & \mathbf{G}_{32}^B & \mathbf{G}_{33}^B & \mathbf{G}_{34}^B & \mathbf{0} & \mathbf{0} & \mathbf{0} & \mathbf{0} & \mathbf{0} \\ \mathbf{G}_{41}^B & \mathbf{G}_{42}^B & \mathbf{G}_{43}^B & \mathbf{G}_{44}^B & \mathbf{0} & \mathbf{0} & \mathbf{0} & \mathbf{0} & \mathbf{0} \\ \mathbf{0} & \mathbf{0} & \mathbf{0} & \mathbf{T}_{13}^A & \mathbf{0} & \mathbf{G}_{12}^A & \mathbf{0} & \mathbf{0} & \mathbf{0} \\ \mathbf{0} & \mathbf{0} & \mathbf{0} & \mathbf{T}_{23}^A & \mathbf{0} & \mathbf{G}_{22}^A & \mathbf{0} & \mathbf{0} & \mathbf{0} \\ \mathbf{0} & \mathbf{0} & \mathbf{0} & \mathbf{T}_{33}^A & \mathbf{0} & \mathbf{G}_{32}^A & \mathbf{0} & \mathbf{0} & \mathbf{0} \\ \mathbf{0} & \mathbf{0} \\ \mathbf{0} & \mathbf{0} \end{bmatrix} \begin{bmatrix} \mathbf{T}_0 \\ \mathbf{0} \\ \mathbf{T}_1 \\ \mathbf{0} \\ \mathbf{0} \\ \mathbf{T}_5 \\ \mathbf{0} \\ \mathbf{0} \\ \mathbf{0} \end{bmatrix},$$

TABLE 1: Comparisons with truncated locations at  $\bar{x} = \pm 60\lambda_L/H$  ( $\lambda_L$  being the Love wavelength for the lowest mode) for the unit line source problem.

Frequency $\bar{\omega}$	Modal	BEM results (far-field amplitudes)	Theoretical far-field Green's functions
1.2	Modal 1	0.13562i	0.13557i
6.5	Modal 1	0.01634i	0.01635i
	Modal 2	0.01335i	0.01335i
10.8	Modal 1	0.00709i	0.00705i
	Modal 2	0.00983i	0.00983i
	Modal 3	-0.0358i	-0.0358i

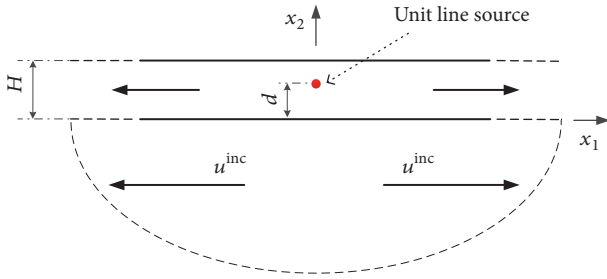


FIGURE 4: Schematic diagram for the unit line source problem.

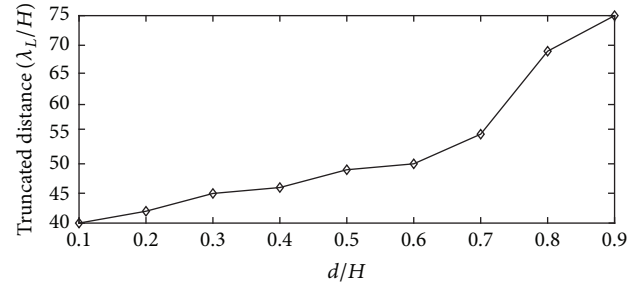


FIGURE 5: Proper truncation distance with various  $d$  for the unit line source problem.

where

$$\mathbf{A}^{B\pm} = \begin{bmatrix} \mathbf{A}_0^{B\pm} \\ \mathbf{A}_{3-}^{B\pm} \\ \mathbf{A}_1^{B\pm} \\ \mathbf{A}_{3+}^{B\pm} \end{bmatrix} \quad (34)$$

$$\mathbf{A}^{A\pm} = \begin{bmatrix} \mathbf{A}_{3-}^{A\pm} \\ \mathbf{A}_5^{A\pm} \\ \mathbf{A}_{3+}^{A\pm} \end{bmatrix}.$$

## 5. Numerical Results

In this section, some numerical examples are illustrated to show the validity and effectiveness of this modified BEM for 2D Love-wave model. In the following numerical examples, the material parameters of the layer and half-plane are dimensionless, which have a shear modulus ratio of  $\mu^B/\mu^A = 1.8$  and a longitudinal wave velocity ratio of  $c_T^B/c_T^A = 0.78$ , and the dimensionless frequency is taken as  $\bar{\omega} = 2\omega H/(c_T^A\pi)$ . The element size is selected to have at least 32 elements per Love wavelength  $\lambda_L$ , which provides accurate results for 2D elastodynamic problem.

Firstly, the numerical results obtained by the modified BEM will be compared with theoretical far-field Green's functions. As shown in Figure 4, this numerical model is a 2D semifinite space with unit harmonic line source acting in  $x_3$  direction, with the distance  $d$  between source and lower interface of the upper-layer. The far-field amplitudes are presented in Table 1 for various frequencies  $\bar{\omega} = 1.2, 6.5, 10.8$ , while a fixed height  $d = 0.5H$ . The far-field

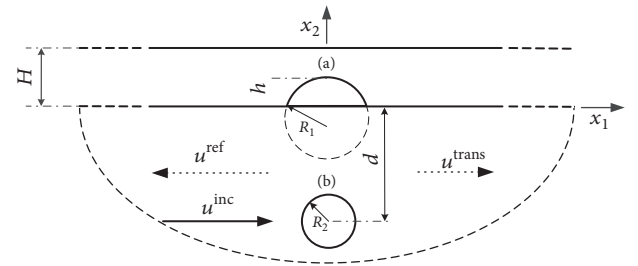


FIGURE 6: Schematic diagram for Love-wave scattering problem: (a) a cavity defect of arc surface on the bonding interface, with radius  $R_1$  and height  $h$ ; (b) a circle defect in half-plane with radius  $R_2$  and depth  $d$ .

coefficients of Love-waves are obtained by modified BEM and compared with theoretical results [1, 2]. The results are in excellent agreement (see Table 1), which show the validity of this modified BEM for a certain range of frequencies. From additional parametric study, it is found from Figure 5 that, as the source moved closer to the top surface, for example,  $d = 0.1 - 0.9H$ , longer surface lengths should remain in the BEM model to ensure the accuracy, which should be kept in mind as a criterion for accurate calculations of these numerical results.

Next, the lowest incident Love-wave mode for a fixed frequency is selected to impinge onto a cavity defect of arc surface on the bonding interface, with radius  $R_1 = H$  and height  $h$  (see Figure 6). The transmission and reflection coefficients for each modal at various frequencies:  $\bar{\omega} = 0.8, 5, 9.5$ , are shown in Table 2. And the normalized displacements for the same frequency range which are here defined as  $U_{\text{scat}}^\pm / \sum_{i=1}^n R_i^\pm U^{i\pm}$  are plotted. It is observed from Figures 7(a)–7(c) that the scattered displacements are approximated

TABLE 2: The transmission and reflection coefficients with truncated locations at  $\bar{x} = \pm 60\lambda_L/H$ ,  $h = 0.2$  ( $\lambda_L$  being the Love wavelength for the lowest mode), for a circle arc defect at the bonding interface.

Frequency $\bar{\omega}$	Modal	Reflection coefficients	Transmission coefficients
0.8	Modal 1	0.00039 – 0.07060i	–0.00582 + 0.03457i
5	Modal 1	–0.04383 + 0.10690i	0.01638 + 0.02342i
	Modal 2	–0.11344 + 0.06911i	0.07724 + 0.11906i
	Modal 1	–0.03315 + 0.08802i	0.00531 + 0.00383i
9.5	Modal 2	–0.19330 + 0.36373i	0.04204 + 0.03600i
	Modal 3	–0.22045 – 0.05598i	0.07071 + 0.09606i

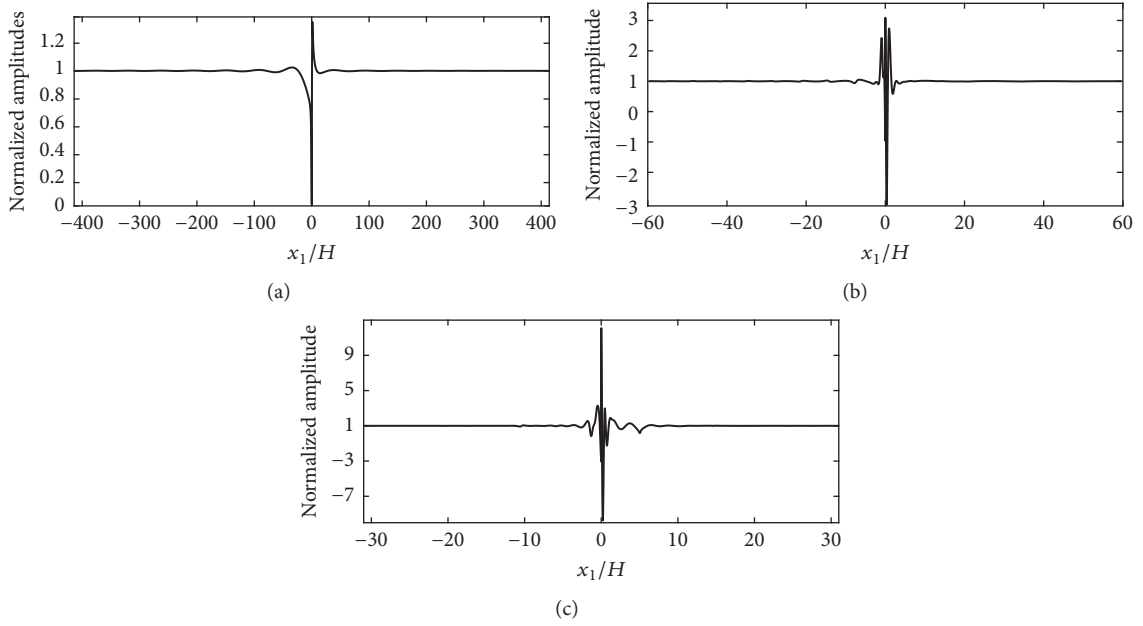


FIGURE 7: Normalized amplitudes of upper boundary due to a defect at the bonding interface: (a)  $\bar{\omega} = 0.8$ ; (b)  $\bar{\omega} = 5$ ; (c)  $\bar{\omega} = 9.5$ .

by Love surface waves at far ends, which satisfy the assumptions of (6).

For basic check purposes, propagations in the opposite directions for the same frequency range are considered, and numerical solutions show very good agreement in all cases owing to the symmetry of the defect. Furthermore, a parametric study has been carried out to analyze the influence of defect height  $h = 0.2, 0.4, 0.6, 0.8$ , on the reflected and transmitted amplitudes which are defined as  $A^{\text{ref}} = u_{\text{scat}}^-/u^-$  and  $A^{\text{trans}} = (u_{\text{scat}}^+ + u^{\text{inc}})/u^+$ . It is found from Figure 8 that as the defect becomes larger, the absolute value of the transmitted amplitude gradually decreases and the absolute value of the reflected amplitude is diverse.

Finally, we consider the lowest incident Love-wave mode for a fixed frequency impinging onto the circle defect in half-plane with radius  $R_2 = 0.2H$  and depth  $d = 0.5H$ , in the positive direction of  $x_1$  (see Figure 6(b)). The transmission and reflection coefficients of various frequencies:  $\bar{\omega} = 0.8, 5, 9.5$ , are performed in Table 3. As the relative normalized displacements are plotted in Figure 9(a)–9(c), we could get the same conclusion that the scattered displacements are approximated by Love surface waves at far ends. Also, numerical results for propagation in opposite direction

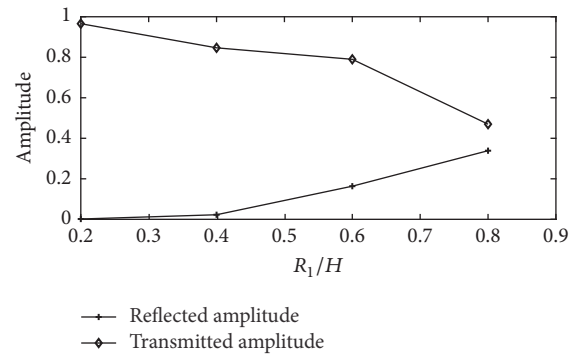


FIGURE 8: Reflected and transmitted amplitudes due to a defect at the bonding interface.

show very good agreement due to the symmetry of the defect.

## 6. Conclusion

In this paper, we proposed a modified BEM for scattering problem of Love surface wave by a defect. The guided

TABLE 3: The transmission and reflection coefficients with truncated locations at  $\bar{x} = \pm 60\lambda_L/H$ ,  $R_2 = 0.2$ , and  $d = 0.5$  ( $\lambda_L$  being the Love wavelength for the lowest mode) for a circle defect in half-plane.

Frequency $\bar{\omega}$	Modal	Reflection coefficients	Transmission coefficients
0.8	Modal 1	$-0.00026 + 0.00746i$	$-0.00026 + 0.00758i$
5	Modal 1	$-0.00004 + 0.00052i$	$-0.00028 + 0.00202i$
	Modal 2	$0.00046 + 0.00494i$	$-0.00190 + 0.01682i$
9.5	Modal 1	$0.00001 - 0.00001i$	$-0.00002 + 0.00010i$
	Modal 2	$0.00003 - 0.00005i$	$-0.00017 + 0.00090i$
	Modal 3	$0.00018 - 0.00027i$	$-0.00060 + 0.00375i$

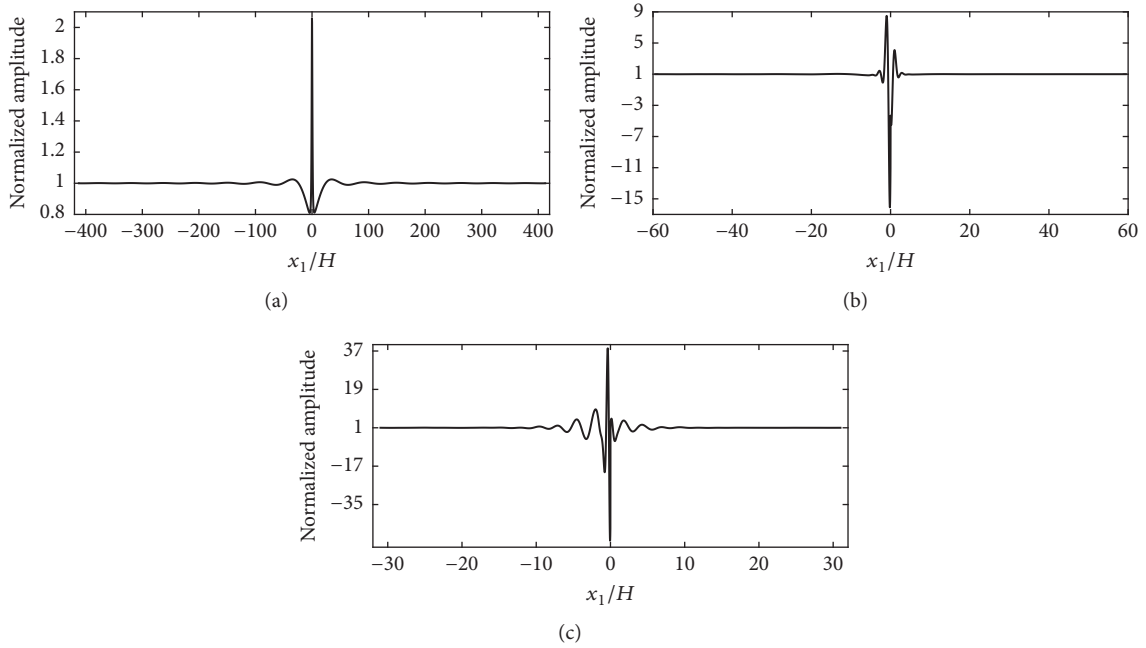


FIGURE 9: Normalized amplitudes of upper boundary due to a circle defect in half-plane: (a)  $\bar{\omega} = 0.8$ ; (b)  $\bar{\omega} = 5$ ; (c)  $\bar{\omega} = 9.5$ .

Love-wave displacement patterns are assumed on the far-field infinite boundaries previously omitted, and they are incorporated into the BEM system as the modified items. With this improvement, the spurious reflected waves were eliminated. The validity and effectiveness of this modified BEM were numerically checked by theoretical far-field Green's functions. Various parametric results show that this method can be applied on the Love-wave model with a defect of arbitrary shape and location, and as the geometrical size of the defect becomes larger, the transmitted wave gradually decreases and the reflected wave is diverse.

In the future, the scattering data from forward analysis by this modified BEM will be used for the inverse analysis of reconstructing both the location and specific geometric information of the debonding cavities.

### Conflicts of Interest

The authors declare that they have no conflicts of interest.

### Acknowledgments

This work was supported by the National Natural Science Foundation of China (nos. 11502108, 11611530686, and 11232007), the Natural Science Foundation of Jiangsu Province (no. BK20140037), and a project funded by the Priority Academic Program Development of Jiangsu Higher Education Institutions (PAPD).

### References

- [1] J. L. Rose, "A baseline and vision of ultrasonic guided wave inspection potential," *Journal of Pressure Vessel Technology, Transactions of the ASME*, vol. 124, no. 3, pp. 273–282, 2002.
- [2] A. Raghavan and C. E. S. Cesnik, "Review of guided-wave structural health monitoring," *The Shock and Vibration Digest*, vol. 39, no. 2, pp. 91–114, 2007.
- [3] M. Capriotti, H. E. Kim, F. L. di Scalea, and H. Kim, "Non-destructive inspection of impact damage in composite aircraft panels by ultrasonic guided waves and statistical processing," *Materials*, vol. 10, no. 6, article no. 616, 2017.

- [4] K. M. Qatu, A. Abdelgawad, and K. Yelamarthi, "Structure damage localization using a reliable wave damage detection technique," in *Proceedings of the 2016 International Conference on Electrical, Electronics, and Optimization Techniques, ICEEOT 2016*, pp. 1959–1962, India, March 2016.
- [5] H. F. Wu, A. L. Gyekenyesi, P. J. Shull et al., "Numerical and experimental simulation of linear shear piezoelectric phased arrays for structural health monitoring," in *Proceedings of the SPIE Smart Structures and Materials + Nondestructive Evaluation and Health Monitoring*, p. 1016912, Portland, Oregon, United States.
- [6] E. V. Malyarenko and M. K. Hinders, "Ultrasonic Lamb wave diffraction tomography," *Ultrasonics*, vol. 39, no. 4, pp. 269–281, 2001.
- [7] B. Wang and S. Hirose, "Inverse problem for shape reconstruction of plate-Thinning by guided SH-Waves," *Materials Transactions*, vol. 53, no. 10, pp. 1782–1789, 2012.
- [8] B. Wang and S. Hirose, "Shape reconstruction of plate thinning using reflection coefficients of ultrasonic lamb waves: a numerical approach," *ISIJ International*, vol. 52, no. 7, pp. 1328–1335, 2012.
- [9] B. Wang, Y. Da, and Z. Qian, "Reconstruction of surface flaw shape using reflection data of guided Rayleigh surface waves," *International Journal of Applied Electromagnetics and Mechanics*, vol. 52, no. 1-2, pp. 41–48, 2016.
- [10] R. Kakar, "Love waves in Voigt-type viscoelastic inhomogeneous layer overlying a gravitational half-space," *International Journal of Geomechanics*, vol. 16, no. 3, Article ID 04015068, 2016.
- [11] P. Destuynder and C. Fabre, "Few remarks on the use of Love waves in non destructive testing," *Discrete and Continuous Dynamical Systems - Series S*, vol. 9, no. 2, pp. 427–444, 2016.
- [12] X. Jiang, P. Li, J. Lv, and W. Zheng, "An adaptive finite element method for the wave scattering with transparent boundary condition," *Journal of Scientific Computing*, vol. 72, no. 3, pp. 936–956, 2017.
- [13] J. D. Achenbach, "Acoustic emission from a surface-breaking crack in a layer under cyclic loading," *Journal of Mechanics of Materials and Structures*, vol. 4, no. 4, pp. 649–657, 2009.
- [14] A. Gunawan and S. Hirose, "Mode-exciting method for Lamb wave-scattering analysis," *The Journal of the Acoustical Society of America*, vol. 115, no. 3, pp. 996–1005, 2004.
- [15] P. C. Waterman, "Matrix theory of elastic wave scattering," *The Journal of the Acoustical Society of America*, vol. 60, no. 3, pp. 567–580, 1976.
- [16] I. Herrera, "On a method to obtain a Green's function for a multi-layered half-space," *Bulletin of the Seismological Society of America*, vol. 54, no. 4, pp. 1087–1096, 1964.
- [17] J. D. Achenbach, *Reciprocity in elastodynamics*, Cambridge Monographs on Mechanics, Cambridge University Press, Cambridge, 2003.
- [18] B. Michel, "Beskos, D. E., Boundary Element Methods in Mechanics. Computational Methods in Mechanics Vol. 3. Amsterdam etc., North-Holland 1987. X, 598 pp., Dfl. 300.-. ISBN 0-444-87990-0 (Mechanics and Mathematical Methods)," *ZAMM - Journal of Applied Mathematics and Mechanics / Zeitschrift für Angewandte Mathematik und Mechanik*, vol. 69, no. 1, pp. 54–54, 1989.

## Research Article

# Dynamic Characteristic and Fatigue Accumulative Damage of a Cross Shield Tunnel Structure under Vibration Load

Qixiang Yan,<sup>1</sup> Hang Chen ,<sup>1</sup> Wenyu Chen,<sup>1</sup> Junchen Zhang,<sup>1</sup> Shuqi Ma ,<sup>1</sup> and Xi Huang<sup>2</sup>

<sup>1</sup>Key Laboratory of Transportation Tunnel Engineering, Ministry of Education, Southwest Jiaotong University, Chengdu 610031, China

<sup>2</sup>Chengdu Survey, Design and Research Co. Ltd., Chengdu 610031, China

Correspondence should be addressed to Hang Chen; [chenhangssd@163.com](mailto:chenhangssd@163.com) and Shuqi Ma; [shuqima@qq.com](mailto:shuqima@qq.com)

Received 19 September 2017; Accepted 9 January 2018; Published 13 March 2018

Academic Editor: Sandris Ručevskis

Copyright © 2018 Qixiang Yan et al. This is an open access article distributed under the Creative Commons Attribution License, which permits unrestricted use, distribution, and reproduction in any medium, provided the original work is properly cited.

This study presents an improved constitutive model for concrete under uniaxial cyclic loading which considers the fatigue stiffness degradation, fatigue strength degradation, and fatigue residual strain increment of concrete fatigue damage. According to the constitutive model, the dynamic response and cumulative damage of the tunnel cross structure under various train operation years were analyzed. The results show that the vibration in the middle of the main tunnel is most violent. With the increase of train operation period, the acceleration in the middle of the transverse passage floor, both sides of the wall corner and the vault increase significantly, and the maximum principal stress increases significantly only in both sides of the wall corner. The compressive damage is mainly distributed at both sides of the wall corner, while tensile damage is distributed in both sides of the inner wall corner. The accumulative damage of the cross structure exhibits a two-stage profile. The size and range of accumulative tensile damage of the connecting transverse passage are greater than those of accumulative compressive damage.

## 1. Introduction

For long and large tunnels, a certain number of connecting transverse passages are normally set up to meet the needs of the operating ventilation, accident evacuation, fire rescue, and other functions. The use of these passages forms the cross tunnel structures. This kind of structure is complex, which lead to uneven distributed forces for the whole structure. The stress concentration most often appears at the intersection due to the train vibration loads [1–4]. In addition, during the service life of the tunnel, the cross tunnel structure is subjected to the vibration loads caused by the train for a long time. The concrete material deteriorates continuously, and the structure is damaged and cracked all the time, which ultimately results in structural damage and poses serious threat to the operational safety of the structure [5–10]. Therefore, it is very important to study the dynamic response and fatigue cumulative damage law of the special structure of the cross tunnel under long-term train which caused loads for the safety of long and large tunnels.

For the properties of the tunnel lining structure material, the tunnel lining structure is mainly made of reinforced concrete in China [11–15]. The fatigue of concrete structures under cyclic loading causes the damage and cracking of concrete lining. At present, the fatigue performance of concrete structure is mainly studied using indoor fatigue tests. Aas-Jakobsen [16] proposed a general formula for logarithmic lifetime and cyclic stress; Tepfer and Kutti [17] identified the general formula of the basic parameters by the fatigue test; Holmen [18] studied compressive fatigue performance of concrete cylindrical specimens under fatigue load; Huang et al. [19] studied the propagation law of the main crack of reinforced concrete beams strengthened with prestressed CFRP sheet under the fatigue load; Cao et al. [20] studied the fractal characterization in the evolving damage of concrete structures based on physical model experiments and found the surface-crack distribution of the damaged concrete structures.

The fatigue test can accurately describe the fatigue performance of the material, but the test is very time-consuming,

and it is difficult to conduct full-scale tests. Researchers started to use numerical methods to study the fatigue damage of the complex structure. Teng and Wang [21] proposed a two-dimensional damage constitutive model of a reinforced concrete structure; Petryna and Krätzig [22] proposed a calculation method for long-term performance evaluation of reinforced concrete structures considering the accumulated damage; Zhang and Shi [23] used the finite element method to study the interface peel stress and its influencing factors on reinforcement and concrete under the fatigue load; J.-S. Zhu and X.-C. Zhu [24] proposed a simplified method for numerical simulation of the fatigue failure process of reinforced concrete bridge structures under operating loads; Wang [25] established a stochastic damage constitutive model based on modified elastomeric Helmholtz free energy under tension and compressive conditions; Wang [26] proposed an equivalent static analysis method for the fatigue cumulative damage process of concrete components.

For the vibration effects caused by train, studies have been conducted on the dynamic response characteristics of tunnels under the train vibration. Gharehdash and Barzegar [27] used a complex elastoplastic 3D dynamic finite difference model by fully considering the joints to study the dynamic response of the shield tunnel buried in soft soil under the vibration loads; Gupta et al. [28] presented the experimental validation of a numerical model for the prediction of subway induced vibrations; Gupta et al. [29] used a coupled periodic finite element-boundary element model to study the vibration response from a Thalys high-speed train in the Groene Hart tunnel; Lin [30] studied the dynamic response of the tunnel under different conditions, such as the reconstruction of the train vibration load.

However, most of the current methods are complex in theory and cannot simulate the fatigue damage behavior of concrete structures under high cyclic loads. Most of the studies only focus on the fatigue analysis of concrete beams, aiming at the dynamic response of the tunnel under the train causing vibration loads. There is a lack of research on dynamic responses of the tunnel structure under the high cyclic loads and lack of the fatigue damage analysis of the cross tunnel structure, formed by the main tunnel and the transverse passage.

The improved uniaxial cyclic loading constitutive model for concrete is proposed based on the latest concrete uniaxial monotone load constitutive model given by “Code for Design of Concrete Structures” (GB50010-2010) [31], together with the concrete fatigue constitutive relation proposed by J. S. Zhu and X. C. Zhu [24]. This model is able to more accurately simulate the mechanical behavior of the commonly used concrete. The formulas for calculating the concrete fatigue stiffness variables, fatigue residual strength variables, and fatigue residual strain variables are included in the cyclic loading constitutive model. Based on the actual situation of the Shiziyang tunnel project of Guangzhou-Shenzhen-Hongkong Railway Passenger Dedicated Line, numerical analysis models were established, and the dynamic response and cumulative damage characteristics of the tunnel cross structures under train vibration load were analyzed.

## 2. Constitutive Model of Concrete Uniaxial Monotone Loading

The stress-strain curves of concrete under monotonic compression were obtained according to the test data fitting in the “Code for Design of Concrete Structures” (GB50010-2010) and are as follows [31]:

$$\sigma_c = k_c E_c \varepsilon, \quad (1)$$

where

$$k_c = \begin{cases} \frac{\rho_c n}{n-1+x^n}, & x \leq 1 \\ \frac{\rho_c}{\alpha_c (x-1)^2 + x}, & x > 1, \end{cases} \quad (2)$$

$$x = \frac{\varepsilon}{\varepsilon_{cr}},$$

$$\rho_c = \frac{f_c}{E_c \varepsilon_{cr}},$$

$$n = \frac{E_c \varepsilon_{cr}}{E_c \varepsilon_{cr} - f_c},$$

$$\alpha_c = 0.157 f_c^{0.785} - 0.905,$$

where  $\varepsilon$  is concrete strain;  $E_c$  is nondestructive elastic modulus of concrete;  $\sigma_c$  is compressive stress of concrete;  $f_c$  is peak compressive stress;  $\varepsilon_{cr}$  is peak compressive strain corresponding to the peak compressive stress and can be taken as  $\varepsilon_{cr} = (700 + 172\sqrt{f_c}) \times 10^{-6}$ .

When the concrete is monotonically tensile, the stress-strain curve is as follows [32]:

$$\sigma_t = k_t E_c \varepsilon, \quad (3)$$

where

$$k_t = \begin{cases} \rho_t (1.2 - 0.2x^5), & x \leq 1 \\ \frac{\rho_t}{\alpha_t (x-1)^{1.7} + x}, & x > 1, \end{cases} \quad (4)$$

$$x = \frac{\varepsilon}{\varepsilon_{tr}},$$

$$\rho_t = \frac{f_t}{E_c \varepsilon_{tr}},$$

$$\alpha_t = 0.312 f_t^2,$$

where  $\sigma_t$  is concrete tensile stress;  $f_t$  is peak tensile stress;  $\varepsilon_{tr}$  is the peak tensile strain corresponding to the peak tensile stress and can be taken as  $\varepsilon_{tr} = 65 f_t^{0.54} \times 10^{-6}$ .

## 3. Constitutive Model of Concrete under Uniaxial Cyclic Loading

The related research [33] shows that the fatigue damage of concrete structures under cyclic loading is mainly demonstrated in three aspects: stiffness decrease, strength degradation, and residual strain increase. Therefore, according to

concrete uniaxial constitutive model of the above specification and the concrete fatigue constitutive relation proposed by J. S. Zhu and X. C. Zhu [24], the fatigue constitutive model of concrete under uniaxial compression can be proposed: that is, the stress-strain curve is as follows:

$$\sigma_c = k'_c E_c(N) (\varepsilon - \Delta\varepsilon_r(N-1)), \quad (5)$$

where the residual strain of concrete  $\Delta\varepsilon_r(N-1)$  after  $N-1$  times fatigue loads, the peak compressive strain  $\varepsilon_{cr}(N)$ , and the modulus of elasticity  $E_c(N)$  after  $N$  times fatigue loads are considered, and the relevant revised parameters for the constitutive model are as follows:

$$k'_c = \begin{cases} \frac{\rho'_c n'}{n' - 1 + x^{n'}}, & x \leq 1 \\ \frac{\rho'_c}{\alpha_c (x-1)^2 + x}, & x > 1, \end{cases} \quad (6)$$

$$x = \frac{\varepsilon - \Delta\varepsilon_r(N-1)}{\varepsilon_{cr}(N)},$$

$$\rho'_c = \frac{\sigma_{rc}(N)}{E_c(N) \varepsilon_{cr}(N)},$$

$$n' = \frac{E_c(N) \varepsilon_{cr}(N)}{E_c(N) \varepsilon_{cr}(N) - \sigma_{rc}(N)},$$

$$\alpha'_c = 0.157 \sigma_{rc}^{0.785}(N) - 0.905.$$

Considering the effect of peak compressive stress  $\sigma_{rc}(N)$  after  $N$  times fatigue loads, the peak compressive strain can be obtained after  $N$  times fatigue loads:

$$\varepsilon_{cr}(N) = \left(700 + 172 \sqrt{\sigma_{rc}(N)}\right) \times 10^{-6}. \quad (7)$$

Similarly, when concrete is subjected to tensile loads, the formula can be proposed as follows:

$$\sigma_t = k'_t E_c(N) (\varepsilon - \Delta\varepsilon_r(N-1)), \quad (8)$$

where the residual strain of concrete  $\Delta\varepsilon_r(N-1)$ , peak tensile strain  $\varepsilon_{tr}(N)$ , and elastic modulus  $E_c(N)$  are considered, and the parameters are revised as follows:

$$k'_t = \begin{cases} \rho'_t (1.2 - 0.2x^5), & x \leq 1 \\ \frac{\rho'_t}{\alpha_t (x-1)^{1.7} + x}, & x > 1, \end{cases} \quad (9)$$

$$x = \frac{\varepsilon - \Delta\varepsilon_r(N-1)}{\varepsilon_{tr}(N)},$$

$$\varepsilon_{tr}(N) = 65 \sigma_{rt}^{0.54}(N) \times 10^{-6},$$

$$\rho'_t = \frac{\sigma_{rt}(N)}{E_c(N) \varepsilon_{tr}(N)},$$

$$\alpha'_t = 0.312 \sigma_{rt}^2(N),$$

where  $\sigma_{rt}(N)$  is the structural concrete peak tensile stress after loading the  $N$  times fatigue load and  $\varepsilon_{tr}(N)$  is the peak tensile strain after loading  $N$  times fatigue load.

3.1. *Concrete Fatigue Stiffness Related Variable  $E_c(N)$* . According to the relevant fatigue test, Holmen [18] proposed the degradation formula for the concrete elastic modulus:

$$E_c(N) = \left(1 - \frac{0.33N}{N_f}\right) E_c, \quad (10)$$

where  $N_f$  is the concrete fatigue life.

3.2. *Concrete Fatigue Residual Strength Variables  $\sigma_{rc}(N)$  and  $\sigma_{rt}(N)$* . The residual fatigue strength of concrete is related to the number of fatigue load cycles and the maximum and minimum stresses of the load [21].

The study [32] shows that the maximum total strain when concrete is broken under tensile and compressive fatigue loads is equivalent to the strain corresponding to the maximum stress of fatigue load in monotonic loading softening section, as shown in Figure 1, the point B in the stress-strain curve of concrete under uniaxial static load and fatigue process. It is assumed that the concrete fatigue residual strength envelope [34] is represented by the shape of softening section of monotonic loading stress-strain curve of the concrete. Therefore, the concrete residual strength envelope can be obtained by the softening section shape of monotonic loading stress-strain curve of the concrete.

According to the softening section shape of the monotonic stress-strain relationship curves of the concrete, the envelope equation of the residual fatigue strength of the concrete can be obtained as follows: [24]

$$\sigma_{rc}(N) = \frac{x(N) f_c}{\alpha_c (x(N) - 1)^2 + x(N)}, \quad (11)$$

where  $x(N)$  is the function of fatigue load times  $N$ : that is [24],

$$x(N) = \frac{\lg N}{\lg N_f} [x(N_f) - 1] + 1. \quad (12)$$

The tensile residual strength envelope of concrete is shown by the following equation [24]:

$$\sigma_{rt}(N) = \frac{x(N) f_t}{\alpha_t (x(N) - 1)^{1.7} + x(N)}. \quad (13)$$

Considering the initial conditions of concrete residual strength and failure criterion, the boundary conditions were taken into account in the concrete compressive and tensile fatigue residual envelope equation. The concrete compressive and tensile dependent variables A and B were available. Substituting those variables to formulas (11) and (13), the fatigue residual strength of concrete can be obtained.

3.3. *Residual Strain of Concrete Fatigue  $\Delta\varepsilon_r(N)$* . Holmen obtained the formula of the fatigue residual strain of concrete by the curve fitting the experimental data, without considering the stress ratio. The formula is as follows: [19]:

$$\Delta\varepsilon_r(N) = \Delta\varepsilon_r(1) + \frac{k_1 \varepsilon_{\max}^{k_2} (1 - \varepsilon_{\min}/\varepsilon_{\max})^{k_3}}{\varepsilon_k^{k_5}} N^{k_4}, \quad (14)$$

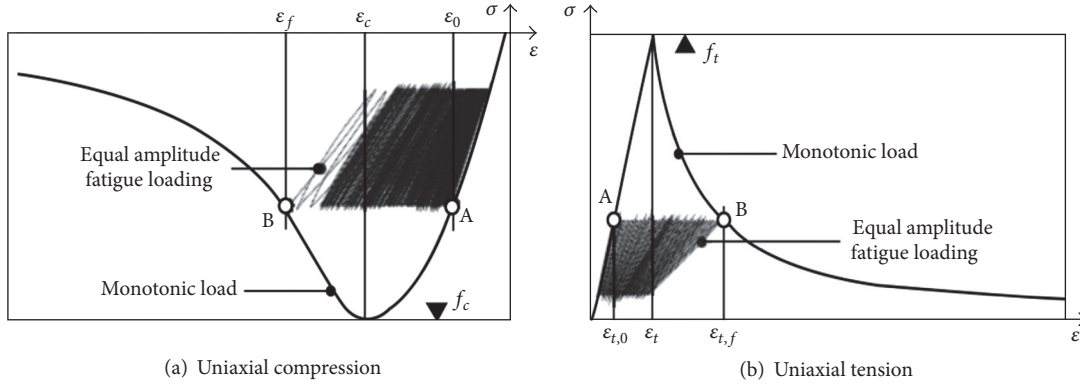


FIGURE 1: The concrete uniaxial static load and fatigue stress-strain curves.

where  $\Delta\epsilon_r(1)$  is the residual strain of the structure after 1 time fatigue load;  $\epsilon_{\max}$ ,  $\epsilon_{\min}$  are the maximum stress and minimum stress of the structure when the fatigue load reaches the upper or lower limit of stress, respectively.  $\epsilon_k$  is the longitudinal total strain when the residual strain of concrete enters the final stage. The experimental result shows that it is close to the peak strain in the uniaxial stress-strain curve of concrete [33]. Wang et al. [35] obtained fatigue residual strain formula with the material constants through the fatigue test data fitting analysis and is as follows:

$$\Delta\epsilon_r(N) = \Delta\epsilon_r(1) + \frac{0.00105\epsilon_{\max}^{1.98}(1 - \epsilon_{\min}/\epsilon_{\max})^{5.27}}{\epsilon_k^{1.41}} N^{0.395}. \quad (15)$$

#### 4. Life Analysis Method of Concrete Structure

Life estimation was based on FE-SAFE fatigue analysis software. Firstly, the ABAQUS calculation was used to obtain the dynamic response of the cross structure in the process of the train operation in the tunnel. Secondly, the concrete stress-life curve (i.e., S-N curve) of concrete was determined by formulas (16) and (17). Based on FE-SAFE's nominal stress prediction method, the dynamic response and N-S curve of the cross structure were analyzed, so that the fatigue life of the structure can be obtained.

The fitting formula for the tensile fatigue life and fatigue load curves of concrete [17] was obtained by the uniaxial compression test of concrete, proposed by Tepfers and Kutti:

$$\lg N_{c,f} = \frac{1}{\beta} \left[ \frac{1 - f_{c,\max}/f_{cu}}{1 - f_{c,\min}/f_{c,\max}} \right], \quad (16)$$

where  $\beta$  is the material constant of concrete, the value range is 0.064~0.080, Teng and Wang [21] suggested an average of 0.072;  $f_{c,\max}$ ,  $f_{c,\min}$  are the maximum compressive stress value and the minimum compressive stress value of cyclic load, respectively.  $f_{cu}$  is the compressive strength of concrete.

The tensile fatigue life and fatigue load curves of concrete were obtained by the fitting formula based on concrete fatigue splitting test [17]:

$$\lg N_{t,f} = \frac{1}{\beta} \left[ 1 - \frac{1 - ((f_{t,\max} - f_{t,\min})/f_t)}{1 - f_{t,\min}/f_t} \right], \quad (17)$$

where  $f_{t,\max}$  and  $f_{t,\min}$  are the maximum tensile stress and the minimum tensile stress of the cyclic load, respectively;  $f_t$  is the tensile strength of concrete.

#### 5. Damage Analysis Theory

Plastic flow, microcracks, and microvoids are the fundamental reasons of nonlinearity of concrete. From the macroscopic performance, it shows the obvious difference of concrete tensile strength and compressive strength and the residual deformation of concrete [36]. The plastic damage constitutive model of concrete (CDP model) based on continuous medium was adopted to better simulate the nonlinear properties of concrete subjected to external load [37].

According to the energy equivalent principle proposed by Sidoroff [38], the structural damage factor is as follows:

$$D = 1 - \sqrt{\frac{\tilde{E}}{E_c}}, \quad (18)$$

where  $\tilde{E}$  is the elastic modulus when the concrete is damaged.

According to the plastic damage theory of concrete, when the concrete is tensile, the cracking strain is [37]

$$\epsilon_t^{ck} = \epsilon - \frac{\sigma_t}{E_c}, \quad (19)$$

where  $\sigma_t$  is the tensile stress of concrete.

When the concrete is compressive, the inelastic strain is [37]

$$\epsilon_c^{in} = \epsilon - \frac{\sigma_c}{E_c}, \quad (20)$$

where  $\sigma_c$  is the tensile stress of concrete.

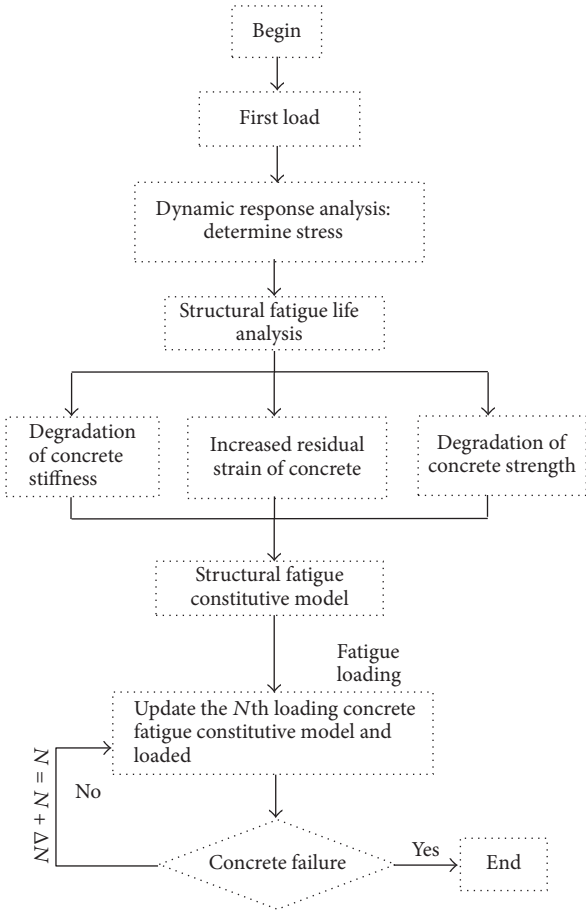


FIGURE 2: Flowchart of structural damage analysis.

### 6. Dynamic Fatigue Damage Analysis Progress and Model of Tunnel Structure

The complex cross structures of the tunnel with the designed service life up to 100 years are subjected to high cycle fatigue problems under the train caused vibration loads. It is uneconomical to calculate the dynamic impact of train on the tunnel every time. Petryna and Krätzig proposed the idea of high cycle structural fatigue [32, 39]. The dynamic response of the train operation in the cross tunnel structure under the vibration load for the first time can be simulated. Then, based on the response law of the structure under the vibration load of train for the first time, the fatigue life of the cross structure can be calculated to obtain the concrete uniaxial cyclic loading constitutive model of the cross tunnel after  $N$ th train vibration load. Finally, based on the concrete constitutive model after  $N$  times of train operation, the dynamic response and fatigue cumulative damage of tunnel cross structure after the specific operation years can be simulated. Specific analysis process is shown in Figure 2.

### 7. Project Overview

Guangzhou-Shenzhen-Hong Kong Railway Passenger Dedicated Line is a fast railway channel connecting Guangzhou,



FIGURE 3: The planar graph of the Shiziyang subsea tunnel.

Shenzhen, and Hong Kong, which is an important part of the intercity railway network in the Pearl River Delta. The full length of the Shiziyang subsea tunnel is 10.8 km, and it is the longest and highest standard subsea railway tunnel in China. Guangzhou-Shenzhen-Hong Kong Passenger Dedicated Line Shiziyang Tunnel is located at Dongyong Station, Humen Station interval. The ground layers where the tunnel run through are mainly soil, mucky soil, silty clay and fine sand, coarse sand, weathered and weak weathered argillaceous siltstone, siltstone, and fine sandstone. The planar graph and the vertical sectional profile of the Shiziyang subsea tunnel are shown in Figures 3 and 4.

According to the actual situation of the project, the connecting transverse passage cross structure of Shiziyang railway shield tunnel was selected and studied here. The dynamic response of cross structure was simulated when the marshalling train is running in the A tunnel. It is assumed that the train is running in the main tunnel A. The clear distance between two tunnels is 5.0 m and the design speed is 300 km/h. The buried depth of the selected section of the tunnel is 19.0 m, located in the weak weathered muddy siltstone, topsoil layer covered with lighter silty clay layer, and fine sand layer. The outer and inner diameters of the shield tunnel are 10.8 m and 9.8 m. The lining is assembled in a 7 + 1 block way with a universal wedge ring reinforced concrete single segment. In order to consider the impact of the segment on the structure, the stiffness reduction ring is set at the main tunnel spacing, and the reduction factor is 0.8. The width and height of connecting transverse passage are 4.0 m and 5.0 m, respectively. The length, width, and height of the stratigraphic structure model are 800.0 m, 80.0 m, and 50.0 m, respectively. All the boundaries except for the upper boundary are simulated using a continuously distributed parallel spring-damper system. This boundary treatment can effectively solve the near field fluctuation problem at soil-structure dynamic interaction.

Marshalling train does not consider the connection between the carriages. The train contains 8 carriages with single carriage length of 25.0 m. Each carriage at the front and rear part has two pairs of axles, a total of 32 pairs of axles. The physical and mechanical parameters of surrounding rock,

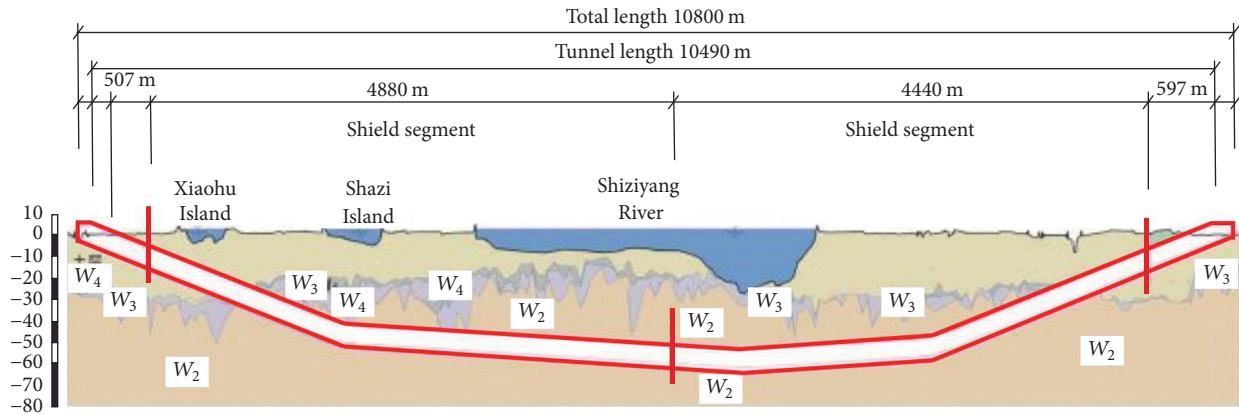


FIGURE 4: The vertical profile of the Shiziyang subsea tunnel.

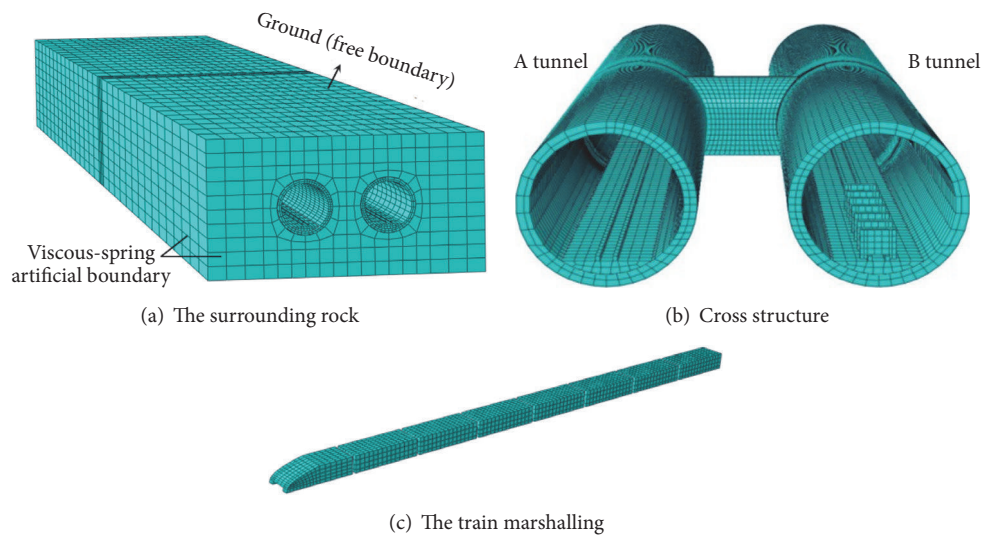


FIGURE 5: The model of the structure.

lining concrete, and track are shown in Table 1. The numerical analysis models of cross tunnel are shown in Figure 5.

The profile irregularity of a railway line is one of the essential vibration sources for vehicles and track [40]. Assuming that the high-speed trains run 40 times per day in the tunnel, the vibration load of the train was selected by the measured load curve of train vibration at 300 km/h, as shown in Figure 6.

In order to simulate the variation of the spatial position and the vibration load time in the upper tunnel where the high-speed train is running, the travel speed of 300 km/h was applied to the marshalling train, to simulate the space driving effect of the train, as shown in Figure 7.

Track and train were simulated using linear elastic materials, the surrounding rock was simulated by the elastic-plastic model with damping, and the vibration system damping used Rayleigh damping. According to the above analysis process and the dynamic response analysis model of the cross tunnel structure under the train vibration, the train vibration response and fatigue cumulative damage analysis of the shield tunnel cross structure were carried out.

## 8. Result Analysis

Firstly, the fatigue life of the tunnel cross structure under the vibration load of the train was analyzed. The stress time-history of the tunnel cross structure obtained by the calculation during the train operation in the tunnel for the first time was introduced into the FE-SAFE software. The logarithmic life distribution nephogram of the cross tunnel structure was calculated as shown in Figure 8.

From Figure 8, the shorter part of the cross structural life is mainly concentrated in the main tunnel A near the middle of the vault and connecting transverse passage on both sides of the wall corner. The minimum logarithmic life of the cross structure is 6.491. The minimum life of the structure is about  $3.10 \times 10^6$  times.

### 8.1. Dynamic Response and Cumulative Damage of Main Tunnel

**8.1.1. Structural Acceleration.** Based on the response law and fatigue life of the structure under the train vibration load for

TABLE 1: Physical and mechanical parameters table.

Material	Density ( $\text{kg/m}^3$ )	Elastic modulus (GPa)	Poisson's ratio	Friction angle ( $^\circ$ )	Cohesion (MPa)
Track	7850	200	0.2	-	-
Lining	2400	34.5	0.2	43.0	1.10
Surrounding rock	2000	3.65	0.325	33.0	0.45

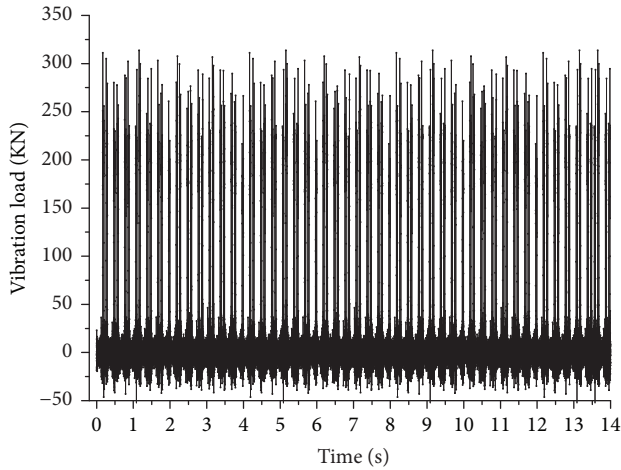


FIGURE 6: Measured train vibration load curve (300 km/h).

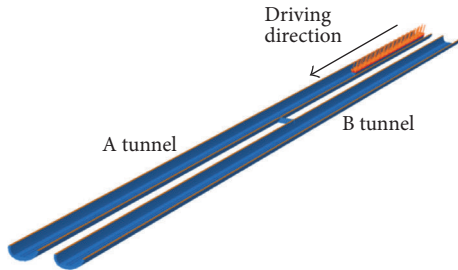


FIGURE 7: Schematic diagram of train vibration load.

the first time, the fatigue constitutive model of the structure can be obtained. Then, the dynamic response and cumulative damage effect of the cross tunnel structure after operating a certain period of time can be calculated.

Four positions of the tunnel arch bottom were selected as the analysis points, and the analysis points layouts are shown in Figure 9. The analysis points are located at the arch bottom of the tunnels. The longitudinal spacing between the points is 20 m.

The acceleration amplitude of the main tunnel analysis points A1, A2, A3, and B were extracted, after high-speed trains ran in the tunnel 1,  $1 \times 10^3$ ,  $1 \times 10^4$ ,  $1 \times 10^5$ ,  $2 \times 10^5$ ,  $5 \times 10^5$ ,  $1 \times 10^6$ ,  $1.5 \times 10^6$  times, as shown in Table 2.

From Table 2, the vibration acceleration amplitudes of tunnel analysis points have a certain degree of increase with the increasing train operation time. The acceleration amplitude of the main tunnel A with the train operation is

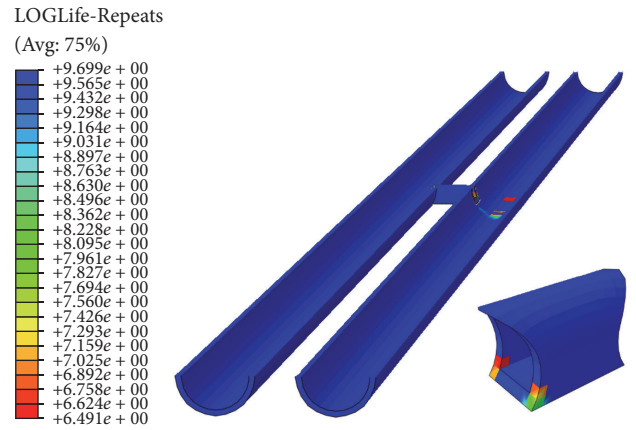


FIGURE 8: Distribution nephogram of fatigue life of cross tunnel structure.

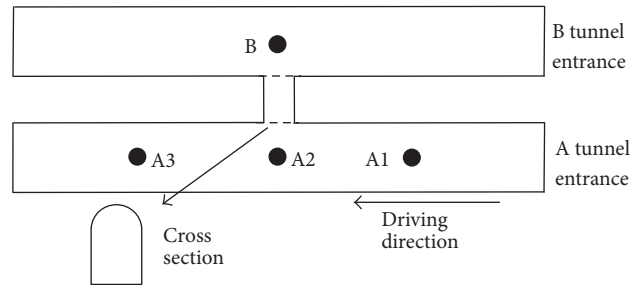


FIGURE 9: Diagram of tunnel analysis points.

obviously larger than that of the adjacent tunnel B. The maximum growth amplitude of the tunnel A is  $0.21 \text{ m/s}^2$ .

**8.1.2. The Maximum Principal Stress of Structure.** The maximum principal stress time-history curve of point A2 of the main tunnel A is shown in Figure 10, when the train is running in a cross shield tunnel for the first time.

Figure 10 shows that when the train is running in the main tunnel for the first time, the closer the train is to the point of analysis, the more intense it vibrates. At 3.7 s, the vibration at the arch bottom A2 is the most violent, and the maximum principal stress reaches 0.94 MPa.

The maximum principal stress curves of the analysis points are shown in Figure 11.

From Figure 11, the maximum principal stress peaks of the tunnel analysis points increase with the increasing

TABLE 2: Acceleration amplitude of tunnel analysis points.

Number of runs (Times)	Running time (Years)	A1 (m/s <sup>2</sup> )	A2 (m/s <sup>2</sup> )	A3 (m/s <sup>2</sup> )	B (m/s <sup>2</sup> )
1	0	0.89	2.28	0.73	0.35
$1.0 \times 10^3$	0.07	0.91	2.29	0.76	0.35
$1.0 \times 10^4$	0.69	0.93	2.30	0.77	0.35
$1.0 \times 10^5$	6.85	0.94	2.30	0.81	0.35
$2.0 \times 10^5$	13.70	0.94	2.33	0.87	0.36
$5.0 \times 10^5$	34.25	0.94	2.36	0.89	0.37
$1.0 \times 10^6$	68.49	0.95	2.43	0.90	0.39
$1.5 \times 10^6$	102.74	0.99	2.51	0.99	0.41

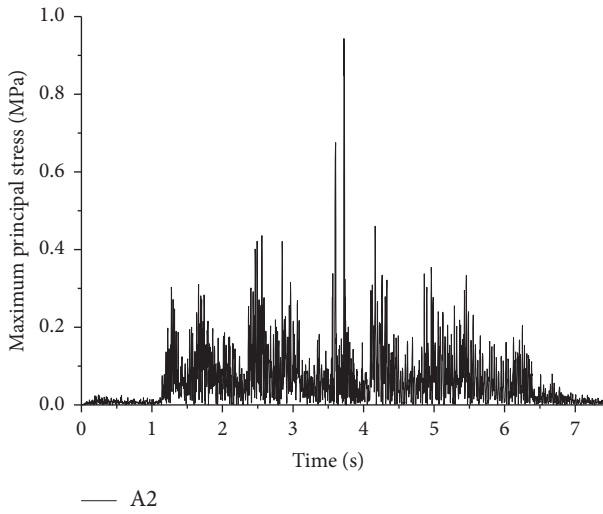


FIGURE 10: Time-history curve of maximum principal stress (A2).

train operation time. During the tunnel design period, the maximum principal stress at the analysis points presents a two-stage change characteristic: in the first stage, from 0 to 13.70 years, the maximum principal stress amplitude of the analysis points A1, A2, and A3 increases rapidly. In the second stage, from 13.70 to 102.74 years, the growth rates of analysis point of the main tunnel arch bottom are relatively slow and close to the linear development. The maximum principal stress of the analysis point B in the tunnel operation period is basically linear trend, which is only 17.4% of the point A2. It is concluded that the adjacent tunnel B belongs to passive vibration; therefore, the vibration load of the train has little effect on the adjacent main tunnel B.

Figure 12 shows the development trend of the maximum principal stress of the main tunnel segment. It can be seen from Figure 10 that the maximum principal stress of the main tunnel arch bottom is the largest, and the right analysis point near the transverse passage is the second, and the left analysis point away from the transverse passage is the smallest.

**8.1.3. Structural Cumulative Damage.** The distribution nephogram of the cumulative tensile damage of the cross structure after tunnel operation 102.74 years is shown in Figure 13.

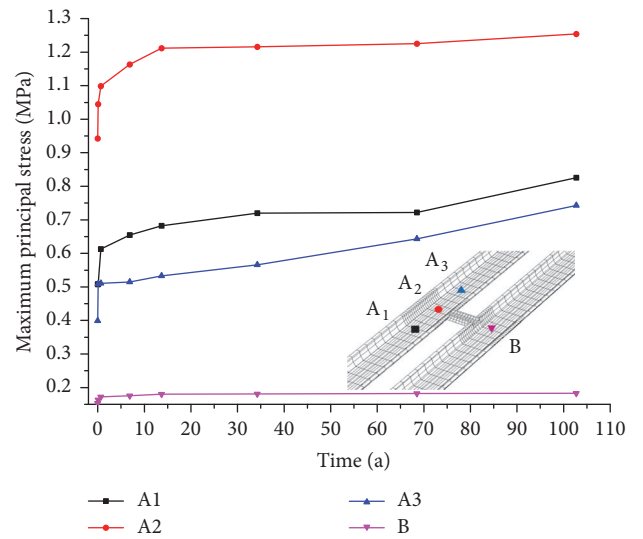


FIGURE 11: The variation curves of the maximum principal stress of tunnel analysis points.

Figure 13 shows that the cumulative tensile damage is mainly concentrated near the invert of the main tunnel A. The size and range of the cumulative tensile damage value in the middle invert of the main tunnel A are obviously higher than those of other positions. In addition, the cumulative tensile damage develops from near the arch bottom to the side wall of the connecting transverse passage in the middle of the main tunnel A, due to the presence of the connecting transverse passage.

The development trend of the tensile damage of the analysis points C1, C2, and C3 is shown in Figure 14 to further analyze the cumulative damage development of the main tunnel structure.

Figure 14 shows that the cumulative tensile damage of the main tunnel segment increases with the increase of the train operation time. The cumulative tensile damage of the point C3 in the arch bottom is the largest. The cumulative tensile damage of the right analysis point C2 is obviously larger than the left analysis point C1 when the high-speed train operation is 102.27 years, because the right analysis point C2 is connected with the transverse passage, leading to the structural stress concentration.

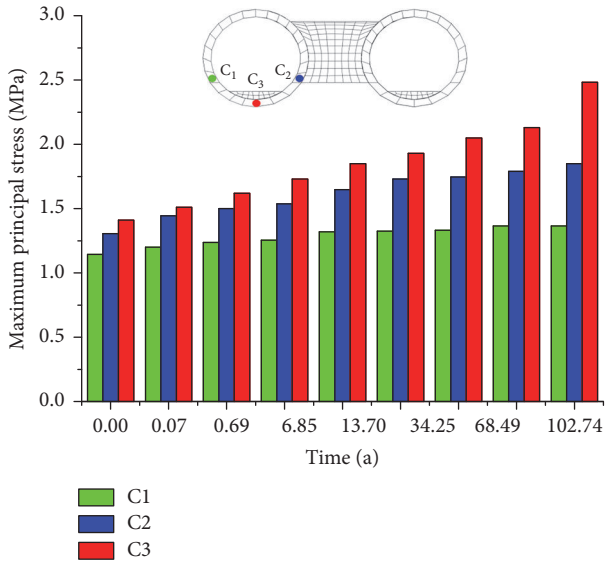


FIGURE 12: Development trend of maximum principal stress of main tunnel segment.

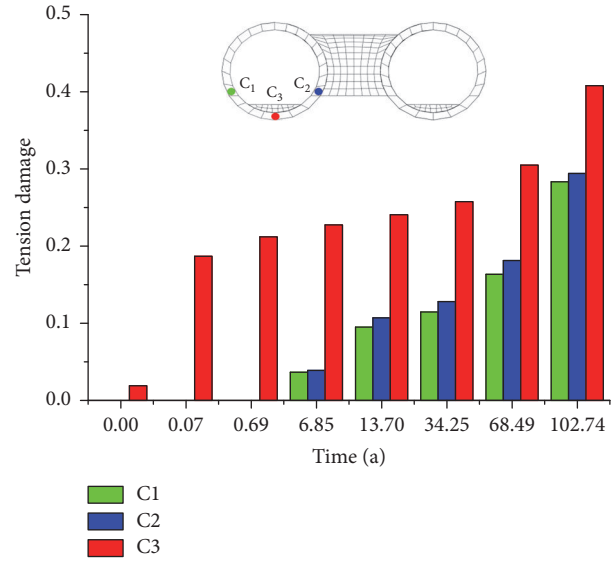


FIGURE 14: The development trend of tensile damage of the main tunnel segment.

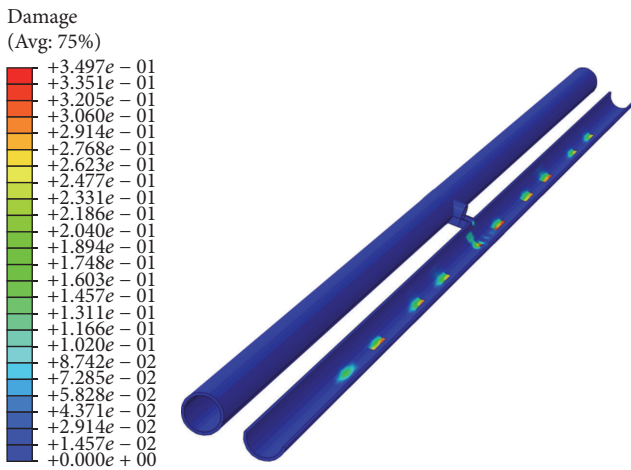


FIGURE 13: Distribution nephogram of cumulative tensile damage of cross structure (102.74 a).

## 8.2. Dynamic Response and Cumulative Damage of Connecting Transverse Passage Structure

**8.2.1. Structural Acceleration.** As can be seen from the above, the connection location is a weak part of the structure due to the stiffness singularity of main tunnel and connected transverse passage. Therefore, the interface of the connected transverse passage and the main tunnel was taken as the analysis section, and the maximum envelope of the acceleration in the time-history range was obtained by extracting the acceleration of the interface of the typical time point (the train first operation, operating for 0.07, 70.68, 49, and 102.44 years), as shown in Figure 15.

Figure 15 shows that the train is running for the first time in the tunnel, the acceleration of the connecting transverse

passage mainly focuses on the middle of the transverse passage floor, and the acceleration maximum value is  $4.26 \text{ m/s}^2$ . The minimum value of acceleration is about  $0.76 \text{ m/s}^2$  in the vault of connected transverse passage. With the increase of the operation time, the acceleration of the middle of the connecting transverse passage floor, both sides of the wall corner and vault increase significantly.

**8.2.2. Maximum Principal Stress of the Structure.** The maximum principal stress values of the analysis point of the left side wall corner of the transverse passage were extracted, when the train is running for the first time, as shown in Figure 14.

Figure 16 shows that the vibration of the left side wall corner of the transverse passage is more intense when the distance of the train from the connecting transverse passage becomes closer. When the train runs to the analysis point A2, at 3.7 s, the vibration of the analysis point is the most intense, and the maximum principal stress reaches 1.06 MPa. It is concluded that the vibration response of the left side wall corner of the transverse passage is more intense than that of arch bottom of the main tunnel, due to the singularity of the main tunnel and connecting transverse passage stiffness.

The maximum envelope of maximum principal stress in time-history range when the train is running for the first time was obtained by extracting the maximum principal stress at the typical time point interface, as shown in Figure 17.

Figure 17 shows that the principal stress of the connecting transverse passage is mainly concentrated near the side wall corner. The maximum principal stress at the right side wall corner reaches 1.06 MPa. As the operation time increases, the maximum of maximum principal stress moves upward from the skewback along the side wall to upside and its range gradually increases.

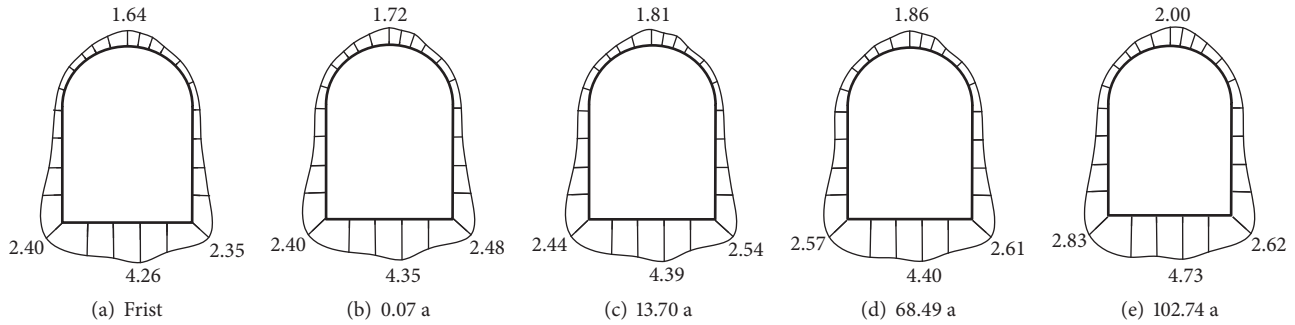


FIGURE 15: Maximum envelope of acceleration at different operation times (MPa).

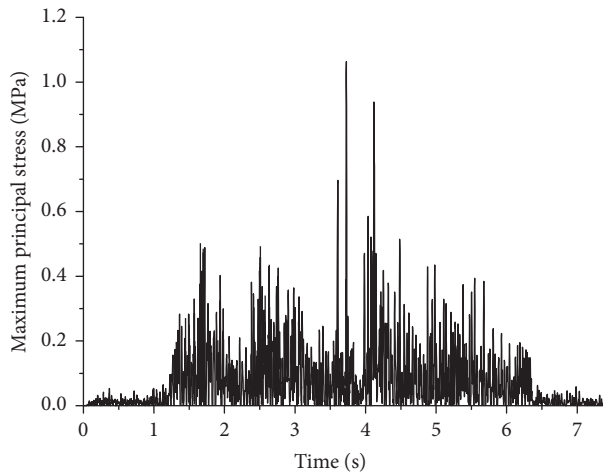


FIGURE 16: The maximum principal stress time-history curve of the left side wall for the first running.

**8.2.3. Cumulative Damage of Structure.** Cumulative compressive and tensile damage of connecting transverse passage was extracted to further analyze damage situation of connecting transverse passage, as shown in Figures 18 and 19.

Figures 18 and 19 show that the cumulative damage of the connecting transverse passage is mainly distributed in both sides of side wall corner. As the operation time increases, the damage develops towards the side wall and the floor; especially after the tunnel operation for 102.74 years, the damage is particularly evident. In addition, the damage size and range of the side wall corner are greater than those of the right side wall corner. The cumulative compressive damage of connecting transverse passage is mainly distributed in the outer wall corner position, while cumulative tensile damage is mainly distributed in the inner wall corner. The size and range of tensile damage of structure are larger than those of the compressive damage. The results show that the tensile damage of transverse passage is the main factor of structure damage.

Considering that the connecting transverse passage is mainly affected by the tensile damage, the cumulative maximum damage values of the transverse passage at the different operation times were extracted and the maximum development curve was shown in Figure 20.

Figure 20 shows that, in the first stage of the train operation of 0~6.85 years, the damage of connecting transverse passage develops rapidly with the duration of 6.8 years. In the second stage of 6.85~68.49 years, the cumulative damage development is relatively gentle and close to the linear development, which can be used to predict structure damage development. In the third stage of 68.49~102.74 years, cumulative damage development is intense. It shows nonlinear development trend, with the duration of 68.5 years. It is concluded that the initial microcracks in the interior of the material caused by the defects of the concrete itself are developed due to the reciprocating vibration load of the train. The longitudinal development is faster in the first stage of the train operation. In the second stage, because the concrete is constrained by other aggregates, the number of microcracks does not increase significantly. But the existing cracks continue to expand, the material strength decreases continuously, and the damage is close to linear accumulation. In the third stage, the microcracks of concrete are interconnected and expanded with each other, and they continue to damage the bond between the aggregate and the mortar, and cracks are rapidly expanding.

## 9. Conclusions

Considering the driving effects of high-speed train, the vibration fatigue life of tunnel cross structure was calculated using fatigue analysis software. The dynamic response and cumulative damage characteristics of cross tunnel structure of Shiziyang railway shield tunnel at various operation years were analyzed, which meet the requirements of the designed life of 100 years according to the Chinese standard. The following main conclusions are obtained:

(1) According to the latest concrete design code, the uniaxial cyclic loading constitutive model of concrete is proposed by taking into account the factors such as the stiffness degradation of concrete, the strength decrease of concrete, and the increase of fatigue residual strain. The proposed model is suitable for high cycle vibration fatigue analysis of train and can reflect the current commonly used concrete mechanical properties.

(2) The high-speed train ran in the cross tunnel structure and the middle area of the main tunnel in which the train runs were the most violent. The dynamic response of the

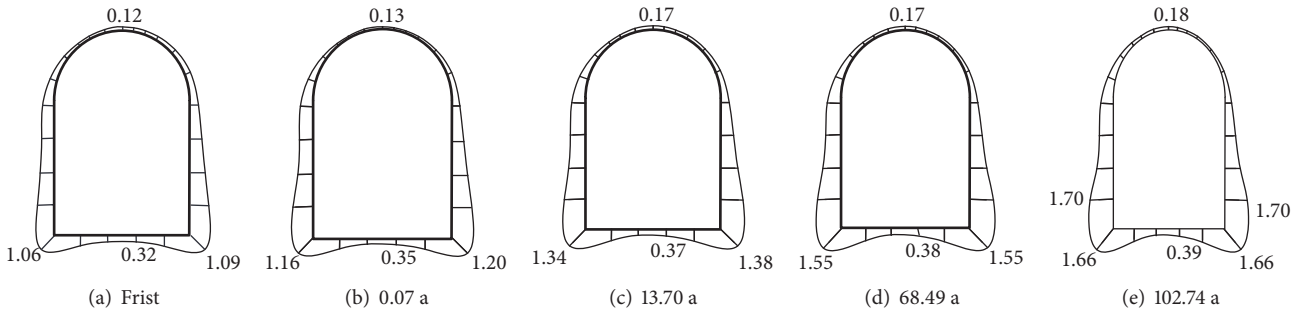


FIGURE 17: Maximum envelope of maximum principal stress at different operation times (MPa).

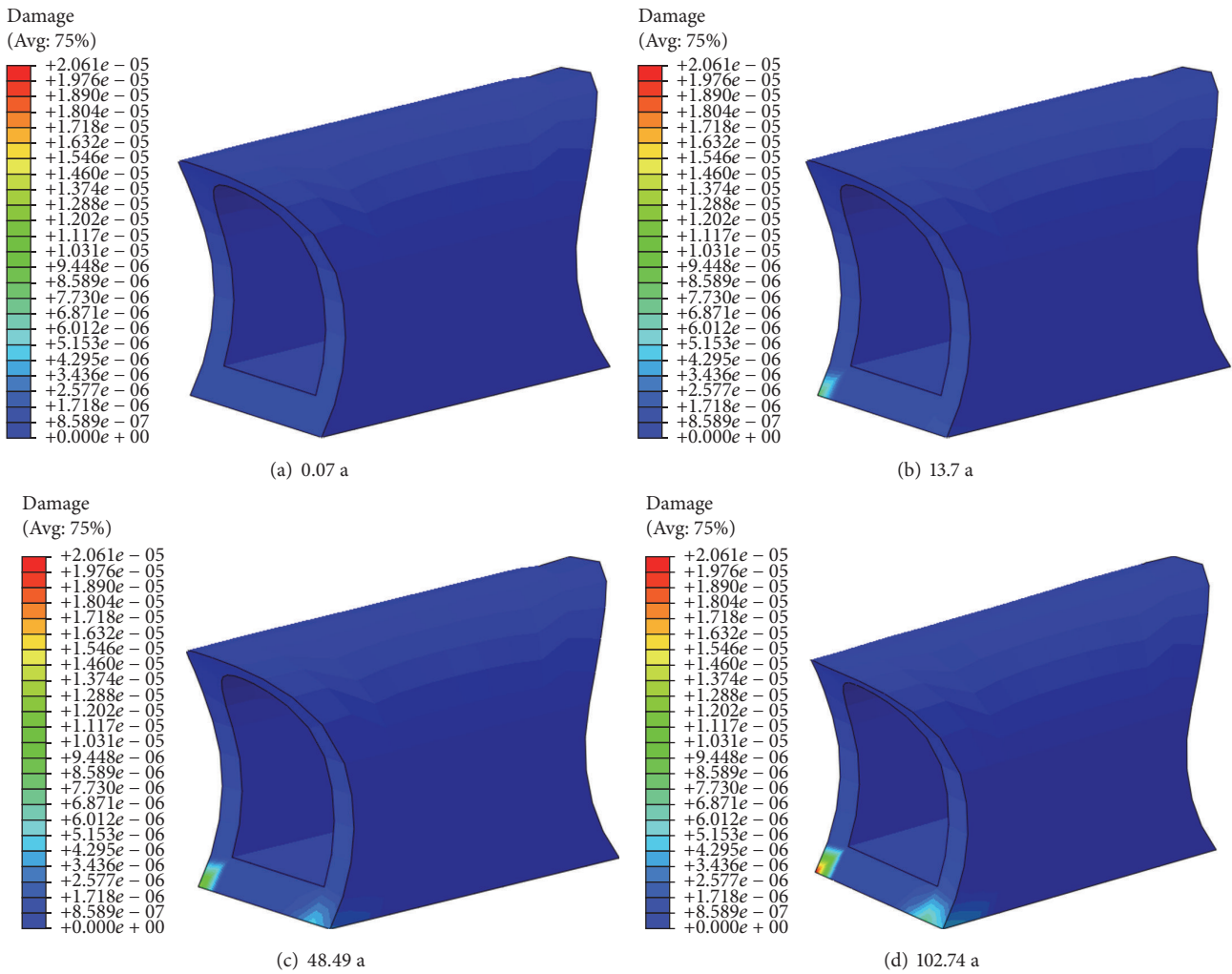


FIGURE 18: Compressive damage nephogram of the connecting transverse passage at different operation times.

arch bottom in the middle of the main tunnel opposite the transverse passage was the largest. The vibration response of the hance of the main tunnel near the transverse passage was larger than that of the opposite of the main tunnel hance.

(3) The stiffness singularity between the connecting transverse passage and the main tunnel caused large stress concentration phenomenon at the interface, and the stress and acceleration were relatively large at the interface. The maximum

principal stress of the transverse passage mainly appeared near the side wall corner, while the maximum acceleration mainly appeared near the middle of the transverse passage floor.

(4) The maximum principal stress and acceleration of the connecting transverse passage increased with the increasing train operation years. The acceleration increased significantly in the middle of the transverse passage floor, both sides of side

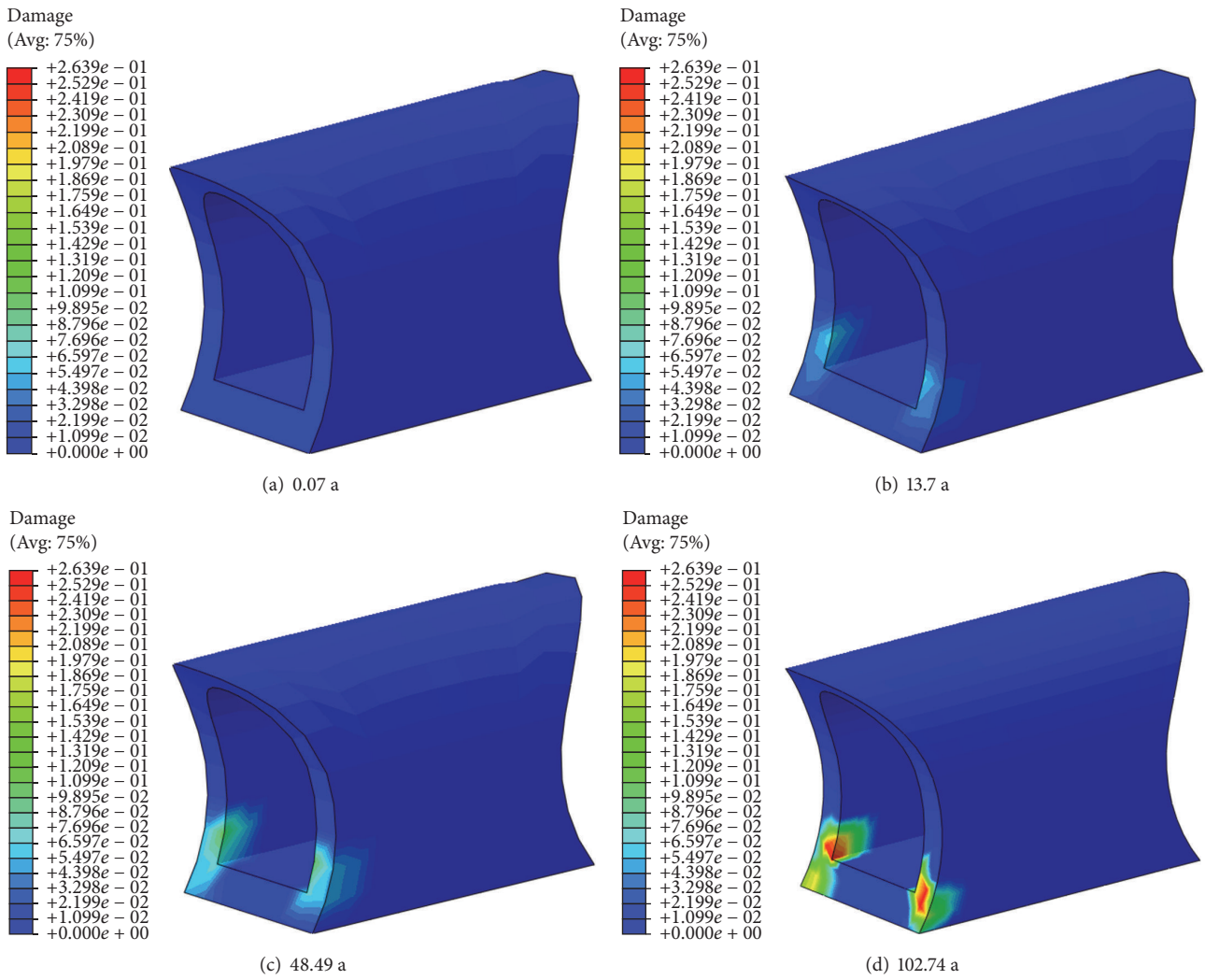


FIGURE 19: Tensile damage nephogram of the connecting transverse passage at different operation times.

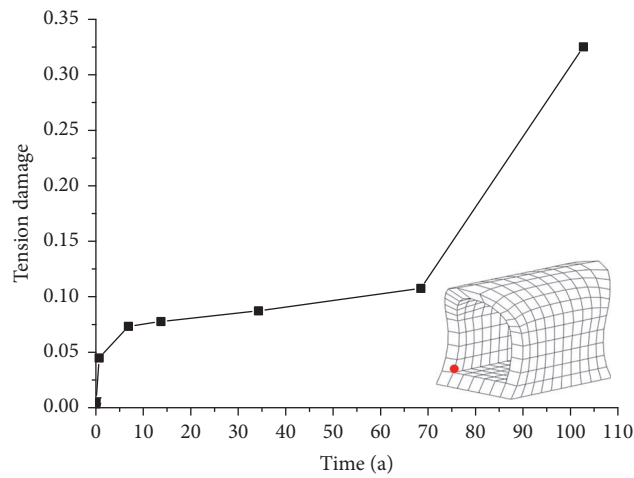


FIGURE 20: Maximum development curve of tensile damage of the transverse passage.

wall corner and vault, while the maximum principal stress developed obviously only in both sides of side wall corner.

(5) The cumulative damage of connecting transverse passage was mainly distributed in both sides of side wall corner. With the increasing operation years, the accumulative damage developed towards the side wall and floor of connecting transverse passage. The damage value and range of the left side wall corner were larger than the corresponding position of the right side wall.

(6) The cumulative compressive damage of connecting transverse passage was mainly distributed in the outer wall corner position, while cumulative tensile damage was mainly distributed in the inner wall corner, which was close to the linear development. The size and range of tensile damage of structure were larger than those of the compressive damage.

## Conflicts of Interest

The authors declare that there are no conflicts of interest regarding the publication of this paper.

## Acknowledgments

Financial support for this work provided by the National Key R&D Program of China (Grant no. 2016YFC0802205) and the National Science Foundation of China (Grants nos. 51178400, 51278425, and U1361210) is gratefully acknowledged.

## References

- [1] J. X. Lai, K. Y. Wang, and J. L. Qiu, "Vibration response characteristics of the cross tunnel structure," *Shock and Vibration*, vol. 2016, Article ID 9524206, 16 pages, 2016.
- [2] F. Ye, C. F. Gou, H. D. Sun, Y. P. Liu, Y. X. Xia, and Z. Zhou, "Model test study on effective ratio of segment transverse bending rigidity of shield tunnel," *Tunnelling and Underground Space Technology*, vol. 41, no. 1, pp. 193–205, 2014.
- [3] J. Lai, F. Niu, K. Wang et al., "Dynamic effect of metro-induced vibration on the rammed earth base of the Bell Tower," *SpringerPlus*, vol. 5, no. 1, article no. 935, 2016.
- [4] H. Yu, C. Cai, X. Guan, and Y. Yuan, "Analytical solution for long lined tunnels subjected to travelling loads," *Tunnelling and Underground Space Technology*, vol. 58, pp. 209–215, 2016.
- [5] W. B. Shi, L. C. Miao, Z. X. Wang, and J. H. Luo, "Settlement behaviors of metro tunnels during the metro operation," *Shock and Vibration*, vol. 2015, Article ID 863961, 11 pages, 2015.
- [6] J. X. Lai, X. L. Wang, J. L. Qiu et al., "A state-of-the-art review of sustainable energy based freeze proof technology for cold-region tunnels in China," *Renewable and Sustainable Energy Reviews*, vol. 82, pp. 3554–3569, 2018.
- [7] H. Lai, X. Zhao, Z. Kang, and R. Chen, "A new method for predicting ground settlement caused by twin-tunneling undercrossing an existing tunnel," *Environmental Earth Sciences*, vol. 76, no. 21, 2017.
- [8] J. Lai, J. Qiu, H. Fan et al., "Structural safety assessment of existing multiarch tunnel: a case study," *Advances in Materials Science and Engineering*, vol. 2017, Article ID 1697041, 11 pages, 2017.
- [9] J. Lai, S. He, J. Qiu et al., "Characteristics of seismic disasters and aseismic measures of tunnels in Wenchuan earthquake," *Environmental Earth Sciences*, vol. 76, no. 2, article 94, 2017.
- [10] C. Shi, C. Cao, and M. Lei, "Construction technology for a shallow-buried underwater interchange tunnel with a large span," *Tunnelling and Underground Space Technology*, vol. 70, pp. 317–329, 2017.
- [11] J. Qiu, Y. Xie, H. Fan, Z. Wang, and Y. Zhang, "Centrifuge modelling of twin-tunnelling induced ground movements in loess strata," *Arabian Journal of Geosciences*, vol. 10, no. 22, 2017.
- [12] Q. Yan, Z. Deng, Y. Zhang, and W. Yang, "Failure Characteristics of Joint Bolts in Shield Tunnels Subjected to Impact Loads from a Derailed Train," *Shock and Vibration*, vol. 2017, Article ID 2829783, 17 pages, 2017.
- [13] J. Qiu, X. Wang, S. He et al., "The catastrophic landslide in Maoxian County, Sichuan, SW China, on June 24, 2017," *Natural Hazards Journal of the International Society for the Prevention & Mitigation of Natural Hazards*, vol. 89, no. 3, pp. 1485–1493, 2017.
- [14] J. L. Qiu, H. Q. Liu, J. X. Lai et al., "Investigating the long term settlement of a tunnel built over improved loessial foundation soil using jet grouting technique," *Journal of Performance of Constructed Facilities*, 2018.
- [15] T. Balendra, C. G. Koh, and Y. C. Ho, "Dynamic response of buildings due to trains in underground tunnels," *Earthquake Engineering & Structural Dynamics*, vol. 20, no. 3, pp. 275–291, 1991.
- [16] K. Aas, *Fatigue of concrete beams and columns*, Bulltin 70-1, NTH Institute of Beton konstruksjoner, Trondheim, Norway, 1970.
- [17] R. Tepfers and T. Kutti, "Fatigue strength of plain, ordinary, and lightweight concrete," *Journal - American Concrete Institute*, vol. 6, no. 5, pp. 635–652, 1979.
- [18] J. O. Holmen, "Fatigue of concrete by constant and variable amplitude loading," *ACI Special Publication, Fatigue of Concrete Structures*, vol. 75, no. 4, pp. 71–110, 1982.
- [19] J. Huang, P. Huang, and X. Zheng, "Experimental study on propagation behavior of main fatigue crack in RC beam strengthened with prestressed CFRP plate," *China Railway Science*, vol. 37, no. 6, pp. 27–33, 2016.
- [20] M. S. Cao, Q. W. Ren, and A. L. Zhai, "Experimental study on fractal characterization in damages of concrete structures," *Rock & Soil Mechanics*, vol. 33, no. 5, pp. 2738–2741, 2005.
- [21] S. Teng and F. Wang, "Finite element analysis of reinforced concrete deep beams under fatigue loading," *ACI Structural Journal*, vol. 98, no. 3, pp. 315–323, 2001.
- [22] Y. S. Petryna and W. B. Krätzig, "Computational framework for long-term reliability analysis of RC structures," *Computer Methods Applied Mechanics and Engineering*, vol. 194, no. 12-16, pp. 1619–1639, 2005.
- [23] R. Zhang and Z. Shi, "Numerical simulation of rebar/concrete interface debonding of FRP strengthened RC beams under fatigue load," *Materials and Structures/Materiaux et Constructions*, vol. 41, no. 10, pp. 1613–1621, 2008.
- [24] J. S. Zhu and X. C. Zhu, "Study on simplified method for the analysis of fatigue failure process of RC bridges," *Journal of Engineering Mechanics*, vol. 29, no. 5, pp. 107–121, 2012.
- [25] Z. W. Wang, Y. M. Zhao, Q. L. Zhang et al., "Stochastic damage model for concrete structure of high-speed railway tunnel substrate," *China Railway Science*, vol. 38, no. 1, pp. 59–67, 2017.
- [26] Q. Wang, J. Wei, X. Liu, and G. Xu, "Equivalent static analysis method for fatigue cumulative damage process of reinforced

- concrete beam,” *Journal of Central South University (Science and Technology)*, vol. 48, no. 1, pp. 247–253, 2016.
- [27] S. Gharehdash and M. Barzegar, “Numerical modeling of the dynamic behaviour of tunnel lining in shield tunneling,” *KSCE Journal of Civil Engineering*, vol. 19, no. 6, pp. 1626–1636, 2015.
- [28] S. Gupta, G. Degrande, and G. Lombaert, “Experimental validation of a numerical model for subway induced vibrations,” *Journal of Sound and Vibration*, vol. 321, no. 3-5, pp. 786–812, 2009.
- [29] S. Gupta, H. Van den Berghe, G. Lombaert, and G. Degrande, “Numerical modelling of vibrations from a Thalys high speed train in the Groene Hart tunnel,” *Soil Dynamics and Earthquake Engineering*, vol. 30, no. 3, pp. 82–97, 2010.
- [30] Z. P. Lin, “Analysis on dynamic response of overlapped tunnel structure under vibration load,” *Journal of Railway Science and Engineering*, vol. 13, no. 9, pp. 1789–1795, 2016.
- [31] National Standard of the People’s Republic of China, *GB50010-2010 Code for Design of Concrete Structures*, China Building Industry Press, Beijing, China, 2010.
- [32] W. Qian, D.-Q. Qi, and W.-C. Xue, “Full-range analysis on behaviors of concrete beams prestressed with CFRP tendons under fatigue load cycles,” *Journal of Vibration and Shock*, vol. 27, no. 5, pp. 125–129, 2008.
- [33] J.-K. Kim and Y.-Y. Kim, “Experimental study of the fatigue behavior of high strength concrete,” *Cement and Concrete Research*, vol. 26, no. 10, pp. 1513–1523, 1996.
- [34] Y. J. Park, “Fatigue of concrete under random loadings,” *Journal of Structural Engineering (United States)*, vol. 116, no. 11, pp. 3228–3235, 1990.
- [35] R. M. Wang, G. F. Zhao, and Y. P. Song, “Research on compression fatigue performance of concrete,” *China Civil Engineering Journal*, vol. 24, no. 4, pp. 38–47, 1991.
- [36] J. Li and J. Y. Wu, “Elastoplastic damage constitutive model for concrete based on damage energy release rates, part I: basic formulations,” *China Civil Engineering Journal*, no. 9, pp. 14–20, 2005.
- [37] ABAQUS Inc., *Abaqus Theory Manual*, Providence: ABAQUS Inc., 2007.
- [38] F. Sidoroff, “Description of anisotropic damage application to elasticity,” in *Proceedings of the IUTAM Colloquium on physical Non-Linearities in Structural Analysis*, pp. 237–244, Springer, 1981.
- [39] Y. S. Petryna, D. Pfanner, F. Stangenberg, and W. B. Krätzig, “Reliability of reinforced concrete structures under fatigue,” *Reliability Engineering & System Safety*, vol. 77, no. 3, pp. 253–261, 2002.
- [40] R. Burdzik and B. Nowak, “Identification of the Vibration Environment of Railway Infrastructure,” in *Proceedings of the Transportation Science and Technology: Proceedings of the 10th International Scientific Conference, TRANSBALTICA 2017*, pp. 556–561, May 2017.

## Research Article

# Detection of Delamination in Laminate Wind Turbine Blades Using One-Dimensional Wavelet Analysis of Modal Responses

Łukasz Doliński , Marek Krawczuk, and Arkadiusz Żak

*Department of Mechatronics and High Voltage Engineering, Faculty of Electrical and Control Engineering, Gdansk University of Technology, Gdansk, Poland*

Correspondence should be addressed to Łukasz Doliński; [lukasz.dolinski@pg.edu.pl](mailto:lukasz.dolinski@pg.edu.pl)

Received 27 October 2017; Accepted 30 January 2018; Published 1 March 2018

Academic Editor: Rafał Burdzik

Copyright © 2018 Łukasz Doliński et al. This is an open access article distributed under the Creative Commons Attribution License, which permits unrestricted use, distribution, and reproduction in any medium, provided the original work is properly cited.

This paper demonstrates the effectiveness of a nondestructive diagnostic technique used to determine the location and size of delamination in laminated coatings of wind turbine blades. This is realized based on results of numerical and experimental investigations obtained by the use of the finite element method (FEM) and laser scanning vibrometry (LSV). The proposed method is based on the one-dimensional continuous wavelet transform of vibration parameters of a wind turbine blade. The investigations were conducted for a 1:10 scaled-down blade of a 36 m rotor wind turbine. Glass fibres and epoxy resin were used as laminate components. For numerical studies, a simple delamination model was proposed. The results obtained by the authors were used to determine the optimal set of parameters of the continuous wavelet transform. The application of high-quality LSV for experimental measurements allowed determining the optimal conditions of measuring procedures. At the same time the capabilities and limitations, resulting from the nature of the measurement method, were identified. In order to maximize the effectiveness of the detection method, preliminary signal processing was performed. Beside base wavelets also different waveform families were tested. The results obtained by the authors showed that it is possible to identify and localize even relatively small damage.

## 1. Introduction

For every technical device, there are many various factors that can start irreversible processes changing its condition and gradually deteriorate its operating characteristics. This also applies to wind turbines, where rotor blades are particularly sensitive to different kinds of defects. Rotor blades are the most important subassembly of wind turbines, which are responsible for converting the wind kinetic energy into mechanical energy. Thanks to aerodynamic forces acting on rotor blades, it is possible to generate torque, which is necessary to drive electric generators. The efficiency of wind turbines is directly related to the effective swept area of rotor blades. The simplest way to increase the power of wind turbines is to increase the diameter of their rotors [1]. The construction of large wind turbines, as well as the optimization of aerodynamic parameters of rotor blades, requires new constructional materials of predefined mechanical properties which provide high mechanical strength at relatively low weight, when compared to metallic materials. Such materials

are laminated composite materials. The main components of laminates are the matrix and the reinforcement. The matrix holds laminate components together, whereas the reinforcement provides transfer of loads. The reinforcement usually takes form of very stiff and durable fibres. Nowadays, wind turbine blades are made of glass or carbon fibre laminates, which consist of several composite layers. Individual layers can possess the same or different mechanical properties. By changing the configuration of reinforcing fibres, or laminated components materials, the optimal material features can be obtained. This makes it possible to decrease the overall mass of wind turbine blades, while maintaining or enhancing the value of permitted loads. Honeycomb composites and additional noncomposite stiffeners can be used in some designs of wind turbine blades. Their designs should also include elements of lightning protection systems [2]. As a result, very complex products are obtained. Despite many advantages of laminated composite materials, they turn out to be vulnerable to very specific damage types that are characteristic only for these types of materials. In

most cases their damage is related to degradation of their internal structure, which is also the most dangerous type of damage and very difficult to detect. A typical example can be the loss of cohesion between individual fibres (so-called fibre splitting/debonding) or between laminate layers (delamination) [3]. There are no external symptoms visible on the surface of wind turbine blades, which would indicate damage presence. Thin-walled components are particularly vulnerable to delamination. This applies to wind turbine blades, where the cause of damage is not only due to wind or centrifugal forces, but also due to dynamic loads resulting from long-term vibrations of rotor blades around resonance frequencies. The expected lifetime of wind turbine rotor blades varies from 10 to 30 years and the number of vibrations cycles during that time span is considerable. Therefore the influence of operating fatigue on the strength reduction of wind turbine rotor blades is high. Damage can also be caused by impact (e.g., bird collisions) or by lightning. These factors are particularly important for the durability and reliability of wind turbine blades. Downtime of wind turbines caused by failure recovery is associated with significant financial costs. Disassembling and replacing damaged parts at heights of several dozen meters is always a very difficult operation. This process gets even more complicated in the case of offshore wind turbine installations. Because of that intensive work is carried out to create delamination detection, identification, and localization methods in laminated coatings of wind turbine blades. Thanks to real time condition monitoring of wind turbine blades it is possible to detect damage at its early stage of development. This also makes it possible to create favourable conditions for failure-free work in assumed time or even to prolong wind turbine blades life. Appropriately quick response can significantly minimize the influence of damage to other elements of wind turbine structures. In modern designs of wind turbines, diagnostic systems are often integral parts of rotor blade structures. Examples of such systems can be found in [4–7]. Solutions proposed there could be autonomous systems of sensors used for collecting and processing data directly from working rotor blades. Most of diagnostic techniques currently used for in-service wind turbine rotor blades requires rotor stopping for the time of assessment. A field assessment of their technical condition is usually carried out during periodical inspections and is mainly based on a subjective visual assessment of rotor blade shells. This is because diagnostic methods leading to more accurate results require complex measuring instrumentation and stable measurement conditions. An example can be ultrasonic techniques [8] or computed tomography [9] used to generate surface maps of visible material defects. The main disadvantage of these techniques is that they are time consuming. For this reason ultrasonic methods can be used at the stage of production quality control and admission of rotor blades to use. Another method of considerably greater fields of applications is the image analysis employing infrared thermal cameras to observe surface temperature of wind turbine rotor blades during fatigue tests. This method effectively indicates coating cracks as well as areas at risk of failure [10, 11]. A large number of methods used to assess the technical condition of wind turbine blades are based

on classical assumptions of vibroacoustics. The popularity of these methods is due to a large amount of information transmitted by mechanical waves and their proven effectiveness in other areas of technology. One of such methods is the analysis of acoustic emission signals, which examines correlation between characteristic features of sound propagating within tested objects and their mechanical properties [12–14]. Fundamental drawbacks of these methods are due to the necessity to separate useful diagnostic information from noise. In addition, as shown in [15], relatively high static loads are required to indicate damage. Basic modal parameters such as natural frequencies, mode shapes, and transmittance functions are also used. The location and size of damage can be determined by examination of differences between dynamic characteristics of undamaged and damaged states. Any detectable changes in inertia or stiffness properties of the objects under investigation and caused by damage are reflected in measured frequencies or vibration patterns that will differ from the initial undamaged state [16–20]. New methods for measuring known physical quantities (e.g., velocities or deformations), such as laser vibrometry [21] or optic fibres [22], allow for new approaches to classical vibration diagnostics, as collection of measurement data is much simpler. In addition to this improved measurement accuracy makes results more useful. The development of measurement techniques also requires the development of signal processing methods. This allows for faster, more accurate, and comprehensive data analysis. Signal processing methods include nowadays wavelet transform [23–26], fractal analysis [27], genetic algorithms [28, 29], and neural networks [30, 31].

The detection method proposed by the authors in this paper assumes measurements and analysis of vibration parameters of a scaled-down composite wind turbine rotor blade, which allows for early damage detection. A universal nature of this method also allows for its application to existing installations, regardless of their locations, the size, or type of rotor blades, as well as without the necessity for rotor stopping.

## 2. Methodology

The main objective of the investigation presented in this paper is the development of a nondestructive diagnostic method in order to determine the location and size of damage in a laminated coating of a wind turbine rotor blade. A general research methodology is schematically depicted in Figure 1. As first, modal responses of the blade are determined in terms of its natural frequencies and modes of vibrations, which next are used as the basis of the proposed diagnostic method. Also results of computer simulations and experimental measurements are presented and discussed.

Selection of useful modal parameters resulted from the requirements for the detection and localization of delamination in a relatively small area. The literature indicates that vibration frequency analysis is effective in the case of damage lengths greater than 15% of the total length of specimens [32, 33]. In addition, it should be mentioned that natural frequencies are global parameters and thus contain

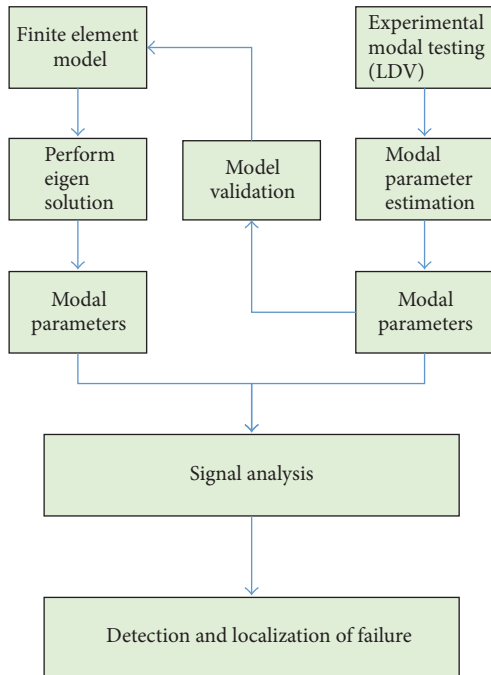


FIGURE 1: A scheme of a general research methodology.

no direct information about the location and size of damage. Therefore, it is necessary to analyse spatial domain signals searching for any discontinuities that could indicate any local stiffness changes. Modes of natural vibrations are these signal features. A continuous wavelet transform can be employed as a subsequent method of data analysis.

Figure 2 shows a more detailed concept of the presented diagnostic method. It can be seen that it assumes the application of a continuous wavelet transform (CWT) to analyse the first 10 bending modes of natural vibrations of the wind turbine blade under investigation. In order to maximize the effectiveness of the detection and localization method, preliminary signal processing was performed. Beside base wavelets also different waveform families were tested by the authors. Three different damage scenarios were taken into account, as presented in Figure 3.

**2.1. Research Object.** Investigations were carried out for a 1:10 scaled-down blade of a real wind turbine rotor, 36 m in diameter. The blade under investigation, 1.74 m in length, was based on a ClarkY aerodynamic profile. The blade was strengthened by one longitudinal spar, as shown in Figure 3. Glass fibres and epoxy resin were used as laminate components. The reinforcing fibres were symmetrically arranged as  $[\pm 45^\circ]_N$ . The blade was divided into three sections, and each sections was characterized by a different number  $N$  of laminate layers.

In order to avoid any sudden changes in the blade stiffness, a linear change in the coating thickness between the sections was ensured, which have a great effect of the results of wavelet analysis.

In general, the motion of wind turbine blades can be characterized by three types of vibrations: bending in the

plane perpendicular to the rotor plane in the direction of the axis of rotation, bending in the rotor plane, and torsion, as shown in Figure 4. The optimal choice for spatial signal analysis presents vibrations of rotor blades perpendicular to the rotor plane.

**2.2. Numerical Model.** The rotor blade was modeled by the FEM. The shell finite elements used by the authors had eight nodes and six degrees of freedom at each node. The total number of finite elements of the blade numerical model was 5,409. It was also assumed that the blade was fixed at one of its end. Numerical calculations included computations of the first 10 bending natural frequencies and modes of vibrations of the blade, with and without damage. It should be mentioned here that the current study was focused on delamination detection and localization, which is one of the most common type of damage in laminates. As a result of the forces acting on the blade during its motion, particular layers of the blade coating can be separated, leading to delamination. Figure 5 shows this damage scheme.

Characteristic features of delamination include no material loss, two possible states of damage (open and closed), and the occurrence at different depths within the laminate. This makes it difficult to develop numerical models of delamination with realistic influence on dynamic behaviour. In general, numerical models of delamination can be divided according to the research purpose. Models based on specific criteria, such as Hashin's failure criteria [34] or critical energy release rates [35], can be used to determine where and when delamination occurs, as well as how it propagates [36, 37]. The second group of numerical models focuses on the impact of delamination on the dynamic behaviour of the objects under investigation. The simplest method of delamination modelling is the reduction of stiffness at the delamination position based on certain local changes in the thickness of laminates or based on the reduction of their Young modulus [38]. This approach gives no satisfactory results and is much better suited for crack modelling. In contrast to delamination cracks presents changes in the cross-sectional area of laminates. Other, more advanced analytical delamination models can be found in the literature [39–41]. Most of them can be assigned to one of two groups. The first group is region approaches, where laminates are divided into three distinct segments: delamination itself and two adjacent undamaged segments on both sides. The second group is layer-wise models, where multilayer theories are used directly. The main problems with both these types of delamination modelling methods result from their complexity. Therefore, in this study, a simpler delamination model was proposed. The idea used by the authors is the reduction of the shear modulus in the lamination plane ( $G_{XY}$ ), which is related to zero tangential stresses within the delamination zone. The value of the shear modulus in the case of a damaged laminate was determined by examination of natural vibrations of a simple cantilever beam. The beam natural frequencies were consistent with a reference model, when the shear modulus was lowered to 14% of its initial value [32, 42]. This method of delamination modelling is a compromise between the exact representation of damage and the ease of implementation.

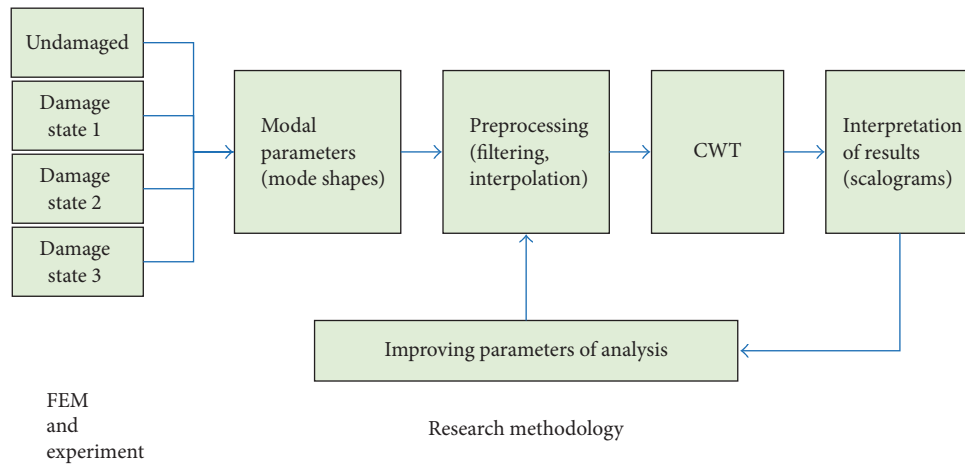


FIGURE 2: A scheme of detailed research methodology.

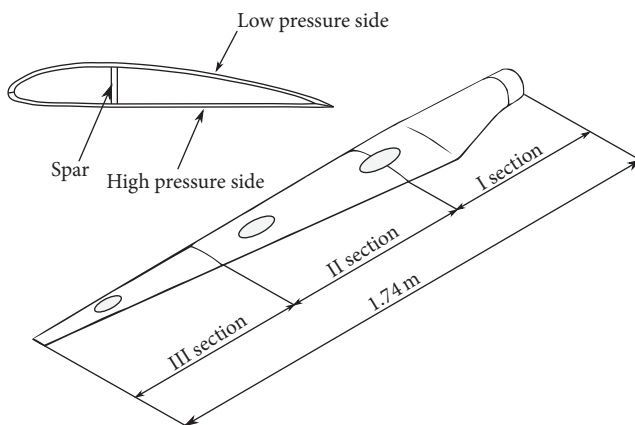


FIGURE 3: A scheme of a scaled-down wind turbine rotor blade.

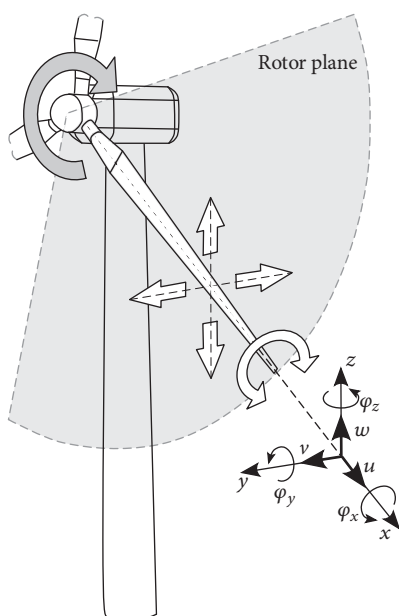


FIGURE 4: Fundamental types of vibrations of wind turbine blades.

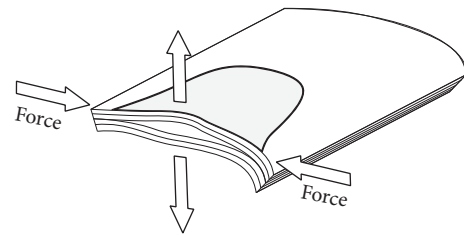


FIGURE 5: A scheme of delamination initiation.

**2.3. Experimental Investigation.** The main purpose of experimental measurements was validation of the numerical model of a wind turbine rotor blade proposed by the authors. Glass fibres and epoxy resin were used as laminate components. The reinforcing fibres were symmetrically arranged as  $[\pm 45^\circ]_N$ . The total mass of the blade was 2 kg. A measurement stand used by the authors is schematically presented in Figure 5. The stand consisted the following elements: the object of investigation (1), an electromechanical shaker (7) with the maximum excitation sinusoidal force of 31 N, and a laser vibrometer (3)–(6). The experiment was carried out using a PSV-400 Laser Scanning Vibrometer by Polytec Ltd., which enabled the authors for fast, accurate, and noncontact vibration measurements. The main and most important element of the vibrometer is a precise optical sensor (3), which is used to determine the velocities of vibrating objects. The device employs the principle of the Doppler effect to measure changes in the frequency of light reflected from vibrating objects. The vibrometer set includes a vibrometer controller, a junction box, and a control unit. The unit automatically moves a laser beam from point to point on the surface of vibrating objects over a grid of user predefined points.

The experiment conducted a series of measurements in order to determine natural frequencies and modes of vibrations of the wind turbine rotor blade under consideration at a certain initial reference state as well as three locations of simulated damage. Measurement data were collected from 200 points. A steel element fixed to the blade surface was used

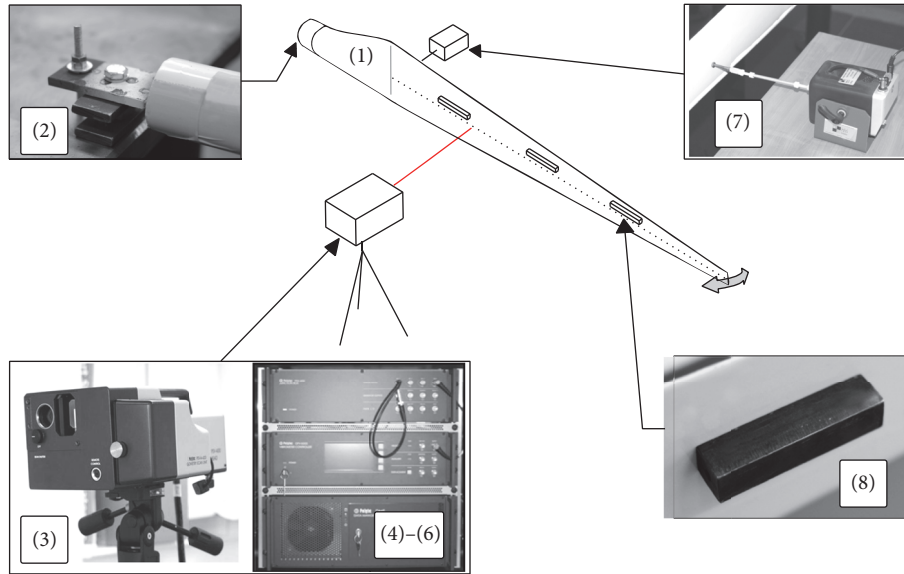


FIGURE 6: A scheme of a laboratory stand: (1) rotor blade; (2) blade fixing; (3) head of laser scanning vibrometer; (4) signal amplifier; (5) signal generator; (6) computer; (7) shaker; (8) model of damage.

to simulate damage in the form of a stiffness change in the composite coating, as shown in Figure 6.

Correct interpretation of the results of experimental data is dependent on the level of measurement noise. High noise values can mask information about the damage presence and consequently can prevent its detection. Therefore, during laboratory tests, appropriate measurement conditions were ensured, in order to maximize the signal level received by the vibrometer (the blade surface was coated by a special retroreflective foil) as well as isolate the blade from any external vibrations. The results of measurements are frequency response functions (FRFs), used to determine the values of natural frequencies and corresponding modes of induced vibrations. The induced vibrations of the blade were excited by a sinusoidal force of a constant amplitude and a linearly varying instantaneous frequency, as presented in Figure 7. Figure 8 shows a typical frequency response function obtained from all measurements points and next averaged, with peaks corresponding to resonance frequencies. Experimental measurements were conducted in the frequency range from 0 Hz to 550 Hz, with a resolution of 6400 FFT lines. It should be pointed out here that the modes of induced vibrations obtained by this method do not provide sufficiently low noise levels.

For this reason, in order to minimize the noise level, a *FastScan* mode of measurements was used, in which each mode of vibration was determined separately based on a sinusoidal excitation at a constant frequency equal to the frequency of the measured resonant vibrations. Such measurements were carried out for a narrow frequency bandwidth of 0.02 Hz. Figure 9 compares the results of FFT and *FastScan* modes for the first mode shape measured. The accuracy of data obtained is directly related to the extended measurement time. For example, the most accurate measurements of the first form of vibrations, for 200 measurement

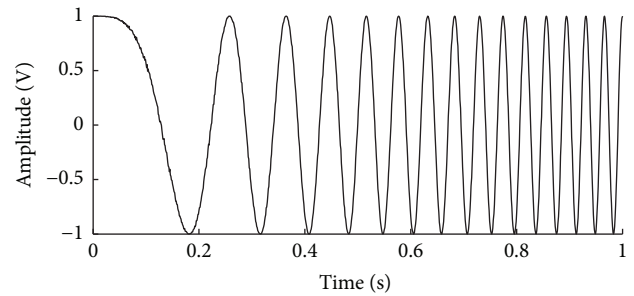


FIGURE 7: A typical form of an excitation signal used during experimental measurements.

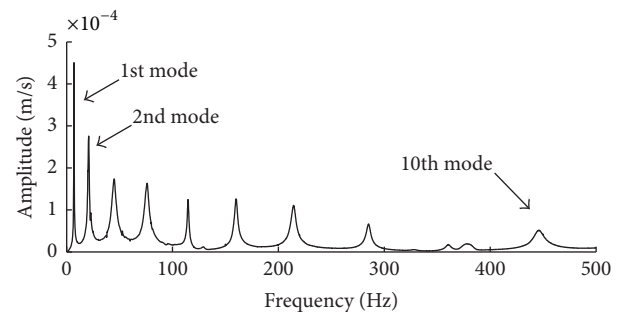


FIGURE 8: A typical frequency response function measured experimentally.

points, took about 3 hours. It is worth mentioning that it is impossible to provide stable excitation parameters and operating conditions in the case of a real wind turbine blade for such a long time.

Based on measured frequency response functions, presented in Figure 8, natural frequencies of the intact blade

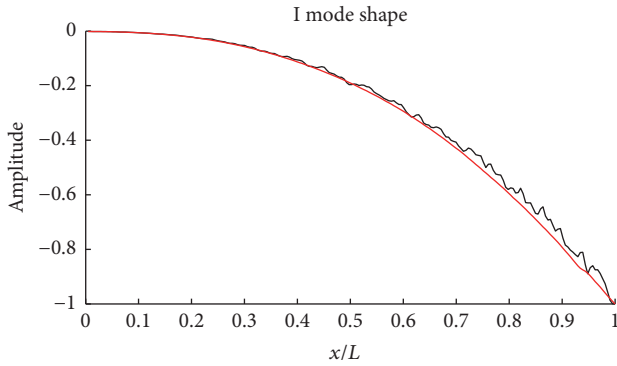


FIGURE 9: The first mode of blade natural vibrations measured experimentally: FFT (black) and FastScan (red).

were determined and compared to the values obtained from numerical simulations by the FEM. These results are shown in Table 1, where  $f_{\text{Exp}}$  are the frequencies obtained experimentally and  $f_{\text{FEM}}$  are the frequencies obtained numerically, while appropriate differences of these frequencies are denoted as  $\Delta f = |f_{\text{Exp}} - f_{\text{FEM}}|$ .

Calculated differences for individual vibration modes up to 22.5% were primarily due to the lack of precise information about the arrangement of additional masses and local stiffeners within the blade coating. Possibly, they are all related to the bonding technology used to join the high and low pressure surfaces of the blade. However, in the case of the diagnostic method proposed in this work the source of information about the presence of damage is carried primarily by the modes of natural vibrations rather than the values of natural frequencies. Assessment of individual mode shapes, which are shown in Figure 10, allow the authors to state that the numerical model applied for FEM simulations is sufficiently precise.

**2.4. Data Analysis Method.** A wavelet transform was used by the authors in order to analyse the data obtained experimentally. A wavelet transform represents a process of signal decomposition into, and subsequent representation by, a linear combination of base functions called wavelets. This transformation can be seen in the context of five types of wavelets: orthogonal (Haar, Daubechies, and Symlets), biorthogonal (BiorSplines, ReversBiors), with scaling function (Meyer), without scaling function (Morlet, Mexican hat, and Gaussian), and complex (Shannon, Complex Gaussian, and Complex Morlet). Members of each family are shown in Figure 11. A full set of wave functions used in signal transformation consists of a chosen basic waveform as well as certain functions that are scaled and shifted in time by output copies. This process leads to a scalable, hierarchical representation of the signal under consideration [43, 44].

Wavelets are mathematical functions characterized by zero-mean, a finite signal strength, as well as a limited range and rapid decay. These characteristics determine that wavelets are well-localized both in time (or space) and frequency domains. For this reason they are particularly useful in representing signals with singular points or discontinuities.

TABLE 1: Comparison of the first 10 natural frequency values obtained experimentally and numerically.

Lp.	$f_{\text{Exp}}$ [Hz]	$f_{\text{FEM}}$ [Hz]	$\Delta f$ [Hz]	$\Delta f$ [%]
(1)	7,03	6,69	0,34	5,10
(2)	20,78	22,48	1,70	7,56
(3)	44,84	51,07	6,23	12,19
(4)	75,94	91,55	15,61	17,05
(5)	114,69	142,37	27,68	19,44
(6)	159,84	206,18	46,34	22,47
(7)	214,22	273,06	58,84	21,55
(8)	285,16	350,80	65,64	18,71
(9)	360,63	430,97	70,35	16,32
(10)	445,78	513,01	67,23	13,10

The wavelet analysis can be continuous (CWT) or discrete (DWT). In the case of DWT signal decomposition is iterative and in each iteration the original signal is decomposed into components of lower resolution. Each iteration decreases signal resolution by half. For this reason the DWT has a limited number of decomposition levels and is ineffective for low sample rates. Contrary to that the CWT makes it possible to decompose signals for any scale and allows for smooth shifting. Due to these features the CWT was used by the authors in this study. Its application leads to certain coefficients determining the similarity between a selected wavelet and the signal under investigation. These coefficients are defined by the following formula:

$$\text{CWT}_f(a, b) = \int_{-\infty}^{+\infty} f(t) \psi(t) dt, \quad (1)$$

where  $a$  is a scale factor,  $b$  is a shift factor, and  $f(t)$  represents an analysed signal, while  $\psi(t)$  denotes the fundamental wave expressed as

$$\psi_{ab}(t) = \frac{1}{\sqrt{a}} \psi\left(\frac{t-b}{a}\right) dt; \quad a \in R^+, b \in R. \quad (2)$$

The scale and shift coefficients  $a$  and  $b$  in (2) determine the wavelength/frequency, and they change the wavelet position on the appropriate space/time axis. An important advantage of the CWT is its ability to change the transformation time resolution (frequency dependent). At low frequencies global signal information is obtained, which feature is useful for isolation of important signal characteristic. On the other hand, at high frequencies better resolution is achieved, which allows for identification of short-term characteristics obtained at the level of signal details. The results of the application of the CWT are presented in the form of scalograms in Figure 12, which graphically represent changes in wavelet coefficients at all assumed decomposition levels. High coefficient values indicate continuity of source signals.

The efficiency of the wavelet analysis is determined by the correct selection of signal preprocessing parameters and wavelet transform attributes. In the case of signals located in the spatial domain, such as are modes of natural vibrations,

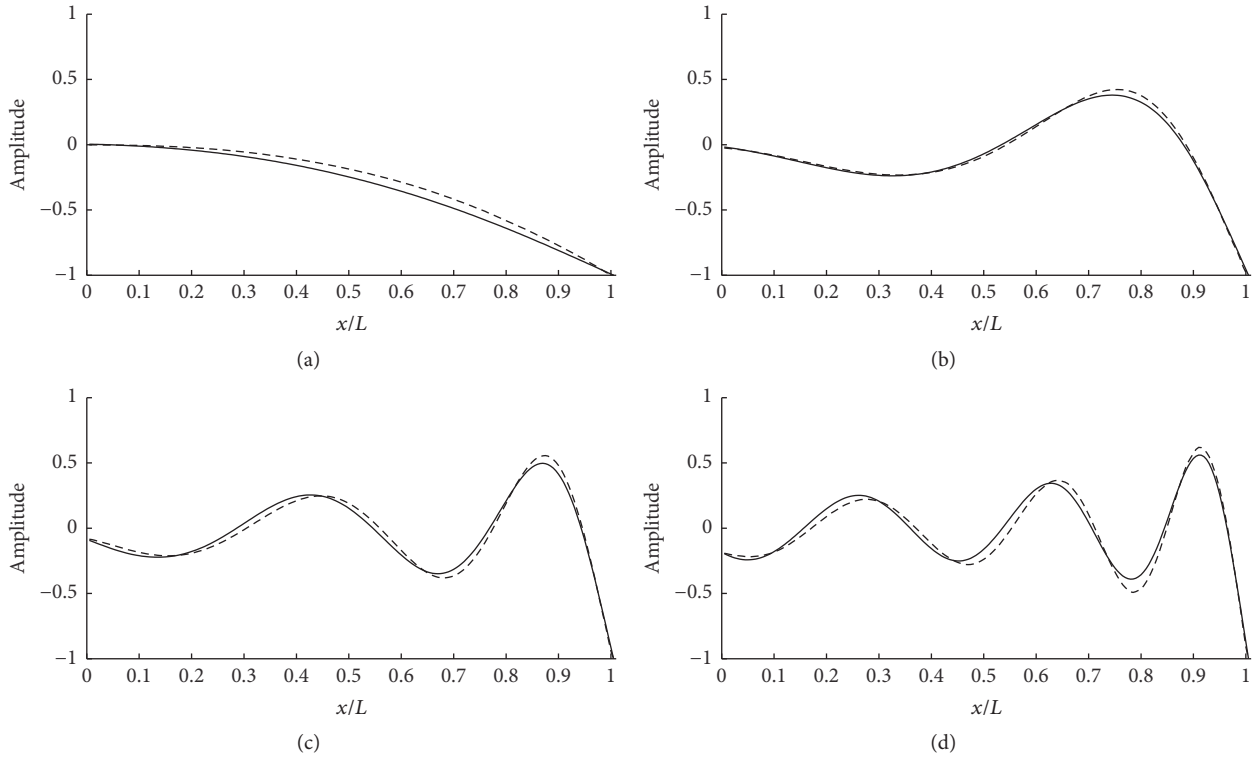


FIGURE 10: Selected modes of natural vibrations: (a) I mode, (b) III mode, (c) V mode, and (d) VII mode (experimental data: dashed line, computational data: continuous line).

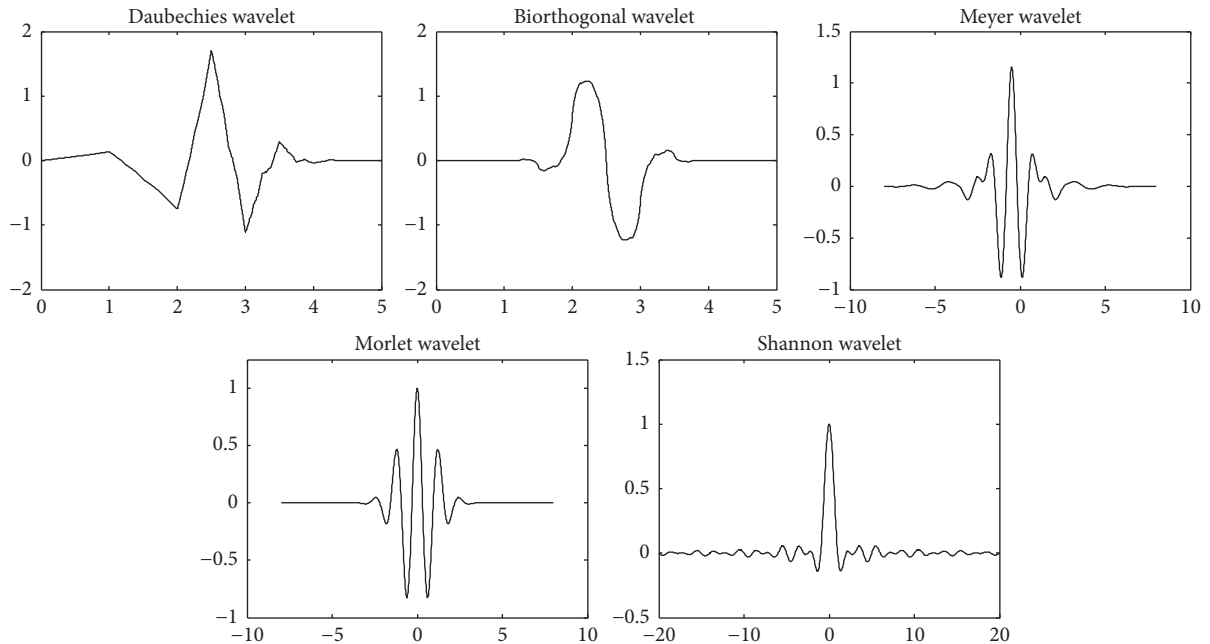


FIGURE 11: Selected examples of basic wavelet functions: Daubechies, Bior, Meyer, Morlet, and Shannon.

an even distribution of measurement points has overriding importance. It should be stated here that in the case of signals of uneven distributions of measurement points the results of wavelet analysis can be falsified. If measurements cannot be carried out for even distribution of measurement points,

interpolated signals should be produced first. Interpolation is also very useful in the case of signals with small numbers of samples.

Another problem is the effect of high wavelet coefficients at the beginning and end of signals. This prevents detecting

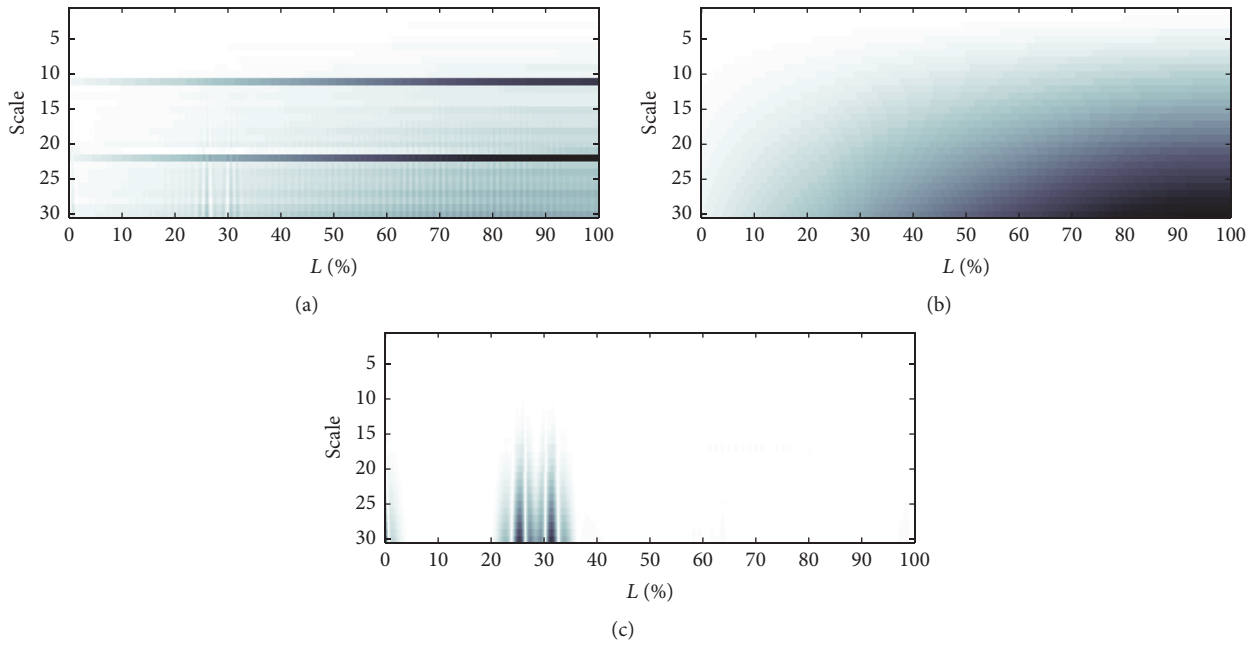


FIGURE 12: Typical scalograms obtained using different wavelet functions: (a) Morlet; (b) Haar; (c) Gauss.

and localizing damage properly. The solution to this problem is to extrapolate signals under examination at their ends, so that the zones of increased coefficient values, resulting from boundary effects, stay outside the range of interest. The type of applied interpolation and extrapolation algorithms, such as linear, polynomial, or different, depends on the form of source signals and should be chosen carefully not to introduce any additional discontinuities.

Another important aspect presents the appropriate selection of correct base wavelets. It turns out that the wavelets of orders lower than 4 generate nonzero wavelet coefficients in the entire signal lengths [45]. This feature prevents proper interpretation of calculated results. On the other hand the wavelets of large numbers of vanishing moments require high computational power and their repeated usage is time consuming. For the reasons described above in the present study base wavelets representing different families were tested in order to choose the most appropriate ones for diagnostic purposes. Figure 12 shows exemplary results of wavelet analysis obtained in the case of the blade under investigation with simulated damage located at 30% of its length, for three types of wavelets. It can be seen from Figure 12 that the most suitable base functions for the analysis of the wind turbine rotor blade is a Gauss wavelet function with four vanishing moments.

### 3. Results

Numerical results obtained by the use of the FEM model were employed to determine preprocessing parameters of signals and wavelet transform parameters such as the type of wavelet and scale. Proper interpretation of computed scalograms, in

terms of damage detection, localization, and estimation its size, was obtained for

- (i) linear extrapolation in order to extend the representation of selected modes of natural vibrations from initial 200 samples to 230 samples by adding 15 extra points on both signal ends,
- (ii) cubic spline interpolation in order to supplement selected modes of natural vibrations with additional samples by adding 10 extra points between each two subsequent signal samples,
- (iii) fourth-order Gauss base wavelet.

Scalograms for the second mode of natural vibration in the case of the intact, as well as three damage scenarios, are shown in Figures 13(a)–13(d). The simulated damage to the blade coating was successively spanning over 3, 6, and 10 measurement points.

For a majority of natural vibration modes the location of damage was identified correctly. However, for small defects of blade coating it is impossible to indicate accurately defect edges. For the 10th mode of natural vibrations detection was practically impossible, as shown in Figure 14(a).

The right side of the scalogram indicates nonzero wavelet coefficients as dark and blurry trails, that is, as the location of possible damage, whereas this part of the blade remains intact. This effect, which is noticed mainly for higher modes of natural vibrations, may obfuscate the scalogram and consequently can prevent proper damage localization. A solution to this problem is to adjust wavelets individually with higher order numbers, as seen in Figure 14(b).

Through the analysis of scalograms, in the case of one mode of natural vibrations, for all three damage locations, it

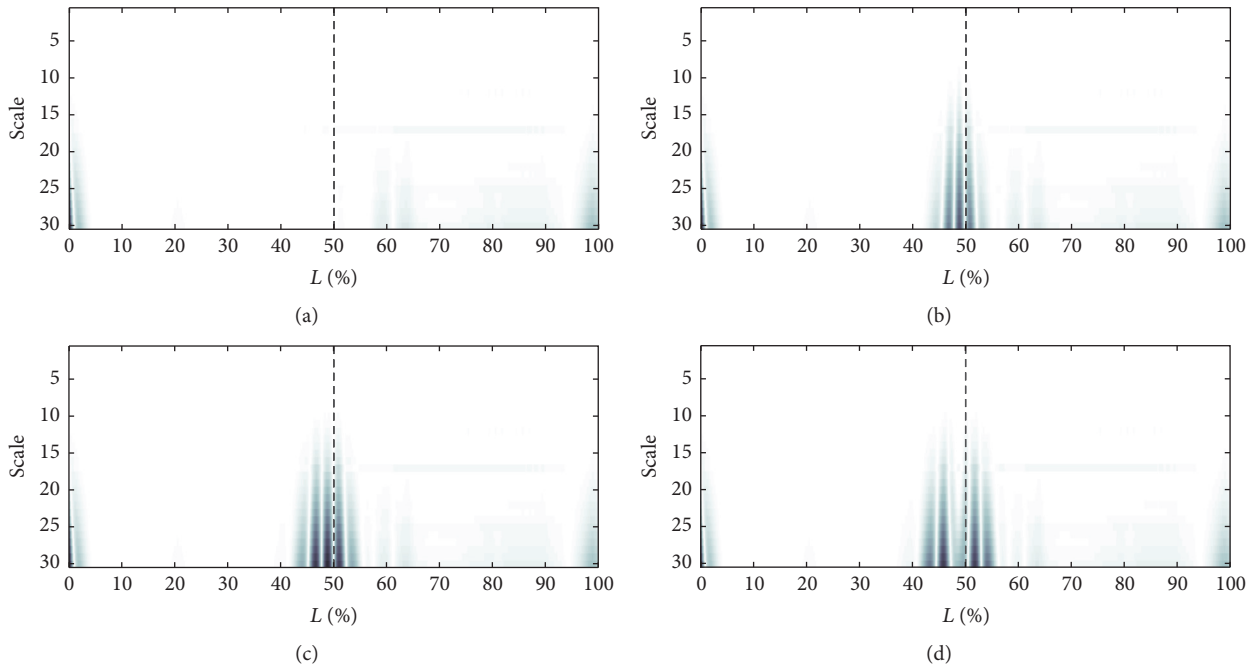


FIGURE 13: Numerical results of wavelet analysis of the 2nd mode on natural vibrations in the case of the intact and three damage scenarios.

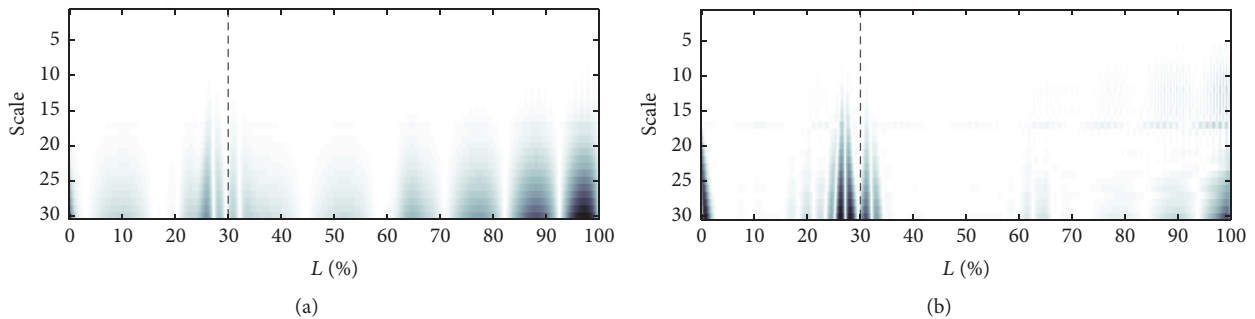


FIGURE 14: Numerical results of wavelet analysis of the 10th mode of natural vibrations in the case of Gauss4 (a) and Gauss6 (b) wavelet functions.

can be seen from Figure 15 that the visibility of damage of the same size varies according to the damage location. As shown in Figure 15(a) the effect of damage is relatively small there, where the cross-section of the blade has high stiffness values, as it is at the blade fixing. Changing the location of damage towards the tip of the blade results in an increase in the visible width of the damage zone, as presented in Figures 15(b) and 15(c). This is due to the fact that in this direction the stiffness of the blade decreases, due to a decrease in the cross-section of the blade as well as a decrease in the thickness of the blade coating.

In the first stage of the analysis of experimental signals, data processing and the analysis of CWT parameters were based on the results of numerical simulations. Figure 16 shows comparison of scalograms for the first 10 bending modes of natural vibrations obtained in the case of the blade

measurements with additional stiffeners. Vertical dashed lines indicate the location of damage defining the limits of the damage zone. Based on experimental data two conclusions can be drawn as starting points in order to improve the effectiveness of the proposed damage detection method. Through the comparison of modes of natural vibrations with corresponding scalograms it is possible to correlate the location of damage with characteristic points of source signals. An increase in wavelet coefficients indicating discontinuities was observed only, if damage coincided with local signal extremes.

The second conclusion concerns the noise level observed, which is directly related to the quality of measurement signals. High noise levels make it difficult to interpret results, as local stiffness changes can result in an increase in wavelet coefficients in the same range as noise. Therefore it was

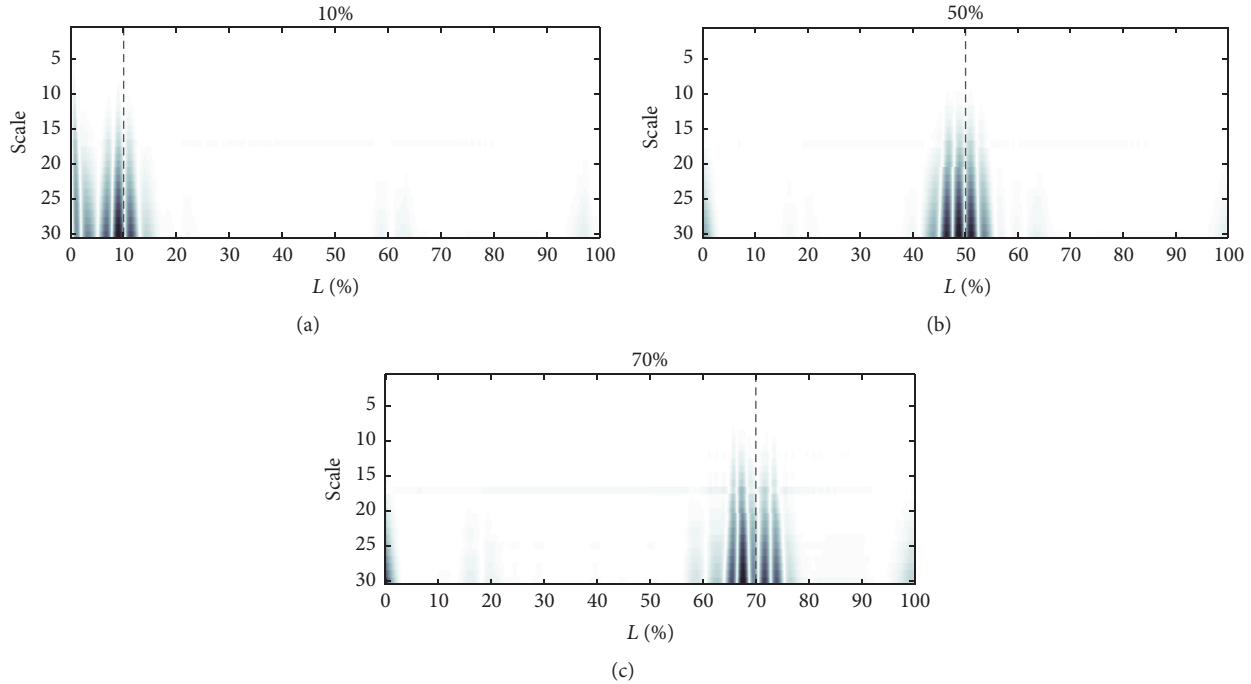


FIGURE 15: Numerical results of wavelet analysis in the case of three damage location scenarios.

necessary to modify the approach proposed by the authors to extract sharper information about the location and size of defects. It should be noticed that limited methods available to increase the accuracy of measurements make it necessary to modify signal analysis parameters.

#### 4. Discussion

The main element of signal preprocessing that influences the performance of wavelet analysis is interpolation. It separates one sample of the original signal from the other by increasing signal resolution, which can be described by a one-dimensional vector. The consequence is sharpening the boundaries of any discontinuities on scalograms, which may include measurement distortions. The level of details can be reduced by reducing the number of interpolation points, thus exposing the sought after changes in a wider range, as shown in Figure 17. The effect of this is the reduction of noise visible in scalograms as well as the appearance of a clear triangular formation that indicates the damage zone.

Thanks to the approach proposed scalograms were obtained also in the case of the remaining damage location scenarios. Figure 18 shows scalogram obtained for the 8th mode of natural vibrations in the case of damage in two extreme locations and spanning over 6 interpolation points.

It can be seen that the reduction in the number of interpolation points enabled the authors to detect damage very accurately. However, this process can cause loss of precise information about the width of the damage zone. Figure 19 shows scalograms for three different sizes of the damage zone close to the central location. Damage spanning

over 12, 10, and 8 measurement points, corresponding to 6%, 5%, and 4% of the total measurement line, were considered.

The analysis of the experimental results shows that the key element for correct interpretation of scalograms is a low noise level as well as precise knowledge about the structure of the object under investigation. For this reason, reference signals are indispensable. Figure 20 shows the results of the CWT based on the difference between modes of natural vibrations obtained for damaged and undamaged states. In this manner the signal-to-noise ratio was improved and positive results for more cases were achieved.

Based on the results obtained for all considered cases, it can be concluded that measured signals should be analysed and assessed in a multistage manner with respect to a reference state by

- (i) starting from a small number of interpolation points,
- (ii) registering global changes (damage identification),
- (iii) gradual increasing of the number of interpolation points, narrowing the window of determination of the damage nature and its exact boundaries.

#### 5. Summary and Conclusions

The paper presents certain results of numerical simulations and calculations as well as experimental measurements aimed at developing a method for delamination detection and localization in composite wind turbine blades. Numerically and experimentally determined modes of natural vibrations of a wind turbine blade were assessed for local changes that may indicate the presence of damage. For numerical simulation a simple delamination model was proposed that allowed the

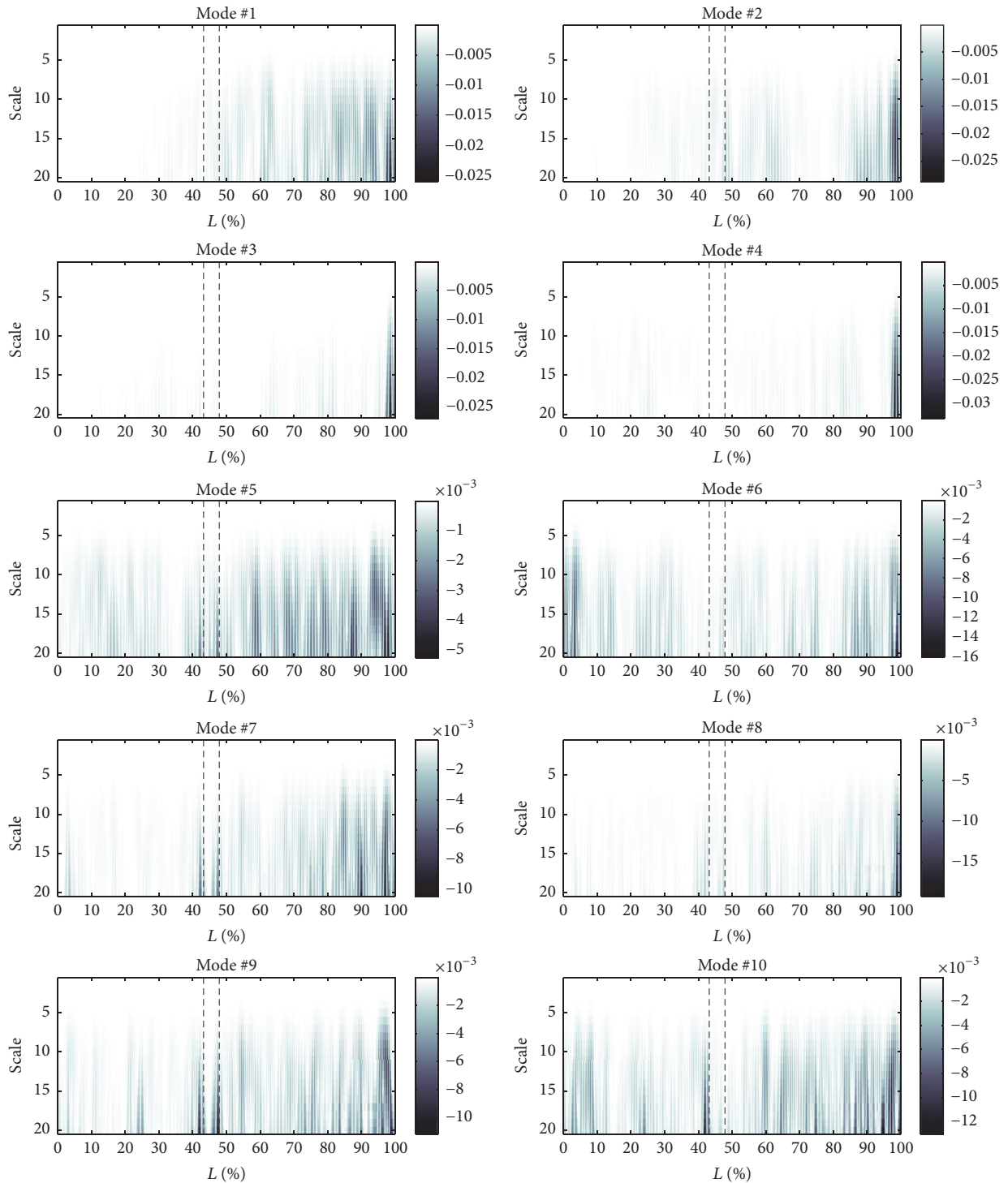


FIGURE 16: Scalograms obtained from measured data in the case of all modes of natural vibrations.

authors to calculate eight simulated damage levels in three different locations. Next the results obtained were used to determine an optimal set of parameters of the continuous wavelet transform (CWT). The second stage of the analysis included experimental research in order to verify both finite element method (FEM) based model predictions as well as

the damage detection method developed. The use of high-quality Scanning Laser Vibrometry allowed the authors to determine the optimal conditions and measuring procedures, which led to the required accuracy of measurement. At the same time the capabilities and limitations resulting from the nature of the measurement method were identified.

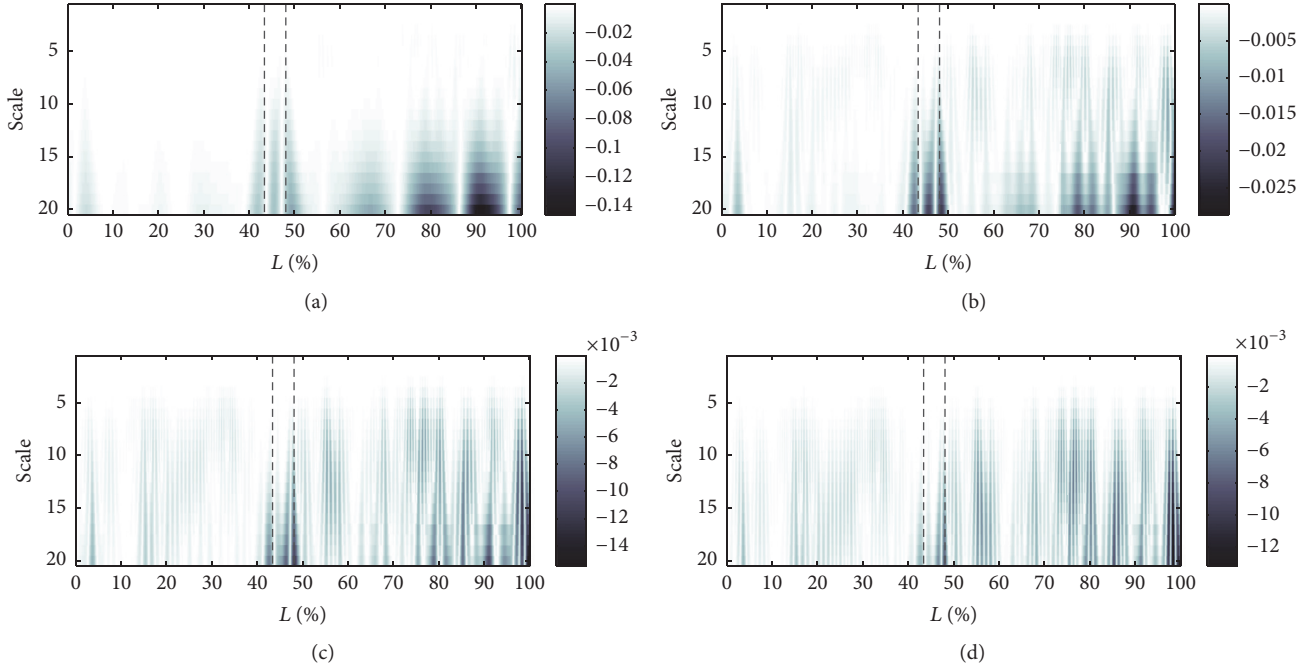


FIGURE 17: Scalograms of the 7th mode of natural vibrations in the case of different numbers of interpolation points: (a) 2; (b) 4; (c) 6; (d) 8.

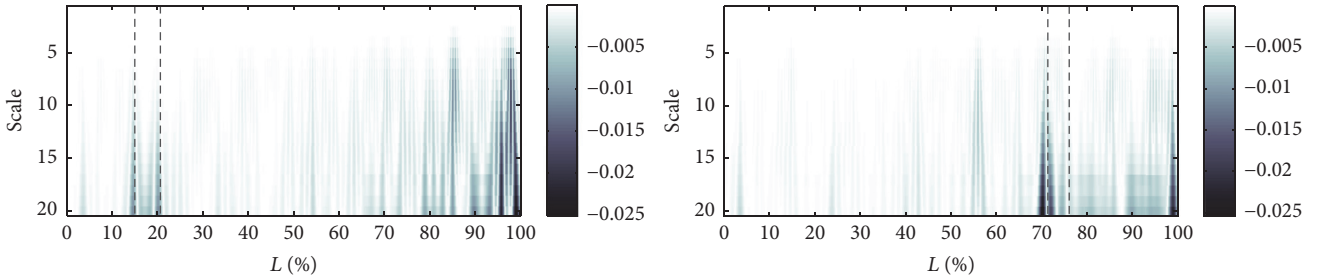


FIGURE 18: Scalograms of the 8th mode of natural vibrations obtained in the case of six interpolation points.

The main challenge in the practical implementation of a diagnostic system based on the proposed method comes from low levels of signal distortions that are sought after. The damage detection method presented can be used on an operating wind turbine based on data obtained from a system of piezoelectric or fibre optic sensors. Vibration measurements can also be performed by means of laser vibrometry supplemented by additional devices, such as is a derotator equipped with a special optical system, whose rotational motion is fully synchronized with the rotation of the object under investigation, such as are wind turbine blades.

The results of the research presented in this paper confirm the effectiveness of wavelet methods in detection of signal discontinuities. Based on them the following conclusions can be made:

(i) For best results, wavelet transform analysis should be preceded by some signal preprocessing in the form of extrapolation and interpolation. Extrapolation

reduces effects of increased values of wavelet coefficients at signal ends, while interpolation increases signal resolution.

- (ii) Analysis of modes of natural vibrations and corresponding scalograms makes it possible to correlate the damage location and size with characteristic points of source signals. Only in the case when damage zones coincide with local signal extremes, it is possible to detect damage.
- (iii) In the case of experimental data that are subjected to measurement noise, too many interpolation points block proper interpretation of scalograms. For this reason signals obtained experimentally should be analysed in a multistage manner, starting from a small number of interpolation points in order to observe more general changes. A gradual increase in the number of interpolation points allows determining the type of damage and its precise location.

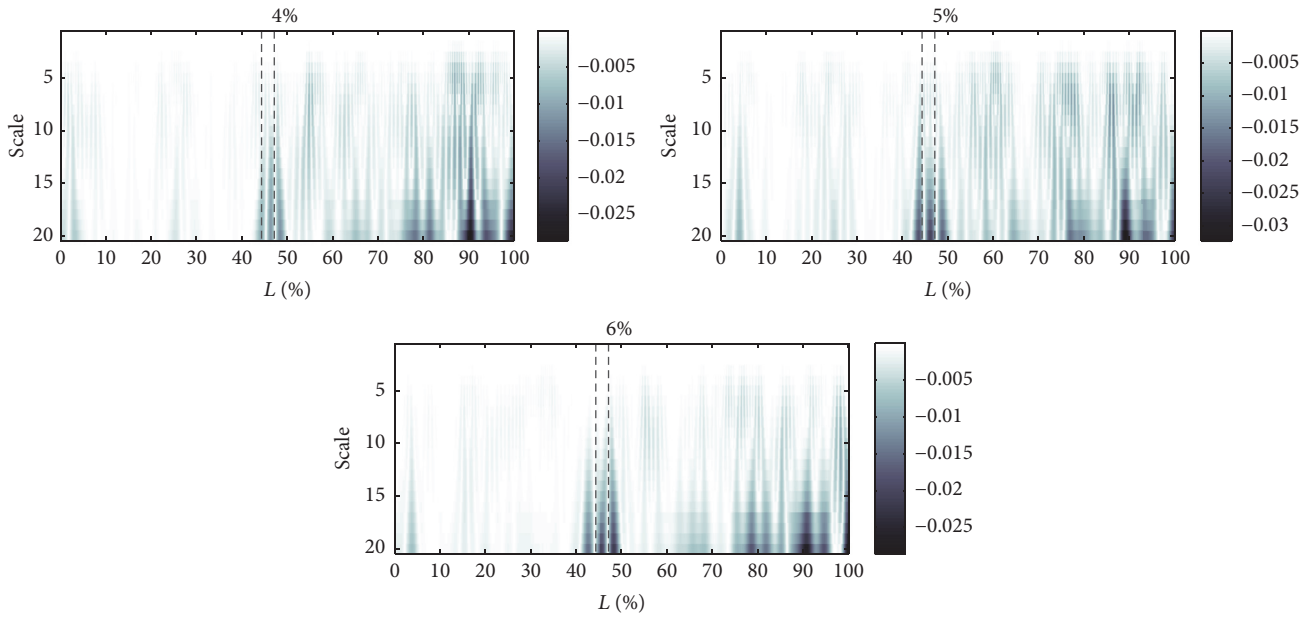


FIGURE 19: Scalograms of the 7th mode of natural vibrations obtained in the case of three different damage sizes.

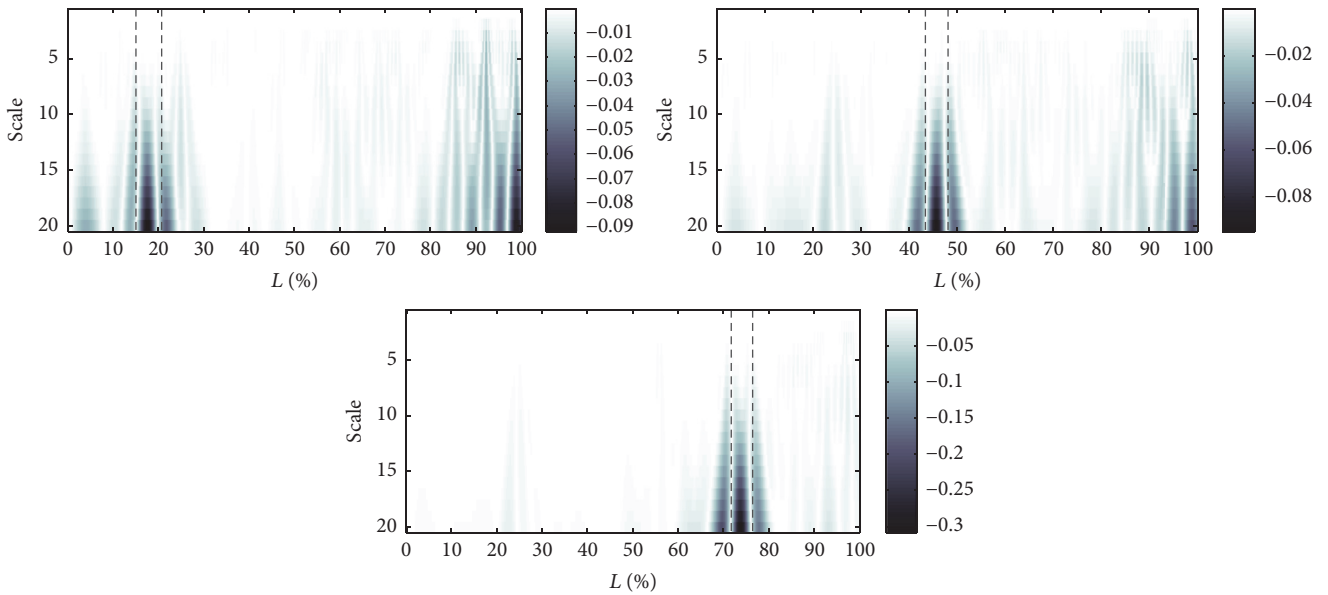


FIGURE 20: Scalograms of differential signals (damaged to reference) obtained for the 9th mode of natural vibrations for three damage locations.

(iv) Signal windowing increases the sharpness of the damage zone. This solution may be particularly important in the case of damage that has a small effect on the object dynamics.

Both experimental and numerical data indicate that the key to the correct interpretation of CWT analysis results, in the case of complex structures, is the knowledge about initial, undamaged state of the object under investigation. In the case of experiments carried out the availability of reference signals made it possible to reduce the influence of noise on the results of subsequent CWT computations.

**Conflicts of Interest**

The authors declare that there are no conflicts of interest regarding the publication of this paper.

**References**

[1] H.-J. Wagner and J. Mathur, *Introduction to Wind Energy Systems – Basics, Technology and Operation*, Springer, 2009.  
 [2] A. Ayub, W. Siew, and S. MacGregor, “External lightning protection system for wind turbine blades – further considerations,” in *Proceedings of the Asia-Pacific International Conference on Lightning (APL)*, Nagoya, Japan, 2015.

- [3] B. F. Sørensen, E. Jørgensen, C. P. Debel et al., "Improved design of large wind turbine blade of fibre composites based on studies of scale effects (Phase 1) Summary Report," 2004.
- [4] G. R. Kirikera, M. J. Schulz, and M. J. Sundaresan, "Multiple damage identification on a wind turbine blade using a structural neural system," in *Proceedings of the SPIE Smart Structures and Materials & Nondestructive Evaluation and Health Monitoring*, San Diego, CA, USA, 2007.
- [5] M. J. Schulz and M. J. Sundaresan, "Smart sensor system for structural condition monitoring of wind turbines," Tech. Rep. NREL/SR-500-40089, National Renewable Energy Laboratory, 2006.
- [6] M. J. Sundaresan, M. J. Schulz, and A. Ghoshal, "Structural health monitoring static test of a wind turbine blade," Tech. Rep. NREL/SR-500-28719, National Renewable Energy Laboratory, 2002.
- [7] M. Sundaresan, M. Schulz, and A. Ghoshal, "Intelligent blade for wind turbines," in *Proceedings of the 39th AIAA/ASME Aerospace Sciences Meeting and Exhibit, Wind Energy Symposium*, Reno, NV, USA, 2001.
- [8] J. Gieske and M. Rumsey, "Non-destructive Evaluation (NDE) Of Composite/Metal Bond Interface Of A Wind Turbine Blade Using An Acousto-ultrasonic Technique," in *Proceedings of the AIAA Aerospace Sciences Meeting*, pp. 249–254, 1997.
- [9] A. Katunin, M. Dańczak, and P. Kostka, "Automated identification and classification of internal defects in composite structures using computed tomography and 3D wavelet analysis," *Archives of Civil and Mechanical Engineering*, vol. 15, no. 2, pp. 436–448, 2015.
- [10] A. G. Beattie and M. Rumsey, "Non-destructive evaluation of wind turbine blades using an infrared camera," in *Proceedings of the ASME Wind Energy Symposium, 18th Aerospace Sciences Meeting and Exhibit*, 1999.
- [11] G. M. Smith, B. R. Clayton, A. G. Dutton, and A. D. Irving, "Infra-red thermography for condition monitoring of composite wind turbine blades feasibility studies using cyclic loading tests," in *Proceedings of the 15th British Wind Energy Association Conference*, York, UK, 1993.
- [12] J. Wei and J. McCarty, "Acoustic emission evaluation of composite wind turbine blades during fatigue testing," *Wind Engineering*, vol. 17, no. 6, pp. 266–274, 1993.
- [13] H. Sutherland, A. Beattie, B. Hansche et al., *The Application of Non-Destructive Techniques to the Testing of a Wind Turbine Blade*, Sandia National Laboratories, 1993.
- [14] A. G. Beattie, "Acoustic emission monitoring of a wind turbine blade during a fatigue test," in *Proceedings of the AIAA Aerospace Sciences Meeting*, 1997.
- [15] M. J. Blanch and A. G. Dutton, "Acoustic emission monitoring of field tests of an operating wind turbine," *Key Engineering Materials*, vol. 245–246, pp. 475–480, 2003.
- [16] J.-T. Kim, Y.-S. Ryu, H.-M. Cho, and N. Stubbs, "Damage identification in beam-type structures: frequency-based method vs mode-shape-based method," *Engineering Structures*, vol. 25, no. 1, pp. 57–67, 2003.
- [17] L. M. Khoo, P. R. Mantena, and P. Jadhav, "Structural damage assessment using vibration modal analysis," *Structural Health and Monitoring*, vol. 3, no. 2, pp. 177–194, 2004.
- [18] Y. Aoki and O.-I. Byon, "Damage detection of CFRP pipes and shells by using localized flexibility method," *Advanced Composite Materials: The Official Journal of the Japan Society of Composite Materials*, vol. 10, no. 2-3, pp. 189–198, 2001.
- [19] N.-G. Park and Y.-S. Park, "Identification of damage on a substructure with measured frequency response functions," *Journal of Mechanical Science and Technology*, vol. 19, no. 10, pp. 1891–1901, 2005.
- [20] A. Furukawa, H. Otsuka, and J. Kiyono, "Structural damage detection method using uncertain frequency response functions," *Computer-Aided Civil and Infrastructure Engineering*, vol. 21, no. 4, pp. 292–305, 2006.
- [21] M. Radziński, Ł. Doliński, M. Krawczuk, and M. Palacz, "Damage localisation in a stiffened plate structure using a propagating wave," *Mechanical Systems and Signal Processing*, vol. 39, no. 1-2, pp. 388–395, 2013.
- [22] J. Sierra-Pérez, M. A. Torres-Arredondo, and A. Güemes, "Damage and nonlinearities detection in wind turbine blades based on strain field pattern recognition. FBGs, OBR and strain gauges comparison," *Composite Structures*, vol. 135, pp. 156–166, 2016.
- [23] P. Pratumnopharat, P. S. Leung, and R. S. Court, "Wavelet transform-based stress-time history editing of horizontal axis wind turbine blades," *Journal of Renewable Energy*, vol. 63, pp. 558–575, 2014.
- [24] A. Katunin, "Stone impact damage identification in composite plates using modal data and quincunx wavelet analysis," *Archives of Civil and Mechanical Engineering*, vol. 15, no. 1, pp. 251–261, 2015.
- [25] A. Katunin and P. Przystałka, "Damage assessment in composite plates using fractional wavelet transform of modal shapes with optimized selection of spatial wavelets," *Engineering Applications of Artificial Intelligence*, vol. 30, pp. 73–85, 2014.
- [26] A. Katunin, "Vibration-based spatial damage identification in honeycomb-core sandwich composite structures using wavelet analysis," *Composite Structures*, vol. 118, pp. 385–391, 2014.
- [27] A. Banerjee and G. Pohit, "Crack investigation of rotating cantilever beam by fractal dimension analysis," in *Proceedings of the 2nd International Conference on Innovations in Automation and Mechatronics Engineering, ICIAME*, 2014.
- [28] J.-H. Chou and J. Ghaboussi, "Genetic algorithm in structural damage detection," *Computers & Structures*, vol. 79, no. 14, pp. 1335–1353, 2001.
- [29] A. Raich and T. Liszkai, "Benefits of implicit redundant genetic algorithms for structural damage detection in noisy environments," in *Proceedings of the Lecture Notes in Computer Science - GECCO*, Berlin, Germany, 2003.
- [30] C. Y. Kao and S.-L. Hung, "Detection of structural damage via free vibration responses generated by approximating artificial neural networks," *Computers & Structures*, vol. 81, no. 28-29, pp. 2631–2644, 2003.
- [31] Q. Chen, Y. W. Chan, and K. Worden, "Structural fault diagnosis and isolation using neural networks based on response-only data," *Computers & Structures*, vol. 81, no. 22-23, pp. 2165–2172, 2003.
- [32] A. Zak, M. Krawczuk, and W. Ostachowicz, "Numerical and experimental investigation of free vibration of multi-layer delaminated composite beams and plates," *Computational Mechanics*, vol. 26, no. 3, pp. 309–315, 2000.
- [33] C. N. Della and D. Shu, "Free vibration analysis of composite beams with overlapping delaminations," *European Journal of Mechanics - A/Solids*, vol. 24, no. 3, pp. 491–503, 2005.
- [34] W. Sprenger, F. Gruttmann, and W. Wagner, "Delamination growth analysis in laminated structures with continuum-based

- 3D-shell elements and a viscoplastic softening model,” *Computer Methods Applied Mechanics and Engineering*, vol. 185, no. 2-4, pp. 123–139, 2000.
- [35] O. Allix and P. Ladevèze, “Interlaminar interface modelling for the prediction of delamination,” *Composite Structures*, vol. 22, no. 4, pp. 235–242, 1992.
- [36] L. Daudeville, O. Allix, and P. Ladevèze, “Delamination analysis by damage mechanics: Some applications,” *Composites Part B: Engineering*, vol. 5, no. 1, pp. 17–24, 1995.
- [37] S. N. Wosu, D. Hui, and P. K. Dutta, “Dynamic mixed-mode I/II delamination fracture and energy release rate of unidirectional graphite/epoxy composites,” *Engineering Fracture Mechanics*, vol. 72, no. 10, pp. 1531–1558, 2005.
- [38] S. V. Kulkarni and D. Frederick, “Frequency as a Parameter in Delamination Problems—A Preliminary Investigation,” *Journal of Composite Materials*, vol. 5, no. 1, pp. 112–117, 1971.
- [39] S. Keshava Kumar, R. Ganguli, and D. Harursampath, “Partial delamination modeling in composite beams using a finite element method,” *Finite Elements in Analysis and Design*, vol. 76, pp. 1–12, 2013.
- [40] M. Marjanović and D. Vuksanović, “Layerwise solution of free vibrations and buckling of laminated composite and sandwich plates with embedded delaminations,” *Composite Structures*, vol. 108, no. 1, pp. 9–20, 2014.
- [41] D. Li and F. Zhang, “Full extended layerwise method for the simulation of laminated composite plates and shells,” *Computers & Structures*, vol. 187, 2017.
- [42] M. Krawczuk, W. Ostachowicz, and A. Zak, “Dynamics of cracked composite material structures,” *Computational Mechanics*, vol. 20, no. 1-2, pp. 79–83, 1997.
- [43] S. G. Mallat, “Theory for multiresolution signal decomposition: the wavelet representation,” *IEEE Transactions on Pattern Analysis and Machine Intelligence*, vol. 11, no. 7, pp. 674–693, 1989.
- [44] I. Daubechies, *Ten Lectures on Wavelets*, Society for Industrial and Applied Mathematics, 1992.
- [45] M. Rucka and K. Wilde, “Application of continuous wavelet transform in vibration based damage detection method for beams and plates,” *Journal of Sound and Vibration*, vol. 297, no. 3–5, pp. 536–550, 2006.

## Research Article

# An Integrated Cumulative Transformation and Feature Fusion Approach for Bearing Degradation Prognostics

Lixiang Duan <sup>1</sup>, Fei Zhao,<sup>2</sup> Jinjiang Wang,<sup>1</sup> Ning Wang,<sup>1</sup> and Jiwang Zhang<sup>1</sup>

<sup>1</sup>School of Mechanical and Transportation Engineering, China University of Petroleum, Beijing 102249, China

<sup>2</sup>Sichuan Special Equipment Inspection and Research Institute, Chengdu 610051, China

Correspondence should be addressed to Lixiang Duan; [duanlx@cup.edu.cn](mailto:duanlx@cup.edu.cn)

Received 4 August 2017; Revised 21 December 2017; Accepted 15 January 2018; Published 18 February 2018

Academic Editor: Rafał Burdzik

Copyright © 2018 Lixiang Duan et al. This is an open access article distributed under the Creative Commons Attribution License, which permits unrestricted use, distribution, and reproduction in any medium, provided the original work is properly cited.

Aimed at degradation prognostics of a rolling bearing, this paper proposed a novel cumulative transformation algorithm for data processing and a feature fusion technique for bearing degradation assessment. First, a cumulative transformation is presented to map the original features extracted from a vibration signal to their respective cumulative forms. The technique not only makes the extracted features show a monotonic trend but also reduces the fluctuation; such properties are more propitious to reflect the bearing degradation trend. Then, a new degradation index system is constructed, which fuses multidimensional cumulative features by kernel principal component analysis (KPCA). Finally, an extreme learning machine model based on phase space reconstruction is proposed to predict the degradation trend. The model performance is experimentally validated with a whole-life experiment of a rolling bearing. The results prove that the proposed method reflects the bearing degradation process clearly and achieves a good balance between model accuracy and complexity.

## 1. Introduction

In order to improve production efficiency, quality, and flexibility, modern manufacturing highly depends on the trouble-free operation of components in manufacturing machines [1, 2]. Therefore, the timely monitoring and estimation of the running status of important machine components are necessary [3]. Prognostics, as an important process of monitoring the condition of components or a system [4], is regarded as a predictive maintenance strategy that can anticipate the occurrence of component defects to ensure the availability, reliability, and security of critical components (such as bearings, gears, or cutting tools) [5, 6]. A bearing is at the heart of rotating machinery and is viewed as a frequent contributor to the breakdown of such machinery [7, 8]; hence, accurate prognostics of bearing degradation trends is of substantial practical relevance.

In general, prognostics can be roughly classified into model-based, data-driven, and hybrid approaches [9]. Among these, data-driven approaches are easier to deploy and have been widely used [10]. They usually follow a road map of data acquisition, feature extraction, and prognostic

modeling. Of the three steps above, the key step is feature extraction, because it has a direct influence on predictor performance. Features that can properly reflect the degradation progression could yield accurate and simple prognostics [11–13].

Various features extracted from time domain, frequency domain, and time-frequency domain have been investigated for bearing degradation prognostics. Time domain methods extract statistical features, such as root mean square (RMS), kurtosis, crest factor, and peak-to-peak value. The energy of bearing defect frequency is extracted as features by frequency domain methods, such as ball-pass frequency of outer ring  $f_{BPFO}$ , ball-pass frequency of inner ring  $f_{BPFI}$ , and ball-spin frequency  $f_{BSF}$ . Time-frequency domain methods extract features, such as short time Fourier transform (STFT) [14], wavelet transform (WT) [15, 16], and empirical mode decomposition (EMD) [17].

These features are extracted to serve as degradation prognostics; however, the original features often show nonideal evolution, fail to reflect the degradation trend, and even cause problems for the prognostics tasks.

In the current research, these questions are studied from different aspects. Some methods are proposed from the smoothing aspect to reduce the influence of fluctuation and obtain a smoothed trend feature. For example, Sutrisno et al. [18] used a moving average filter to reduce the fluctuation of original features and the smoothed features were put into the least squares support vector regression (LS-SVR) for bearing remaining life estimation. Following a similar idea, Loutas et al. [19] employed a moving average filter to suppress the high noise and volatility of condition-based maintenance features. Ben Ali et al. [20] proposed a feature extraction method based on a combination of a sliding average and Weibull distribution to avoid feature fluctuation for accurate bearing remaining useful life prediction. Although smoothing methods are easy to implement, they could lose some useful information. More generally, new indexes have been constructed using some further processing methods on the original features. For instance, Qiu et al. [21] developed a robust degradation indicator based on a self-organizing map neural network to evaluate the bearing degradation performance. Sassi et al. [22] developed two new scalar indicators by combining six conventional features to evaluate the severity of bearing degradation. Zhang et al. [23] used a continuous hidden Markov model combined with various features to construct an effective degradation indicator of rolling bearings for residual life prediction. Xi et al. [24] established a virtual health index based on a transformation formula to quantify the health degradation of an engineering system and further performed a health state prediction process. Liao [25] discovered prognostic features to represent the fault progression by using genetic programming, in which monotonicity is used as fitness function. Sun et al. [26] proposed a nonprobabilistic metric to assess the operational reliability of aeroengines by utilizing the cosine function to map kernel principal angles extracted from condition information into a similarity index.

The above feature extraction methods process only a single signal fragment and ignore the relationship of the whole signal. The extracted features are easily affected by other factors such as noise and show some local fluctuations, so they do not clearly describe the state of the machinery degradation. Bearing degradation is a cumulative process, and thus we can consider the entire degradation process from a cumulative perspective. By continuously accumulating data, each extracted feature is able to take advantage of all the previous data, thereby achieving the purpose of mining the overall data, to reduce the influence of fluctuations and extract trend feature with more reliable trend characteristics.

Considering these problems, this study proposes a novel prognostics method based on a cumulative transformation technique and feature fusion approach for bearing degradation trend prognostics. To consider the overall relationship of the data and obtain features with a good monotonic trend characteristic, a novel cumulative transformation algorithm is proposed. However, each cumulative feature only contains partial information of bearing status. To more comprehensively reflect the degradation process, an effective and popular feature fusion method KPCA is used to fuse multi-dimensional cumulative features and develop a degradation

index. Furthermore, the degradation index is reconstructed by phase space reconstruction (PSR) to better grasp its nature and input into an extreme learning machine (ELM) for bearing degradation trend prognostic. The effectiveness of the proposed method is validated with a whole-life experiment of a rolling bearing.

The main merits of this study are as follows: (1) a novel cumulative transformation algorithm is proposed to extract features with better trend characteristics; (2) an integrated cumulative transformation and feature fusion method is investigated for bearing degradation prognostics; (3) a prediction model based on PSR and ELM is built to perform the prognostic task. The remainder of this article is organized as follows: The theoretical background of cumulative transformation is introduced in Section 2. The proposed method is then described in Section 3. In Section 4, the bearing experimental test demonstrated the effectiveness of the method. Finally, the conclusions of this study are drawn in Section 5.

## 2. Theoretical Framework

*2.1. The Theory of Cumulative Damage.* Generally, degradation of many units or systems, such as parts or machinery, is a damage accumulation process under different running environments, which grows as time passes. To explore the relationship between the degradation process and cumulative damage and find an effective way to reflect the degradation process, some methods have been investigated from the perspective of accumulation. These methods can be roughly divided into two categories: model-based and data-driven.

Model-based methods suppose that the degradation process can be expressed by a series of mathematical equations regarding cumulative system damage and time, and a model is set up by investigating the failure mechanism and the degradation paths. For instance, in [27, 28], different cumulative damage models are constructed to describe the system degradation process by considering different degradation paths and distributions, and a preventive maintenance policy is obtained to minimize the maintenance cost. In [29], a nonparametric model called cumulative incidence functions and logical analysis are integrated to solve the problem of multi-failure-mode in prognosis. The curves of cumulative incidence functions are calculated to reflect the running time on the degradation status of the monitored bearing by using the lifetime data of different failure modes. Model-based cumulative damage methods can describe the degradation process well using an accurate model, although an accurate model is hard to build in most cases, and the applicability of the model is limited for different systems.

Compared with model-based cumulative methods, data-driven methods are easier to achieve by transforming condition monitoring data into an appropriate cumulative form to infer the system status and estimate the useful remaining life. In [30], cumulative energy functions and mathematical morphology gradient in both the time and frequency domains from partial discharge waveforms are calculated as feature parameters to detect defects and assess the insulation conditions of high-voltage equipment. In [31], a smoothed accumulation method for bearing remaining

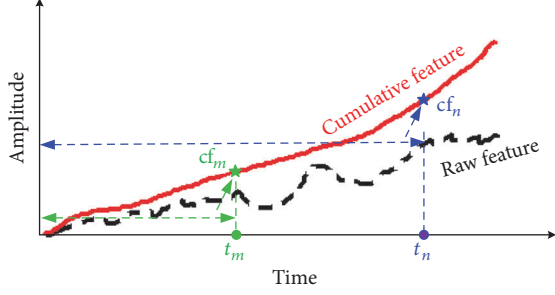


FIGURE 1: Diagram of cumulative transformation.

useful life estimation is proposed, in which the acceleration values instead of directly measured vibration values were used to estimate the bearing degradation. In [4], a cumulative method is applied to describe the degradation process from a data-driven perspective, in which the condition monitoring lifetime data are used to obtain cumulative descriptors to reflect the bearing degradation process.

In summary, a system degradation process is usually regarded as a continuous damage accumulation process over time. Therefore, we can reveal the essence of the degradation process from the perspective of accumulation by building a cumulative damage model or extracting a cumulative feature.

**2.2. Cumulative Transformation Algorithm.** For most mechanical components, such as bearings, gears, and rotors, the degradation is a constant damage accumulation process without self-recovery when these parts exceed the service life, so the appropriate degradation features should exhibit good trend characteristics, such as monotonicity, trendability, and robustness. Monotonicity characterizes the potential monotonic increasing or decreasing trend of the feature, and it is an essential characteristic of a degradation feature. Trendability is related to the characteristic form and its correlation with time, which reflects how the characteristic sequence changes with time and has some universality. Robustness is used to measure the fluctuation of the feature sequence. However, the features extracted from the raw vibration data often do not show good trend characteristics. Thus, a new concise and effective strategy is proposed to get monotonic and trendable features.

A new cumulative transformation algorithm is introduced by transforming an extracted feature into its corresponding cumulative form. The sketch map of cumulative transformation is shown in Figure 1. Mainly, the cumulative function is defined as the accumulation of a given time series, to which a pointwise running sum of squares of difference and scaling operations are simultaneously applied to achieve the transformation task as follows:

$$cf_n = \sqrt{\sum_{i=1}^n (f(i) - f_{\text{nor}})^2}, \quad (1)$$

where  $f_{\text{nor}}$  represents the normal value, which is defined as the corresponding average of a segment stationary trend of feature  $f(i)$  in normal conditions, and  $cf_n$  represents the

cumulative total of feature up to  $n$  observations. It should be noted that the cumulative sum of a feature is sensitive to noise. To get a cumulative feature with better monotonicity and trendability, the smoothing should be applied a priori, before accumulation.

To quantitatively evaluate the suitability of the extracted features, the trend characteristics, such as monotonicity, trendability, and robustness, are further investigated. Monotonicity is given by the absolute difference between the number of positive and negative derivatives of each feature. It can be seen that the value of monotonicity is in the range from 0 to 1. The higher the monotonicity is, the greater the fitness of the feature is presented. The range of trendability is from 0 to 1, and the larger the trend index is, the higher the linear correlation degree of the feature sequence with time is. The range of robustness is also from 0 to 1; the more the feature fluctuates, the smaller the robustness is, and the greater the uncertainty is when the trend prognostics is carried out.

The criteria of monotonicity, trendability, and robustness are, respectively, defined as follows: [32]:

$$\begin{aligned} \text{Mon} &= \left| \frac{\text{number of } d/df > 0}{n-1} - \frac{\text{number of } d/df < 0}{n-1} \right|, \\ \text{Tre}(F, T) &= \frac{|n \sum_i f_i t_i - \sum_i f_i \sum_i t_i|}{\sqrt{[n \sum_i f_i^2 - (\sum_i f_i)^2] [n \sum_i t_i^2 - (\sum_i t_i)^2]}}, \\ \text{Rob}(F) &= \frac{1}{n} \sum_i \exp\left(-\frac{f_i - \tilde{f}_i}{f_i}\right), \end{aligned} \quad (2)$$

where  $f$  is the original feature curve,  $n$  is the feature number of observations,  $d/df$  is the differentiation operator which is the differential of the original feature,  $t$  is time index, and  $\tilde{f}$  is the feature curve after smooth processing of  $f$ .

A single evaluation metric can only measure the suitability of the degradation feature from a certain aspect. In order to evaluate the feature more comprehensively, a linear weighted comprehensive indicator is proposed to realize the effective fusion of evaluation metrics. The specific form of weighted fusion is as follows:

$$\begin{aligned} W_{F \in \Omega} &= \omega_1 \text{Tre}(F, T) + \omega_2 \text{Mon}(F) + \omega_3 \text{Rob}(F) \\ \text{s.t. } &\omega_i > 0 \\ &\sum_i \omega_i = 1, \end{aligned} \quad (3)$$

where  $W$  is a comprehensive evaluation index,  $F$  is the feature sequence, and  $\omega$  is the weight.  $\omega$  is usually determined by empirical knowledge. It can be seen from the derivation that  $W$  is positively related to the three evaluation indexes, so the greater  $W$  is, the more effective the description of the degradation process is, and the more favorable to the prediction the degradation trend is.

### 3. Proposed Method

**3.1. Framework of Proposed Method.** The goal of the present study is to develop a degradation index with a better trend and achieve simpler and more accurate prognostics. The complete procedure of bearing degradation trend prognostics is depicted in Figure 2. First, some typical features in the time and time-frequency domains are extracted based on raw vibration data. Second, cumulative transformation is proposed to gain the cumulative features with better trend characteristics from the original features. Following that, the feature fusion KPCA [33] is used to get a degradation trend index to reflect degradation process. Next, the mutual information method is adopted to choose the time delay and the process of CAO is employed to determine the embedded dimension. Meanwhile, the degradation index is reconstructed by PSR [34]. Finally, the reconstructed degradation index is input into ELM for bearing degradation trend prognostic.

To quantitatively assess the proposed method, three criteria are investigated, including mean absolute percent error (MAPE) and root mean square error (RMSE). The mathematical expressions are as follows:

$$e_{\text{MAPE}} = \frac{1}{n} \sum_{i=1}^n \left| \frac{y_i - \hat{y}_i}{y_i} \right|, \quad (4)$$

$$e_{\text{RMSE}} = \sqrt{\frac{1}{n} \sum_{i=1}^n (y_i - \hat{y}_i)^2},$$

where  $n$  is the number of data and  $y_i$  and  $\hat{y}_i$  represent the true and predicted values, respectively.

**3.2. Cumulative Feature Extraction and Fusion.** The failure of machinery represents the procedure of an abnormal phenomenon from the incipient failure to deterioration. Many types of signals are used to reflect the abnormal phenomena. Vibration signals acquired via sensors are the most widely used for condition monitoring, although they usually contains redundant dimensions, and the vibration signal generated by a certain bearing is often overwhelmed by noise or other components' vibrations; hence, it is seldom used directly.

In order to solve this problem, the useful features are extracted from the time domain, frequency domain, and time-frequency domain for fault diagnosis and prognostics. In this study, 12 time domain features and four frequency domain features are extracted, as shown in Table 1. In Table 1,  $x_i$  is the original time domain signal set (seeing Section 4.1),  $n$  is the sample points of  $x_i$ ,  $\mu$  and  $\sigma$  represent the mean value of  $x_i$  and standard deviation, respectively,  $s(k)$  is the frequency spectrum of  $x_i$ ,  $K$  is the number of spectral lines of  $s(k)$ , and  $X_{\text{fm}}$  represents the mean value of  $s(k)$ .

However, time domain and frequency domain analyses cannot simultaneously deal with the signals in the time and frequency domains; furthermore, some useful information could be discarded. To solve this problem, more information is obtained by time-frequency domain analysis. The most

TABLE 1: Features and corresponding formulas.

Feature	Formula
Mean absolute value (MAV)	$X_{\text{am}} = \frac{1}{n} \sum_n  x_i $
Maximum	$X_{\text{max}} = \max(x)$
Variance	$X_{\text{var}} = \frac{1}{n-1} \sum_n (x_i - \mu)^2$
Skewness	$X_{\text{skew}} = E \left[ \left( \frac{x_i - \mu}{\sigma} \right)^3 \right]$
Shape factor	$X_{\text{sf}} = \frac{X_{\text{rms}}}{X_{\text{abs}}}$
Clearance factor	$X_{\text{clf}} = \frac{X_{\text{max}}}{X_{\text{smr}}}$
Average frequency	$X_{\text{fm}} = \frac{\sum_{k=1}^K s(k)}{K}$
Frequency skew	$X_{\text{fs}} = \frac{\sum_{k=1}^K (s(k) - X_{\text{fm}})^3}{K X_{\text{fa}}^3}$
RMS	$X_{\text{rms}} = \sqrt{\frac{1}{n} \sum_n x_i^2}$
Peak-to-peak	$X_{\text{p-p}} = \max(x) - \min(x)$
Square mean root (SMR)	$X_{\text{smr}} = \left( \frac{1}{n} \sum_n \sqrt{ x_i } \right)^2$
Kurtosis	$X_{\text{kurt}} = \frac{1}{n} \sum_n \left( \frac{x_i - \mu}{\sigma} \right)^4$
Crest factor	$X_{\text{cf}} = \frac{X_{\text{max}}}{X_{\text{rms}}}$
Impulse factor	$X_{\text{if}} = \frac{X_{\text{max}}}{X_{\text{abs}}}$
Standard deviation frequency (SDF)	$X_{\text{fa}} = \sqrt{\frac{\sum_{k=1}^K (s(k) - X_{\text{fm}})^2}{K - 1}}$
Frequency kurtosis	$X_{\text{fk}} = \frac{\sum_{k=1}^K (s(k) - X_{\text{fm}})^4}{K X_{\text{fa}}^4}$

commonly used time-frequency analysis methods are STFT, WT, and EMD. Among them, the difficulty of STFT is how to select the proper window function, and the main weakness of EMD is its high sensitivity to noise and mode mixing. In addition, WT is reported to have better applicability in dealing with vibration data from rotating machinery such as bearings [35]. In this study, a specific wavelet "db4" from Daubechies family wavelets in three levels is applied to extract the eight features of wavelet packet energy  $P_{d,n}$ .

Assuming that  $E_{d,n}$  is the energy of the  $n$ th frequency band in the  $d$ th layer, which is defined as [36]

$$E_{d,n} = \sum_{k=1}^M \|W_{d,n}^k\|^2, \quad (5)$$

where  $W_{d,n}^k$  is the wavelet coefficient of the  $k$ th discrete point of the decomposition signal  $x_{d,n}(i)$  and  $M$  is the number of  $x_{d,n}(i)$ , the contribution of the  $n$ th band in the  $d$ th layer wavelet coefficient to the energy of the signal is defined as

$$P_{d,n} = \frac{E_{d,n}}{\sum_{n=1}^{2^d} E_{d,n}}. \quad (6)$$

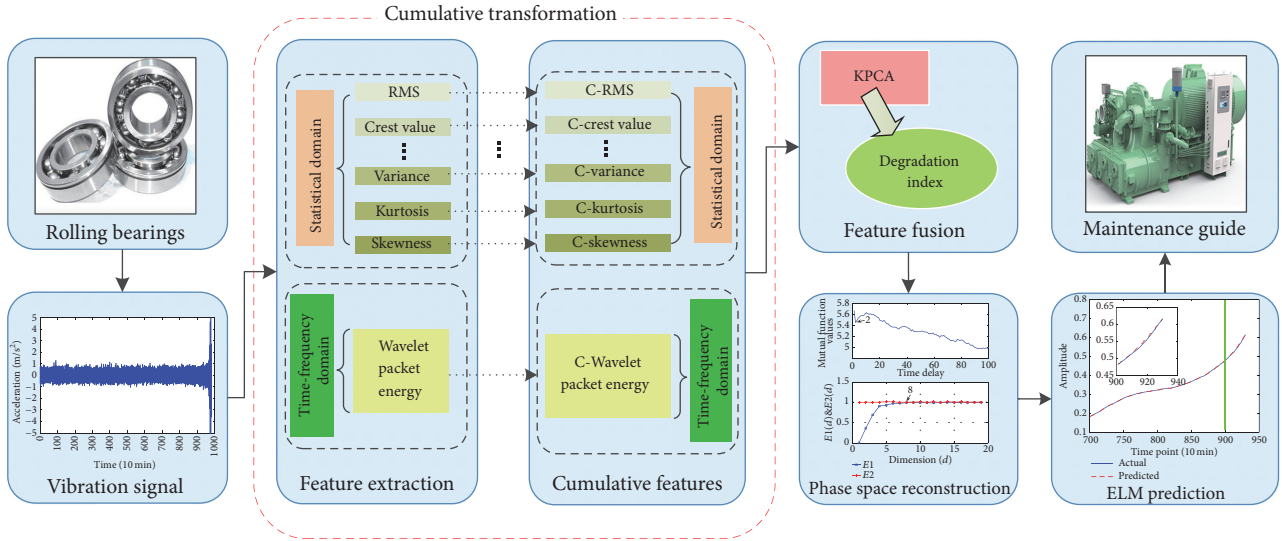


FIGURE 2: Flowchart for bearing degradation trend prognostic.

After the original features are extracted, each feature is mapped to its respective cumulative form by cumulative transformation algorithm, and a total of 24 cumulative features are obtained. Each cumulative feature contains partial information of bearing status and reflects the bearing degradation process from different aspects. To comprehensively describe the degradation process, KPCA is used to fuse all cumulative features and obtain a degradation index.

**3.3. PSR and ELM.** In the data-driven prognostic methods, a number of methods are used to build prediction models, for example, ARIMA, artificial neural network (ANN), and support vector machine (SVM). Among these methods, ELM is a new, simple, and effective single hidden layer feedforward neural network (SLFN) learning algorithm, which was first proposed by Huang et al. for both classification and regression purposes [37]. The structure parameter of ELM is randomly chosen, and iteration is not required. Compared with other gradient-based machine learning algorithms, ELM has the advantages of high computational efficiency, easy implementation, and good generalization performance. Owing to these advantages, ELM is employed to build a model to perform the prediction tasks in this study.

In addition, the time sequences prognostic supposes that the future values are determined by certain past values. The bearing degradation index is a one-dimensional time sequence, and the challenge is how to train the ELM model. PSR is able to extend a one-dimensional time sequence to a high-dimensional phase space that has an equivalent space with the original dynamic system in topology, and it can effectively grasp the nature of time series. Therefore, it is employed to deal with the model's import problem. The time lag and embedded dimension of the one-dimensional degradation index are determined by mutual information method and CAO's method, respectively. The degradation index reconstructed by PSR is then used as an import to the ELM model.

## 4. Experiment and Results

**4.1. Experimental Setup.** To assess the effectiveness of the proposed method, the vibration signals originating from Center for Intelligent Maintenance Systems (IMS), University of Cincinnati [38], are used. The designed experiment platform is shown in Figure 3 and the experiments are carried out under constant load and speed conditions. Four Rexnord ZA-2115 double-row bearings are erected on the axis of the test rig. The rotation speed is maintained at 2000 rpm. The axis and bearings bear a radial load of 6000 lbs through a spring mechanism, and all bearings are forced lubricated. The acceleration sensors are installed on the bearing housing. The new bearings are tested under this condition for full life cycle test. All failures occurred after exceeding designed lifetime of the bearing which is more than 100 million revolutions. It is found that the data in 10000 minutes before bearing failure can well reflect the whole failure process of the bearing, so the data in this period are analyzed. Each data set ( $x_i$ ) of bearing 1 used in this study is 1-second vibration signal snapshots recorded at 10-minute intervals and consists of 20480 points with the sampling rate of 20 kHz.

**4.2. Data Processing.** The 12 time domain features, four frequency domain features, and eight time-frequency domain features are extracted from the vibration signal as described in Section 3.2. The original features are shown in Figures 4–7. From Figures 4–7, we can see some of the extracted original features (e.g., square mean root, RMS, skewness, standard deviation frequency, and WPE2), which can reflect the bearing degradation process to some extent. By contrast, some other features cannot reflect the bearing degradation trend appropriately. For example, frequency kurtosis and WPE1 are almost constant; the crest factor, clearance factor, and so on contain a lot of noise information and show no trendability. Moreover, the evolution of the original feature curves always

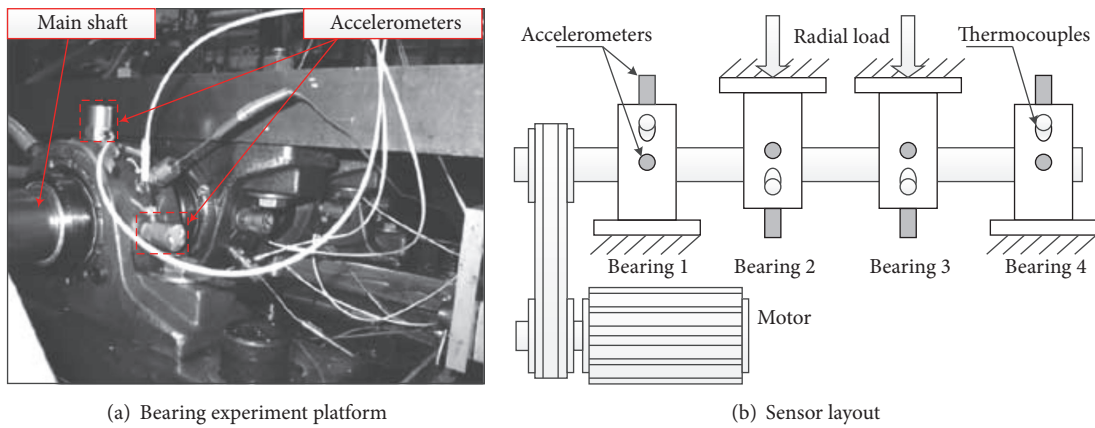


FIGURE 3: Illustration of the bearing experiment platform.

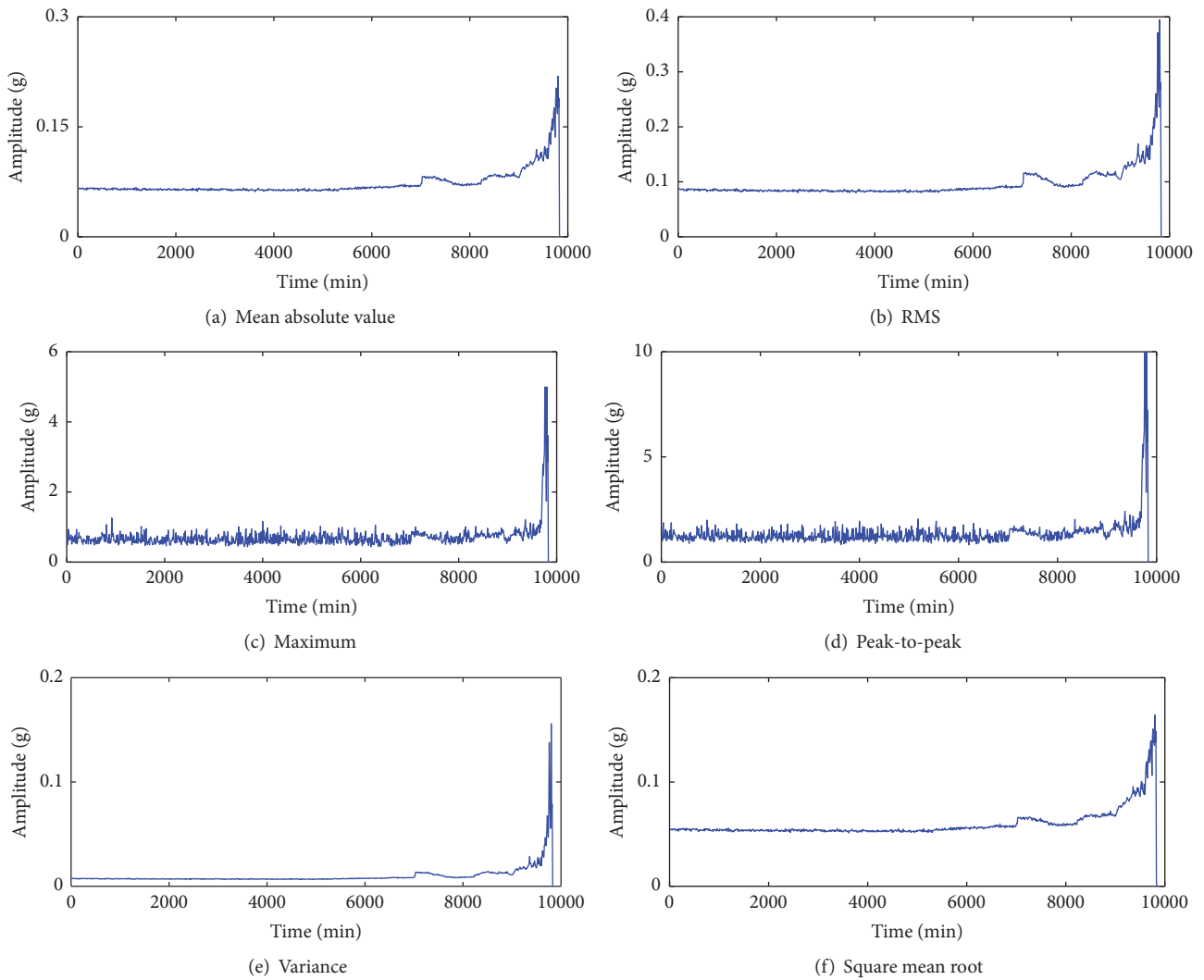


FIGURE 4: Six dimensional time domain features.

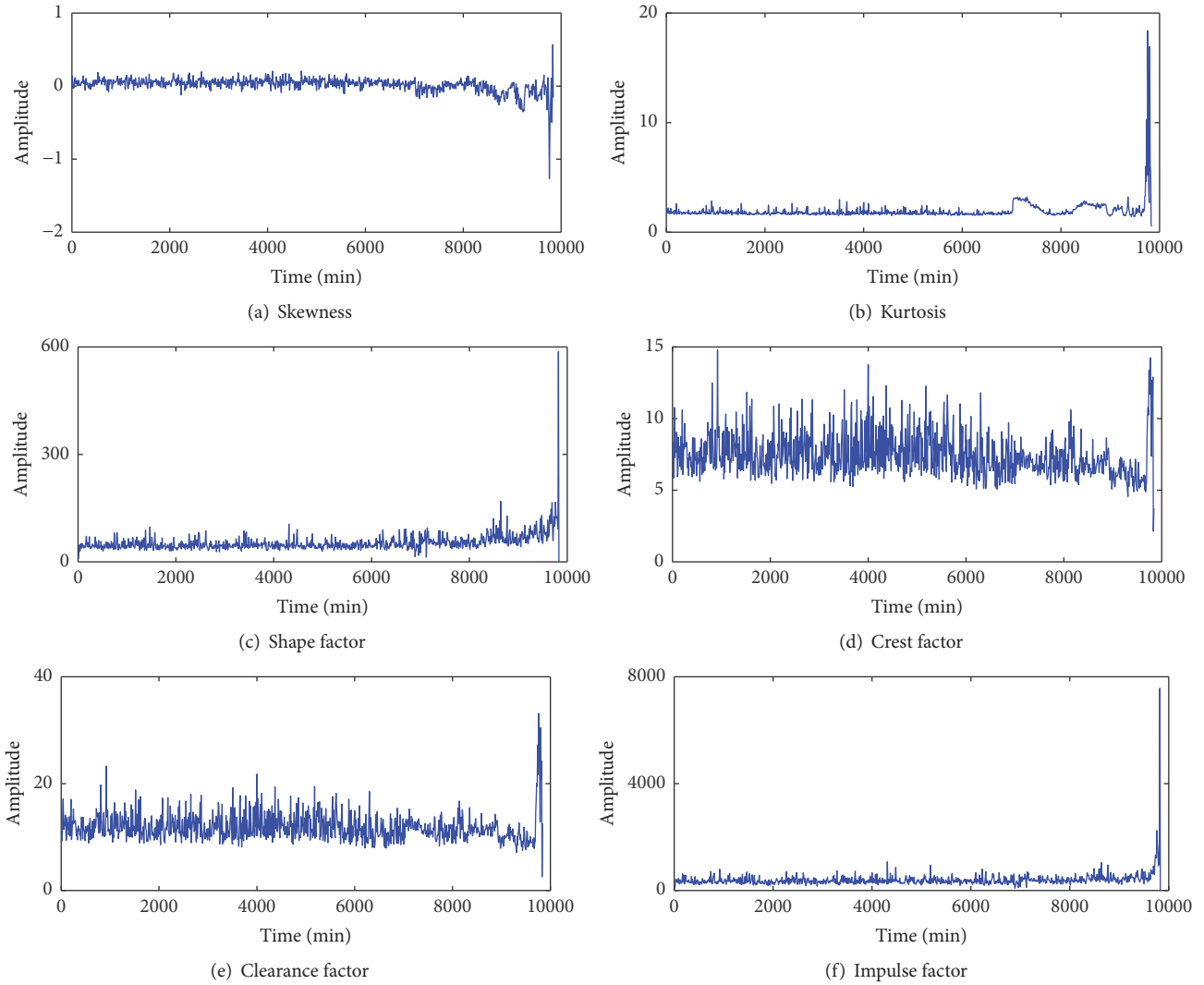


FIGURE 5: Six dimensionless time domain features.

shows some fluctuation and low trend characteristics owing to the background noise or some significantly stronger signals (e.g., gears and bars), which fail to track degradation trend effectively and even cause problems for the prognostic task.

In order to quantitatively describe the trend characteristics of the original features, a comprehensive evaluation indicator is proposed for feature evaluation. Table 2 shows the evaluation results of the eight optimal features, which indicate that the evaluation results and waveforms can show good agreement. It is found that even the comprehensive index of the eight optimal primitive features is relatively small.

To obtain the features that have better trend characteristics and can better reflect the bearing degradation process, the original features are transformed to build respective cumulative features. The eight optimal features and their corresponding cumulative features are shown in Figures 8 and 9. Compared with the original features, all the cumulative features show a smooth, monotonically increasing trend and can more clearly reflect the bearing degradation process.

The evaluation results of cumulative features are shown in the Table 3. Compared with Table 2, it can be seen that the monotonicity, trendability, and robustness of the eight features are obviously improved by the cumulative transformation. The monotonicity of each cumulative feature is increased to 1. Although there are some differences in the trendability, they have been greatly improved. The difference in robustness is small, and it remains at a high level.

In order to verify that the cumulative transformation has strong versatility, 24 original features of a rolling bearing are transformed to obtain the corresponding cumulative features, and the original and cumulative features are normalized and displayed by waterfalls. The feature waveforms are shown in Figures 10 and 11.

It can be seen that the trend between original features is different, and the characteristics of each feature also show more violent fluctuations, whereas cumulative features show a similar monotonically increasing trend, and the waveforms of cumulative features are very smooth.

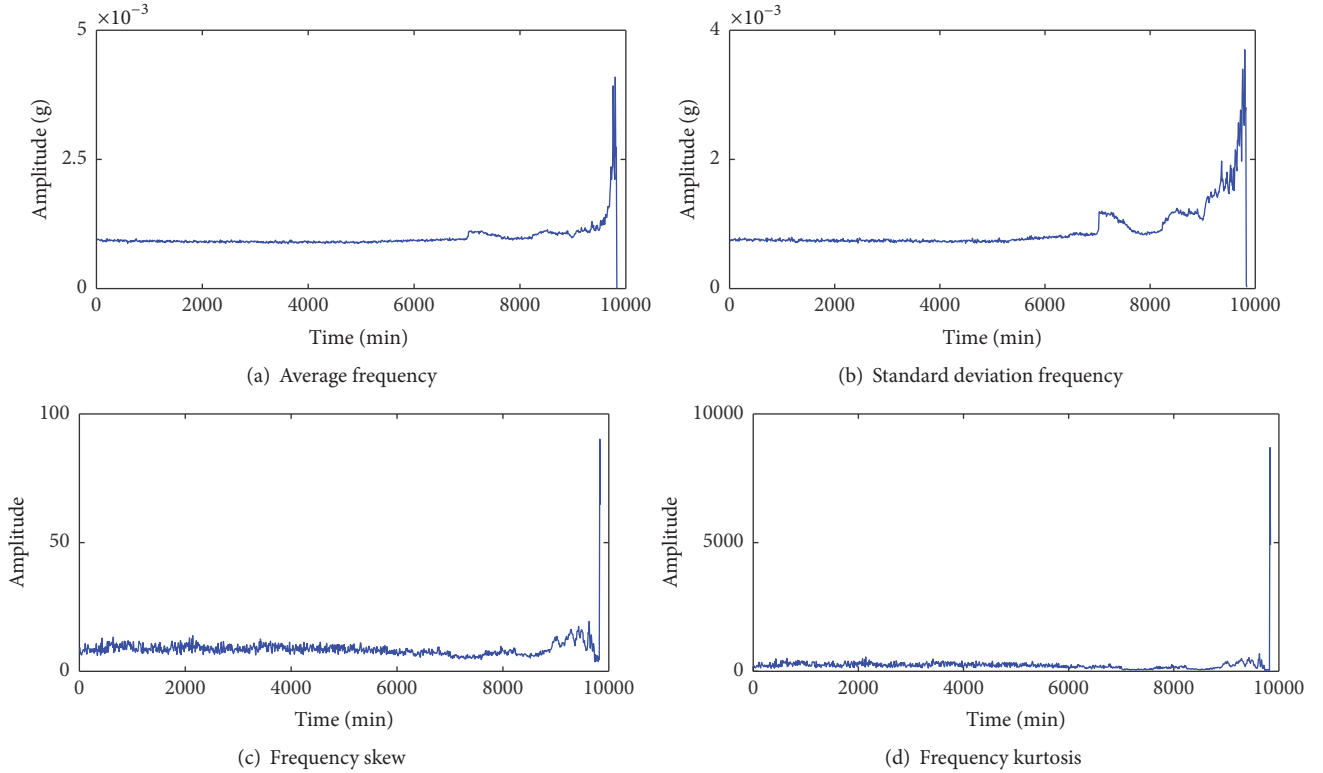


FIGURE 6: Four frequency domain features.

TABLE 2: Evaluation results of the first eight best bearing features.

Feature	Monotonicity	Trendability	Robustness	Comprehensive indicator
WPE2	0.0081	0.7834	0.9813	0.4353
WPE5	0.0163	0.7262	0.9837	0.4228
WPE8	0.0203	0.6945	0.9811	0.4147
SDF	0.0163	0.6211	0.9739	0.3893
SMR	0.0224	0.5842	0.9826	0.3830
MAV	0.0183	0.5807	0.9820	0.3798
RMS	0.0163	0.5527	0.9790	0.3698
Skewness	0.0142	0.4845	0.9564	0.3437

Different cumulative features can reflect the bearing degradation process from different aspects; the entire bearing degradation process cannot be described comprehensively by only one cumulative feature. Therefore, these cumulative features are fused to construct the fusion degradation index by the KPCA method, and the first principal component is selected as the degradation index. It can be seen from Figure 12 that the degradation index is monotonically increasing, and the different life states clearly characterize the entire life of the bearing. Accordingly, the index constructed by KPCA can reflect the degradation more effectively and comprehensively.

As can be seen from Figure 12, the bearing is in normal operation before the first 7000 minutes, after which the condition of the bearing suddenly changed and the curve increased sharply, which shows there are certain faults occurring in the bearing.

In the degradation trend prognostics, an improper input may lead to a bad prognostics result, and thus the key problem is how to validly import the one-dimensional degradation index into the model. PSR can effectively extend the one-dimensional time signal to its corresponding high-dimensional equivalent, which can be used to deal with the model's import problem. In the present study, the time delay  $\tau$  is set as 2 through the mutual information method. Then, the embedded dimension  $d$  is set to 8 through the CAO method (as shown in Figure 13.). Based on the selected optimal delay time and embedded dimension, the ELM model is used to predict the bearing degradation trend.

**4.3. Results and Discussion.** A nonlinear function, that is, a sigmoid function, is selected as the activation function in ELM for bearing degradation trend prediction, and the number of hidden nodes is set as 10. As mentioned above, the

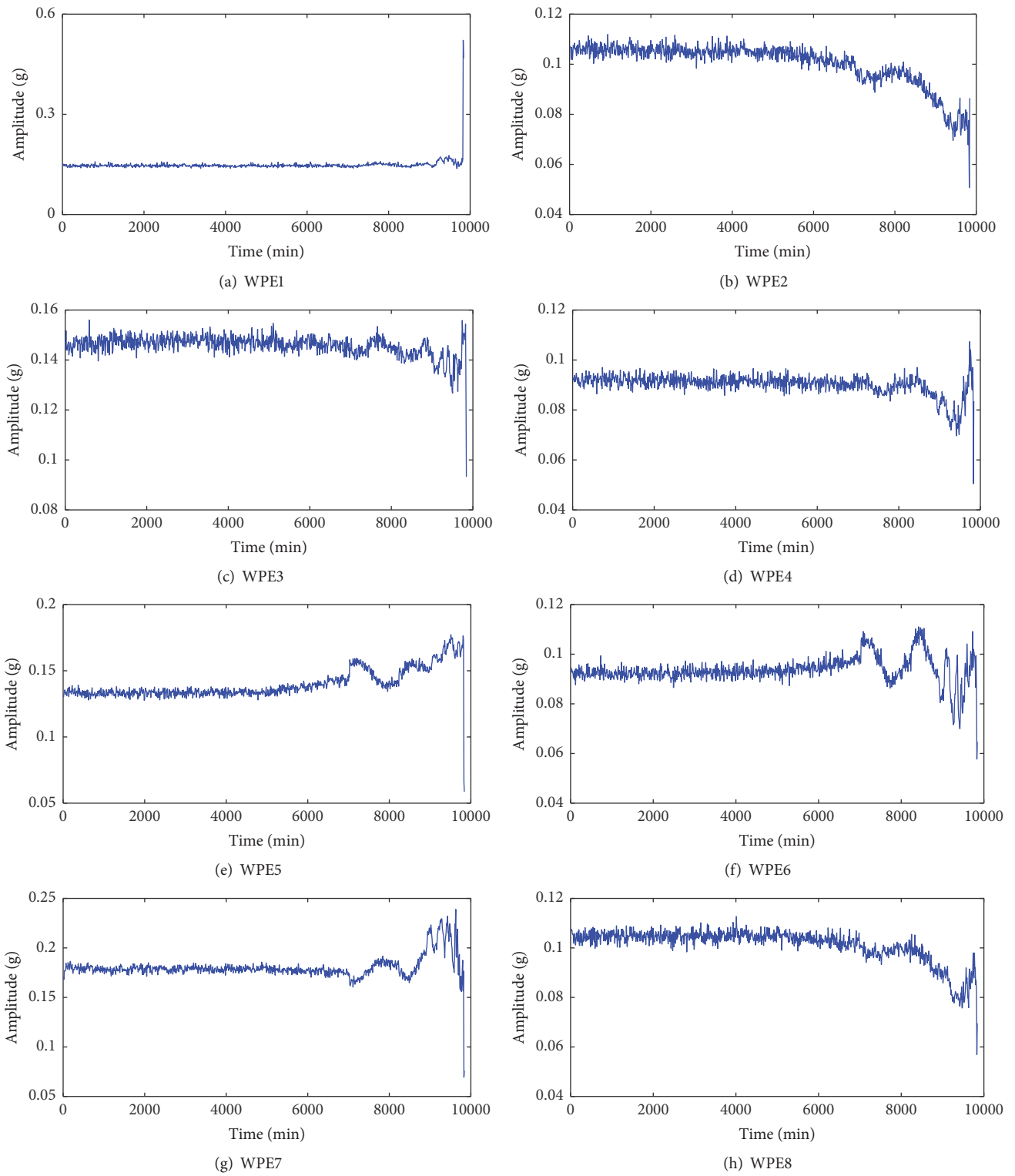


FIGURE 7: Eight wavelet packet energy features.

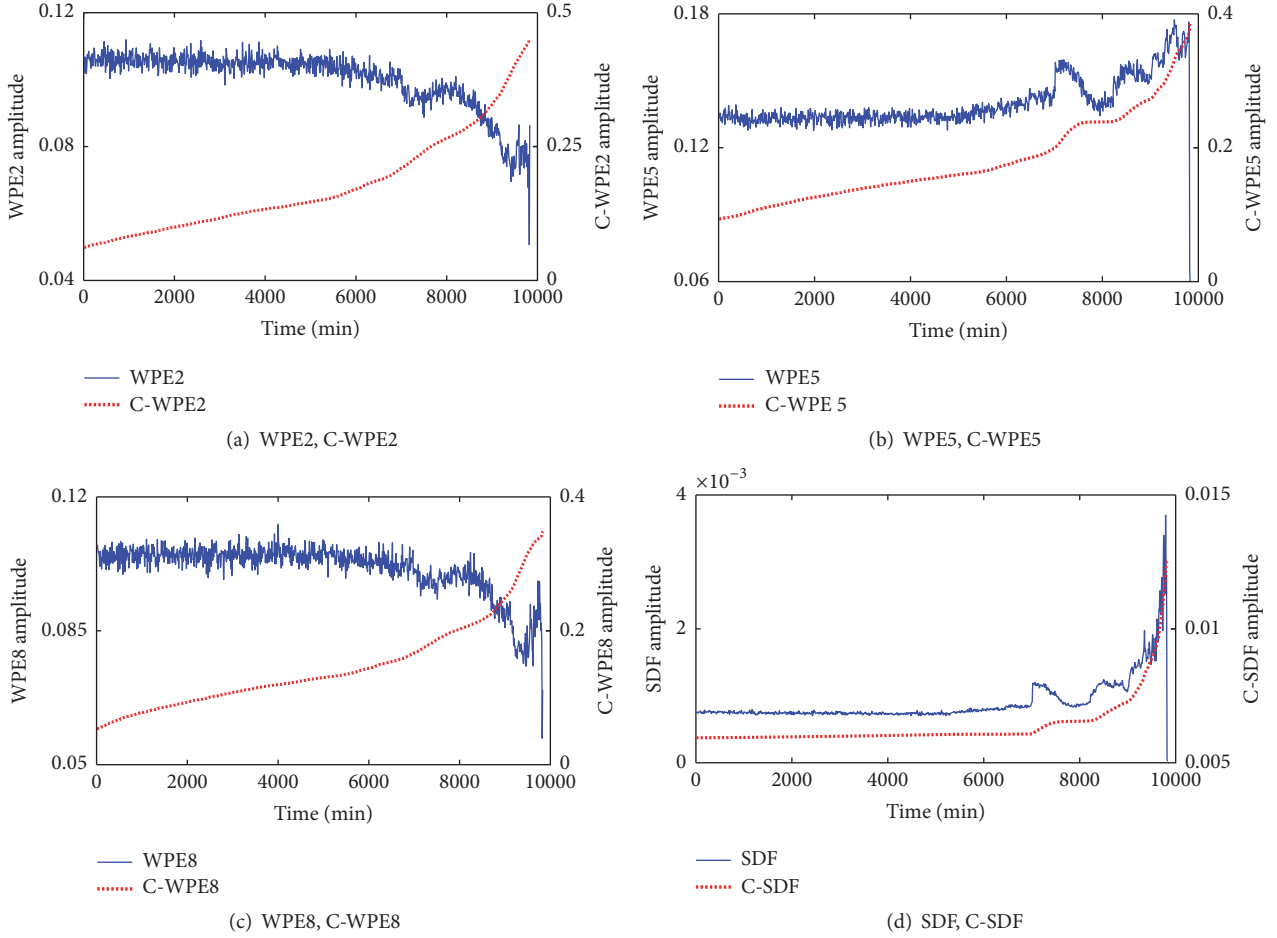


FIGURE 8: First four preferred features and corresponding cumulative features.

TABLE 3: Evaluation results of cumulative features of the first eight best original features.

Feature	Monotonicity	Trendability	Robustness	Comprehensive indicator
C-WPE2	1.0000	0.9302	0.9895	0.9770
C-WPE5	1.0000	0.9195	0.9929	0.9744
C-WPE8	1.0000	0.9295	0.9900	0.9769
C-SDF	1.0000	0.6228	0.9961	0.8861
C-SMR	1.0000	0.7268	0.9891	0.9159
C-MAV	1.0000	0.7495	0.9882	0.9225
C-RMS	1.0000	0.7797	0.9864	0.9312
C-Skewness	1.0000	0.9559	0.9868	0.9841

bearing is in a normal state before the 7000 minutes, so the points from 701 to 900 are used to train the ELM model and the following 30 points are used for testing.

The actual value and the predicted result of the original and cumulative fused index are shown in Figure 14. It can be seen that the predicted result of the cumulative fused index is consistent with the actual degradation curve.

The present method is compared with other methods to verify the advantages in the bearing degradation trend prognostics. Kurtosis, RMS, and WPE2 of the original and cumulative form are, respectively, used as the degradation

index to feed input to the ELM model, determining the import parameters of the ELM model with the mutual information method and CAO method. For illustration, Figures 15–17 show different prediction results.

From Figures 15–17, it can be seen that, owing to the fluctuation and bad trend, the degradation progression cannot be reflected clearly by the original features; furthermore, the prediction difficulty has also been increased, which leads to bad performance of the prognostic model. Compared with the original features, the cumulative features achieve better prediction result than the corresponding original

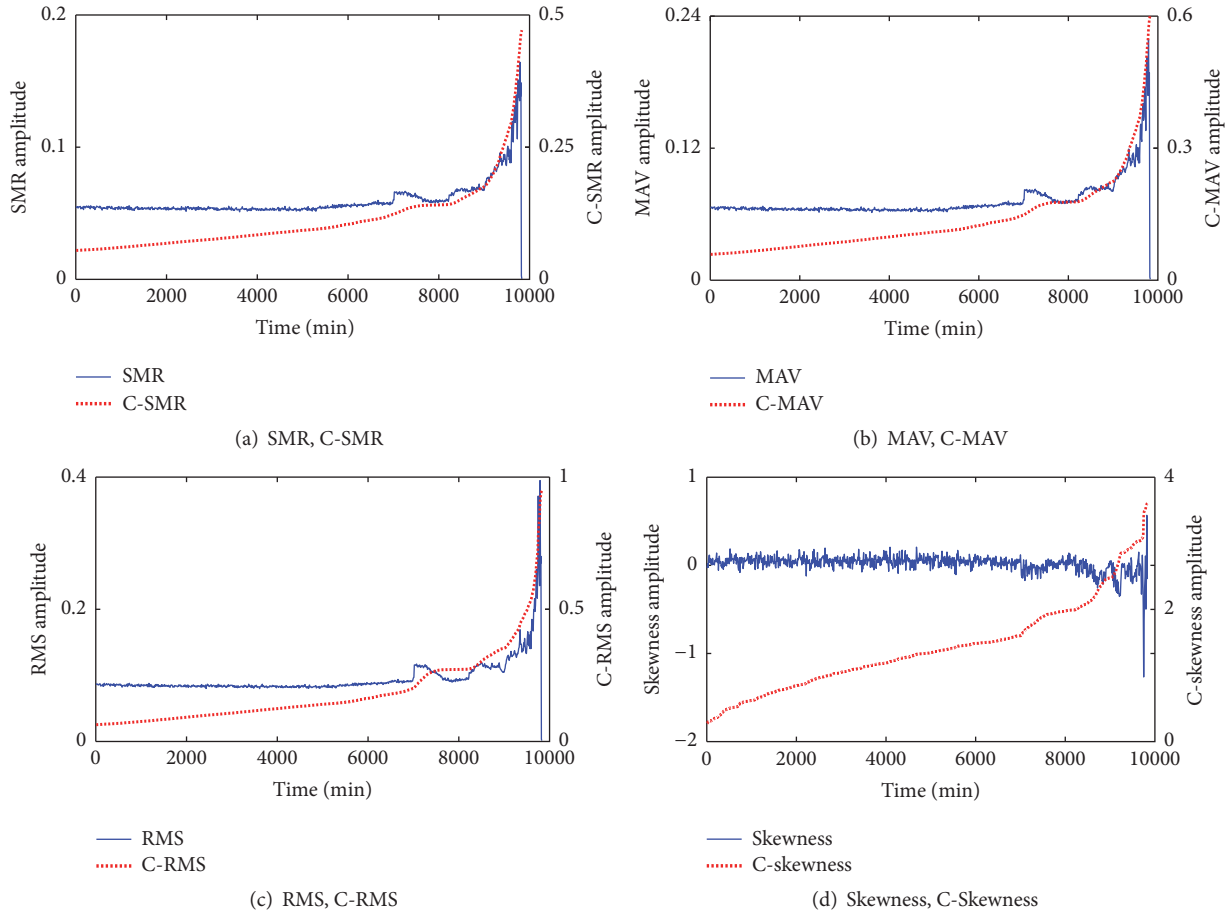


FIGURE 9: Fifth to eighth preferred features and corresponding cumulative features.

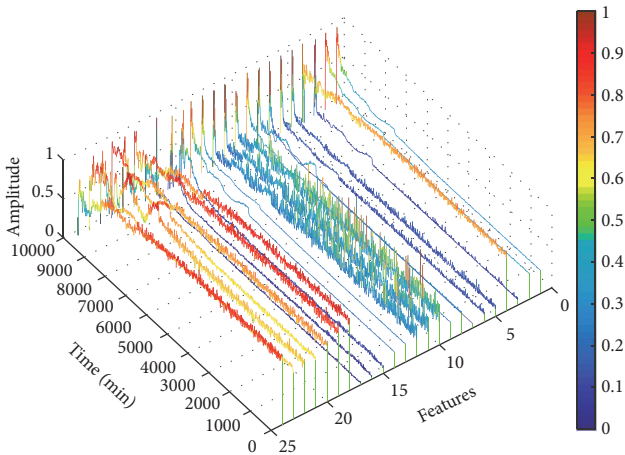


FIGURE 10: Waterfall of original features.

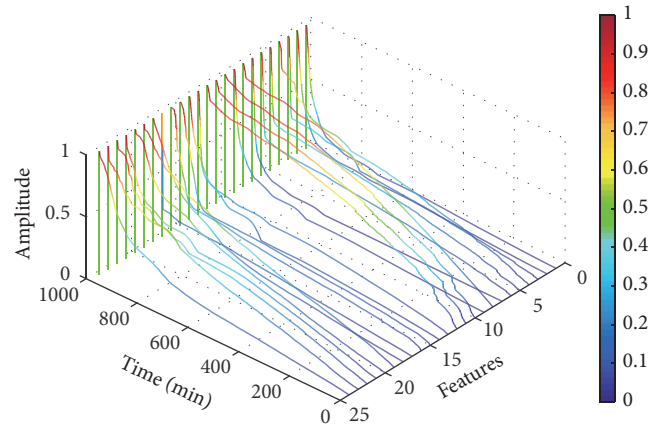


FIGURE 11: Waterfall of cumulative features.

features. On the whole, the predicted results have the same trend as the actual cumulative features, and there are only minor differences between the predicted results and actual cumulative features.

To quantitatively evaluate the performance of different methods, the MAPE and RMSE values of different degradation indexes are summarized in Table 4. We note that the cumulative features can achieve higher accuracy than the original features.

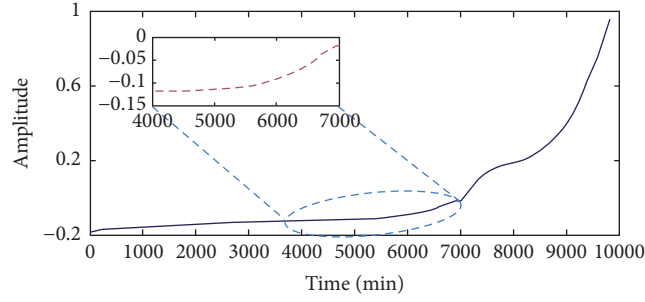
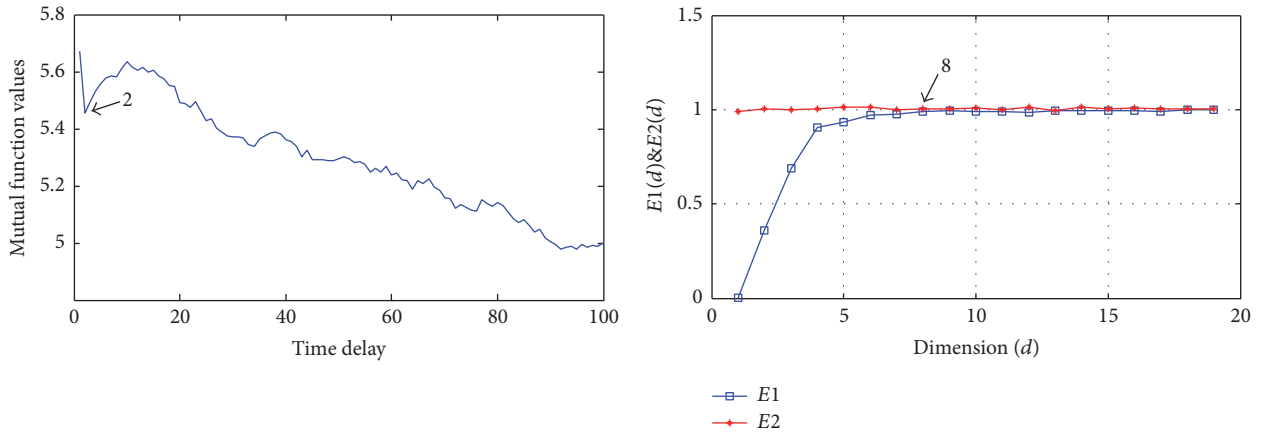


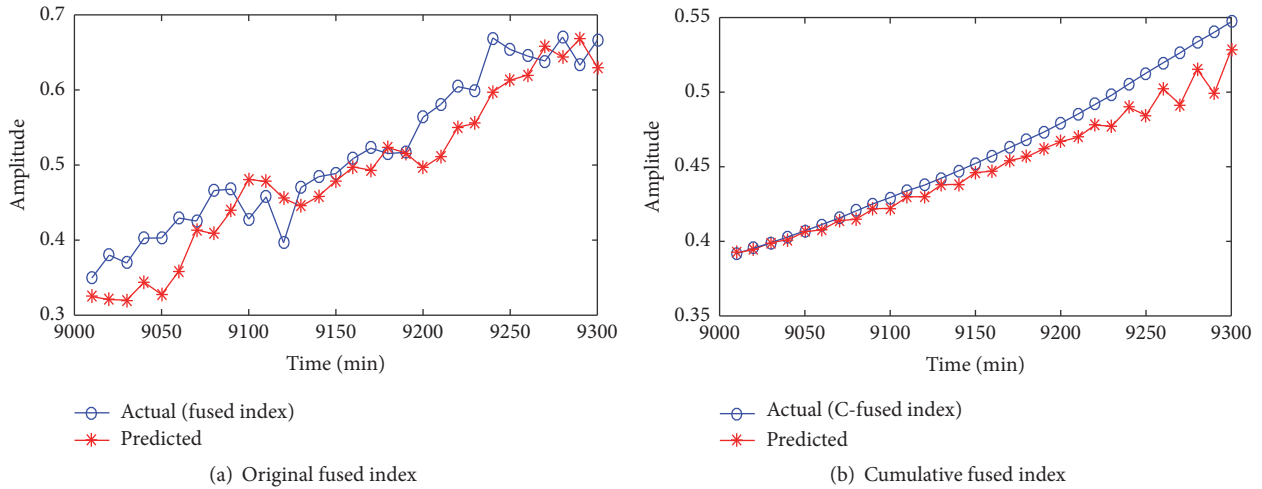
FIGURE 12: Degradation index constructed by KPCA.



(a) Mutual information method

(b) CAO method

FIGURE 13: Delay time and the embedded dimension of phase space reconstruction.



(a) Original fused index

(b) Cumulative fused index

FIGURE 14: Prediction results of original fused index and cumulative fused index.

TABLE 4: Prediction error comparison of different degradation indexes.

Degradation index	MAPE	RMSE	Degradation index	MAPE	RMSE
Kurtosis	0.1643	1.0213	C-Kurtosis	0.0059	0.0625
RMS	0.1425	0.8548	C-RMS	0.0131	0.0051
WPE2	0.0815	0.0056	C-WPE2	0.0052	0.0032
Fused index	0.0799	0.0455	C-Fused Index	0.0226	0.0149

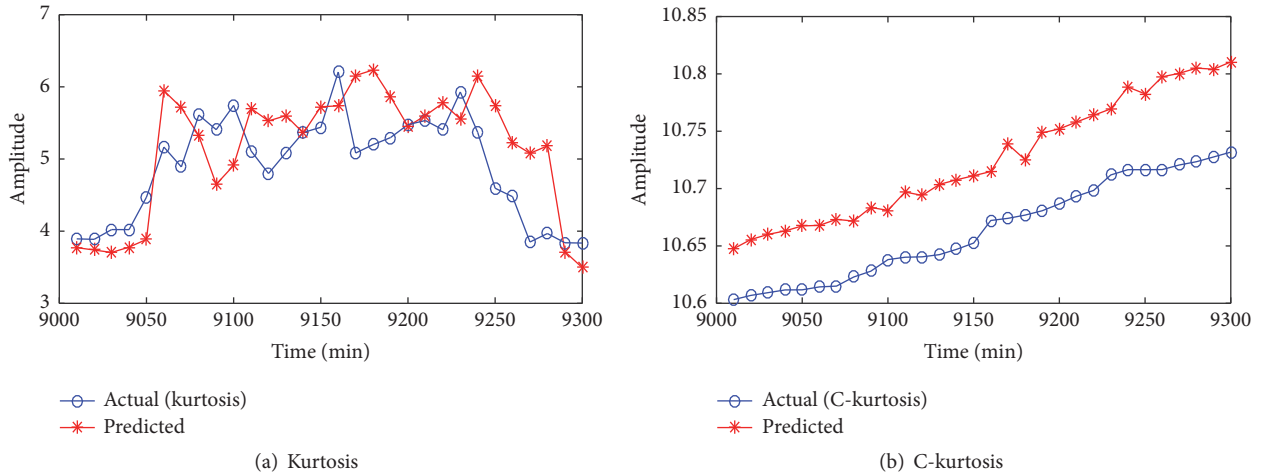


FIGURE 15: Prediction results of kurtosis and C-kurtosis.

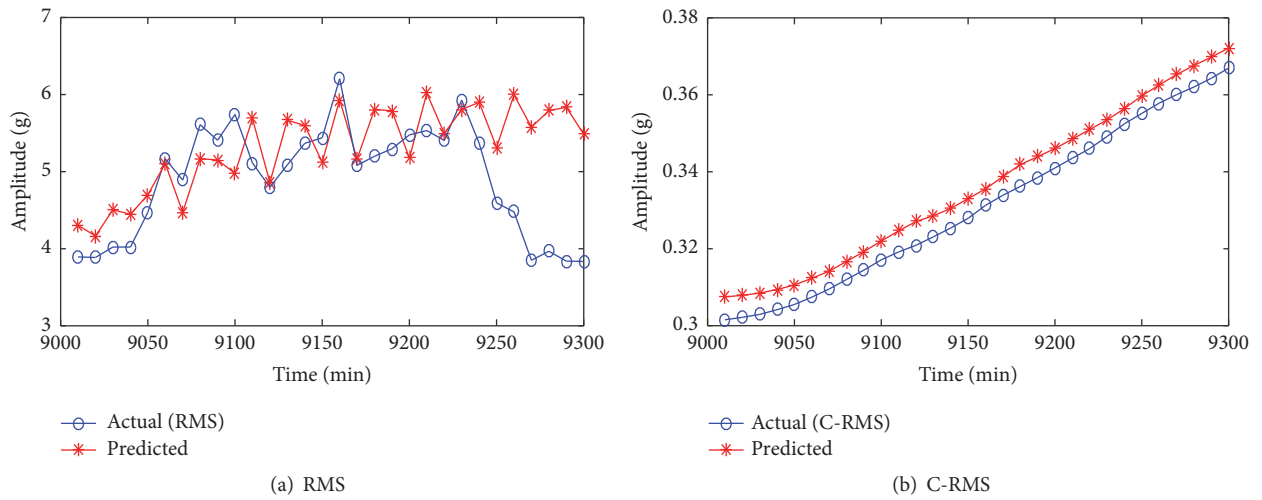


FIGURE 16: Prediction results of RMS and C-RMS.

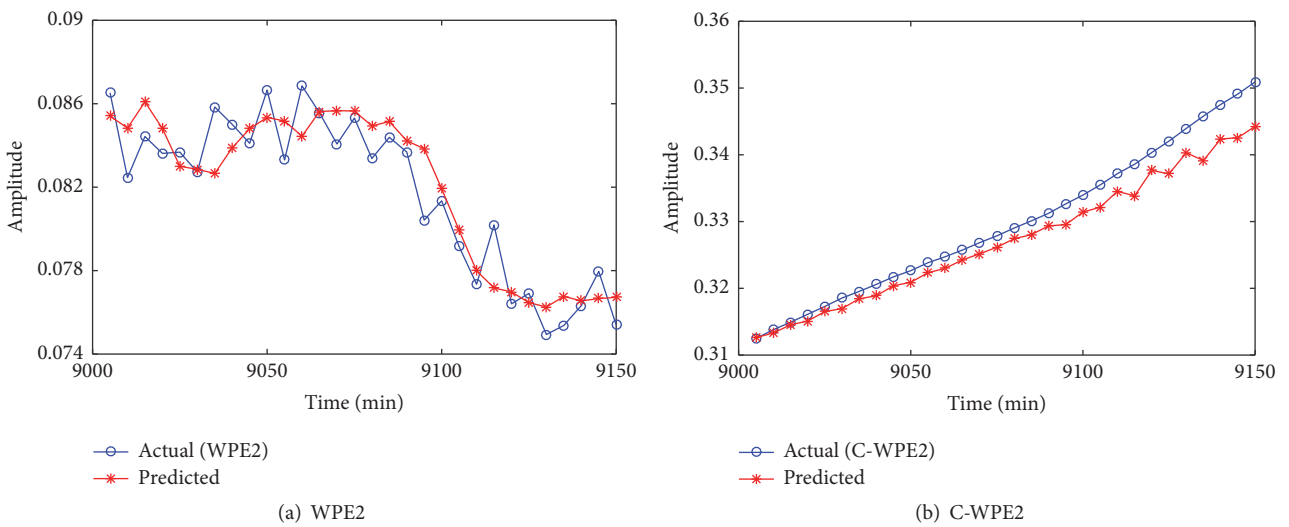


FIGURE 17: Prediction results of WPE2 and C-WPE2.

The reason for this is that the cumulative features are calculated based on the whole bearing life data, unlike the traditional features, which are based on a piece of data; thus, the cumulative transformation can partly ignore data fluctuation and extract significant monotonic trend information. Moreover, the KPCA can effectively fuse different features that describe the signal characteristics from different aspects and get more useful information. Therefore, the proposed degradation index can effectively reflect the bearing degradation trend and benefit the prognostic tasks.

## 5. Conclusion

In this study, a novel rolling bearing degradation prognostics method based on cumulative transformation and KPCA is proposed. More specifically, cumulative transformation and KPCA are integrated to obtain a degradation index to reflect the bearing degradation process. A prediction model based on ELM and PSR is built to perform the prognostics task. The following conclusions can be drawn:

(1) The features of the time domain, frequency domain, and time-frequency domain are extracted, and cumulative transformation is proposed to achieve features with high monotonicity and trendability from the original features, which can benefit the prognostic tasks.

(2) A new degradation index system is constructed, which fuses multidimensional cumulative features by KPCA and reflects the bearing degradation process properly.

(3) A prediction model based on PSR and ELM is proposed to achieve bearing degradation trend prediction. The whole-life experiment of the bearing shows that the proposed method reflects the bearing degradation process clearly and achieves a good balance between model accuracy and complexity.

## Conflicts of Interest

The authors declare that they have no conflicts of interest.

## Acknowledgments

The authors acknowledge the financial support provided by National Natural Science Foundation of China (nos. 51674277 and 51504274) and National Key Research and Development Program of China (no. 2017YFC0805803).

## References

- [1] M. Ge, Y. Xu, and R. Du, "An intelligent online monitoring and diagnostic system for manufacturing automation," *IEEE Transactions on Automation Science and Engineering*, vol. 5, no. 1, pp. 127–138, 2008.
- [2] X. An, H. Zeng, and C. Li, "Demodulation analysis based on adaptive local iterative filtering for bearing fault diagnosis," *Measurement*, vol. 94, no. 12, pp. 554–560, 2016.
- [3] Z. K. Peng and F. L. Chu, "Application of the wavelet transform in machine condition monitoring and fault diagnostics: a review with bibliography," *Mechanical Systems and Signal Processing*, vol. 18, no. 2, pp. 199–221, 2004.
- [4] K. Javed, R. Gouriveau, N. Zerhouni, and P. Nectoux, "A feature extraction procedure based on trigonometric functions and cumulative descriptors to enhance prognostics modeling," in *Proceedings of the 2013 IEEE International Conference on Prognostics and Health Management, PHM 2013*, pp. 1–7, June 2013.
- [5] S. Dong and T. Luo, "Bearing degradation process prediction based on the PCA and optimized LS-SVM model," *Measurement*, vol. 46, no. 9, pp. 3143–3152, 2013.
- [6] X. H. Liang, M. J. Zuo, and M. R. Hoseini, "Vibration signal modeling of a planetary gear set for tooth crack detection," *Engineering Failure Analysis*, vol. 48, pp. 185–200, 2015.
- [7] J. Lee, F. Wu, W. Zhao, M. Ghaffari, L. Liao, and D. Siegel, "Prognostics and health management design for rotary machinery systems—reviews, methodology and applications," *Mechanical Systems and Signal Processing*, vol. 42, no. 1-2, pp. 314–334, 2014.
- [8] C. Shen, D. Wang, F. Kong, and P. W. Tse, "Fault diagnosis of rotating machinery based on the statistical parameters of wavelet packet paving and a generic support vector regressive classifier," *Measurement*, vol. 46, no. 4, pp. 1551–1564, 2013.
- [9] A. K. S. Jardine, D. Lin, and D. Banjevic, "A review on machinery diagnostics and prognostics implementing condition-based maintenance," *Mechanical Systems and Signal Processing*, vol. 20, no. 7, pp. 1483–1510, 2006.
- [10] K. Javed, R. Gouriveau, N. Zerhouni, and P. Nectoux, "Enabling health monitoring approach based on vibration data for accurate prognostics," *IEEE Transactions on Industrial Electronics*, vol. 62, no. 1, pp. 647–656, 2015.
- [11] S. Kumar and M. Pecht, "Modeling approaches for prognostics and health management of electronics," *International Journal of Performability Engineering*, vol. 6, no. 5, pp. 222–229, 2010.
- [12] F. Camci, K. Medjaher, N. Zerhouni, and P. Nectoux, "Feature evaluation for effective bearing prognostics," *Quality and Reliability Engineering International*, vol. 29, no. 4, pp. 477–486, 2013.
- [13] B. Zhang, L. Zhang, and J. Xu, "Degradation feature selection for remaining useful life prediction of rolling element bearings," *Quality and Reliability Engineering International*, vol. 32, no. 2, pp. 547–554, 2016.
- [14] J. Yan, C. Guo, and X. Wang, "A dynamic multi-scale Markov model based methodology for remaining life prediction," *Mechanical Systems and Signal Processing*, vol. 25, no. 4, pp. 1364–1376, 2011.
- [15] P. Li, F. Kong, Q. He, and Y. Liu, "Multiscale slope feature extraction for rotating machinery fault diagnosis using wavelet analysis," *Measurement*, vol. 46, no. 1, pp. 497–505, 2013.
- [16] H. Hong and M. Liang, "Fault severity assessment for rolling element bearings using the Lempel-Ziv complexity and continuous wavelet transform," *Journal of Sound and Vibration*, vol. 320, no. 1-2, pp. 452–468, 2009.
- [17] W. Guo, P. W. Tse, and A. Djordjevic, "Faulty bearing signal recovery from large noise using a hybrid method based on spectral kurtosis and ensemble empirical mode decomposition," *Measurement*, vol. 45, no. 5, pp. 1308–1322, 2012.
- [18] E. Sutrisno, H. Oh, A. S. S. Vasani, and M. Pecht, "Estimation of remaining useful life of ball bearings using data driven methodologies," in *Proceedings of the IEEE Conference on Prognostics and Health Management (PHM '12)*, pp. 1–7, Denver, Colo, USA, June 2012.
- [19] T. H. Loutas, D. Roulias, and G. Georgoulas, "Remaining useful life estimation in rolling bearings utilizing data-driven probabilistic E-support vectors regression," *IEEE Transactions on Reliability*, vol. 62, no. 4, pp. 821–832, 2013.

- [20] J. Ben Ali, B. Chebel-Morello, L. Saidi, S. Malinowski, and F. Fnaiech, "Accurate bearing remaining useful life prediction based on Weibull distribution and artificial neural network," *Mechanical Systems and Signal Processing*, vol. 56, pp. 150–172, 2015.
- [21] H. Qiu, J. Lee, J. Lin, and G. Yu, "Robust performance degradation assessment methods for enhanced rolling element bearing prognostics," *Advanced Engineering Informatics*, vol. 17, no. 3-4, pp. 127–140, 2003.
- [22] S. Sassi, B. Badri, and M. Thomas, "Tracking surface degradation of ball bearings by means of new time domain scalar indicators," *International Journal of COMADEM*, vol. 11, no. 3, pp. 36–45, 2008.
- [23] S. Zhang, Y. Zhang, and D. Zhu, "Residual Life Prediction for Rolling Element Bearings Based on an Effective Degradation Indicator," *Journal of Failure Analysis and Prevention (JFAP)*, vol. 15, no. 5, pp. 722–729, 2015.
- [24] Z. Xi, R. Jing, P. Wang, and C. Hu, "A copula-based sampling method for data-driven prognostics," *Reliability Engineering & System Safety*, vol. 132, no. 4, pp. 72–82, 2014.
- [25] L. Liao, "Discovering prognostic features using genetic programming in remaining useful life prediction," *IEEE Transactions on Industrial Electronics*, vol. 61, no. 5, pp. 2464–2472, 2014.
- [26] C. Sun, Z. He, H. Cao, and Z. Zhang, "A non-probabilistic metric derived from condition information for operational reliability assessment of aero-engines," *IEEE Transactions on Reliability*, vol. 64, no. 1, pp. 1–15, 2014.
- [27] Y. Wang and H. Pham, "Imperfect preventive maintenance policies for two-process cumulative damage model of degradation and random shocks," *International Journal of Systems Assurance Engineering and Management*, vol. 2, no. 1, pp. 66–77, 2011.
- [28] X. Ni, J. Zhao, X. Zhang, X. Lv, and J. Zhao, "System degradation process modeling for two-stage degraded mode," in *Proceedings of the 2014 Prognostics and System Health Management Conference, PHM 2014*, pp. 186–189, August 2014.
- [29] A. Ragab, S. Yacout, M.-S. Ouali, and H. Osman, "Prognostics of multiple failure modes in rotating machinery using a pattern-based classifier and cumulative incidence functions," *Journal of Intelligent Manufacturing*, pp. 1–20, 2016.
- [30] M. X. Zhu, J. N. Zhang, Y. Li, and Y. H. Wei, "Partial discharge signals separation using cumulative energy function and mathematical morphology gradient," *IEEE Transactions on Dielectrics Electrical Insulation*, vol. 23, no. 1, pp. 482–493, 2016.
- [31] S. Porotsky and Z. Bluvband, "Remaining useful life estimation for systems with non-trendability behaviour," in *Proceedings of the 2012 IEEE International Conference on Prognostics and Health Management: Enhancing Safety, Efficiency, Availability, and Effectiveness of Systems Through PHM Technology and Application, PHM 2012*, pp. 1–6, June 2012.
- [32] J. B. Coble, *Merging data sources to predict remaining useful life—an automated method to identify prognostic parameters*, [Ph.D. thesis], University of Tennessee, 2010.
- [33] Q. He, F. Kong, and R. Yan, "Subspace-based gearbox condition monitoring by kernel principal component analysis," *Mechanical Systems and Signal Processing*, vol. 21, no. 4, pp. 1755–1772, 2007.
- [34] F. Takens, "Detecting strange attractors in turbulence," in *Dynamical systems and Turbulence*, D. A. Rand and L. S. Young, Eds., vol. 898 of *Lecture Note in Mathematics*, pp. 366–381, Springer, Berlin, Germany, 1981.
- [35] A. Bellini, F. Filippetti, C. Tassoni, and G.-A. Capolino, "Advances in diagnostic techniques for induction machines," *IEEE Transactions on Industrial Electronics*, vol. 55, no. 12, pp. 4109–4126, 2008.
- [36] L. Liao and J. Lee, "A novel method for machine performance degradation assessment based on fixed cycle features test," *Journal of Sound and Vibration*, vol. 326, no. 3-5, pp. 894–908, 2009.
- [37] G. B. Huang, Q. Y. Zhu, and C. K. Siew, "Extreme learning machine: theory and applications," *Neurocomputing*, vol. 70, no. 1–3, pp. 489–501, 2006.
- [38] <http://ti.arc.nasa.gov/tech/dash/pcoe/prognostic-data-repository>.

## Research Article

# Optimal Sensor Placement for Spatial Structure Based on Importance Coefficient and Randomness

Haoxiang He , Honggang Xu, Xiaobing Wang, Xiaofu Zhang, and Shaoyong Fan

*Beijing Key Laboratory of Earthquake Engineering and Structural Retrofit, Beijing University of Technology, Beijing 100124, China*

Correspondence should be addressed to Haoxiang He; [hxx7856@163.com](mailto:hxx7856@163.com)

Received 26 June 2017; Revised 18 December 2017; Accepted 1 January 2018; Published 7 February 2018

Academic Editor: Maosen Cao

Copyright © 2018 Haoxiang He et al. This is an open access article distributed under the Creative Commons Attribution License, which permits unrestricted use, distribution, and reproduction in any medium, provided the original work is properly cited.

The current methods of optimal sensor placement are majorly presented based on modal analysis theory, lacking the consideration of damage process of the structure. The effect of different minor damage cases acting on the total spatial structure is studied based on vulnerability theory in structural analysis. The concept of generalized equivalent stiffness is introduced and the importance coefficient of component is defined. For numerical simulation, the random characteristics for both structural parameters and loads are considered, and the random samples are established. The damage path of each sample is calculated and all the important members on the damage failure path are listed; therefore the sensor placement scheme is determined according to the statistical data. This method is extended to dynamic analysis. For every dynamic time-history analysis, time-varying responses of the structure are calculated by selecting appropriate calculating interval and considering the randomness of structural parameters and load. The time-varying response is analyzed and the importance coefficient of members is sorted; finally the dynamic sensor placement scheme is determined. The effectiveness of the method in this paper is certified by example.

## 1. Introduction

Spatial structures, such as latticed shell and space truss, are three-dimensional representations of equilibrium equations and symbols of structural design, simulation, and construction in civil engineering. Spatial structures are widely used for many advantages such as large stiffness, light mass, and low cost, and structural styles are also novel and diversified.

Spatial structure has these mechanical characteristics as follows. It has three-dimensional mechanical characteristics and presents a space working state under loads [1]. It belongs to high-order statically indeterminate structure, but it is generally flexible and can be easily damaged and even destroyed under special loads and sudden disasters. Most of the spatial structures are symmetrical, the natural frequencies are usually close, and the dynamic characteristics are complex. The major loads have strong randomness, and the overall structure has a high sensitivity to defects. The initial defect and the damage of local elements can significantly influence the bearing capacity and the mechanical characteristics.

The operating environment of the spatial structure is complex, and the potential risk of damage and destruction is

larger. In addition, spatial structures are inevitable to subject to environmental corrosion, long-term fatigue effects, or natural disasters, and then the damage accumulates during long service period [2, 3]. Furthermore, many large spatial structures are constructed as important building such as gymnasium, exhibition hall, and station hall. Therefore, it is necessary to detect the potential damage accurately and promptly in order to ensure structural capacity and safety. Under this background, intelligent health monitoring, sensors selection, and optimal placement and damage detection in construction and operation have an important theoretical value and practical significance [4, 5].

Over the past twenty years, various problems in health monitoring of spatial structure have been studied and many research achievements have been obtained, and some theoretical results and techniques have been applied to practical engineering. However, there are still some problems in the health monitoring of spatial structure, which need to be further studied and then get improved in the aspects such as optimal sensor placement, model updating, damage detection, and safety assessment.

According to the structural style and mechanical characteristics of spatial structures, placing the main sensors on the key joints of the spatial structure so as to detect the damage is reasonable and effective. However, there are a large number of joints, elements, and more degrees of freedom for large spatial structures; it is inconceivable and irrational to place the sensors on all the joints since the economy and the feasibility cannot be fulfilled. Hence, the locations and the number of the joints which will be placed on sensors should be optimized to achieve effective data acquisition and improve the accuracy of damage detection and maintenance efficiency, according to the specific type and performance of sensors. The methods on the optimal sensor placement have been developed from various aspects and many methodologies [6–8]. The most important methods are introduced and discussed in the following content from the dynamic mechanism and the applicability.

The most widely used method is modal assurance criterion (MAC) method or MinMAC method, which is carried out based on minimizing the value of the nondiagonal elements on the modal assurance criterion matrix when new sensors are added on the structure [9–11]. Minimizing the maximal off-diagonal term indicates less correlation exists in the corresponding mode shape vectors and renders the mode shapes discriminable from each other. This method, which belongs to the category of modal analysis, is to maximize the angles formed by unit mode shape vectors, which is equivalent to minimizing the dot product between them.

Although the modal information is sufficient and accurate for modal identification by MinMAC method, the damage detection cannot be achieved only by modal results. The energy is generally assumed as another parameter related to damage. For the energy concept, the most important sensor placement method is the modal kinetic energy (MKE) method [12]. It is established on the traditional heuristic visual inspection, which is to visually inspect the structural response, to examine the interested mode shapes, and to select locations with high amplitudes of responses. The MKE method gives a measure of the dynamic contribution of each degree of freedom for each of the target mode shapes and provides a rough idea where the maximum responses could be measured. Although MKE is suitable for simple structures, it encounters difficulty in large complicated structures; thus, the bottleneck problem occurs. The MKE method starts first from the selection of target modes by the modal kinetic energy as follows.

As another famous method, the effective independence (EI) method aims to select measurement positions that make the mode shapes of interest as linearly independent as possible while containing sufficient information about the target modal responses in the measurements [13, 14]. This method roots in the estimation theory by sensitivity analysis of the parameters to be estimated, and then it arrives at the maximization of the Fisher information matrix. There are many variants of the EI method. The so-called energy optimization technique is derived from EI by optimizing the kinetic energy matrix measured by candidate sensor locations.

The QR decomposition method proposed by Schedlinski and Link aims to locate the effective subset of the modal matrix [15]. The original modal matrix is decomposed into one unitary matrix and one trigonometric matrix by QR decomposition. The fundamental idea is to find the most linear independent rows of the modal matrix to minimize the off-diagonal terms of the MAC matrix.

The Guyan reduction method selects the master degrees as the locations of sensors during the process of Guyan reduction [16]. It is based on the assumption that low ratios of leading diagonal stiffness to mass terms indicate good degree of freedom to be retained in terms of describing the kinetic energy and that the inertia forces at slave coordinates are negligible compared with the elastic forces. A major disadvantage of the reduction methods is that they strongly depend on the meshing size of the FEM and are interested only in the lower modes, which are not always the case. It is useful to note that other sophisticated reduction techniques can also be employed. A relative promising method is static flexibility approach [17]. This method optimizes the static transformation matrix with the assumption that the best master degrees of freedom are those for which the FEM mode shapes can be represented as a linear combination of static flexibility shapes.

In conclusion, the deficiency in the current study on the optimal sensors placement method can be summarized as follows. Different optimal placement schemes can be obtained according to different placement criteria, and the guideline of comprehensive evaluation for various placement criteria and selecting the appropriate placement scheme according to the structural form and the engineering requirements needs intensive study. The current optimal sensor placement methods are mainly established based on dynamic analysis and modal analysis, which are only suitable for the dynamic sensors such as the accelerometer and the dynamic displacement meter. However, the optimal placement strategy on the static parameters such as stress, strain, crack, and long-term deformation is not comprehensive enough, and the placement scheme is usually determined by experience or the simple simulation. On the other hand, the existing optimal placement scheme is usually determined by combining the algorithm and the finite element model, but it is not enough to pay attention to the difference of the loading pattern, the randomness of materials and structures, and the model error and updating, which affects the feasibility of the theoretical optimization placement scheme. In addition, the minor damage and the damage evolution process are not adequately considered, which leads to the flexibility and the adaptability of the placement scheme being unsatisfactory.

In recent years, the concept, philosophy, and application of structural vulnerability continue to be valued [18–23]. Structural vulnerability, also viewed as the antonym of robustness, is usually defined as the characteristics and circumstances of a structural system that makes it susceptible to the damaging effects of a hazard. For example, the seismic vulnerability is the degree of damage to the built environment for a given intensity of earthquake motion [24]. Structural vulnerability can be expressed on a scale of 0 to 1, where 0 is no damage and 1 defines complete destruction. It is apparent that

the structural health monitoring and the sensor placement method can be studied within the system framework of structural vulnerability, and new methods and ideas maybe occur, which will be beneficial to the development of health monitoring.

According to the deficiency of the traditional method of optimal sensor placement, a new static-dynamic sensor placement method based on structural vulnerability and importance coefficient is presented in this paper, and the random characteristics are also involved, which can provide new ideas and methods for optimal sensor placement and application for complex spatial structures.

## 2. Structural Analysis considering Random Characteristics

The practical engineering structures inevitably have all kinds of initial random defects due to the material characteristics and the construction error; thus, the parameters such as structural stiffness, mass, and geometric size are not equal to the design value but fluctuate within a certain range and the design value is probably the mean value, so these parameters are stochastic. In addition, the actual value of the load on the structure is also random [25]. This randomness generates the difference of geometrical properties, bearing capacity, and damage evolution mechanism between the actual structure and the ideal design model.

Hence, the modal characteristics, damage performance, and the optimal sensor placement scheme based on the ideal model cannot be fully consistent with the actual condition, and there is a considerable deviation in many cases. Based on previous discussion, it is apparent that the structural performance will be recognized more intensively if the load pattern and the randomness of structure materials and dimensions are involved in structural analysis, and the statistical parameters and characterization of the structural static-dynamic performance can be calculated by probability statistical method [26–28]. On this basis, the optimal sensor placement will be more realistic and comprehensive, which can improve the accuracy of damage identification and health monitoring.

The Monte Carlo method is mostly used in the random analysis; the load pattern and the randomness of structural parameters can be considered. First, the probability distribution function (PDF) of load and parameters should be determined, and then a certain number of samples are selected randomly from the total sample library which are in conformity with the corresponding PDFs, in order to generate the operating cases with different load patterns. After that, the mechanical properties and the optimal scheme of each operating case are studied and the statistical results are achieved; then the final analysis result or the optimal scheme is determined based on the occurrence probability.

The advantages of the structure random analysis based on Monte Carlo method include the high accuracy and the precision which can be controlled, but the disadvantage is the low computational efficiency and being time consuming.

On the other hand, a function or a surface which is easy to be established substitutes for the implicit or complex real

function or limit state surface in response surface method; the accuracy and the convenience are achieved simultaneously. For complex structures, the basic structural features can be represented by response surface function. On this basis, Monte Carlo sampling is carried out. Because only the value of special response surface function is calculated for each sample rather than restarting structural analysis, this method will obviously improve the computational efficiency than Monte Carlo method.

It is worth noting that the probabilistic design system (PDS) can be provided by some finite element software, such as ANSYS, and both Monte Carlo method and response surface method can be used by users to realize the structural random parameters analysis or reliability analysis. However, there are still many problems in this module, such as the limitation on the number of random input variables and the total amount of input and output, which lead to the bottleneck problem of the random analysis for large and complex structures.

Thus, the mathematical software such as MATLAB is suggested to be used for the preprocessing of parameters and the random variables generation especially for complex structures and then importing the data into the finite element command and carry out structural analysis in finite element software. Finally, the result data are saved and converted into the recognizable format; then the probability statistics and numerical analysis are performed in MATLAB.

## 3. Vulnerability Evaluation Based on the Importance Coefficient

Spatial structures will inevitably damage due to various natural hazards and environmental effect. The damage includes the change of the materials property and the geometrical feature of the total structure or local members, besides the deterioration on the stiffness, the strength, the boundary, and the connection conditions.

The incident natural disasters such as earthquake and hurricane will cause serious structural damage in a very short period of time, and these damage types belong to the sudden damage. In addition, a certain degree of damage will occur in the structure due to the factors like environmental change, component degradation, fatigue, corrosion, and others, and these cases belong to the cumulative damage. Both the sudden damage and cumulative damage can be understood and analyzed through the concept of structural vulnerability.

The general definition of structural vulnerability indicates the conditional probability of the actual damage exceeds the designated damage degree when structure is subjected to a given load [22, 23]; this concept represents the relationship between the initial disturbance caused by an unexpected event or overload and the final consequence, and it also stands for the structural fragility and the bearing capacity for accidental damage.

As a derived concept, the importance coefficient of component based on vulnerability represents the influence on the performance of whole structure when the individual members damage or become invalid if the structure is subjected to unexpected events under normal loads, which

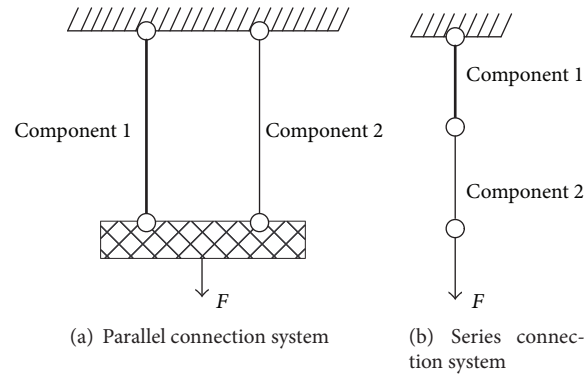


FIGURE 1: Illustration of importance coefficient in different structures.

also indicates the constraint capacity of the component in a certain extent [29].

The current research on engineering vulnerability analysis mainly focuses on the seismic vulnerability of buildings and bridges, and the application of structural vulnerability in the field of structural health monitoring is not popular. In this paper, it is assumed that structural vulnerability can fully represent the characteristics of the structural damage and be used to evaluate the safety grade. In the theoretical framework of the structural vulnerability analysis, the importance coefficient and damage demand of structural component are analyzed in order to search for the structural vulnerable path and then install sensors according to important path. Hence, the needs of the cumulative damage and the sudden damage are both considered and the large scale of damage caused by local damage can be prevented. Furthermore, the robustness and the reliability of the structure are effectively ensured. Thus, the optimal sensor placement based on vulnerability analysis and important coefficient is studied in this paper.

In the traditional structural vulnerability analysis, it is usually necessary to simultaneously calculate the importance coefficient of the components and the energy which can destroy the components so as to find the circumstance that the components are most important or prone to damage; then the vulnerable path is determined according to the possible damage sequence. However, the components are fully removed in the process of damage analysis when the traditional method is used; that is, the components are completely destroyed. However, the actual possibility of a certain critical component completely destroyed is very small in normal state. On the contrary, the damage is often cumulative. Therefore, the traditional method should be improved for the application of optimal sensor placement.

In this study, the minor damage states, that is, the percent decrease of stiffness is less than 20%, which often occurs in the early stage of cumulative damage, are mainly discussed, and the target of the optimal sensor placement is to detect the minor damage rapidly and accurately. Since the required destruction energy of each component is small, all the components are assumed to be prone to damage, so there are no special damage demands for designated components

in vulnerability analysis. Moreover, it should be pointed out that the initial random imperfections are not equivalent to the minor damage. The initial random imperfections are the inevitable errors in the process of material production and construction, and the minor damage is the damage that occurs in the operation process of structural members. In view of damage degree, the minor damage is obviously larger than the value of random imperfections.

From the above analysis, it is obvious that the definition and calculation of importance coefficient are the critical part to realize the vulnerability analysis and to search vulnerable path. There are two types of methods for evaluating the importance coefficient of structural component. The first type of methods mainly focuses on the intrinsic properties of the structural system, which is independent of the load patterns. The other type of methods belongs to the evaluation method related to load, which pays attention to both the properties of the structural system and the effects of the load on the structure.

In fact, the effective vulnerable path of the structure is not merely related to the structure geometry and the stiffness distribution but also intrinsically related to the load pattern. The stiffness involved in the evaluation method independent of load is not the effective stiffness of the structure resisting the external loads. For example, the practical importance of a redundant component with larger stiffness is very small because it has no contribution to load transfer, but the corresponding important coefficient calculated by above method may be larger than the value of the component with the great contribution to the load transfer but the stiffness is less.

In order to deeply illustrate the significance of importance coefficient and previous discussion, two simple systems are shown in Figure 1. In the parallel connection system, if the stiffness of component 1 is larger, the corresponding importance coefficient is larger because the sharing force of this component is large and the consequence is more serious if it is removed. In contrast, if either component is removed in the series connection system, the structure will be invalid; thus, the importance coefficients of these two components are the same though the stiffness is different. Hence, both

the structural characteristics and the load pattern should be considered in the importance evaluation for structural health monitoring, especially for the optimal sensor placement.

The applications of vulnerability and importance coefficient in health monitoring and sensor placement are necessary. The damage capacity of current damage detection methods is preferable for the structure with medium damage, but the results of minor damage detection are not satisfactory. For spatial structure, the minor damage of the components not only generates the potential safety hazard and reduces the structural service life, but also is directly harmful to the whole structure and weakens the normal operational performance. With the development of the damage, it will finally bring about serious damage on the structure and causes heavy casualties and property losses. Therefore, it is very necessary to study the consequence and the transfer path of minor damage by combining the random properties of the structure and the load pattern based on the structural vulnerability analysis. The study on searching possible damage path and installing various sensors on the important components becomes the first task to be solved.

#### 4. Calculation of Component Importance Coefficient

To carry out vulnerability analysis and importance coefficient calculation, the quantifiable index must be presented. In view of the previous conclusion about the importance coefficient, the concept of the generalized equivalent stiffness is introduced into the calculation method of the importance coefficient of component. The relationship of the joint deformation  $\Delta$  in a specified direction and the force  $F$  which is applied on the joint in the corresponding direction is given by

$$F = k\Delta, \quad (1)$$

where  $k$  is the equivalent stiffness of the component in the specified direction. If the structure is merely subjected to the load  $F$ , the components that participate in transferring the force, that is, contribute to the equivalent stiffness  $k$ , have importance, whereas the component, which has no contribution to the equivalent stiffness  $k$ , does not influence the state of the structural bearing capacity even if it is removed, so it is not important.

The above conclusion can be generalized to the larger and complex structure which is usually subjected to multiple loads. When the load distribution on the structure is determined, the joint deformation distribution can be also determined.

Assuming the resultant force acting on the joint  $i$  is  $F_i$ , the component force of  $F_i$  in the direction  $l$  is  $F_{li}$ , and the deformation of the joint  $i$  in the direction  $l$  is  $d_{li}$ . Then the structural equivalent stiffness of the joint  $i$  in the direction  $l$  is defined as

$$K_{li} = \frac{F_{li}}{d_{li}}. \quad (2)$$

On this basis, the generalized equivalent stiffness of the structure corresponding to the load pattern in the direction  $l$  is given by

$$K_{lg} = \sum_{i=1}^n K_{li} = \sum_{i=1}^n \frac{F_{li}}{d_{li}}, \quad (3)$$

where  $n$  is the number of joints.

The resultant forces acting on each joint can be generally decomposed into three principal axis directions including  $x$ ,  $y$ , and  $z$ , and the generalized equivalent stiffness of the structure with respect to a given load pattern in three principal axis is  $K_{zg}$ ,  $K_{yg}$ , and  $K_{xg}$ , respectively. The actual structure generalized equivalent stiffness is the vector sum of the generalized equivalent stiffness in all directions and is expressed as follows:

$$K_g = \sqrt{K_{xg}^2 + K_{yg}^2 + K_{zg}^2}. \quad (4)$$

The generalized equivalent stiffness of the structure with respect to a specified load pattern is a whole physical quantity which indicates the deformation capacity of the overall structure resisting a given load, which is related to the load distribution pattern on the structure and the structural stiffness. Under the action of a given load, the contribution of one component to the actual structural equivalent generalized stiffness evidently represents the significance in the force system; it also represents the importance of the components of the whole structure.

Therefore, the loss rate of the actual structural equivalent generalized stiffness caused by the component damage is used as an importance evaluation index of the structure system. The index is defined as the importance coefficient  $I$ , and the expression is

$$I = \frac{(K_{gp} - K_{gd})}{K_{gp}}, \quad (5)$$

where  $K_{gp}$  is the initial generalized equivalent stiffness of the intact structure;  $K_{gd}$  is the generalized equivalent stiffness of the damaged structure. The component importance coefficient  $I$  is a constant range between 0 and 1. When  $I$  is 0, it indicates that the designated component has no effect on the actual generalized equivalent stiffness of the structure and does not contribute to the transmission path in the structural system; that is, this component is not important in the structure. If  $I$  is 1, it is evident that the component is very important, and once the failure occurs, the structure will not be able to sustain the given load.

In order to further explain the method and calculation process of the component importance coefficient based on the above formulae, a simple truss with 7 members is selected for analysis. The structural composition, the number of the joints, and the members are shown in Figure 2. All the members in the structure are the same, and the length is 3.0 m, the outer diameter of the member is 102 mm, and the wall thickness is 4 mm. Both the Compressive stiffness and the tensile stiffness are 460 kN/m.

TABLE 1: Importance coefficients of each member for different load patterns.

Importance coefficients	Member number						
	1	2	3	4	5	6	7
$I_{A2}$	0.018	0.018	0.079	0.000	0.000	0.079	0.023
$I_{A5}$	0.079	0.079	0.251	0.000	0.000	0.251	0.095
$I_{B2}$	0.023	0.023	0.072	0.011	0.011	0.072	0.044
$I_{B5}$	0.069	0.069	0.222	0.014	0.014	0.222	0.1417

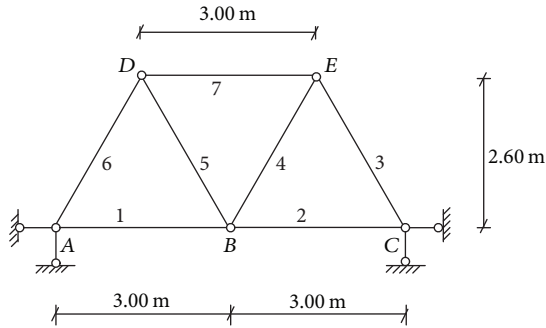


FIGURE 2: Illustration of importance coefficient in different structures.

The importance coefficient of each member under different static loading modes is calculated. In this study, two load patterns are considered; that is, load pattern A and load pattern B. For load pattern A, 10 kN vertical force is applied on joints D and E, respectively. For load pattern B, 20 kN vertical force is applied on joint B. It is assumed that each member has two types of degree of damage, so that the importance coefficient of each member is calculated according to (2), (3), and (5), and the calculation results are shown in Table 1.

Specifically,  $I_{A2}$  is the importance coefficient of the designated element when the load pattern A is applied and the damage degree of the corresponding element is 20% and other elements are intact.  $I_{A5}$  is the importance coefficient of the designated element when the load pattern A is applied and the damage degree of the corresponding element is 50% and other elements are intact.  $I_{B2}$  is the importance coefficient of the designated element when the load pattern B is applied and the damage degree of the corresponding element is 20% and other elements are intact.  $I_{B5}$  is the importance coefficient of the designated element when the load pattern B is applied and the damage degree of the corresponding element is 50% and other elements are intact.

It can be seen from the above results that the importance coefficient of certain member is different for different loading modes; a variety of possible load modes should be considered in order to calculate the importance of the members in a comprehensive way. In addition, for any damage degree and loading mode, the sequence of the importance of the member is given as members 3 and 6, member 7, members 1 and 2, and members 4 and 5, although the values are varied. Priority should be given to the strengthening and monitoring of the most important components.

## 5. Sensor Placement considering Importance Coefficient and Randomness

For spatial structures subjected to static loads, once the most important component damages, the stress distribution and the transfer path of the whole structure will change due to the change of the stiffness distribution. Therefore, the importance coefficient of each component will vary, and the maximum importance coefficient of all the remaining components can be obtained by recalculating the importance coefficient of each component. Following this set pattern, the multiple components with maximum importance coefficient can be gradually identified.

If the structure damages in the sequence of the permutation of the multiple components with maximum importance coefficient, the hazard of the whole structure is most severe. The damage of the multiple most important components will lead to much more loss of the generalized equivalent stiffness under given load condition. Thus, it causes a large deformation on the structure and deterioration of the normal performance.

From the perspective of the transfer path, the emergency capacity of the structure also greatly decreases, which will lead to structure destruction at top speed with the damage evolution and even causes the collapse. Hence, if the top important components are obtained by vulnerability analysis and the sensors are installed on corresponding joints to collect static response signals, the weak parts of the structure can be effectively monitored and the structural safety and reliability can be ensured.

For the minor damage detection and normal health monitoring, it is adequate to calculate the top three important members of the structure in the vulnerability analysis.

In addition, when the structure is subjected to ground motion or wind load, the applied forces on the structure involve the inertia force, gravity, and other dynamic actions at any moment in the dynamic process. Thus, the multiple most important members at any time step can be obtained according to the above method. Once the important components damage, the distribution of dynamic action will rearrange and the dynamic response will change obviously. Therefore, in order to evaluate the structural capacity to resist dynamic action, an appropriate time interval for vulnerability calculation should be determined and the time-varying responses of the structure in a dynamic process are extracted so as to calculate the importance coefficients of component. At last, the important members of the structure in a dynamic hazard are obtained and the static-dynamic parameters of these

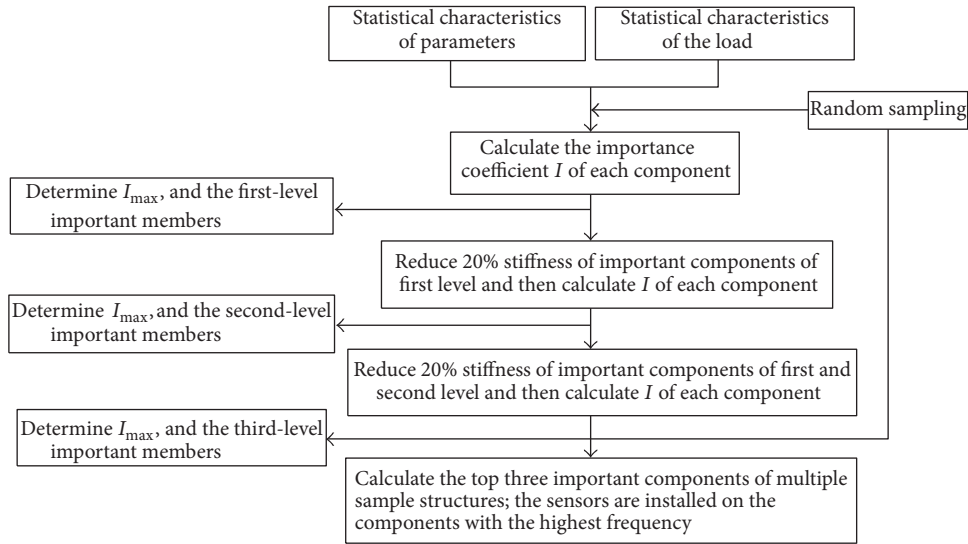


FIGURE 3: Flow chart of sensor placement considering static load.

members are monitored by statistical time-history analysis results.

The important coefficient calculation method for the deterministic structure and the specified load pattern is described above. For random cases, it is necessary to study a large number of sample conditions by considering the random characteristics of load and structure parameters. The most important components of each sample are obtained, respectively, and then the important members of all samples are counted. The components with the highest frequency are determined as the important components; then the sensors are installed on the components or the adjacent joint and the static-dynamic parameters are monitored.

In summary, the calculation flow diagram of the optimal sensor placement considering the importance coefficient and the randomness of structural parameters and static or dynamic load is shown in Figures 3 and 4, respectively.

## 6. Example Analysis

To verify the proposed method of optimal sensor placement considering importance coefficient and randomness, a single-layer spherical rib-circle latticed dome structure is selected as an analysis example, and the structural constitution is shown in Figures 5 and 6. The span of the structure is 40 m, the rise-span ratio is 1/4, and the material is normal carbon constructional steel with yield strength  $2.35 \times 10^8$  N/m<sup>2</sup>. For all the steel components, the external diameter is 200 mm and the internal diameter is 20 mm. The solid sphere with 160 mm diameter is used as the joint of the structure and welded with corresponding components. The assigned dead load to each joint on the surface is calculated as 15 kN/m<sup>2</sup>.

The importance coefficient of the components when the structure is subjected to the static load is calculated. The normal uniform load and the snow load are involved, and the possible load patterns include the following four types: uniform load (load pattern I), combination of the

uniform load and half edge uniform load (load pattern II), combination of the whole uniform load and 1/4 area uniform load (load pattern III), and the combination of the whole uniform load and the apex load (load pattern IV). According to the study [30], when randomness is considered, the statistical characteristics of the structure and load parameters are shown in Table 2, where  $L$  is the span.

The size of the random sample is determined according to the statistical characteristics and the amount of calculation. 100 random samples are simulated for each load pattern, and these loads are applied to 100 structures with random geometric parameters, respectively. Thus, 100 random models considering both the load and structural parameters are established. The first three important components of each model are calculated by finite element software ANSYS and numerical calculation software MATLAB. In the calculation of the importance coefficient of each component, the stiffness decreased by 20% to achieve the minor damage.

The initial displacements of joint 12 subjected to each type of load patterns in different random structures are shown in Figure 7; it is evident that the value has obvious randomness and discreteness. The importance coefficients  $I$  of the first level of element 51 near joint 12 in random structures are shown in Figure 8, and the results show the importance coefficient also has obvious randomness.

The importance coefficients of the structure under static load are calculated, and the vulnerability is evaluated based on different load patterns and statistical characteristics.

When the structure is subjected to a uniform load, as shown in Figure 9, the importance coefficients of different levels are calculated and analyzed. The frequency numbers of importance coefficients in the first three levels are shown in Figures 10(a)–10(c), respectively. The total frequency number of importance coefficients is shown in Figure 10(d). The numberings of the components whose frequency number is small are not listed. It is found that the probability that the rib

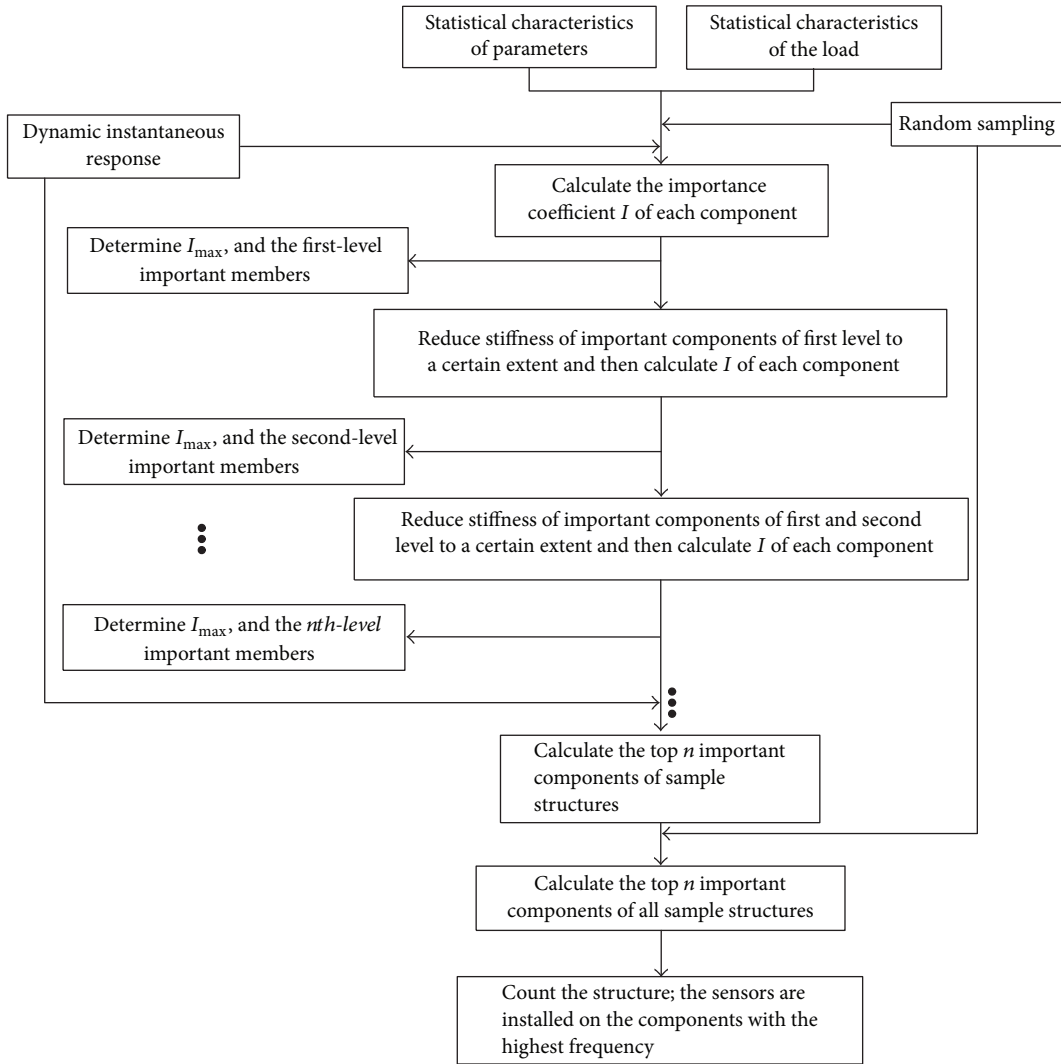


FIGURE 4: Flow chart of sensor placement considering dynamic load.

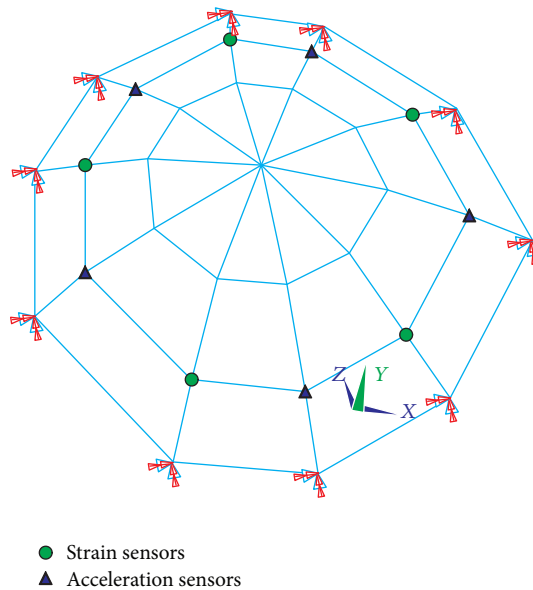


FIGURE 5: Reticulated dome structure and the sensors layout.

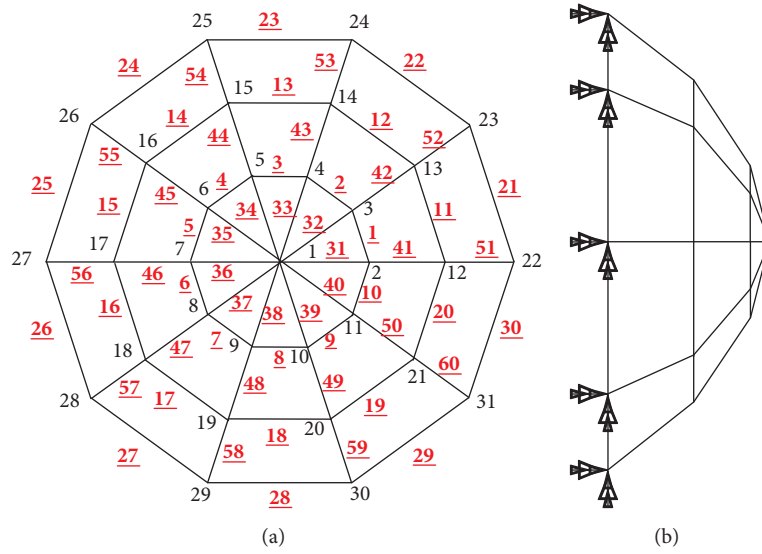


FIGURE 6: Number of joints and components in dome.

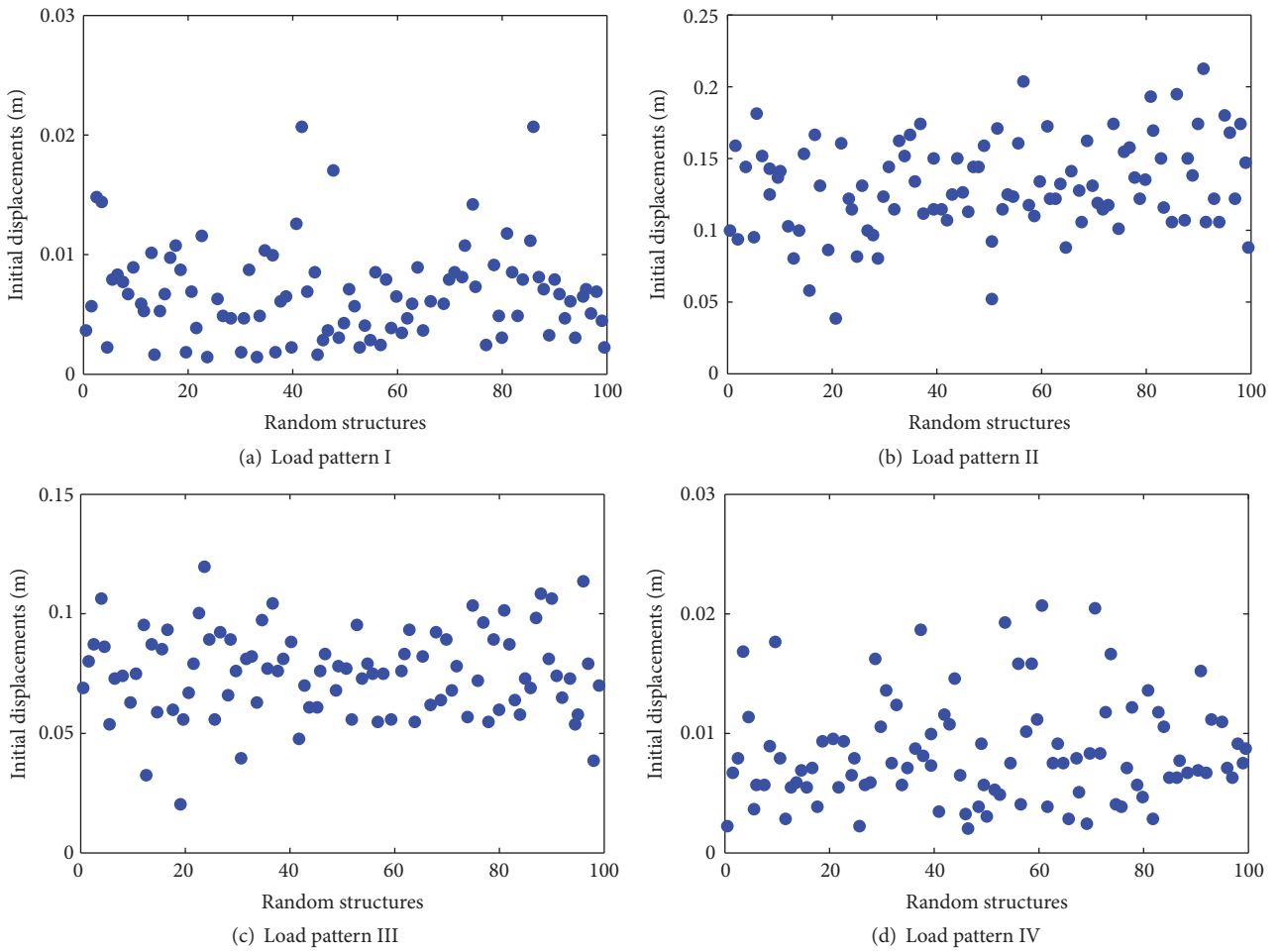


FIGURE 7: Random initial displacement of joint 12.

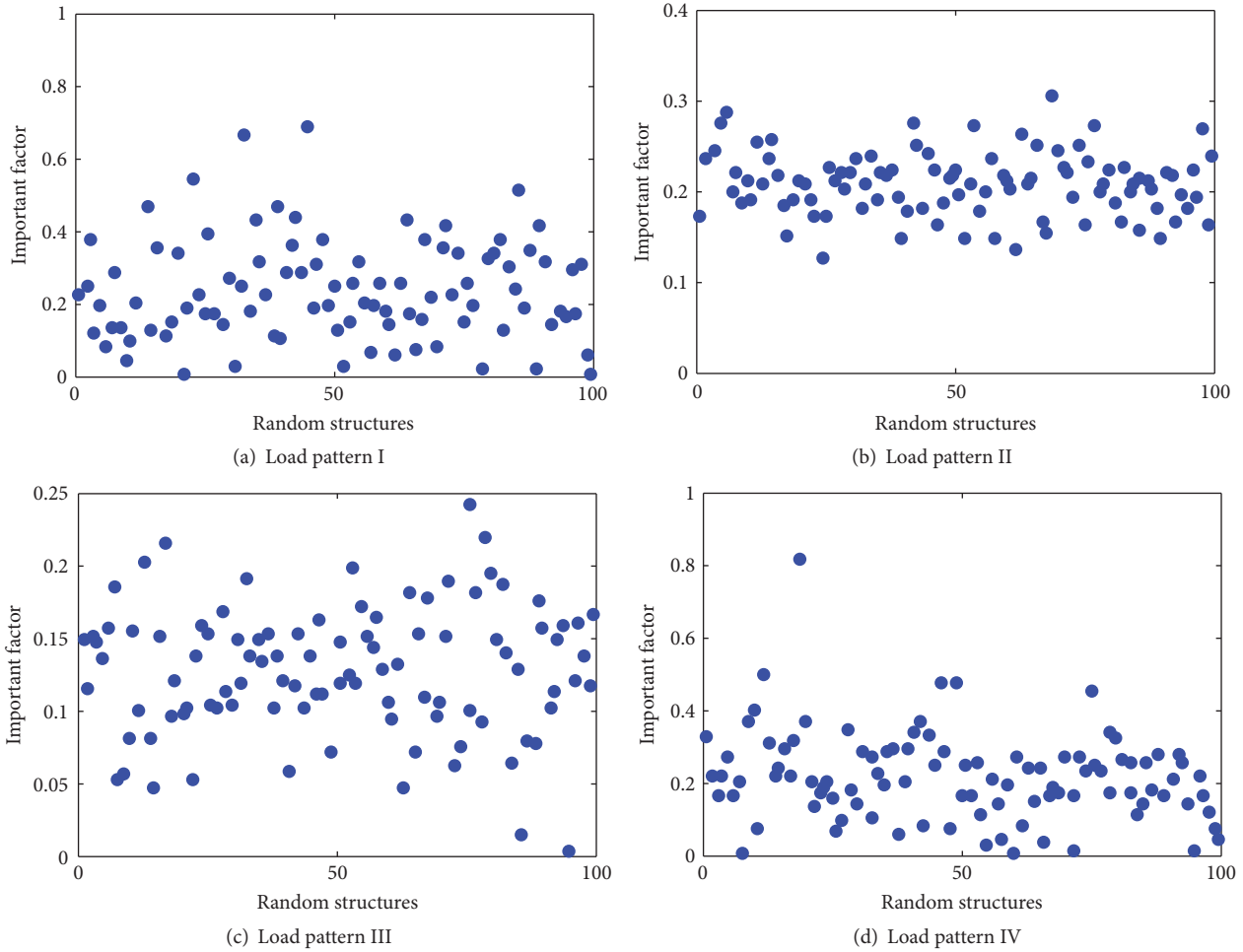


FIGURE 8: The first important factor of component 51.

elements in the base circle become important components is largest when the structure is subjected to uniform load.

Similar analysis is carried out according to the above method, the cumulated frequency where the main components become important components under various loads is shown in Figure 11, and the numberings of the components whose frequency number is less than 2 are not listed.

When the structure is subjected to the uniform load or the combination of the whole uniform load and the top load, the probability that the rib elements in the base circle become the important components is largest. When the structure is subjected to the combination of the uniform load and half or 1/4 uniform load, the rib elements in the base circle and the adjacent vertical elements especially at the junction of two kinds of uniform loads are the most important components.

Hence, the most important components range in element 51 to element 60 in most cases, that is, the rib elements at the base circle. Therefore, static strain sensors should be placed on these elements or corresponding joints. The definitive optimal placement scheme of static sensors is shown in Figure 3.

In what follows, the importance coefficients of the structure under dynamic action are analyzed and discussed. In

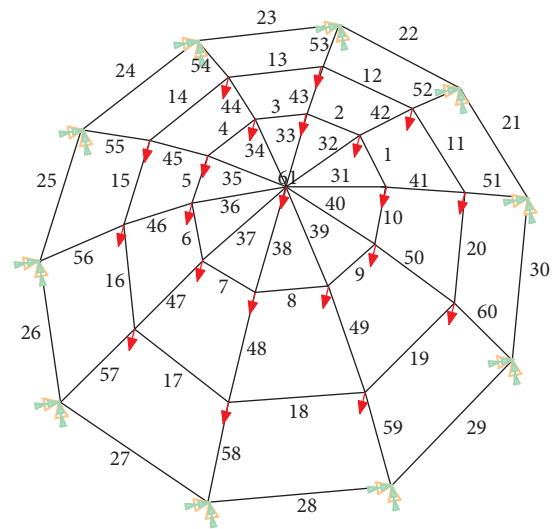


FIGURE 9: Uniform load pattern.

earthquake, the apparent deformation will occur in the shell structure subjected to the inertia force, and the importance coefficient of the components may vary in a short time. Thus,

TABLE 2: Statistical parameter for sample structure.

Parameter	Probability distribution	Mean	Standard deviation
Elastic modulus	Gaussian distribution	$2.10 \times 10^{11} \text{ N/m}^2$	$6.18 \times 10^9 \text{ N/m}^2$
Pipe diameter	Gaussian distribution	0.2 m	0.0002 m
Concentrated force on top	Gaussian distribution	50 KN	0.5 KN
Uniform load on joint	Gaussian distribution	10 KN	0.1 KN
Initial imperfections of position	Gaussian distribution	$(L/1000 + L/300)/2 = 0.087 \text{ m}$	0.047 m

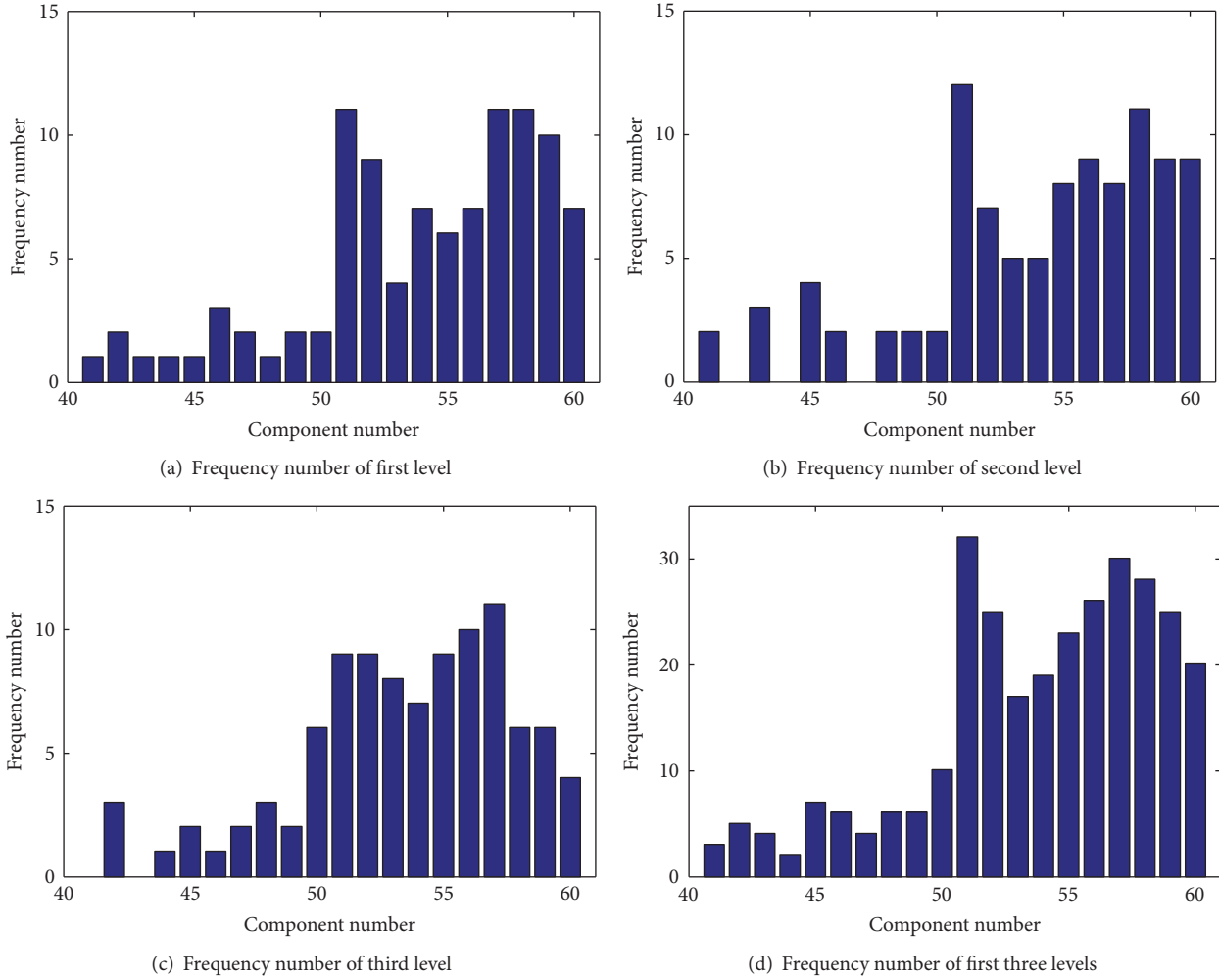


FIGURE 10: Frequency number under uniform load pattern.

the dynamic time-history analysis and adequate research are needed.

According to the site type, El Centro waves, Taft waves, Tianjin waves, and Kobe waves are used in dynamic analysis. Each earthquake wave comprises two horizontal seismic waves and one vertical seismic wave, the time interval is 0.02 s, the selected duration is 4.8 s, and the waveforms contain the maximum amplitudes.

In order to simplify the calculation, the dynamic displacement and the generalized equivalent stiffness of the structure are calculated by the time interval 0.2 s, which is equivalent

to select 25 instantaneous states of the structure and calculate the statistical results from each earthquake wave.

The random parameters and their statistical distributions are in Table 1. For each group of earthquake waves, 30 random structure models are established. Therefore, the importance coefficients of 750 elements are calculated. According to the process in Figure 4, the probability values of the important coefficient of all elements are obtained by statistical calculation. Taking component 55 as an example, the importance coefficient results in different dynamic actions which are shown in Figure 12.

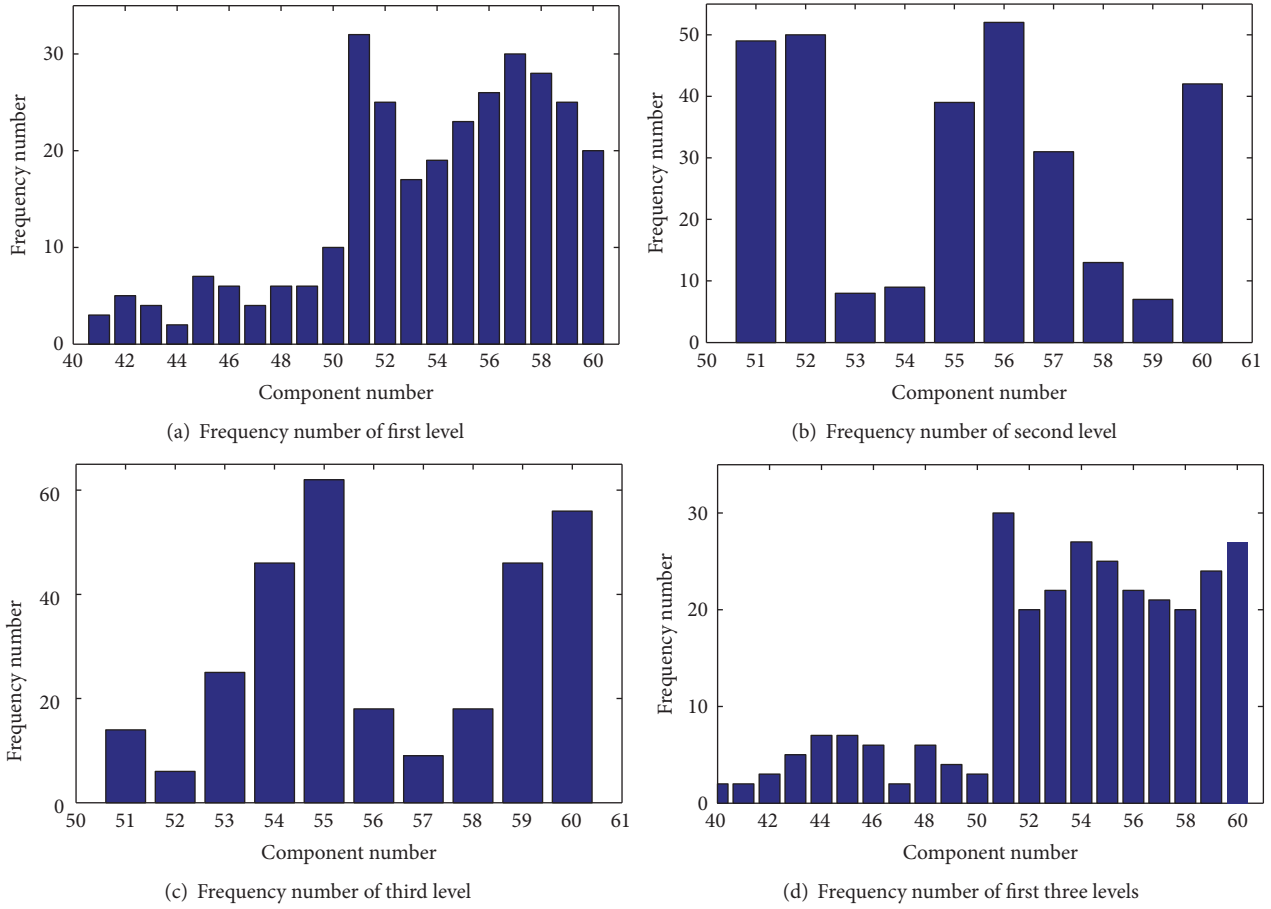


FIGURE 11: Accumulated frequency of members under various loads.

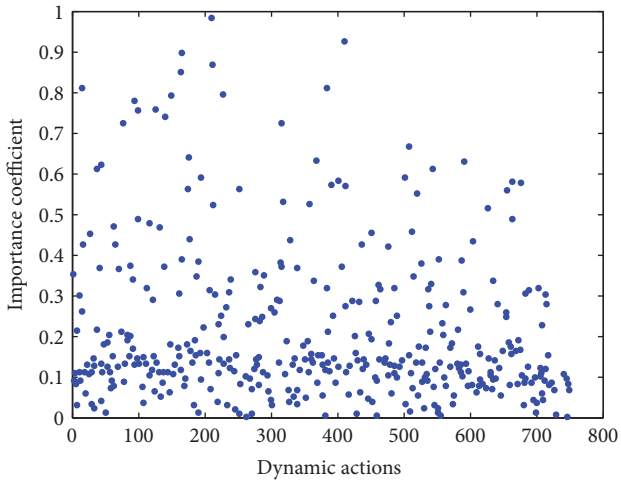


FIGURE 12: Importance coefficient of member 51 in various dynamic cases.

As the earthquake has great uncertainty, the elements of the similar location can be treated equally for the spatial structure with symmetry in evaluating the importance coefficient of each member.

In this case, according to the locations, the elements on the first circle (elements 1–10) are classified as type 1, the elements on the second circle (elements 11–20) are classified as type 2, and the elements on the third circle (elements 21–30) are recorded as type 3.

The rib elements of the first circle (elements 31–40) are classified as type 4, the rib elements of the second circle (elements 41–50) are classified as type 5, and the rib elements of the third circle (elements 51–60) are classified as type 6. The accumulated frequency and the mean value of these six types of elements becoming the important members in three different earthquakes are shown in Figure 13.

From the above results, it can be seen that although the earthquake effect is random and the distribution of the importance coefficient of the components is slightly different in various earthquakes, the most important elements mainly belong to type 6 and type 5, that is, the rib elements of the second and third circle.

The final placement scheme of acceleration sensors is shown in Figure 4 according to the statistical calculation results and the experience of sensors placement.

It is worth noting that the optimal sensor locations according to modal assurance criteria method or energy method are generally at the top of the joints, which are

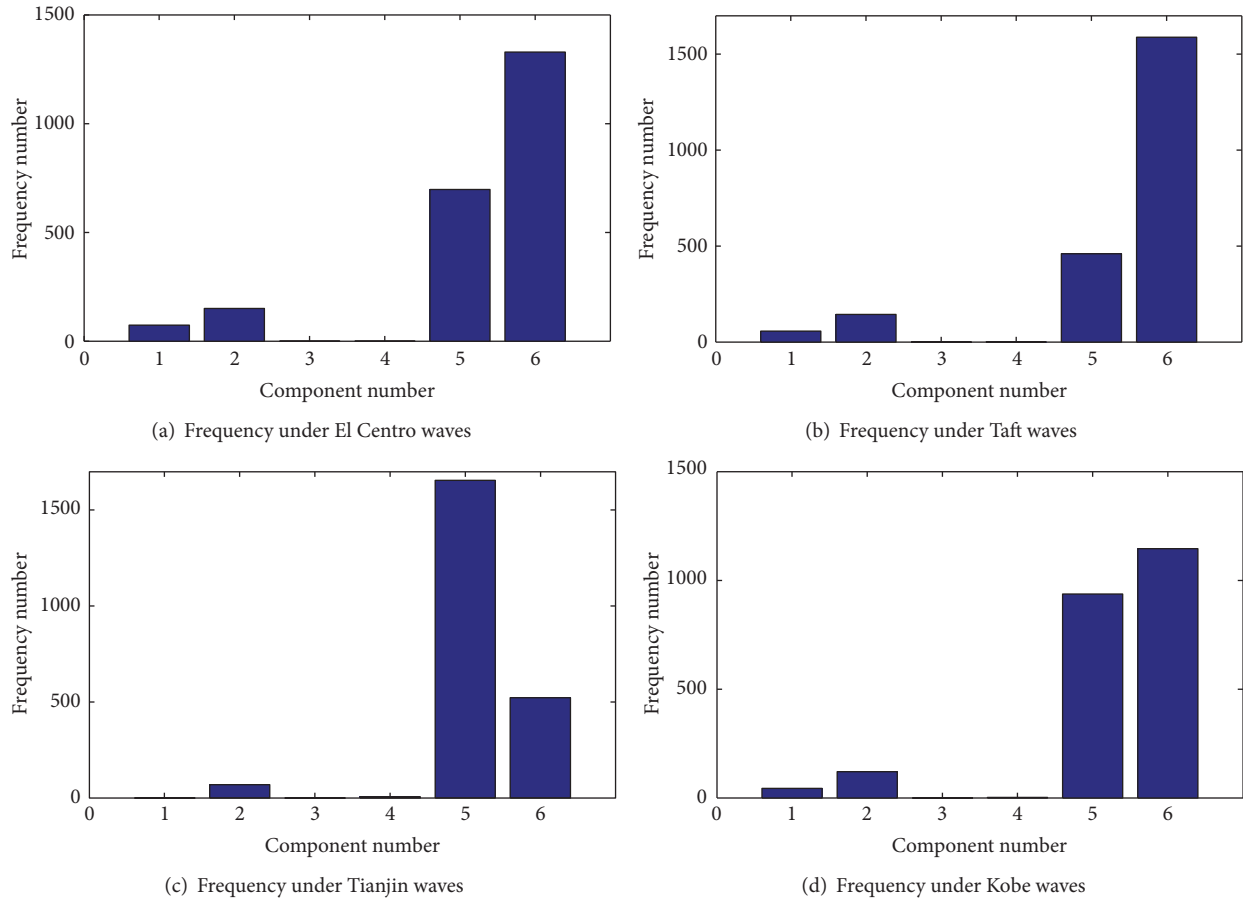


FIGURE 13: Frequency of importance coefficient of 6 types of components.

different from the results based on vulnerability method. Hence, the final placement scheme can be determined by sufficiently considering the results by various methods.

## 7. Conclusion

In the premise of considering randomness of the actual structure parameters and load patterns, the optimal sensor placement scheme based on the vulnerability is the effective application of the vulnerability theory in the field of health monitoring. The evaluation of the importance coefficient according to the change of the global generalized equivalent stiffness of the structure is a reasonable improvement and development for the vulnerability theory.

In addition, in order to meet the practical needs of health monitoring, the effect of components failure is replaced by the minor damage in the components in structural vulnerability analysis, and the most vulnerable path and important components involving the random characteristics of the structure and load pattern are intensely studied.

In general, the weak parts of the spatial structure in the actual operational environment can be effectively monitored by the sensors placement method proposed in this paper, and the identification capacity for initial damage stage is especially excellent. The corresponding method has significant application value in the field of health monitoring.

Different from the traditional method of optimal sensor placement based on modal theory or information theory, the optimal sensor placement based on vulnerability and importance coefficient is emphasized in searching the weak part firstly and to deduce the damage path, and it also can fully consider the random characteristics, which is different from the traditional methods. Although the results from different methods can vary slightly, they can absorb advantages from each other and ultimately achieve the goal of multiobjective optimization.

In the future, intensive studies can be carried out on reducing the number of simulated random samples effectively, exploring the mechanism of damage evolution, and fully combining with other sensors placement methods.

## Conflicts of Interest

The authors declare that there are no conflicts of interest regarding the publication of this paper.

## Acknowledgments

This work is partially supported by Natural Science Foundation of China, under Grant nos. 51478024 and 51108009, Foundation of Beijing Key Lab of Earthquake Engineering and Structural Retrofit under Grant no. USDE201403,

Program for Innovative Research Team “Anti-Seismic and Control in Civil Engineering” of Education Ministry of China, and Beijing Municipal University Innovation Team Building and Teacher Occupation Development Program.

## References

- [1] A. K. Noor and M. M. Mikulas, “Continuum Modeling of Large Lattice Structures: Status and Projections,” in *Large Space Structures: Dynamics and Control*, Springer Series in Computational Mechanics, pp. 1–34, Springer Berlin Heidelberg, Berlin, Heidelberg, 1988.
- [2] C.-Y. Wang, C.-C. Chuang, R.-Z. Wang, and T.-Y. Wu, “Non-linear dynamic analysis of reticulated space truss structures,” *Journal of Mechanics*, vol. 22, no. 3, pp. 199–212, 2006.
- [3] X.-D. Zhi, F. Fan, and S.-Z. Shen, “Failure mechanisms of single-layer reticulated domes subjected to earthquakes,” *Journal of the International Association for Shell and Spatial Structures*, vol. 48, no. 153, pp. 29–44, 2007.
- [4] H. Sohn, C. R. Farrar, and F. Hemez, A review of structural health monitoring literature: 1996-2001, Los Alamos, New Mexico, USA, Los Alamos National Laboratory, 2003.
- [5] R. Kothamasu, S. H. Huang, and W. H. VerDuin, “System health monitoring and prognostics—a review of current paradigms and practices,” *The International Journal of Advanced Manufacturing Technology*, vol. 28, no. 9, pp. 1012–1024, 2006.
- [6] W. J. Staszewski and K. Worden, “An overview of optimal sensor location methods for damage detection,” in *Proceedings of the Smart Structures and Materials 2001-Modeling, Signal Processing, and Control in Smart Structures-*, pp. 179–187, USA, March 2001.
- [7] M. Meo and G. Zumpano, “On the optimal sensor placement techniques for a bridge structure,” *Engineering Structures*, vol. 27, no. 10, pp. 1488–1497, 2005.
- [8] T. H. Yi and H. N. Li, “Methodology developments in sensor placement for health monitoring of civil infrastructures,” *International Journal of Distributed Sensor Networks*, vol. 2012, Article ID 612726, 11 pages, 2012.
- [9] G. C. Thomas and R. D. Clark, A modal test design strategy for modal correlation, Proc 13Th Int Modal Anal Conf, Union College, Schenectady, NY, USA, pp.927-933, 1995.
- [10] T. G. Carne and C. R. Dohmann, “Modal test design strategy for modal correlation,” in *Proceedings of The Proceedings of The 13Th International Modal Analysis Conference*, pp. 13–16, Schenectady, NY, USA, 1995.
- [11] C. R. Pickrel, “Practical approach to modal pretest design,” *Mechanical Systems and Signal Processing*, vol. 13, no. 2, pp. 271–295, 1999.
- [12] M. Papadopoulos and E. Garcia, “Sensor placement methodologies for dynamic testing,” *AIAA Journal*, vol. 36, no. 2, pp. 256–263, 1998.
- [13] D. C. Kammer, “Sensor placement for on-orbit modal identification and correlation of large space structures,” *Journal of Guidance, Control, and Dynamics*, vol. 14, no. 2, pp. 251–259, 1991.
- [14] D. C. Kammer and M. L. Tinker, “Optimal placement of triaxial accelerometers for modal vibration tests,” *Mechanical Systems and Signal Processing*, vol. 18, no. 1, pp. 29–41, 2004.
- [15] C. Schedlinski and M. Link, “An approach to optimal pick-up and exciter placement,” in *Proceedings of The Proceedings of The 14Th International Modal Analysis Conference*, 1996.
- [16] J. E. T. Penny, M. I. Friswell, and S. D. Garvey, “Automatic choice of measurement locations for dynamic testing,” *AIAA Journal*, vol. 32, no. 2, pp. 407–414, 1994.
- [17] C. Flanigan and D. Botos, “automated selection of accelerometer locations for modal survey tests,” in *Proceedings of the international modal analysis conference*, San Diego, Ca, USA, 1992.
- [18] K. S. Murray, in *Proceedings of the, Risk-based structural design*, Proceedings of Symposium on Risk Analysis, Michigan, USA, University of Michigan, 1994.
- [19] M. Shinozuka, M. Q. Feng, H.-K. Kim, and S.-H. Kim, “Nonlinear static procedure for fragility curve development,” *Journal of Engineering Mechanics*, vol. 126, no. 12, pp. 1287–1295, 2000.
- [20] M. Shinozuka, M. Q. Feng, J. Lee, and T. Naganuma, “Statistical analysis of fragility curves,” *Journal of Engineering Mechanics*, vol. 126, no. 12, pp. 1224–1231, 2000.
- [21] J. W. Smith, “Structural robustness analysis and the fast fracture analogy,” *Structural Engineering International: Journal of the International Association for Bridge and Structural Engineering (IABSE)*, vol. 16, no. 2, pp. 118–123, 2006.
- [22] J. Agarwal, D. Blockley, and N. Woodman, “Vulnerability of 3-dimensional trusses,” *Structural Safety*, vol. 23, no. 3, pp. 203–220, 2001.
- [23] J. England, J. Agarwal, and D. Blockley, “The vulnerability of structures to unforeseen events,” *Computers & Structures*, vol. 86, no. 10, pp. 1042–1051, 2008.
- [24] D.-E. Choe, P. Gardoni, D. Rosowsky, and T. Haukaas, “Probabilistic capacity models and seismic fragility estimates for RC columns subject to corrosion,” *Reliability Engineering & System Safety*, vol. 93, no. 3, pp. 383–393, 2008.
- [25] N. Shome, *probabilistic seismic demand analysis of nonlinear structures*, stanford university, Stanford, Calif, USA, 1999.
- [26] N. Catbas, H. Burak Gokce, and D. M. Frangopol, “Predictive analysis by incorporating uncertainty through a family of models calibrated with structural Health-Monitoring data,” *Journal of Engineering Mechanics*, vol. 139, no. 6, pp. 712–723, 2013.
- [27] A. Lorton, M. Fouladirad, and A. Grall, “A methodology for probabilistic model-based prognosis,” *European Journal of Operational Research*, vol. 225, no. 3, pp. 443–454, 2013.
- [28] R. K. Sharma, V. Sugumaran, and H. Kumar, “condition monitoring of roller bearing by k-star classifier and k-nearest neighborhood classifier using sound signal,” *structural durability & health monitoring*, vol. 12, no. 1, pp. 1–16, 2014.
- [29] Yang Gao, *Importance Coefficients of Components in Quantitative Evaluation of Structural Robustness*, Shanghai: Shanghai Jiao Tong University, China, 2008.
- [30] Tengfei Ge, Theoretical and experimental research on damage detection of latticed shells considering random defects, Beijing: Beijing university of technology, China, 2013.

## Research Article

# The Time-Space Joint Response Characteristics of AE-UT under Step Loading and Its Application

Xiaoran Wang,<sup>1,2</sup> Xiaofei Liu ,<sup>1,2</sup> Enyuan Wang ,<sup>1,2</sup> Chong Zhang,<sup>1,2</sup> Haishan Jia,<sup>1,2</sup> and Dexing Li<sup>1,2</sup>

<sup>1</sup>Key Laboratory of Gas and Fire Control for Coal Mines, China University of Mining and Technology, Ministry of Education, Xuzhou 221116, China

<sup>2</sup>School of Safety Engineering, China University of Mining and Technology, Xuzhou 221116, China

Correspondence should be addressed to Xiaofei Liu; liuxiaofei@cumt.edu.cn and Enyuan Wang; weytop@cumt.edu.cn

Received 12 August 2017; Revised 24 November 2017; Accepted 5 December 2017; Published 18 January 2018

Academic Editor: Andrzej Katunin

Copyright © 2018 Xiaoran Wang et al. This is an open access article distributed under the Creative Commons Attribution License, which permits unrestricted use, distribution, and reproduction in any medium, provided the original work is properly cited.

The acoustic emission (AE) and ultrasonic (UT) simultaneous monitoring program is designed using concrete samples under step loading. The time-varying response characteristics of AE-UT are studied and the cross-correlation analysis between AE-UT parameters is obtained. Moreover, the joint response of UT-AE spatial distribution field is analyzed, and an AE-UT joint monitoring method to detect early-warning signals of a rockburst disaster in a coal seam is proposed. The results show the following. (1) During the loading process, the AE pulses/energy and UT attenuation coefficient first slowly decrease and then increase steadily and finally rapidly increase, while the UT velocity shows a trend of first gradually increasing and then slowly decreasing and finally a sharp decline. (2) AE pulses and energy are significantly or highly correlated with the UT velocity and attenuation coefficient. The AE energy and UT attenuation coefficient can better characterize the damage evolution of concrete under step loading. (3) The UT field evolves ahead of the rupture on the surface, and the long/narrow strip distribution region of UT parameters is consistent with the future failure zone; meanwhile, the AE events can visually reflect the evolution path of internal damage as well as the dynamic migration mechanism of UT field.

## 1. Introduction

Concrete as a raw material is widely used in construction engineering such as buildings, roadways, bridges, and tunnels. It is very important for public safety to carry out damage analysis, stability monitoring, and remaining life estimation of those constructions using appropriate methods [1]. Various techniques such as surface topography, scanning electron microscopy (SEM), infrared thermal imaging, computerized tomography (CT), and electromagnetic radiation (EMR) have been used to observe the damage process in laboratory tests [2, 3]. In recent years, passive (acoustic emission, AE) and active (ultrasonic, UT) testing techniques have been gradually applied to the structural instability and safety monitoring [4, 5].

UT monitoring technique is a kind of active nondestructive testing method. Analyzing the response laws of the

received UT wave, we can retrieve the material's damage state, predict the material's intensity, and provide an early warning of structural instability disasters [6–9]. Many scholars have carried out a number of researches on the correlation between UT parameters and stress in the crack evolution process. Nur [10] studied the influence of microcracks on the wave velocity, and the quadratic function relationship between wave velocity and stress was concluded in the crack closure stage. Liu et al. [11] established polynomial regression between the UT parameters (velocity, amplitude, and frequency) and stress levels of coal under step loading and discussed the relationship between UT velocity, crack width, and damage variable. Molina and Wack [12] described the fracture field characteristics combining the surface crack images and UT attenuation, and they explained that UT attenuation had a high sensitivity to crack propagation. Sun and Zhu [13] reported the relationship between wave velocity



TABLE 1: The positions of AE probes and UT test points (based on coordinate system in Figure 1).

Number	UT test points				AE sensors			
	Generating	x/mm	receiving	y/mm	z/mm	x/mm	y/mm	z/mm
(1)	100	0	0	10	90	10	10	100
(2)	100	0	0	10	10	90	10	100
(3)	100	0	0	90	10	90	90	100
(4)	100	0	0	90	90	10	90	100
(5)	100	0	0	30	70	10	10	0
(6)	100	0	0	30	30	90	10	0
(7)	100	0	0	70	30	90	90	0
(8)	100	0	0	70	70	10	90	0
(9)	100	0	0	50	50	-	-	-

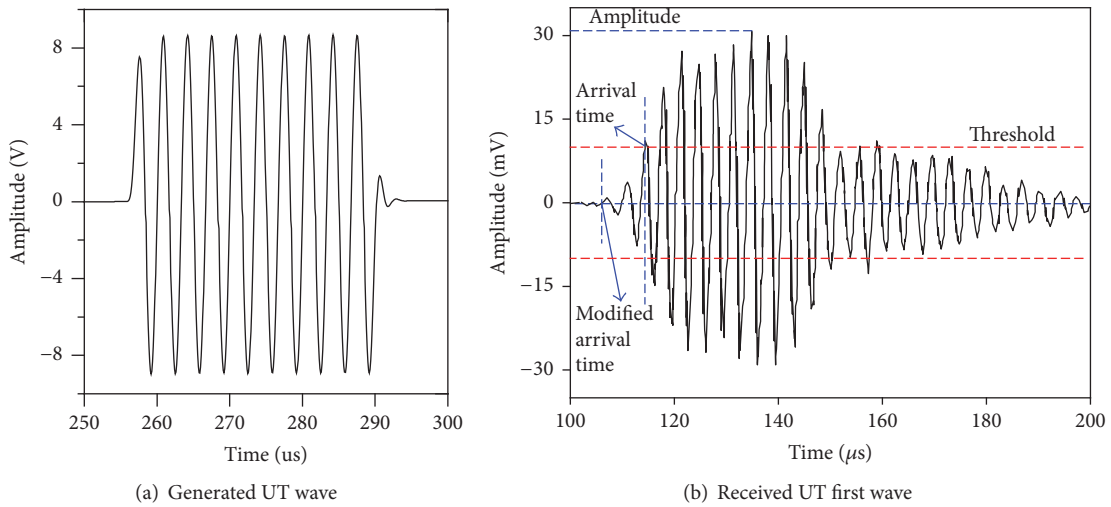


FIGURE 2: The generated UT wave and received UT first wave.

function, 8 AE sensors (NONA-30) are arranged at different coordinate positions (Figure 1 and Table 1). The AE locating algorithm is based on the time-difference locating method. The P-wave threshold crossing technique is used to determine the AE arrival time, and velocity is the average value of 9 points per stress level in Section 3.3. The AE sensors are attached and fixed to the sample's surface with a special coupling agent. Lead break amplitude should be above 90 dB to make sure that the coupling quality between AE sensors and the sample is good. The preamplifier value and AE threshold are both 40 dB, and the AE sampling rate is 1 MSPS.

The UT monitoring system mainly includes the generated and received system of UT signals (ARB-1410 card), generated and received UT probes (NANO-30), and a preamplifier. The ARB-1410 card can generate various UT signals with different frequencies and amplitudes, and the detailed information of the generated UT signals is shown in Figure 2(a) and Table 2. To obtain the UT field, we employ 9 UT test points as shown in Figure 1 and Table 1. UT velocity and attenuation coefficient are the most basic UT parameters which correlate

strongly with applied stress. The calculations of UT velocity and attenuation coefficient are shown below [11, 24]:

$$v = \frac{L}{t_1 - t_0} \quad (1)$$

$$\alpha = 8.686 \frac{\ln A_0 - \ln A_1}{L}, \quad (2)$$

where  $v$  is the UT velocity (m/s);  $L$  is the distance traveled in samples (m);  $t_0$  and  $t_1$  are the modified arrival times of the generated and received UT first wave, respectively (s);  $\alpha$  is the attenuation coefficient (dB/m);  $A_0$  and  $A_1$  are the amplitude of the generated and received UT first wave, respectively (dB).

The UT signals will be recorded in the voltage form by software. So, before formula (2) can be calculated, the voltage signals must be converted into wave signals by the following formula:

$$A = 20 (6 + \lg B) - \text{pre}, \quad (3)$$

TABLE 2: The detailed information of the generated UT signals.

Waveform	Dominant frequency	Firing interval	Threshold value	Sampling frequency	Amplitude	Preamplifier value
Sine wave	300 kHz	2 s	40 dB	10 MHz	8.5 V	40 dB

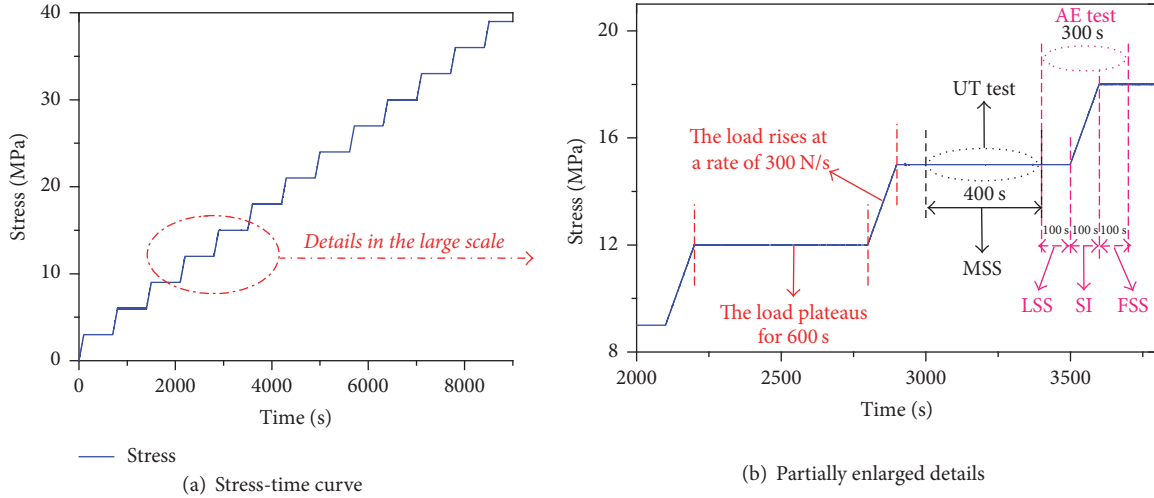


FIGURE 3: The step-loading path of concrete and experimental test program.

where  $A$  is the amplitude of the UT wave (dB);  $B$  is the voltage of the recorded UT wave (V);  $pre$  is the preamplifier value in Table 2.

The arrival time of the UT signal is determined using the first wave threshold crossing technique by the software automatically. But the arrival time determination is not accurate sometimes, so it is necessary to modify the arrival time of UT signals manually (as shown in Figure 2(b)) [11].

**2.2. Sample Preparation.** The concrete samples used in this paper are cube (100 mm × 100 mm × 100 mm) with a total number of 4. The materials of concrete samples mainly contain cement, sand, coarse aggregates, and water with a mass ratio of 1:1.6:0.5:0.58. Mix and stir these materials evenly and then pour the mixture into the mold and strongly vibrate it to reduce bubbles inside the samples. Then, we should put these concrete samples in a cool and ventilated place for 28 days before the experiments.

**2.3. Experimental Test Program.** We assume step loading in the experiments with 30 kN in each loading step (Figure 3). The applied loading rate is 300 N/s. In order to realize the AE and UT synchronous monitoring, we carry out AE monitoring in the stress increase (SI) stage, former 100 s of stress stable (FSS) stage, and latter 100 s of stress stable (LSS) stage. In the middle 400 s of the stress stable (MSS) stage, we test the UT signals. After finishing the above preparation, we should start the loading machine and AE monitoring system. When the applied load reaches the stress stable stage, we should suspend the AE monitoring system and meanwhile start the UT test system to collect UT signals. After finishing

the UT test of the 9 points, we should close the UT monitoring system and restart the AE monitoring system. This cycle is repeated until the samples reach complete failure. The cracks evolution process on the surface of concrete samples is recorded by a digital camera under the whole loading process.

**2.4. Data Processing Method.** In this paper, cross-correlation analysis (CCA) is used to analyze the correlation of these two signals. The discrete series of AE parameters (AE pulses and energy) is  $X$ , and the discrete series of UT parameters (velocity and attenuation coefficient) is  $Y$ . So, the degree of correlation between AE and UT signals can be represented by a correlation coefficient  $r_{xy}$ .

$$r_{xy} = \frac{\sum_{i=1}^n (x_i - \bar{x})(y_i - \bar{y})}{\sqrt{\sum_{i=1}^n (x_i - \bar{x})^2} \sqrt{\sum_{i=1}^n (y_i - \bar{y})^2}} \quad (4)$$

$$\bar{x} = \frac{1}{n} \sum_{i=1}^n x_i,$$

$$\bar{y} = \frac{1}{n} \sum_{i=1}^n y_i,$$

where  $i$  represents the  $i$ th step loading;  $n$  is the total number of load steps;  $x_i$  is the AE parameters in the  $i$ th step loading, which is the AE pulses and energy accumulative sum of the SI stage, the FSS stage in the  $i$ th step, and the FSS stage in the  $(i-1)$ th step;  $y_i$  is the UT velocity and attenuation coefficient variation in the  $i$ th step loading;  $\bar{x}$  and  $\bar{y}$  are the average values of  $x_i$  and  $y_i$ , respectively;  $r_{xy}$  is the correlation coefficient of AE and UT signals, and its value range is  $[-1, 1]$ ; when  $|r_{xy}|$

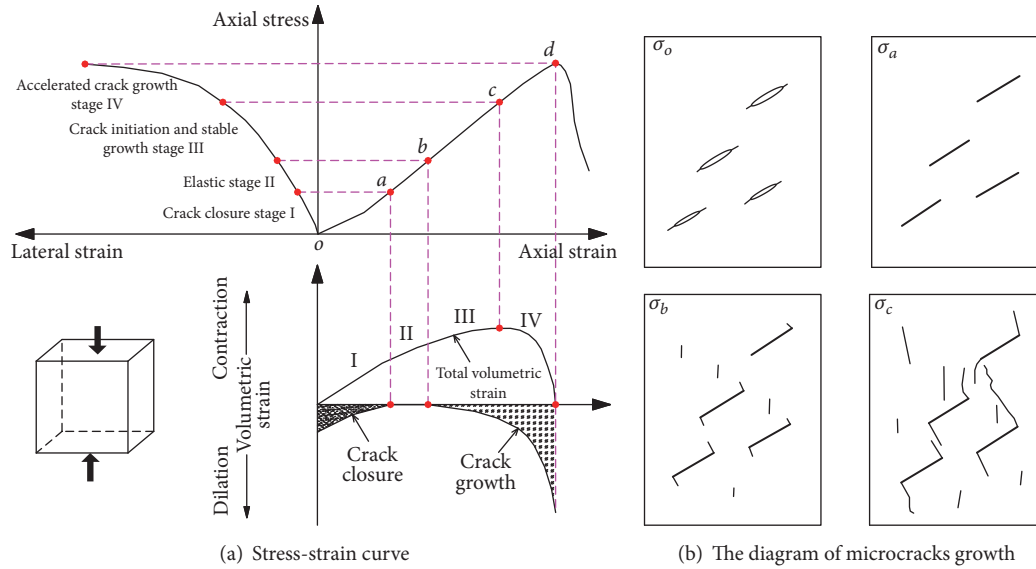


FIGURE 4: Typical stress-strain curve and microcracks growth of concrete (from the literature [13]).

is closer to 1, the correlation is higher, and when  $|r_{xy}|$  is closer to 0, the correlation of the two signals is low.

The correlation degree of the two signals can be divided into 4 grades according to the correlation coefficient: ①  $0 < |r_{xy}| \leq 0.3$ , weak or no correlation; ②  $0.3 < |r_{xy}| \leq 0.5$ , low correlation; ③  $0.5 < |r_{xy}| \leq 0.8$ , significant correlation; ④  $0.8 < |r_{xy}| \leq 1.0$ , high correlation.

### 3. AE-UT Temporal Response Characteristics of Concrete under Step Loading

**3.1. Mechanics and Cracks Growth Characteristics of Concrete under Loading.** According to the literature [13] and previous test results of concrete mechanical properties, the loading process of concrete can be divided into the following stages (as shown in Figure 4): (1) microcrack closure stage I (*oa* stage): the original microcracks inside concrete are compacted, and the stress-strain curve presents a concave type; (2) elastic stage II (*ab* stage): the stress-strain curve is approximately linear, in which a small amount of microcracks will begin to grow accompanied by the occurrence of cracks closure, and the cracks are randomly distributed; (3) microcrack initiation and stable growth stage III (*bc* stage): the microcracks expand steadily, the stress-strain curve exhibits nonlinear characteristics, and the specimen begins to exhibit damage; (4) accelerated microcrack growth stage IV (*cd* stage): the development of microcracks exhibits a qualitative change and the internal cracks propagation speed is accelerated. At this stage, a large number of internal cracks inside concrete samples gradually converge and nucleate to form the main rupture.

**3.2. AE Time-Varying Response Characteristics.** In the internal microcracks development process, there will be accompanying AE signals. The AE time-varying response characteristics of SI, FSS, and LSS stage under different loading steps are

shown in Figure 5. The AE pulses mainly reflect the frequencies of microruptures while AE energy represents the energy released during the fracture process of loading concrete.

At the initial stage of loading, the AE pulses and energy of the SI stage are large because of the internal microcracks compaction. With the applied load increasing, the original internal microcracks become fewer because the applied load does not reach the crack initiation stress to generate new cracks. Therefore, the AE signals gradually reduce. However, at FSS and LSS stage, the stress is small and the cumulative damage effect is relatively weak, so initial microcracks cannot close, and the AE pulses and energy both show low values but an increasing tendency. Compared with the LSS stage, the AE signals of the FSS stage are more active relatively. When the applied stress enters the linear-elastic and microcrack stable growth stage (12–27 MPa), the microcracks begin to generate inside the sample. These generated cracks are random and the number is relatively stable. So, in the SI, FSS, and LSS stages, AE pulses and energy show a steady increasing trend with a small amplitude. When the specimen enters the microcrack accelerated growth stage (27–36 MPa), irreversible deformation will occur, and the small cracks expand and coalesce to form larger cracks. The AE signals at SI, FSS, and LSS stages all show a rapid increasing trend. It is worth noting that the AE signals of the LSS stage begin to exceed the FSS stage, because the cracks will also develop with time although the stress is maintained. The specimen exhibits fatigue damage and shows a strong creep rheological property. When the specimen is approaching the failure stage (36–42 MPa), a large number of cracks are connected to form the macroscopic main failure. The AE signals of SI, FSS, and LSS stages reach the maximum value, and the total AE signals in the LSS stage exceed the SI stage when the specimen reaches complete failure in 9500 s.

**3.3. UT Time-Series Response Characteristics.** According to formulas (1)–(3), the UT velocity and attenuation coefficient

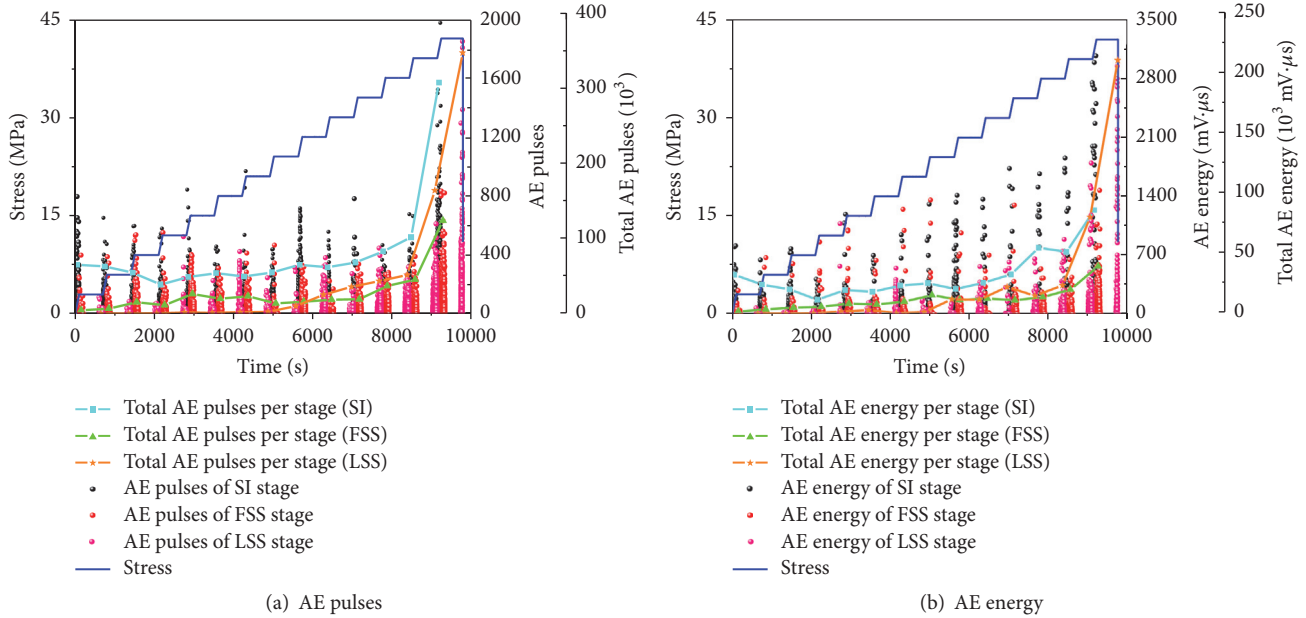


FIGURE 5: AE time-varying characteristics of concrete under step loading.

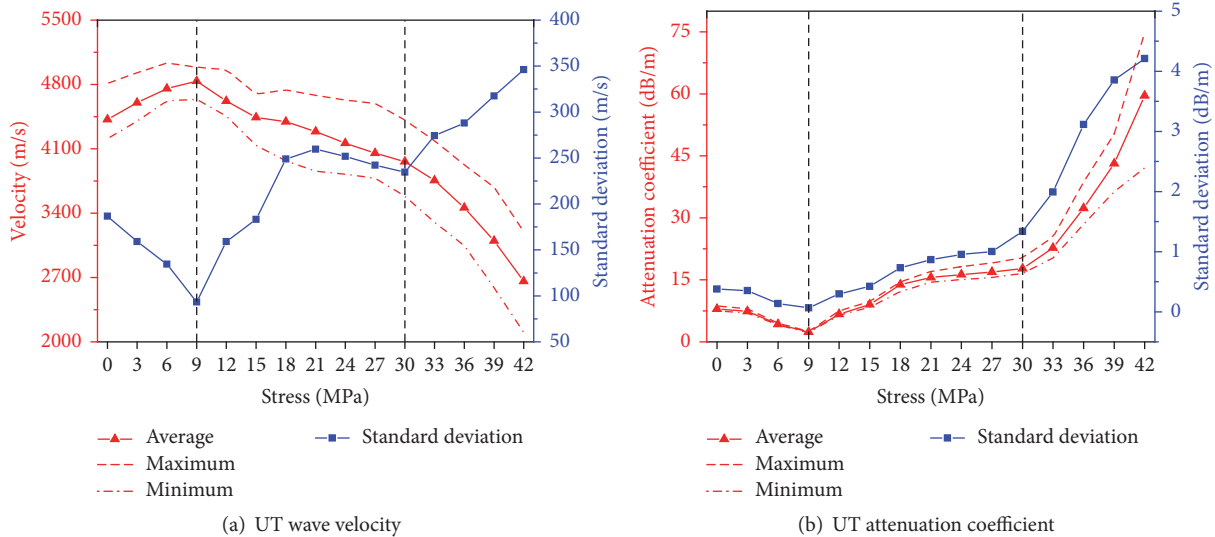


FIGURE 6: The evolution of UT parameters under different applied stresses.

under different stresses are calculated, respectively, and shown in Figure 6. Due to the irregular shape, size, and distribution of the cracks inside the concrete specimen, the stress field is inhomogeneous and the UT response characteristics are different in different test points albeit with a similar character of change generally. Therefore, this paper uses the average, maximum, minimum, and standard deviation value of the 9 UT test points to analyze the UT response characteristics at each stress level.

From Figure 6, we can see that the UT response goes through three stages on the whole. At the initial loading stage (0–9 MPa), the internal microcracks are compacted, and the

concrete sample presents an obvious loading strengthening characteristic. The UT velocity increases but the attenuation coefficient decreases gradually. With the applied stress increasing, the UT average velocity decreases slowly from 4836 m/s at 9 MPa to 3961 m/s at 30 MPa, while the attenuation coefficient increases from 2.36 dB/m to 17.72 dB/m and increases by 15.36 dB/m. In this stage, the applied stress exceeds the crack initiation stress, and the cracks begin to develop stably. After that, the specimen enters the accelerated microcrack growth stage, in which the specimen produces a large number of irreversible deformations and the small cracks grow to form large cracks. The UT velocity and

TABLE 3: Correlation coefficient between AE and UT parameters.

AE	UT							
	UT velocity				UT attenuation coefficient			
		Test result		Average	$ r_{xy} $	Test result		Average
AE pulses	0.7383	0.7524	0.7689	0.7532	0.8501	0.8106	0.8371	0.8326
AE energy	0.7744	0.8265	0.7693	0.7901	0.8706	0.8902	0.8446	0.8685

attenuation coefficient both reach the critical turning point corresponding to about 70% of the peak stress. Then, the UT velocity begins to decrease sharply and the average velocity reduces by nearly 40% at the peak stress which is only 2659 m/s. But the average attenuation coefficient shows a sharp increasing trend and reaches 59.58 dB/m at peak stress, which increases by over 7.5 times compared with the value under no applied loading. In the whole loading process, the maximum and minimum values of UT parameters (velocity, attenuation coefficient) at the 9 test points show the same trend as the average value. But the full range (difference between the maximum and minimum values) and the standard deviation of the 9 UT test points both decrease first and then increase. This phenomenon reveals that the concrete failure process is the combination of the identity and diversity change processes, in which the physical properties of concrete change from intrinsic heterogeneity to homogeneity and then to heterogeneity.

## 4. Discussion

**4.1. Correlation Analysis between AE and UT Parameters.** The rupture inoculation process of concrete samples is a continuous development process, including initial microcracks closure, initiation, propagation, and coalescence. These are the root causes of the UT parameters' changes. Therefore, there must be a certain correlation between UT and AE parameters. According to formula (4), the correlation coefficients between the AE and UT parameters are calculated, and the results are shown in Table 3.

From Table 3, the ranges of  $|r_{xy}|$  between AE and UT parameters are 0.7383–0.7689, 0.8106–0.8501, 0.7693–0.8265, and 0.8446–0.8902, with average values of 0.7532, 0.8326, 0.7901, and 0.8685, respectively. In contrast, the correlations between AE energy and UT parameters are better than that of AE pulses, which indicates that the AE energy can better characterize the damage state of concrete samples. The values of  $|r_{xy}|$  between UT attenuation coefficient and AE pulses and energy are both more than 0.8, showing a high degree of correlation, while the UT velocity is significantly correlated with AE parameters, which has a lower correlation compared with the attenuation coefficient. The essence of the fracture evolution process is the energy accumulation, transference, redistribution, and release. AE energy and UT attenuation coefficient both are the parameters coming from the energy point of view. They show obvious advantages on representing the damage state of the specimen and there is a high degree of correlation between them.

**4.2. Joint Response Characteristics of AE and UT Spatial Distribution Field.** The physical properties of concrete samples are inhomogeneous in space distribution. So, it is of great importance from the aspect of spatial field distribution to fully understand the damage process and its mechanical mechanism [25, 26]. The spatial distribution of damage and stress can be obtained at a certain time (stress) using UT monitoring, but it cannot get the dynamic migration path and its mechanism in real time. The development and evolution path of internal cracks can be observed visually in real time by AE locating technology, which can provide a tool for revealing the evolution process of the UT spatial field distribution.

In the initial loading stage (6 MPa, Figure 7(a)), the internal cracks close and the sample becomes homogeneous gradually. The ranges of the UT velocity and attenuation coefficient of 9 test points are 4621 m/s~5033 m/s and 4.09 dB/m~4.52 dB/m, respectively. And the top right area is the low velocity zone which is consistent with the large energy AE event concentration area. There is no obvious crack growth in the surface rupture image.

When the sample is in the linear-elastic stage (15 MPa, Figure 7(b)), a faintly visible fine crack appears on the right side of the sample surface, and its position is consistent with the large energy AE events concentration region. The distribution of UT velocity decreases while UT attenuation coefficient increases from the center to the boundary. The greater the density of AE events, the smaller the UT velocity and the greater the UT attenuation coefficient. Large energy AE events begin to appear and the damage begins to develop on the left area based on the AE locating results. All of those indicate that the right area of the sample is still in high stress, but the stress in the left side significantly increases and high stress begins to migrate to the left from the right area.

In the microcrack stable growth stage (21 MPa, Figure 7(c)), the ranges of UT velocity and attenuation coefficient are 3856 m/s~4682 m/s and 14.44 dB/m~17.04 dB/m, respectively. The dispersions of UT parameters increase obviously. The high energy AE events further increase in the left area, which indicates that the high stress zone continues to migrate to the left. Some visible fine cracks begin to appear on the left side corresponding to the low UT velocity, and the cracks on the right side further extend to the bottom of the specimen corresponding to the dense area of AE events.

While the sample enters the microcrack accelerated growth stage (30 MPa, Figure 7(d)), the cracks on the right side connect with each other to form a macroscopic crack. And there also forms an obvious fine crack on the left side

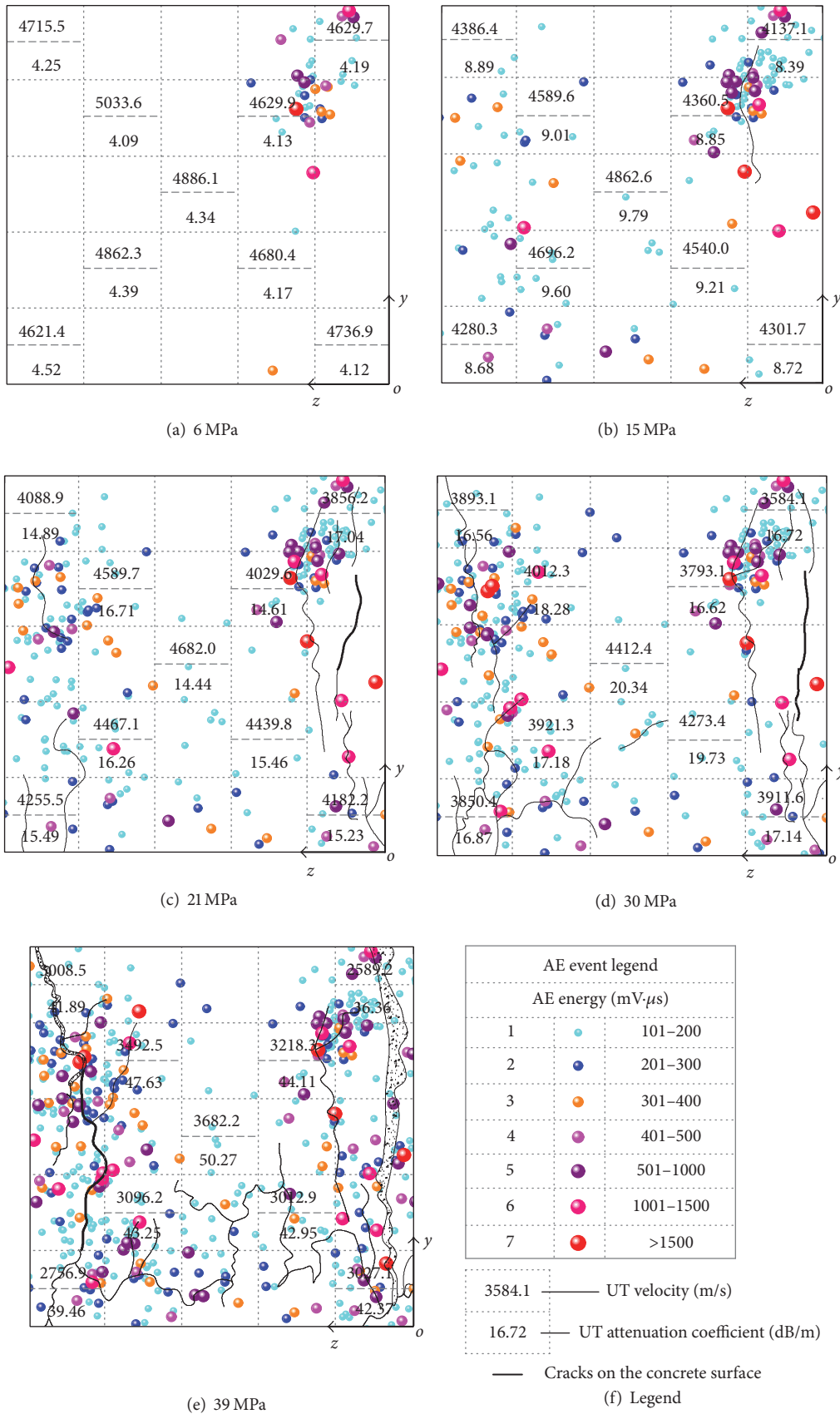


FIGURE 7: The spatial joint response characteristics of UT-AE.

of the sample. The UT velocity severely attenuates due to the existence of the macroscopic crack on the right side. The left side is a high stress concentration area corresponding to the low velocity (high attenuation coefficient) zone. The UT field presents a long and narrow strip distribution characteristic. The large energy AE events are also distributed in a long strip shape, which are concentrated in the left and right sides of the specimen. This long and narrow strip distribution region is the future macro failure zone.

When the specimen is near failure (39 MPa, Figure 7(e)), the cracks on both the left and the right sides continue to grow and merge to form a macroscopic main failure. The failure mode is similar to the "X" conjugate wedge splitting type. Due to the existence of macroscopic cracks, the UT parameters severely attenuate (the velocity decreases and attenuation coefficient increases) sharply. So, both the left and the right sides are low velocity (high attenuation coefficient) zones. According to the AE event field and the surface rupture image, there are little cracks in the middle upper part of the sample, so it corresponds to the high velocity region (low attenuation coefficient). In the middle lower area of the sample, there are a large number of high energy AE events and serious cracks development corresponding to the low velocity region. The velocity and attenuation coefficient distribution ranges of the 9 test points are 2589 m/s~3682 m/s and 36.36 dB/m~50.27 dB/m, respectively. The dispersions of UT parameters reach their maximum values.

## 5. Field Application Prospects and the Significance of AE-UT Joint Monitoring

Rockburst disaster is a serious geological dynamic disaster in coal mines which can cause a large number of casualties. Particularly, with the increase of the mining depth, underground engineering faces special severe geographical environments such as high crustal stress, high geotemperature, high seepage pressure, and strong disturbance. In such geographical regions, the occurrence frequencies and intensity of rockburst disaster are gradually increasing. During the mining process, in front of the longwall face, a high stress concentration zone will occur. Besides, the mining activities will generate strong disturbance stress. Under the comprehensive effect of high static stress and strong disturbance stress, the zones in front of the working face are more likely to exhibit rockburst disasters where we should pay much attention.

According to the experiments and analysis in Sections 3 and 4, the AE-UT joint monitoring has the potential to be an effective tool of the rockburst early warning. So, we propose using the AE-UT joint monitoring method to forecast the rockburst disasters in the longwall working face. The detailed AE-UT joint monitoring prospect in the coal seam is shown in Figure 8. The AE-UT monitoring area is within 200 m in front of the working face. There are five measuring groups on both the upper roadway and the lower roadway. Each group has four UT test points and two AE monitoring sensors as shown in Figure 8(b), and the distance between the UT and AE sensors in each group is 5 m. The first group is located at 20 m ahead of the working face,

and the distance between each group is 40 m. The real-time monitoring data of each AE-UT sensor are sent and stored in the substations underground. Then, the monitoring data will be transferred to the ground host computer through the communication port. Then, we can analyze the AE-UT time-space response characteristics to provide an early warning against rockburst disasters. The AE-UT monitoring method in the longwall working face has a guiding significance for rockburst monitoring mainly in the following two aspects.

(1) It can help determine the critical precursor characteristics of rockburst disasters more comprehensively and evaluate the danger degree more accurately. The AE parameters begin to rise sharply and UT parameters reach the critical turning point. The UT field distribution begins to present long and narrow strip distribution characteristics, and the large energy AE events fields are gathered together. When the above cases appear, we can indicate that the coal seam has entered the damage accelerated development stage. And the computer will issue the early-warning alert about when and where the rockburst disasters will occur. Then, mining workers will take some measures to prevent the occurrence or reduce the consequences of disasters.

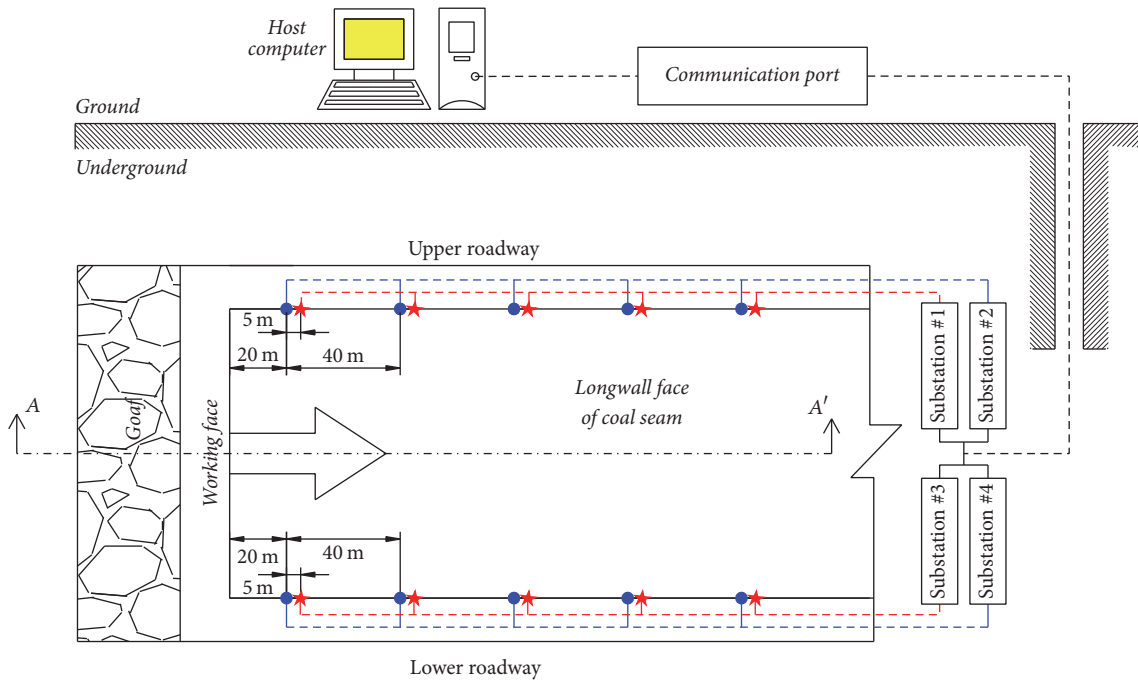
(2) It is beneficial to further understand the damage evolution process and the mechanism of rockburst disasters. During the development of the rockburst disaster, small fractures converge to form large fractures and the large fractures coalesce to form the main failure. The evolution of UT field can reflect the migration of stress field, while the location of AE events can well represent the development of microcracks and explain the dynamic migration path of the UT field distribution.

## 6. Conclusion

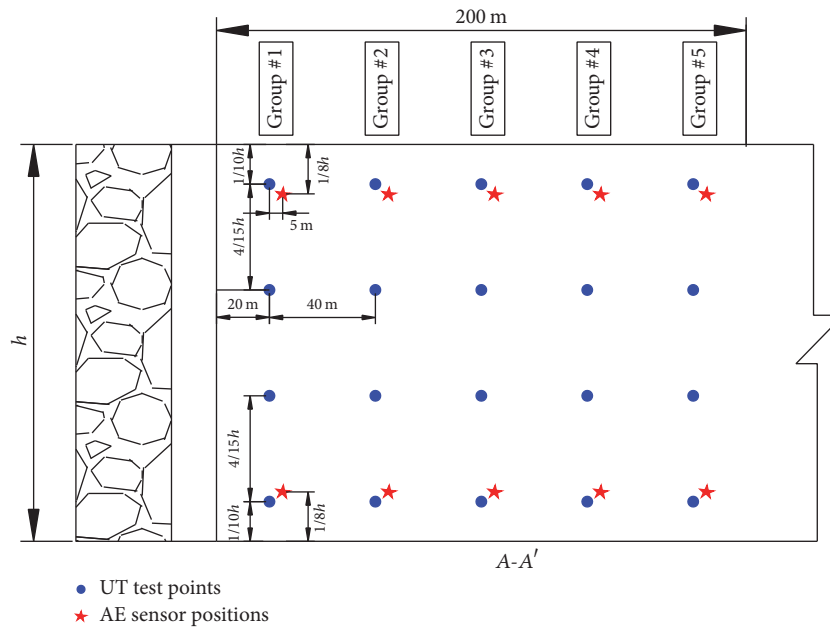
(1) In the compaction stage, AE pulses/energy showed a decreasing trend, and the UT velocity showed an increasing trend, while the attenuation coefficient decreases gradually. During the crack stable growth stage, the AE pulses/energy showed a trend of steady increase with a small amplitude, the UT velocity slowly declined, and the attenuation coefficient slowly increased. In the microcrack accelerated growth stage, AE pulses/energy and UT attenuation coefficient present a rapid growing trend and reach the maximum value, while the velocity greatly reduces to the lowest value.

(2) AE pulses and energy are significantly correlated with UT velocity, while UT attenuation coefficient variation is highly correlated with AE pulses and energy. From the energy point of view, AE energy and UT attenuation coefficient can carry more abundant information of the damage state, which shows obvious advantages on representing the continuous damage evolution process.

(3) The failure process of concrete is the combination of the identity and diversity changes, in which the physical properties of loaded concrete change from intrinsic heterogeneity to homogeneity and then to heterogeneity. The dispersions of the UT parameters decrease firstly and then increase. In this process, the small cracks converge to form large cracks



(a) Layout of sensors at the longwall face



(b) Detailed AE-UT sensors arrangement

FIGURE 8: The AE-UT joint monitoring prospect in the coal seam.

and the large cracks coalesce to form the main failure; the evolution of the UT field can reflect the migration of the stress field, while the location of AE events can well represent the development of microcracks and explain the dynamic migration path of the UT field distribution. The UT and AE field distributions evolve ahead of the surface failure. The long/narrow strip distribution region of UT parameters and the large energy AE event concentrated area are consistent with the future failure zone.

### Conflicts of Interest

The authors declare that they have no conflicts of interest regarding the publication of this paper.

### Acknowledgments

This work is supported by the Fundamental Research Funds for the Central Universities (2017BSCXB13).

## References

- [1] T. Wen, H. M. Tang, Y. R. Liu, Z. X. Zou, K. Wang, and C. Y. Lin, "Newly modified damage statistical constitutive model of rock based on impact factor," *Journal of Chinese University of Mining & Technology*, vol. 45, no. 1, pp. 141–149, 2016.
- [2] B. Kong, E. Wang, Z. Li et al., "Electromagnetic radiation characteristics and mechanical properties of deformed and fractured sandstone after high temperature treatment," *Engineering Geology*, vol. 209, pp. 82–92, 2016.
- [3] G. H. Ge, C. Wang, and L. Li, "Acoustic wave propagation characteristics of the soft sandstone under loading," *Science Technology and Engineering*, vol. 15, no. 18, pp. 85–90, 2015.
- [4] H. Li, C. Yang, B. Li, and X. Yin, "Damage evolution and characteristics of ultrasonic velocity and acoustic emission for salt rock under triaxial multilevel loading test," *Yanshilixue Yu Gongcheng Xuebao/Chinese Journal of Rock Mechanics and Engineering*, vol. 35, no. 4, pp. 682–691, 2016.
- [5] J. Zhu and Y. Song, "Research on fatigue damage of concrete under biaxial compressive loading using ultrasonic velocity method," *Journal of Rock Mechanics and Engineering*, vol. 23, no. 13, pp. 2230–2234, 2004.
- [6] J. Chen, Z. Xu, Y. Yu, and Y. Yao, "Experimental characterization of granite damage using nonlinear ultrasonic techniques," *NDT & E International*, vol. 67, pp. 10–16, 2014.
- [7] H.-L. Wang and Y.-P. Song, "Ultrasonic pulses behavior in various-size concrete specimens under compression," *Journal of Dalian University of Technology*, vol. 47, no. 1, pp. 90–94, 2007.
- [8] L. Peyras, P. Rivard, P. Breul, A. Millet, and G. Ballivy, "Characterization of rock discontinuity openings using acoustic wave amplitude-application to a metamorphic rock mass," *Engineering Geology*, vol. 193, pp. 402–411, 2015.
- [9] N. Li, J. Sun, J. Jiao, B. Wu, and C. He, "Quantitative evaluation of micro-cracks using nonlinear ultrasonic modulation method," *NDT & E International*, vol. 79, pp. 63–72, 2016.
- [10] A. Nur, "Effects of stress on velocity anisotropy in rocks with cracks," *Journal of Geophysical Research*, vol. 76, no. 8, pp. 2022–2034, 1971.
- [11] X. Liu, X. Wang, E. Wang, Z. Liu, and X. Xu, "Study on ultrasonic response to mechanical structure of coal under loading and unloading condition," *Shock and Vibration*, vol. 2017, Article ID 7643451, 12 pages, 2017.
- [12] J.-P. Molina and B. Wack, "Crack field characterization by ultrasonic attenuation-preliminary study on rocks," *International Journal of Rock Mechanics and Mining Sciences*, vol. 19, no. 6, pp. 267–278, 1982.
- [13] Q. Sun and S. Zhu, "Wave velocity and stress/strain in rock brittle failure," *Environmental Earth Sciences*, vol. 72, no. 3, pp. 861–866, 2014.
- [14] A. Behnia, H. K. Chai, and T. Shiotani, "Advanced structural health monitoring of concrete structures with the aid of acoustic emission," *Construction and Building Materials*, vol. 65, pp. 282–302, 2014.
- [15] P. Hou, F. Gao, Z. Zhang, Y. Yang, and T. Teng, "Evaluation method of rock brittleness based on acoustic emission and energy evolution," *Journal of China University of Mining and Technology*, vol. 45, no. 4, pp. 702–708, 2016.
- [16] S. De Santis and A. K. Tomor, "Laboratory and field studies on the use of acoustic emission for masonry bridges," *NDT & E International*, vol. 55, pp. 64–74, 2013.
- [17] F. Xiao, G. Liu, Z. Zhang, Z. Shen, F. Zhang, and Y. Wang, "Acoustic emission characteristics and stress release rate of coal samples in different dynamic destruction time," *International Journal of Mining Science and Technology*, vol. 26, no. 6, pp. 981–988, 2016.
- [18] X. Wang, X. Liu, E. Wang et al., "Experimental research of the AE responses and fracture evolution characteristics for sand-paraffin similar material," *Construction and Building Materials*, vol. 132, pp. 446–456, 2017.
- [19] Q. S. Liu, J. Xu, X. W. Liu, J. Jiang, and B. Liu, "The role of flaws on crack growth in rock-like material assessed by AE technique," *International Journal of Fracture*, vol. 193, no. 2, pp. 99–115, 2015.
- [20] X. R. Wang, E. Y. Wang, X. F. Liu, H. Wang, X. L. Li, and D. X. Li, "Experimental study on the static loading rate effects of sandstone specimen containing pre-existing echelon cracks," *Journal of China Coal Societ*, vol. 42, no. 10, pp. 2582–2591.
- [21] C. Liu, S. Li, C. Cheng, and J. Xue, "Activation characteristics analysis on concealed fault in the excavating coal roadway based on microseismic monitoring technique," *International Journal of Mining Science and Technology*, vol. 27, no. 5, pp. 883–887, 2017.
- [22] T. C. Liang, H. K. Ge, Z. W. Guo, L. L. Song, and J. W. Zhang, "Evaluation of rock damage state with acoustic emission and velocity variation," in *Earthquake Research in China*, vol. 28, pp. 154–166, Earthquake research in China, 2012.
- [23] H.-R. Li, C.-H. Yang, F. Chen, H.-L. Ma, and S.-W. Wu, "Development and application of an integrative testing device for acoustic waves and acoustic emission of rock," *Yantu Lixue/Rock and Soil Mechanics*, vol. 37, no. 1, pp. 287–296, 2016.
- [24] M. Auberger and J. S. Rinehart, "Ultrasonic velocity and attenuation of longitudinal waves in rocks," *Journal of Geophysical Research: Atmospheres*, vol. 66, no. 1, pp. 191–199, 1961.
- [25] Y. Chen, X. W. Yang, and B. Han, "Spatial velocity variations of P waves during rock deformations," *Acta Geophysica Sinica*, vol. 12, no. 1, pp. 54–62, 1990.
- [26] K. Luxbacher, E. Westman, P. Swanson, and M. Karfakis, "Three-dimensional time-lapse velocity tomography of an underground longwall panel," *International Journal of Rock Mechanics and Mining Sciences*, vol. 45, no. 4, pp. 478–485, 2008.

## Research Article

# A Novel Faults Diagnosis Method for Rolling Element Bearings Based on ELCD and Extreme Learning Machine

Mingliang Liang,<sup>1</sup> Dongmin Su,<sup>1</sup> Daidi Hu,<sup>2</sup> and Mingtao Ge <sup>2</sup>

<sup>1</sup>Zhengzhou Railway Vocational & Technical College, Zhengzhou 451460, China

<sup>2</sup>College of Electronics and Information Engineering, SIAS International University, Xinzheng 451150, China

Correspondence should be addressed to Mingtao Ge; [stevenget@126.com](mailto:stevenget@126.com)

Received 31 August 2017; Accepted 16 November 2017; Published 15 January 2018

Academic Editor: Rafał Burdzik

Copyright © 2018 Mingliang Liang et al. This is an open access article distributed under the Creative Commons Attribution License, which permits unrestricted use, distribution, and reproduction in any medium, provided the original work is properly cited.

A rolling bearing fault diagnosis method based on ensemble local characteristic-scale decomposition (ELCD) and extreme learning machine (ELM) is proposed. Vibration signals were decomposed using ELCD, and numerous intrinsic scale components (ISCs) were obtained. Next, time-domain index, energy, and relative entropy of intrinsic scale components were calculated. According to the distance-based evaluation approach, sensitivity features can be extracted. Finally, sensitivity features were input to extreme learning machine to identify rolling bearing fault types. Experimental results show that the proposed method achieved better performance than support vector machine (SVM) and backpropagation (BP) neural network methods.

## 1. Introduction

Rolling bearing is among the most important components of any mechanical equipment and is often found in various industrial applications. Due to its widespread industrial applications, roller bearing fault diagnosis is critical to prevent catastrophic failure of machines, thereby preventing economic losses [1, 2]. Status of rolling element bearings is typically monitored by processing vibration signals [3]. When a fault occurs, collected vibration signals are nonstationary. Hence, reliable fault detection systems need to adopt appropriate methods to process vibration signals.

Traditional signal processing methods such as Wavelet and Fourier transforms are widely used to process vibration signals. Rafiee et al. applied Wavelets to fault diagnosis of rolling bearing and obtained good results [4]. Short-time Fourier transforms have been proved to be superior in mechanical fault diagnosis [5]. Wavelet and Fourier transform methods cannot accurately analyze vibration signals because of poor adaptation. The empirical mode decomposition (EMD) represents a classical time-frequency analysis method, and EMD has been widely adopted in mechanical fault diagnosis, earthquake monitoring, and bridge and

constructions state monitoring [6–8]. However, EMD suffers from over-envelope, under-envelope, end-effect, and other shortcomings [9]. Local mean decomposition (LMD) methods have been widely used in different fields such as electroencephalogram (EEG) processing and mechanical fault diagnosis. This is because of its strong ability to deal with nonstationary signals and superior time-frequency analysis performance. However, LMD itself also has a large amount of iterative computation and problems associated with end effects [10, 11]. Recently, Cheng et al. proposed a new self-adaptive signal processing method, local characteristic-scale decomposition (LCD), which can decompose a nonstationary signal into several intrinsic scale components (ISCs) [12–14]. By analyzing each ISC, characteristic information of the original signal can be extracted effectively with higher accuracy. Due to superior time-frequency analysis performance, LCD method has been widely used to analyze nonstationary signals in mechanical fault diagnosis. As with the EMD method, LCD method also causes mode-mixing effect [13]. Therefore, an improved LCD method, ensemble local characteristic-scale decomposition (ELCD) method, has been proposed to decompose vibration signals.

This effectively eliminates mode-mixing and allows accurate intrinsic scale components to be obtained.

There are two major challenges in the development of real-time fault diagnostic systems. The first one is that there is a large amount of data collected from the real-time monitoring system, which are multivariate and nonlinear. The second challenge is related to the demand for quick fault identification within a short time. It is well known that only a few seconds are needed for a fault to propagate and cause catastrophic failure. This would cause significant financial loss and could result in injury or death of personnel. Therefore, if any fault exists, a diagnostic system should be able to detect the fault immediately and send an alarm signal to inform the control center so that the necessary correction action can be taken immediately. Conventional pattern recognition methods, like backpropagation (BP) neural network and support vector machine (SVM), are widely applied for fault diagnosis [15, 16]. Yang et al. distinguished signals at different corrosion stages using BP neural networks in the acoustic emission testing of a tank bottom [17, 18]. Nevertheless, BP neural network has disadvantages related to abundant parameter settings and slow convergence and is easily caught in a local minimum. All these issues restrict accuracy and wide application of the diagnosis [19, 20]. Compared to BP neural network, SVM generalization performance has been improved greatly, but requires artificial assignment of kernel function and kernel function parameters. This significantly restricts application of SVM [21, 22]. Extreme learning machine (ELM) is a new classifier based on neural networks [23, 24]. In theory, this algorithm tends to provide the best generalization performance at an extremely fast learning speed. As a result, it is widely used in gear fault diagnosis, energy fields, and sales forecasting. Moreover, ELM has been proven to require less human intervention and less running time than support vector machine (SVM) [25]. Due to these advantages of ELM, ELM has been proposed to realize real-time state classification of rolling bearings under variable conditions.

In this work, a new method based on ELCD and ELM is proposed to identify different rolling bearing working conditions. First, ELCD is used to decompose vibration signals into multiple intrinsic scale components. Applied to ISC feature values, a distance-based evaluation method is adopted to calculate bearing sensitive features for different working conditions. These features are input into the ELM to identify roller bearing fault patterns.

## 2. Brief Introduction of LCD and ELCD

**2.1. Ensemble Local Mean Decomposition.** LCD is a new self-adaptive signal decomposition method. Any two decomposed ISCs are mutually independent, with instantaneous frequency of physical significance. ISC needs to meet the following two conditions [12, 13].

(1) A signal  $X(t)$  should have both positive and negative valued maxima and minima, respectively, and any adjacent maxima and minima should witness a monotonic relationship.

(2) For the data, let all the maximal points be denoted as  $(\tau_k, X_k)$ . The line formed by any two adjacent extreme points,  $l_k$ , at  $\tau_{k+1}$  as  $A_{k+1}$ , is specified as follows:

$$l_k = \frac{X_{k+2} - X_k}{\tau_{k+2} - \tau_k} (t - \tau_k) + X_k. \quad (1)$$

Then, the relation

$$A_{k+1} + X_{k+1} = 0 \quad (2)$$

should be true, where

$$A_{k+1} = X_k + \frac{\tau_{K+1} - \tau_k}{\tau_{K+2} - \tau_k} (X_{K+2} - X_k), \quad (3)$$

$$k = 1, 2, \dots, M.$$

Any complex signal  $X(t)$  may have its LCD results written as follows:

$$X(t) = \sum_{p=1}^n \text{ISC}_p(t) + r_n(t), \quad (4)$$

where  $r_n(t)$  denotes the residual component.

Intrinsic scale components with different characteristic scales are obtained via the LCD method. Mode-mixing phenomenon of the decomposition process generates some IS components that have unclear physical meaning. Therefore, the ensemble local characteristic-scale decomposition (ELCD) method is used in this study for signal processing. This method solves the mode-mixing problem by using statistical features of white noise; that is, they have evenly distributed frequencies. White noise of finite amplitude is repeatedly added to the signal to form a composite signal. Then, this composite signal is decomposed using LCD, and the average multi-decomposed component is calculated. Mode-mixing effect of LCD method is eliminated. The ELCD algorithm is shown in Figure 1.

**2.2. Algorithm Simulation.** In order to verify the algorithm, an impact component, a high-frequency sinusoidal wave, and a low-frequency sinusoidal wave are used to form a simulation signal. The results are shown in Figures 2(a)–2(d).

The simulated signals are decomposed by the LCD method and ELCD method. In this study, noise added for the ELCD has a signal amplitude of 0.01 times the signal standard deviation and has a total mean of 120 times. The results are shown in Figures 3 and 4.

In Figure 3, decomposition results using the LCD method are shown. It can be seen that the decomposed components of simulated signals have mode-mixing effect. High-frequency components and distortions components are present in the ISC1 component and the ISC2 component. As seen in Figure 4, impact components along with the high-frequency and low-frequency sine waves are accurately decomposed by ELCD. Moreover, mode-mixing phenomenon does not occur in the ELCD method.

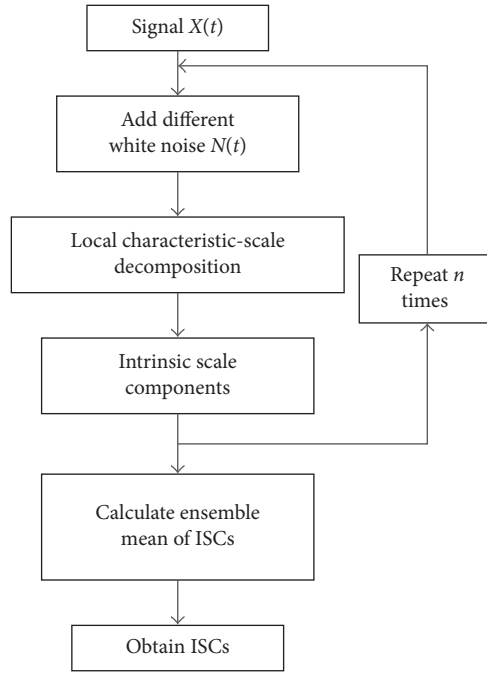


FIGURE 1: Ensemble local characteristic-scale decomposition algorithm.

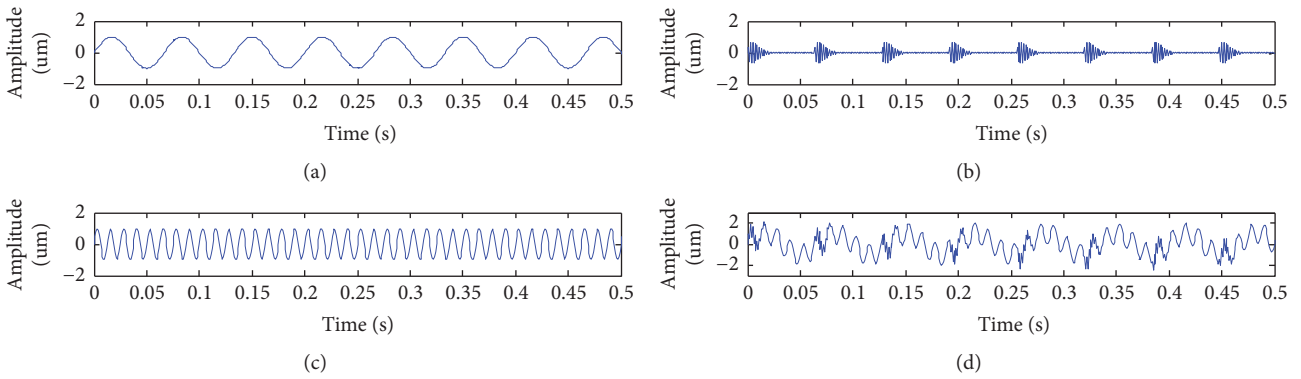


FIGURE 2: Simulation signal and its constituents: (a) low-frequency sinusoidal wave, (b) impact component, (c) high-frequency sinusoidal wave, and (d) simulation signal.

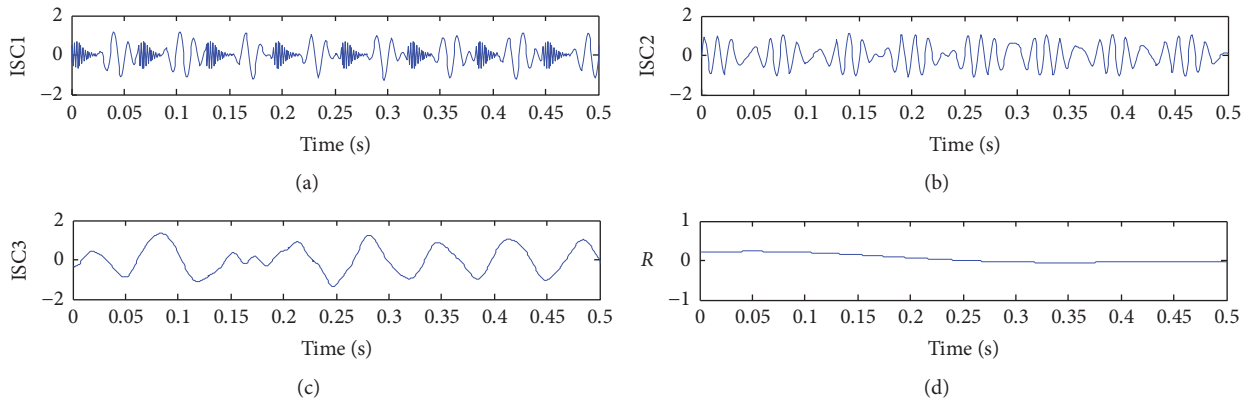


FIGURE 3: Simulation signal LCD results.

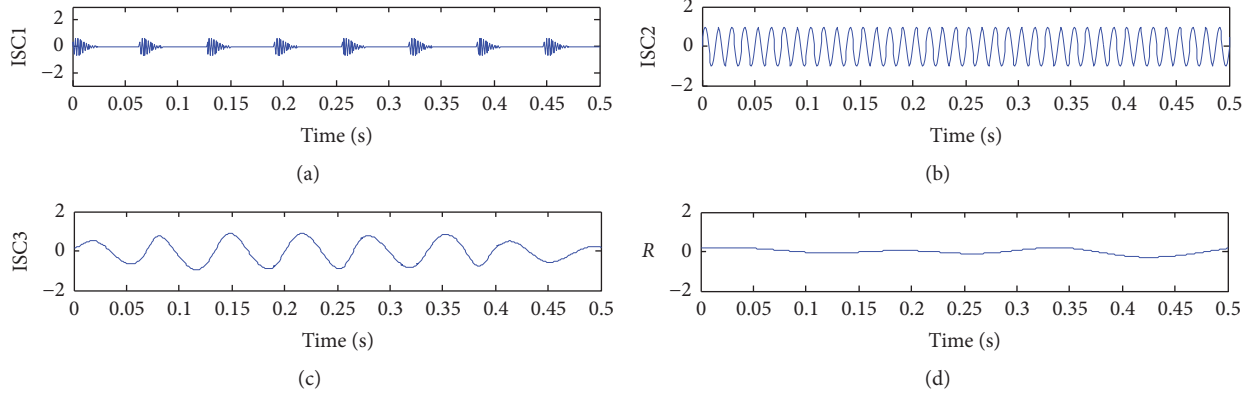


FIGURE 4: Simulation signal ELCD results.

### 3. Feature Extractions

**3.1. Feature Calculation.** Single time-domain or frequency-domain features cannot effectively represent mechanical faults, suffering from low diagnostic accuracy and low universality. In this work, frequency-domain is used; time-domain and other parameters are used to represent different rolling bearing working conditions. As dimensionless indices, skewness, kurtosis, peak indicators, waveform index, pulse index, and margin index can be used to represent rolling bearing fault features. These quantities are widely used in mechanical fault diagnosis [2]. Kullback–Leibler (K-L) divergence is called relative entropy. It can be used to measure similarity of the two signals. Decomposed different vibration signals are different from the original signal in terms of similarity and K-L divergence. Energy can reflect signal strength. Bearings in different working conditions have different energy in different frequency bands. Against any signal  $S = (s_1, s_2, \dots, s_t)$ , the above parameter indicators are defined as follows:

$$\begin{aligned}
 S &= \frac{\sum_{t=1}^T (s_t - \bar{s})^3}{(T-1)\sigma^3}, \\
 K &= \frac{\sum_{t=1}^T (s_t - \bar{s})^4}{(T-1)\sigma^4}, \\
 CF &= \frac{\max |s_t|}{\sqrt{(1/T) \sum_{t=1}^T (s_t)^2}}, \\
 SF &= \frac{\sqrt{T \sum_{t=1}^T (s_t)^2}}{\sum_{t=1}^T |s_t|}, \\
 IF &= \frac{\max |s_t|}{(1/T) \sum_{t=1}^T |s_t|}, \\
 CLF &= \frac{\max |s_t|}{\left( (1/T) \sum_{t=1}^T \sqrt{|s_t|} \right)^2}, \\
 E &= \int_{-\infty}^{+\infty} |s_t|^2 d_t.
 \end{aligned} \tag{5}$$

The following symbols have been used:  $S$ : skewness,  $K$ : kurtosis,  $\bar{s}$  and  $\sigma$ : signal's mean and standard difference,  $CF$ : peak indicator,  $SF$ : waveform index,  $IF$ : pulse index,  $CLF$ : margin index, and  $E$ : energy. The K-L divergence method is follows.

Nonparametric estimation method is used to calculate probability distribution of signals, and then the K-L distance is given as

$$\delta(p, q) = \sum_{x \in N} p(x) \log \frac{p(x)}{q(x)}, \tag{6}$$

where  $p(x)$ ,  $q(x)$  are the probability distribution of signals.

Calculate K-L divergence  $D(p, q)$ :

$$D(p, q) = \delta(p, q) + \delta(q, p). \tag{7}$$

**3.2. Distance-Based Feature Selection.** The ELCD process obtains multiple ISCs of the signal from different vibration signals, parameter indexes of 8 ISCs are calculated, and a series of features indicators are obtained. Some of these parameters are associated with fault information. Other parameters are not irrelevant and therefore it is necessary to further process them to extract sensitive features. In this work, Yang et al. [17] proposed the distance-based evaluation approach. Principal feature is chosen from the entire feature using distance-based evaluation approach. Distance-based evaluation approach is one of the most popular feature selection methods; therefore, it is used widely in parallel with the Pearson correlation coefficient and information gain [2]. The basic idea of a distance-based evaluation method is that smaller distances between samples within the same category are better when features characterize the samples and greater distances between different classes are more favorable. The steps involved in this method are as follows.

(1) Evaluate the average distance, where distance is given by

$$d_{c,j} = \frac{1}{M_c \times (M_c - 1)} \sum_{l=1}^{M_c} \sum_{\substack{m=1 \\ m \neq l}}^{M_c} |q_{m,c,j} - q_{l,c,j}|, \tag{8}$$

$j = 1, 2, \dots, J, \quad c = 1, 2, \dots, C.$

Here,  $M_c$  stands for the number of samples belonging to the  $c$ th class;  $J$  is the size of a feature set; and  $q_{m,c,j}$  is the value of the  $j$ th feature of the  $m$ th sample in the  $c$ th class. The average distance  $d_j^{(w)}$  of the  $j$ th feature belonging to all the  $C$  classes is given by

$$d_j^{(w)} = \frac{1}{C} \sum_{c=1}^C d_{c,j}. \quad (9)$$

(2) Compute average value:

$$u_{c,j} = \frac{1}{M_c} \sum_{m=1}^{M_c} q_{m,c,j} \quad (10)$$

and evaluate average distance  $d_j^{(b)}$  of the  $C$  different classes:

$$d_j^{(b)} = \frac{1}{C \times (C - 1)} \sum_{c=1}^c \sum_{\substack{e=1 \\ e \neq c}}^c |u_{e,j} - u_{c,j}|, \quad (11)$$

where  $c$  and  $e$  are two different classes.

(3) Calculate assessment factor of  $j$ th feature by

$$\alpha_j = \frac{d_j^{(b)}}{d_j^{(w)}}. \quad (12)$$

The assessment factor reflects sensitivity of the feature. Larger evaluation factors denote more sensitive features.

(4) Calculate threshold value  $\lambda$  and take feature with its assessment factor greater than  $\lambda$  as a sensitive factor:

$$\lambda = \max \frac{(\alpha_j)}{\varepsilon}, \quad j = 1, 2, 3 \dots \quad (13)$$

Repeated experiments showed that a value of  $\varepsilon = 2$  leads to optimal results.

#### 4. Extreme Learning Machine

ELM, proposed by Huang et al., was originally developed for single-hidden-layer feed forward neural networks and then extended to "generalized" single-hidden-layer feed forward networks (SLFNs). ELM is a new learning algorithm with faster learning speed and better generalization performance [24, 25]. Details about ELM algorithm can be found in [24]. The ELM output expression reads

$$y_i = \omega^T g(W_{in}x_i + b), \quad i = 1, 2, \dots, N, \quad (14)$$

where  $W_{in}$ ,  $b$ , and  $\omega$  are input weight, concealed layer deviation, and output weight, respectively. Input and output vectors are denoted by  $x_i$  and  $y_i$ . Number of samples and the activation function are denoted by  $N$  and  $g$ , respectively. For the latter, in practice, a sigmoid function is often used. Assuming  $N$  samples  $\{(x, y)\}_{i=1}^N$  and a number of concealed layer sections  $M$  for training and testing, the ELM procedures are the following:

(1) Initialize and maintain weight  $w_{in}$  and deviation  $b$ .

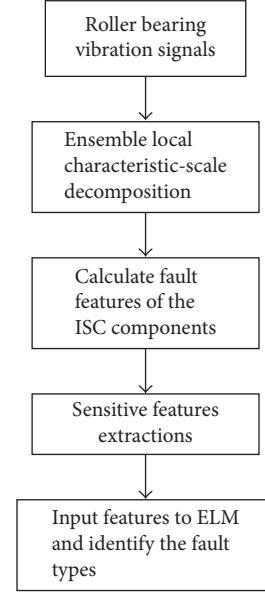


FIGURE 5: Flow chart of fault diagnosis using ELCD and ELM.

(2) Calculate concealed layer output matrix  $H$ .

(3) Calculate output weight  $\omega$ ,  $\omega = H * T$ .

(4) Output feature vector for testing.

In this section, the proposed rolling bearing fault detection method based on ELCD and ELM is presented. Fault features can be obtained by processing the vibration signals collected by multiple sensors. As mentioned previously, some of them are associated with fault information and others are not irrelevant. Therefore, the other parameters are used to further extract sensitive features of the fault. ELM is used to identify roller bearing fault patterns. A summary of the process for the fault diagnosis using ELCD and ELM is shown schematically in Figure 5.

#### 5. Experimental Analysis

**5.1. Experiments.** This study adopted rolling bearing data of US Case Western Reserve University for processing. Experiments adopted 6205-2RS JEM SKF deep groove ball bearings, with a rotating motor load of 735.5 W. The rolling bearing speed was set to 1797 rpm, adopting EDM technology to process the bearing into one with fault diameter as 0.3556 mm and fault depth as 0.2794 mm. In this study, sensor sampling frequency was 12 kHz, collecting four working state vibration signals, respectively, referring to the normal state, rolling element fault, inner race, and outer race faults, with each data sample's length  $N$  as 2500 points. The collected four signals are shown in Figure 6.

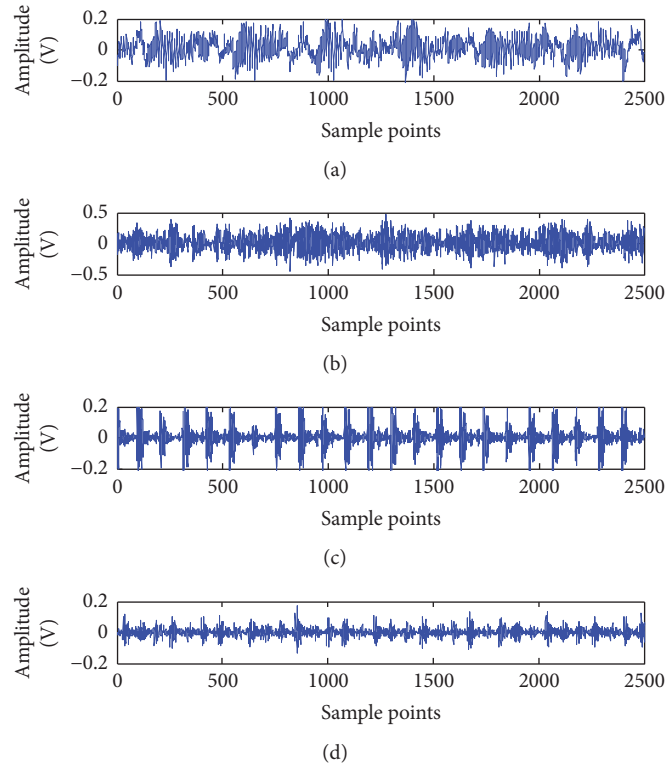


FIGURE 6: Four vibration signals collected by the sensor: (a) normal, (b) rolling element fault, (c) outer race fault, and (d) inner race fault.

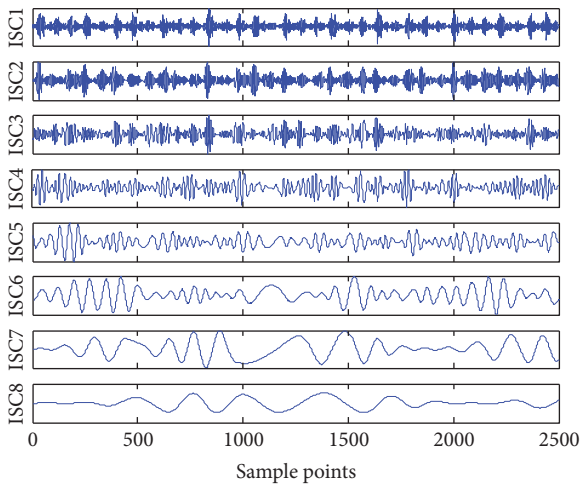


FIGURE 7: Inner race fault signal ELCD results.

IS components of the decomposition by ELCD of a vibration signal from the inner race fault are shown in Figure 7.

As can be seen in Figure 7, eight IS components were derived. Then, skewness, kurtosis, peak indicators, waveform index, pulse index, margin index, energy, and relative entropy of 8 ISCs were calculated. This was used to obtain a series of features, some of which contained principal information and

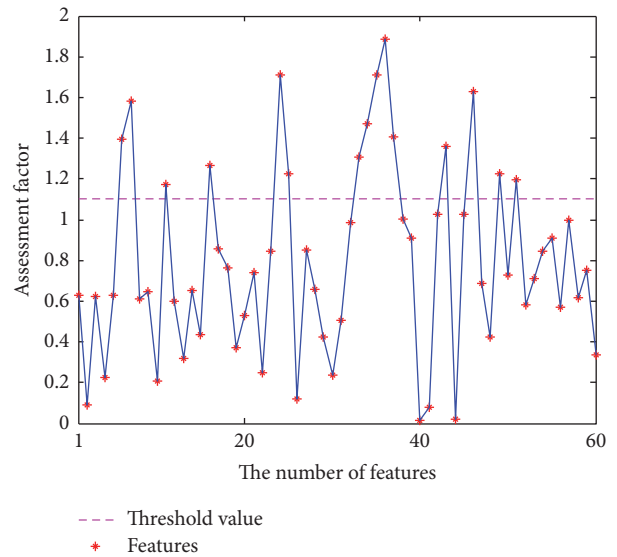


FIGURE 8: Feature assessment factor.

others contained little information. Therefore, the distance-based evaluation approach was adopted to calculate distance factor and threshold value, as shown in Figure 8.

Figure 8 shows that the threshold value evaluation can obtain 15 sensitive features. In order to distinguish between

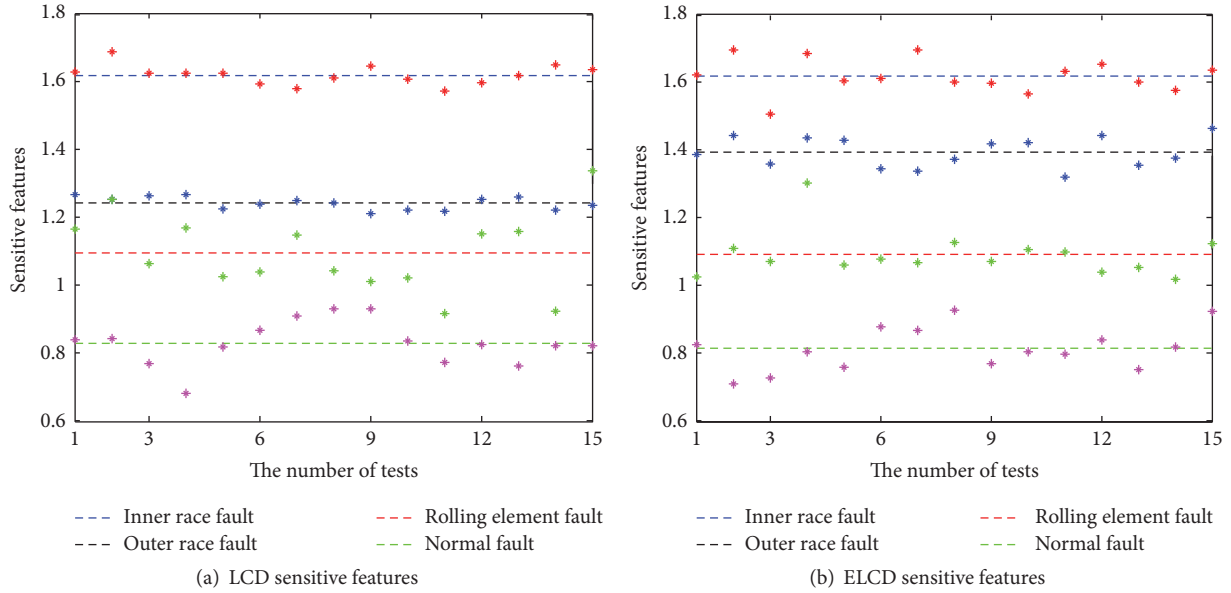


FIGURE 9

advantages and disadvantages of ELCD and LCD, rolling bearing sensitivity features in different working conditions were calculated, taking mean of multiple experiments, with the comparison results shown in Figure 9.

Figure 9 shows that LCD witnesses mode-mixing, calculation sensitive features and uneven mean distribution, and unobvious differences between different working conditions. The ELCD experiences an even distribution of sensitivity features, overcoming decomposition mode-mixing. To accurately identify faults in different working conditions, the ELM classifier is employed.

**5.2. Pattern Recognition.** In accordance with results in the previous section, sensitivity features were calculated for different vibration signals and chosen as input data to train and test the extreme learning machine. At the same time, this study adopted ELCD, LCD, EMD, and LMD methods for processing vibration signals. Results of the test samples are shown in Figure 10 and are compared with those using ELCD. Test accuracy of two methods is listed in Table 1.

As seen in Figure 11 and Table 1, both EMD and LCD methods suffer from mode-mixing. Therefore, results of the test samples are poor. LMD method also has a large amount of iterative computation and end effects. As a result, test accuracy of LMD-ELM is not good. ELCD method can effectively eliminate mode-mixing and obtain accurate intrinsic scale components. Hence, experimental results show that the ELCD-ELM method can effectively identify different rolling bearing working conditions, at a recognition rate higher than other methods. 60 groups of data were chosen for training and testing, of which 40 groups were used for training and 20 groups were used

for testing. Three classifiers, SVM, BP, and ELM, were used for data training and testing. Test results are shown in Figure 11.

As seen in Figure 11, all three classifiers can distinguish different conditions of rolling bearing, but compared to BP and SVM, the ELM classifier achieves the highest mean recognition rate and identifies roller bearing fault patterns, because of the lower human intervention and lower running time.

## 6. Conclusions

The collected vibration signals are often mixed with substantial ambient noise, which makes fault signal features insignificant for rolling bearings fault diagnosis. In this study, a novel fault diagnosis methodology for rolling bearings based on ELCD and ELM is proposed. The ELCD method was proposed to process nonstationary vibration signals and overcome mode-mixing phenomenon of the LCD method. A distance-based evaluation method is adopted to calculate bearing sensitive features for different working conditions. In order to address disadvantages of traditional BP and SVM classifiers, such as complex parameter setting and low convergence rate, ELM was used to identify roller bearing fault patterns. A theoretical analysis and experimental results show that the ELCD-ELM method has higher accuracy than other methods.

## Conflicts of Interest

The authors declare that they have no conflicts of interest.

TABLE I: Test accuracy.

Specification	Normal condition	Rolling element	Inner race fault	Outer race fault
EMD-ELM	75	81	79	83
LMD-ELM	78	77	82	79
LCD-ELM	80	84	83	82
ELCD-ELM	100	100	100	100

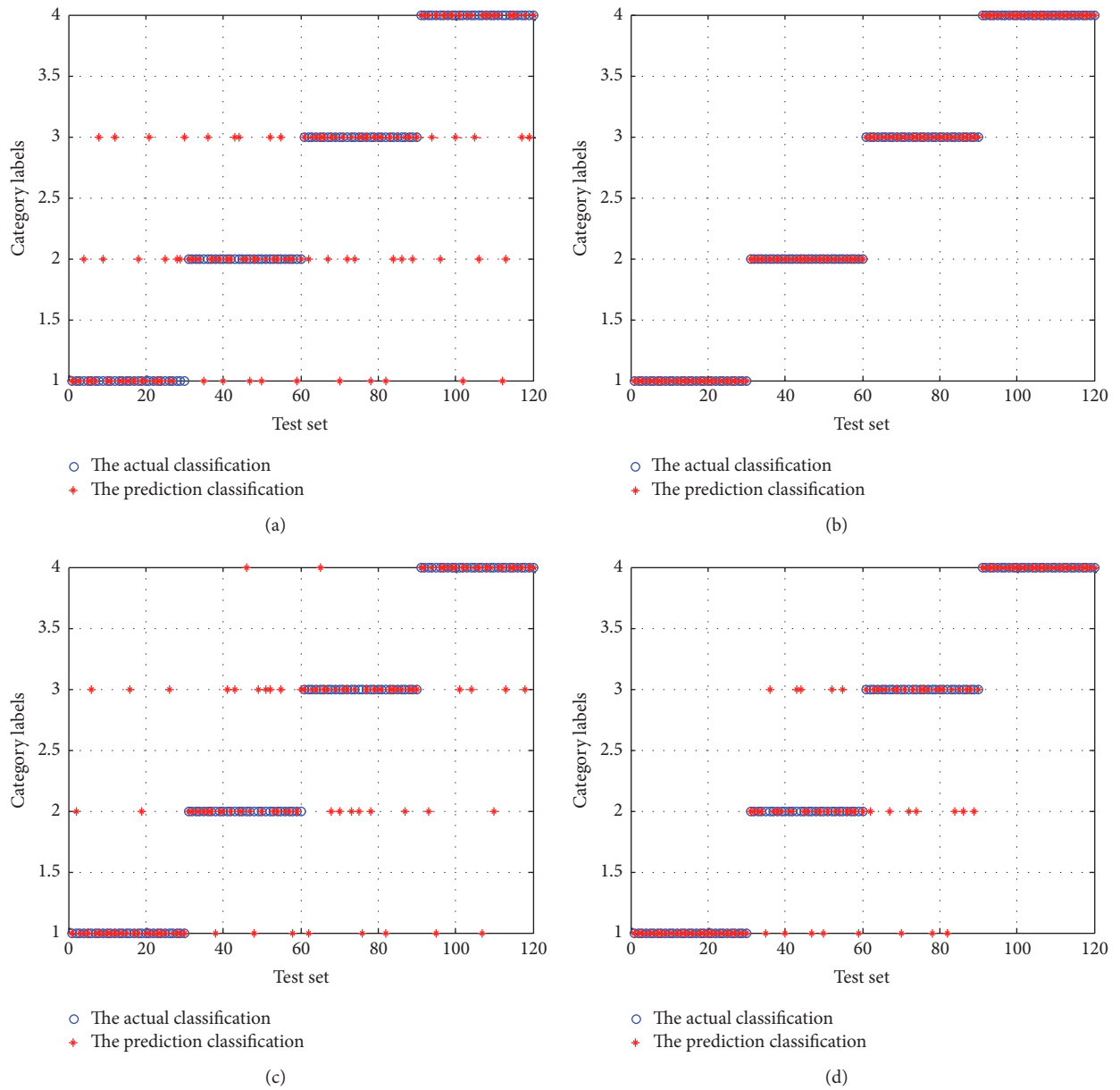


FIGURE 10: Test classification: (a) LCD-ELM method, (b) ELCD-ELM method, (c) EMD-ELM method, and (d) LMD-ELM method.

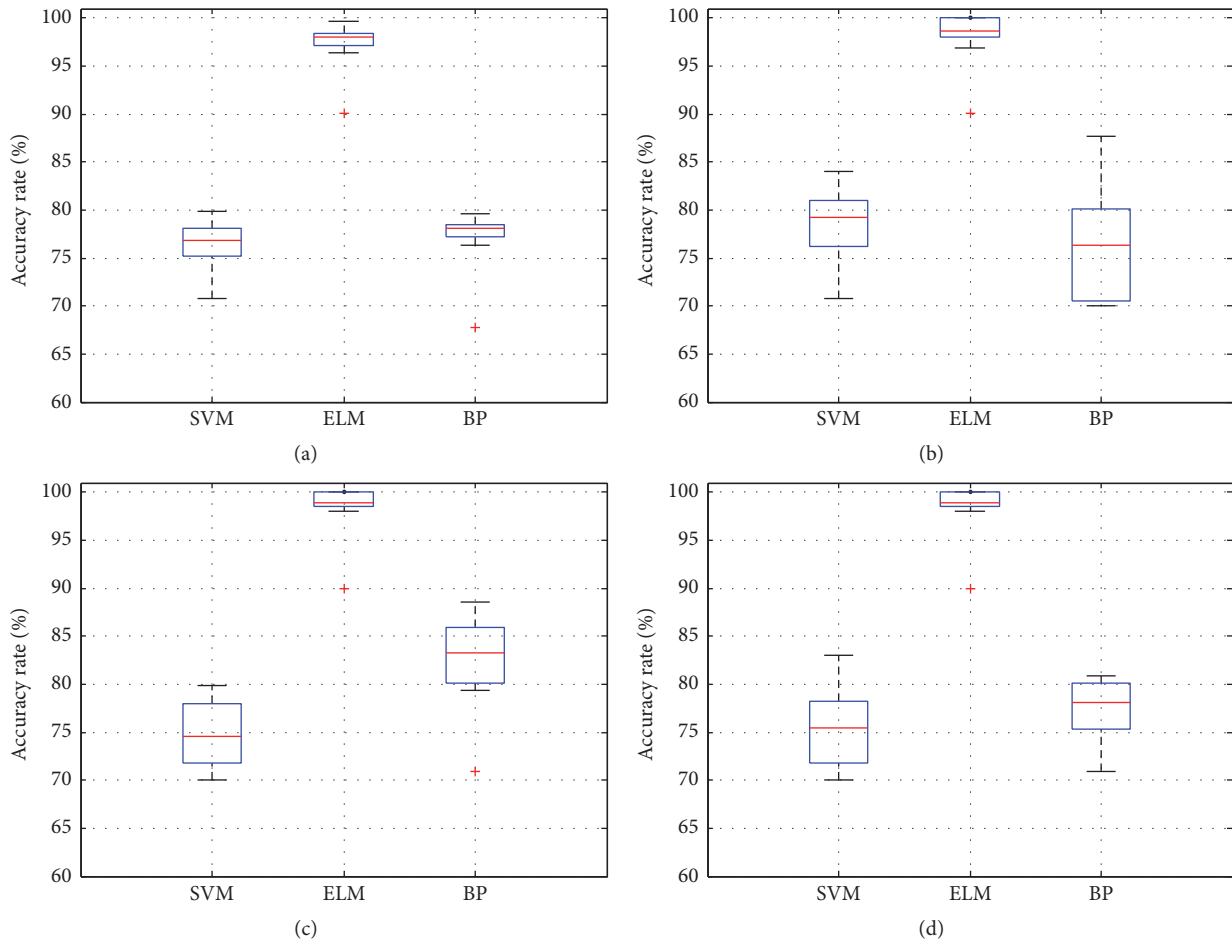


FIGURE 11: Test accuracy of classifiers: (a) normal, (b) rolling element fault, (c) outer race fault, and (d) inner race fault.

## Acknowledgments

This work was supported by Henan High-Speed Railway Operation and Maintenance Engineering Research Center and was also supported by the Key Project of China Spark Program (2015GA750005) and Key Science and Technology Program of Henan Province, China (152102210130).

## References

- [1] Y. G. Lei and M. J. Zuo, "Fault diagnosis of rotating machinery using an improved HHT based on EEMD and sensitive IMFs," *Measurement Science and Technology*, vol. 20, no. 12, Article ID 125701, 2009.
- [2] F. Zhang, Y. Liu, C. Chen, Y.-F. Li, and H.-Z. Huang, "Fault diagnosis of rotating machinery based on kernel density estimation and Kullback-Leibler divergence," *Journal of Mechanical Science and Technology*, vol. 28, no. 11, pp. 4441–4454, 2014.
- [3] Z. Gao, C. Cecati, and S. X. Ding, "A survey of fault diagnosis and fault-tolerant techniques—part I: fault diagnosis with model-based and signal-based approaches," *IEEE Transactions on Industrial Electronics*, vol. 62, no. 6, pp. 3757–3767, 2015.
- [4] J. Rafiee, M. A. Rafiee, and P. W. Tse, "Application of mother wavelet functions for automatic gear and bearing fault diagnosis," *Expert Systems with Applications*, vol. 37, no. 6, pp. 4568–4579, 2010.
- [5] Z. P. Feng, M. J. Zuo, J. Qu, T. Tian, and Z. L. Liu, "Joint amplitude and frequency demodulation analysis based on local mean decomposition for fault diagnosis of planetary gearboxes," *Mechanical Systems and Signal Processing*, vol. 40, no. 1, pp. 56–75, 2013.
- [6] J.-D. Zheng, J.-S. Cheng, and Y. Yang, "A rolling bearing fault diagnosis method based on LCD and permutation entropy," *Journal of Vibration Measurement & Diagnosis*, vol. 34, no. 5, pp. 802–806, 2014.
- [7] T. Wang, M. Zhang, Q. Yu, and H. Zhang, "Comparing the applications of EMD and EEMD on time-frequency analysis of seismic signal," *Journal of Applied Geophysics*, vol. 83, pp. 29–34, 2012.
- [8] W.-C. Wang, K.-W. Chau, D.-M. Xu, and X.-Y. Chen, "Improving Forecasting Accuracy of Annual Runoff Time Series Using ARIMA Based on EEMD Decomposition," *Water Resources Management*, vol. 29, no. 8, pp. 2655–2675, 2015.
- [9] J. B. Ali, N. Fnaiech, L. Saidi, B. Chebel-Morello, and F. Fnaiech, "Application of empirical mode decomposition and artificial

- neural network for automatic bearing fault diagnosis based on vibration signals,” *Applied Acoustics*, vol. 89, pp. 16–27, 2015.
- [10] Z. Shi, W. Song, and S. Taheri, “Improved LMD, permutation entropy and optimized K-means to fault diagnosis for roller bearings,” *Entropy*, vol. 18, no. 3, article no. 70, 2016.
- [11] H. Liu and M. Han, “A fault diagnosis method based on local mean decomposition and multi-scale entropy for roller bearings,” *Mechanism and Machine Theory*, vol. 75, pp. 67–78, 2014.
- [12] J. Cheng S, J. Zheng D, and Y. Yang, “A non-stationary signal analysis approach-LCD,” *Journal of Vibration Engineering*, vol. 25, no. 2, pp. 215–220, 2012.
- [13] H. L. Ao, J. Cheng, K. Li, and T. K. Truong, “A roller bearing fault diagnosis method based on LCD energy entropy and ACROA-SVM,” *Shock and Vibration*, vol. 2014, Article ID 825825, 12 pages, 2014.
- [14] H. Liu, X. Wang, and C. Lu, “Rolling bearing fault diagnosis based on LCD-TEO and multifractal detrended fluctuation analysis,” *Mechanical Systems and Signal Processing*, vol. 60-61, pp. 273–288, 2015.
- [15] M. Riahi, H. Shamekh, and B. Khosrowzadeh, “Differentiation of leakage and corrosion signals in acoustic emission testing of aboveground storage tank floors with artificial neural networks,” *Russian Journal of Nondestructive Testing*, vol. 44, no. 6, pp. 436–441, 2008.
- [16] B. Gu and Sheng. S. V., “A robust regularization path algorithm for  $\nu$ -support vector classification,” *IEEE Transactions on Neural Networks Learning Systems*, vol. 28, no. 5, pp. 1241–1248, 2016.
- [17] B. S. Yang, T. Han, and J. L. An, “ART-KOHONEN neural network for fault diagnosis of rotating machinery,” *Mechanical Systems and Signal Processing*, vol. 18, no. 3, pp. 645–657, 2004.
- [18] B. Gu, X. Sun, and V. S. Sheng, “Structural minimax probability machine,” *IEEE Transactions on Neural Networks and Learning Systems*, vol. 28, no. 7, pp. 1646–1656, 2017.
- [19] B. Gu, V. Sheng S, and Y. K. Tay, “Incremental support vector learning for ordinal regression,” *IEEE Transactions on Neural Networks Learning Systems*, vol. 26, no. 7, p. 1403, 2014.
- [20] Z. Xia, X. Wang, X. Sun, Q. Liu, and N. Xiong, “Steganalysis of LSB matching using differences between nonadjacent pixels,” *Multimedia Tools and Applications*, vol. 75, no. 4, pp. 1947–1962, 2016.
- [21] Z. Xia, X. Wang, X. Sun, and B. Wang, “Steganalysis of least significant bit matching using multi-order differences,” *Security and Communication Networks*, vol. 7, no. 8, pp. 1283–1291, 2014.
- [22] Z. Qu, H. Feng, Z. Zeng, J. Zhuge, and S. Jin, “A SVM-based pipeline leakage detection and pre-warning system,” *Measurement*, vol. 43, no. 4, pp. 513–519, 2010.
- [23] K. Zhu, X. Song, and D. Xue, “A roller bearing fault diagnosis method based on hierarchical entropy and support vector machine with particle swarm optimization algorithm,” *Measurement*, vol. 47, no. 1, pp. 669–675, 2014.
- [24] G. Huang, D. H. Wang, and Y. Lan, “Extreme learning machines: a survey,” *International Journal of Machine Learning and Cybernetics*, vol. 2, no. 2, pp. 107–122, 2011.
- [25] Y. Tian, J. Ma, C. Lu, and Z. Wang, “Rolling bearing fault diagnosis under variable conditions using LMD-SVD and extreme learning machine,” *Mechanism and Machine Theory*, vol. 90, pp. 175–186, 2015.

## Research Article

# A SVDD and $K$ -Means Based Early Warning Method for Dual-Rotor Equipment under Time-Varying Operating Conditions

Zhinong Jiang , Minghui Hu, Kun Feng , and Hao Wang

*College of Mechanical and Electrical Engineering, Beijing University of Chemical Technology, Beijing, China*

Correspondence should be addressed to Kun Feng; [kunfengphd@163.com](mailto:kunfengphd@163.com)

Received 15 August 2017; Revised 4 December 2017; Accepted 12 December 2017; Published 4 January 2018

Academic Editor: Sandris Ručevskis

Copyright © 2018 Zhinong Jiang et al. This is an open access article distributed under the Creative Commons Attribution License, which permits unrestricted use, distribution, and reproduction in any medium, provided the original work is properly cited.

Under frequently time-varying operating conditions, equipment with dual rotors like gas turbines is influenced by two rotors with different rotating speeds. Alarm methods of fixed threshold are unable to consider the influences of time-varying operating conditions. Hence, those methods are not suitable for monitoring dual-rotor equipment. An early warning method for dual-rotor equipment under time-varying operating conditions is proposed in this paper. The influences of time-varying rotating speeds of dual rotors on alarm thresholds have been considered. Firstly, the operating conditions are divided into several limited intervals according to rotating speeds of dual rotors. Secondly, the train data within each interval is processed by SVDD and the allowable ranges (i.e., the alarm threshold) of the vibration are determined. The alarm threshold of each interval of operating conditions is obtained. The alarm threshold can be expressed as a sphere, whose controlling parameters are the coordinate of the center and the radius. Then, the cluster center of the test data, whose alarm state is to be judged, can be extracted through  $K$ -means. Finally, the alarm state can be obtained by comparing the cluster center with the corresponding sphere. Experiments are conducted to validate the proposed method.

## 1. Introduction

Gas turbines, representative equipment of dual rotors, are the key power equipment in aviation, shipping, electric power, petroleum, and so on. Once a gas turbine undergoes a fault or accident, the relevant production and management will suffer a lot. And even worse, those problems will probably lead to fatal disasters [1, 2]. Therefore, it is very important to ensure the efficient and normal operation of a gas turbine [3].

Vibration monitoring is one of the main methods for mechanical faults monitoring. An early warning of gas turbines' state can be realized through a vibration alarm before a serious fault occurs. To create an alarm for the vibration conditions of certain equipment, the main steps include collecting vibration signals in the main parts of the equipment, computing the vibration overall amplitude, and setting a fixed alarm threshold. The fixed threshold alarm is usually able to ensure the safety and reliable operation for the equipment to some extent. However, this alarm method is mainly suitable

for single-rotor equipment under steady operating conditions. This method applies the same alarm threshold under every operating condition and cannot deal with problems that are caused by variable operating conditions. Because the mentioned characteristic of a fixed threshold can easily lead to missing alarms under low operating conditions and false alarms under high operating conditions, this method is not applicable in the warning for the vibration state for a gas turbine under time-varying operating conditions.

Unlike general equipment with one rotor, dual-rotor equipment has two rotors, whose rotational speeds are usually different. A complete description of the operating conditions of rotating machinery should include the speed and the load. The object of this research, however, is dual-rotor equipment including gas turbines and aircraft engines. As for the equipment, the load is the output power or the thrust. Two speeds and load are generated when the rotor is shocked by high temperature and high pressure gas. There is a positive correlation between the speed set and the load. The load does not change

when the speed set is constant. The load factor is included in the speed factor in this research, so only speed set is analyzed to study the operating conditions for dual-rotor equipment. In engineering applications, the operating conditions of the dual-rotor equipment are usually characterized by rotating speeds. In conclusion, different speeds can be used for characterizing the time-varying operating conditions due to the special research object. Namely, vibration is affected by two different and variable rotational speeds simultaneously, and thus an effective warning for early faults in this type of equipment cannot be realized through the fixed alarm threshold. As previously mentioned, missing and false alarms occur when variable operating conditions are not considered, making traditional alarm methods unable to warn against early faults for this type of equipment effectively. It is necessary to consider the following two aspects of alarm thresholds for dual-rotor equipment: One is to learn alarm threshold values and identify alarm status. And the other is to consider variable operating conditions influenced by two varying rotating speeds.

To solve problems concerning the computation of alarm thresholds and the identification of alarm state, a great number of researches have been carried out for improving the algorithm based on Support Vector Machine (SVM) or Artificial Neural Network (ANN). Empirical Mode Decomposition (EMD) has been applied to obtain the feature set [4]. Then, the ANN has been trained and tested for warning against bearing faults. In recent years, a huge number of scholars have utilized SVM to achieve fault alarms and identify faults. The principle of SVM is that two types of data are separated by finding the optimal hyperplane that has the same distance from itself to both types of data. This means that SVM can warn against faults better than ANN does [5]. SVM, a classifier based on statistical learning theory, was initially proposed to deal with problems when the number of fault samples is not enough [6]. At present, SVM has been used to monitor equipment of various kinds and has been increasingly improved. SVM, whose kernel function is Gaussian, has been utilized to solve classification issues for nonlinear datasets [7], but how to set parameters was still unclear. Immune algorithms that imitate the artificial immune system have been used to optimize parameters of SVM, which plays a significant role in obtaining a classifier with better performance [8]. Several SVMs have been utilized simultaneously to warn against and identify various faults [9]. Then, outputs of each SVM on the basis of the inference of the case database have been obtained. Next, all kinds of the outputs have been compared through the same standard, and the SVM model, suitable for identifying the corresponding fault, has been selected. Those efforts have made great contributions to warning against and identifying faults of bearings. From the above descriptions, it is clear that SVM can achieve higher accuracy and better generalization ability in mechanical fault alarm and recognition [10].

To solve issues caused by variable operating conditions for dual-rotor equipment, a large number of researches focus on how to extract fault features from nonstationary signals in time domain [11–13]. So far, those researches have brought about great benefits. Feature extraction is not concerned

in this paper. Nevertheless, there are seldom published researches on early warning methods, which consider varying alarm thresholds caused by operating conditions in dual-rotor equipment. The gearbox used in wind turbines is currently mainly studied for the early warning method under time-varying operating conditions. Considering the gearbox under time-varying operating conditions, Ren et al. have obtained influences of speeds and loads on the vibration signal through a large number of experiments, but they have not solved fault warning problems under time-varying operating conditions [14]. Using order tracking and feature extraction in the angle domain, Gu et al. have obtained the vibration features and load index. Then, they have set up different relevant index models under different operating conditions to recognize gearbox faults, realizing the fault warning under time-varying operating conditions [15]. After extracting the features of the vibration signal at different speeds when the equipment was under normal operating conditions, Lin and Makis have determined the time series models under normal operating conditions. Then, these models have been compared with real-time data to define the status of the equipment. Additionally, load intervals have been divided based on the torque and speed. Then, the gearbox faults were recognized by the Bayesian model [16]. For solving problems of the constantly changeable vibration signal component of the gearbox under time-varying operating conditions, Shao et al. have used an autoregressive model and hypothetical test method to warn against faults in the equipment [17]. Kouadri et al. proposed a method based on the statistical test. This method can define the status of the gearbox by comparing the confidence intervals of the vibration signal between normal and fault experiments. The validity of fault warning for the gearbox under time-varying operating conditions was proved through experimental data [18]. The fault mechanism of dual-rotor equipment is different from that of gearboxes, so the above methods cannot be directly applied to dual-rotor equipment.

This paper proposes an early warning method for dual-rotor equipment under time-varying operating conditions using support vector domain description (SVDD) and  $K$ -means algorithm. To solve problems caused by variable conditions, the range of operating conditions is divided into finite intervals, with each interval considered as a steady operating condition. Alarm thresholds of all intervals are computed one by one. Because the two rotating speeds affect the vibration value simultaneously when the dual-rotor equipment works, SVDD is used to decide the allowable ranges of vibration for the equipment under normal conditions, determining the alarm threshold under each operating condition. Meanwhile,  $K$ -means clustering algorithm is used to obtain the cluster center of vibration data whose alarm state is uncertain. The early warning of vibration state can be realized by comparing the cluster center with the alarm threshold under the corresponding operating condition.

The rest of this paper is organized as follows. Section 2 introduces the theoretical backgrounds of this work, including the SVDD, the  $K$ -means, and the parameter optimization algorithm. Section 3 describes this proposed early warning method. The experimental results are presented to verify this

proposed method in Section 4. The conclusions are drawn in Section 5. Section 6 presents some discussions about this study.

## 2. Basic Theory

**2.1. Support Vector Domain Description.** SVM, a statistical learning theory based on machine learning method, can classify data according to structural risk minimization [5]. SVM is mainly utilized for data classification and regression prediction, and this paper only studies the former. SVM is suitable for small sample data, so it is used in this paper to classify data.

Classification problems in engineering practice can be divided into two categories: relatively simple linearly separable problems and linearly inseparable nonlinear problems. SVM initially solves problems when an optimal separating hyperplane is computed in linear separable problems [19]. SVM projects nonlinear separable data onto a high dimension through a nonlinear kernel function to make it a linearly separable problem. Thus, linear distinction of nonlinear data in high dimension will be realized [20].

As a derivative of SVM, one-class SVM is different from binary classification SVM, as it only has one class of data [21]. Currently, there are two types of one-class SVM: one-class-SVM and support vector domain description (SVDD). All of them can be used to distinguish abnormal data from normal one [22]. As for SVDD, it is used to discriminate the data by constructing a hypersphere in a high-dimensional space. The center and radius of the hypersphere can be obtained by using the penalty parameter [23]. In this method, spatial features of vibration data under multivariable factors can be shown better. Therefore, SVDD is applied to classify data in this paper.

A training vector  $x_i$  ( $x_i \in R^n$ ,  $i = 1, \dots, l$ ) is known and there is no class label; the optimization objective of SVDD is to obtain an optimal hypersphere [24], whose center is  $a$  and radius is  $R$ . It can be expressed as

$$F(R, a, \xi_i) = R^2 + C \sum_i \xi_i. \quad (1)$$

As it is shown in (2), the fixed proportional training data points are included in this sphere.

$$(x_i - a)^T (x_i - a) \leq R^2 + \xi_i, \quad (\forall_i, \xi_i \geq 0), \quad (2)$$

where  $\xi_i$  represents the relaxation variable. To set  $\xi_i$  is to prevent interference of individual outliers in the hypersphere. If there is no relaxation variable, the hypersphere will be worse because of few outliers.  $C$  is used to adjust the influences of  $\xi_i$ . If  $C$  is larger, more outliers will be included. On the contrary, if  $C$  is smaller, it is likely that no outliers will be here. Therefore, optimization of  $C$  is of great significance. This problem will be explained in Section 2.3.

The hypersphere can solve nonlinear problems. For this purpose, data points must be projected onto high-dimensional space for finding the optimal hyperplane, that

is, a kernel function  $k(x, x')$ , which can satisfy the following equation:

$$k(x, x') = \varphi(x) \varphi(x'), \quad (3)$$

where  $x$  and  $x'$  denote coordinates of the data and  $\varphi(\cdot)$  represents the function which can project the coordinate onto high-dimensional space. Thus, the optimization problem is shown as follows:

$$\min R^2 + C \sum_{i=1}^N \xi_i, \quad (4)$$

which is subjected to

$$\begin{aligned} [\varphi(\varphi_i) - a] [\varphi(\varphi_i) - a]^T &\leq R^2 + \xi_i, \\ (\xi_i \geq 0, i = 1, \dots, N). \end{aligned} \quad (5)$$

$N$  in (4)-(5) denotes the number of training samples. The dual form of (5) is shown as

$$\min \sum_{i,j=1}^N \alpha_i \alpha_j k(x_i, x_j) - \sum_{i=1}^N \alpha_i k(x_i, x_i). \quad (6)$$

The constraint of (6) is

$$\sum_{i=1}^N \alpha_i = 1, \quad (0 \leq \alpha_i \leq C, i = 1, \dots, N), \quad (7)$$

where  $\alpha_i$  denotes the coefficient of Lagrange function. In solving the above optimization problem, most  $\alpha_i$  is zero. If  $\alpha_i$  is nonzero, it is a support vector, which decides the shape and size of the hypersphere. Based on all the support vectors,  $a$ , the center of the sphere, is shown as follows:

$$a = \sum_{i \in I_{SV}} \alpha_i \varphi(x_i), \quad (8)$$

where  $I_{SV}$  represents the set of support vectors. As for support vector with  $0 \leq \alpha_i \leq C$ ,  $x_i$  satisfies

$$R^2 - \left[ k(x_i, x_i) - 2 \sum_{j \in I_{SV}} \alpha_j k(x_j, x_i) + C^2 \right] = 0. \quad (9)$$

The radius  $R$  of the sphere can be obtained from the above equation.

As mentioned earlier, the kernel function can be divided into two types: linear and nonlinear. Nonlinear kernel functions include polynomial, Gaussian, sigmoid, and self-defined types. **The** Gaussian kernel function, one of the most commonly used kernel functions, can be used easily and nearly without problems of numerical solutions [25]. Thus, the Gaussian kernel function is used as a mapping function in high dimension in this paper, as it is shown in

$$e^{-\gamma \|u-v\|^2}, \quad (10)$$

where  $u$  denotes the sample point,  $v$  represents the center decided by the sample points, and  $\gamma$  denotes the parameter which decides the change rate of the kernel function. When  $\gamma$  becomes larger, the corresponding parting surface will be more complex. On the contrary, when  $\gamma$  is less, the relevant parting surface will become smoother. Therefore, choosing the value of  $\gamma$  is also very important. This problem will be explained in Section 2.3.

**2.2. *K*-Means Clustering Algorithm.** The clustering algorithm is to determine the distribution of data through a statistical method. The distribution can be regarded as a certain kind of geometry, and the cluster center is the barycenter of the geometry [26, 27]. Actually, it is difficult to find this center in many data. Meanwhile, the dataset must be divided into several different classes. *K*-means clustering algorithm has been initially introduced and has been applied widely into various research fields [28]. In this paper, the cluster center of test data can be found in three-dimensional spaces via the *K*-means clustering algorithm. When compared with the distribution of the data points, the cluster center of data is a more stable feature and can characterize the state of equipment better [29]. This is because misjudgment due to individual points is avoided by the cluster center.

$X = \{x_1, x_2, \dots, x_i, \dots, x_l\}$  is a  $d$ -dimensional dataset including  $l$  samples, where  $x_i \in R^d$ .  $K$  in the *K*-means algorithm represents the notion that  $X$  is divided into  $K$  subclasses. Each subclass is expressed as  $c_i$  ( $i = 1, 2, \dots, K$ ), and every  $c_i$  has its own cluster center  $u_i$ . Firstly, select  $K$  elements randomly to be the initial cluster centers of  $K$  subclasses. Then, compute the distance from each data point to every subclass center. The initial classification can be realized according to the criterion of the shortest distance. Next, calculate the average Euclidean distance of each subclass, update the cluster center on account of this average, and renew the classification according to the principle of the shortest distance. Equations (11) and (12) are, respectively, the quadratic sum of distance from the data point in each subclass to the corresponding class center  $u_i$  and the quadratic sum of the total distance of all classes [30].

$$J(c_k) = \sum_{x_i \in c_k} \|x_i - u_k\|^2 \quad (11)$$

$$\begin{aligned} J(C) &= \sum_{k=1}^K J(c_k) = \sum_{k=1}^K \sum_{x_i \in c_k} \|x_i - u_k\|^2 \\ &= \sum_{k=1}^K \sum_{i=1}^l d_{ki} \|x_i - u_k\|^2, \end{aligned} \quad (12)$$

where

$$d_{ki} = \begin{cases} 1, & x_i \in c_i \\ 0, & x_i \notin c. \end{cases} \quad (13)$$

*K*-means clustering algorithm aims at minimizing the quadratic sum of distance of all classes. Update the cluster centers and classifications constantly according to the above

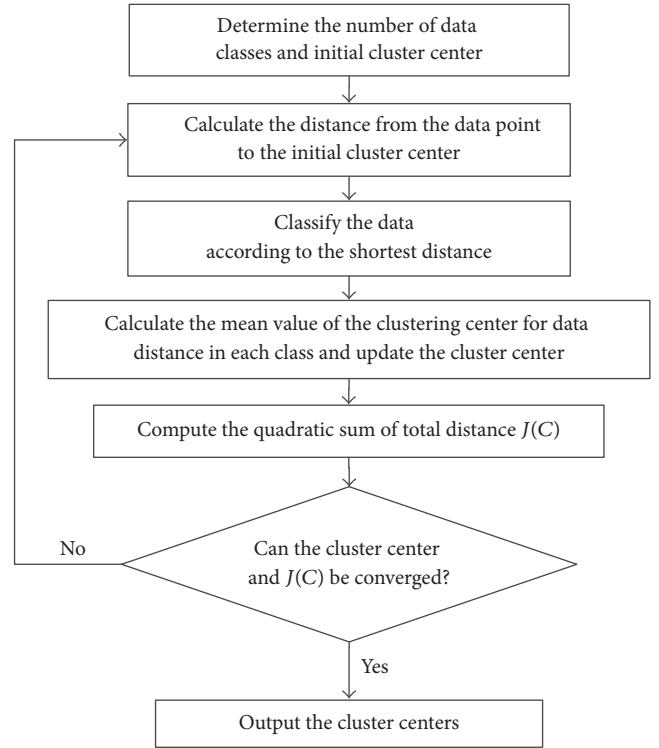


FIGURE 1: Flow chart of the *K*-means clustering algorithm.

steps when the quadratic sum is convergent. The flow chart of the *K*-means clustering algorithm is shown in Figure 1.

**2.3. *Parameter Optimization Algorithm.*** As per the description in Section 2.1, the penalty factor  $C$  adjusts the confidence interval when SVDD defines the data subspace, and it is also the balance between the misclassification ratio and the algorithm complexity [31]. When  $C$  is smaller, the algorithm is less complex and the empirical risk is greater. With the increase of  $C$ , the complexity is increased and the value of the experience risk is reduced. When  $C$  is larger, the classification results of datasets which have large samples are unsatisfactory. Therefore, the value of  $C$  should be appropriate. Each data should have at least one reasonable value of  $C$  to make the best generalization performance of SVDD.

According to Section 2.1, linearly inseparable datasets can be converted to linearly separable datasets through a kernel function [31]. The Gaussian kernel function selected in this paper has a few parameters and a high classification accuracy. Parameter  $\gamma$  in the kernel function affects the nonlinear transformation function, and its change will affect the distribution dimension of the sample data in the space. If  $\gamma$  is large, the value of the kernel function will approach 0, which will lead to overlearning. In other words, the classifier can only correctly classify the training samples and fails to classify the unknown testing samples. On the contrary, less learning will occur, and all testing samples will be classified into one class, which leads to a wrong classification.

From the above, the penalty factors  $C$  and  $\gamma$  play a significant role in the performance of SVDD. Therefore, the

property of SVDD will be improved to a great extent if a more appropriate parameter set ( $C$ ,  $\gamma$ ) is selected.

The question of which is the best parameter optimization method for SVDD still has no answer in academic circles. The commonly used methods for optimizing SVDD's parameters are Grid Search, Genetic Algorithm, and Particle Swarm Optimization [32–34].

Each of the three optimization algorithms has its advantages. If the search interval is large enough and the search step is small enough, the Grid Search can find the global optimal solution. However, it will take a long time to traverse all the parameter groups in the grid. The Genetic Algorithm and Particle Swarm Optimization are heuristic algorithms. They can find the global optimal solution without traversing all the parameter groups in the interval. However, the operation of the two algorithms is often complex, and it is easy for them to fall into the local optimum rather than the global optimal solution. When the number of samples contained in the dataset is small, it is better to use Grid Search to optimize the parameters of SVDD. On the contrary, the Genetic Algorithm and Particle Swarm Optimization are better. The computation time required for GA is longer than that of PSO, but the classification accuracy of GA is higher.

Therefore, different algorithms may be used for obtaining the best results in different applications or operating conditions. In order to obtain the best results as much as possible, three algorithms are selected for optimization and the most effective one is selected under each condition. Therefore, it is necessary to determine them through three optimization algorithms.

**2.3.1. Grid Search.** The processes of optimization algorithm of Grid Search are as follows. Firstly, set ranges of parameters  $C$  and  $\gamma$ ; these two parameters, respectively, correspond to the horizontal and vertical axes of a planar coordinate system. Then, set a certain step length for the two parameters and obtain a value and draw a line on the coordinate diagram according to the parameters. Finally, there will be a grid, which can determine the final optimal parameters through the obtained parameters in the grid point [35]. This method, however, is used not only to calculate results but also to make cross-validation. The procedures of Grid Search are shown in Figure 2.

**2.3.2. Genetic Algorithm.** The genetic parameters optimization algorithm can be realized according to Darwin's theory of evolution, survival of the fittest. Similar to human gene evolution, the Genetic Algorithm can achieve parameter changes according to imitating competition between superior and degradation genes, selection of superior genes, combination of genes, and genovariation. Additionally, it computes the fitness value of population parameters through the fitness function. Higher fitness value shows that the parameter is better [36]. Firstly, the Genetic Algorithm generates a parameter population randomly. Then, relatively optimal parameters can be selected via the fitness function and the corresponding parameter population will be obtained. Parameters can be updated using the above steps and the iteration terminating condition can be set according to the actual requirements.

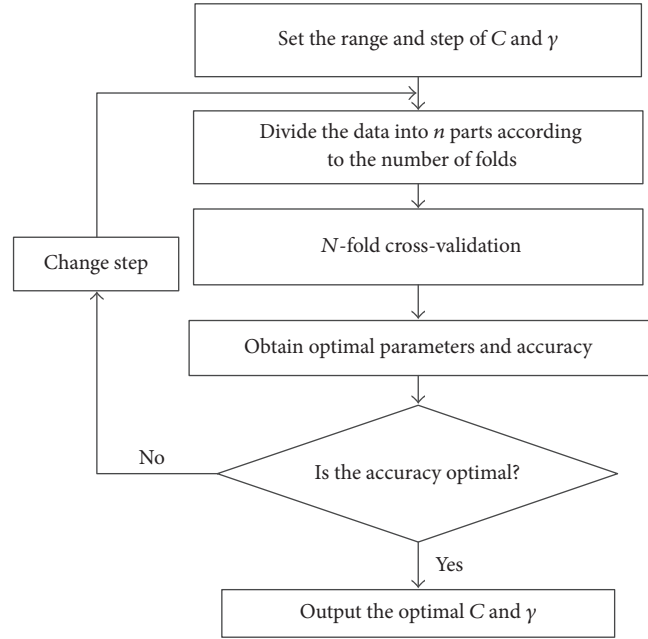


FIGURE 2: Flow chart of Grid Search.

Once the iteration is terminated, optimal parameters that satisfy certain conditions will be obtained [37].

The flow chart of a commonly used Genetic Algorithm is shown in Figure 3.

**2.3.3. Particle Swarm Optimization.** Particle Swarm Optimization (PSO) mainly simulates migration and aggregation behaviors of birds foraging. Similar to the Genetic Algorithm, PSO seeks the optimal particle as the last parameter in the constant iteration [38]. Firstly, a group of random particles are selected as the initial solution. During the iteration, the solution can be updated when particles track two extremums. One is the extremum of the particles themselves and can be called the individual extremum. The other is the one that has been found from the whole population. Advancing direction and speed of those particles can be updated by constantly computing optimal values of particles and the population. Those steps make the particle swarm continuously move towards the direction of the optimal solution. Thus, the optimal solution of parameters can be found ultimately [39]. The flow chart of PSO is shown in Figure 4.

**2.3.4. Cross-Validation Accuracy.** The parameter optimization algorithm which is selected in each operating condition is chosen from the above three algorithms according to the maximum cross-validation accuracy. These algorithms all divide the dataset into  $n$  subsets and regard the  $n-1$  subsets as training ones. The left one is used as a prediction set to judge the above training state. The  $n$  subsets all need prediction sets for their relevant accuracies, and the accuracy of the algorithm can be obtained by computing the average of these

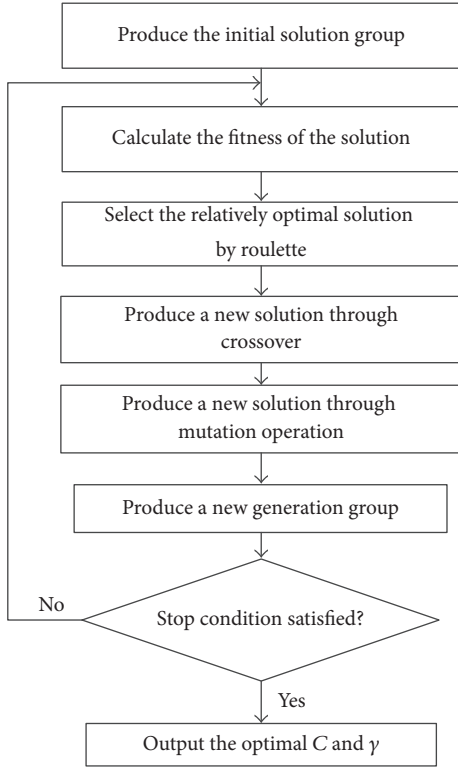


FIGURE 3: Flow chart of the Genetic Algorithm.

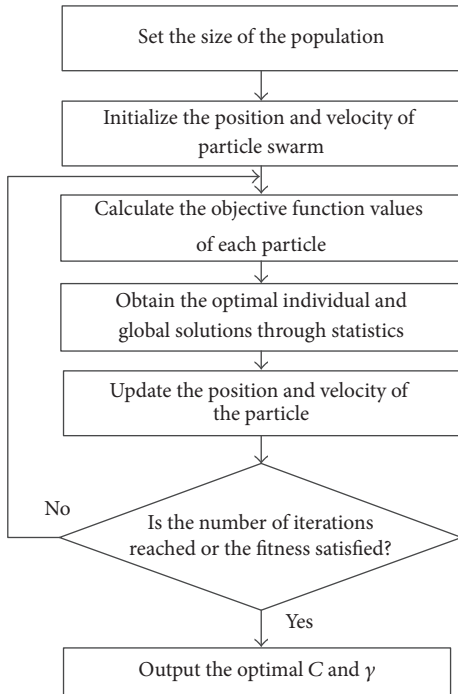


FIGURE 4: Flow chart of the PSO algorithm.

above accuracies [40]. The cross-validation accuracy  $e_n$  is shown in

$$e_n = \frac{1}{n} \sum_{i=1}^n \left[ \frac{\text{num}(y_i = \hat{y}_i)}{m} \right], \quad (14)$$

where  $m$  denotes the number of data in each subset;  $y_i$  and  $\hat{y}_i$  represent the actual value and predicted value of the data element, respectively;  $\text{num}(\cdot)$  denotes the number of data elements in which the condition  $\cdot$  is satisfied.

### 3. The Proposed Method for Early Warning

This paper studies an early warning method for dual-rotor equipment under time-varying operating conditions. The method is based on SVDD and  $K$ -means algorithm, as represented graphically in Figure 5. The main procedures are expressed as follows.

(1) *Interval Partition of Baseline Vibration.* When a piece of equipment works normally, vibration feature values such as peak or RMS of acceleration, RMS or peak of velocity, and peak to peak of displacement are divided into several intervals according to the dual-rotor speeds. Under an interval of an operating speed,  $l$  signal sequences can be described as  $S_i = [N1_i, N2_i, As_i]$ ,  $i = 1, 2, \dots, l$ , where  $l$  is the number of datasets within this operating condition (running speed) interval. The three elements of  $S_i$  are, respectively, rotating speed 1, rotating speed 2, and vibration feature.

(2) *Optimization of Parameters  $C$  and  $\gamma$  in SVDD.*  $l$  signal sequences  $S_i$  are inputs of Grid Search, Genetic Algorithm, and Particle Swarm Optimization within an operating condition interval. After the parameters are optimized, their results and accuracies can be shown as  $[C_1, \gamma_1, e_1]$ ,  $[C_2, \gamma_2, e_2]$ , and  $[C_3, \gamma_3, e_3]$ . Then, select  $C$  and  $\gamma$  with the highest accuracy rate among  $e_1$ ,  $e_2$ , and  $e_3$ . They can be regarded as the optimum parameters. The parameters in every interval of an operating condition should be optimized as the above steps and the optimal solution of  $C$  and  $\gamma$  under each operating condition will be obtained.

(3) *Calculation of Alarm Threshold Parameters  $O_{ia}$  and  $R_{ia}$ .* Regard  $l$  signal sequences  $S_i$ , under an operating condition range, as the input of SVDD. Insert the optimal solutions  $C_o$  of  $C$  and  $\gamma_o$  of  $\gamma$  into (8), (9), and (10). Then, the center  $O_{ia}$  and the radius  $R_{ia}$  of the optimal sphere will be known.  $O_{ia}$  and  $R_{ia}$  can show the normal variation range of vibration data for equipment under an operating condition range; this normal range can be defined as the alarm threshold value under this operating condition range. Apply the above calculation to each range of the operating condition to obtain all alarm threshold values.

(4) *Determination of Cluster Center of the Test Data Whose Alarm State Is Unknown.* The test dataset whose alarm state is unknown is taken as the input of  $K$ -means algorithm. Cluster center  $O_N = (N1_N, N2_N, AS_N)$  can be obtained according to (12). This cluster center can denote the operating state of the equipment steadily and reduce false alarms caused by few outliers as much as possible.

(5) *Judgment of the Alarm State.* When the distance  $r_N$  from  $O_N$ , cluster center of the test data, to  $O_{ia}$ , the center of the optimal sphere in the corresponding operating condition

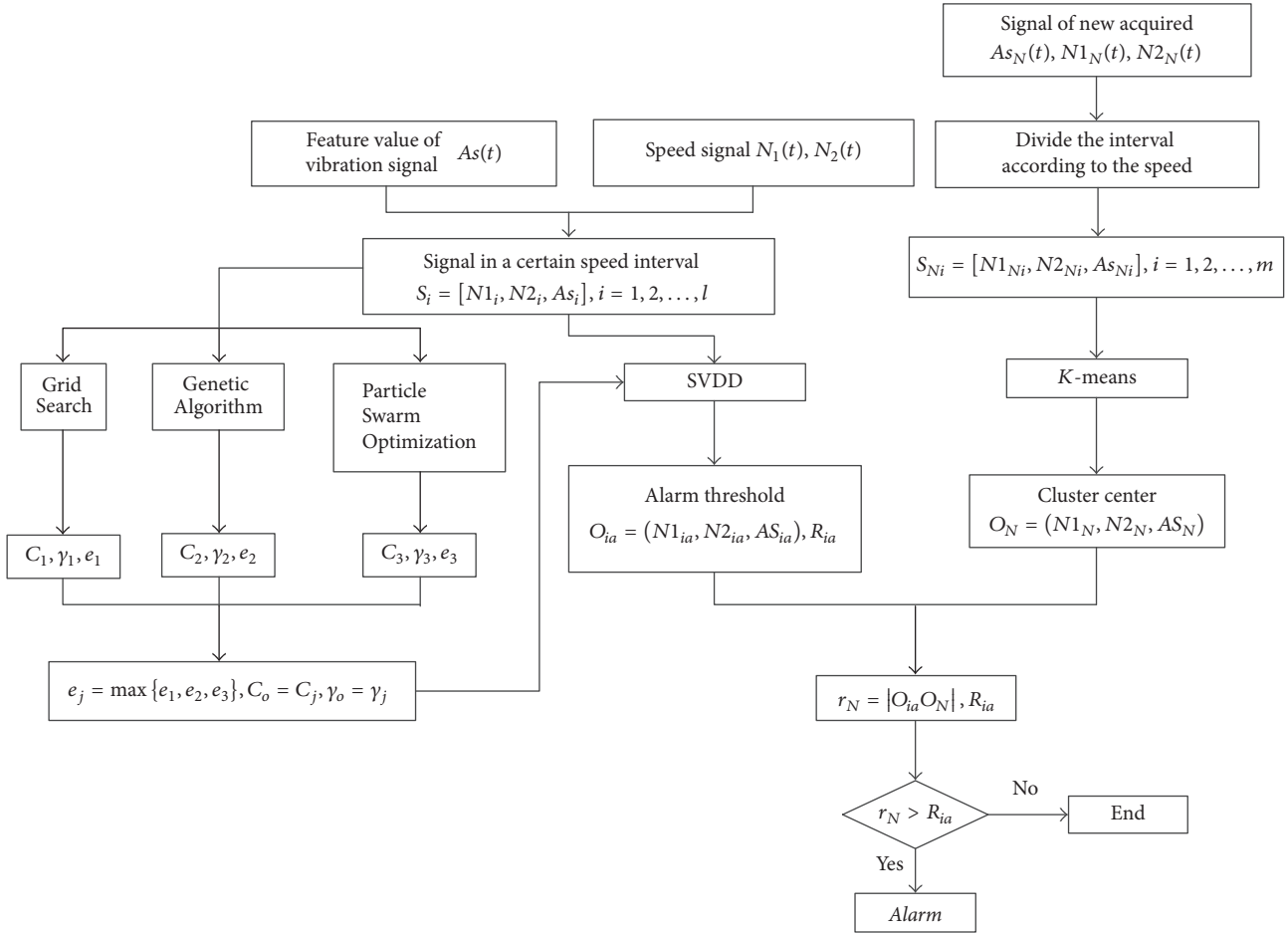


FIGURE 5: Schematic of the proposed method.

range, satisfies the following condition that  $r_N \leq R_{ia}$ , the equipment can be considered to work normally. Oppositely, if  $r_N > R_{ia}$ , it means that the equipment is on alarm.

## 4. Experiments

A dual-rotor test rig has been set up to simulate the operating environment of the real dual-rotor equipment. To carry out the experimental study, two datasets of vibration in bearing housing and rotating speeds of dual rotors have been collected, respectively, when there were no faults and defects in 1# intershaft bearing.

**4.1. Experiments Setup.** The dual-rotor test rig, applied in the experiment, is shown in Figure 6.

In the experiment, intershaft bearings under normal and fault conditions are installed. The experiment can be divided into two groups: (1) the test rig under normal conditions and (2) faults in the outer ring of the intershaft bearing (1 mm deep and 1 mm wide groove (simulation of initial fault) across the axis on the inner surface of the outer ring).

The vibration data is collected by LMS SCADAS [41]. The vibration sensor is BK4519 accelerometer, and the key

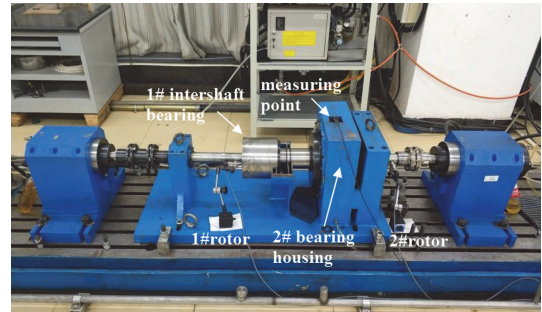


FIGURE 6: Test rig for dual-rotor faults simulation.

phase sensor is a proximity switch. The accelerometer has been mounted vertically on the 2# bearing housing. Speeds of 1# rotor and 2# rotor can be controlled through two motorized spindles. Vibration and rotating speed signals can be collected when dual-rotor speeds are variable.

The selected data to be processed in the following part can be divided into two groups: (1) data under normal conditions (the rotating speed  $N_1$  of 1# rotor slightly fluctuates at 300 rpm, 900 rpm, and 1500 rpm; the rotating speed  $N_2$  of 2#

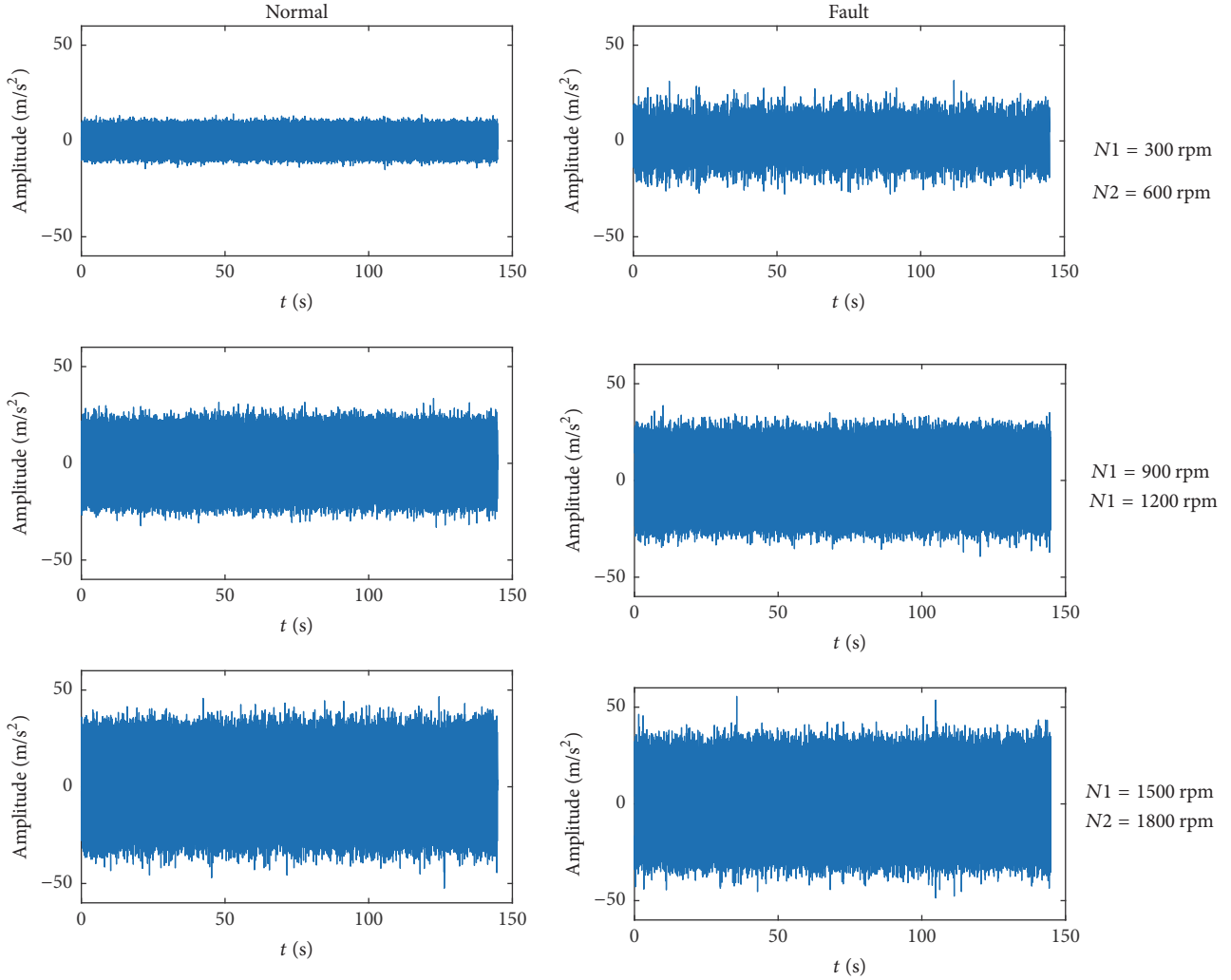


FIGURE 7: Waveforms of normal and fault vibration signals.

rotor slightly fluctuates at 600 rpm, 1200 rpm, and 1800 rpm, resp.; the sampling rate is 25.6 kHz) and (2) fault data of the outer ring in the intershaft bearing (the operating condition and sampling rate are the same with the above data). The waveforms of normal and fault vibration signals at different speeds are shown in Figure 7.

Because RMS can steadily represent the operating state of equipment, this paper selects RMS of acceleration as the vibration feature value. It can be calculated by (14).

$$X_{\text{rms}} = \sqrt{\frac{\sum_{i=1}^N X_i^2}{N}}. \quad (15)$$

**4.2. Analysis through Fixed Threshold Alarm.** The fixed threshold alarm means that one threshold is adopted to warn for the equipment under every operating condition without considering influences of time-varying conditions. In this section, a fixed alarm threshold has been set according to vibration data of the dual-rotor test rig under normal condition. Vibration acceleration can be selected when the test rig works at normal conditions: 1# rotor speed is 900 r/min and

TABLE 1: Fixed alarm threshold for the test rig.

	1# rotor	2# rotor
Speed (r/min)	900	1200
Max. RMS ( $\text{m/s}^2$ )		6.32
Alarm threshold ( $\text{m/s}^2$ )		7.90

2# rotor speed is 1200 r/min. Then, the RMS can be computed. The alarm threshold is 1.25 times the maximum RMS [42], as is shown in Table 1.

Fault data of intershaft bearings are analyzed when the rotating speed of 1# rotor is 300 r/min and that of 2# rotor is 600 r/min. The RMS of vibration acceleration is about  $3 \text{ m/s}^2$ , which is the fault data at a low speed, as is shown in Figure 7. The figure shows that fault data, under this operating condition, is lower than the fixed alarm threshold,  $7.9 \text{ m/s}^2$ . Thus, the above fixed threshold alarm cannot accurately warn against initial faults in low operating conditions.

The data under the normal condition can also be analyzed when the rotating speed of 1# rotor is 1500 r/min and that

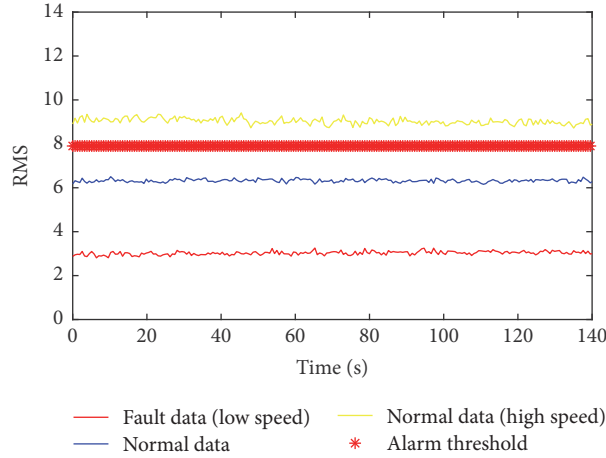


FIGURE 8: Analysis results of the fixed threshold alarm.

TABLE 2: Interval division of experimental data.

Operating condition	1	2	3
Speed of 1# rotor (rpm)	300	900	1500
Speed of 2# rotor (rpm)	600	1200	1800

of 2# rotor is 1800 r/min. The RMS of acceleration is about  $9 \text{ m/s}^2$ . It is shown as normal data at a high speed in Figure 8. From the figure, it is obvious that the data under this condition is higher than the fixed alarm threshold,  $7.9 \text{ m/s}^2$ . Thus, a false alarm is produced through the alarm method based on the fixed threshold under high operating conditions.

From the above analysis, influences from two rotating speeds of the dual-rotor equipment on vibration are ignored by the fixed threshold alarm method. Hence, this method is commonly applied to equipment with a constant speed, but it is inadaptable to warn against faults for dual-rotor ones. A higher value of the fixed threshold means that it is easier for equipment with faults to miss fault warning under low operating conditions; namely, the missing alarm rate will be higher. Similarly, a lower value of the fixed threshold means that it is easier for equipment without faults to warn under high operating conditions; namely, the false alarm rate will be higher. Utilizing a fixed threshold to warn for the equipment will make it difficult to keep the balance between missing alarm rate and false alarm rate.

**4.3. Analysis by the Proposed Method.** The algorithm proposed in this paper is used to analyze the data of the test rig. Processes are as follows.

**4.3.1. Interval Division of Baseline Vibration Features.** The data, under normal and fault conditions, are divided into three groups according to the dual-rotor rotating speeds, as shown in Table 2.

**4.3.2. Parameter Optimization.** The experimental data without faults, under the above three operating conditions, have been analyzed through Grid Search, Genetic Algorithm, and

TABLE 3: Parameters setting and optimization results of Grid Search.

Parameters	$C$	$\gamma$
Range of values	$[2^{-8}, 2^8]$	$[2^{-8}, 2^8]$
Step	1	1
Optimization result	0.5	0.25
Fold of cross-validation	10	
Cross-validation accuracy	98.3516%	

Particle Swarm Optimization. This is to obtain parameters  $C$  and  $\gamma$  under each operating condition for SVDD algorithm. Take operating condition 1 as an example; the processes of parameter optimization are shown as follows.

(1) *Grid Search.* In order to achieve optimum parameters  $C$  and  $\gamma$ , Grid Search is utilized to analyze three-dimensional data under operating condition 1. Those data include dual-rotor speeds and RMS of the acceleration. A contour map and the 3D chart of SVC selection results can be obtained as soon as the parameters are optimized, as is shown in Figure 9. The settings of main parameters and optimization results are shown in Table 3.

(2) *Genetic Algorithm.* The Genetic Algorithm is used to analyze three-dimensional data including dual-rotor speeds and RMS of the acceleration under operating condition 1. A fitness curve can be obtained, as is shown in Figure 10. Main parameters' setting and optimization results are shown in Table 4.

(3) *Particle Swarm Optimization.* Particle Swarm Optimization is applied to analyzing three-dimensional data including dual-rotor speeds and RMS of the acceleration under operating condition 1. Then, a fitness curve can be obtained, as is shown in Figure 11. The settings of main parameters and optimization results are shown in Table 5.

A cross-validation accuracy of 98.8889%, obtained through Particle Swarm Optimization, is the highest value among all the accuracies of all three optimization algorithms

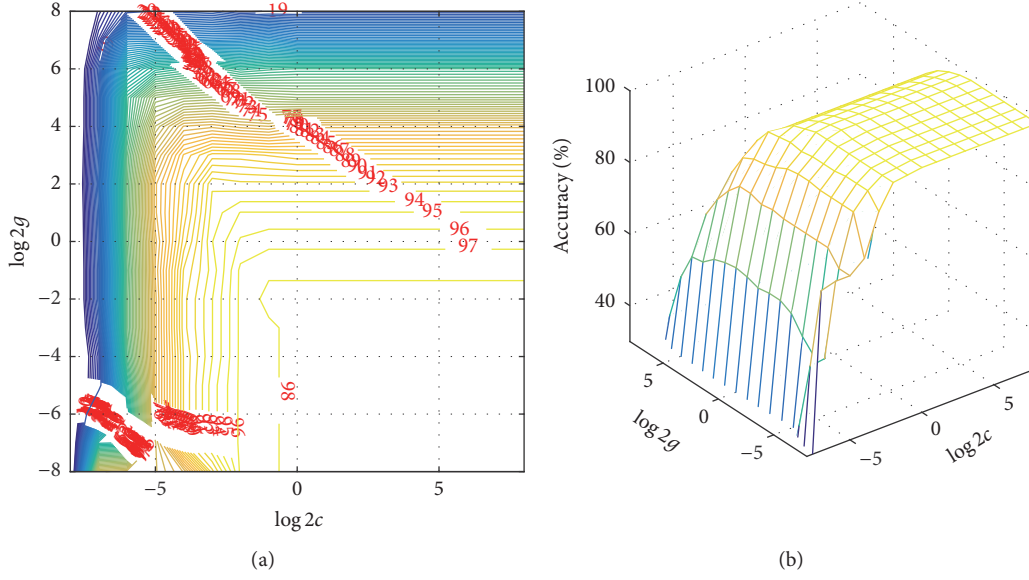


FIGURE 9: Results of the Grid Search algorithm: (a) contour chart; (b) 3D view.

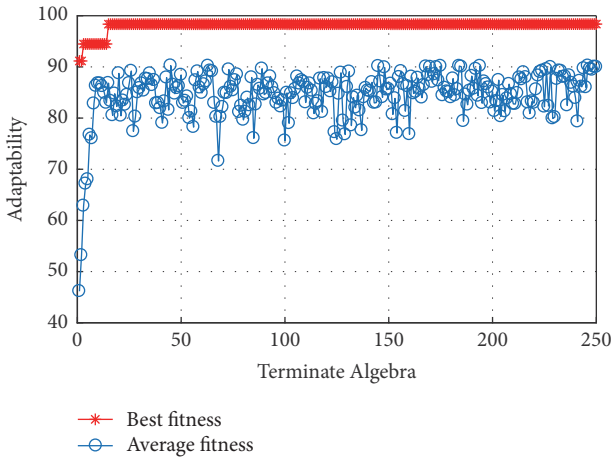


FIGURE 10: Fitness curve of the Genetic Algorithm.

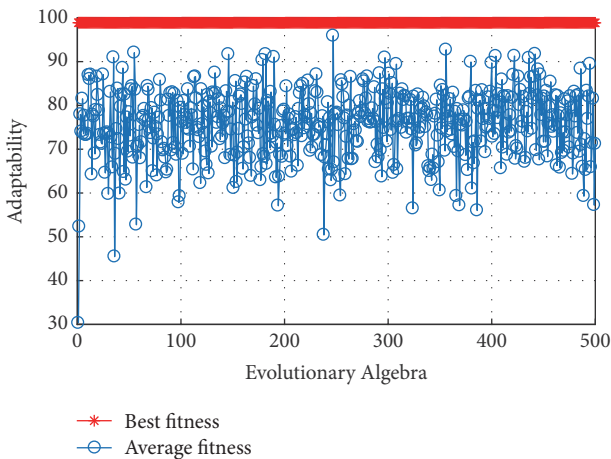


FIGURE 11: Fitness curve of Particle Swarm Optimization.

TABLE 4: Parameters setting and optimization results of the Genetic Algorithm.

Parameters	$C$	$\gamma$
Range of values	[0, 256]	[0, 256]
Maximum population		20
Maximum generation		500
Fold of cross-validation		10
Optimization results	0.74438	0.17261
Cross-validation accuracy		98.3425%

TABLE 5: Parameters setting and optimization results of PSO.

Parameters	$C$	$g$
Range of values	[0.1, 100]	[0.01, 1000]
Maximum evolution		500
Maximum population		20
Local search speed		1.5
Global search speed		1.7
Fold of cross-validation		7
Optimization results	0.52958	0.01
Cross-validation accuracy		98.8889%

that have been used to process experimental data without faults under operating condition 1. Thus, under this operating condition, optimization results of Particle Swarm Optimization are regarded as the values of  $C$  and  $\gamma$ ; namely,  $C_1 = 0.52985$  and  $\gamma_1 = 0.01$ .

Under each operating condition, those three optimization algorithms can be utilized to determine  $C$  and  $\gamma$ . Take parameters obtained through an algorithm whose cross-validation accuracy is the highest among all the accuracies as the trained parameters of SVDD. The final results are shown with boldface letters in Table 6.

TABLE 6: Results of parameter optimization.

Operating condition		1	2	3
Grid Search	Accuracy (%)	98.3516	96.6667	98.3333
	$C$	0.5	0.5	0.5
	$\gamma$	0.25	0.0039063	0.0039063
Genetic Algorithm	Accuracy (%)	98.3425	<b>98.3471</b>	<b>98.3471</b>
	$C$	0.74438	<b>1.332</b>	<b>2.3611</b>
	$\gamma$	0.17261	<b>0.087738</b>	<b>0.099182</b>
Particle Swarm Optimization	Accuracy (%)	<b>98.8889</b>	96.6667	98.3333
	$C$	<b>0.52985</b>	0.912166	1.0021
	$\gamma$	<b>0.01</b>	0.01	0.01

TABLE 7: Alarm threshold of the dual-rotor test rig.

Operating condition	1	2	3
Center of sphere	[300, 600, 2.79648]	[897, 1199, 6.30922]	[1502, 1803, 9.0504]
Radius of sphere	0.2023	0.6035	0.6362

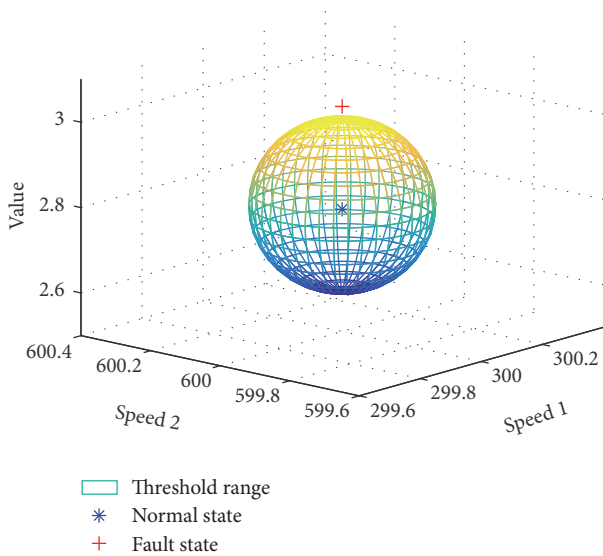


FIGURE 12: Alarm system simulation.

**4.3.3. Determination of the Alarm Threshold.** Optimization results of  $C$  and  $\gamma$  in Section 4.3.2 are adopted by the SVDD algorithm to process experimental data without faults under three operating conditions in sequence. Hence, alarm threshold values under each operating condition are obtained. The alarm threshold can be shown as a sphere, whose controlling parameters are the coordinate of center and the radius. Take operating condition 1 as an example; the sphere representing the alarm threshold is shown in Figure 12. When the data is in the inner part or on the surface of the sphere, as the blue point shown in the figure, the equipment works at a normal condition. However, when data is on the outside of the sphere, as the red point shown in the figure, the equipment is in a state of alarm.

Alarm threshold values of the test rig under all the operating conditions can be obtained through the SVDD algorithm, as is shown in Table 7.

**4.3.4. Judgment of the Alarm State.** The cluster center of experimental data with and without faults under the above three operating conditions can be computed through the  $K$ -means algorithm. Then, distances from all the cluster centers to the corresponding centers of the sphere can be calculated, as is shown in Table 8.

Compare the distance from the cluster center in Table 8 to the center of the sphere with the radius of the sphere in Table 7. If the distance is longer than the radius of the sphere, the equipment is in a state of alarm. On the contrary, if the distance is shorter than the radius of the sphere, the equipment works at a normal condition.

The distances, obtained on the basis of experimental data without faults under each operating condition, are compared with the corresponding radius of the sphere. As is shown in Figure 13, yellow cylinders representing the distances are lower than the red cylinders which represent alarm threshold values; therefore, this equipment works normally under all operating conditions. This analysis result corresponds to the fact that there are no faults on the test rig; namely, there are no false alarms in this experiment.

The distances, obtained on the basis of fault data in intershaft bearing under each condition, are compared with the corresponding radius of the sphere. As is shown in Figure 14, yellow cylinders which represent the distance are higher than the red cylinders representing the alarm threshold value. Thus, under every operating condition, this equipment is judged to be in a state of alarm. This analysis result corresponds to the fact that there are faults in intershaft bearing on the test rig; namely, no missing alarms occur in this experiment.

TABLE 8: Cluster center and distance under normal and fault data.

Operating condition		1	2	3
Without fault	Cluster center	[300, 600, 2.7864]	[897, 1199, 6.3217]	[1502, 1803, 9.0282]
	Distance	0.0613	0.5346	0.3083
Fault	Cluster center	[304, 600, 3.0273]	[901, 1199, 7.3804]	[1499, 1800, 9.0774]
	Distance	3.7661	4.4019	3.5541

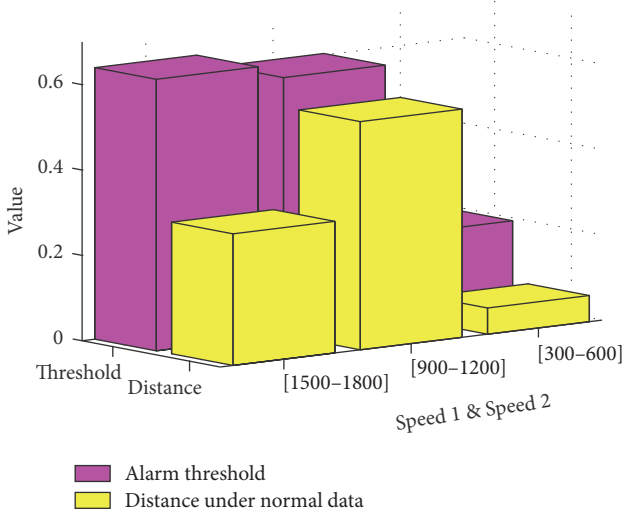


FIGURE 13: Alarm results for the normal data of the dual-rotor test rig.

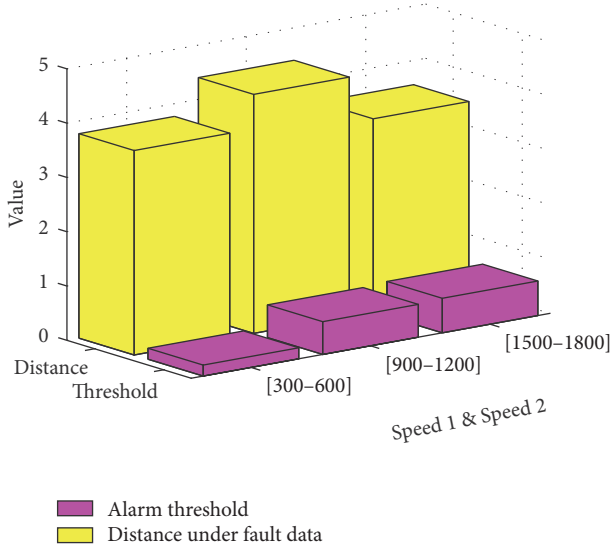


FIGURE 14: Alarm results for the fault data of the dual-rotor test rig.

By analyzing the above experimental data, it is obvious that the algorithm, proposed in this paper, is applicable to warning against faults early for dual-rotor equipment under time-varying operating conditions.

## 5. Conclusions

This paper proposes an early warning method based on SVDD and  $K$ -means for dual-rotor equipment under time-varying operating conditions. Vibration alarm thresholds suitable for different operating conditions can be decided by training SVDD with vibration data under each operating condition without faults. This alarm threshold can be expressed as several spheres whose different coordinates of center and radiuses are their controlling parameters. The cluster center of multigroup data, whose alarm states are to be determined, can be obtained through  $K$ -means algorithm. An early warning of vibration can be realized according to this relative position between the cluster center and the sphere. The proposed method, which combines the above two algorithms, has been tested through the vibration signals of a test rig for dual-rotor faults simulation. Consequently, it has been proved that the proposed method is valid on the early warning for dual-rotor equipment under time-varying conditions.

## 6. Discussion

There is a positive correlation between the speeds set and the load due to the special research object, and the load does not change when the speed set is constant. In other words, the speed factor considered in this paper can represent load. Therefore, only the influences of rotational speed set on the alarm threshold are studied in this paper.

If the present method will be used in other equipment (such as an electric motor whose speeds are the same but loads may be different), a parameter representing the load can be added to the speed set as an independent one easily. This can realize the early warning of comprehensive speed and the load parameters under time-varying operating conditions.

## Conflicts of Interest

The authors declare no conflicts of interest.

## Acknowledgments

Support for this research is provided by the National Key Technologies R&D Program of China under Grant no. 2016YFF0203305 and the Fundamental Research Funds for the Central Universities under Grant no. JD1715.

## References

- [1] H. R. Depold and J. Siegel, "Using diagnostics and prognostics to minimize the cost of ownership of gas turbines," in *Proceedings of the 2006 ASME 51st Turbo Expo*, pp. 845–851, May 2006.
- [2] E. Hindle, R. Van Stone, C. Brogan, J. Vandike, K. Dale, and N. Gibson, "A prognostic and diagnostic approach to engine health management," in *Proceedings of the 2006 ASME 51st Turbo Expo*, pp. 673–680, May 2006.
- [3] D. Balevic, "Heavy-duty gas turbine operating and maintenance considerations," *GER*, 2003.
- [4] J. B. Ali, N. Fnaiech, L. Saidi, B. Chebel-Morello, and F. Fnaiech, "Application of empirical mode decomposition and artificial neural network for automatic bearing fault diagnosis based on vibration signals," *Applied Acoustics*, vol. 89, pp. 16–27, 2015.
- [5] A. Widodo and B. Yang, "Support vector machine in machine condition monitoring and fault diagnosis," *Mechanical Systems and Signal Processing*, vol. 21, no. 6, pp. 2560–2574, 2007.
- [6] V. N. Vapnik, *The Nature of Statistical Learning Theory*, Springer, 1995.
- [7] B.-S. Yang, T. Han, and W.-W. Hwang, "Fault diagnosis of rotating machinery based on multi-class support vector machines," *Journal of Mechanical Science and Technology*, vol. 19, no. 3, pp. 846–859, 2005.
- [8] I. Aydin, M. Karakose, and E. Akin, "A multi-objective artificial immune algorithm for parameter optimization in support vector machine," *Applied Soft Computing*, vol. 11, no. 1, pp. 120–129, 2011.
- [9] S. Lee and K.-K. Seo, "Intelligent fault diagnosis based on a hybrid multi-class support vector machines and case-based reasoning approach," *Journal of Computational and Theoretical Nanoscience*, vol. 10, no. 8, pp. 1727–1734, 2013.
- [10] Z. Yin and J. Hou, "Recent advances on SVM based fault diagnosis and process monitoring in complicated industrial processes," *Neurocomputing*, vol. 174, pp. 643–650, 2016.
- [11] K. R. Fyfe and E. D. S. Munck, "Analysis of computed order tracking," *Mechanical Systems and Signal Processing*, vol. 11, no. 2, pp. 187–202, 1997.
- [12] P. Borghesani, R. Ricci, S. Chatterton, and P. Pennacchi, "A new procedure for using envelope analysis for rolling element bearing diagnostics in variable operating conditions," *Mechanical Systems and Signal Processing*, vol. 38, no. 1, pp. 23–35, 2013.
- [13] Z. Jiang, M. Hu, K. Feng, and Y. He, "Weak fault feature extraction scheme for intershaft bearings based on linear prediction and order tracking in the rotation speed difference domain," *Applied Sciences-Basel*, vol. 7, no. 937, 2017.
- [14] G. Q. Ren, W.-C. Zhang, and B. Li, "Research on the gearbox fault signal relation to the sensitivity of variable working conditions," *Applied Mechanics and Materials*, vol. 494–495, pp. 921–924, 2014.
- [15] Y. Gu, L. Song, T. Xu, L. Su, and G. Wu, "Research on Wind Turbine Gearbox Fault Warning Method under Variable Operational Condition," *Acta Press*, 2014.
- [16] C. Lin and V. Makis, "Optimal Bayesian maintenance policy and early fault detection for a gearbox operating under varying load," *Journal of Vibration and Control*, vol. 22, no. 15, pp. 3312–3325, 2016.
- [17] Y. Shao, K. M. Chris, J. Ou, and Y. Hu, "Gearbox deterioration detection under steady state, variable load, and variable speed conditions," *Chinese Journal of Mechanical Engineering*, vol. 22, no. 2, pp. 256–264, 2009.
- [18] A. Kouadri, G. R. Ibrahim, and A. Albarbar, "Varying load detection in a gearbox system based on adaptive threshold estimation," in *Proceedings of the International Conference on Mechanical, Manufacturing, Modeling and Mechatronics, IC4M 2016*, Kuala Lumpur, Malaysia, February 2016.
- [19] Z. Fu and A. Robles-Kelly, "On mixtures of linear svms for nonlinear classification," *Joint Iaprr International Workshop on Structural, Syntactic, and Statistical Pattern Recognition*, vol. 5342, pp. 489–499, 2008.
- [20] J. A. K. Suykens, J. De Brabanter, L. Lukas, and J. Vandewalle, "Weighted least squares support vector machines: robustness and sparse approximation," *Neurocomputing*, vol. 48, pp. 85–105, 2002.
- [21] Q.-A. Tran, X. Li, and H. Duan, "Efficient performance estimate for one-class support vector machine," *Pattern Recognition Letters*, vol. 26, no. 8, pp. 1174–1182, 2005.
- [22] B. Schölkopf, J. C. Platt, J. Shawe-Taylor, A. J. Smola, and R. C. Williamson, "Estimating the support of a high-dimensional distribution," *Neural Computation*, vol. 13, no. 7, pp. 1443–1471, 2001.
- [23] D. M. J. Tax and R. P. W. Duin, "Support vector domain description," *Pattern Recognition Letters*, vol. 20, no. 11–13, pp. 1191–1199, 1999.
- [24] Y. N. Can, "Modeling and fault prediction of complex system support vector machine," *National Defense Industry Press*, 2015.
- [25] O. L. Mangasarian and M. E. Thompson, "Chunking for massive nonlinear kernel classification," *Optimization Methods & Software*, vol. 23, no. 3, pp. 365–374, 2008.
- [26] K. R. Žalik, "An efficient k-means clustering algorithm," *Pattern Recognition Letters*, vol. 29, no. 9, pp. 1385–1391, 2008.
- [27] A. K. Jain, "Data clustering: 50 years beyond K-means," *Pattern Recognition Letters*, vol. 31, no. 8, pp. 651–666, 2010.
- [28] J. MacQueen, "Some methods for classification and analysis of multivariate observations," *Proc. of Berkeley Symposium on Mathematical Statistics and Probability*, pp. 281–297, 1967.
- [29] V. S. Ananthanarayana, M. N. Murty, and D. K. Subramanian, "Efficient clustering of large data sets," *Pattern Recognition*, vol. 34, no. 12, pp. 2561–2563, 2001.
- [30] A. Likas, N. Vlassis, and J. J. Verbeek, "The global k-means clustering algorithm," *Pattern Recognition*, vol. 36, no. 2, pp. 451–461, 2003.
- [31] X. Xu, *SVM Parameter Optimization and Its Application in the Classification [Ph.D. thesis]*, Dalian Maritime University, Dalian City, China, December 2014.
- [32] X. Liu, D. Jia, and H. Li, "Research on Kernel Parameter Optimization of Support Vector Machine in Speaker Recognition," *Science Technology and Engineering*, vol. 10, no. 7, pp. 1669–1673, 2010.
- [33] P. Chen, J. Wang, and H. Lee, "Model selection Of SVMs using GA approach," in *Proceedings of the 2004 IEEE International Joint Conference on Neural Networks*, Piscataway, NJ, USA, 2004.
- [34] R. C. Eberhart and J. Kennedy, "A new optimizer using particle swarm theory," in *Proceedings of the 6th International Symposium on Micro Machine and Human Science (MHS '95)*, Piscataway, NJ, USA, October 1995.
- [35] T. Xiao, D. Ren, S. Lei et al., "Based on grid-search and PSO parameter optimization for Support Vector Machine," *Intelligent Control and Automation, IEEE*, 2015.
- [36] D. W. Coit, "Genetic algorithms and engineering design," *The Engineering Economist*, vol. 43, no. 4, pp. 379–381, 1998.

- [37] D. E. Goldberg and J. H. Holland, "Genetic algorithms and machine learning," *Machine Learning*, vol. 3, no. 2-3, pp. 95–99, 1998.
- [38] K. Muthulakshmi, R. M. Sasiraja, and V. Suresh Kumar, "The proper location and sizing of multiple distributed generators for maximizing voltage stability using PSO," *Journal of Circuits, Systems and Computers*, vol. 26, no. 4, Article ID 1750057, 2017.
- [39] J. Kennedy and R. Eberhart, "Particle swarm optimization," in *Proceedings of the IEEE International Conference on Neural Networks*, pp. 1942–1948, Perth, Australia, December 1995.
- [40] P. C. Bhat, H. B. Prosper, S. Sekmen, and C. Stewart, "Optimizing event selection with the random grid search," *High Energy Physics-Phenomenology*, 2017, High Energy Physics-Phenomenology.
- [41] "Siemens, LMS SCADAS [EB/OL]," 2017, <https://www.plm.automation.siemens.com/zh/products/lms/testing/scadas/lab.shtml>.
- [42] ISO 10816-4:2009, Mechanical vibration, Evaluation of machine vibration by measurements on non-rotating.

## Research Article

# A New Method for Weak Fault Feature Extraction Based on Improved MED

Junlin Li,<sup>1</sup> Jingsheng Jiang,<sup>1</sup> Xiaohong Fan,<sup>2</sup> Huaqing Wang ,<sup>1</sup> Liuyang Song ,<sup>1,3</sup> Wenbin Liu,<sup>1</sup> Jianfeng Yang,<sup>1</sup> and Liangchao Chen<sup>1</sup>

<sup>1</sup>School of Mechanical & Electrical Engineering, Beijing University of Chemical Technology, Chaoyang District, Beijing 100029, China

<sup>2</sup>College of Mechanical and Energy Engineering, Jimei University, Jimei District, Xiamen 361021, China

<sup>3</sup>Graduate School of Bioresources, Mie University, 1577 Kurimamachiya-cho, Tsu, Mie 514-8507, Japan

Correspondence should be addressed to Huaqing Wang; hqwang@mail.buct.edu.cn and Liuyang Song; xq-0703@163.com

Received 27 September 2017; Accepted 9 December 2017; Published 2 January 2018

Academic Editor: Sandris Ručevskis

Copyright © 2018 Junlin Li et al. This is an open access article distributed under the Creative Commons Attribution License, which permits unrestricted use, distribution, and reproduction in any medium, provided the original work is properly cited.

Because of the characteristics of weak signal and strong noise, the low-speed vibration signal fault feature extraction has been a hot spot and difficult problem in the field of equipment fault diagnosis. Moreover, the traditional minimum entropy deconvolution (MED) method has been proved to be used to detect such fault signals. The MED uses objective function method to design the filter coefficient, and the appropriate threshold value should be set in the calculation process to achieve the optimal iteration effect. It should be pointed out that the improper setting of the threshold will cause the target function to be recalculated, and the resulting error will eventually affect the distortion of the target function in the background of strong noise. This paper presents an improved MED based method of fault feature extraction from rolling bearing vibration signals that originate in high noise environments. The method uses the shuffled frog leaping algorithm (SFLA), finds the set of optimal filter coefficients, and eventually avoids the artificial error influence of selecting threshold parameter. Therefore, the fault bearing under the two rotating speeds of 60 rpm and 70 rpm is selected for verification with typical low-speed fault bearing as the research object; the results show that SFLA-MED extracts more obvious bearings and has a higher signal-to-noise ratio than the prior MED method.

## 1. Introduction

Rolling bearings are one of the most widely used elements in rotary machines. The mechanical failure of bearings may result in financial loss, and even death. Therefore, condition monitoring and fault diagnosis of rolling bearings are critically important for production efficiency and plant safety in modern enterprises [1, 2]. When a rolling bearing fault is weak at an early stage or at a low shaft speed, weak fault features are often embedded in background noise. So it is not an easy task to extract the representative features from the original signal [3]. For instance, the fast Fourier transform cannot obtain ideal transient extraction, even as an increased signal-to-noise ratio assists weak fault feature extraction. Many scholars have reviewed the problem of fault diagnosis taken from weak signals and have made progress. In [4], wavelet transformation is applied to the problem of weak, abnormal vibration signal extraction, but reliance

upon a single wavelet transform makes the extraction of complex vibration signals difficult [5, 6]. Many approaches to improved wavelet transform signal extraction have been proposed, by combination with other diagnostic tools: neural networks, hidden Markov models, or singular value decomposition. In some cases, good results were obtained, but these approaches require the setting of a great many parameters, and yet when the signal is quite weak or the noise strong, these approaches give poor results [7–10]. Huang et al. in 1998 proposed empirical mode decomposition (EMD), an adaptive signal processing method that yields intrinsic mode functions (IMFs) [11]. EMD algorithms are widely used for rolling bearing fault type identification. However, there is a serious pattern mixing and endpoint effect in the EMD method. Wu and Huang proposed ensemble empirical mode decomposition (EEMD) to overcome the shortcoming of mode mixing, but end effects remain a problem. So the

EMD and EEMD methods cannot be qualified for weak fault diagnosis [12, 13]. Stochastic resonance is usually used to enhance weak fault signals and to extract rolling bearing characteristic frequency components [14, 15]. Given the difficulty of choosing the parameters of a band-pass filter, spectral kurtosis (SK) is another useful tool; it provides a moderate way of detecting weak fault in rotation even under the background of strong noise [16, 17]. Liu et al. put forward a new method to extract new features using kernel joint approximate diagonalization of eigenmatrices (KJADE) [18]. Sparse decomposition derived from application of a matching pursuit algorithm to fault signal data can detect the amplitude, the frequency, and the phase of weak signals under the background of strong noise [19]. These results are not obvious because of the loss of signal details.

Wiggins introduced minimum entropy deconvolution (MED) in 1978. MED has been applied to seismic signal processing, especially for the separation of convolutional components of reflection signals [20]. In 2007, Sawalhi et al. first applied MED to detection of faults in rolling bearings and other gear. MED is usually combined with spectral kurtosis or AR filtering to enhance rolling bearing fault detection and diagnosis [21, 22]. MED is also a valid approach to the period estimation problem [23]. However, given strong noise, the failure impact component will be lost by MED, and this is because of the following reasons [24–26].

MED is used as a linear operator and so is ill-adapted to process a limited frequency bandwidth. For noisy data, the limitation of the linear operator is difficult to overcome.

The filter coefficients obtained by the objective function method (OFM) are local optima, not global optima.

To address the latter limitation, an improved MED method based on the shuffled frog leaping algorithm (SFLA-MED) is proposed. In the new method, a shuffled frog leaping algorithm (SFLA) is applied to select an optimal set of filter coefficients that provide maximum kurtosis. So, the filtered signal will be acquired by taking advantage of a global optimal inverse filter. The envelope spectrum of the filtered signal is calculated with Hilbert transform (HHT) and fast Fourier transform (FFT). In the envelope spectrum, the characteristic frequency of a rolling bearing is quite obvious, and the bearing faults can be diagnosed.

## 2. Overview of the Improved Algorithm

**2.1. Minimum Entropy Deconvolution Algorithm.** Deconvolution is an inverse filter that is typically applied to seismic data, for the purpose of recovering reflection coefficients. The main benefit is compression of the seismic reflection pulse and to improve estimation of the subsurface reflection interface reflection coefficient. Deconvolution is particularly important to the bright spot technique of oil-gas exploration and to the analysis of seismic data associated with lithological study on the formation of seismology. Deconvolution can remove the interference from short cycle reverberation and multiple waves [27, 28]. Deconvolution can be divided into deterministic deconvolution and predictive deconvolution. There are many commonly known deconvolutions, including

east square deconvolution, predictive deconvolution, homomorphic deconvolution, surface-consistent deconvolution, maximum entropy deconvolution, minimum entropy deconvolution, change mould deconvolution, Q deconvolution, Noah deconvolution, and minimum information deconvolution.

The MED technique is a type of system identification method that was originally developed to aid extraction of reflectivity information in seismic data. The reflectivity information can be used to identify and locate layers of subterranean minerals [23]. The essence of the method is to acquire a linear operator that maximizes the characteristics of the spike pulse [29, 30]. Maximum kurtosis defines a stop condition [30].

Rolling bearing fault vibration signal can be expressed as

$$y(n) = h(n) * x(n) + e(n), \quad (1)$$

where  $x(n)$  is the impact sequence of the rolling bearing vibration signal,  $h(n)$  is the transfer function, and  $e(n)$  is the noise component. To facilitate analysis,  $e(n)$  can be ignored. The purpose of MED is to find a deconvolution optimal inverse transfer function  $f(n)$  to calculate an input signal  $x(n)$  from the output signal  $y(n)$  through (\*).

$$x(n) = f(n) * y(n). \quad (*)$$

From (3) one may find the best inverse filter that maximizes the kurtosis index of original signal.

$$o_2^4(f(n)) = \frac{\sum_{i=1}^N x^4(i)}{[\sum_{i=1}^N x^2(i)]^2} \quad \text{that is} \quad \frac{\partial o_2^4(f(n))}{\partial f(n)} = 0. \quad (**)$$

Therefore, MED makes the recovery of signal by construction of an “optimal” filter possible.

MED can be summarized in five steps [26]:

(1) Initialization:

$$f^{(0)} = 1. \quad (***)$$

(2) Iteration computing:

$$x(n) = f(n)^{(i-1)} * y(n). \quad (2)$$

(3) Calculate the cross-correlation:

$$b^{(i)}(l) = a \sum_{n=1}^N x^3(n) y(n-l). \quad (3)$$

(4) Calculate the coefficient of filtering:

$$f^{(i)} = A^{-1} b^{(i)}. \quad (4)$$

(5) Terminate condition.

Assume that the given threshold is 0.01. If  $\|f^{(i)} - f^{(i-1)}\|_2^2 < 0.01$ , the iteration ends; else  $i = i + 1$ , and iterate.

**2.2. Shuffled Frog Leaping Algorithm.** SFLA combines the global breadth search of the entire frog populations and the local depth search of frogs individual information, leading the algorithm towards the global optimum direction [25, 31]. The frog representing the solution is divided into several subgroups, and each population has its own culture. Then the frogs evolve according to fitness in the population. After searching in each memplex, the frogs from all memplexes are shuffled and then frogs are redistributed forming new memplexes, which makes searching process less possible to be trapped in local optimum [31].

Its steps include the following:

- (1) Initialize population size.
- (2) Initialize population generation  $U(i)$ ; calculate the  $U(i)$  performance of  $f(i)$ :

$$U(i) = (U_i^1, U_i^2, \dots, U_i^d). \quad (5)$$

- (3) Rank the frogs  $U(i)$ , and arrange the array according to  $f(i)$ :

$$X = \{U(i), f(i), i = 1, 2, \dots, F\}. \quad (6)$$

- (4) The frogs  $U(i)$  are placed in different populations in turn.
- (5) Within populations, frogs begin to evolve (update the worst frogs in the population):

$$Di = \text{rand}() * (Pb - Pw). \quad (7)$$

- (6) After the evolution of the population, the subgroups are combined and arranged in descending order. By constantly iterating, then find out the best frogs to update.

The output signal of a linear time invariant system (LTI) system can be expressed as follows:

$$y(n) = \sum_{i=0}^{N-1} b_i x(n-i) - \sum_{i=1}^M a_i y(n-i). \quad (*a)$$

$x(n)$  is the input signal,  $a_i$  and  $b_i$  represent filtering coefficients, and  $N$  is the filter order. In this paper,  $a_i = 0$ ,

$$y(n) = \sum_{i=0}^{N-1} b_i x(n-i). \quad (*b)$$

The best filter coefficient ( $f_i$ ) obtained by the leapfrog algorithm is substituted into the formula (\*b); then the denoising signal  $x'(n)$  becomes

$$x'(n) = \sum_{i=0}^{N-1} f_i x(n-i). \quad (*c)$$

Then the denoising signal  $x'(n)$  is demodulated by HILBERT-FFT envelope. Finally, the validity of SFLA-MED is verified by comparing the envelope spectrum with the fault characteristic value.

**2.3. Diagnosis Method by the SFLA-MED.** Figure 1 shows the differences between MED and the SFLA-MED. The MED filter is implemented by the objective function method (OFM) given in reference [26]. The OFM is an optimization process designed to maximize the kurtosis of the MED output. It is pointed out that the filter coefficients obtained by OFM are merely local optima, not global optima. So the SFLA-MED uses SFLA to find these optimal coefficients.

The process of fault diagnosis is shown in Figure 2. Vibration signals are measured in a low-speed bearing experiment. The SFLA-MED method does not need to set threshold parameters during the iteration and directly filters the original signal so that a new signal formed. Envelope demodulation is then applied to the new signal. Envelope demodulation consists of a Hilbert transform (HHT) and a fast Fourier transform (FFT). To further verify the reliability and feasibility, the proposed method is compared to MED and theoretical characteristic frequency.

### 3. Experimental Validation

**3.1. Simulation Signal Analysis.** Assume the expression of the bearing simulation signal:

$$x(t) = s1 \times (1 + \cos(2\pi F_{r1}t) + \cos(2\pi F_{r2}t)) \times \cos(2\pi F_n t) + s2 \times \text{randn}(\text{size}(t)). \quad (* * a)$$

$s1$  is the amplitude of the shock component; the value was set to 1.5. The characteristic frequency  $F_{r1} = 12$  Hz,  $F_{r2} = 30$  Hz, and carrier frequency  $F_n = 150$  Hz. The noise component is  $\text{randn}(\text{size}(t))$ , amplitude was 0.2. The time-domain waveform is shown in Figure 3.

Hilbert-FFT was used to demodulate the signals obtained by the MED method and the SFLA-MED method, and then the amplitude of the frequency domain was normalized for a clear contrast. As can be seen from Figure 4(a), after the signal had been reduced and processed by the MED method, the characteristic frequency was drowned in the noise signal, which cannot accurately extract the fault characteristics of the bearing. After the SFLA-MED method was adopted, the signal can be accurately extracted with 12 Hz and 30 Hz, and the harmonic characteristics were obvious, as shown in Figure 4(b). In addition, as can be seen from Figure 3, the modulation characteristics of the simulation signal were obvious, so the envelope analysis was carried out here, as shown in Figure 4(c). After the signal was enveloped, the submerged feature of the mixed white noise was well detected. It should be pointed out that the noise contained in the actual bearing fault signal was usually rather complicated. So the paper uses the method of SFLA-MED and envelope analysis to detect the weak fault signal of bearing.

#### 3.2. Experimental Verification of Low-Speed Bearings

**3.2.1. Experimental System.** The experimental signals to be analyzed were collected from low-speed bearing experiments as shown in Figure 5. In order to better verify the effectiveness of the method put forward in this paper, the outer-race fault data and inner-race fault data of a rolling bearing were taken,

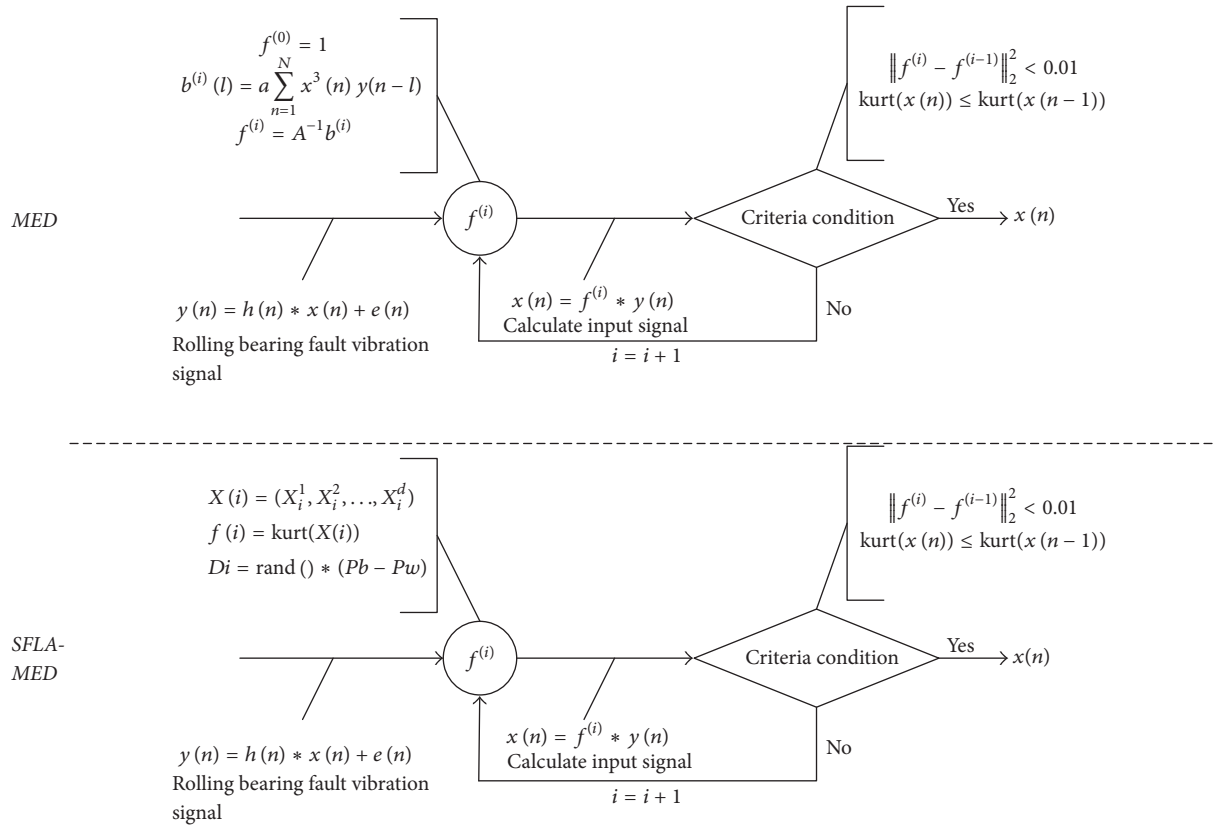


FIGURE 1: The calculation process of MED and the SFLA-MED.

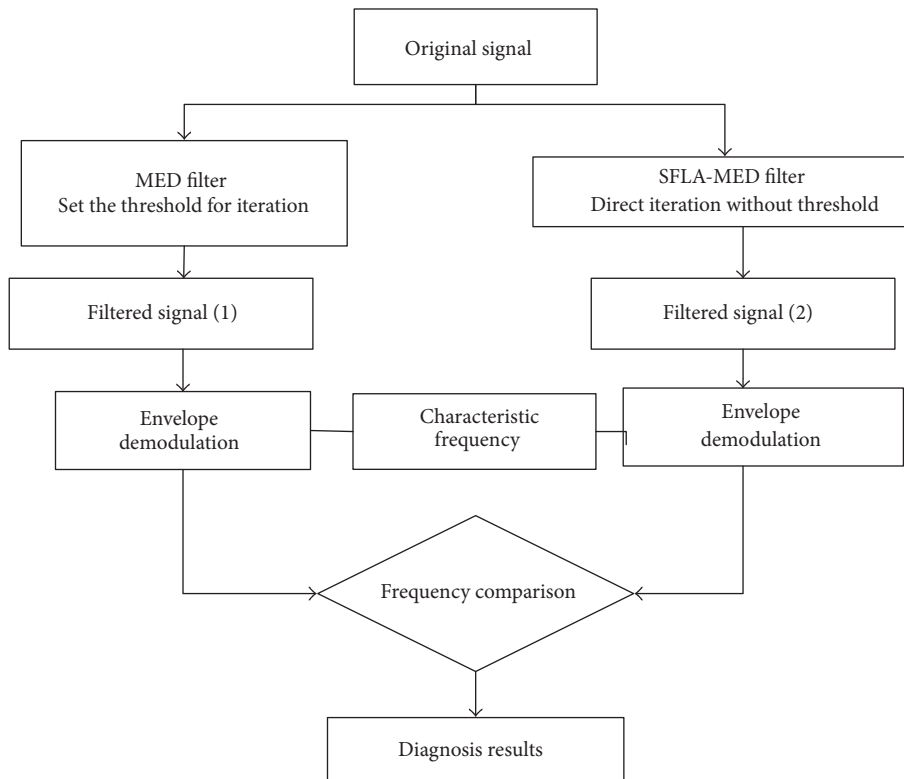


FIGURE 2: The flowchart of fault diagnosis.

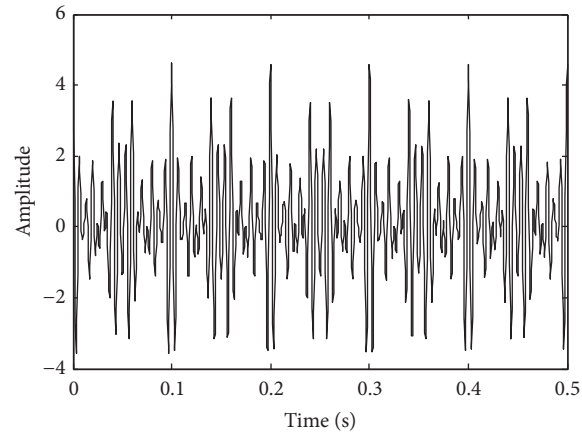


FIGURE 3: Time-domain waveform of simulation signal.

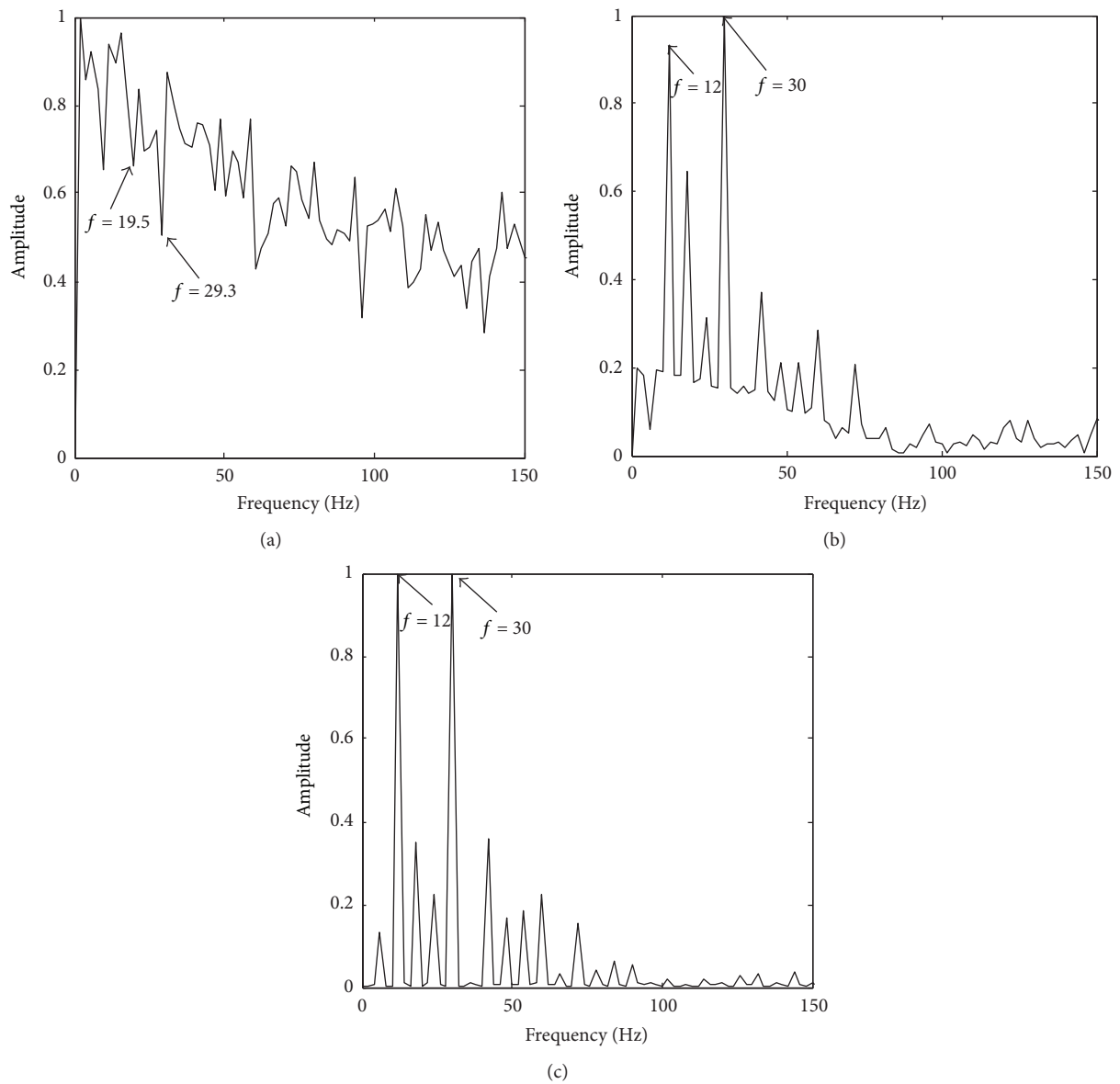


FIGURE 4: Diagnostic results of simulated signals. (a) MED method detection; (b) SFLA-MED method detection; (c) Hilbert-FFT method detection.

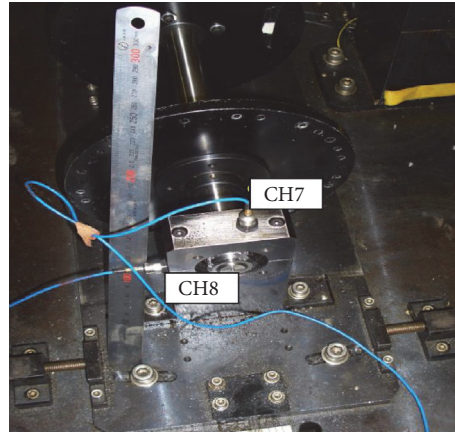


FIGURE 5: Low-speed bearing experimental system.



FIGURE 6: Fault bearings. (a) Outer-race fault; (b) inner-race fault.

and those flaws were artificially made with the use of a wire-cutting machine as shown in Figure 6. The sizes of the flaws are as follows:

Outer-race flaw: 5.0 mm \* 0.5 mm (width \* depth)

Inner-race flaw: 5.0 mm \* 0.5 mm (width \* depth).

**3.2.2. Bearing Data Set Description.** In order to fully analyze signal features and acquire more comprehensive information for the research of the fault diagnosis, the sampling frequency is set at 100 kHz, the sampling time is 10 seconds, and the rotation speed of spindle is 60 rpm and 70 rpm. So four kinds of vibration signal are obtained and they are outer-race fault vibration signal at 60 rpm, inner-race fault vibration signal at 60 rpm, outer-race fault vibration signal at 70 rpm, and the inner-race fault vibration signal at 70 rpm, respectively. By varying rotation speed, the time-domain wave form of vibration signals is shown in two figures. Figure 7 indicates the time-domain wave form of outer-race and inner-race fault vibration signals when the rotation speed is 60 rpm and Figure 8 shows the time-domain waveform of outer-race

and inner-race vibration signals when the rotation speed is 70 rpm.

Bearing defects will generate a series of impact vibrations that emit at bearing characteristic frequencies every time a running roller passes over a defect [32]. Therefore the fault type can be determined by identifying the characteristic frequency [33].

Computed pass-frequencies are shown in Table 1. Pure rolling motion is a condition of the above equations. As there may be some sliding motion in practice, the results in Table 1 are approximate values.

## 4. Results and Discussion

**4.1. Feature Extraction of MED and SFLA-MED.** Envelop spectrum analysis based on the Hilbert transform has been widely used in bearing fault diagnosis [34]. It separates modulating signal from the collected signal, and this contains information that indicates the fault type. Envelope spectrum analysis is obtained from the FFT of the envelop signal. Figure 9 shows the normalized envelop spectrum of outer-race and

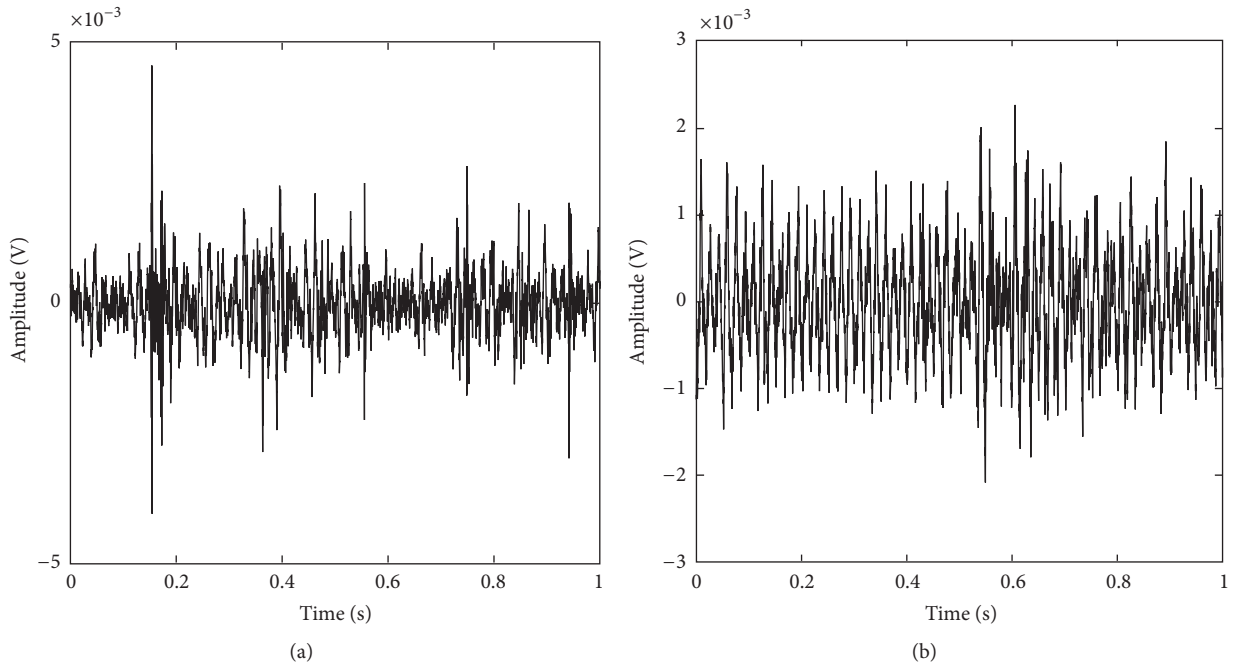


FIGURE 7: The time-domain waveform of vibration signals (60 rpm): (a) outer-race fault; (b) inner-race fault.

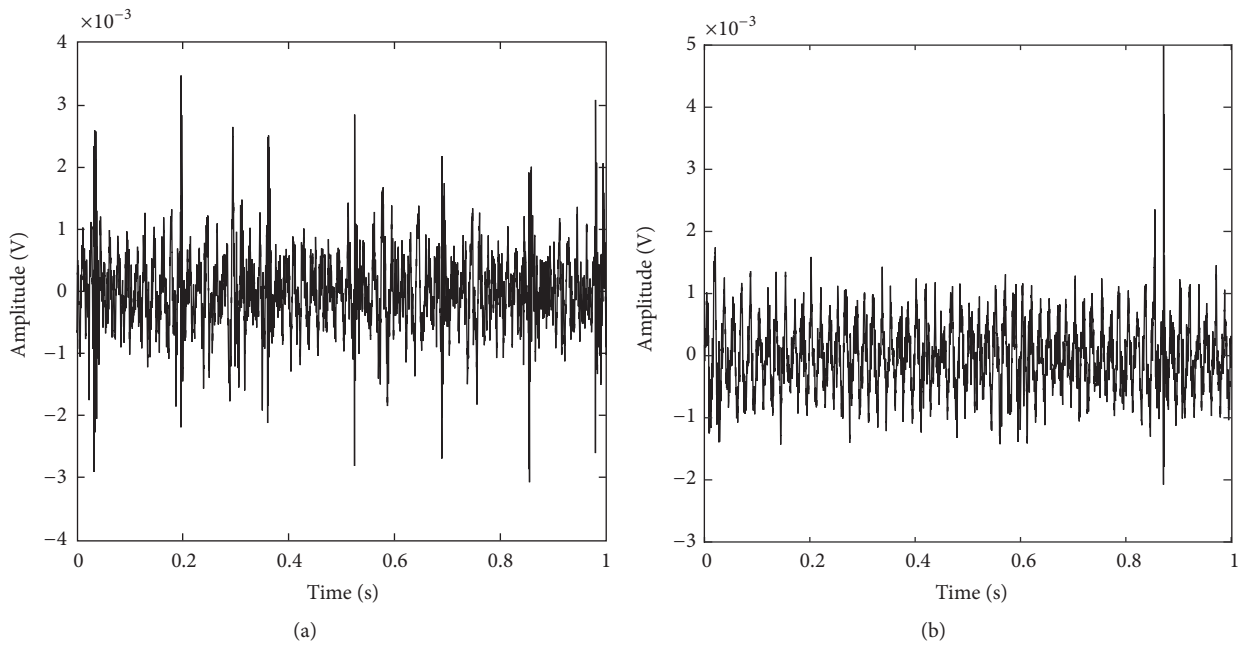


FIGURE 8: The time-domain waveform of vibration signals (70 rpm): (a) outer-race fault; (b) inner-race fault.

inner-race fault vibration signals at the speed of 60 rpm filtered by MED method. As shown in Figure 9(a), the theoretical characteristic frequency is not clearly shown by the spectrum peaks. Although there is a clear spectrum peak appearing near the theoretical characteristic frequency as shown in Figure 9(b), it is not the highest spectral peak and cannot be identified for the first time. Hence, the MED method extracts the fault characteristic frequency with contingency.

Shuffled Frog Leaping Algorithm optimization improves the MED method. Based on theoretical study, the frequency equation of bearing fault characteristics is based on the assumption of a pure rolling motion. These vibrations occur at bearing characteristic frequencies, which are estimated based on the geometry of the bearing, its rotational speed, and the location of the defect. However, in practice, some unexpected status may occur, which causes slight deviation

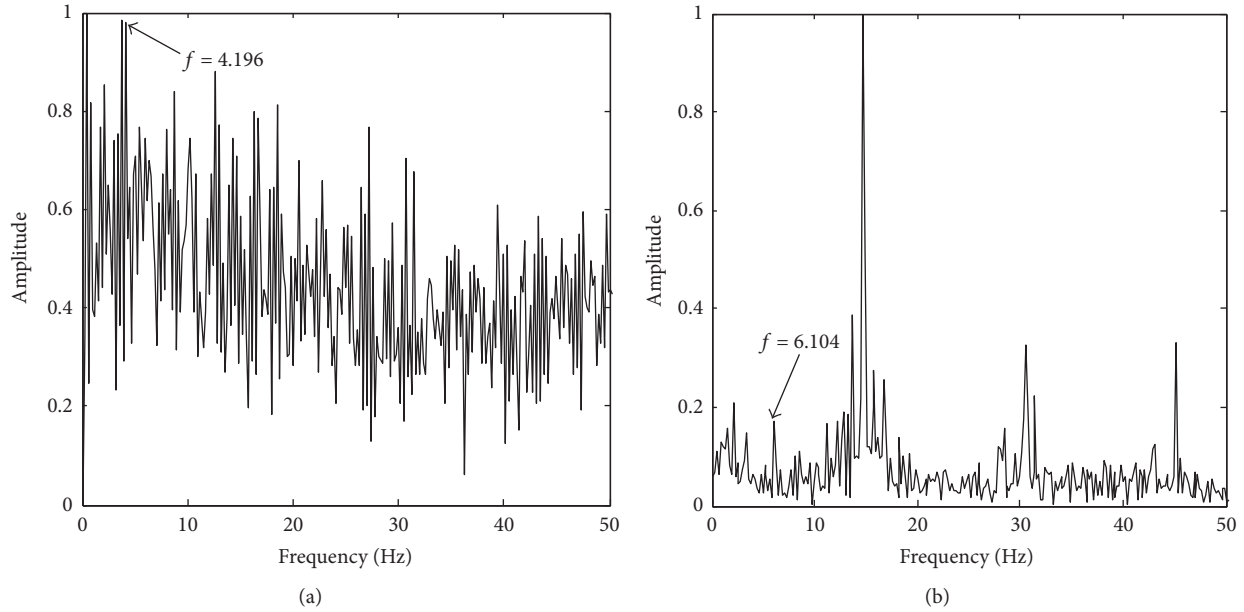


FIGURE 9: The envelope spectrum of vibration signals filtered by MED (60 rpm): (a) outer-race fault; (b) inner-race fault.

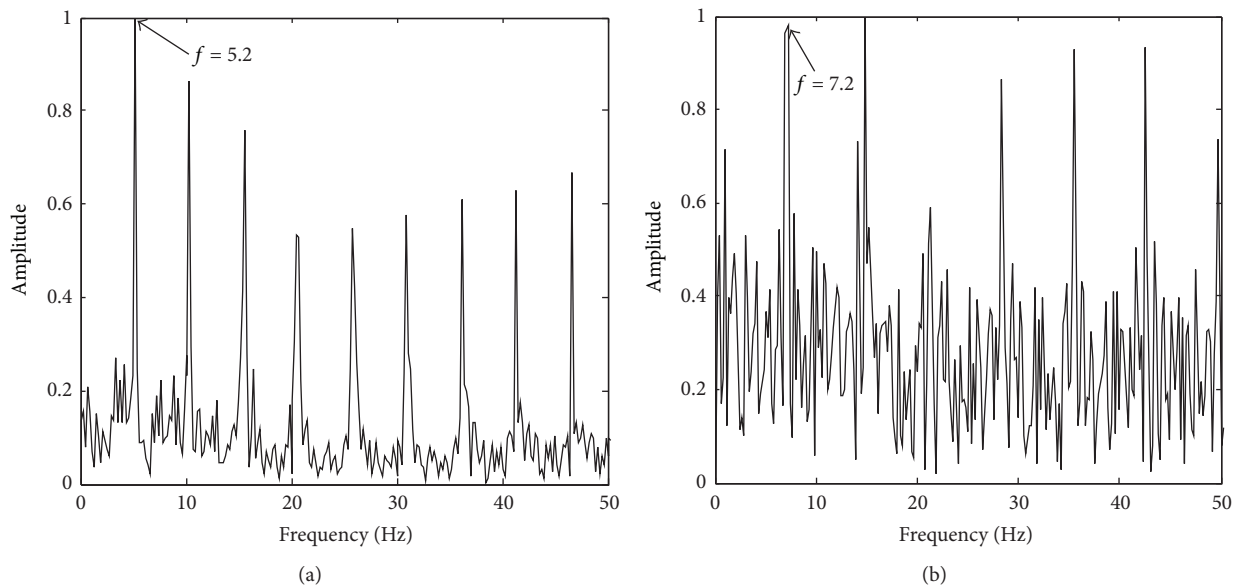


FIGURE 10: The envelope spectrum of vibration signals filtered by SFLA-MED (60 rpm): (a) outer-race fault; (b) inner-race fault.

of the characteristic frequency locations. Figure 10 shows the normalized envelop spectrum of outer-race and inner-race fault vibration signals at the speed of 60 rpm filtered by SFLA-MED. From Figure 10, it can be seen that there is an obvious spectrum peak corresponding to the theoretical characteristic frequency, so the results obtained from SFLA-MED meet the diagnostic accuracy requirement. In summary, the SFLA-MED method can better extract the fault characteristic frequency.

According to the experimental results in Figure 11, the traditional MED method can recognize the bearing failure, which shows the effectiveness of the MED method. The

SFLA-MED are used to analyze the experimental data, and it can also identify bearing failure, as shown in Figure 12. The two methods are good to identify fault bearing fault characteristics under 70 rpm. Compared with the 60 rpm experimental data, the SFLA-MED algorithm recognizes the characteristic frequency of the bearing fault under different speeds, which shows that it has a better universality and is more suitable for application.

**4.2. Effect Comparison of MED and SFLA-MED.** As is known, signal-to-noise ratio (SNR) is one of the most basic indicators to measure an algorithm. Combining the experimental data

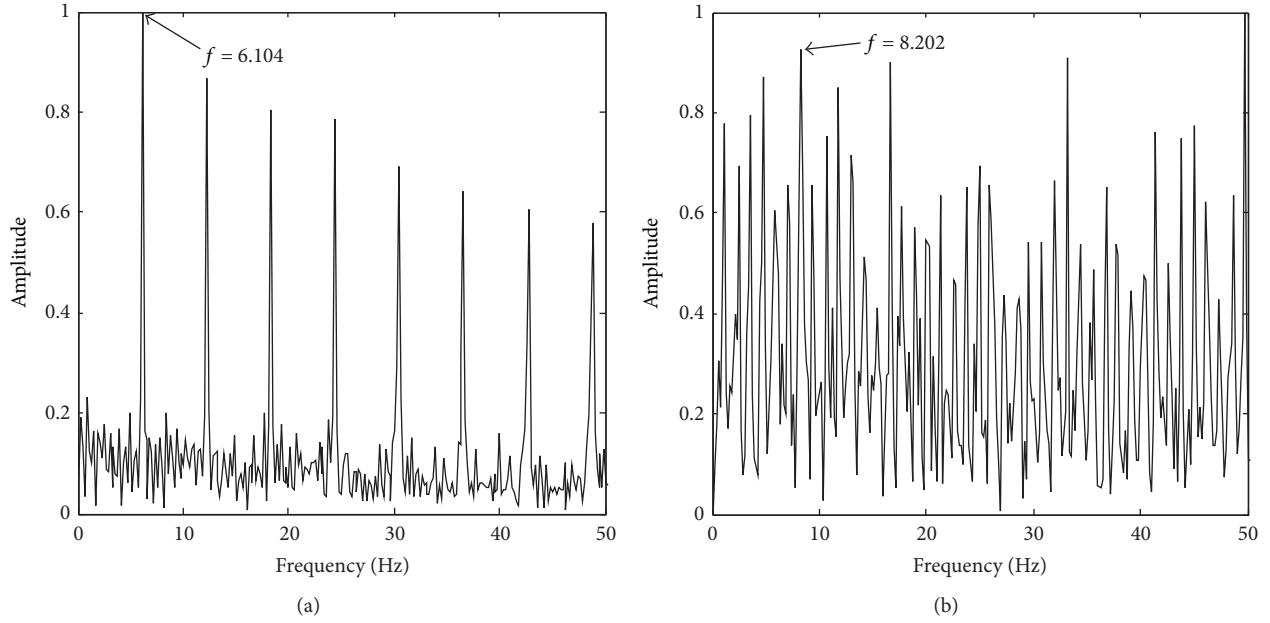


FIGURE 11: The envelope spectrum of vibration signals filtered by MED (70 rpm): (a) outer-race fault; (b) inner-race fault.

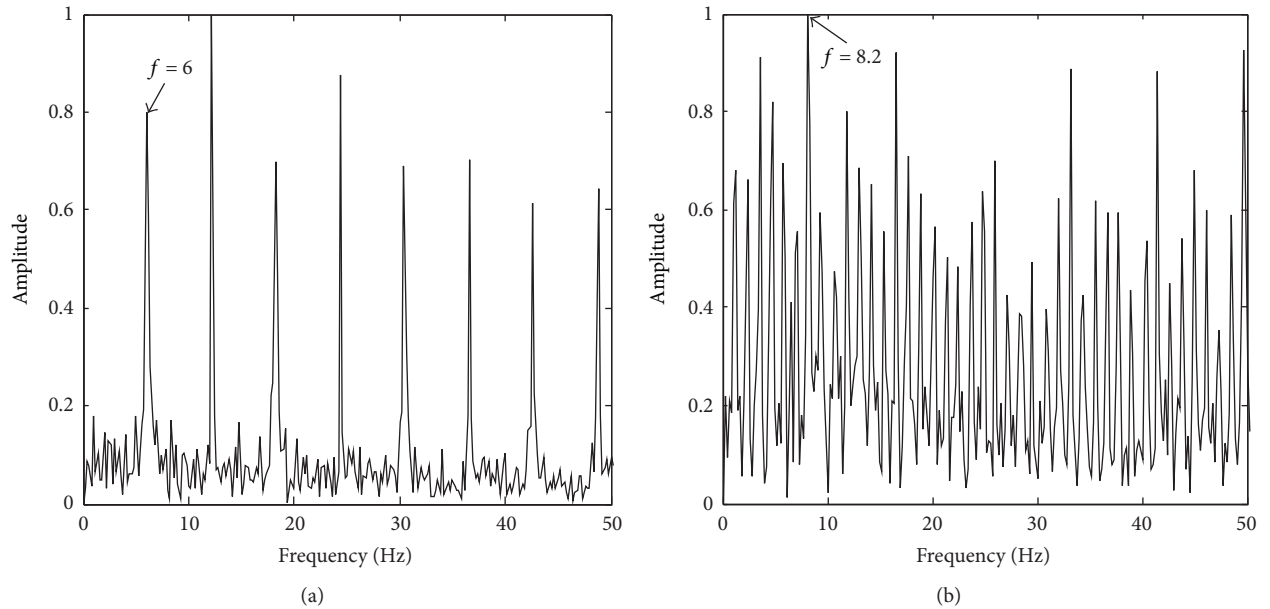


FIGURE 12: The envelope spectrum of vibration signals filtered by SFLA-MED (70 rpm): (a) outer-race fault; (b) inner-race fault.

of the four groups, it is found that the characteristic frequency signals of the SFLA-MED method are not drowned by noise, and they are more easily identified with the fault characteristics (highest spectrum peaks). In addition, compared with the experimental result of signals at the speed of 60 rpm, the SFLA-MED method has higher signal-to-noise ratio than the original MED method as shown in Table 2. Therefore, the SFLA-MED can extract the failure frequency more accurately and reduce the possibility of miscalculation.

The calculation formula of frequency domain signal-to-noise ratio is shown in.

$$R = \lg \frac{\sum_{r=1}^3 A_{F_r}^2}{\sum_{i=1}^N A_i^2 - \sum_{r=1}^3 A_{F_r}^2}. \quad (***)$$

$N$  is the sampling length,  $A_{F_r}$  is the corresponding amplitude of the first three-order characteristic frequency, and  $A_i$  is the frequency domain signal amplitude.

TABLE 1: Pass-frequencies of rolling bearing.

Rotation speed	60 rpm	70 rpm
Outer-race fault	4.91 (Hz)	5.73 (Hz)
Inner-race fault	7.09 (Hz)	8.27 (Hz)

TABLE 2: SNR of two methods (dB).

	60 rpm Inner-race	60 rpm Outer-race
MED	-0.4814	-0.8050
SFLA-MED	-0.2691	1.8908

## 5. Conclusions

In this paper, an SFLA-MED combined with envelope demodulation is applied to the weak fault diagnosis of rolling bearings. Compared with the previous MED method, the proposed method extracts more obvious fault features of rolling bearings and is better adapted to engineering application. It is pointed out that the improved MED obtains a global optimal solution but that MED does not. SFLA makes the selection of filtering coefficients more flexible. As can be seen from the algorithm flow diagram, there is no error accumulation in the SFLA-MED, because the process of finding filter coefficients is not affected by the last filtered signal. There are no extra frequency components beyond the characteristic frequency that appears in the envelope spectrum.

## Conflicts of Interest

The authors declare that there are no conflicts of interest regarding the publication of this paper.

## Authors' Contributions

The presented work was carried out by collaboration of all authors. Huaqing Wang conceived and designed the experiments; Junlin Li and Jingshen Jiang performed the experiments and the simulations; Xiaohong Fan and Liuyang Song analyzed the data; Wenbin Liu, Jianfeng Yang, and Liangchao Chen performed the simulation and revised the paper; Junlin Li and Huaqing Wang wrote the paper. All authors read and approved the final manuscript.

## Acknowledgments

This paper is supported by the National Natural Science Foundation of China (Grant no. 51675035) and Petro-China Science and Technology Innovation Fund (Grant no. 2015D50060606).

## References

- [1] N. Tandon and A. Choudhury, "Review of vibration and acoustic measurement methods for the detection of defects in rolling element bearings," *Tribology International*, vol. 32, no. 8, pp. 469–480, 1999.
- [2] J. Wang, L. L. Cui, H. Q. Wang, and P. Chen, "Improved complexity based on time-frequency analysis in bearing quantitative diagnosis," *Advances in Mechanical Engineering*, vol. 2013, Article ID 258506, 11 pages, 2013.
- [3] P. D. McFadden and J. D. Smith, "Vibration monitoring of rolling element bearings by the high-frequency resonance technique—a review," *Tribology International*, vol. 17, no. 1, pp. 3–10, 1984.
- [4] R. B. Randall and J. Antoni, "Rolling element bearing diagnostics—a tutorial," *Mechanical Systems and Signal Processing*, vol. 25, no. 2, pp. 485–520, 2011.
- [5] Z. K. Peng, P. W. Tse, and F. L. Chu, "A comparison study of improved Hilbert-Huang transform and wavelet transform: application to fault diagnosis for rolling bearing," *Mechanical Systems and Signal Processing*, vol. 19, no. 5, pp. 974–988, 2005.
- [6] X. S. Lou and K. A. Loparo, "Bearing fault diagnosis based on wavelet transform and fuzzy inference," *Mechanical Systems and Signal Processing*, vol. 18, no. 5, pp. 1077–1095, 2004.
- [7] H. C. Wang, J. Chen, and G. M. Dong, "Feature extraction of rolling bearing's early weak fault based on EEMD and tunable Q-factor wavelet transform," *Mechanical Systems and Signal Processing*, vol. 48, no. 1-2, pp. 103–119, 2014.
- [8] G. Yu, C. Li, and S. Kamarthi, "Machine fault diagnosis using a cluster-based wavelet feature extraction and probabilistic neural networks," *The International Journal of Advanced Manufacturing Technology*, vol. 42, no. 1-2, pp. 145–151, 2009.
- [9] J. Yan and L. Lu, "Improved Hilbert-Huang transform based weak signal detection methodology and its application on incipient fault diagnosis and ECG signal analysis," *Signal Processing*, vol. 98, pp. 74–87, 2014.
- [10] H. Demirel, C. Ozcinar, and G. Anbarjafari, "Satellite image contrast enhancement using discrete wavelet transform and singular value decomposition," *IEEE Geoscience and Remote Sensing Letters*, vol. 7, no. 2, pp. 333–337, 2010.
- [11] N. E. Huang, Z. Shen, S. R. Long et al., "The empirical mode decomposition and the Hilbert spectrum for nonlinear and non-stationary time series analysis," *Proceedings A*, vol. 454, pp. 903–995, 1998.
- [12] Z. H. Wu and N. E. Huang, "Ensemble empirical mode decomposition: a noise-assisted data analysis method," *Advances in Adaptive Data Analysis (AADA)*, vol. 1, no. 1, pp. 1–41, 2009.
- [13] Z. H. Wu and N. E. Huang, "A study of the characteristics of white noise using the empirical mode decomposition method," *Proceedings of the Royal Society A Mathematical, Physical and Engineering Sciences*, vol. 460, no. 2046, pp. 1597–1611, 2004.
- [14] N. Hu, M. Chen, G. Qin, L. Xia, Z. Pan, and Z. Feng, "Extended stochastic resonance (SR) and its applications in weak mechanical signal processing," *Frontiers of Mechanical Engineering in China*, vol. 4, no. 4, pp. 450–461, 2009.
- [15] X. Zhang, N. Hu, Z. Cheng, and L. Hu, "Enhanced detection of rolling element bearing fault based on stochastic resonance," *Chinese Journal of Mechanical Engineering*, vol. 25, no. 6, pp. 1287–1297, 2012.
- [16] F. Cong, J. Chen, and G. Dong, "Spectral kurtosis based on AR model for fault diagnosis and condition monitoring of rolling bearing," *Journal of Mechanical Science and Technology*, vol. 26, no. 2, pp. 301–306, 2012.
- [17] F. Combet and L. Gelman, "Optimal filtering of gear signals for early damage detection based on the spectral kurtosis," *Mechanical Systems and Signal Processing*, vol. 23, no. 3, pp. 652–668, 2009.

- [18] Y. Liu, B. He, F. Liu, S. Lu, and Y. Zhao, "Feature fusion using kernel joint approximate diagonalization of eigen-matrices for rolling bearing fault identification," *Journal of Sound & Vibration*, vol. 385, pp. 389–401, 2016.
- [19] C. Zhang, Z. Yin, X. Chen, and M. Xiao, "Signal overcomplete representation and sparse decomposition based on redundant dictionaries," *Chinese Science Bulletin*, vol. 50, no. 23, pp. 2672–2677, 2005.
- [20] R. A. Wiggins, "Minimum entropy deconvolution," *Geoprospection*, vol. 16, no. 1-2, pp. 21–35, 1978.
- [21] N. Sawalhi, R. B. Randall, and H. Endo, "The enhancement of fault detection and diagnosis in rolling element bearings using minimum entropy deconvolution combined with spectral kurtosis," *Mechanical Systems and Signal Processing*, vol. 21, no. 6, pp. 2616–2633, 2007.
- [22] H. Endo and R. B. Randall, "Enhancement of autoregressive model based gear tooth fault detection technique by the use of minimum entropy deconvolution filter," *Mechanical Systems and Signal Processing*, vol. 21, no. 2, pp. 906–919, 2007.
- [23] G. González, R. E. Badra, R. Medina, and J. Regidor, "Period estimation using minimum entropy deconvolution (MED)," *Signal Processing*, vol. 41, no. 1, pp. 91–100, 1995.
- [24] E. A. Robinson, S. Treitel, R. A. Wiggins, and P. R. Gutowski, *Digital seismic inverse methods*, International Human Resources Development Corp., Boston, Mass, USA, 1983.
- [25] P. Sharma, N. Sharma, and H. Sharma, "Elitism based Shuffled Frog Leaping algorithm," in *Proceedings of the 5th International Conference on Advances in Computing, Communications and Informatics, ICACCI 2016*, pp. 788–794, India, September 2016.
- [26] J.-Y. Lee and A. K. Nandi, "Extraction of impacting signals using blind deconvolution," *Journal of Sound and Vibration*, vol. 232, no. 5, pp. 945–962, 2000.
- [27] D. W. Eaton and J.-M. Kendall, "Improving seismic resolution of outermost core structure by multichannel analysis and deconvolution of broadband SmKS phases," *Physics of the Earth and Planetary Interiors*, vol. 155, no. 1-2, pp. 104–119, 2006.
- [28] G. F. Margrave, M. P. Lamoureux, and D. C. Henley, "Gabor deconvolution: Estimating reflectivity by nonstationary deconvolution of seismic data," *Geophysics*, vol. 76, no. 3, pp. W15–W30, 2011.
- [29] M. Bano, "Modeling and inverse Q imaging of ground penetrating radar waves in 1 and 2D," *Geophysical Research Letters*, vol. 23, no. 22, pp. 3123–3126, 1996.
- [30] J. Longbottom, A. Walden T, and E. White R, "Principles and application of maximum kurtosis phase estimation," *Geophysical Prospecting*, vol. 36, no. 2, pp. 115–138, 1988.
- [31] J. Zhao, M. Hu, H. Sun, and L. Lv, "Shuffled frog leaping algorithm based on enhanced learning," *International Journal of Intelligent Systems Technologies and Applications*, vol. 15, no. 1, pp. 63–73, 2016.
- [32] N. Rehman, C. Park, N. E. Huang, and D. P. Mandic, "EMD via MEMD: multivariate noise-aided computation of standard EMD," *Advances in Adaptive Data Analysis (AADA)*, vol. 5, no. 2, 2013.
- [33] P. Chen and T. Toyota, "Sequential fuzzy diagnosis for plant machinery," *JSME International Journal Series C Mechanical Systems, Machine Elements and Manufacturing*, vol. 46, no. 3, pp. 1121–1129, 2003.
- [34] D. Ho and R. B. Randall, "Optimisation of bearing diagnostic techniques using simulated and actual bearing fault signals," *Mechanical Systems and Signal Processing*, vol. 14, no. 5, pp. 763–788, 2000.

## Research Article

# Acoustic Emission Monitoring and Failure Precursors of Sandstone Samples under Various Loading and Unloading Paths

Jie Xu,<sup>1</sup> Jingdong Jiang,<sup>2</sup> Lingling Zuo,<sup>3</sup> and Yufeng Gao<sup>1</sup>

<sup>1</sup>Geotechnical Research Institute, Hohai University, Nanjing 210098, China

<sup>2</sup>Nanjing Hydraulic Research Institute, Nanjing 210029, China

<sup>3</sup>Laixi Water Conservancy Bureau, Laixi 266600, China

Correspondence should be addressed to Jingdong Jiang; 365354266@qq.com

Received 21 July 2017; Accepted 17 October 2017; Published 27 December 2017

Academic Editor: Rafał Burdzik

Copyright © 2017 Jie Xu et al. This is an open access article distributed under the Creative Commons Attribution License, which permits unrestricted use, distribution, and reproduction in any medium, provided the original work is properly cited.

To explore the failure precursors of hard rock, a series of triaxial loading and unloading experiments were carried out on sandstone sample using the acoustic emission systems. The extreme-point symmetric mode decomposition method (ESMD method) was used to denoise and reconstruct the AE data. The AE quiet period in Scheme I becomes much more obvious with the confining pressure increasing, which can be regarded as the precursor information of the sample failure under conventional triaxial compression. Unlike Scheme I, there are no obvious precursory characteristics before failure in Schemes II and III, and the count rate reaches the maximum at the peak point. When the stress ratio ranges from 0.8 to 1.0, the fractal values of acoustic emission can be used to investigate the failure precursors of samples at a lower confining pressure. When the time ratio is greater than 0.8 under higher confining pressures, the fractal values of sandstone samples under unloading paths are rapidly reduced, which can be used to predict rock failure at higher confining pressures.

## 1. Introduction

The rock material properties, various stress paths, and wall rock conditions are complex and diverse, severely restricting the study on failure precursors of rock materials. The deformation and failure behavior of rock are the process of the inner micro cracks initiation, propagation, and coalescence [1–5]. During this process, the strain energy is continuously released in the form of the elastic wave, which is referred to as the acoustic emission (AE). It is helpful to investigate the failure mechanism of rock materials to study the AE characteristics during the failure process and the relationship between the AE parameters and rock fracture [6–11].

Chmel and Shcherbakov [12] carried out experimental study on the AE characteristics of compression and dynamic fracture in granite, which contributes to assessing the relationship between events occurring under nonequilibrium conditions. Based on the biaxial compression tests, Baddari et al. [13] adopted electromagnetic radiation and acoustic emission to study the failure process of large rock samples, and the

results can provide an analysis platform for forecasting the dynamic disaster. Three triaxial compression tests on granite samples were carried out by Thompson et al. [14], and new observations of fracture nucleation were proposed according to AE monitoring. The results showed that the fracture nucleation in intact rock and the nucleation of dynamic instabilities in stick slip tests had similarity. The strength variation and AE features of skarn were investigated by Xu et al. [15] through uniaxial cyclic loading and unloading tests. The results showed that there is an apparent relative quiet stage of AE signals before failure. Zhang et al. [16] performed the uniaxial loading to research the AE characteristics of rock failure process, and the AE parameters such as cumulative AE events, AE energy release rate, and the  $b$ -value were used to investigate the precursory information of rock failure.

Existing AE studies are mainly concentrated on the relationship between stress or strain and AE parameters under a single stress path condition such as compression, tension, and shear. By contrast, there are fewer studies on the theoretical research of AE activity under a complex stress path.



FIGURE 1: Standard cylindrical sandstone samples used in this study.

In our paper, a series of triaxial loading and unloading experiments on sandstone samples were carried out under different stress conditions. The extreme-point symmetric mode decomposition method (ESMD method) was used to denoise and reconstruct the AE data, and the AE characteristics of sandstone samples under different stress paths were investigated. Based on the fractal theory, the influence of unloading paths on AE characteristics was quantified, which could be used to explore the failure precursors of rock and provide a theoretical basis for assessing and preventing the stress-induced stability of hard rock.

## 2. Test Method and Sample Preparation

**2.1. Sample Preparation.** The sandstone used in our study was collected from the Huainan coal mine in Anhui province, China. The results of X-ray diffraction (XRD) show that the minerals of this sandstone are 12.1% quartz, 10.9% K-feldspar, 38.7% plagioclase, 13.4% calcite, 12.7% dolomite, 2.8% hematite, and 9.4% clay minerals. The connected porosity and bulk density of the sandstone are 7.02% and 2613 kg/m<sup>3</sup>, respectively. All sandstone samples were cored from the same block of material to an actual diameter of 50 mm and length of 100 mm, as shown in Figure 1. The permissible error of end flatness is  $\pm 0.05$  mm, the diameter error is less than 0.3 mm, and the maximum deviation between the end face and axial line is not more than  $0.25^\circ$ . The machining precisions of all samples are in accordance with the demand of technical specifications.

**2.2. Testing Equipment and Procedure.** All experiments were conducted using an MTS 815 servo-controlled rock mechanics experimental system. The integral rigidity of the experiment framework is  $11.0 \times 10^9$  N/m, the maximum axial force is 4600 KN, the maximum lateral pressure is 140 MPa, and the sensitivity of servo valve is 290 Hz. The whole experimental process is controlled by a computer, allowing for automatic data acquisition and processing. Acoustic emissions were monitored with a 16-channel PCI-II system. The resonant frequency and operating frequency range were 500 kHz and 200~750 kHz, respectively, and the amplification of the preamplifier and threshold were set at 55 dB to improve signal to noise ratio. The sampling frequency and the sampling length were fixed at 500 kHz and 8192, respectively. To ensure three-dimensional position precision, 6 sensors were fixed on the outside of the triaxial pressure cell as a sensor matrix.

The type of the sensors was Nano30, of which the operating frequency is 100–400 kHz. The sensors were coated with Vaseline, a coupling agent, and fixed on the surface of the samples by plastic tapes. To ensure the coupling effect of the AE sensor with the sample, a pencil lead break (PLB) should be performed before the tests began (Figure 2).

The detailed testing schemes under different stress paths are shown as follows.

(1) *Conventional Triaxial Loading Tests (Scheme I).* The conventional triaxial tests were conducted under different confining pressures of 10, 20, 40, and 50 MPa. First, the confining pressure was loaded to the design value at a constant rate of 0.1 MPa/s, and the samples were put into a state of uniform hydrostatic stress. Second, the confining pressure remained unchanged, and the axial stress was loaded to the sandstone samples at a constant axial displacement rate of 0.001 mm/s until failure, ensuring that complete stress-strain curves would be obtained. The peak strength obtained through conventional triaxial tests can provide a basis for the determination of the unloading point in the unloading confining pressure tests.

(2) *Increasing Axial Pressure and Confining Pressure Unloading Tests (Scheme II).* First, the confining pressure was loaded to the design value (10, 20, 40, and 50 MPa). Second, the confining pressure remained unchanged, and the axial stress was loaded to 80% of the peak strength obtained from conventional triaxial tests. Then, the axial stress was loaded at a constant rate of 0.3 MPa/s, and the confining pressure was simultaneously unloaded at a constant rate of 0.5 MPa/s until failure.

(3) *Constant Axial Pressure and Confining Pressure Unloading Tests (Scheme III).* First, the confining pressure was loaded to the design value (10, 20, 40, and 50 MPa). Second, the confining pressure remained unchanged, and the axial stress was loaded to 80% of the peak strength obtained from conventional triaxial tests. Then, the axial stress remained unchanged, and the confining pressure was simultaneously unloaded at a constant rate of 0.5 MPa/s until failure.

## 3. Extreme-Point Symmetric Mode Decomposition Method (ESMD Method)

**3.1. Method Introduction.** The background noise inevitably mixes into the AE signals during data acquisition process. Even if the experiments are carried out in the relatively sealed laboratory, the servo valve adjustment also generates mechanical noise. The noise signals can interfere in the analysis of experimental data; thus the noise-suppressed processing of AE signals is the precondition of accurate quantitative analysis of rock failure process. In this study, the ESMD method was used to denoise and reconstruct the AE data.

The ESMD method is proposed to improve the Hilbert-Huang Transform (HHT) based on four prospects: (1) The sifting process is performed by means of several inner interpolating curves, which divides these methods into ESMD I, ESMD II, ESMD III, and so on; (2) the last residual

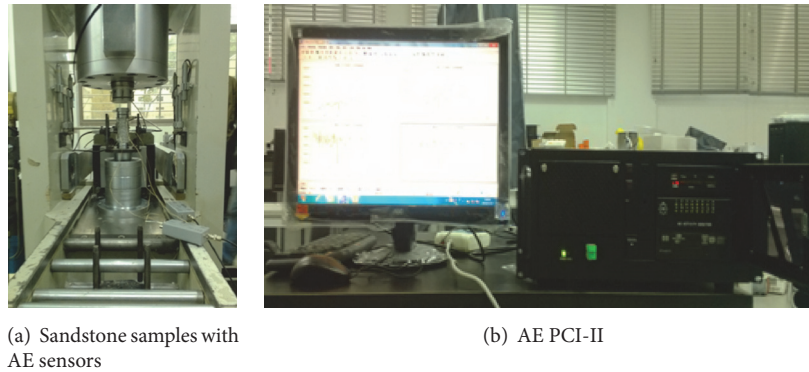


FIGURE 2: Sandstone samples in MTS 815 servo-controlled rock mechanics experimental system and AE PCI-II system.

is defined as an optimal curve possessing a certain number of extreme points, instead of general trend with at most one extreme point, which allows the optimal sifting times and decomposition; (3) the extreme-point symmetry is applied instead of the envelop symmetry; (4) the data-based direct interpolating approach is developed to compute the instantaneous frequency and amplitude. One advantage of the ESMD method is to determine an optimal global mean curve in an adaptive way which is better than the common least-square method and running-mean approach; another one is to determine the instantaneous frequency and amplitude in a direct way which is better than the Hilbert-spectrum method. These will improve the adaptive analysis of the data from many fields [17].

**3.2. Denoising Process of AE Signals.** The data decomposition of AE signals based on the ESMD can be carried out in three steps: (1) the data file named Variance\_II.sce was defined according to the data file regulations, and then AE signals such as data volume and time interval were input to this data file; (2) the file established in the first step operated through the Scilab platform, which uses the least-square method to optimize the residual mode, gives the optimum screening frequency of data, and determines the optimal global mean curve in an adaptive way; (3) the self-developed file (ESMD\_II.sce) operated, which can not only give the number of extreme points, but also acquire abundant information of AE data, including the trend chart, energy diagram, and spectrogram.

## 4. AE Characteristics of Sandstone Samples under Different Stress Paths

**4.1. AE Characteristics of Samples under Loading Conditions.** Figure 3 gives the curves of axial stress difference and ringing count rate with time during sandstone failure process under various confining pressures in Scheme I. At the early loading stage, the AE activity is relatively active, which comes from the closure of the initial fissure and holes. When entering into the plastic stage, the ringing count rate gradually increases, indicating that the new cracks begin to initiate in the samples. The volume expansion of samples due to the dilatation

effect appears upon reaching the expansion stress, and the AE signals are enhanced significantly. When the relatively large crack occurs inside the sample, the tips of the cracks generate the stress redistribution, which accompanies the energy dissipation. During this process, the energy release rate gradually slows down, and the AE parameters such as the ringing count rate decrease, that is, the AE quiet period. As shown in Table 1 and Figure 3, the AE quiet period becomes much more obvious with the confining pressure increasing, because the amount of new cracks is relatively less due to the restriction of higher confining pressure. The time of quiet period lasts from 20 s to 57 s with the confining pressure increasing from 10 MPa to 50 MPa, and the crack propagation process transits from generation oriented to coalescence oriented small cracks.

The stress and AE characteristics of sandstone samples during the deformation process under various confining pressures are shown in the following aspects: (1) the shear failure is the main failure mode of the samples under the conventional triaxial compression, which have the higher residual strengths; (2) the stress drops after the peak becomes less distinct with the confining pressure increasing, and the residual strengths gradually increase, which comes from the more obvious restraining effect of high confining pressure to the samples; (3) the AE signals almost exist during the whole process, which as a whole are stronger; (4) with the confining pressure increasing, the ringing count rate at the peak rises from 59 times per second to 145 times per second, indicating that the sandstone samples accumulated more energy before failure and released more energy at failure due to higher confining pressure; (5) the maximum ringing count rate appears after peak instead of peak positions, which also rises with the confining pressure increasing. The reason is that the samples have larger load bearing capacity at peak positions due to the confining pressure constraints, and the obvious friction slip of broken blocks takes place only when the stress falls to the residual stress. This is consistent with the characteristics of crack propagation and coalescence during the process of rock breaking simulated by [18].

The quiet period can be regarded as the precursor information of the sample failure under conventional triaxial compression. The confining pressure changes the stress state

TABLE I: Count rate of sandstone sample under various confining pressures in Scheme I.

Scheme I	Confining pressure/MPa	Axial stress difference at the peak/MPa	Time at the peak/s	Count rate at the peak/(times/s)	Time of quiet period/s	Maximum count rate/(times/s)
	10	118.1	78.3	59	20	96
	20	154.1	93.4	100	22	140
	40	199.9	134.2	118	33	134
	50	210.60	184.0	145	57	169

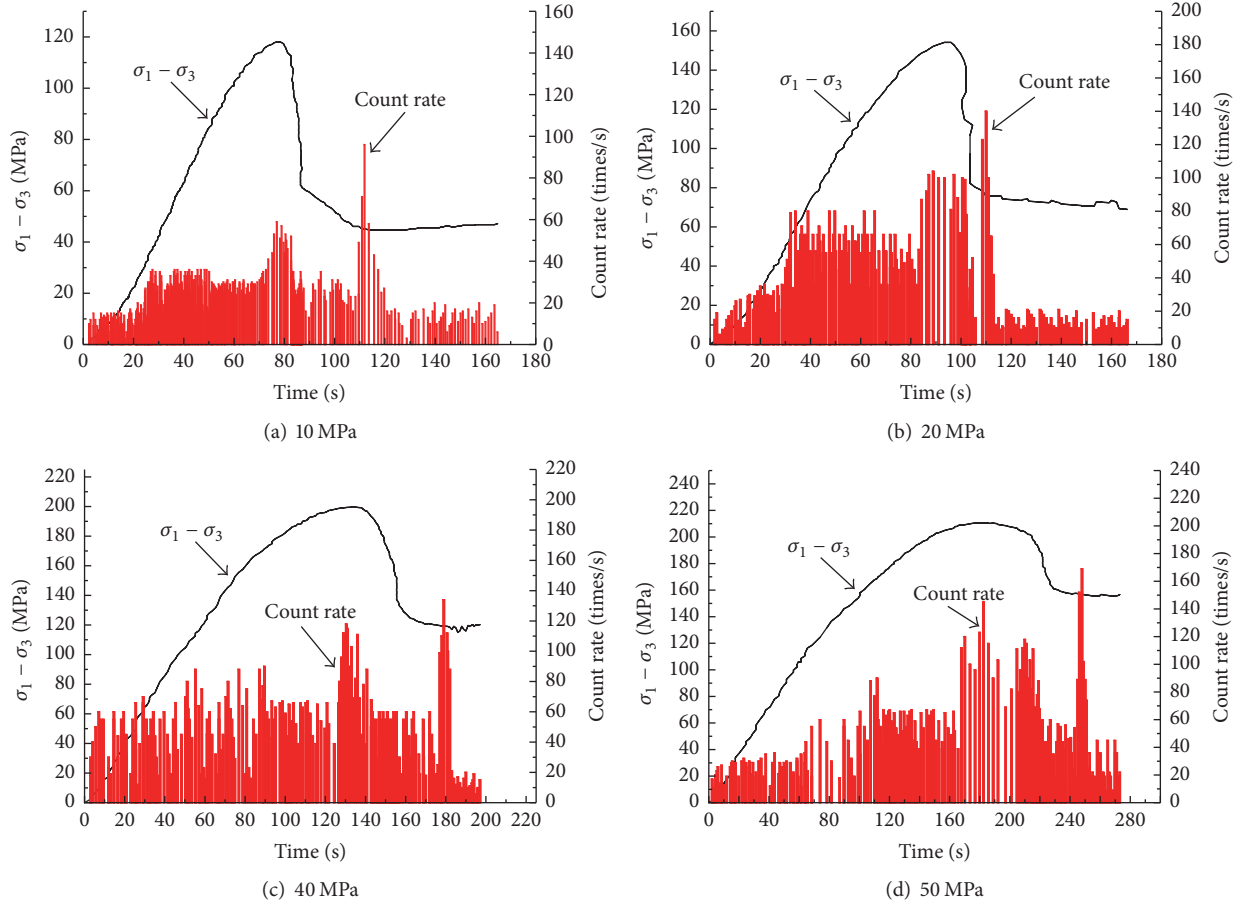


FIGURE 3: Curves of axial stress difference and count rate with time in sandstone failure process under various confining pressures in Scheme I.

of samples, prolongs the crack propagation process, delays the breaking moment, and increases the AE ringing count rate, which can provide the basis for identifying the failure point.

**4.2. AE Characteristics of Samples under Unloading Conditions.** Figures 4 and 5 show the curves of axial stress difference and count rate with time in sandstone failure process under various confining pressures in Scheme II and Scheme III, respectively. In Scheme II, as shown in Figure 4(a), the ringing rate gradually increases before unloading point. The results show that there exists an apparent turning point at the unloading point in the stress-strain curves and there is a sudden increase in the count rate. The sandstone sample is suddenly destroyed 10 s after unloading point, and the

count rate comes to the maximum value of 131 times/s at 74.9 s. As shown in Table 2, the count rate at the peak increases from 131 times/s to 296 times/s with the confining pressure increasing from 10 MPa to 50 MPa, indicating that the samples are destroyed more fiercely with the confining pressure increasing. As shown in Figure 4(b), the count rate-time curve emerges with a quiet period of 30 s before unloading. There are no new cracks to initiate in the samples, so they cannot be regarded as the precursor information of sample failure. When the sample begins to be unloaded, the count rate has a sudden increase, indicating that the new cracks occur in the samples. The count rate continues to increase with unloading until the axial stress difference at the peak rises to 148.03 MPa.

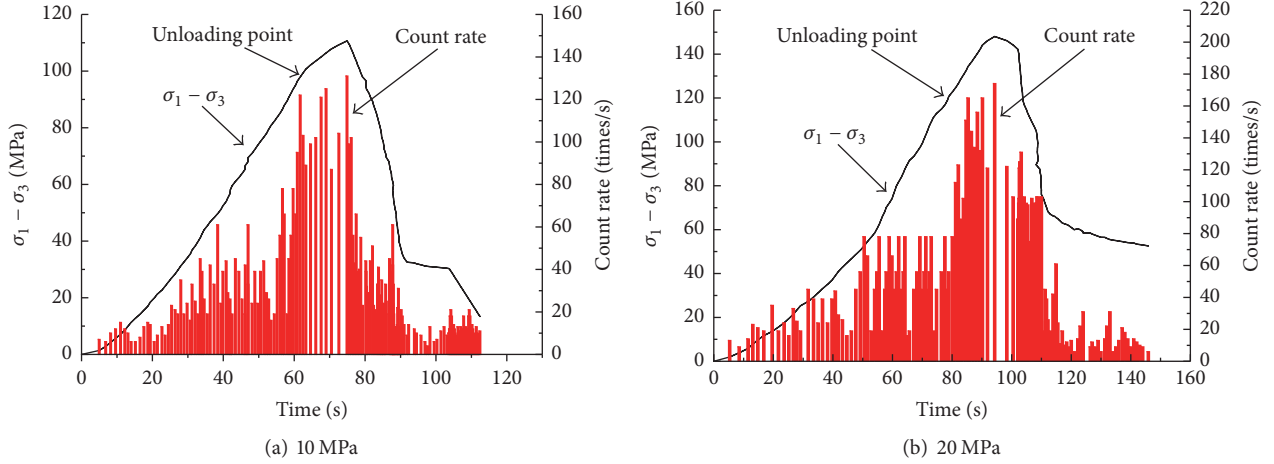


FIGURE 4: Curves of axial stress difference and count rate with time in sandstone failure process under various confining pressures in Scheme II.

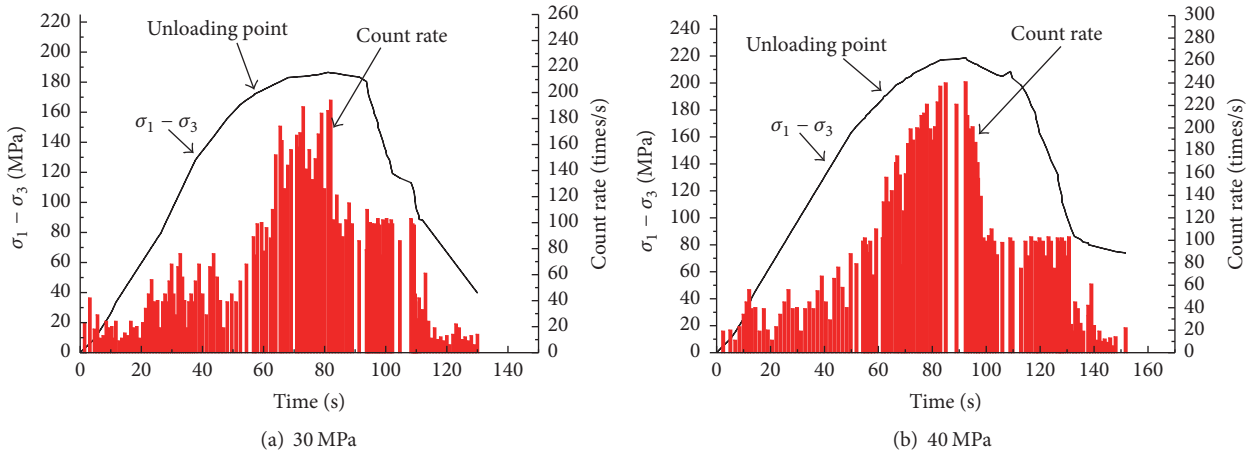


FIGURE 5: Curves of axial stress difference and count rate with time in sandstone failure process under various confining pressures in Scheme III.

The count rate of Scheme III has the same change rules as that of Scheme II. Unlike the Scheme I, there are no obvious precursory characteristics before failure in Schemes II and III, and the count rate reaches the maximum at failure.

## 5. Acoustic Emission Failure Precursors of Sandstone under Different Loading and Unloading Paths

**5.1. The Calculation of Fractal Dimension.** To further investigate the failure precursors of sandstone samples under different stress paths, it is necessary to quantify the characteristics of the acoustic emission during the whole failure process [19–22]. The acoustic emission count rate has a fractal feature in the time series analysis. The delay-coordinate method is adopted to reconstruct the space phase and fully reveal the information contained in the time series. Assuming that the relationship between dimension  $m$  of delay-coordinate and dimension  $d$  of the sequence is  $m \geq 2d + 1$ , the calculation process based on the G-P algorithm is as follows: the strength

sequence of acoustic emission of one sample in the process of the tests is studied, which corresponds to a sequence set with a capacity of  $n$ .

$$X = \{x_1, x_2, \dots, x_n\}. \quad (1)$$

Taking  $m$  paratactic numbers in the sequence as the first vector in  $m$ -dimensional space,

$$Y_1 = \{x_1, x_2, \dots, x_m\}. \quad (2)$$

Moving the  $m$  paratactic numbers back for one position and taking another  $m$  paratactic number in the sequence as the second vector in  $m$ -dimensional space,

$$Y_2 = \{x_2, x_3, \dots, x_{m+1}\}. \quad (3)$$

Then,  $N = n - m + 1$  vectors are formed. According to the Takens principle, the correlation dimension of the sequence is calculated. The correlation dimension is the cumulative

TABLE 2: Count rate of sandstone sample under various confining pressures in Schemes II and III.

Stress path	Confining pressure/MPa	Axial stress difference at the peak/MPa	Time at the peak/s	Count rate at the peak/(times/s)	Maximum count rate/(times/s)
Scheme II	10	110.67	74.9	131	131
	20	148.03	94.3	174	174
	40	186.03	122.6	211	211
	50	207.39	146.9	296	296
Scheme III	10	109.57	57.13	112	112
	20	152.31	72.3	159	159
	40	186.49	81.12	194	194
	50	218.74	92.4	241	241

distribution function  $W(r)$ , that is, the probability that the distance of two points is less than  $r$  in the space.

$$W(r) = \frac{1}{N^2} \cdot \sum_{i,j}^N u(r - |Y_i - Y_j|), \quad (4)$$

where  $u$  is the Heaviside function.

$$u(r - |Y_i - Y_j|) = \begin{cases} 1 & (u(r - |Y_i - Y_j|) \geq 0) \\ 0 & (u(r - |Y_i - Y_j|) < 0). \end{cases} \quad (5)$$

$|Y_i - Y_j|$  is the distance between  $Y_i$  and  $Y_j$ , and  $r$  is the measurement scale. The slope can be obtained based on of straight-line fitting of data point ( $\lg W(r)$ ,  $\lg r$ ):

$$D(m) = \frac{\lg W(r)}{\lg r}. \quad (6)$$

This is the fractal feature of the strength sequence of acoustic emission within the measurement scale. The line slope  $D$  gradually converges to a stable value with the dimension  $m$  increasing; otherwise, the sequence set is a random sequence. When the strength sequence of acoustic emission is constant, the smaller the fractal dimensions, the narrower the distribution of strength in the sequence, and the strength values are close.

*5.2. Variation of Fractal Dimension with the Stress Ratio.* Programs are made to calculate the fractal dimensions of acoustic emission of sandstone samples during the failure process. Rock samples usually fail as the stress is loaded to the peak value of compressive strength. Thus, using the peak stress difference as a baseline, the stress ratio is defined as the ratio of axial stress difference and peak stress difference. The maximum of the stress ratio is 1.

Table 3 gives the fractal values of AE of sandstone samples under different stress ratios, and Figure 6 shows the curves of the fractal values. As shown in Figures 6(a) and 6(b), when the stress ratio ranges from 0.2 to 0.4, the sandstone samples are at the stage of transferring from initial compression to elastic deformation. Under the influence of confining pressure, the growth rate of fractal values is slow, which even shows a decrease. When the stress ratio ranges from 0.4 to 0.8, the cracks in the samples under conventional triaxial

loading tests propagate slowly, and the fractal values first increase and then decrease. The samples under unloading conditions enter into the plastic deformation stage from the elastic deformation stage; thus, the crack growth rates increase obviously and the fractal values first decrease and then increase. When the stress ratio ranges from 0.8 to 1.0, the stress of the samples approaches the peak value and the cracks in the samples expand and communicate into a shear band. The formation of the shear band induces the brittle failure of the samples, and the fractal values under different stress paths decrease rapidly. The acoustic emission at this stage can be used to investigate the failure precursors of the samples under different stress paths. By contrast, the decreasing rate of the fractal values of Scheme II is the highest, followed by that of Scheme III. The decreasing rate of Scheme I is the lowest.

When the confining pressure increases, as shown in Figures 6(c) and 6(d), the fractal values of the sandstone samples show different changing tendencies. As the stress ratio ranges from 0.4 to 0.8, the initiation, propagation, and coalescence of cracks in the sandstone samples slow down when subjected to the high confining pressure. The variation trend of the fractal values of the samples under unloading conditions is similar to that under conventional triaxial loading conditions; that is, they first increase and then decrease. When the stress ratio ranges from 0.8 to 1.0, the increase in the confining pressure not only reduces the difference in the AE characteristics between the different stress ratios, but also changes the decreasing regularity of the fractal values of the samples before failure. Therefore, the relationship between AE characteristics and stress ratios is not obvious when the confining pressure is higher (40 MPa or 50 MPa).

*5.3. Variation of Fractal Dimension with the Time Ratio.* Taking the failure time as a benchmark, the time ratio is designed as the loading time and the failure time. The maximum of the time ratio is 1. Table 4 gives the fractal values of AE for sandstone samples under different time ratios, and Figure 7 shows the curves of the fractal values. According to Figures 7(a) and 7(b), it is found that when the time ratio ranges from 0.4 to 0.8, the fractal values of the sample under different stress paths first decrease and then increase. The variation trend of the AE characteristics is not obvious when the time ratio is greater than 0.8. As shown in Figures 7(c) and 7(d), the fractal values of sandstone samples in Scheme I under

TABLE 3: Fractal values of AE of samples under different stress ratios.

Stress ratio	Scheme I					Scheme II					Scheme III					
	10 MPa	20 MPa	40 MPa	50 MPa	10 MPa	20 MPa	40 MPa	50 MPa	10 MPa	20 MPa	40 MPa	50 MPa	10 MPa	20 MPa	40 MPa	50 MPa
0.2	1.51	0.90	1.41	1.31	1.21	0.67	0.67	1.26	0.69	0.67	0.67	1.26	0.69	0.73	0.83	0.56
0.4	1.34	0.96	1.21	1.23	1.26	0.69	0.98	0.98	0.63	0.69	0.98	0.98	0.63	0.62	0.92	0.98
0.6	1.38	1.01	1.29	1.34	1.03	0.61	1.19	1.19	0.51	0.63	1.19	1.19	0.51	0.48	0.90	1.12
0.8	1.12	0.79	1.23	1.31	1.19	0.85	1.16	1.16	0.72	0.85	1.16	1.16	0.72	0.54	0.83	1.08
1.0	0.91	0.69	1.51	1.40	0.62	0.30	1.20	1.20	0.31	0.31	1.20	1.20	0.31	0.41	0.97	0.98

TABLE 4: Fractal values of AE of samples under different time ratios.

Time ratio	Scheme I				Scheme II				Scheme III			
	10 MPa	20 MPa	40 MPa	50 MPa	10 MPa	20 MPa	40 MPa	50 MPa	10 MPa	20 MPa	40 MPa	50 MPa
0.2	1.33	0.96	1.34	1.34	1.21	0.71	0.69	1.10	0.79	0.69	0.82	0.58
0.4	1.26	1.10	1.36	1.30	1.24	0.66	0.69	1.21	0.56	0.51	0.95	1.11
0.6	1.16	0.78	1.39	1.41	1.13	0.16	0.66	1.06	0.51	0.43	0.87	1.02
0.8	1.19	0.76	1.32	1.41	1.34	0.26	0.86	0.78	0.64	0.64	0.91	0.95
1.0	1.24	0.51	1.34	1.40	1.12	0.69	0.30	0.31	0.66	0.11	0.36	0.08

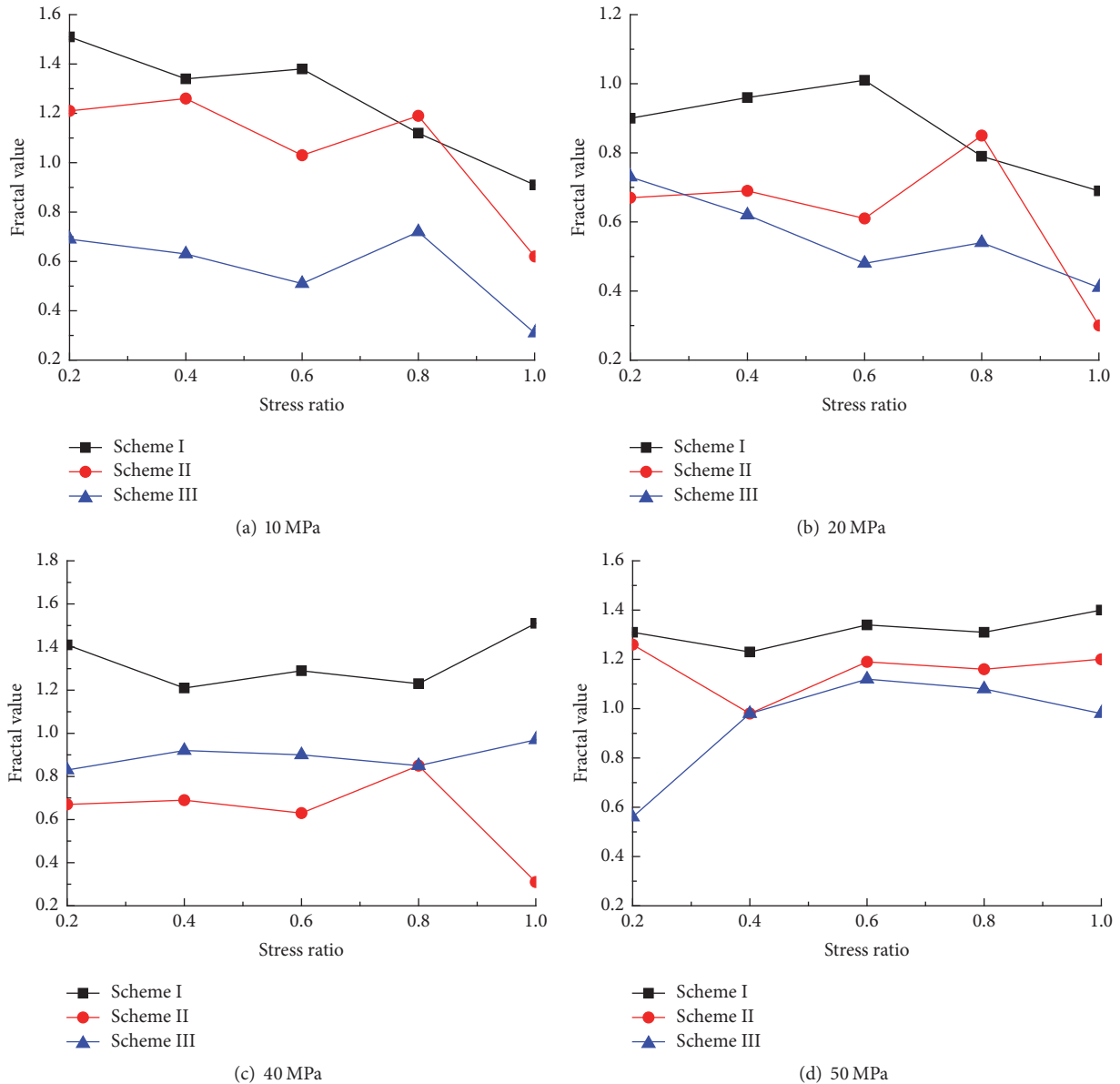


FIGURE 6: Fractal values of AE of sandstone samples under different stress paths (stress ratio).

different time ratios show little change. When the time ratio is greater than 0.8, the fractal values of sandstone samples under unloading paths are rapidly reduced, which indicates that the fractal value changing with the time ratio can be used to predict rock failure at higher confining pressures.

The failure of rock mass is an energy dissipation process, and the fractal law of the laboratory sample is united with that of engineering rock mass. Theoretically, the fractal dimension of acoustic emission is the efficacious index that evaluates the rock mass stability, and the lowest level of the fractal dimension means that the rock engineering disaster is a strong possibility. In engineering applications, the microseismic (MS) monitoring system can be established to carry out the real time monitoring to the deformation and failure of rock mass, and the AE signals obtained from the MS monitoring

can be used to predict the instability of rock mass. In addition, the critical value of the AE signals needs to be studied further.

## 6. Conclusion

In this paper, a series of triaxial loading and unloading tests of sandstone samples were carried out under different stress conditions. The AE characteristics of sandstone samples under different stress paths were investigated. Based on the fractal theory, the influence of loading and unloading paths on AE characteristics was quantified. The results drawn from the experiments can provide a theoretical basis for assessing the stress-induced stability of hard rock.

(1) The AE quiet period in Scheme I becomes much more obvious with the confining pressure increasing, because the

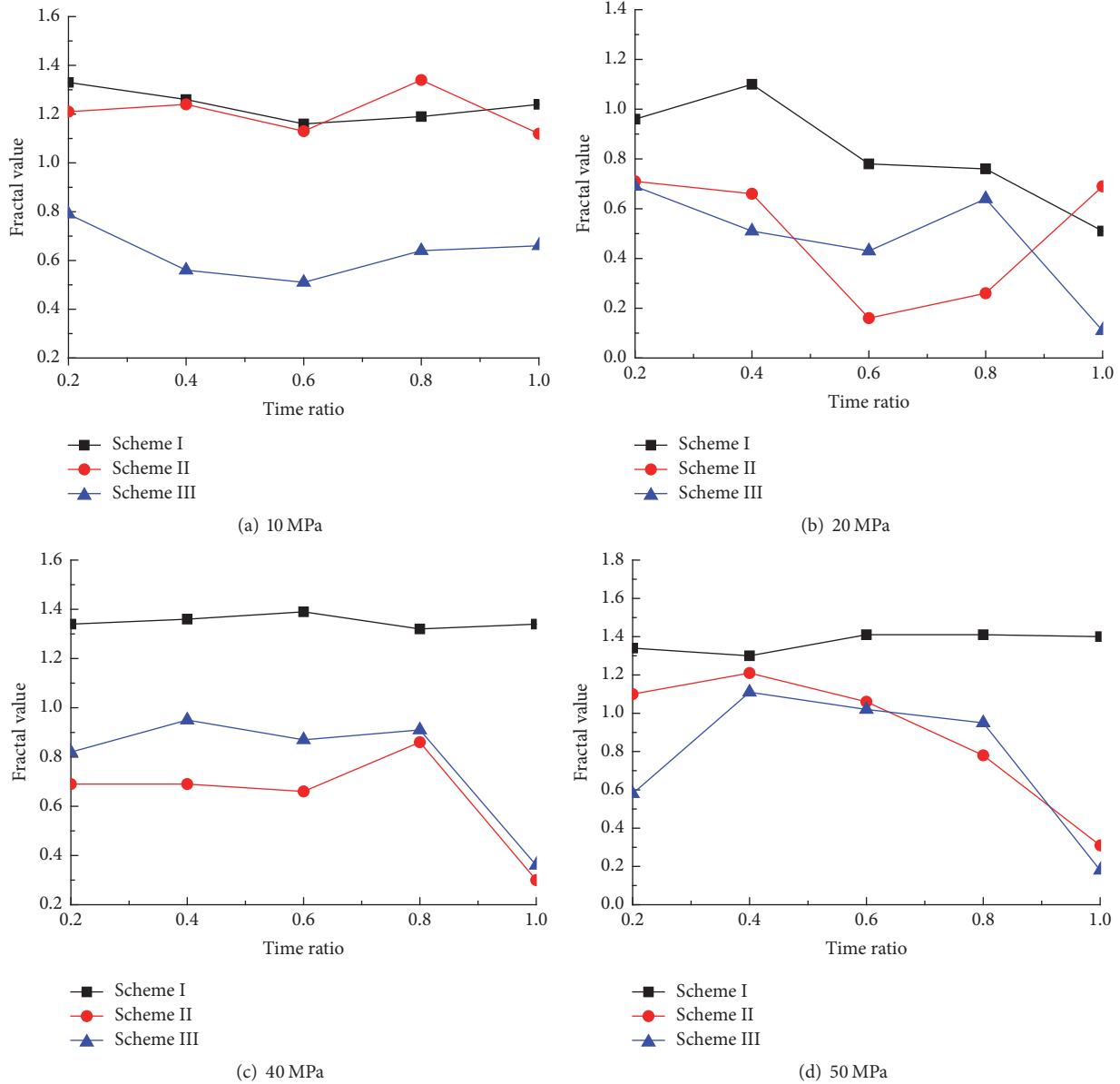


FIGURE 7: Fractal values of AE of sandstone samples under different stress paths (time ratio).

amount of new cracks is relatively less due to the restriction of higher confining pressure. The time of quiet period lasts from 20 s to 57 s with the confining pressure increasing from 10 MPa to 50 MPa, and the crack propagation process transits from generation oriented to coalescence oriented small cracks. The AE quiet period can be regarded as the precursor information of the sample failure under conventional triaxial compression. The maximum ringing count rate appears after peak instead of peak positions, which also rises with the confining pressure increasing. The reason is that the samples have larger load bearing capacity at peak positions due to the confining pressure constraints, and the obvious friction slip of broken blocks takes place only when the stress falls to the residual stress.

(2) The ringing count rate of Scheme III has the same change rules as that of Scheme II. Unlike Scheme I, there are no obvious precursory characteristics before failure in Schemes II and III, and the ringing count rate reaches the maximum at the peak point.

(3) When the stress ratio ranged from 0.8 to 1.0 under lower confining pressure, the formation of a shear band induced the brittle failure of the samples, and the fractal values under different stress paths decreased rapidly. The fractal values of acoustic emission at this stage can be used to investigate the failure precursors of samples under different stress paths. By contrast, the decreasing rate of the fractal values of Scheme II was the highest, followed by that of Scheme III, and the decreasing rate of Scheme I was the

lowest. However, the relationship between AE characteristics and stress ratios was not obvious when the confining pressure was higher (40 MPa or 50 MPa).

(4) When the time ratio was greater than 0.8 under higher confining pressures, the fractal values of sandstone samples under the unloading paths were rapidly reduced, which indicated that the fractal value changing with the time ratio can be used to predict rock failure at higher confining pressures.

## Conflicts of Interest

The authors declare that there are no conflicts of interest regarding the publication of this paper.

## Acknowledgments

This work was supported by China Postdoctoral Science Foundation (Grant no. 2017M611676), Jiangsu Province Postdoctoral Research Funding Scheme (Grant no. 1701091B), the National Natural Science Foundation of China (Grant no. 41630638), and the National Key Basic Research Program of China ("973" Program) (Grant no. 2015CB057901).

## References

- [1] D. A. Lockner, J. D. Byerlee, V. Kuksenko, A. Ponomarev, and A. Sidorin, "Quasi-static fault growth and shear fracture energy in granite," *Nature*, vol. 350, no. 6313, pp. 39–42, 1991.
- [2] J. F. Shao and R. Khazraei, "A continuum damage mechanics approach for time independent and dependent behaviour of brittle rock," *Mechanics Research Communications*, vol. 23, no. 3, pp. 257–265, 1996.
- [3] M. S. Diederichs, "Manuel rocha medal recipient rock fracture and collapse under low confinement conditions," *Rock Mechanics and Rock Engineering*, vol. 36, no. 5, pp. 339–381, 2003.
- [4] Y. Fialko, D. Sandwell, D. Agnew, M. Simons, P. Shearer, and B. Minster, "Deformation on nearby faults induced by the 1999 Hector Mine earthquake," *Science*, vol. 297, no. 5588, pp. 1858–1862, 2002.
- [5] F. Rojat, V. Labiouse, P. K. Kaiser, and F. Descoedres, "Brittle rock failure in the steg lateral adit of the lötschberg base tunnel," *Rock Mechanics and Rock Engineering*, vol. 42, no. 2, pp. 341–359, 2009.
- [6] V. B. Smirnov, A. V. Ponomarev, and A. D. Zavyalov, "Acoustic structure in rock samples and the seismic process," *Physics of the Solid Earth*, vol. 31, pp. 38–58, 1995.
- [7] A. Zang, F. C. Wagner, S. Stanchits, G. Dresen, R. Andresen, and M. A. Haidekker, "Source analysis of acoustic emissions in Aue granite cores under symmetric and asymmetric compressive loads," *Geophysical Journal International*, vol. 135, no. 3, pp. 1113–1130, 1998.
- [8] M. Cai, P. K. Kaiser, and C. D. Martin, "Quantification of rock mass damage in underground excavations from microseismic event monitoring," *International Journal of Rock Mechanics and Mining Sciences*, vol. 38, no. 8, pp. 1135–1145, 2001.
- [9] S. Colombo, I. G. Main, and M. C. Forde, "Assessing damage of reinforced concrete beam using 'b-value' analysis of acoustic emission signals," *Journal of Materials in Civil Engineering*, vol. 15, no. 3, pp. 280–286, 2003.
- [10] A. Schiavi, G. Niccolini, P. Tarizzo, A. Carpinteri, G. Lacidogna, and A. Manuello, "Acoustic emissions at high and low frequencies during compression tests in brittle materials," *Strain Journal*, vol. 47, no. 2, pp. 105–110, 2011.
- [11] Q. S. Liu, J. Xu, X. W. Liu, J. Jiang, and B. Liu, "The role of flaws on crack growth in rock-like material assessed by AE technique," *International Journal of Fracture*, vol. 193, no. 2, pp. 99–115, 2015.
- [12] A. Chmel and I. Shcherbakov, "A comparative acoustic emission study of compression and impact fracture in granite," *International Journal of Rock Mechanics and Mining Sciences*, vol. 64, pp. 56–59, 2013.
- [13] K. Baddari, A. D. Frolov, V. Tourtchine, and F. Rahmoune, "An integrated study of the dynamics of electromagnetic and acoustic regimes during failure of complex macrosystems using rock blocks," *Rock Mechanics and Rock Engineering*, vol. 44, no. 3, pp. 269–280, 2011.
- [14] B. D. Thompson, R. P. Young, and D. A. Lockner, "Fracture in Westerly granite under AE feedback and constant strain rate loading: nucleation, quasi-static propagation, and the transition to unstable fracture propagation," *Pure and Applied Geophysics*, vol. 163, no. 5-6, pp. 995–1019, 2006.
- [15] S. C. Xu, X. T. Feng, and B. R. Chen, "Acoustic emission characteristics and mechanical behavior of skarn under uniaxial cyclic loading and unloading," *Controlling Seismic Hazard and Sustainable Development of Deep Mines*, vol. 1, 2009.
- [16] S. Zhang, J. Liu, and C. Shi, "Study on precursory characteristics of rock failure based on acoustic emission experiment," *Metal Mine*, 2008.
- [17] J.-L. Wang and Z.-J. Li, "Extreme-point symmetric mode decomposition method for data analysis," *Advances in Adaptive Data Analysis (AADA)*, vol. 5, no. 3, pp. 135–170, 2013.
- [18] L. A. M. Camones, E. do Amaral Vargas, R. P. de Figueiredo, and R. Q. Velloso, "Application of the discrete element method for modeling of rock crack propagation and coalescence in the step-path failure mechanism," *Engineering Geology*, vol. 153, no. 2, pp. 80–94, 2013.
- [19] S. Yuyama, T. Okamoto, M. Shigeishi, and M. Ohtsu, "Quantitative evaluation and visualization of cracking process in reinforced concrete by a moment tensor analysis of acoustic emission," *Materials Evaluation*, vol. 53, no. 6, pp. 751–752, 1995.
- [20] T. Shiotani, M. Ohtsu, and K. Ikeda, "Detection and evaluation of AE waves due to rock deformation," *Construction and Building Materials*, vol. 15, no. 5-6, pp. 235–246, 2001.
- [21] D. G. Aggelis, S. Verbruggen, E. Tsangouri, T. Tysmans, and D. Van Hemelrijck, "Characterization of mechanical performance of concrete beams with external reinforcement by acoustic emission and digital image correlation," *Construction and Building Materials*, vol. 47, pp. 1037–1045, 2013.
- [22] G. Ma and H. Li, "Acoustic emission monitoring and damage assessment of FRP-strengthened reinforced concrete columns under cyclic loading," *Construction and Building Materials*, vol. 144, pp. 86–98, 2017.

## Research Article

# Analysis of the Impacts of Bearing on Vibration Characteristics of Rotor

Peiji Yang,<sup>1,2</sup> Qi Yuan,<sup>1,3</sup> Chao Huang,<sup>1,3</sup> Yafeng Zhou,<sup>2</sup> Hongliang Li,<sup>2</sup> and Yu Zhou<sup>2</sup>

<sup>1</sup>School of Energy and Power Engineering, Xi'an Jiaotong University, Xi'an 710049, China

<sup>2</sup>Xi'an Shaangu Power Co., Ltd., Xi'an, China

<sup>3</sup>Shaanxi Engineering Laboratory of Turbomachinery and Power Equipment, Xi'an, China

Correspondence should be addressed to Qi Yuan; [qyuan@xjtu.edu.cn](mailto:qyuan@xjtu.edu.cn)

Received 23 July 2017; Accepted 1 November 2017; Published 12 December 2017

Academic Editor: Sandris Ručevskis

Copyright © 2017 Peiji Yang et al. This is an open access article distributed under the Creative Commons Attribution License, which permits unrestricted use, distribution, and reproduction in any medium, provided the original work is properly cited.

Aiming at a Top Gas Recovery Turbine Unit (TRT) with double support rotor and the extending disk end, theoretical and experimental analysis about influence of cylindrical bearing and four-lobe bearing on vibration of TRT rotor system are conducted in this paper. The results indicate that vibration of the rotor supported by cylindrical bearing is more stable than that supported by four-lobe bearing at the driving end (DE) and the nondriving end (NDE). The amplitude of rotor is supported by both of these types of bearing increases as the speed increases at the NDE, while the amplitude of the DE remains unchanged. Comparing with the result of theoretical analysis, the practical test results are more consistent with the theoretical response analysis conducted by applying unbalanced mass at the extending disk end. This paper presents an analysis method of the critical characteristics of a double support rotor system with the extending disk end and provides reference value for dealing with vibration fault of double support rotor system with the extending disk end.

## 1. Introduction

The vibration problems of the rotor system within rotating machinery are an important safety issue in engineering. With the development of industry, more complex rotor structure and higher operating parameters (high rotational speed, large flow rate, high operating pressure, etc.) will bring more challenges for the vibration problems of rotor system. Since Jeffcott discovered the phenomenon that rotor will automatically center after exceeding the critical state in 1919 which laid the foundation of the theory of rotating machinery operating in high rotational speed [1], the research of vibration problem evolves and matures continually. The research of dynamic characteristics of rotor system [2, 3], dynamic balancing technology [4], and vibration control [5] which were involved in the vibration issue also gets continuous improvement and development in the modeling, calculation methods, technology, and so on. In addition to the study of rotor structure, the bearing-based rotor dynamics research is also the main field of the study. The effects of different structure parameters [6], operating parameters [7],

and oil parameters [8] of the bearing on the vibration characteristics of the rotor are obvious, and this research provides the basis for the analysis and processing of current vibration problem. Although the relevant theory tends to be matured and there are specific researches [6] about the impacts of bearing support characteristics on the dynamic characteristics of shaft, the impact of different types of bearing on the rotor's vibration characteristics is still not very clear. Related research is rare due to the restriction of some conditions.

In this paper, the dynamic characteristics of a double support rotor with extending disk end in a Top Gas Recovery Turbine Unit (TRT) is analyzed and tested to study the impacts of bearing on vibration characteristics of rotor.

## 2. Theoretical Basis of Rotor System Dynamics Model

The analysis of TRT rotor system dynamic model is the same as the classic finite element analysis method of multidisc rotor system. Through the analysis of the axial discs, shaft section,

TABLE 1: The structural and operating parameters of the four-lobe bearing.

Structural parameters	Value	Operating parameters	Value
Bearing diameter/mm	180	Fulcrum coefficient	0.5
Bearing width/mm	150	The type of oil	L-TSA46
Gap ratio/%	1.5	Preload	0.892
Cornerite of pad/°	71	Load/N	20210/21530

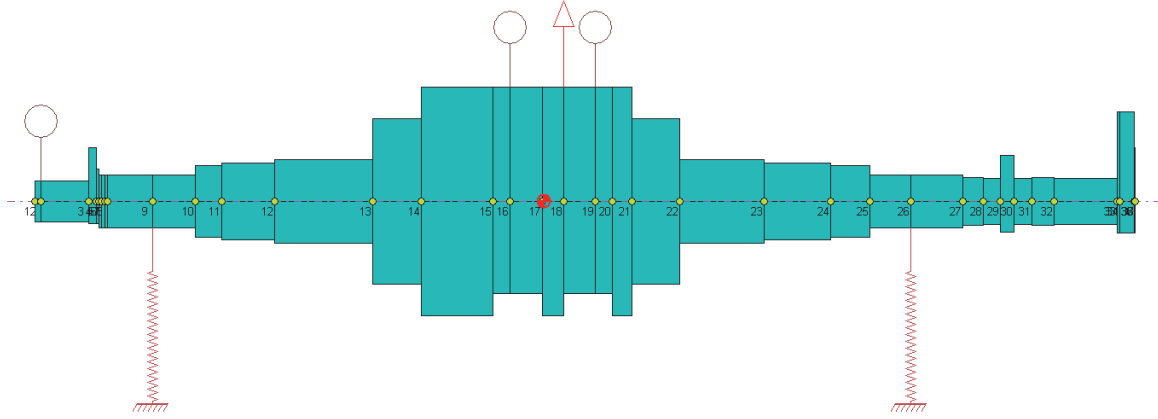


FIGURE 1: TRT rotor model.

and bearing seat, the relationship between node force and node displacement is established, combining the equation of motion of each unit. Finally, the motion differential equation of system with the node displacement as generalized coordinates can be obtained. Thus converting the problem into a rotor vibration problem with finite degree of freedom, the critical speed of the rotor can be obtained by solving a set of linear algebraic equations [9].

For a rotor system with  $N$  nodes which consists of  $N - 1$  shaft segments, the equations of motion of the rotor system can be obtained by integrating the equations of motion of each disc and shaft segment. It can be written as

$$\begin{aligned} [M_1] \{\ddot{U}_1\} + \Omega [J_1] \{U_2\} + [K_1] \{U_1\} &= \{Q_1\}, \\ [M_2] \{\ddot{U}_2\} + \Omega [J_2] \{U_1\} + [K_2] \{U_2\} &= \{Q_2\}, \end{aligned} \quad (1)$$

where the overall mass matrix  $[M_1]$ , rotation matrix  $\Omega [J_1]$ , and stiffness matrix  $[K_1]$  are all  $2N \times 2N$  order symmetric matrixes.  $U_1$  and  $U_2$  are the displacement vectors of the system.  $\{Q_1\}$  and  $\{Q_2\}$  are the corresponding generalized forces.

TRT is a typical double support rotor system with extended discs whose impeller and hub are located between the two bearings. The free end is fitted with a gear plate for turning the rotor at start-up. The rotor model is shown in Figure 1. In this paper, the commercial software DyRoBes is used to establish the TRT rotor dynamic model, and the

structural components such as gimbal, tachometer disc, and gear plate, are substituted by the equivalent stiffness of the shaft. As for the blade, it is replaced by additional mass because of its uniform distribution on the spindle.

### 3. Theoretical Analysis of the Dynamics of TRT Rotor-Bearing System

**3.1. Four-Lobe Bearing-Rotor Dynamics.** The working speed of the TRT is  $3000 \text{ r}\cdot\text{min}^{-1}$  and its original bearing is four-lobe bearing. The structural parameters and operating parameters of the bearing are shown in Table 1.

The results of eigenvalue analysis of four-lobe bearing-rotor system are shown in Figure 2. As can be seen from Figure 2, the response in the middle and the extending end (free end) of the rotor is greater than other positions. According to the rules of typical vibration mode of double support rotor system in API617 and engineering experiences, it is enough to do the unbalance response analysis which is applied to the middle position for the expander. However, it is necessary to apply unbalanced mass at the cantilever end for response analysis. The results are shown in Figures 3(a) and 3(b).

The bode charts of the two bearings of the rotor which can be obtained by applying unbalance of  $14.93 \text{ kg}\cdot\text{mm}$  at the middle of the rotor are shown in Figure 3(a). It can be seen from the figure that the horizontal and vertical critical speed in the DE (driving end) are  $3420 \text{ r}\cdot\text{min}^{-1}$  and  $3300 \text{ r}\cdot\text{min}^{-1}$ ,

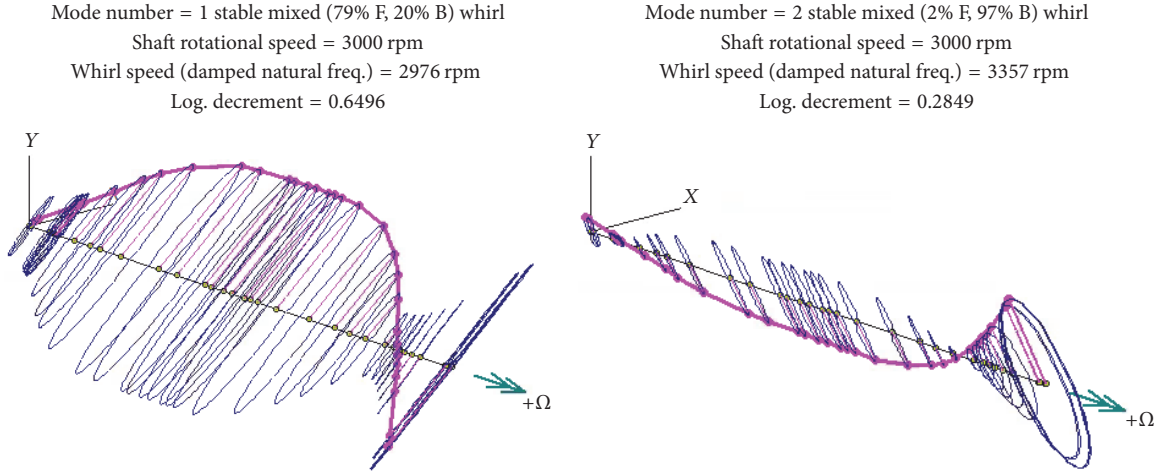


FIGURE 2: Modal analysis of four-lobe bearing-rotor system.

respectively, the NDEs (non-driving end) are  $3420 \text{ r}\cdot\text{min}^{-1}$  and  $3300 \text{ r}\cdot\text{min}^{-1}$ , respectively, and the avoidance rate is above 11% to meet the design requirements. There is a vibration peak in horizontal direction at  $3000 \text{ r}\cdot\text{min}^{-1}$  which coincides with the working speed.

The bode charts of the two bearings of the rotor which can be obtained by applying unbalance of  $14.93 \text{ kg}\cdot\text{mm}$  at the cantilever end of the rotor are shown in Figure 3(b). It can be seen from the figure that the horizontal and vertical critical speed of the DE-bearing and NDE-bearing of the four-lobe bearing-rotor system are  $3000 \text{ r}\cdot\text{min}^{-1}$  and  $4500 \text{ r}\cdot\text{min}^{-1}$ , respectively.

**3.2. Cylindrical Bearing-Rotor Dynamics.** After systematically analysis of the various structures and parameters of tilting pad bearing, elliptical bearing, and cylindrical journal bearing, it can be found that the response characteristics of the rotor system supported by cylindrical bearing are the best. The structural parameters of the cylindrical bearing are shown in Table 2. The results which can be obtained by applying eigenvalue analysis and unbalanced response analysis to the rotor system supported by cylindrical bearing are shown in Figures 4 and 5, respectively. It can be seen from Figure 4 that the first-order modal shows the first-order bending vibration, and the second-order mode is taper. Similarly, the response analyses with unbalanced mass applied in the middle and the extending end of rotor are carried out, respectively. It can be seen from Figure 5(a) that the horizontal and vertical critical speed in the DE-bearing are  $3420 \text{ r}\cdot\text{min}^{-1}$  and  $3300 \text{ r}\cdot\text{min}^{-1}$ , respectively; the NDE-bearings are  $3420 \text{ r}\cdot\text{min}^{-1}$  and  $3300 \text{ r}\cdot\text{min}^{-1}$ , respectively; the avoidance rate is above 16% to meet the design requirements. From Figure 5(b), it can be seen that the horizontal and vertical critical speed of the DE-bearing are  $4000 \text{ r}\cdot\text{min}^{-1}$  which is the same as the NDE-bearings. For the cylindrical bearing, the process of acceleration is stable and there is no vibration peak existing near the working speed and the magnification factor is smaller, which makes the characteristics of the rotor system supported by cylindrical bearing better.

TABLE 2: The structural and operating parameters of the cylindrical bearing.

Parameters	Value
Bearing diameter/mm	180
Gap ratio/%	1.5
Bearing width/mm	135

## 4. Experimental Study on the Effects of Different Bearings on Rotor Vibration

**4.1. Test Rig.** The test of this paper is for a real energy recovery turbine unit, and it was carried out by conducting a trial run in a table driven by a  $3200 \text{ kW}$  motor. Through the variable speed fluid coupling and gearbox, the power is transmitted to the TRT device to realize the control of speed and force. Each device including TRT, gear case, and motor carries out bearing pad temperature monitoring and shaft's vibration monitoring. At the same time, the inlet and outlet temperature of lubricating oil are tested and these monitoring data are fed back to the control platform by converting into electrical signals. The specific test system is no longer detailed. The test object of this paper is a TRT unit and the vibration of rotor supported by four-lobe bearing and cylindrical bearing is tested separately. The temperature of the bearing and the temperature of the lubricating oil at the inlet and outlet will not be presented in this paper. The bearing temperature test rig and the installation of vibration and speed probe are shown in Figure 6; the physical photos of two kinds of bearings are shown in Figure 7; the parameters of the bearing are shown in Tables 1 and 2.

**4.2. Results of Vibration Test.** The vibration tests of four-lobe bearing and cylindrical bearing are carried out, respectively, under the condition of speed-up, operation, and shutdown. The test results are shown in Figures 8–10. Figure 8 shows the vibrational trend of the rotor supported by four-lobe bearings, Figure 9 shows the vibrational trend of the rotor

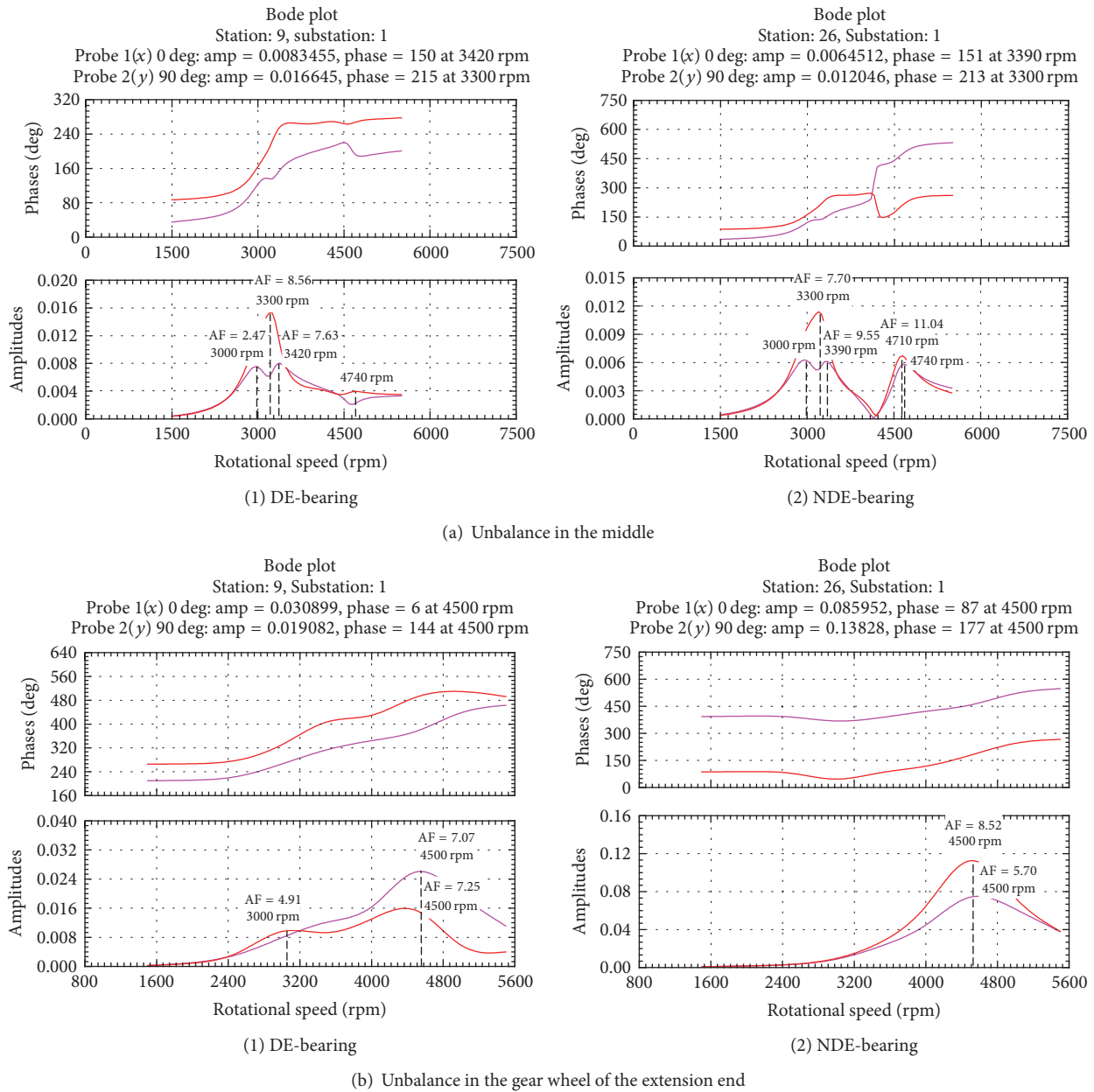


FIGURE 3: The bode charts of unbalanced response of four-lobe bearing.

supported by cylindrical bearings, and Figure 10 shows the comparison of these two types of bearings operating at the same speed.

It can be seen from Figure 8 that the vibration at the DE of the rotor supported by the four-lobe bearings is stable. The amplitude is maintained at about  $13 \mu\text{m}$ , but there is a vibration catastrophe at  $2660 \text{ r}\cdot\text{min}^{-1}$ . However the amplitude at the NDE increases as the speed increases and reaches the maximum which is nearly  $30 \mu\text{m}$  at  $3000 \text{ r}\cdot\text{min}^{-1}$ . Besides, there is a vibration peak at the speed of  $2240 \text{ r}\cdot\text{min}^{-1}$ .

As for the cylindrical bearing, it can be seen from Figure 9 that the vibrational trend of the DE-bearing is stable, and the amplitude is maintained at about  $10 \mu\text{m}$ . However the amplitude at DE increases as the speed increases and

reaches the maximum which is nearly  $30 \mu\text{m}$  at  $3000 \text{ r}\cdot\text{min}^{-1}$ . Comparing with the four-lobe bearing, there is no vibration catastrophe of the rotor supported by cylindrical bearing in the process of acceleration and deceleration.

From Figure 10, it can be seen that the vibration characteristics of the rotor supported by cylindrical bearing are better than four-lobe bearing at the driving end (DE) and nondriving end (NDE). The amplitude at NDE supported by the circular bearing is  $10.5 \mu\text{m}$  lower than that supported by the four-lobe bearing at the same speed, while the amplitude at DE is less than  $8 \mu\text{m}$ .

4.3. Analysis on Test Results. The vibration characteristics of the rotor supported by the cylindrical bearing are better

Mode number = 1 stable forward precession  
 Shaft rotational speed = 3000 rpm  
 Whirl speed (damped natural freq.) = 2114 rpm  
 Log. decrement = 0.7584

Mode number = 1 stable forward precession  
 Shaft rotational speed = 3000 rpm  
 Whirl speed (damped natural freq.) = 2305 rpm  
 Log. decrement = 4.1396

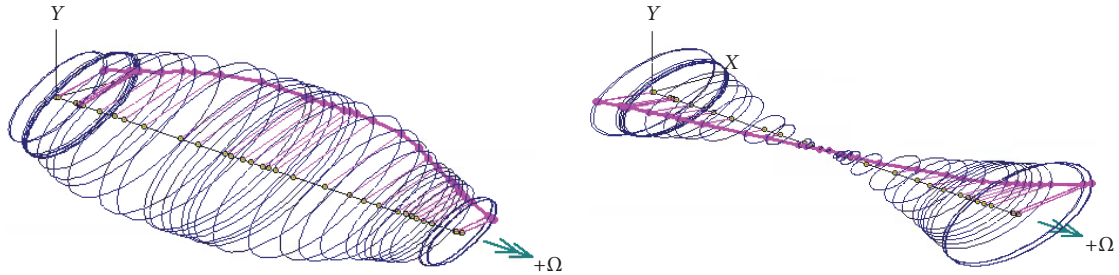
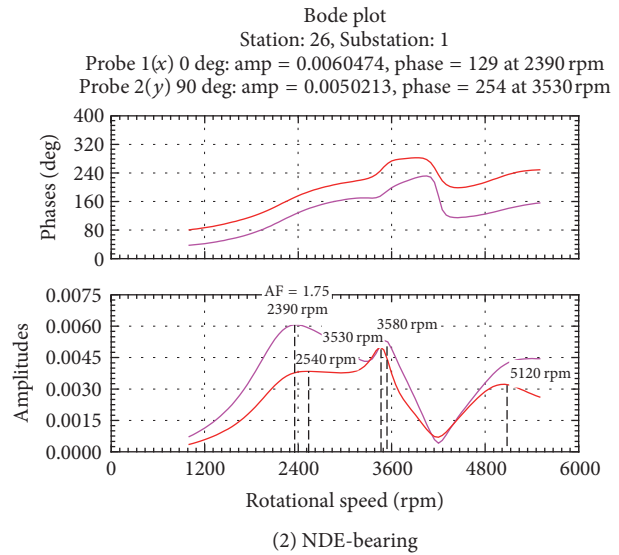
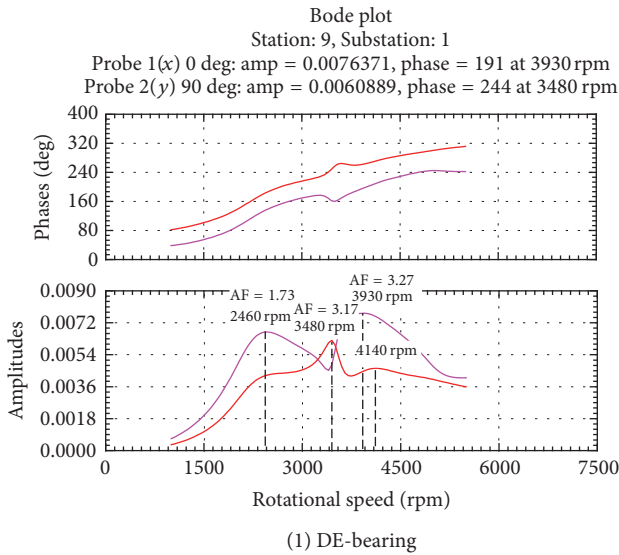
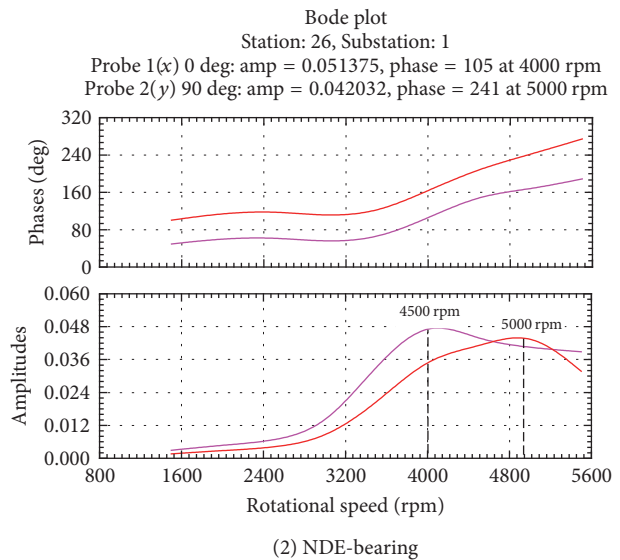
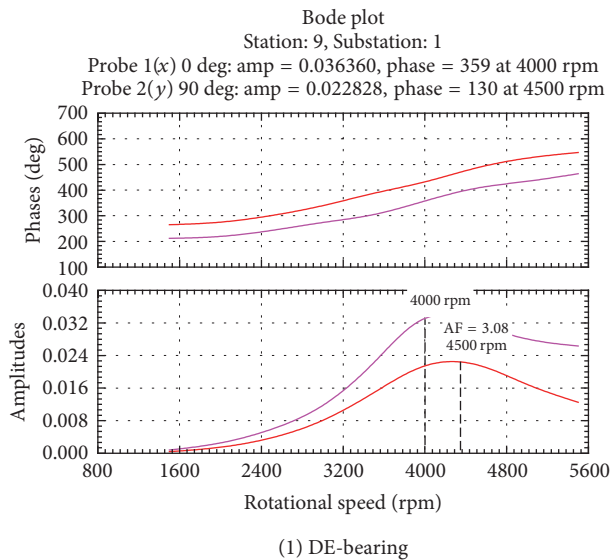


FIGURE 4: Modal analysis of the cylindrical bearing-rotor system.



(a) Unbalance in the middle



(b) Unbalance in the gear wheel of the extension end

FIGURE 5: The bode chart of unbalanced response of cylindrical bearing.



FIGURE 6: TRT test platform and the installation of vibration and speed probe.

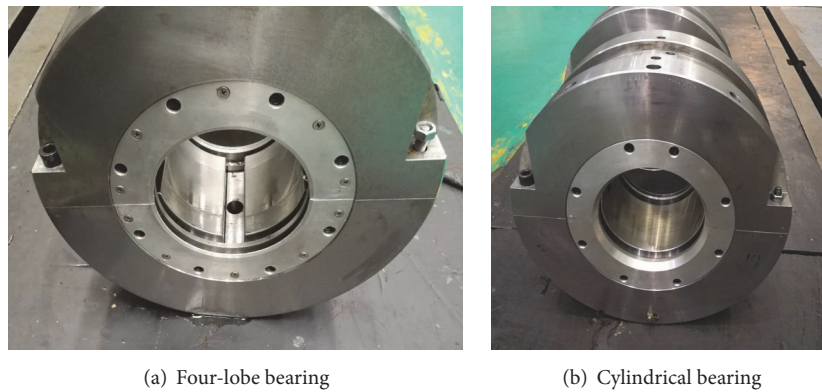


FIGURE 7: Two types of bearings.

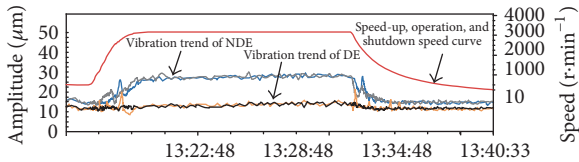


FIGURE 8: The vibrational trend of four-lobe bearing-rotor system.

than four-lobe bearing. The amplitude at the NDE of rotor supported by both of these types of bearing increases as the speed increases, while the amplitude at the DE remains unchanged. Comparing with the theoretical analysis, it can be found that the actual test results of the double supports rotor system with extending disc are more in agreement with theoretical analysis conducted by applying unbalance at the extending end. Besides, there is a vibration catastrophe of the four-lobe bearing-rotor system at the NDE when the speed reaches  $2240 \text{ r}\cdot\text{min}^{-1}$ . It should be caused by the low frequency eddies (approximately half of the critical speed which is  $4500 \text{ r}\cdot\text{min}^{-1}$ ), while the vibration catastrophe of the test results of 2# probe at DE when the speed is  $2660 \text{ r}\cdot\text{min}^{-1}$  is mainly caused by the influences of external environment.

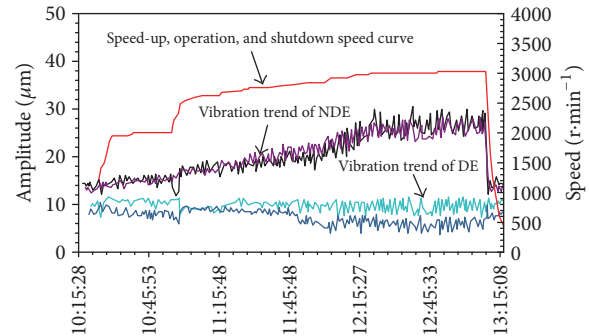


FIGURE 9: The vibrational trend of cylindrical bearing-rotor system.

The bearing affects the critical characteristics of the rotor. For a double support bearing-rotor system with an extending end, if the vibration of cantilever end is severe after applying eigenvalue analysis, it is necessary to conduct the unbalance response analysis of the cantilever end and dynamic balance treatment even though the unit is expander and its rotor is stubby.

At the working speed of  $3000 \text{ r}\cdot\text{min}^{-1}$ , the amplitude at NDE is about  $20 \mu\text{m}$  larger than the value at DE, which indicates that there is residual unbalance in the gear disc at the NDE.

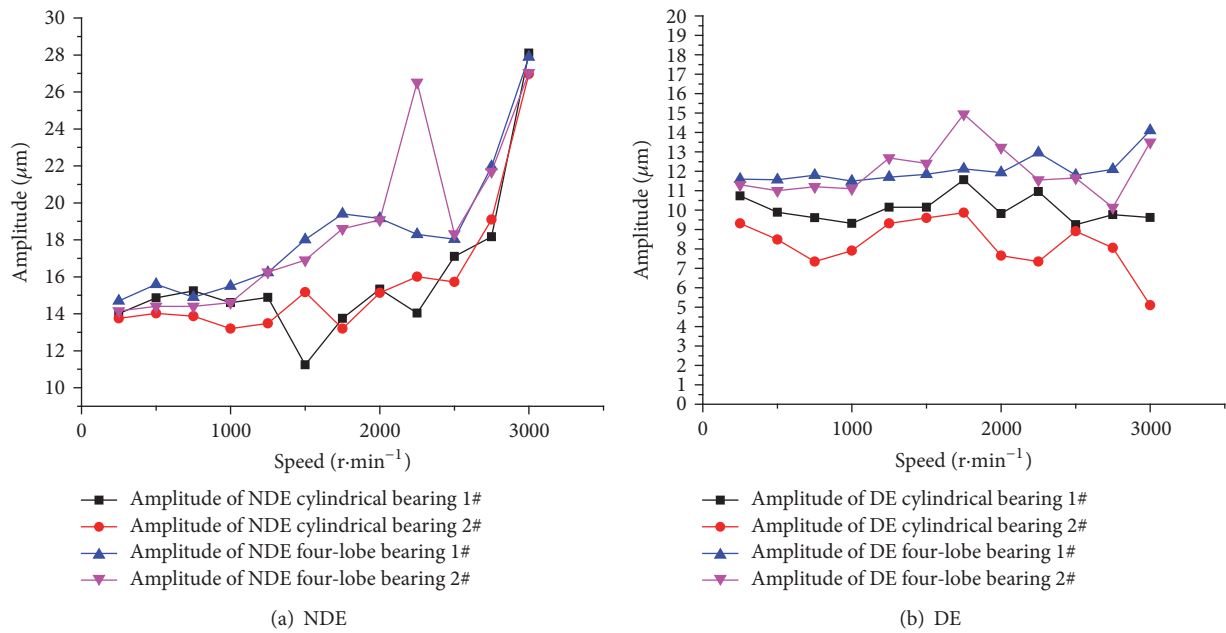


FIGURE 10: Comparison of the vibration of rotor supported by four-lobe bearing and cylindrical bearing.

## 5. Conclusion

- (1) This paper studies the impacts of cylindrical bearing and four-lobe bearing on the vibration of rotor system combining theoretical analysis and experimental analysis. The result shows that different bearing types have effects on the critical characteristics of rotor system, and the vibration of rotor supported by cylindrical bearing is more stable than four-lobe bearing. The test results are in good agreement with theoretical analysis.
- (2) For a double support bearing-rotor system with an extending end, if the vibration of cantilever end is severe after applying eigenvalue analysis, the unbalance response analysis of the cantilever end and dynamic balance treatment are necessary to conduct.

## Conflicts of Interest

The authors declare that they have no conflicts of interest.

## Acknowledgments

This work is supported by the National Natural Science Foundation of China (no. 11372234) and the Key Project of Natural Science Foundation of Xi'an Jiaotong University (no. zrz2017025).

## References

- [1] H. H. Jeffcott, "The Lateral vibration of Loaded Shafts in the Neighborhood of a Whirling Speed," *Philosophical Magazine*, vol. 6, no. 37, pp. 304–314, 1919.
- [2] H. Diken and K. Alnefaie, "Startup dynamic behaviour of a Jeffcott Rotor," *International Journal of Acoustics and Vibration*, vol. 10, no. 2, pp. 83–88, 2005.
- [3] T. Iwatsubo, K. Shimbo, and S. Kawamura, "The study of nonlinear vibration analysis of rotor system using component mode synthesis method (Analysis Using the Harmonic Balance Method)," *JSME International Journal Series C Mechanical Systems, Machine Elements and Manufacturing*, vol. 45, no. 1, pp. 136–141, 2002.
- [4] K.-K. Shin and J. Ni, "Adaptive control of multi-plane active balancing systems for speed-varying rotors," *Journal of Dynamic Systems, Measurement, and Control*, vol. 125, no. 3, pp. 372–381, 2003.
- [5] K. M. Tammi, "Identification and Active Feedback-Feedforward Control of Rotor," *The International Journal of Acoustics and Vibration*, vol. 12, no. 1, 2007.
- [6] J. Ma, J. Dai, B. Sun, X. Kou, and J. Jing, "Supporting Characteristics of Bearings and Their Effects on Dynamical Behaviors of Rotor System," *Noise and Vibration Control*, pp. 22–26, 2011.
- [7] Q. Gao, S. Liu, and Y. Feng, "Analysis and comparison of low-frequency vibration in tilting-pad journal bearing under different load cases," *Journal of Chinese Society of Power Engineering*, vol. 34, no. 4, pp. 286–291, 2014.
- [8] Y. Zhang, J. Wang, M. Cai, and H. Ji, "Research on Viscosity-Temperature Characteristic of the Lubricating Oil of Oil Film Bearing," *Lubrication Engineering*, vol. 03, pp. 75–78, 2014.
- [9] R. Huang, Y. Zhang, and T. Chen, "Rotor dynamics analysis for ball bearing turbocharger considering the sealed construction," *Journal of vibration and shock*, vol. 31, no. 16, pp. 153–182, 2012.

## Research Article

# Planetary Gearbox Fault Diagnosis via Torsional Vibration Signal Analysis in Resonance Region

Kangqiang Li,<sup>1</sup> Zhipeng Feng,<sup>1</sup> and Xihui Liang<sup>2</sup>

<sup>1</sup>*School of Mechanical Engineering, University of Science and Technology Beijing, Beijing 100083, China*

<sup>2</sup>*Department of Mechanical Engineering, University of Alberta, Edmonton, AB, Canada T6G 2G8*

Correspondence should be addressed to Zhipeng Feng; fengzp@ustb.edu.cn

Received 20 August 2017; Accepted 29 October 2017; Published 21 November 2017

Academic Editor: Rafał Burdzik

Copyright © 2017 Kangqiang Li et al. This is an open access article distributed under the Creative Commons Attribution License, which permits unrestricted use, distribution, and reproduction in any medium, provided the original work is properly cited.

Planetary gearbox torsional vibration signals are free from the extra amplitude modulation effect due to time-varying transmission paths and have simpler frequency structure than translational ones. Gear faults result in modulation on the torsional resonance vibration and are manifested by the modulation feature. These merits are exploited for planetary gearbox fault diagnosis in this paper. Gear fault induced torsional vibrations in resonance region are modelled as amplitude modulation and frequency modulation (AM-FM) processes, the explicit equation of Fourier spectrum is derived, and the sideband characteristics are summarized. To avoid complex sideband analysis, amplitude and frequency demodulation analysis methods are exploited. The equations of amplitude and frequency demodulated spectra are derived in closed form, and their frequency structures are revealed. For fault diagnosis based on above theoretical derivations, a resonance frequency identification approach is proposed through time-frequency analysis of torsional vibrations during variable speed processes, according to the independence nature of resonance frequency on running conditions. The theoretical derivations and proposed approach are illustrated by numerical simulated signal analysis and are further validated through dynamics modelling and lab experimental tests. Localized faults on the sun, planet, and ring gears are successfully diagnosed.

## 1. Introduction

Planetary gearboxes are widely used in various types of machines, such as wind turbines, helicopters, and trucks. Once fault occurs in a planetary gearbox, it may lead to reduction in transmission efficiency and even breakdown of the entire drive train. Hence, fault diagnosis has great significance to maintain reliable operation of planetary gearboxes [1, 2].

To date, researchers have made many important contributions to planetary gearbox fault diagnosis, but they mainly focus on translational vibration signals. To name a few, for example, McFadden [3, 4] and Samuel and Pines [5], respectively, proposed a vibration separation method of planet and sun gears by generalizing the time domain averaging method. Liang et al. [6] developed a signal decomposition technique to extract the vibration signal corresponding to one tooth of a planet gear for planet gear tooth crack detection. Barszcz and Randall [7] applied spectral kurtosis to gear fault detection,

and they diagnosed the ring gear tooth crack in a wind turbine planetary gearbox. Lei et al. [8] proposed an adaptive stochastic resonance method to suppress noise interference and enhance fault signature and applied it to weak fault feature extraction of planetary gearboxes. Yoon et al. [9] developed spectral averaging via enveloping and Welch's spectral averaging for planetary gearbox fault diagnosis. These works have enriched our understanding on planetary gearbox fault diagnosis.

Translational vibration signals are subject to extra amplitude modulation (AM) effect caused by the planet carrier rotation, and they exhibit intricate spectral structures. Translational vibration signals are usually measured by sensors fixed on gearbox casing or bearing housing. The distance from sun-planet and planet-ring gear meshing locations to the sensor varies with the planet carrier rotation. This results in a time variant vibration transfer path and thereby an extra AM effect on translational vibrations. McFadden and Smith

[10], McNames [11], and Mosher [12] found that the translational vibration signal spectrum of planetary gearboxes is typically asymmetric due to the planet carrier rotation. The spectral complexity leads to difficulty in planetary gearbox fault diagnosis via translational vibration signal analysis.

Torsional vibration signals are free from the extra AM effect due to the planet carrier rotation and show simpler spectral structures than translational ones. Torsional vibration sensors are usually connected to the input or output shaft of a gearbox, and the distance from sun-planet and planet-ring gear meshing locations to the sensor is isotropic circumferentially. As such, the torsional vibration transfer paths are time invariant, even though the sun-planet and planet-ring gear meshing locations vary during gearbox running. Inspired by this property, Feng and Zuo [13] exploited the merit of torsional vibrations to avoid the intricate spectral structure existing with translational vibrations and extracted the sun, planet, and ring gear fault feature around gear meshing frequency or its harmonics.

Gear fault information is not only carried by gear meshing vibrations, but also conveyed by resonances [14, 15]. Localized defects on a gear tooth surface will generate sudden changes in torque as it meshes with mating gears. These sudden changes will further excite torsional resonances. Torsional resonances vanish due to damping effect, but they arise repetitively at the gear fault frequency during gearbox running. In this sense, the resonance region contains gear fault information. However, to our best knowledge, research on planetary gearbox fault diagnosis via torsional vibration signal analysis, particularly in the resonance region, has been very limited.

In this paper, we propose to extract gear fault torsional vibration signature in resonance region. To implement this idea, we firstly identify the torsional resonance frequency via time-frequency analysis of torsional vibration signals during variable speed processes. This resonance frequency identification method overcomes the difficulty in exciting torsional resonances via traditional hammer impact technique. Then, we extract gear fault features around the resonance frequency via sideband analysis in Fourier spectrum, and amplitude and frequency demodulation analysis. In summary, this proposed methodology does not only offer an alternative solution to avoid the complexity issue existing with translational vibrations due to extra amplitude modulation effect by the time-varying vibration propagation paths, but also provides a new insight into gear fault induced torsional vibration signatures.

Hereafter, this paper is organized as follows. Section 2 derives the explicit equations of Fourier spectrum, envelope spectrum, and the Fourier spectrum of instantaneous frequency in the resonance frequency region, respectively. Section 3 introduces the resonance frequency identification approach and the sensitive component separation method and summarizes the analysis procedure as well. Section 4 illustrates the torsional resonance vibration characteristics via a numerically simulated signal analysis. Sections 5 and 6 validate the proposed method via dynamics modelling data of a planetary gear set and lab experimental signals of a planetary gearbox. Section 7 draws conclusions.

## 2. Gear Fault Characteristics in Torsional Resonance Region

In this section, we extract gear fault features in the torsional resonance frequency region, instead of around gear meshing frequency and its harmonics that are usually focused in conventional methods. Therefore we derive explicit equations of Fourier spectrum, envelope spectrum, and Fourier spectrum of instantaneous frequency, for better understanding their spectral structure.

*2.1. Torsional Vibration Signal Model in Resonance Region.* Suppose we have a localized fault on the tooth surface of sun, planet, or ring gear. Under constant speed operation, as the fault area strikes mating gear teeth, sudden changes in torque will be generated. Consequently, the repeating sudden torque changes excite the torsional resonance of gear-shaft system periodically. Such resonance vanishes rapidly due to damping before the next resonance comes, resulting in the AM phenomenon. Meanwhile, in one repeating cycle, the resonance exists in the early portion and the instantaneous frequency equals approximately the resonance frequency, while in the later portion, the resonance vanishes due to damping and the instantaneous frequency becomes 0. This means the instantaneous frequency changes periodically, resulting in frequency modulation (FM). Therefore, the fault exciting torsional vibration signals around resonance frequency can be modelled as an amplitude modulation and frequency modulation (AM-FM) process, with the carrier frequency equal to resonance frequencies and the modulating frequency equal to the gear fault frequency harmonics.

Without loss of generality, we focus on one resonance frequency  $f_n$  and the fundamental gear fault frequency  $f_g$  only. Then, the torsional vibration signal model in the resonance region can be simplified as

$$x(t) = [1 + A \cos(2\pi f_g t + \phi)] \cdot \cos[2\pi f_n t + B \sin(2\pi f_g t + \varphi) + \theta], \quad (1)$$

where  $A > 0$  and  $B > 0$  are the AM and FM magnitude, respectively, and  $\phi$ ,  $\varphi$ , and  $\theta$  are the initial phases.

*2.2. Fourier Spectrum.* According to the property of Bessel functions [17],

$$\exp[jz \sin(\theta)] = \sum_{m=-\infty}^{\infty} J_m(z) \exp(jm\theta), \quad (2)$$

where  $J_m(z)$  is the first class of Bessel function with integer order  $m$  and argument  $z$  and the identities of trigonometric functions. Then, (1) can be rewritten as

$$x(t) = [1 + A \cos(2\pi f_g t + \phi)] \times \sum_{m=-\infty}^{\infty} J_m(B) \cdot \cos[2\pi(f_n + m f_g)t + m\varphi + \theta] = \sum_{m=-\infty}^{\infty} J_m(B)$$

$$\begin{aligned}
& \cdot \cos \left[ 2\pi (f_n + mf_g)t + m\varphi + \theta \right] + \frac{A}{2} \sum_{m=-\infty}^{\infty} J_m(B) \\
& \cdot \cos \left\{ 2\pi [f_n + (m+1)f_g]t + m\varphi + \theta + \phi \right\} + \frac{A}{2} \\
& \cdot \sum_{m=-\infty}^{\infty} J_m(B) \\
& \cdot \cos \left\{ 2\pi [f_n + (m-1)f_g]t + m\varphi + \theta - \phi \right\}. \tag{3}
\end{aligned}$$

Applying Fourier transform to (3) yields the Fourier spectrum

$$\begin{aligned}
X(f) &= \sum_{m=-\infty}^{\infty} J_m(B) \delta \left[ f - (f_n + mf_g) \right] \\
& \cdot \exp [j(m\varphi + \theta)] + \frac{A}{2} \sum_{m=-\infty}^{\infty} J_m(B) \\
& \cdot \delta \left\{ f - [f_n + (m+1)f_g] \right\} \exp [j(m\varphi + \theta + \phi)] \\
& + \frac{A}{2} \sum_{m=-\infty}^{\infty} J_m(B) \delta \left\{ f - [f_n + (m-1)f_g] \right\} \\
& \cdot \exp [j(m\varphi + \theta - \phi)], \tag{4}
\end{aligned}$$

where  $\delta(\cdot)$  denotes the Dirac delta function.

According to (4), peaks appear in the Fourier spectrum at frequency locations  $f_n \pm mf_g$ . They form sidebands around the resonance frequency  $f_n$ , with a sideband spacing equal to the gear fault frequency  $f_g$ . Based on such characteristics, we can diagnose gear fault according to the presence of sidebands or changes in their magnitudes, and particularly the associated sideband spacing, in the resonance frequency region.

**2.3. Envelope Spectrum.** For the signal model (1), the AM part

$$e(t) = 1 + A \cos(2\pi f_g t + \phi) \tag{5}$$

contains gear fault information, because its modulating frequency equals the gear fault frequency  $f_g$ . This motivates us to reveal gear fault signature via amplitude demodulation analysis.

Applying Fourier transform to (5) yields the envelope spectrum

$$E(f) = \delta(f) + A\delta(f - f_g) \exp(j\phi). \tag{6}$$

According to (6), in the envelope spectrum, peak appears at the gear fault frequency  $f_g$  only. If we consider higher order harmonics of amplitude modulating frequencies, peaks will also appear at the gear fault frequency harmonics  $kf_g$ . Therefore, we can detect gear fault according to the existence of gear fault frequency harmonics  $kf_g$  or increase in their magnitudes in the envelope spectrum.

**2.4. Fourier Spectrum of Instantaneous Frequency.** According to the signal model (1), the FM part also contains gear fault information, since its modulating frequency is the gear fault frequency. Hence, we can detect gear fault via frequency demodulation analysis.

For the signal model, given in (1), its instantaneous phase is

$$\alpha(t) = 2\pi f_n t + B \sin(2\pi f_g t + \varphi) + \theta. \tag{7}$$

The instantaneous frequency can be derived as a derivative of the instantaneous phase  $\alpha(t)$  with respect to time  $t$ :

$$f(t) = \frac{1}{2\pi} \frac{d\alpha(t)}{dt} = f_n + Bf_g \cos(2\pi f_g t + \varphi). \tag{8}$$

Applying Fourier transform to (8) yields the Fourier spectrum of instantaneous frequency

$$F(f) = f_n \delta(f) + Bf_g \delta(f - f_g) \exp(j\varphi). \tag{9}$$

Equation (9) implies that peaks appear at the gear fault frequency  $f_g$  in addition to 0, in the Fourier spectrum of instantaneous frequency. If we consider higher harmonics of the frequency modulating frequency, peaks will also exist at the gear fault frequency harmonics  $kf_g$ . Based on such features, we can detect gear fault according to the frequency locations of peaks present in the Fourier spectrum of instantaneous frequency.

### 3. Analysis Procedure

Figure 1 shows the flowchart of our proposed analysis method. Firstly, we identify the torsional resonance frequency via time-frequency analysis of torsional vibration signals during variable speed processes (to be explained in Section 3.1). Then, we extract gear fault symptoms by sideband analysis around the resonance frequency in Fourier spectrum. Next, we separate the resonance component via bandpass filtering around the resonance frequency and discern gear fault signature in its envelope spectrum. We further decompose the filtered resonance component into monocomponents via ensemble empirical mode decomposition (EEMD), choose a sensitive monocomponent (to be introduced in Section 3.2), and pinpoint gear fault information from the Fourier spectrum of its instantaneous frequency. Finally, we diagnose gear fault by combining the findings from sideband analysis in Fourier spectrum, and amplitude and frequency demodulation analyses.

**3.1. Torsional Resonance Frequency Identification.** To extract gear fault signatures around torsional resonance frequency, it is necessary to identify the resonance frequency first. Hammer impact technique is commonly used in translational resonance identification. However, it is difficult to apply an impact to a gear-shaft torsional vibration system. To overcome this difficulty, we exploit the independence nature of resonance frequency on running conditions, particularly the running speed, and propose a resonance frequency identification approach via time-frequency analysis.

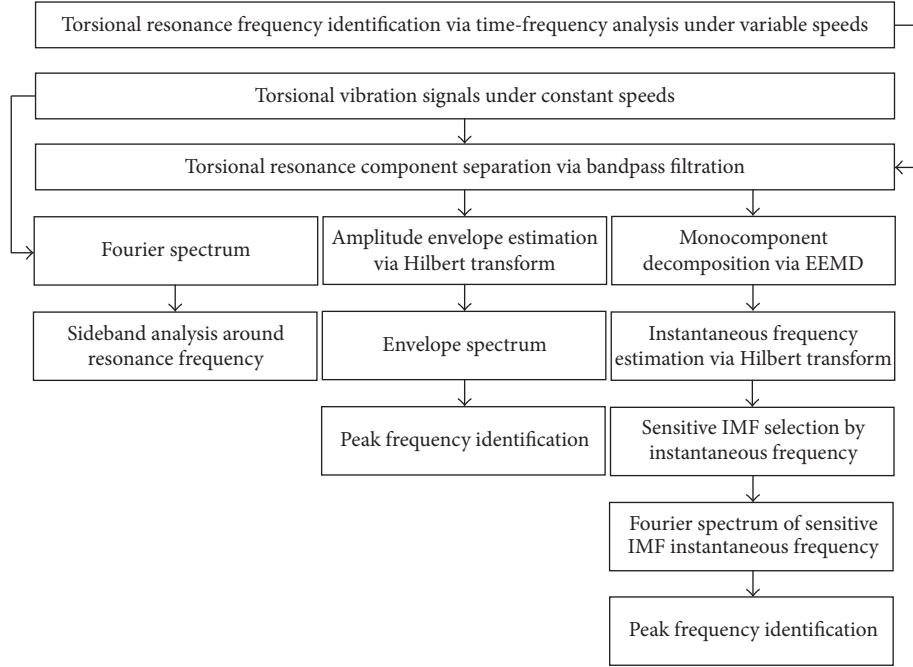


FIGURE 1: Analysis flowchart.

Gear meshing and resonance vibrations are major components of gearbox vibrations, but they exhibit distinct behavior during variable speed conditions. Gear meshing vibrations are manifested by meshing frequency harmonics and associated sidebands with spacing equal to gear characteristic frequencies. These frequencies are proportional to the gearbox running speed. During variable speed processes, they follow the time-varying speed profile and change over time. For resonance vibrations, during gearbox running, sudden changes in meshing stiffness, due to gear fault and/or alternation in number of engaging gear pairs, generate impulses in load torque and further excite torsional resonance vibrations. Resonance frequencies are independent on running conditions, thus being time invariant during variable speed processes. Therefore, resonance frequencies show up as constant ones on time-frequency plane, which are parallel to the time axis but vertical to the frequency axis. On the contrary, gear meshing frequency harmonics and associated sidebands emerge as curves on time-frequency plane. According to this property, resonance frequencies can be discriminated from gear meshing frequency harmonics and associated sidebands and can be recognized as constant frequencies on time-frequency plane. Furthermore, gear fault feature can be extracted in the resonance region via sideband, amplitude, and frequency demodulation analyses.

**3.2. Sensitive Component Separation.** For amplitude demodulation analysis, it is necessary to separate the signal component of interest before envelope spectrum analysis. Because gear fault induced torsional vibration rides on the resonance frequency, we separate the resonance vibration component of interest using a band pass filter centered around the

resonance frequency, to avoid interferences from other components.

For frequency demodulation analysis, instantaneous frequency estimation requires the signal to be monocomponent. To satisfy this requirement, we further decompose the filtered resonance component into monocomponent intrinsic mode functions (IMFs) via ensemble empirical mode decomposition (EEMD) by exploiting its capability to decompose multicomponent signal into constituent monocomponents [18]. Among the obtained IMFs, we choose the earliest IMF with an instantaneous frequency fluctuating around the resonance frequency for further frequency demodulation analysis, because (1) EEMD extracts IMFs in an order from higher to lower frequency [18, 19], (2) impulsive gear fault vibrations have significant features in higher frequency band, and (3) the signal carrier frequency is the resonance frequency.

#### 4. Numerical Simulation

In this section, we illustrate the above theoretical derivations via a numerical simulated signal analysis. Considering the gear fault impulsive vibration nature in resonance region, we generate a numerical simulated signal as a series of damped sinusoids

$$x(t) = \sum_{m=1}^M A_m \exp[-2\pi\zeta f_n(t - mT)] \cdot \sin[2\pi f_n(t - mT)] u(t - mT) + n(t), \quad (10)$$

where the amplitude  $A_m = 1.5$ , the damping ratio  $\zeta = 0.15$ , the natural (resonance) frequency  $f_n = 6550$  Hz, the period

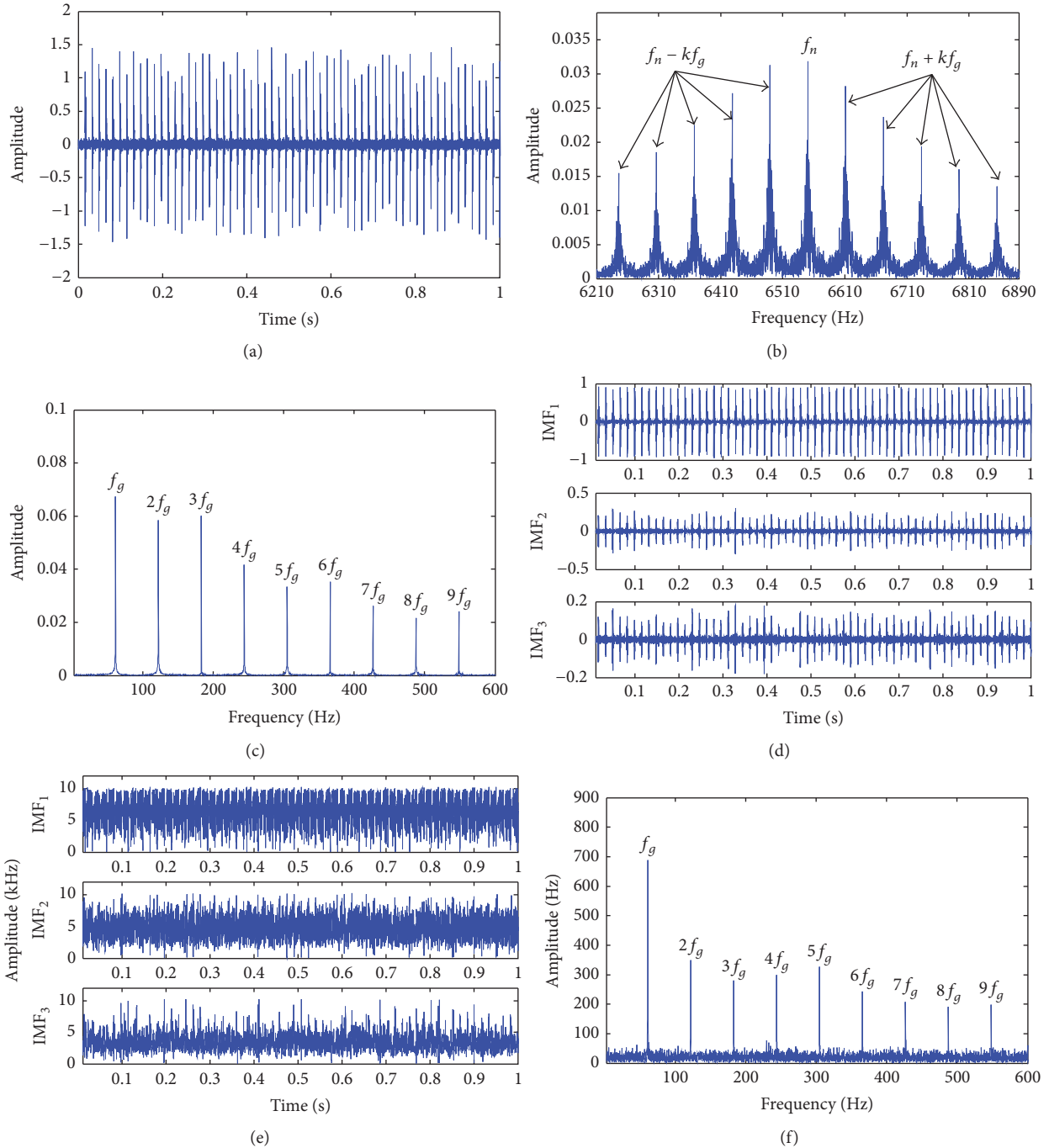


FIGURE 2: Simulated signal analysis: (a) signal waveform, (b) Fourier spectrum, (c) envelop spectrum, (d) IMFs, (e) instantaneous frequencies of IMFs, and (f) Fourier spectrum of instantaneous frequency.

of repeating impulses  $T = 0.0164$  s, accordingly the gear fault frequency  $f_g = 1/T = 61$  Hz,  $u(t)$  is a unit step function, and  $n(t)$  is a Gaussian white noise at a signal to noise ratio of 10 dB to simulate background noise.

Figures 2(a) and 2(b) show the simulated signal waveform and its Fourier spectrum, respectively. In the Fourier spectrum, peaks appear around the resonance frequency  $f_n$ , and their frequency locations correspond to the resonance frequency plus or minus the gear fault frequency harmonics

$f_n \pm kf_g, k = 1, 2, \dots$ . These peaks form sidebands with a regular spacing equal to the gear fault frequency  $f_g$ . This behavior is consistent with the theoretical expectation from equation (4).

To avoid intricate sideband analysis, amplitude demodulation analysis is conducted. Since the simulated signal is mainly composed of resonance, bandpass filtration is omitted here. Figure 2(c) displays the envelope spectrum. The gear fault frequency harmonics  $kf_g$  (where  $k = 1, 2, \dots$ ) are



TABLE 2: Characteristic frequencies (Hz).

Meshing frequency	Rotating frequency			Fault frequency		
	Sun	Planet carrier	Planet	Sun	Ring	
11.97	0.7778	0.1478	0.3861	0.7722	2.52	0.5912

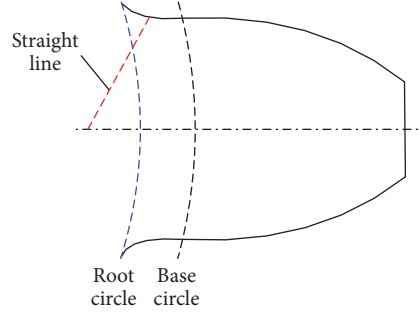


FIGURE 4: Simulated crack on sun gear tooth.

the polar moment of inertia,  $K$  is the linear stiffness in lateral directions (perpendicular to the shaft axis),  $K_t$  is the torsional stiffness, and subscripts  $c$ ,  $r$ ,  $p$ , and  $s$  denote planet carrier, ring, planet, and sun gear, respectively.

Figure 3 shows the dynamic model of a planetary gear at the initial time (time zero). Using the same method of dynamics modelling and simulation, in accordance with the theoretical derivation from (11), as in [16], the first torsional resonance frequency of this planetary gear set is calculated as  $f_n = 3542.7$  Hz. To simulate gear crack fault, a crack of length 3.9 mm along the straight dotted line is introduced to one of the sun gear teeth, as shown in Figure 4. The sun gear rotating frequency is set to 0.7778 Hz. Torsional vibrations are generated and sampled at 10000 Hz. Given the gear configuration and running speed, the planetary gear set characteristic frequencies can be calculated [20, 21], as listed in Table 2.

Equations of motion for the sun gear are

$$\begin{aligned}
 m_s \ddot{x}_s + c_{sx} \dot{x}_s + k_{sx} x_s + \sum F_{spn} \cos \psi_{sn} \\
 &= m_s x_s \Omega^2 + 2m_s \dot{y}_s \Omega + m_s y_s \dot{\Omega}, \\
 m_s \ddot{y}_s + c_{sy} \dot{y}_s + k_{sy} y_s + \sum F_{spn} \sin \psi_{sn} \\
 &= m_s y_s \Omega^2 - 2m_s \dot{x}_s \Omega - m_s x_s \dot{\Omega}, \\
 m_s \ddot{y}_s + c_{sy} \dot{y}_s + k_{sy} y_s + \sum F_{spn} \sin \psi_{sn} \\
 &= m_s y_s \Omega^2 - 2m_s \dot{x}_s \Omega - m_s x_s \dot{\Omega}, \\
 \left( \frac{J_s}{r_s} \right) \ddot{\theta}_s + \sum F_{spn} &= \frac{T_i}{r_s},
 \end{aligned} \tag{11}$$

where  $m$ ,  $c$ ,  $k$  denote mass of sun gear, damping coefficient, and stiffness of sun gear bearing;  $x$  and  $y$  denote the  $x$ -direction and  $y$ -direction displacement of the sun gear;  $\psi_n$  is

circumferential angle of  $n$ th planet;  $\Omega$  is rotation speed of the carrier;  $J_s$  and  $r_s$  are mass moment of inertia and base circle radius of the sun gear;  $T_i$  denotes input torque on the sun gear;  $F_{spn}$  represents the dynamic force of the  $n$ th sun-planet gear mesh:

$$\begin{aligned}
 F_{spn} &= k_{spn} \delta_{spn} + c_{spn} \dot{\delta}_{spn}, \\
 \delta_{spn} &= (x_s - x_{pn}) \cos \psi_{sn} + (y_s - y_{pn}) \sin \psi_{sn} + r_s \theta_s \\
 &\quad + r_{pn} \theta_{pn} - r_c \theta_c \cos \alpha, \\
 \psi_{sn} &= \frac{\pi}{2} - \alpha + \psi_n, \\
 \psi_n &= \frac{2(n-1)\pi}{n},
 \end{aligned} \tag{12}$$

where  $\alpha$  is pressure angle of gear pairs,  $\delta$  is relative displacement on the lines of action, and  $\theta$  is angular displacement.

**5.2. Signal Analysis.** Figure 5 shows the signal analysis result. In the Fourier spectrum, Figure 5(b), we concentrate on the resonance region around  $f_n = 3542.7$  Hz to extract gear fault signature through sideband analysis. In addition to those at  $f_n - 3f_s + 4f_c$  and  $f_n - 5f_s + 4f_c$ , most peaks appear at  $f_n \pm kf_s$ , and they form sidebands with a regular spacing equal to the sun gear fault frequency  $f_s$ . To separate the resonance component for further demodulation analysis, the raw signal is band pass filtered around the resonance frequency  $f_n = 3542.7$  Hz with a bandwidth of 300 Hz. Figure 5(c) displays the envelope spectrum. Most of dominant peaks correspond to the sun gear fault frequency harmonics  $kf_s$ , besides  $5f_s - 4f_c$  and  $10f_s - 4f_c$ . Several IMFs are generated through EEMD of the separated resonance component. In EEMD, the added noise amplitude is set to 0.02, and the ensemble number is set to 100, following the suggestion in [19]. Among them,

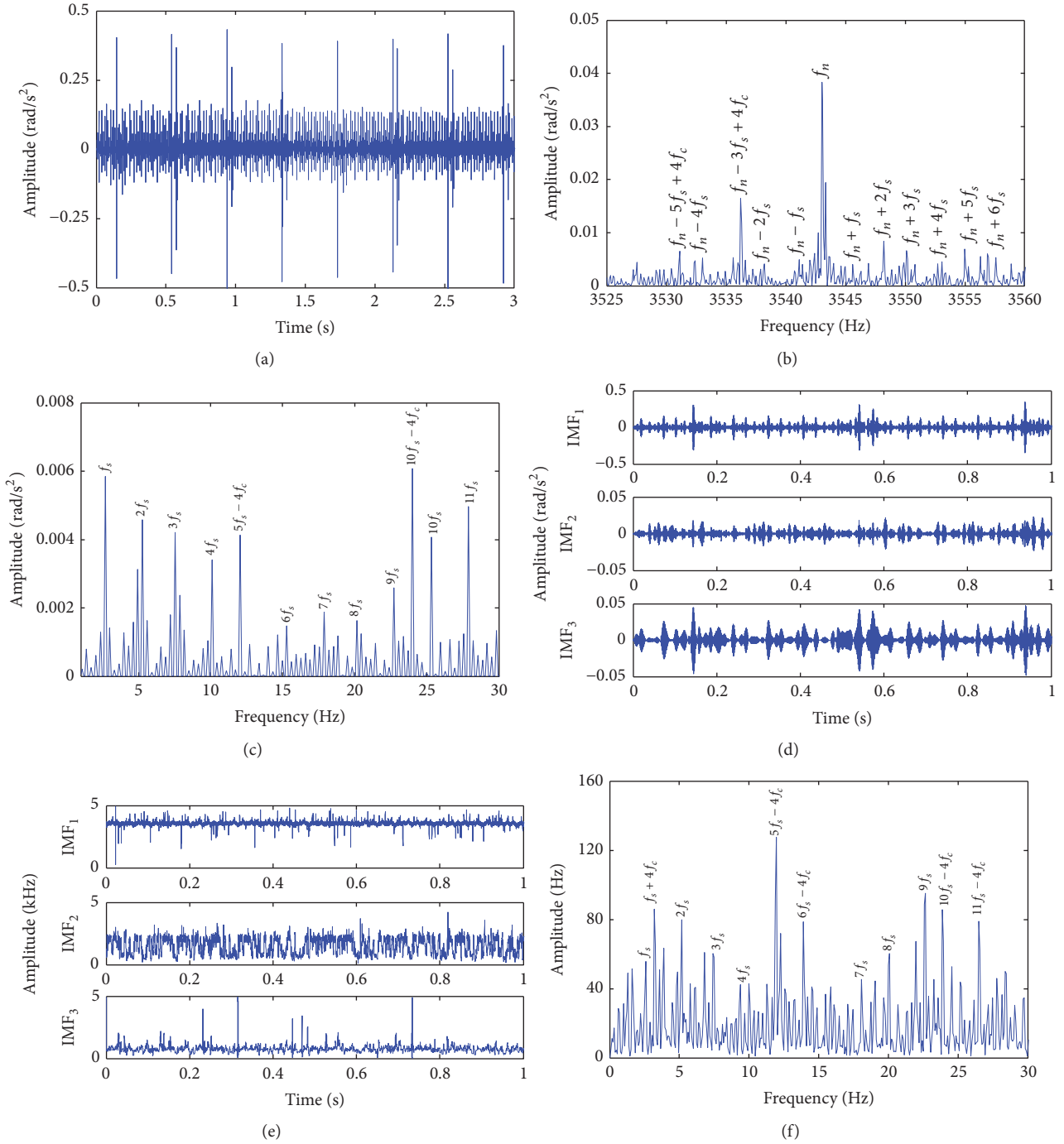


FIGURE 5: Dynamics modelling signal analysis: (a) torsional vibration signal, (b) Fourier spectrum, (c) envelop spectrum, (d) IMFs, (e) instantaneous frequencies of IMFs, and (f) Fourier spectrum of instantaneous frequency.

IMF1 has an instantaneous frequency fluctuating around the resonance frequency  $f_n = 3542.7$  Hz and hence is selected for frequency demodulation analysis. Figure 5(f) shows the Fourier spectrum of IMF1 instantaneous frequency. Although the sun gear fault frequency harmonics plus or minus four times the planet carrier rotating frequency  $kf_s \pm 4f_c$

dominate, the sun gear fault frequency harmonics  $kf_s$  also have prominent magnitudes. In the above Fourier spectrum, and amplitude and frequency demodulated spectra, all the peaks relate to the sun gear fault frequency  $f_s$ . These findings imply the sun gear fault, in accordance with actual settings in dynamics modelling.

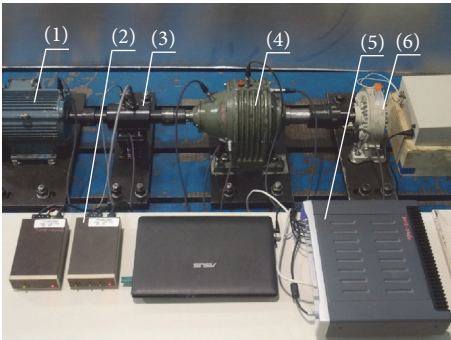


FIGURE 6: Planetary gearbox test rig: (1) drive motor, (2) signal conditioner, (3) torque-speed transducer, (4) planetary gearbox, (5) signal collector, and (6) magnetic powder brake.

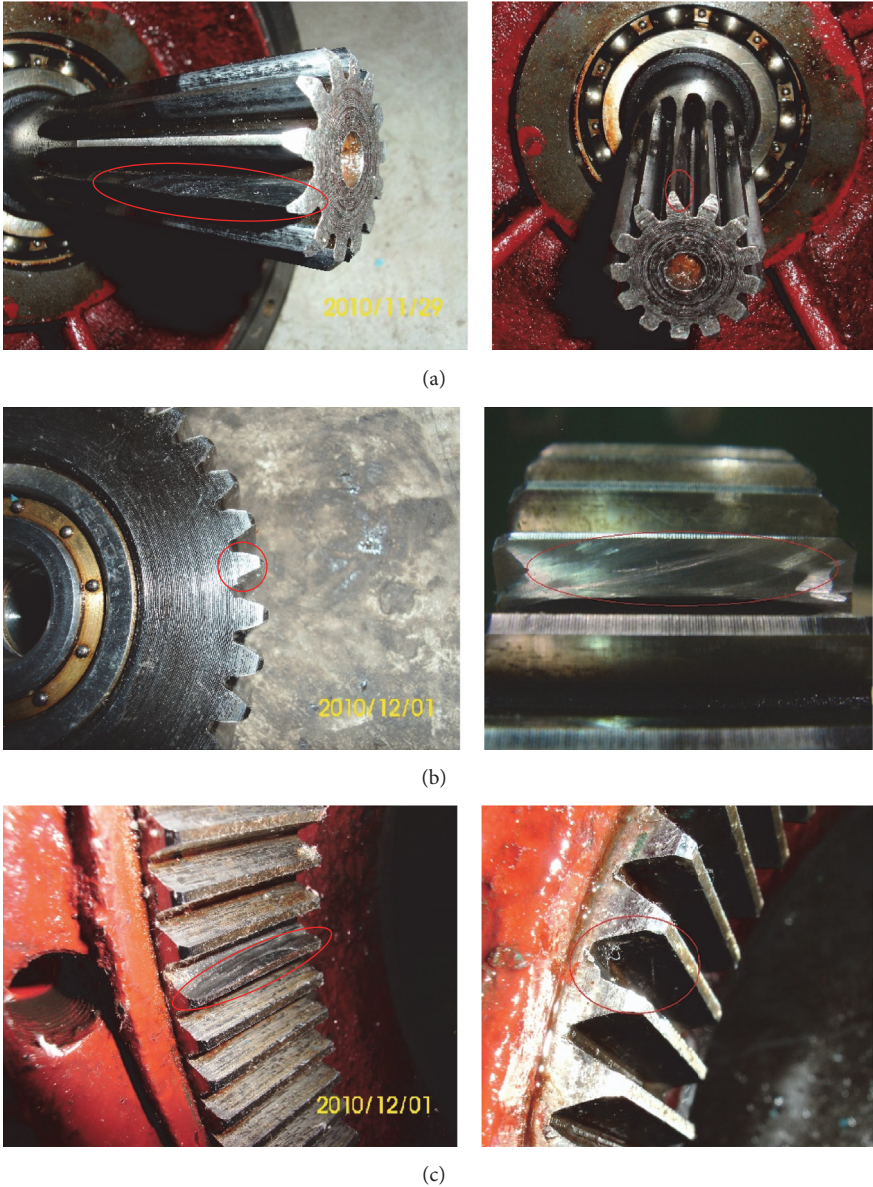


FIGURE 7: Localized fault on (a) sun, (b) planet, and (c) ring gear.

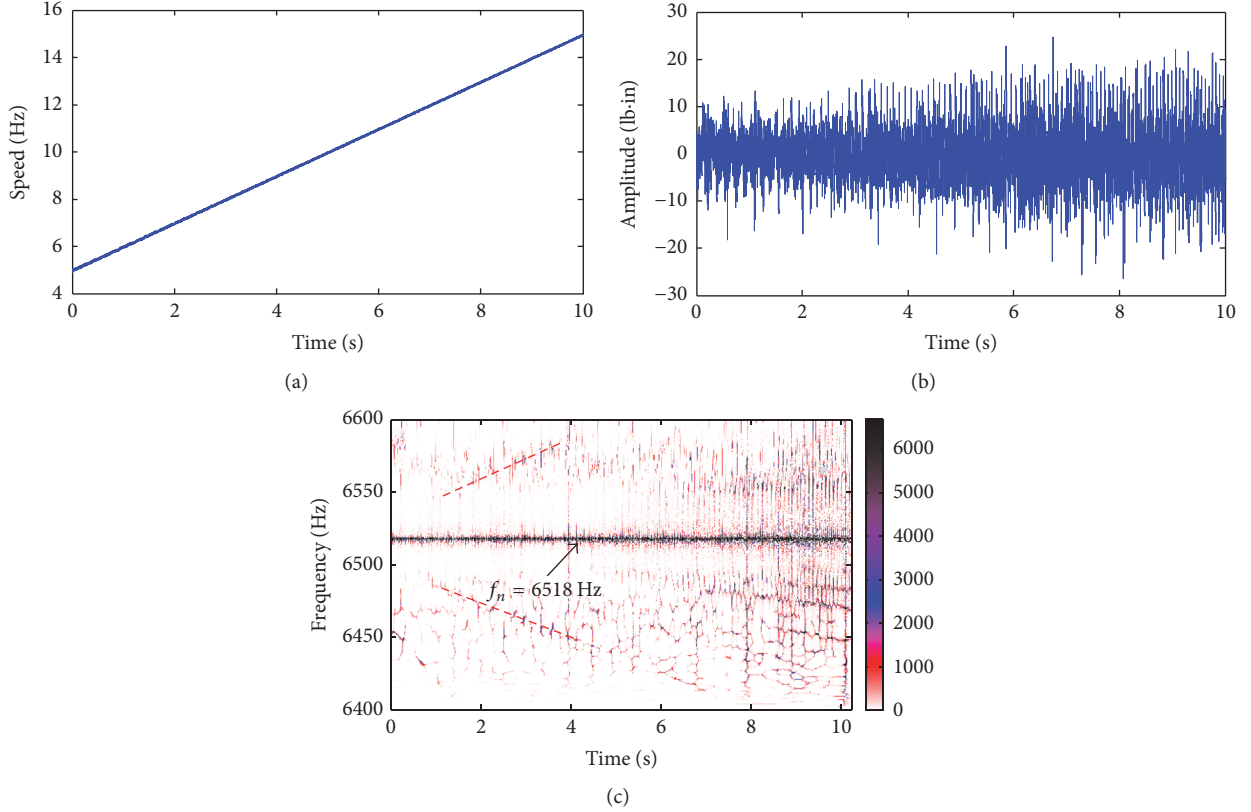


FIGURE 8: Resonance frequency identification: (a) drive motor speed, (b) detrended torsional vibration signal, and (c) reassigned Morlet scalogram.

TABLE 3: Gear configuration parameters.

Gear	Sun	Planet	Ring
Number of gear teeth	13	38 (3)	92

Note. Number of planet gears in parentheses.

## 6. Experimental Validation

In this section, we validate the proposed idea using lab experimental signals of a planetary gearbox under healthy and faulty gear conditions, respectively.

**6.1. Experimental Setting.** Figure 6 shows the planetary gearbox test rig. Table 3 lists the gearbox configuration parameters. The planetary gearbox is driven by a drive motor through the sun gear shaft, and a load of 25 lb-in is applied by a magnetic powder brake via the planet carrier shaft. A speed-torque transducer is installed between the drive motor and the planetary gearbox. The torque sensor we used is an integrated sensor, and its output is torsional vibration signal only. During experiments, the torque (torsional vibration) and speed are collected at 20480 Hz.

To simulate localized gear fault, one tooth of the sun, one planet, and ring gear are locally chipped, respectively, as

shown in Figure 7. Four types of tests are conducted: baseline case when all gears are healthy and faulty sun, planet, and ring gear case when the sun, one planet, and the ring gear alone are locally chipped, respectively. For each case, two running speed conditions are set. One is a constant speed condition to be used for fault feature extraction, when the drive motor speed is set to 23.5 Hz. The other is a variable speed condition for resonance frequency identification, when the drive motor speeds up linearly.

Given the gearbox configuration parameters and running speed, gear characteristic frequency can be calculated [20, 21], as listed in Table 4.

**6.2. Signal Analysis.** In this section, we firstly identify the resonance frequency via time-frequency analysis of torsional vibration signals during speed-up processes. Then, we extract gear fault signature through sideband analysis in Fourier spectrum within resonance region, and amplitude and frequency demodulation analysis of sensitive resonance component. For demodulation analysis, we separate the component of interest using a bandpass filter with a center frequency equal to the identified resonance frequency and a bandwidth of 200 Hz. In EEMD, the added noise amplitude is set to 0.02, and the ensemble number is 100 according to the suggestion in [19].

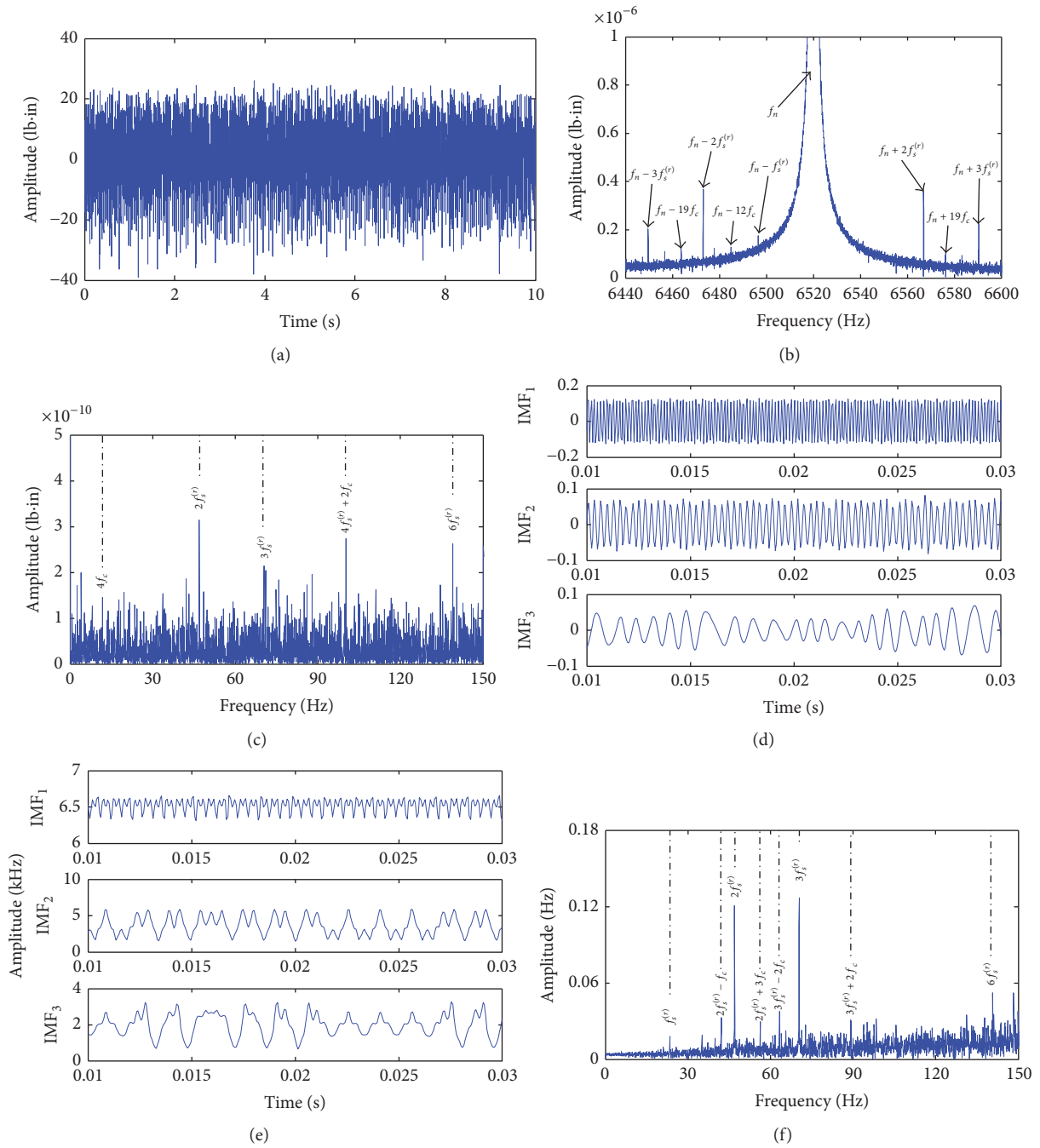


FIGURE 9: Baseline signal analysis: (a) detrended torsional vibration signal, (b) Fourier spectrum, (c) envelop spectrum, (d) IMFs, (e) instantaneous frequencies of IMFs, and (f) Fourier spectrum of instantaneous frequency.

TABLE 4: Gearbox characteristic frequencies (Hz).

Meshing frequency	Rotating frequency		Fault frequency		
	Sun gear	Planet carrier	Sun gear	Planet gear	Ring gear
267.676	23.5	2.91	61.77	7.044	8.73

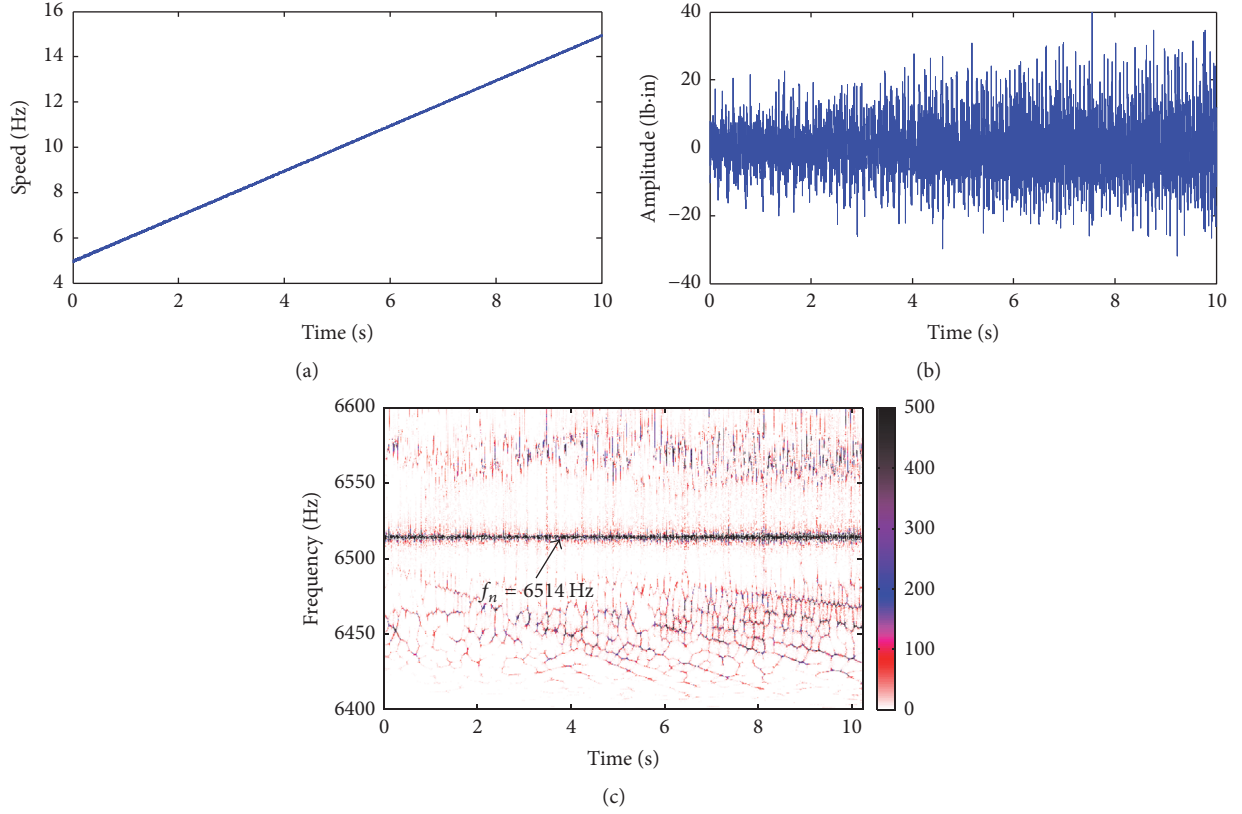


FIGURE 10: Resonance frequency identification: (a) drive motor speed, (b) detrended torsional vibration signal, and (c) reassigned Morlet scalogram.

**6.2.1. Baseline.** In the baseline case, a speed-up test is conducted for resonance frequency identification via time-frequency analysis. The drive motor speeds up from 5 Hz to 15 Hz in 10 seconds approximately. Figures 8(a), 8(b), and 8(c) show the speed, torsional vibration signal, and its reassigned Morlet scalogram, respectively. In Figure 8(c), within the frequency band [6400, 6600] Hz, the dominant frequency is constant and corresponds to 6518 Hz. Other frequencies change over time. The frequencies higher than 6518 Hz increase in direct proportionality to the variable speed, while those lower than 6518 Hz decrease in inverse proportionality to the variable speed. They form a dispersive sideband structure symmetric about 6518 Hz, as indicated by red dash lines. According to this feature, 6518 Hz is treated as a resonance frequency for further sideband analysis in Fourier spectrum, and amplitude and frequency demodulation analysis under constant speed conditions.

Figures 9(a) and 9(b) show the torsional vibration signal and its Fourier spectrum under constant speed. In Fourier spectrum, sidebands appear around the resonance frequency, such as the resonance frequency plus or minus the planet carrier and sun gear rotating frequency harmonics  $f_n \pm kf_c$ ,  $f_n \pm lf_s^{(r)}$ , where  $k, l = 1, 2, \dots$ . This does not indicate any gear fault, because gearbox manufacturing or assembling errors will generate torque fluctuation at the sun gear and planet carrier shaft rotating frequencies, resulting in presence of the sidebands.

For amplitude demodulation analysis, we separate the component of interest using a bandpass filter. Figure 9(c) displays the envelope spectrum of separated resonance component. Prominent peaks exist at the planet carrier rotating frequency harmonics  $kf_c$ , the sun gear rotating frequency harmonics  $lf_s^{(r)}$ , and their combinations  $lf_s^{(r)} \pm kf_c$ , such as  $4f_c, 2f_s^{(r)}, 3f_s^{(r)}, 6f_s^{(r)}$ , and  $4f_s^{(r)} + 2f_c$ . For frequency demodulation analysis, we decompose the separated resonance component via EEMD and calculate their instantaneous frequencies, as shown in Figures 9(d) and 9(e). According to the sensitive IMF selection criterion, we choose IMF1 for further analysis, since its instantaneous frequency fluctuates around the resonance frequency. Figure 9(f) presents the resonance frequency demodulated spectra. Peaks emerge at the sun gear rotating frequency harmonics  $lf_s^{(r)}$ , their combinations with the planet carrier rotating frequency harmonics  $lf_s^{(r)} \pm kf_c$ , such as  $(1, 2, 3, 6)f_s^{(r)}, 2f_s^{(r)} - f_c, 2f_s^{(r)} + 3f_c, 3f_s^{(r)} - 2f_c$ , and  $3f_s^{(r)} + 2f_c$ . In both amplitude and frequency demodulated spectra, the peaks do not link to any gear fault frequency or their harmonics. As such, they do not imply fault existence on any gear.

**6.2.2. Sun Gear Fault.** Figure 10 shows the time-frequency analysis result of torsional vibration signal during a speed-up process under sun gear fault. In this case, the resonance frequency is identified as 6514 Hz, according to its time

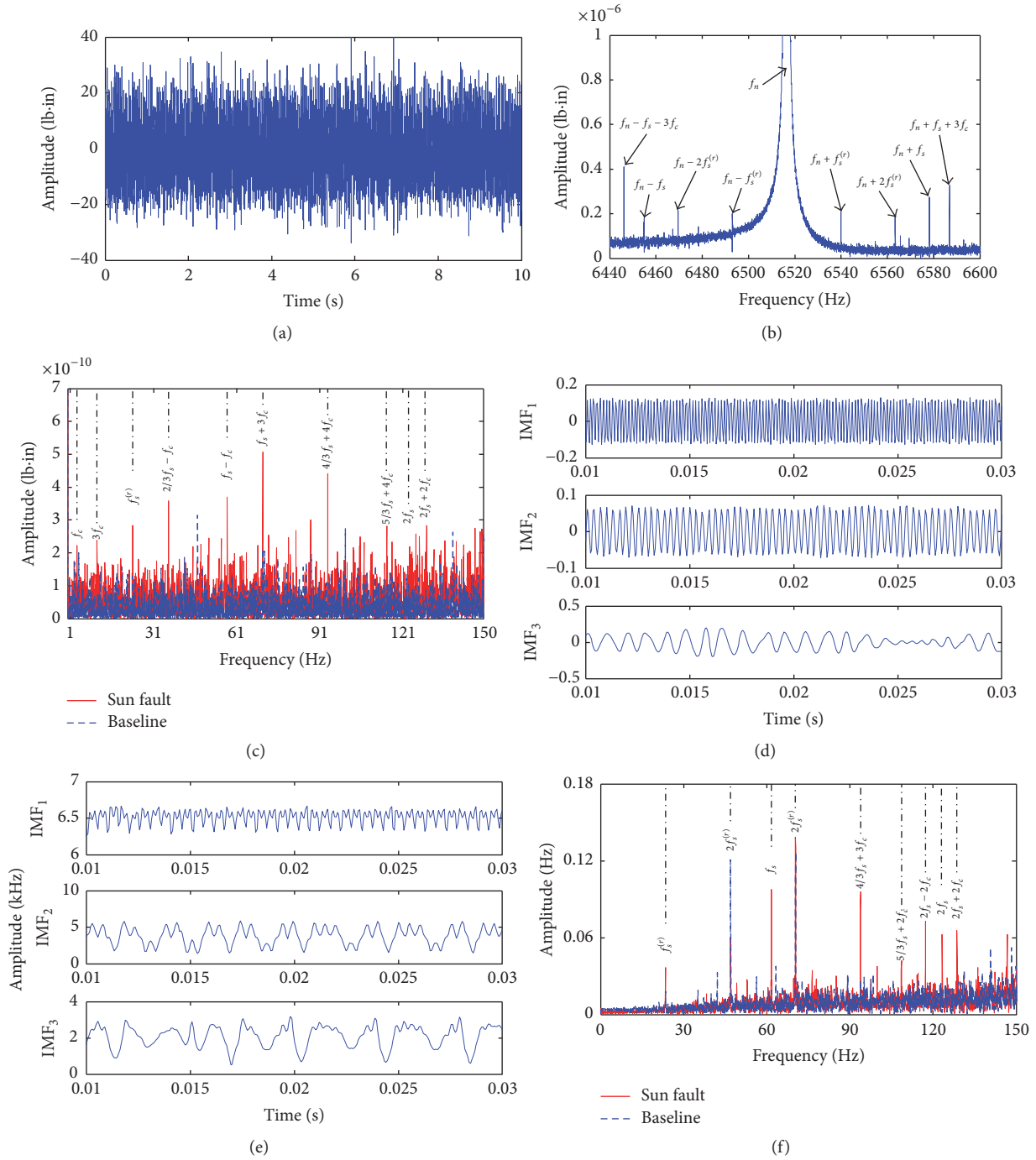


FIGURE 11: Sun gear fault signal analysis: (a) detrended torsional vibration signal, (b) Fourier spectrum, (c) envelop spectrum, (d) IMFs, (e) instantaneous frequencies of IMFs, and (f) Fourier spectrum of instantaneous frequency.

invariant nature under variable speeds; see Figure 10(c). The identified resonance frequency differs somewhat from that in the baseline case, since the gearbox dynamic property might change after replacing a gear.

Figure 11 displays the Fourier spectrum, and amplitude and frequency demodulation analysis results. In the Fourier

spectrum, Figure 11(b), in addition to the sidebands corresponding to the sun gear rotating frequency  $f_n \pm lf_s^{(r)}$ ,  $l = 1, 2, \dots$ , new sidebands emerge. They correspond to the resonance frequency plus or minus the sun gear fault frequency  $f_n \pm f_s$ , and the resonance frequency plus or minus combination (sum or difference) of the sun gear

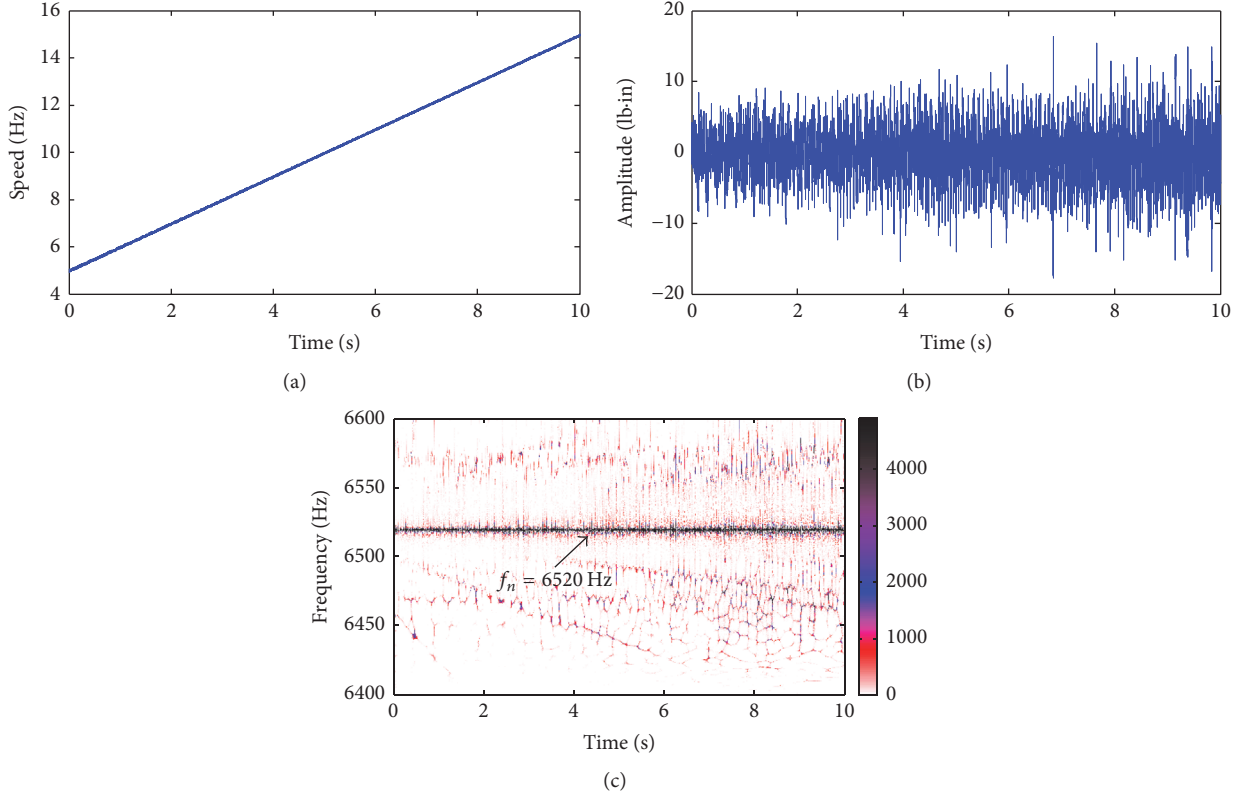


FIGURE 12: Resonance frequency identification: (a) drive motor speed, (b) detrended torsional vibration signal, and (c) reassigned Morlet scalogram.

fault frequency and three times the planet carrier rotating frequency  $f_n \pm f_s \pm 3f_c$ . The expressions in these new sidebands all have a common term equal to the sun gear fault frequency, indicating existence of the sun gear fault.

In the envelope spectrum of filtered resonance component, the sun gear rotating frequency and the planet carrier rotating frequency harmonics still exist. Moreover, pronounced peaks also appear at 1/3 harmonics of the sun fault frequency plus or minus the planet carrier rotating frequency harmonics  $1/3nf_s \pm kf_c$ . In the Fourier spectrum of sensitive IMF1 instantaneous frequency, Figure 11(f), the sun gear rotating frequency and its harmonics  $lf_s^{(r)}$ ,  $l = 1, 2, \dots$ , also show up. Meanwhile, prominent peaks appear at the sun gear fault frequency and its harmonics (such as  $f_s$  and  $2f_s$ ), as well as 1/3 harmonics of the sun fault frequency plus or minus the planet carrier rotating frequency harmonics (e.g.,  $4/3f_s + 3f_c$ ,  $5/3f_s + 2f_c$ ,  $2f_s - 2f_c$ , and  $2f_s + 2f_c$ ). These peaks are higher than those of the baseline signal, and they relate to the sun gear fault frequency, indicating the sun gear fault. Due to manufacturing error, planet gears are not perfectly identical. When they mesh with the faulty sun gear tooth, the generated fault impulses differ among planet gears. In this case, the sun gear fault frequency can be modified by dividing by the number of planet gears 3. This is why 1/3 harmonics of the sun fault frequency are present.

**6.2.3. Planet Gear Fault.** In this case, the resonance frequency is recognized as 6520 Hz; see the time-frequency analysis of torsional vibration signal during a speed-up process, Figure 12(c).

The sideband around the resonance frequency in Fourier spectrum is exhibited in Figure 13(b). In addition to the sidebands related to the sun gear rotating frequency  $f_n \pm lf_s^{(r)}$ ,  $l = 1, 2, \dots$ , prominent peaks exist at the resonance frequency plus or minus the planet gear fault frequency harmonics, such as  $f_n - 6f_p$ ,  $f_n + 3f_p$ , and  $f_n \pm nf_p$ ,  $n = 1, 2, \dots$

In the envelope spectrum of filtered resonance component, Figure 13(c), the planet gear fault frequency harmonics  $nf_p$  (e.g.,  $2f_p$  and  $4f_p$ ) and their sum or difference combination with the planet carrier rotating frequency harmonics  $nf_p \pm kf_c$  are present. In the Fourier spectrum of sensitive IMF1 instantaneous frequency, Figure 13(f), although the sun gear rotating frequency  $f_s^{(r)}$  is dominant, prominent peaks emerge at the planet fault frequency harmonics  $nf_p$ , and their sum or difference combinations with the planet carrier rotating frequency harmonics  $nf_p \pm kf_c$ . These peaks in both amplitude and frequency demodulation spectra relate to the planet gear fault frequency, and they are higher than the baseline signal, implying fault existence on one planet gear.

**6.2.4. Ring Gear Fault.** In this case, the resonance frequency is discerned as  $f_n = 6512 \text{ Hz}$ , through the time-frequency

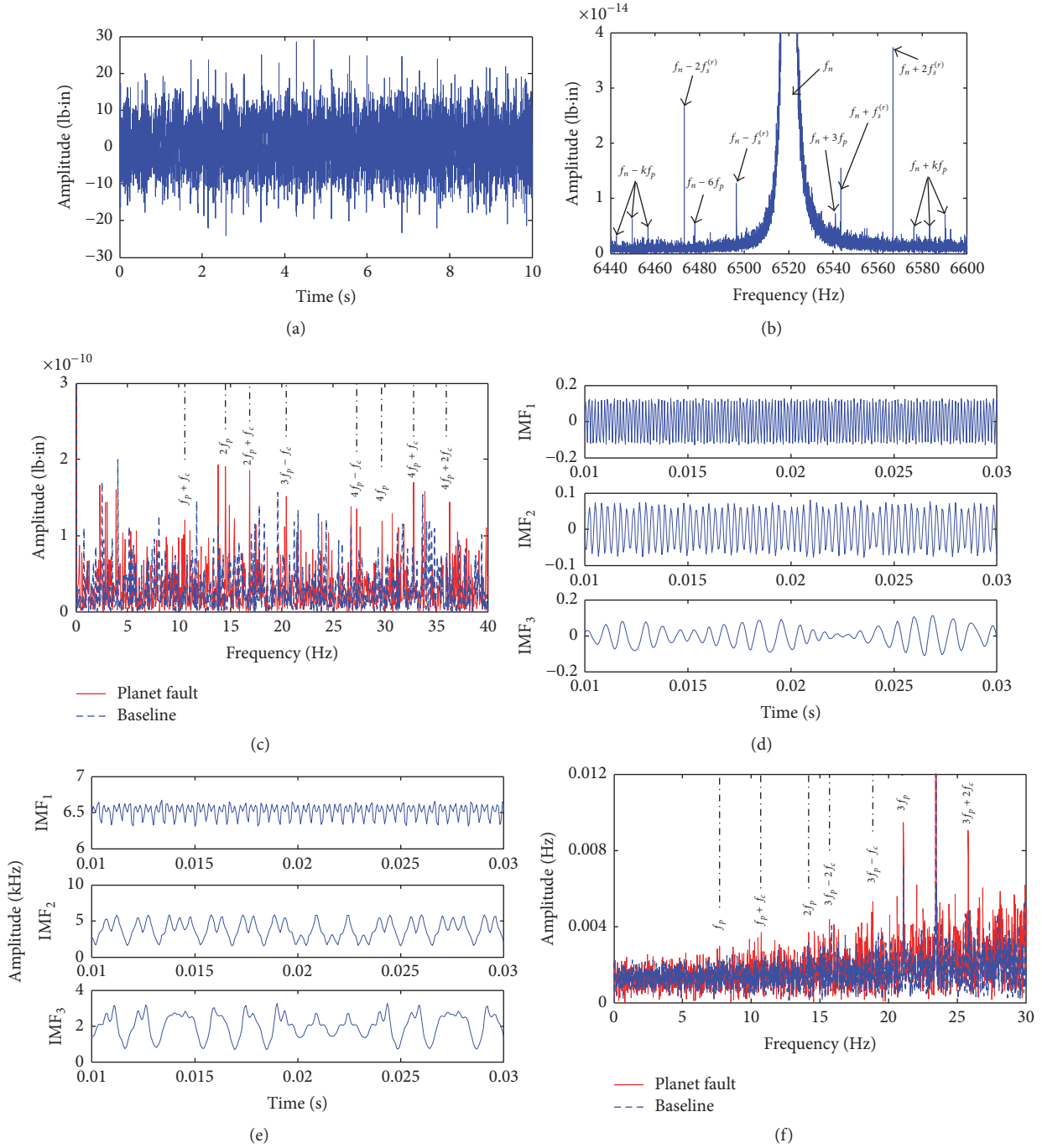


FIGURE 13: Planet gear fault signal analysis: (a) detrended torsional vibration signal, (b) Fourier spectrum, (c) envelop spectrum, (d) IMFs, (e) instantaneous frequencies of IMFs, and (f) Fourier spectrum of instantaneous frequency.

analysis of torsional vibration signal during a speed-up process; see Figure 14(c).

In the Fourier spectrum around the resonance frequency  $f_n = 6512$  Hz, Figure 15(b), sidebands relevant to the ring gear fault frequency  $f_r$  or its 1/3 harmonics  $1/3f_r$  show up (such as  $f_n \pm 4f_r$ ,  $f_n \pm 19/3f_r$ , and  $f_n - 7f_r$ ), in addition to those associated with the sun gear rotating frequency.

In the envelope spectrum of filtered resonance component, Figure 15(c), dominant peaks appear at 1/3 harmonics of ring gear fault frequency  $1/3nf_r$ ,  $n = 1, 2, \dots$  In the Fourier spectrum of sensitive IMF1 instantaneous frequency, Figure 15(f), except the dominant peaks at three times the planet gear fault frequency  $3f_p$  and the sun gear rotating frequency  $f_s^{(r)}$ , all the prominent peaks correspond to 1/3 harmonics

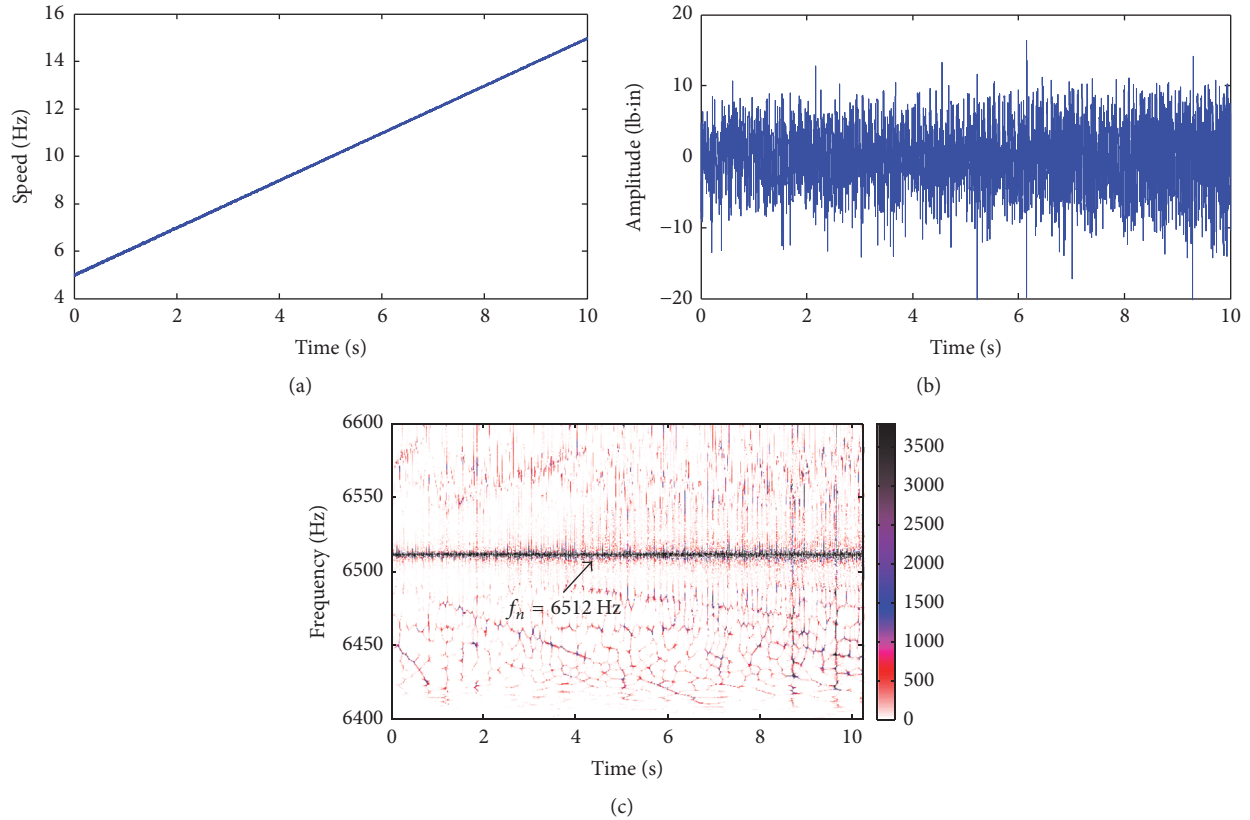


FIGURE 14: Resonance frequency identification: (a) drive motor speed, (b) detrended torsional vibration signal, and (c) reassigned Morlet scalogram.

of the ring gear fault frequency  $1/3nf_r$ . The presence of  $1/3$  harmonics of the ring gear fault frequency is reasonable, because of nonidentical planet gears. In Fourier spectrum, and amplitude and frequency demodulation spectra, all the peaks related to the ring gear fault frequency are higher than the baseline signal. This feature implies the ring gear fault.

The above analyses illustrate the effectiveness of our proposed approach in diagnosing planetary gearbox faults via torsional vibration signal analysis in resonance region.

## 7. Conclusions

Torsional vibration signals are free from the additional amplitude modulation effect due to time-varying vibration transmission paths, and they have simpler spectral structure than translational vibration signals, being able to reflect gear fault more effectively. Localized gear faults generate impulses in load torque, thus exciting torsional resonance vibrations and leading to modulation effect on resonance vibration. Therefore, torsional vibration in resonance region can be modelled as an AM-FM process. Its Fourier spectrum, and amplitude and frequency demodulated spectra are derived explicitly. In Fourier spectrum, the sideband around resonance frequency has a spacing equal to gear fault frequency. In both amplitude and frequency demodulated

spectra, peaks directly link to gear fault frequency harmonics. For fault diagnosis based on above theoretical derivations, a torsional resonance frequency identification method via time-frequency analysis of torsional vibration signals during variable speed process is proposed, by exploiting the independence nature of resonance on running speed. The resonance frequency can be recognized as the frequency corresponding to a straight line parallel to the time axis on the time-frequency plane. Given the resonance frequency, gear fault can be diagnosed by sideband analysis, and amplitude and frequency demodulation analysis of the sensitive component in resonance region. The theoretical derivations and proposed approach are illustrated by a numerical simulation and are validated with both dynamics modelling data of a planetary gear set and lab experimental signals of a planetary gearbox.

## Conflicts of Interest

The authors declare that there are no conflicts of interest regarding the publication of this paper.

## Acknowledgments

This work is supported by National Natural Science Foundation of China (51475038).

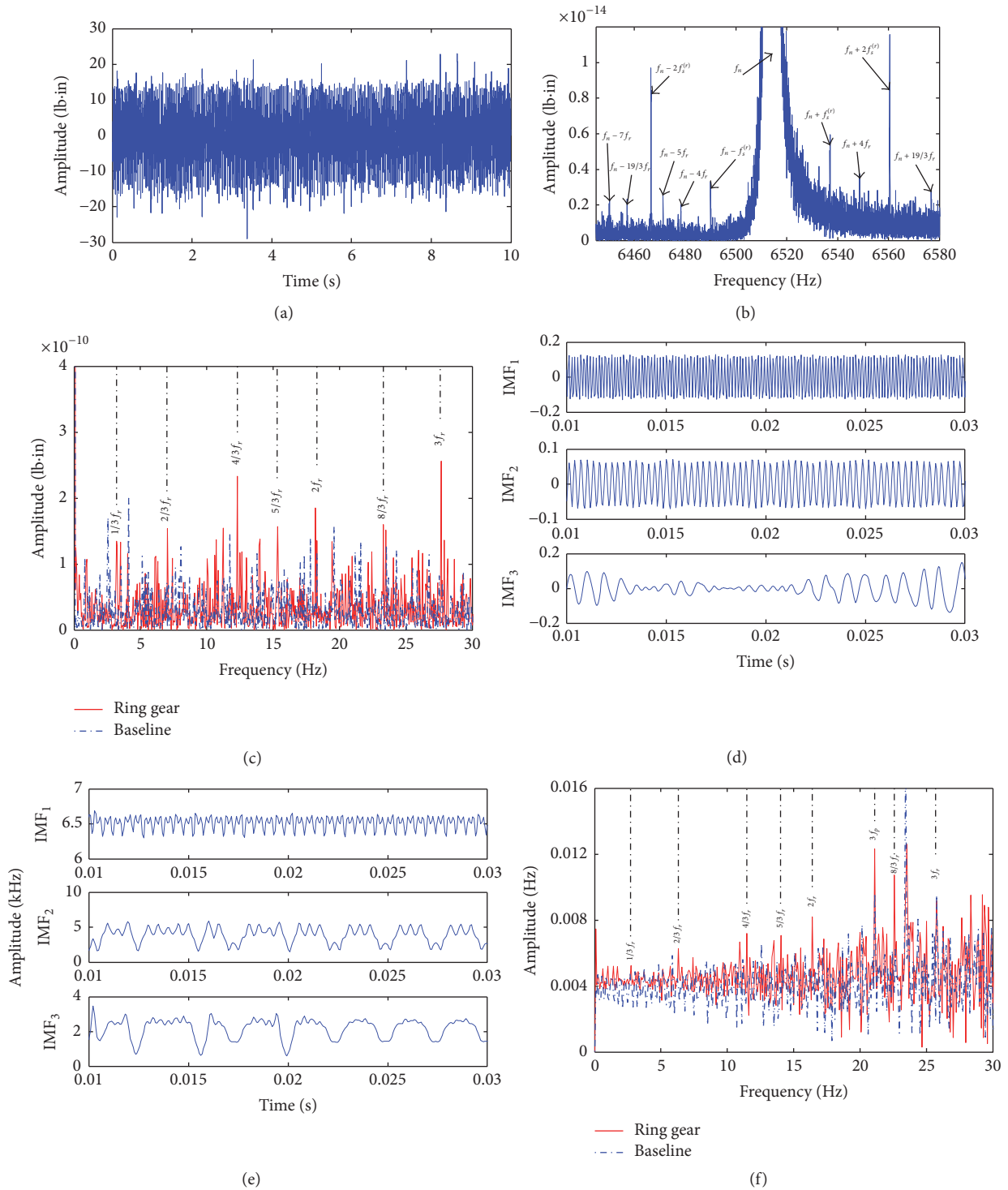


FIGURE 15: Ring gear fault signal analysis: (a) detrended torsional vibration signal, (b) Fourier spectrum, (c) envelop spectrum, (d) IMFs, (e) instantaneous frequencies of IMFs, and (f) Fourier spectrum of instantaneous frequency.

**References**

[1] P. D. Samuel and D. J. Pines, “A review of vibration-based techniques for helicopter transmission diagnostics,” *Journal of Sound and Vibration*, vol. 282, no. 1-2, pp. 475–508, 2005.

[2] Y. G. Lei, J. Lin, M. J. Zuo, and Z. J. He, “Condition monitoring and fault diagnosis of planetary gearboxes: a review,” *Measurement*, vol. 48, no. 2, pp. 292–305, 2014.

[3] P. D. McFadden, “A technique for calculating the time domain averages of the vibration of the individual planet gears and

- the sun gear in an epicyclic gearbox,” *Journal of Sound and Vibration*, vol. 144, no. 1, pp. 163–172, 1991.
- [4] P. D. McFadden, “Window functions for the calculation of the time domain averages of the vibration of the individual planet gears and sun gear in an epicyclic gearbox,” *Journal of Vibration and Acoustics*, vol. 116, no. 2, pp. 179–187, 1994.
- [5] P. D. Samuel and D. J. Pines, “Vibration separation methodology for planetary gear health monitoring,” in *Proceedings of the Proceeding of SPIE*, vol. 3985, pp. 250–260, March 2000.
- [6] X. Liang, M. J. Zuo, and L. Liu, “A windowing and mapping strategy for gear tooth fault detection of a planetary gearbox,” *Mechanical Systems and Signal Processing*, vol. 80, pp. 445–459, 2016.
- [7] T. Barszcz and R. B. Randall, “Application of spectral kurtosis for detection of a tooth crack in the planetary gear of a wind turbine,” *Mechanical Systems and Signal Processing*, vol. 23, no. 4, pp. 1352–1365, 2009.
- [8] Y. G. Lei, D. Han, J. Lin, and Z. J. He, “Planetary gearbox fault diagnosis using an adaptive stochastic resonance method,” *Mechanical Systems and Signal Processing*, vol. 38, no. 1, pp. 113–124, 2013.
- [9] J. Yoon, D. He, B. Van Hecke, T. J. Nostrand, J. Zhu, and E. Bechhoefer, “Vibration-based wind turbine planetary gearbox fault diagnosis using spectral averaging,” *Wind Energy*, vol. 19, no. 9, pp. 1733–1747, 2016.
- [10] P. D. McFadden and J. D. Smith, “An explanation for the asymmetry of the modulation sidebands about the tooth meshing frequency in epicyclic gear vibration,” *Proceedings of the Institution of Mechanical Engineers, Part C: Journal of Mechanical Engineering Science*, vol. 199, no. 1, pp. 65–70, 1985.
- [11] J. McNames, “Fourier series analysis of epicyclic gearbox vibration,” *Journal of Vibration and Acoustics*, vol. 124, no. 1, pp. 150–152, 2002.
- [12] M. Mosher, “Understanding vibration spectra of planetary gear systems for fault detection,” in *Proceedings of ASME Design Engineering Technical Conferences*, pp. 1–8, 2003.
- [13] Z. Feng and M. J. Zuo, “Fault diagnosis of planetary gearboxes via torsional vibration signal analysis,” *Mechanical Systems and Signal Processing*, vol. 36, no. 2, pp. 401–421, 2013.
- [14] M. Inalpolat and A. Kahraman, “A theoretical and experimental investigation of modulation sidebands of planetary gear sets,” *Journal of Sound and Vibration*, vol. 323, no. 3–5, pp. 677–696, 2009.
- [15] M. Inalpolat and A. Kahraman, “A dynamic model to predict modulation sidebands of a planetary gear set having manufacturing errors,” *Journal of Sound and Vibration*, vol. 329, no. 4, pp. 371–393, 2010.
- [16] X. H. Liang, M. J. Zuo, and M. R. Hoseini, “Vibration signal modeling of a planetary gear set for tooth crack detection,” *Engineering Failure Analysis*, vol. 48, pp. 185–200, 2015.
- [17] M. Abramowitz and I. A. Stegun, *Handbook of Mathematical Functions with Formulas, Graphs, and Mathematical Tables*, Dover Publications, New York, NY, USA, 9th edition, 1972.
- [18] N. E. Huang, Z. Shen, S. R. Long et al., “The empirical mode decomposition and the Hilbert spectrum for nonlinear and non-stationary time series analysis,” *Proceedings of the Royal Society A*, vol. 454, no. 1971, pp. 903–995, 1998.
- [19] Z. H. Wu and N. E. Huang, “Ensemble empirical mode decomposition: a noise-assisted data analysis method,” *Advances in Adaptive Data Analysis (AADA)*, vol. 1, no. 1, pp. 1–41, 2009.
- [20] Z. Feng and M. J. Zuo, “Vibration signal models for fault diagnosis of planetary gearboxes,” *Journal of Sound and Vibration*, vol. 331, no. 22, pp. 4919–4939, 2012.
- [21] Z. P. Feng, M. Liang, Y. Zhang, and S. M. Hou, “Fault diagnosis for wind turbine planetary gearboxes via demodulation analysis based on ensemble empirical mode decomposition and energy separation,” *Journal of Renewable Energy*, vol. 47, pp. 112–126, 2012.

## Research Article

# Nonpenetrating Damage Identification Using Hybrid Lamb Wave Modes from Hilbert-Huang Spectrum in Thin-Walled Structures

Zijian Wang,<sup>1</sup> Pizhong Qiao,<sup>2</sup> and Binkai Shi<sup>3</sup>

<sup>1</sup>Department of Dam Safety Management, Nanjing Hydraulic Research Institute, Nanjing 210029, China

<sup>2</sup>Department of Civil and Environmental Engineering and Composite Materials and Engineering Center, Washington State University, Pullman, WA 99164-2910, USA

<sup>3</sup>School of Mechanics and Materials, Hohai University, Nanjing 210098, China

Correspondence should be addressed to Zijian Wang; [zijianwang@nhri.cn](mailto:zijianwang@nhri.cn)

Received 12 June 2017; Revised 19 September 2017; Accepted 16 October 2017; Published 20 November 2017

Academic Editor: Sandris Ručevskis

Copyright © 2017 Zijian Wang et al. This is an open access article distributed under the Creative Commons Attribution License, which permits unrestricted use, distribution, and reproduction in any medium, provided the original work is properly cited.

Lamb waves have shown promising advantages for damage identification in thin-walled structures. Multiple modes of Lamb wave provide diverse sensitivities to different types of damage. To sufficiently utilize damage-related wave features, damage indices were developed by using hybrid Lamb wave modes from Hilbert-Huang spectra. Damage indices were defined as surface integrals of Hilbert-Huang spectra on featured regions determined by time and frequency windowing. The time windowing was performed according to individual propagation velocity of different Lamb wave mode, while the frequency windowing was performed according to the frequency of excitation. By summing damage indices for all transmitter-receiver pairs, pixels were calculated to reconstruct a damage map to characterize the degree of damage at each location on structure. Both numerical and experimental validations were conducted to identify a nonpenetrating damage. The results demonstrated that the proposed damage indices using hybrid Lamb wave modes are more sensitive and robust than the one using single Lamb wave mode.

## 1. Introduction

Applying walls as thin as possible is a natural optimization to minimize dead load and reduce construction cost. These thin-walled structures have been widely used in aircraft fuselages, storage vessels, sluices, and so forth. However, long-period service deteriorates structural resistance and increases the possibility of failure. Impact, abrasion, and corrosion could cause nonpenetrating damage on thin-walled structures. It is imperative to identify this damage as early as possible to prevent it from penetrating the cross-section and causing catastrophic failure.

Recently, Lamb waves have shown promising suitability for damage identification in thin-walled structures. Irradiating through thickness and propagating over substantial areas, Lamb waves can assess structural integrity without

probe movement. Due to high vibration frequency, typically from kilohertz to megahertz [1], Lamb waves are sensitive to small damage at millimeter scale, which are hard to be identified by low-frequency methods. Furthermore, multiple modes of Lamb wave provide diverse sensitivities to identify different types of damage. Among all the Lamb wave modes, fundamental symmetric  $S_0$  [2] and antisymmetric  $A_0$  [3] modes have been widely used because of their great amplitude. Based on the dependence of amplitude on frequency of excitation and propagation velocity, we can intentionally amplify or depress Lamb wave modes to obtain a wave field dominated by single mode. Many researches have been reported to separate Lamb wave mode [4–6] and use single mode to identify damage. Using single Lamb wave mode with nondispersive velocity and low attenuation [7], various kinds of damage, including crack [8], delamination [9],

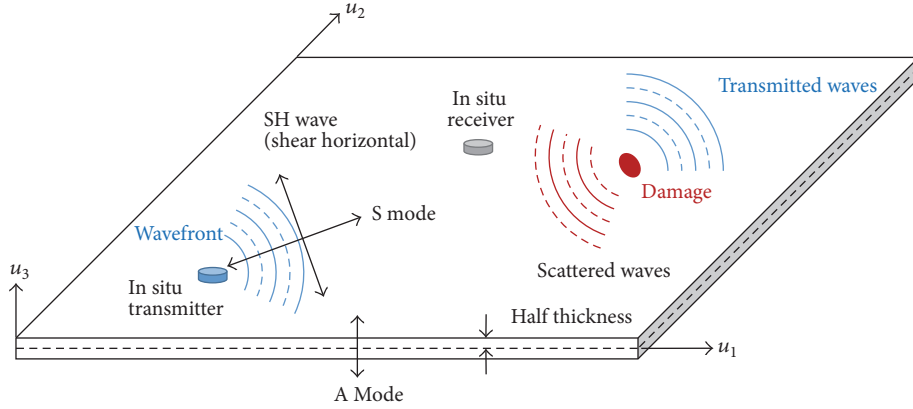


FIGURE 1: Propagating waves in thin-walled structures.

distributed micro defect [10], fatigue [11], and corrosion [12], have been identified. Various damage indices have been developed to interpret Lamb wave signals and alleviate noises by transforming Lamb wave signals to different physical domains. The ways to transform Lamb wave signals include short-time Fourier [13], wavelet [14], and Hilbert-Huang [15] transformations. By plotting damage indices at each location, we can produce a damage map to characterize the degree of damage over structure.

However, using single Lamb wave mode neglects damage-related features of other Lamb wave modes and, accordingly, compromises the identification of nonpenetrating damage. This deficiency becomes serious when adopting sparse sensors to identify nonpenetrating damage in noisy environment. To this end, it is desirable to use hybrid Lamb wave modes to enhance the sensitivity and robustness of sparse sensors to identify nonpenetrating damage. In this study, since there is no conclusive superiority of a specific Lamb wave mode to identify nonpenetrating damage, we used both  $S_0$  and  $A_0$  Lamb wave modes to develop damage indices. By transforming Lamb wave signals to a time-frequency spectrum via Hilbert-Huang transformation, damage indices were defined as surface integrals on featured regions determined by time and frequency windowing. The time windowing was performed according to individual propagation velocity of different Lamb wave mode, while the frequency windowing was performed according to the frequency of excitation. The usage of hybrid Lamb wave modes increased the capability of sparse sensors to identify nonpenetrating damage in noisy environment. Both numerical and experimental implementation presented damage more distinctly on damage map, indicating good improvement of the proposed method over the one using single mode.

## 2. Wave Propagation in Thin-Walled Structures

Wave propagation in thin-walled structures, for example, plates and shells, is guided by upper and bottom surfaces, producing Lamb waves in  $u_1$ - $u_3$  plane, and shear horizontal

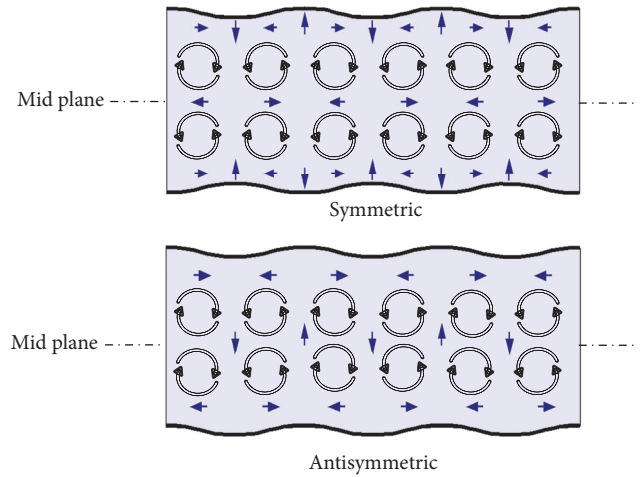


FIGURE 2: Displacement of Lamb wave modes.

(SH) wave in  $u_1$ - $u_2$  plane (see Figure 1). According to the displacement pattern, Lamb waves can be seen as symmetric and antisymmetric modes (see Figure 2). For the application of Lamb waves on damage identification, we use group velocity to characterize wave propagations. The group velocity of SH wave is solved as the velocity of shear vertical wave  $c_T$  [16], while the group velocities of Lamb waves are solved from the Rayleigh-Lamb equation [17]:

$$\frac{\tan ph}{\tan qh} = - \left[ \frac{4k^2 pq}{(k^2 - q^2)^2} \right]^{\pm 1} \quad (1)$$

$$p = \sqrt{\left(\frac{\omega}{c_L}\right)^2 - k^2}$$

$$q = \sqrt{\left(\frac{\omega}{c_T}\right)^2 - k^2},$$

where  $h$  is the half thickness of plate;  $k$  is the wave number;  $\omega$  is the circular frequency;  $c_L$  is the velocity of longitudinal

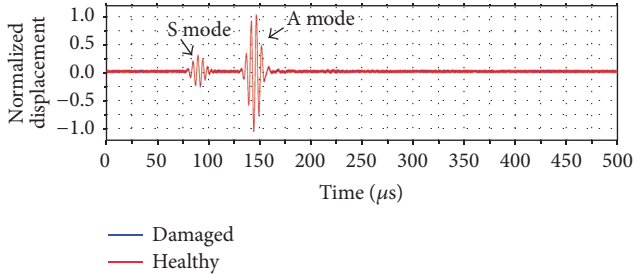


FIGURE 3: Lamb wave signals.

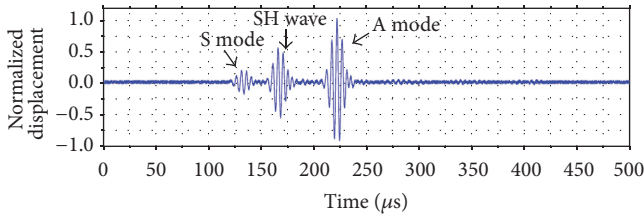


FIGURE 4: Residual signal.

wave;  $c_T$  is the velocity of shear vertical wave; and +1 and -1 represent symmetric and antisymmetric modes, respectively.

### 3. Physical Process of Damage Identification

Figure 3 shows two Lamb signals acquired from healthy and damaged finite element (FE) models, respectively. Details about the FE model are given in Section 6. Two wave peaks around 90 and 140  $\mu\text{s}$  correspond to  $S_0$  and  $A_0$  Lamb wave modes, respectively. Amplitudes of different Lamb wave modes can be controlled by changing the tuning frequency of excitation [18]. In this case,  $A_0$  mode gains triple amplitude as  $S_0$  mode. Since the damaged signal contains direct waves from the excitation and scattered waves from damage, there is small difference between healthy and damaged signals, as shown in Figure 3. To extract scattered waves caused by damage, we subtract healthy signal from damaged one to get a residual signal, as shown in Figure 4. Since boundary reflections are the same for damaged and healthy signals, this subtraction can eliminate the interference of boundary reflection, and the overlap of direct waves and boundary reflections cannot affect the residual signal. At this point, we could see the residual signal as a wave transmitted by damage as a second wave source. Since different waves propagate with individual velocities, we can obtain separated Lamb wave modes as different wave peaks in the residual signal by deploying sensors at a distance from the damage.

In this case, mode conversion at damage generates SH waves in the residual signal along with  $S_0$  and  $A_0$  modes. The phases of these wave peaks indicate the location of damage. By multiplying time interval between excitation and these wave peaks with wave velocity, we can determine the distance from transmitter through damage to receiver

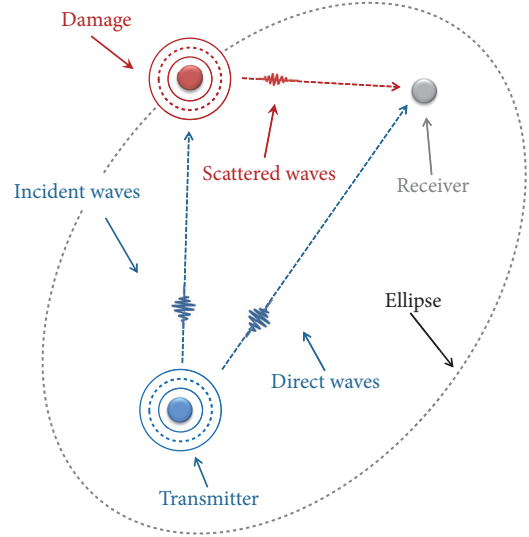


FIGURE 5: Ellipse determined by individual transmitter-receiver pair.

and draw an ellipse on which possible damage locates (see Figure 5). The superposition of multiple ellipses determined by each transmitter-receiver pair finally presents the location of damage.

### 4. Hilbert-Huang Transformation

For real situation, wave peaks in residual signal are inadequate to characterize damage because of their vulnerability to noise and insensitivity to weak damage scattering (e.g., scattered waves caused by nonpenetrating damage). In most cases, we need to develop damage indices from multiple physical domains to characterize damage. Therefore, Hilbert-Huang transformation (HHT) gains its popularity to analyze Lamb wave signals in time and frequency domains. The HHT provides intuitive and direct basis to characterize nonstationary Lamb wave signals based on a simple but reasonable assumption: a signal can be decomposed into a finite and a small number of simple oscillatory modes, with significantly different frequencies, one superimposed on another [19]. This assumption is suitable with real situation, since frequency of Lamb wave signal is significantly higher than environmental noises. These simple oscillatory modes are defined as intrinsic mode functions (IMFs) which satisfy two requirements: the number of extreme values and zero points must be equal or differ at most by one; and the function must be symmetric about the local mean. The IMFs are obtained by a sifting process. The local maxima and minima points of input signal are firstly identified to form an upper and lower envelope together with the mean curve  $m_1(t)$ . The difference between input signal  $x(t)$  and mean curve  $m_1(t)$  is designated as a prototype IMF  $h_1(t)$ . However, the prototype cannot meet the requirements of IMF in most cases, so the sifting process is repeated by treating the prototype IMF as another input signal through the above steps. This repetition

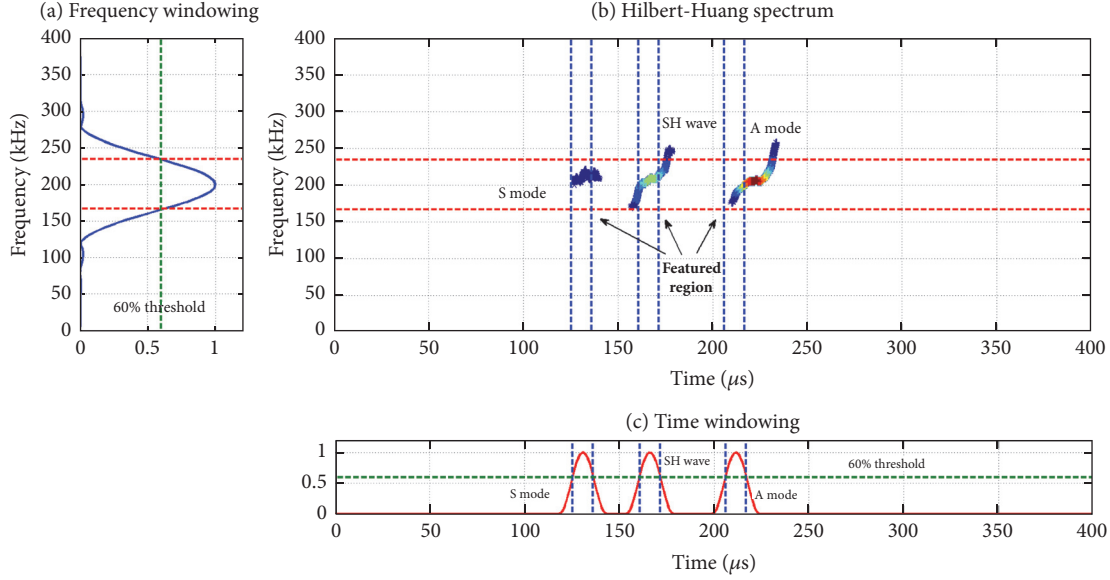


FIGURE 6: Formation of damage index.

aims to eliminate the low-frequency tendency and makes the signal more symmetric to meet the requirements of IMF. This sifting process stops when index  $SD_k$  is smaller than a predetermined value as follows:

$$SD_k = \frac{\sum_{t=0}^T |h_{k-1}(t) - h_k(t)|^2}{\sum_{t=0}^T h_{k-1}^2(t)}, \quad (2)$$

where  $T$  is the sampling period. After  $k$  times sifts, the prototype IMF  $h_{1k}(t)$  becomes the first IMF  $c_1(t)$ , which represents highest-frequency oscillation in input signal  $x(t)$ , whereas the residual  $r_1(t) = x(t) - c_1(t)$  contains lower-frequency oscillation. Then the residual  $r_1(t)$  is treated as another input signal repeatedly in sifting process to obtain successive IMFs of lower frequency, until it becomes a constant or monotonic function, presenting original input signal  $x(t)$  as follows:

$$x(t) = \sum_{j=1}^n c_j(t) + r(t), \quad (3)$$

where  $c_j(t)$  is the  $j$ th IMF and  $r(t)$  is a final constant or a monotonic function.

The IMFs generated by this sifting process lead to a robust Hilbert transformation without the presence of negative frequencies. The Hilbert-Huang spectrum of the input signal  $x(t)$  is obtained by summing the Hilbert spectrum of each IMF as follows:

$$H(t, f) = \sum_{j=1}^n a_j(t) e^{i \int \omega_j(t) dt}, \quad (4)$$

where  $a_j(t)$  and  $\omega_j(t)$  are the instantaneous amplitude and frequency of the  $j$ th IMF, respectively. At this point, the input signal  $x(t)$  is represented as distinct energy distribution in a time-frequency spectrum where a damage index can be developed.

## 5. Formulation of Damage Index

Applying Hilbert-Huang transformation on the Lamb wave signal presented in Figure 4, a time-frequency spectrum is produced in Figure 6. The damage index is formulated by integrating the Hilbert-Huang spectrum on featured regions selected by time and frequency windowing.

For the frequency windowing, damage-related waves are assumed to have the same frequency with excitation. The width of frequency window is determined by a 60% threshold of the amplitude in Fast-Fourier spectrum of excitation (see Figure 6(a)). This threshold is chosen empirically to obtain a narrow frequency window to eliminate interferences from other frequencies and secure sufficient energy to develop robust damage indices.

For the time windowing, scattered waves are assumed to have the same waveform with excitation. At a given location  $(x, y)$ , the time-of-flight  $\Delta t$  for a specific wave mode is estimated by

$$\Delta t = \frac{\sqrt{(x_t - x)^2 + (y_t - y)^2} + \sqrt{(x_r - x)^2 + (y_r - y)^2}}{v}, \quad (5)$$

where  $x_t$ ,  $y_t$ ,  $x_r$ , and  $y_r$  are the coordinates of transmitter and receiver, respectively; and  $v$  is the propagation velocity of a specific wave mode. By shifting envelop of excitation according to the time-of-flight calculated in (5), the envelope of wave peaks in residual signal can be estimated. The estimated time of arrival of  $S_0$ , SH, and  $A_0$  wave modes is shown in Figure 6(c). The envelop  $y(t)$  is calculated by Hilbert transformation as follows:

$$H[x(t)] = \frac{1}{\pi} P \int_{-\infty}^{\infty} \frac{x(\tau)}{t - \tau} d\tau \quad (6)$$

$$y(t) = x(t) + iH[x(t)],$$

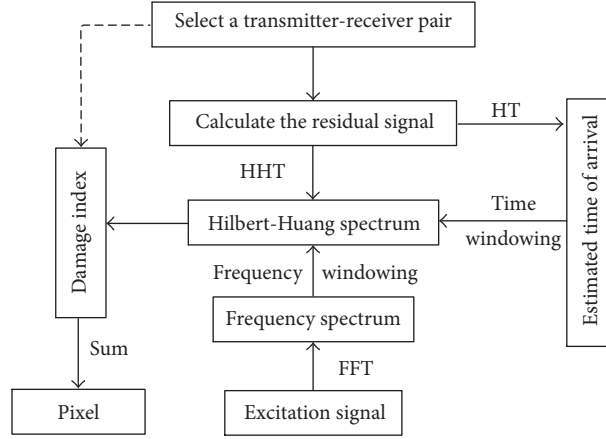


FIGURE 7: Procedure of damage identification.

where  $P$  is the Cauchy principal value. The width of time window is determined by a 60% threshold of the envelop of excitation  $|y(t)|$  (see Figure 6(c)). This threshold is chosen empirically to obtain a narrow time window to eliminate interferences from other wave modes and secure sufficient energy to develop robust damage indices.

After the time and frequency windowing, three rectangular featured regions are shown in Figure 6(b), associated with  $S_0$ , SH, and  $A_0$  wave modes, respectively. A damage index  $DI(x, y)$  is defined as surface integral of Hilbert-Huang spectrum on these featured regions as follows:

$$\begin{aligned}
 DI(x, y) = & \iint_{S_0} HHS(t, f) dt df \\
 & + \iint_{A_0} HHS(t, f) dt df \\
 & + \iint_{SH} HHS(t, f) dt df.
 \end{aligned} \quad (7)$$

The pixel at location  $(x, y)$  on the damage map is defined as the sum of damage index determined by individual transmitter-receiver pair as follows:

$$P(x, y) = \sum_{i=1}^n DI_i, \quad (8)$$

where  $i$  denotes the  $i$ th transmitter-receiver pair.

At this point, damage is identified on a reconstructed map based on the proposed damage indices, by following the procedure, as shown in Figure 7. Pixels on the damage map indicate the degree of damage at this location.

## 6. Numerical Implementation

To validate the effectiveness of proposed damage indices, we simulated the physical process of wave excitation, propagation, and scattering in Abaqus 6.11. The FE model was in

$400 \times 400 \times 4$  (length  $\times$  width  $\times$  depth) mm, discretized by  $1 \times 1 \times 1$  mm C3D8R elements. Damping elements were assigned around the plate to absorb boundary reflections. Four piezoelectric transducers (PZTs) were placed at corners of an AL6061-T6 aluminum plate to excite or receive Lamb waves. The excitation (200 kHz tone burst) was applied as nodal force on a rectangular region ( $5 \times 5$  mm) in  $x$ - $y$  plane (see Figure 8). Considering numerical stability and efficiency, time increment  $\Delta t$  and duration were chosen as  $1 \times 10^{-7}$  s and 1 ms, respectively. Twelve elements were deleted from the mesh to simulate a  $2 \times 2 \times 3$  (length  $\times$  width  $\times$  depth) mm nonpenetrating damage (see Figure 9). The coordinates of transducers and damage are shown in Figure 8, according to the Cartesian coordinate at plate center.

By exciting transducers in turns, Lamb waves were acquired as magnitude of displacements at receivers (see Figure 9), producing 16 signals in healthy and damaged plate, respectively. Transmitted and scattered waves were denoted in a snapshot, as shown in Figure 9. Scattered waves were extracted as residual signals by subtracting healthy signals from damaged ones (see Figure 10). However, mode conversion led to the presence of SH waves as second wave peak in residual signals, along with  $S_0$  and  $A_0$  Lamb wave mode as first and third wave peaks. Based on the velocity measurements on healthy plate, the group velocities of the  $S_0$ ,  $A_0$ , and SH waves were determined as 5183, 2982, and 3892 m/s, respectively. Since scattered waves were affected by incident angles and shape of damage, it is difficult to obtain comparative amplitude for different scattered waves.

To examine noisy immunity of the proposed damage indices, 150% Gaussian noises were blended into residual signals. Following the procedure of damage identification in Figure 7, normalized damage maps were produced using  $S_0$  mode,  $A_0$  mode, SH wave, and hybrid waves, respectively (see Figure 11). Pixels on these damage maps were calculated according to (8). Large pixel indicates strong wave scattering, which relates to the presence of damage. The damage maps using single wave mode are interfered by Gaussian noises,

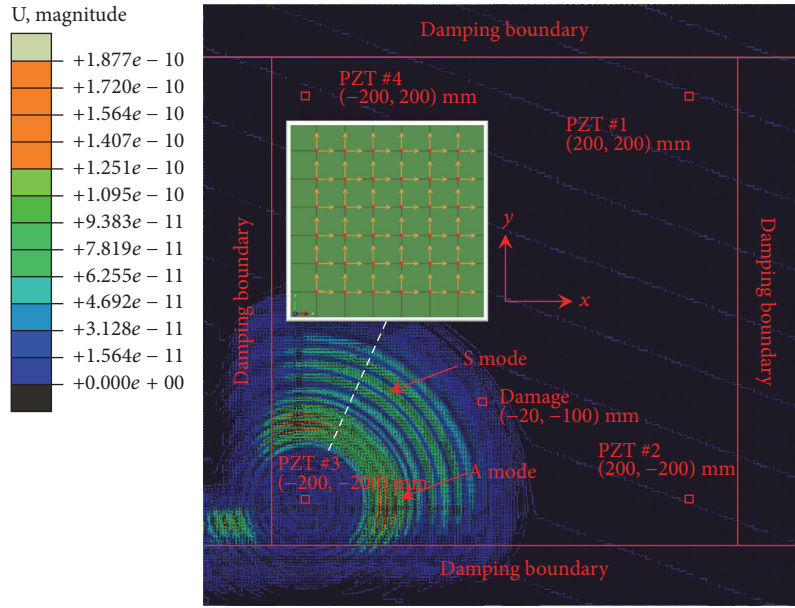


FIGURE 8: Wave excitation in FE model.

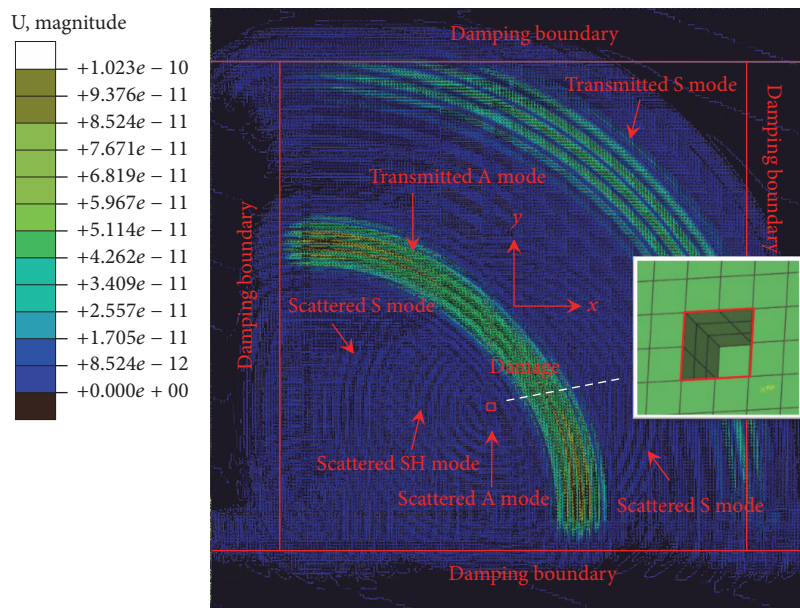


FIGURE 9: Wave scattering at damage.

presenting a blurry damage identification at the location of  $(-20, -100 \text{ mm})$ , along with a lot of false damage spots (red pixel) at other places, while the damage map using hybrid wave modes obtains appropriate amplification of pixel at the location of  $(-20, -100 \text{ mm})$ , presenting a concentrated damage identification. The comparison between these damage maps indicates that the proposed damage indices are more sensitive and robust to identify nonpenetrating damage in noisy environment than the ones using single wave mode.

## 7. Experimental Implementation

In parallel, we conducted an experiment to identify a nonpenetrating damage in an AL6061-T6 aluminum plate, whose dimensions were  $700 \times 800 \times 3$  (length  $\times$  width  $\times$  depth) mm. Four PZT disks (5 mm in diameter, 0.5 mm in thickness) were surface-bonded by epoxy at corners (see Figure 12). A nonpenetrating damage was manufactured by drilling a groove in size of  $4 \times 4 \times 1$  (length  $\times$  width  $\times$  depth) mm.

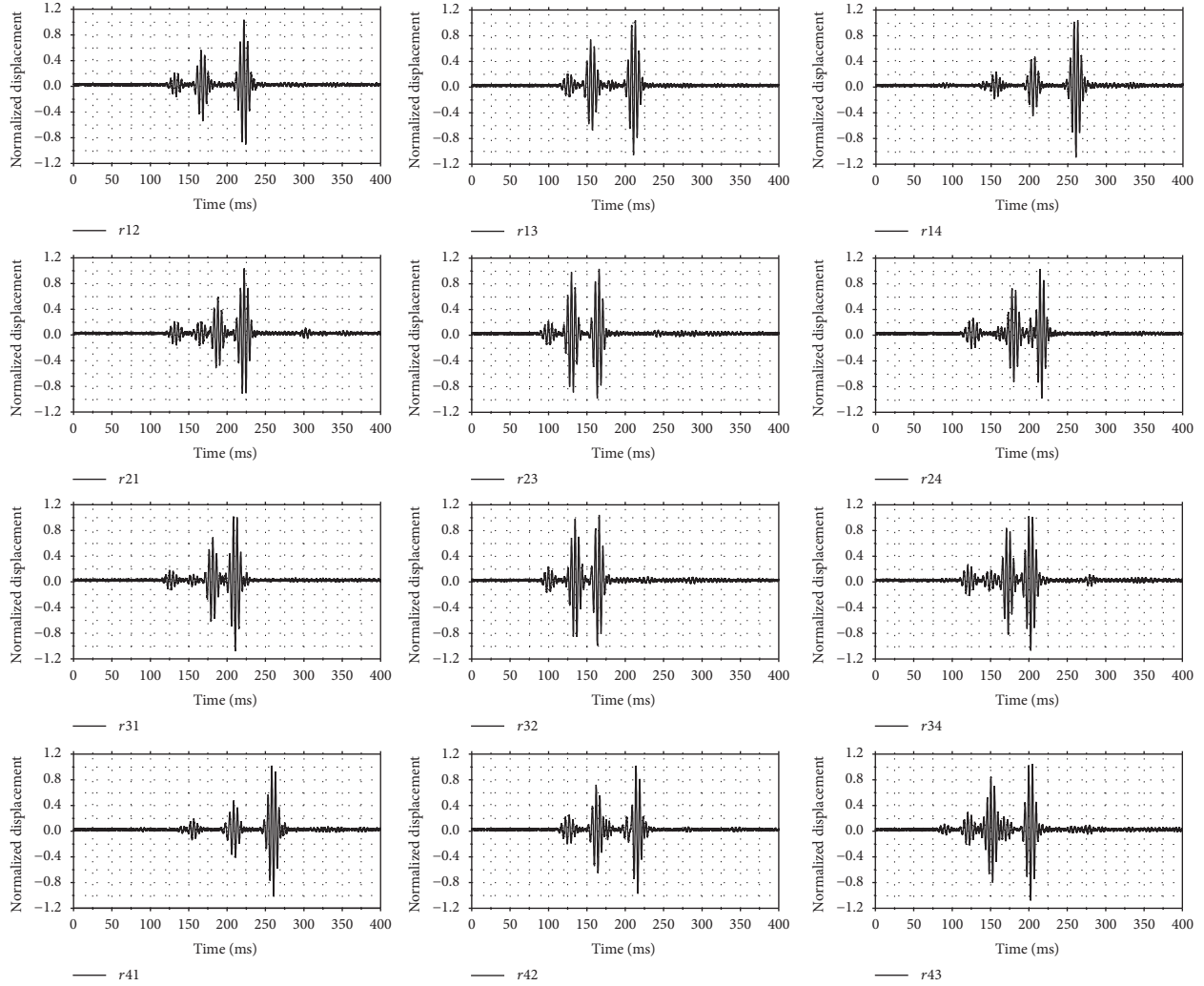


FIGURE 10: Residual signal of different transmitter-receiver pair (FE simulation).

A 190 kHz tone burst was generated by an Agilent 3325A waveform generator. The voltage of tone burst was amplified to 200 Vpp by a PINTOK HA-405 voltage amplifier. A signal that came from monitoring terminal of the voltage amplifier was imported to an Agilent DSO7034B digital oscilloscope as trigger to coordinate excitation and reception. Once a transmitter excited, the oscilloscope recorded voltages of receivers in 1.7 ms with a sampling frequency of 10 MHz (see Figure 13). Since the circular groove scattered waves in all directions evenly, mode conversion at circular groove was not as serious as rectangular damage shown in the numerical FE simulation in Section 6. Only  $S_0$  and  $A_0$  Lamb wave modes were clearly presented, with group velocities of 4822 and 2993 m/s, respectively. Accordingly, damage indices in the following damage mapping adopted the first two terms in (7). Received signals were filtered by a Krohn-Hite 3384 filter (band pass from 180 to 200 kHz) and then blended with 100% Gaussian noises. By calculating pixels according to (8), damage maps reconstructed by  $S_0$  mode,  $A_0$  mode, and hybrid

Lamb wave modes are shown in Figure 14. As presented in the numerical implementation, the proposed damage indices are more sensitive and robust to nonpenetrating damage in noisy environment than the indices using single wave mode. In Figure 14(c), pixels near actual location of the damage (black dot) are amplified by hybrid Lamb wave modes, while random noises are offset by each other, producing small pixels at other places.

## 8. Discussion and Conclusions

In this study, damage indices using hybrid Lamb wave modes were proposed, and they were successively implemented in both numerical and experimental cases. Residual signals generated by transmitter-receiver pairs were calculated by subtracting healthy signals from damaged ones. The subsequent, residual signals were subjected to Hilbert-Huang transformation to produce time-frequency spectra. By windowing Hilbert-Huang spectra from time and frequency

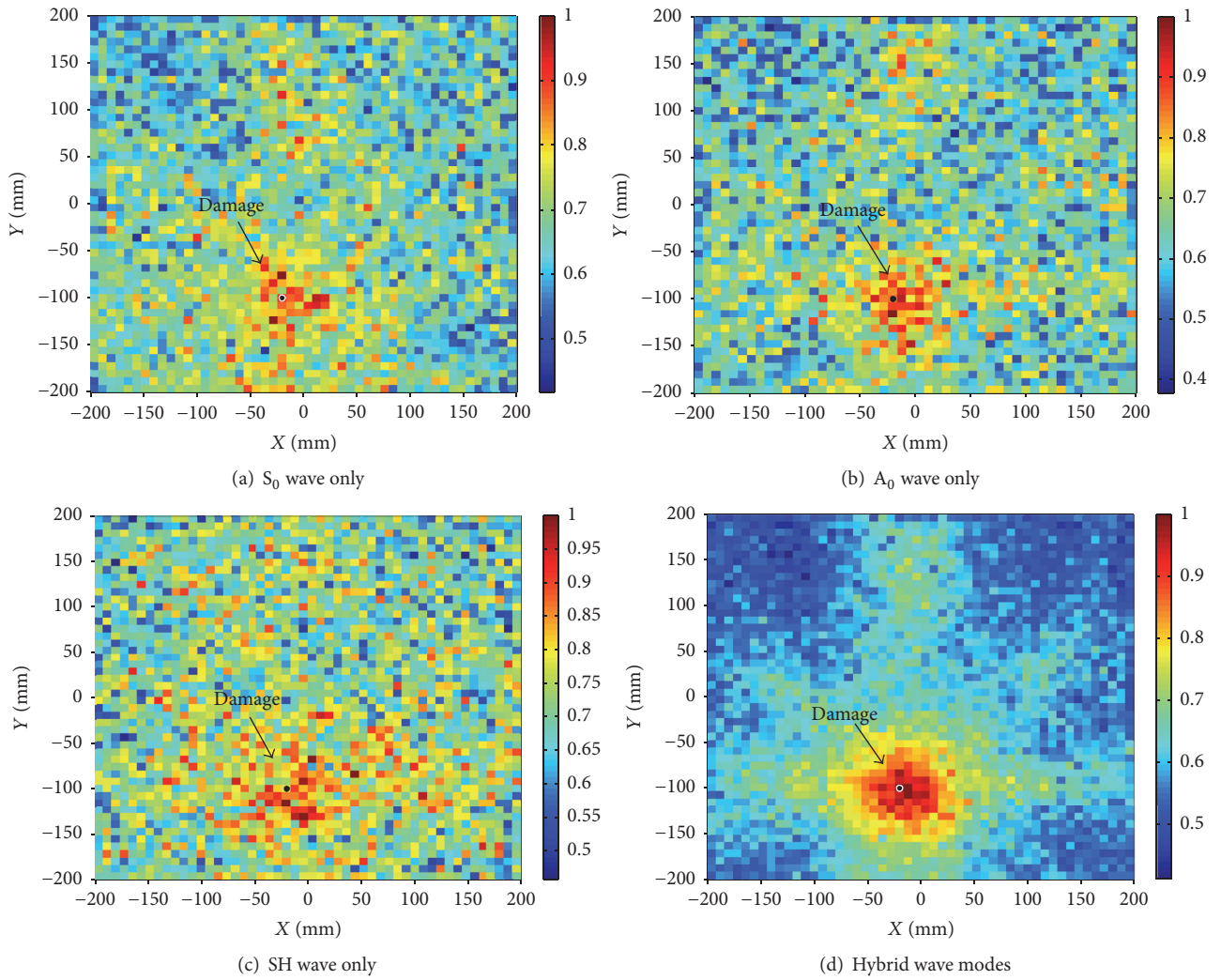


FIGURE 11: Comparison of damage maps (FE simulation).

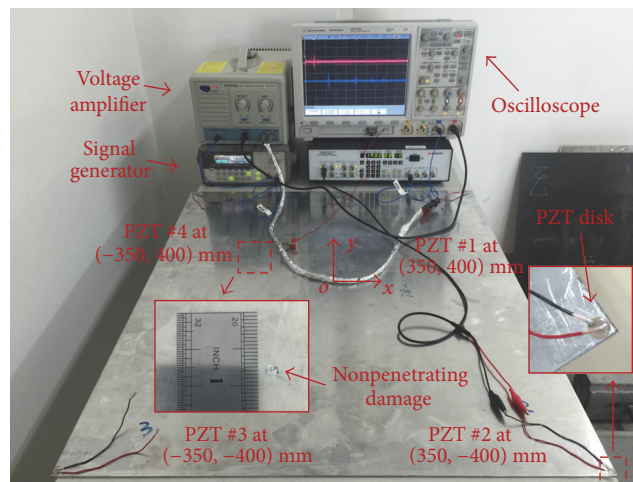


FIGURE 12: Experiment setup.

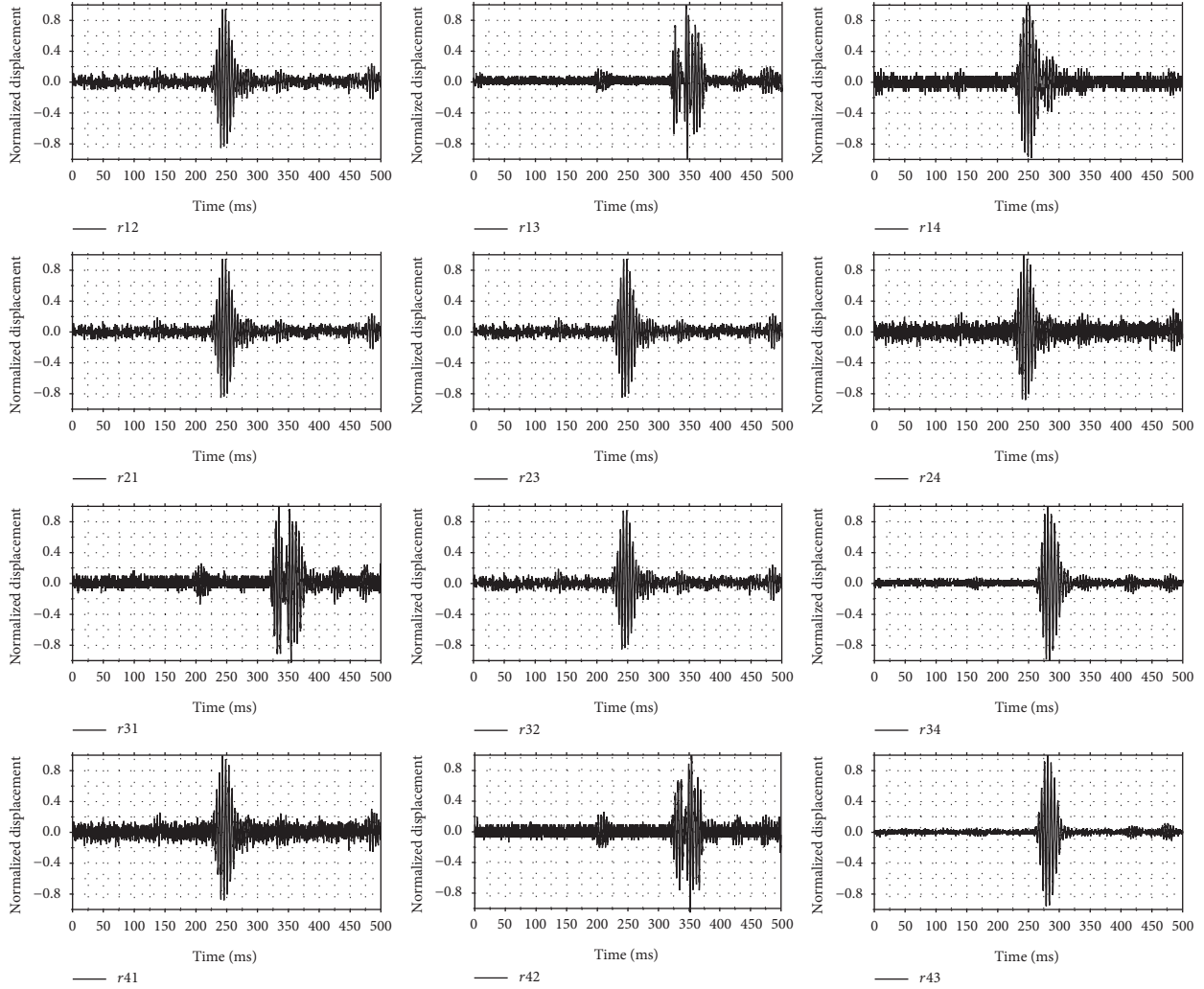


FIGURE 13: Residual signals of different transmitter-receiver pair (experiment).

domains, featured regions were determined where the damage indices were formulated. The time windowing was performed according to individual propagation velocity of different Lamb wave modes, while the frequency windowing was performed according to the Fourier spectrum of excitation. The damage index was defined as surface integrals of Hilbert-Huang spectrum on these featured regions. By summing damage indices produced by all transmitter-receiver pairs, we reconstructed a damage map whose pixels indicate the degree of damage at each location on the plate. As shown in both numerical and experimental implementations, the usage of hybrid Lamb wave modes increases the signal-to-noise ratio, and it consequently improves sensitivity and robustness to nonpenetrating damage.

With successful damage identification before penetrating through wall cross-section, as presented in this study, we are able to warn about potential failure at early stage and, accordingly, improve the reliability of thin-walled structures. Moreover, the implementation of in situ transducers, as

shown in the experiment, facilitates real-time structural health monitoring instead of periodical inspection. However, insufficient consideration of wave scattering at damage leads to varying amplitude for different scattered waves, which compromised the improvement of hybrid wave method in some degree. It is encouraging to study the amplitude changes and mode conversion of scattered waves in the future research.

## Conflicts of Interest

The authors declare that they have no conflicts of interest.

## Acknowledgments

The first author wants to acknowledge the financial support received from the National Key Research and Development Program of China (Grant no. 2016YFC0401603) and the Fund

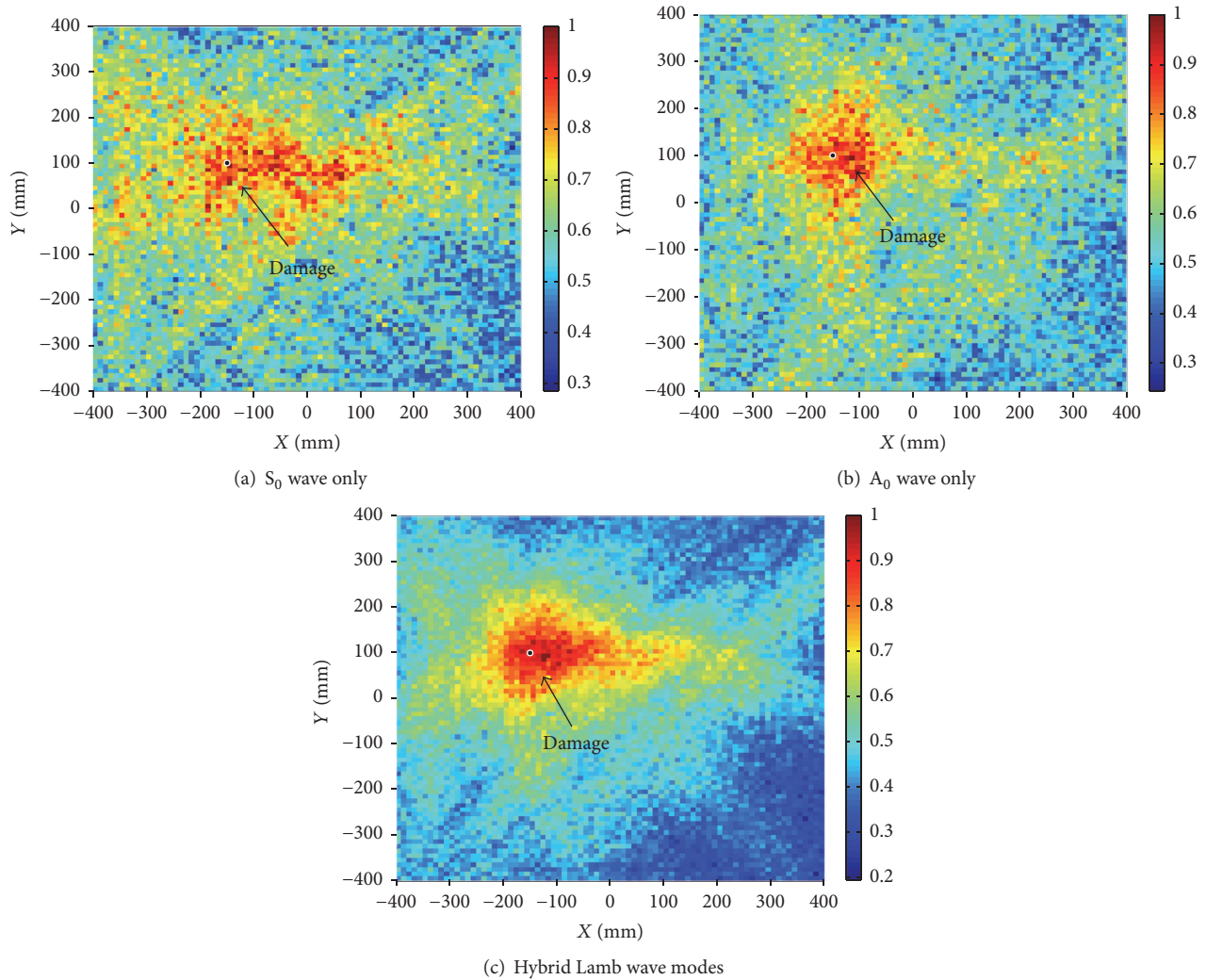


FIGURE 14: Comparison of damage maps (experiment).

of Nanjing Hydraulic Research Institute (Grant no. Y716021) to this study.

## References

- [1] S. Gopalakrishnan, M. Ruzzene, and S. Hanagud, "Signal Processing Techniques," in *Computational Techniques for Structural Health Monitoring*, Springer Series in Reliability Engineering, pp. 97–154, Springer London, London, 2011.
- [2] Z. Wang, P. Qiao, and B. Shi, "Application of soft-thresholding on the decomposed Lamb wave signals for damage detection of plate-like structures," *Measurement*, vol. 88, pp. 417–427, 2016.
- [3] N. Quaegebeur, P. Micheau, P. Masson, and A. Maslouhi, "Structural health monitoring strategy for detection of inter-laminar delamination in composite plates," *Smart Materials and Structures*, vol. 19, no. 8, Article ID 085005, 2010.
- [4] I. Park, Y. Jun, and U. Lee, "Lamb wave mode decomposition for structural health monitoring," *Wave Motion*, vol. 51, no. 2, pp. 335–347, 2014.
- [5] L. Zeng, J. Lin, J. Bao, R. P. Joseph, and L. Huang, "Spatial resolution improvement for Lamb wave-based damage detection using frequency dependency compensation," *Journal of Sound and Vibration*, vol. 394, pp. 130–145, 2017.
- [6] M. Ratssepp, Z. Fan, and K. Lasn, "Wave mode extraction from multimodal wave signals in an orthotropic composite plate," *Ultrasonics*, vol. 71, pp. 223–230, 2016.
- [7] K. Xu, D. Ta, P. Moilanen, and W. Wang, "Mode separation of Lamb waves based on dispersion compensation method," *The Journal of the Acoustical Society of America*, vol. 131, no. 4, pp. 2714–2722, 2012.
- [8] Z. Wang and P. Qiao, "Backward wave separation method in a single transmitter and multi-receiver sensor array for improved damage identification of two-dimensional structures," *International Journal of Damage Mechanics*, vol. 26, no. 2, pp. 229–250, 2017.
- [9] X. Yu, M. Ratssepp, and Z. Fan, "Damage detection in quasi-isotropic composite bends using ultrasonic feature guided waves," *Composites Science and Technology*, vol. 141, pp. 120–129, 2017.
- [10] Y. Zhao, F. Li, P. Cao et al., "Generation mechanism of nonlinear ultrasonic Lamb waves in thin plates with randomly distributed micro-cracks," *Ultrasonics*, vol. 79, pp. 60–67, 2017.

- [11] B. Masserey and P. Fromme, "Analysis of high frequency guided wave scattering at a fastener hole with a view to fatigue crack detection," *Ultrasonics*, vol. 76, pp. 78–86, 2017.
- [12] P. Huthwaite and F. Simonetti, "High-resolution guided wave tomography," *Wave Motion*, vol. 50, no. 5, pp. 979–993, 2013.
- [13] M. Y. Bhuiyan, Y. Shen, and V. Giurgiutiu, "Guidedwave based crack detection in the rivet hole using global analytical with local FEM approach," *Materials*, vol. 9, no. 7, article no. 602, 2016.
- [14] J. Chen, S. Yuan, L. Qiu, J. Cai, and W. Yang, "Research on a lamb wave and particle filter-based on-line crack propagation prognosis method," *Sensors*, vol. 16, no. 3, article no. 320, 2016.
- [15] J. Cai, S. Yuan, and T. Wang, "Signal construction-based dispersion compensation of lamb waves considering signal waveform and amplitude spectrum preservation," *Materials*, vol. 10, no. 1, article no. 4, 2017.
- [16] Z. Su, C. Yang, N. Pan, L. Ye, and L.-M. Zhou, "Assessment of delamination in composite beams using shear horizontal (SH) wave mode," *Composites Science and Technology*, vol. 67, no. 2, pp. 244–251, 2007.
- [17] P. F. Pai, H. Deng, and M. J. Sundaresan, "Time-frequency characterization of lamb waves for material evaluation and damage inspection of plates," *Mechanical Systems and Signal Processing*, pp. 183–206, 2015.
- [18] V. Giurgiutiu, "Piezoelectric wafer active sensors for structural health monitoring of composite structures using tuned guided waves," *Journal of Engineering Materials and Technology*, vol. 133, no. 4, Article ID 041012, 2011.
- [19] N. E. Huang, Z. Shen, S. R. Long et al., "The empirical mode decomposition and the Hilbert spectrum for nonlinear and non-stationary time series analysis," *Proceedings A*, vol. 454, no. 1971, pp. 903–995, 1998.

## Research Article

# Information-Based Construction of High-Speed Railway Tunnel

**Qian Yang and Zhaoling Wang**

*Sichuan Agricultural University, Chengdu, Sichuan 611830, China*

Correspondence should be addressed to Zhaoling Wang; [wong8010@berkeley.edu](mailto:wong8010@berkeley.edu)

Received 30 June 2017; Accepted 3 October 2017; Published 31 October 2017

Academic Editor: Rafał Burdzik

Copyright © 2017 Qian Yang and Zhaoling Wang. This is an open access article distributed under the Creative Commons Attribution License, which permits unrestricted use, distribution, and reproduction in any medium, provided the original work is properly cited.

Nowadays, railway tunnel construction faces huge developments and opportunities, with a tendency for high speed and long distance. How to effectively apply the information in the construction process has been the focus of current research. According to the Xian-nvyan tunnel in Xicheng high-speed railway, our research was based on the geological forecast, selecting appropriate tunneling model parameters to establish the 3D calculation model. Through the numerical simulation of three tunnel excavation and support methods, we analyzed the displacement of surrounding rock and the plastic failure to select the construction method reasonably. Compared with the actual measured data, we judged the rationality of the selected scheme and model parameters, so as to provide design parameters which conform to the surrounding rock properties for the subsequent construction, thus optimizing the construction program and applying the concept of information-based construction in engineering actually.

## 1. Introduction

At present, China has become the largest and the fastest-growing constructor of tunnels in the world. In midwest traffic construction, tunnel engineering has a great and an unprecedented development opportunity. The characteristics of tunnels include the large scale, complicated technology, wide impact, and high risk, which pose great challenges on the construction of tunnel projects. At the same time, the investigation, design, and construction process of tunnels are in a separating state to a certain degree, resulting in the construction of information that cannot be accessed, transferred, and reacted to timely, thus increasing the construction risk and costs. The insufficient information level of the survey, forecast information, and monitoring measurement data lead to various construction information that cannot be communicated, analyzed, and given feedback on timely and efficiently. Therefore, the comprehensive and efficient integration and the instant feedback of tunnel information have great importance in the high efficiency, safety, and economy of tunnel constructions, which possess different connotations and extensions in different development times.

Since the Austrian civil engineer Rabcewicz put forward the new Austrian tunneling method (NATM) in the 1940s, the

tunnel construction technology, which proposes to make the most out of the self-bearing capacity of surrounding rock and integrated design, construction, and monitoring, has been a widely used theory of tunnel monitoring measurement. Meanwhile, the method of combining numerical simulation with measurement was also widely applied in information-based construction. The highly intelligent TMS (Tunnel Measurement System) was used in the Utley tunnel in Switzerland to maximize the measuring time, and it greatly improved the production efficiency and reduced costs [1]. Li Yongsuo's thesis, discussing the numerical simulation for the excavation in tunnel construction, utilized FLAC3D to simulate the mechanical laws of surrounding rock and supporting structure of tunnels and then performed a comparison with the field measurement to optimize the construction scheme and supporting measures [2]. Chen et al. studied the double-arched highway tunnel in Hunan Province, which was based on the field measurements, analyzing the deformation of surrounding rocks and simulating the process of construction with the finite element method [3].

Tunnel engineering depends heavily on the control of construction information; therefore, it is imperative to improve the tunnel information construction. This paper relies on Xicheng Railway Xian-nvyan tunnel, which is a

high-speed railway tunnel, for the analysis of geological investigation, forecast, numerical simulation, and monitoring measurement, discussing the position and function of the different information in the tunnel construction, in order to provide a reference for the development of tunnel information construction systems.

## 2. Project Overview

Located in Guangyuan City, Sichuan Province, Xian-nvyan tunnel is a sole hole double-line tunnel, with full length of 5633.4 m, maximum depth of 390 m, shallow depth of only 15 m, single hole double-line tunnel spacing of 4.6 m, and ground elevation of 500~970 m.

The surface layer of the study section is mainly strong- and weak-weathered sandstone, and the inside part is broken with a gravelly structure. Within the joint fissure development, some areas form perilous rocks, and the diameter of collapsed large stones is several to ten meters. The geological structure is a monocline structure, and the strata tend towards the left line, causing a bedding lateral pressure in the right side of the tunnel, so it is prone to landslide and drop rockfall. Moreover, the groundwater in the tunnel is mainly composed of bedrock fissure water.

## 3. Advanced Forecast Information

Based on the New Austrian Tunneling Method (NATM), tunnel information construction cycles the processes of geological investigation, predesign, simulated construction, and optimization. The information obtained by geological exploration is relatively extensive, which cannot completely control the construction risk and guide the construction, so advanced forecasting becomes an important way to obtain detailed construction information [4].

*3.1. Advanced Horizontal Drilling.* According to the pre-geological investigation, as the mudstone is relatively an aquiclude, the underground part of the sandstone layer forms confined water; thus, multiple boreholes emit groundwater. The MD-50 type DTH (down-the-hole) impact-rotary rig is adopted to drill in the DK425 + 981 tunnel face (which means the tunnel face is 425 kilometers and 981 meters from the railway entrance), with a cumulative drilling length of 23.10 m.

*3.2. TSP Geological Forecasting.* The normal TSP (Tunnel Seismic Prediction) method mainly consists of the three-component geophone, recording cell, and initiation device. The three-component geophone is used to receive seismic wave signals; the recording cell amplifies the received seismic wave signal and performs analog-to-digital conversion and data recording, while also controlling the measuring process, and the initiation device is used for triggering the electric detonator and detonating the explosives and exciting the seismic wave [5].

In this section, parameters such as S-wave velocity, P-wave-to-S-wave velocity ratio, and Poisson's ratio change greatly, with fracture water developing, indicating that the

rock condition is worse than the previous one, especially the representative segment, DK425 + 968~DK425 + 980, owning concentrated reflecting layers. Based on the above analysis, it is inferred that the fault fracture zone existed, suggesting that the section should be constructed by grade IV surrounding rock, noting the partial collapse and piece dropping of the construction, paying attention to the support treatment and construction safety.

On the basis of the pregeological investigation, through the rock mechanics parameters of the geological forecast, shown in Figure 1, and groundwater and karst conditions in front of the tunnel face, we can forecast the width, occurrence, and location of the forward fault zone. In addition, we also obtain the geological investigation and provide the parameter guarantee for the establishment of a numerical simulation model [6].

## 4. Numerical Simulation

The numerical method of tunnel engineering is an effective method to solve the tunnel engineering problem, which heavily depends on the research of the engineering geological conditions and rock property, reflected in the simulation results through the parameters. In this paper, three main tunnel excavation methods are simulated by FLAC3D; the optimal excavation method can be chosen, making a reasonable evaluation and prediction of the stability of tunnel surrounding rock, so as to direct the follow-up construction [7].

*4.1. Numerical Model.* The numerical test parameters are adopted from the "Highway Tunnel Design Code" (JTGD70-2004), combined with the advanced geological forecast. Figure 2 shows a longitudinal section drawing of the simulation section in order to prove the geological condition in front of the tunnel face before construction, and the advanced geological drilling and TSP forecasting data indicate that the tunnel rock of the test section was magenta and highly weathered sandstone, which is loose and soft, explaining the integrity and poor self-stability [8]. As a result of the test section tunnel's weak water, the calculation parameters of surrounding rock are reduced to a certain extent [9].

Based on the TSP forecasting and the geological condition, we calculate the parameters of the tunnel model shown in Table 1, which provides accurate information for model building. The real tested tunnel is a sole hole double-line one with a span of 13.92 m. As shown in Figure 3, the dimensions of the calculated model are 112 m width, eight times the span, 92 m height, and 52 m longitudinal dimension. For the shallow tunnel depth, in order to simulate the actual situation of the test section, the depth of the model is 15 m, and the surface unsymmetrical pressure angle is 10 degrees.

In view of the good stability of the surrounding rock and no obvious rheological behavior after excavation, the geological condition is relatively stable. Therefore, the numerical model can be calculated according to the elastoplastic theory, and the Mohr-Coulomb criterion is adopted to describe the mechanical behavior of rock mass, which contains the shear failure criterion and tensile failure criterion.

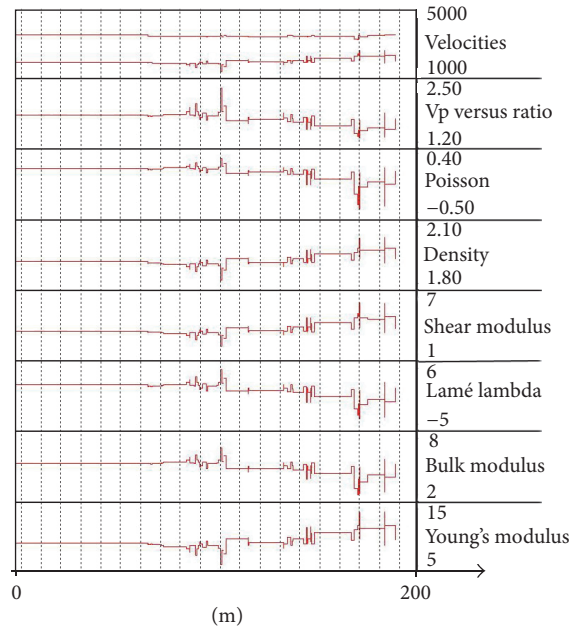


FIGURE 1: Rock mechanics parameters of the geological forecast.

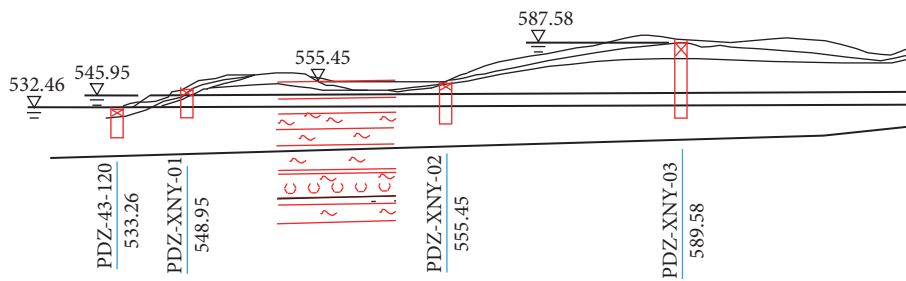


FIGURE 2: Longitudinal section drawing of the simulation section.

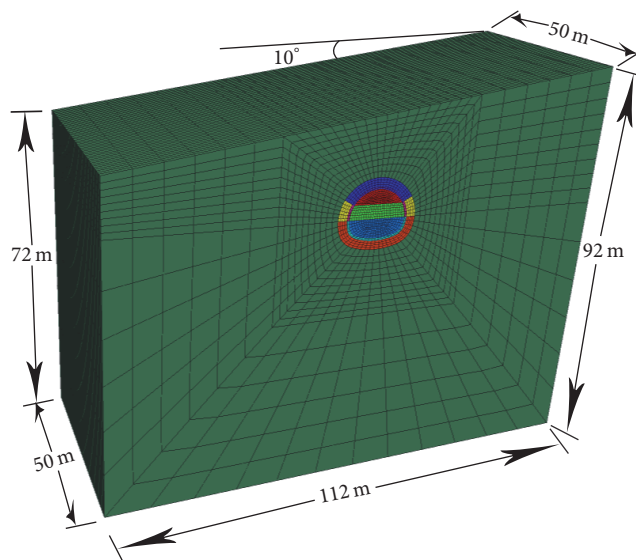


FIGURE 3: Numerical model.

TABLE I: Calculation parameters of the tunnel model.

Number	Material	Elastic modulus (GPa)	Poisson's ratio	Cohesion (MPa)	Internal friction (°)	Bulk density (kN/m <sup>3</sup> )
(1)	Surrounding rock	1.5	0.35	0.1	22	19.6
(2)	Primary support	28	0.2	—	—	24.5
(3)	Grouting in surrounding rock	6	0.35	0.7	39	24.5
(4)	Secondary lining	30	0.2	—	—	24.5

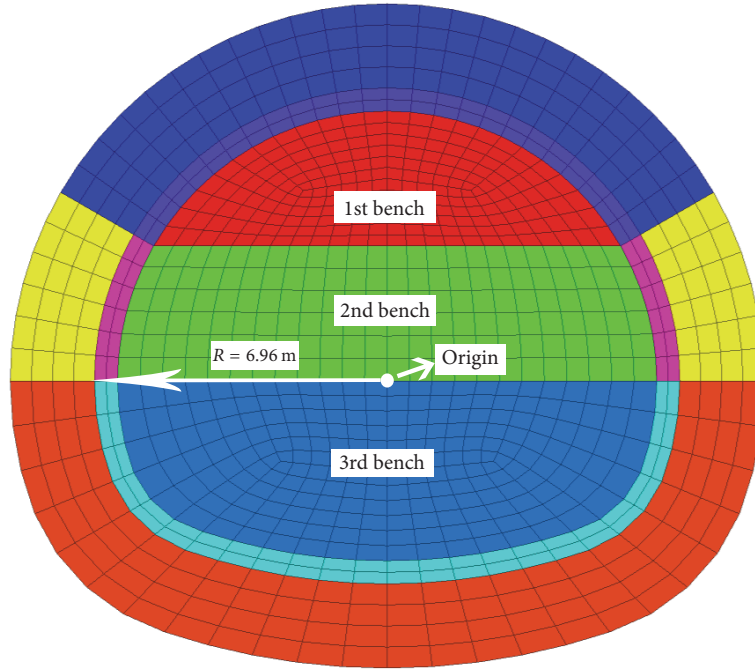


FIGURE 4: Numerical model of the excavation.

The boundary condition for the model is fixed in all directions on the bottom side, normal direction on the side boundaries. The sign for the horizontal displacement is negative (deform to the left) or positive (deform to the right). The sign for the vertical displacement is negative (deform downwards) or positive (deform upwards).

This experiment simulates three excavation methods in Figure 4, that is, full section, two-bench section, and tribench section, monitoring the clearance convergence, ground settlement, and the plastic zone failure of the midpoint section of the model. By comparing the deformation law rule of surrounding rock in different construction methods, analyzing the rock mechanical behavior, and choosing more suitable schemes for this project in excavation and support, the role of numerical simulation technology in tunnel information model is illustrated as an example [10].

#### 4.2. The Result of the Numerical Experiment

**4.2.1. Analysis of Clearance Convergence.** In order to compare the developing process of clearance convergence in different conditions, the paper has taken the mid cross section of

the 50-meter tunnel as the monitoring section. Every two meters of the excavation footage tunneling, we extract the deformation data of the mid cross section. The beginning of the monitoring is when the up-bench was dug to 15 m, and it ends as the tunnel was dug through.

The results in Figure 5 depict the clearance convergence change of the selected section in the process of tunnel excavation. The displacement of all nodes around the hole is magnified 18 times to make the described graph more intuitive.

It can be seen from Figure 5 that the evolution of the tunnel convergence deformation after excavation is closely related to the construction method. In virtue of the unsymmetrical pressure, leading to the skew of the tunnel section, the tunnel convergence deformation tends towards the deeply buried direction.

By comparing the deformation results, we found that the convergence deformation of the full section is relatively small and uniform, which is influenced by the excavation of adjacent sections, and there is no large horizontal or vertical displacement; hence, the deformation rate gradually decreased and then stabilized.

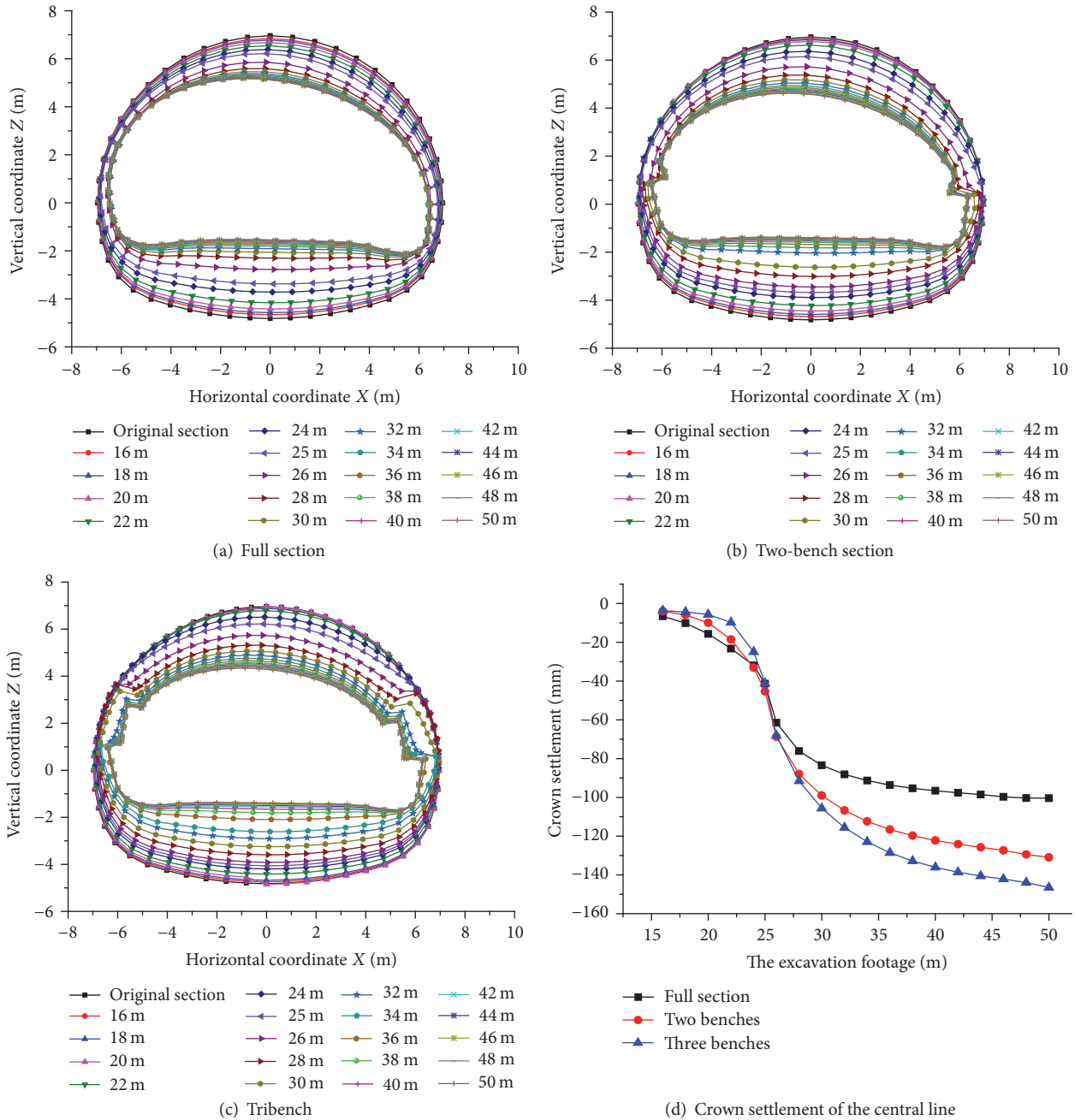


FIGURE 5: The clearance convergence by different methods.

However, in the step excavation, due to the excavation and support disturbance of previous processes and the upper-middle steps, the convergence displacement is not uniform after the excavation of the steps in the monitoring section, and each step, especially the arch, will cause a great deformation and then tend to stabilize. Among these, the vertical deformation of the tribench method is larger than the two-bench method, so the advance support should be strengthened and the surrounding rock ought to be closed into a ring timely in the construction.

In addition, the paper also took the crown settlement of the central line into consideration. From the curve, the deformation of the full-section excavation is minimum among the three methods, which can stabilize in a relatively short time, which requires that the support must be in place timely, increasing the difficulty and insecurity of the support. At the same time, the tribench excavation has the greatest influence on the crown settlement, followed by the two-bench method, and the cumulative deformation is 1.7 and 1.4 times, respectively, the full-section excavation.

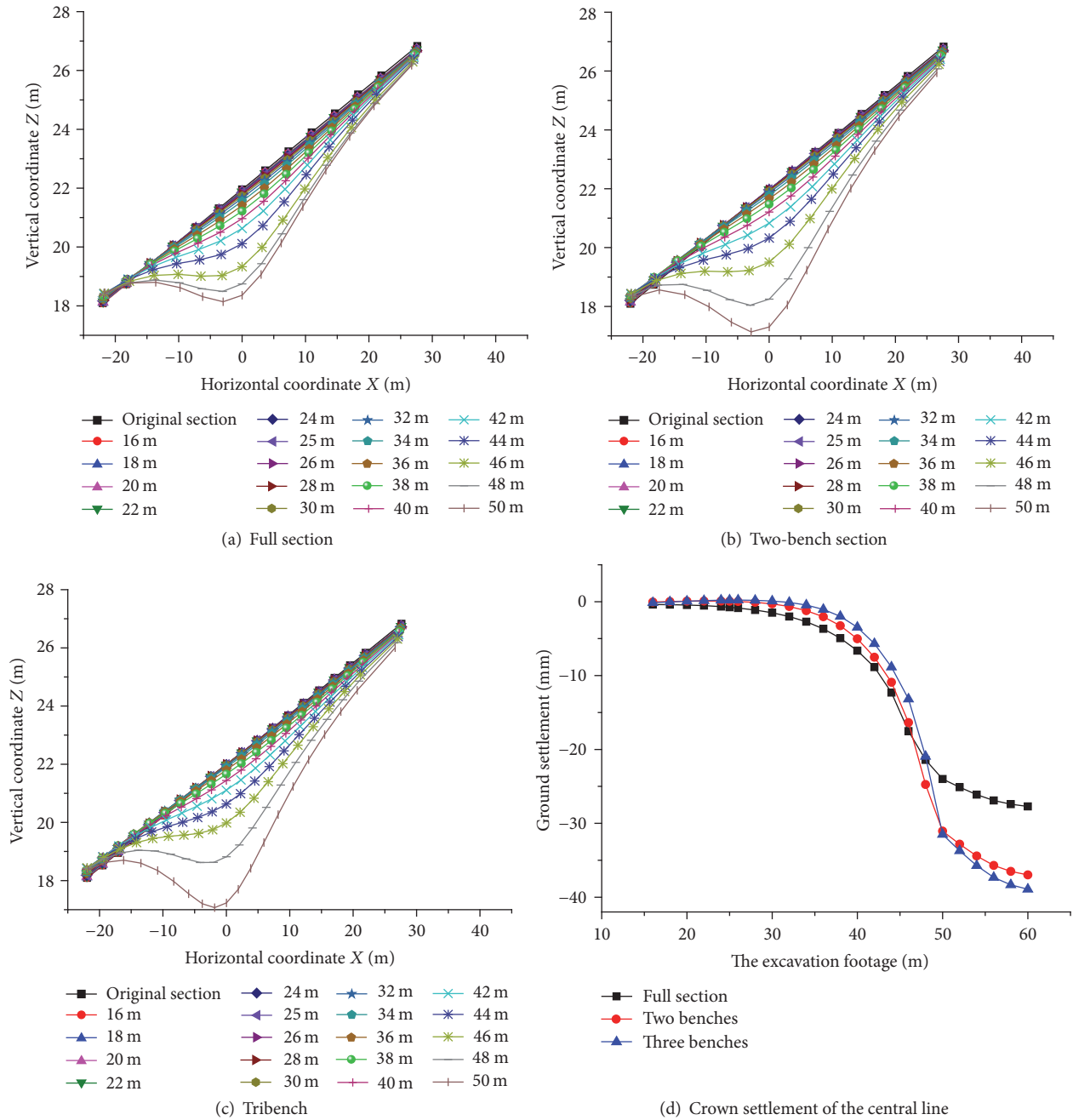


FIGURE 6: The ground settlement by different methods.

4.2.2. Analysis of Ground Settlement. The observation of ground settlement is mainly to investigate the influence of different construction methods. Same as the clearance convergence, the paper monitored the displacement of the mid cross section and took a record every 2 meters forward. In the simulated calculation, seven monitoring points have been placed in the selected cross section, with the ground settlement value expanding 150 times to superimpose directly on the curve that shows the surface node location.

The results are plotted as a sectional groove curve, as Figure 6 shows.

From the ground displacement monitoring data, the maximum sedimentation value is distributed in the vicinity of the centerline of the tunnel section.

As shown in Figure 6, the three kinds of excavation methods did not cause large ground settlement immediately after the excavation of the monitoring section, and the decreasing rate of settlement which is caused by excavation, with the increase of the distance to the tunnel face, is essentially in agreement.

With the excavation, the ground settlement began to increase significantly in the 38 m footage, decreasing

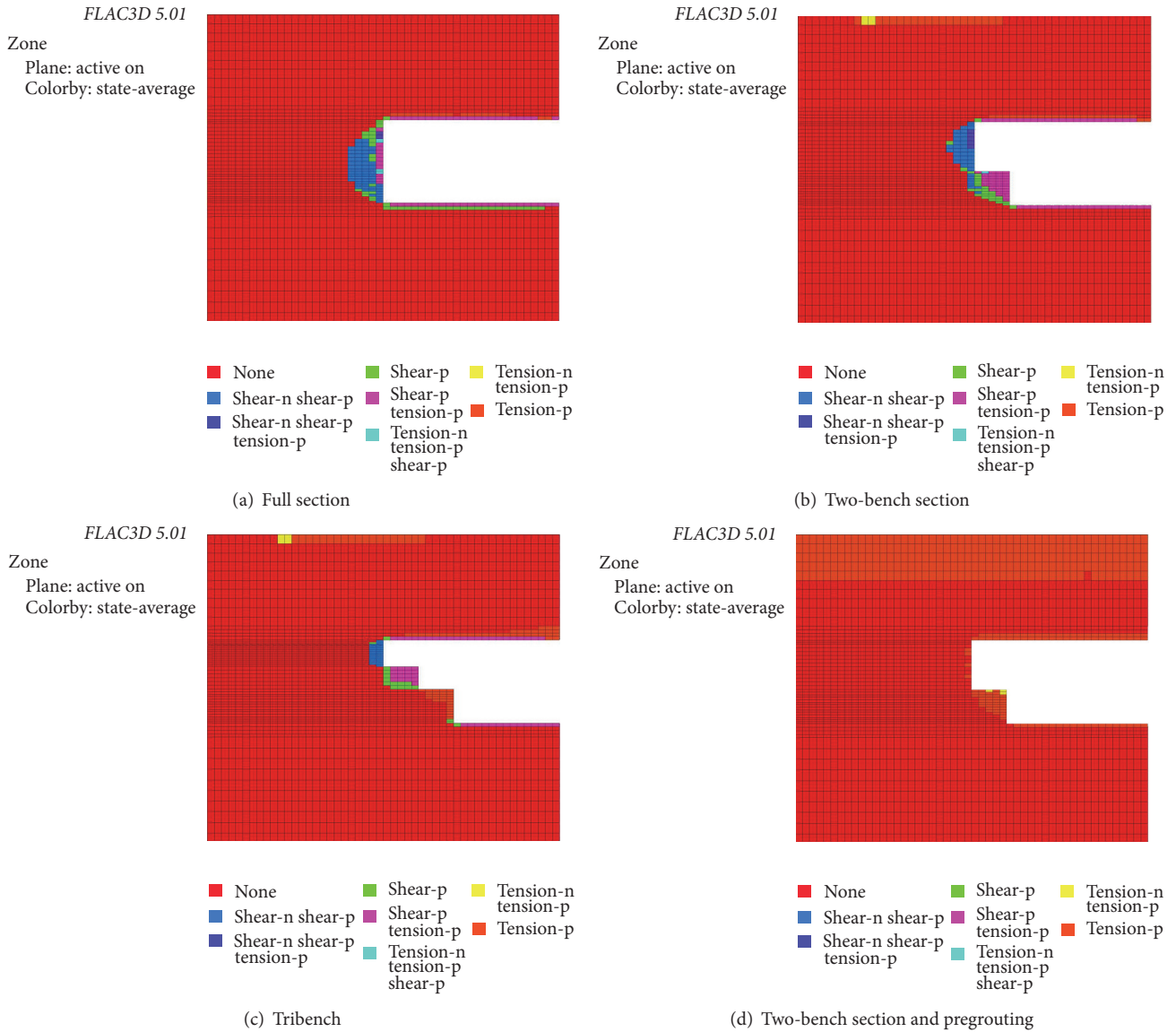


FIGURE 7: The distribution of the plastic zone deformation.

gradually when excavated to 46 m. For the bench method, the largest settlement due to excavation is still the tribench method.

From Figure 6(d), in the crown settlement curve, in the range of starting excavation to 45 m footage, the settlement caused by the three methods is not quite different. Moreover, the full-section method tends to stabilize earlier than others, and the cumulative deformation of the two-bench and tribench methods is about 1.6 times that of the full section; also, the deformation amount of the tribench method is still larger than of the two-bench method.

From the deformation results of the clearance convergence and the ground settlement, we found that different methods have different advantages. The analysis of plastic zone failure is required in the further comparison.

*4.2.3. The Tunnel Face Displacement and Plastic Zone Failure.* For the weak surrounding rock, it is very important to prevent the landslide caused by the tunnel face construction. The tunnel failure mechanism in adverse geological conditions can be depicted graphically by numerical simulation, so as to obtain the potential risks of tunnel construction in different conditions; then, positive prevention has great significance for information construction.

In Figure 7, the numerical simulation compares the displacement of the tunnel face and the development of the plastic zone after excavation in the three methods, analyzing the effect of the small duct grouting to stabilize the tunnel face and confirming the pros and cons of the different conditions on the control of the tunnel face displacement, which provides guidance for tunnel construction.

TABLE 2: Frequency of convergence displacement measurement.

Displacement speed (mm/d)	Distance from the working face	Frequency	Remarks
>5	(1~2) B	1~4 times/1 day	(1) B is the tunnel width.
1~5	(2~5) B	1 time/2 days	(2) When the displacement rate > 5 mm/d, consider dangerous, alert timely
0.2~1	5 B	1 time/1 week	
<0.2		No monitoring	

The plastic zone appeared in the rock strata of the tunnel arch waist after excavation; besides, at the bottom of the wall, due to the stress concentration caused by the geometry of the excavation boundary, a plastic zone is presented with a smaller range but a large strain. Generally speaking, the plastic zone of surrounding rock is mainly distributed in the tunnel arch waist, the side wall, and the bottom of the rock stratum.

In the full-section excavation, a closed plastic zone is formed around the tunnel, and the plastic zone's range in front of the tunnel face is large, so invert construction must be timely and reliable, which increases the construction difficulty.

As for the bench methods, we can see that the plastic zone is smaller than the full section; the reason is that the boundary of the plastic zone in front of the tunnel face of the excavation range is concaved to the face, and the plastic zone in the upper and lower benches appears to be arc-shaped through the area. It is inferred that the tribench excavation method has the best effect on controlling the damage of the face and the smallest range of the plastic zone.

Furthermore, forming the deformation of the plastic zone which applied the two-bench excavation and small duct, the range is smaller than other methods shown in Figure 7(d), so the advanced small duct grouting to strengthen the surrounding rock can control the destruction of the surrounding rock well.

**4.2.4. Reasonable Choice of Construction Methods.** Through analyzing the numerical simulation results of different construction programs, the full-section method to control the deformation effect of the surrounding rock is better than the bench excavation, which is more suitable for the stable surrounding rock but needs higher requirements for the supporting time, increasing the difficulty of construction. However, the tribench method has a large disturbance on the formation and surrounding rock, and the difficulty of closing into a ring timely is higher than in the two-bench method. So, the paper held the view that the two-bench method combined with pregrouting is a better way for the actual construction.

## 5. Monitor Measurement Feedback

As the foundation of information construction, monitoring and measurement are the main basis to test the designed parameters, the rationality of the model, and the evaluation of the construction method, whose authenticity is stronger than of the numerical simulation [11].

**5.1. Observation of Clearance Convergence.** We adopt the LEICA TS09 total station for noncontact measurement and determine the measurement frequency by the surrounding rock level, tunnel section size, and embedded depth. The frequency of convergence displacement measurement was affected by other factors. Table 2 shows the correspondence between measuring frequency and the displacement speed and also the distance from the working face.

After the excavating of the tunnel, the observation piles are embedded in the horizontal wall and the arch waist of the tunnel. The buried depth is 450 mm, and the location of the convergence points around the tunnel is shown in Figure 8. The paper adopted line 2# as the monitored object.

DK425 + 969 section was selected to monitor the horizontal convergence, as shown in Figure 9; during the 20-day monitoring process, the total accumulated amount was 32.51 mm, and the maximum daily convergence was 6.81 mm.

In the initial excavation of the upper bench, the surrounding rock was greatly disturbed due to the construction blasting, making the convergence rate of the deformation increase obviously, and the average daily deformation rate is about 6.61 mm/d.

With the steel arch, feet-lock bolt, and other initial supports constructed timely, the convergence rate of the surrounding rock decreased gradually, the accumulated deformation reached 73.8% of the total deformation on the 6th day, and the average deformation rate dropped below 1 mm/d.

After the excavation of the lower bench, the deformation increases again, and the average rate over the seven days was 1 mm/d. At this stage, the initial support should also be constructed timely to close into a ring, which causes the rapid release of the surrounding rock pressure to be relieved to a certain extent, thus reducing the deformation tendency of the convergence.

**5.2. Observation of Ground Settlement.** Ground settlement measurement refers to the observation from the setting point on the ground, judging the influence on ground settlement by excavating according to the displacement, and the effect on slope due to the excavation by deformation, which can define the stability of the tunnel support structure.

The analysis of the shallow ground settlement measurement in this project combined with DK425 + 985 section and three measuring sections with a pitch of 10 m is set up in the tunnel portal along the tunnel axis. Start measurement when the distance between the measured section and the working face is 30 m and stop when the excavation exceeds the measured section and the settlement stabilizes. Figure 10

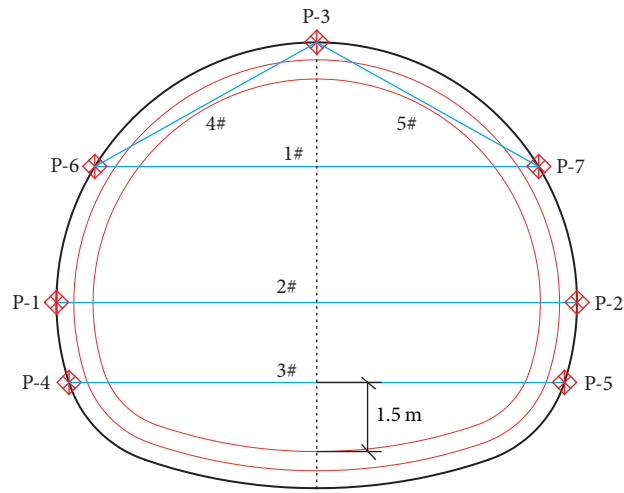


FIGURE 8: Layout of the observation piles.

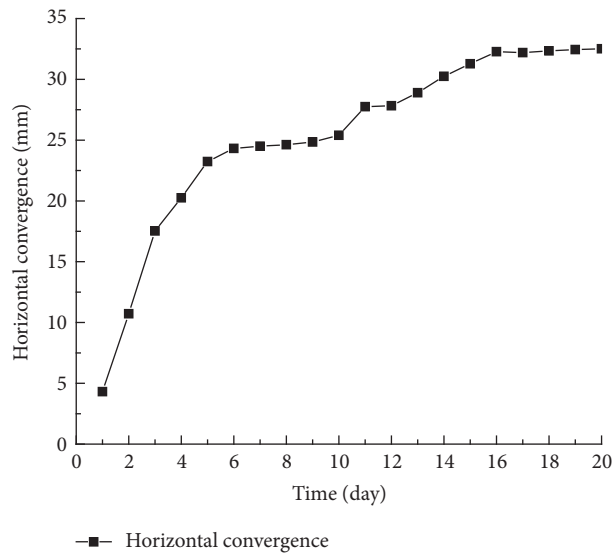


FIGURE 9: Horizontal convergence curve for section DK425 + 969 line 2#.

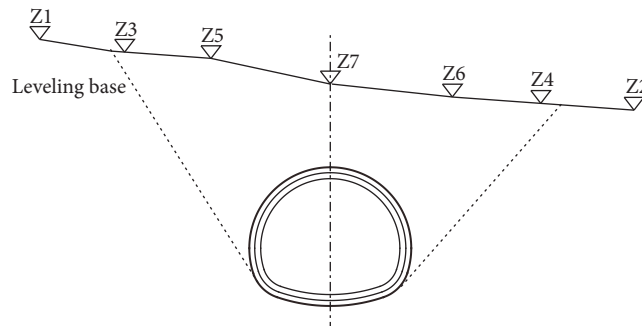


FIGURE 10: The measuring point of entrance and shallow buried section.

TABLE 3: Frequency of the shallow ground settlement measuring.

Project	Excavation condition	Measuring frequency
The shallow ground settlement	The distance between excavation and the measured section $< 2 B$	1~2 times/d
	The distance between excavation and the measured section $< 5 B$	1 time/2 d
	The distance between excavation and the measured section $> 5 B$	1 time/2 weeks

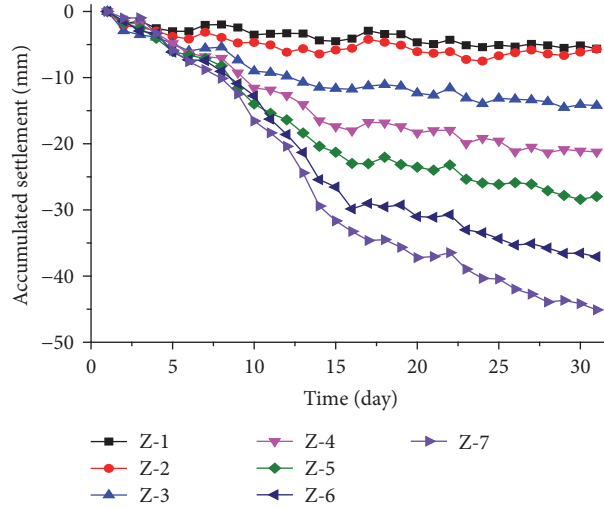


FIGURE 11: Accumulated settlement of the seven measuring points.

shows the location of seven symmetrical measuring points in the entrance of the shallow buried section, and Table 3 shows the measuring frequency.

As shown in Figure 11, we record the accumulated settlement of the seven measuring points, to analyze the deformation process.

Due to the disturbance to the stratum induced by construction in the initial deformation, the original consolidated soil layer became loose, resulting in the bulge or small settlement. The deformation of all the measured points is not obvious, and the smallest is 1 and 2 points with the average deformation of about 7 mm.

As for the bench method, the upper soil is fully excavated, leading to the original balanced three-dimensional soil stress being suddenly destroyed and the geostress being redistributed, causing the deformation of the surrounding soil; moreover, there is the free state of the upper surrounding rock and releasing of a large number of internal stresses. With the initial support that began to play a role, the deformation speed of surrounding rock tends to be gentle. When all the surrounding rock stress is released at the later stage of deformation, the timely construction and backfill of the inverted arch made the rock stable, as well as the ground settlement of each measuring point.

After sixty days of continuous observation, the maximum cumulative deformation of all the measuring points is the 7th point, 45.10 mm, which tends to stabilize. Among all the points, the minimum daily average settling velocity is 0.09 mm/d, and the maximum is 0.75 mm/d, which are in the allowable range, indicating that the selected construction

method is rational and practical; in addition, the support scheme can effectively control the deformation.

From the information construction point of view, the comparison of numerical model deformation and the monitoring measurement data can be a criterion of reliability in tunnel information model. In addition, the feedback of measurement information is beneficial to the optimization of parameters in the model, and if the relevant parameters are reasonable [12], the numerical model possesses practical reference meaning which can provide more accurate guidance for the subsequent construction.

## 6. Conclusions

In this paper, Xian-nvyan tunnel of Xicheng Railway is taken as the research background, combined with concrete engineering example; an intensive study is carried out by the combination of the geological forecast, numerical simulation, and field monitoring measurement. The main conclusions are as follows.

On the basis of the pregeological investigation, the geological forecast can improve the detailed geological information of the monitoring section, obtain the rock mechanics parameters, and reveal the geological situation in the tunnel area.

By comparing the characteristics of displacement deformation and plastic zone failure in the three construction methods, the deformation mechanism is analyzed. It is concluded that the displacement deformation of the full-section excavation is smaller than of the bench excavation

but needs a better geological condition. In contrast, the displacement deformation of the two-bench excavation is in the allowable range and more suitable for the construction of the selected section.

The results of the numerical simulation are the basis of the qualitative analysis, compared with the measured data indicating that the prediction rule is consistent with the actual deformation to some extent, which shows the rationality of the model parameters set by the forecast results.

Only by carrying out numerical simulation and field measuring into design and construction can we ensure the feasibility of mutual certification and feedback and then change the current low level of construction technology quality and apply the concept of information construction to engineering practice.

### Conflicts of Interest

The authors declare that there are no conflicts of interest regarding the publication of this paper.

### Acknowledgments

This research was funded by the National Natural Science Foundation of China (the Experiment and Modeling Studies of the Surface Wavefield by Elliptically Polarization of the Surface Waves) (Approval no. 51508358).

### References

- [1] S. Maurhofer, M. Glaettli, and J. Bolliger, "Uetliberg Tunnel: heading methods and interior works," *Tunnelling & Underground Space Technology*, vol. 19, p. 349, 2004.
- [2] Y.-S. Li, K.-N. Zhang, X. Yang, and C.-B. HuanG, "Numerical simulation for the excavation in tunnel construction," in *Proceedings of the International Conference on Civil Engineering and Transportation*, pp. 90–93, Trans Tech Publications, Jinan, China, 2011.
- [3] Q. Chen, M. Zhao, Y. Zhang, X. Liu, J. Hu, and S. Huang, "Information construction and finite element simulation analysis of unsymmetrical pressure double-arched highway tunnel," *Yanshilixue Yu Gongcheng Xuebao/Chinese Journal of Rock Mechanics and Engineering*, vol. 25, pp. 1723–1727, 2006.
- [4] D. Qiu, S. Li, Y. Xue, and S. Qin, "Prediction study of tunnel collapse risk in advance based on efficacy coefficient method and geological forecast," *Journal of Engineering Science and Technology Review*, vol. 7, no. 4, pp. 156–162, 2014.
- [5] F. Yang, Z.-H. Li, and J.-L. Shi, "Study on application of TSP advanced forecast in tunnel construction," *Journal of Railway Engineering Society*, vol. 30, pp. 76–80, 2013 (Chinese).
- [6] Y. Jia, Y. Li, and H. Liang, "Forecast geological prediction for fault and water gushing in deep-buried super long tunnel," in *Proceedings of the Global Conference on Civil, Structural and Environmental Engineering*, pp. 1294–1297, Trans Tech Publications, Yichang, China, 2012.
- [7] Y. Li, W. Zhu, S. Li, Q. Zhang, H. wang, and W. Kang, "Numerical simulation of a branching-out tunnel construction process using Flac3D," in *Proceedings of the 42nd US Rock Mechanics Symposium (USRMS)*, American Rock Mechanics Association, 2008.
- [8] Y. Huang, Z. Wang, Y. Zhao, N. Hao, and Y. Chen, "Numerical simulation of TSP tunnel fault model of seismic prediction," *International Journal of Earth Sciences and Engineering*, vol. 8, pp. 24–30, 2015.
- [9] J. Guo and Q.-C. Wang, "The numerical simulation analysis of excavation process of loess tunnel," in *Proceedings of the 2011 International Conference on Manufacturing Science and Technology, (ICMST '11)*, pp. 6594–6600, Singapore, Singapore, September 2012.
- [10] H. B. Fan, J. X. Lai, and D. D. Hou, "The bench method numerical simulation of soft rock tunnel," in *Proceedings of the 2nd International Conference on Civil Engineering, Architecture and Sustainable Infrastructure, (ICCEASI '13)*, Zhengzhou, China, July 2013.
- [11] Y. Song, Y. tANG, G. Mu, and G. Wang, "Monitoring of tunnel clearance displacements under condition of TBM construction," *Yanshilixue Yu Gongcheng Xuebao/Chinese Journal of Rock Mechanics and Engineering*, vol. 28, pp. 621–627, 2009.
- [12] J.-H. Yang, J.-Q. Chen, G. He, and Q. Chen, "Research on monitoring and measuring of sandy clay tunnel construction under complex conditions," *Yanshilixue Yu Gongcheng Xuebao/Chinese Journal of Rock Mechanics and Engineering*, vol. 24, pp. 4588–4593, 2005 (Chinese).

## Research Article

# Diagnosis of Localized Faults in Multistage Gearboxes: A Vibrational Approach by Means of Automatic EMD-Based Algorithm

**M. Buzzoni, E. Mucchi, G. D'Elia, and G. Dalpiaz**

*Engineering Department, University of Ferrara, Via Saragat, 1 I-44122 Ferrara, Italy*

Correspondence should be addressed to E. Mucchi; [emiliano.mucchi@unife.it](mailto:emiliano.mucchi@unife.it)

Received 26 July 2017; Accepted 14 September 2017; Published 30 October 2017

Academic Editor: Rafał Burdzik

Copyright © 2017 M. Buzzoni et al. This is an open access article distributed under the Creative Commons Attribution License, which permits unrestricted use, distribution, and reproduction in any medium, provided the original work is properly cited.

The gear fault diagnosis on multistage gearboxes by vibration analysis is a challenging task due to the complexity of the vibration signal. The localization of the gear fault occurring in a wheel located in the intermediate shaft can be particularly complex due to the superposition of the vibration signature of the synchronous wheels. Indeed, the gear fault detection is commonly restricted to the identification of the stage containing the faulty gear rather than the faulty gear itself. In this context, the paper advances a methodology which combines the Empirical Mode Decomposition and the Time Synchronous Average in order to separate the vibration signals of the synchronous gears mounted on the same shaft. The physical meaningful modes are selected by means of a criterion based on Pearson's coefficients and the fault detection is performed by dedicated condition indicators. The proposed method is validated taking into account simulated vibrations signals and real ones.

## 1. Introduction

Multistage gearboxes are employed in a wide range of mechanical systems and represent crucial components for the correct functioning of the entire machine. Since they are often subjected to faults due to manufacturing errors or heavy working conditions, the gear fault identification is of prime importance in order to reduce the maintenance costs as well as to restrict machine downtimes. In this context, the exact knowledge of the fault position by means of nondestructive techniques simplifies the maintenance process avoiding burdensome visual inspections.

Vibration-based diagnosis represents an effective approach for the gear fault diagnosis [1]. In the last decades, many researches have been focused on the development and testing of signal processing techniques for the identification of localized gear faults. The success of the fault identification strongly depends on the employed signal processing techniques, the system typology under investigation, and the working condition. In fact, the state of the art about the identification of localized gear faults covers a wide range of

different approaches such as the following: the cyclostationary theory [2–4], which takes advantage of the hidden periods embodied in the vibration signals; the Kurtogram [5] for the selection of the frequency band associated with the maximum Spectral Kurtosis; time-frequency signal representations like Continuous Wavelet Transform [6]; the blind deconvolution algorithms [7, 8], which estimate the excitation source due to the presence of the fault from the noisy observation; condition indicators based on the Time Synchronous Average [9].

Unfortunately, the aforementioned approaches allow for identifying the rotation period of the shaft synchronous with the faulty gear rather than the faulty gear itself. Hence, the exact identification of the faulty gear is not a trivial task if two or more gears are installed in the same shaft (which is very common in multistage gearboxes). As the authors are aware, no works can be found in the specialized literature dealing with such a tricky problem. Hence, encouraged by this lack, the present research is focused on the investigation of this issue having both industrial and academic interest.

In this work, the signal separation is based on the EMD (Empirical Mode Decomposition) which represents a fascinating approach in the field of time-frequency signal processing techniques. The EMD was introduced for the first time by Huang et al. [10] and it is a self-adaptive time-frequency analysis technique. The EMD decomposes the original signal into a set of oscillatory modes (called also Intrinsic Mode Functions) on the basis of the local time scales of the signal rather than on a predetermined kernel, as in the case of the Continuous Wavelet Transform. The EMD is effective for the analysis of signals that exhibit nonstationary and nonlinear behavior. Since the EMD is fully data-driven and adapted for the analysis of nonstationary signals, it is particularly suitable for the goal of this paper. Many efforts have been made in order to improve the effectiveness of the EMD algorithm, restricting its intrinsic drawbacks [11, 12]. The EEMD (Ensemble Empirical Mode Decomposition) [13], the CEEMD (Complementary Ensemble Empirical Mode Decomposition) [14], and the CEEMDAN (Complete Ensemble Empirical Mode Decomposition with Adaptive Noise) [15] are among the most popular improved EMD methods proposed in the literature.

EMD has been successfully used in a number of different research fields (speech recognition, chemistry, biology, medicine, etc.) but only in the last decade has EMD been exploited also for the identification of the gear faults, as gear cracks [16, 17], broken teeth [18], or wear [19]. In this context, Lin and Chen [20] exploited the EEMD for the extraction of multiple fault information from the vibration signals measured on gearboxes, a diagnostic method for wind turbine planetary gearboxes based on the EEMD has been proposed by Feng et al. [21] and the CEEMD combined with Permutation Entropy has been used for the identification and the severity recognition of gear faults by Zhao et al. [22]. On the other hand, no researches can be found in the literature about the gear fault diagnostic by means of CEEMDAN, even if its effectiveness has been demonstrated in other applications as the bearing fault identification [23, 24]. A complete literature review about the use of EMD for rotating machine diagnostics can be found in [25].

On this basis, the proposed work aims at developing a EMD-based methodology for the identification of the faulty wheel in multistage gearboxes, in the case of synchronous wheels mounted on intermediate shafts. Specifically, this method allows for the precise detection of the faulty gear rather than the faulty stage. In fact, the faulty gear detection is a limitation of the traditional signal processing techniques when a fault occurs in an intermediate stage. As mentioned before, this research tries to fill the gap in the specialized literature by facing this challenging case, being also of particular concern in many industrial applications. In this regard, care has been taken on the validation of the algorithm as well as on the reduction of the user interactions. For this purpose, selection criterion of the oscillatory modes estimated by a EMD-based algorithm have been advanced, in order to separate the Time Synchronous Average of the vibration signal into two representative vibration signals of the investigated wheels. Different EMD algorithms are taken into account (EMD, EEMD, and CEEMDAN) in order to

verify how the signal separation is influenced. The localized fault identification has been quantified by means of dedicated statistical indicators that reflect the gear condition. The method is validated taking into account both simulated signals and real vibration signals.

The paper is structured as follows: Section 2 outlines the theoretical background; Section 3 introduces the problem statement and the description of the method; the methodology has been tested using simulated signals in Section 4; Section 5 focuses on the validation by means of real vibration signals; final remarks are drawn in Section 6.

## 2. Theoretical Background

In this section, the main signal processing tools necessary for the comprehension of the proposed methodology are concisely introduced. Only the fundamental concepts are described avoiding unnecessary theoretical explanations.

*2.1. The Time Synchronous Average.* The vibration signals acquired on gearboxes can be considered as wide-sense cyclostationary signals [26]. The first-order cyclostationary part is particularly significant for the gear fault identification and the Time Synchronous Average (TSA) is a common estimator of such a cyclostationary quantity [3, 27]. In general, the TSA can be considered as the ensemble average of the vibration signal synchronized with a certain rotating component having rotation period  $T$ . Commonly, the TSA is typically performed into the angle domain rather than the time domain. In fact, the cyclostationarity on *mechanical* systems follows the periodicity imposed by the kinematics of the system, which is locked in the angle variable. Thus, many mechanical systems exhibit cyclostationarity with respect to rotation rather than to time.

Let  $x(\theta)$  be the vibration signal synchronized with rotation  $\theta$  of a certain rotating mechanical component taken as reference. Considering a periodicity of  $\Theta = 2\pi$  and an integer number  $N$  of revolutions, the length of  $x(\theta)$  is  $N\Theta$ . Thus, the Time Synchronous Average,  $x_{\text{TSA}}(\theta)$ , of  $x(\theta)$  can be defined as

$$x_{\text{TSA}}(\theta) = \frac{1}{N} \sum_{n=0}^{N-1} x(\theta + n\Theta) \quad \text{with } 0 \leq \theta < 2\pi. \quad (1)$$

The change of variable from time to angle implies that the frequency variable will change accordingly. The new frequency variable is called “order” and it is defined as the ratio between cycles and machine speed. Taking into account a proper number of averages, the main result of the TSA is the strong attenuation of all the nonperiodic components with respect to the reference and the improvement of the SNR (Signal-to-Noise Ratio). Furthermore, the angle domain TSA can strongly reduce the effects of the speed variation that mask the effects due to possible faults. Hence, this signal processing technique is particularly effective with noisy signals that embody a number of components having different periods, as the multistage gearboxes.

*2.2. The Empirical Mode Decomposition.* The EMD is a self-adaptive signal decomposition technique that separates the

signal in several oscillatory components called IMF (Intrinsic Mode Function) or just modes. Each IMF has to meet two properties: (i) the zero-crossing points and the extrema have to be equal or differ by one; (ii) at any point the mean value of the envelope evaluated by the local maxima and by the local minima has to be zero [10]. By virtue of these properties, the last component extracted by the EMD is a monotonic signal, called residue. As the name suggests, there is still a lack of a general theory about EMD. This pitfall has been investigated by some authors [28, 29] in the attempt to formulate a theoretical foundation of the method, but it is still an open question.

For the sake of brevity, the essential steps of the EMD algorithm are described in Figure 1, but a more comprehensive explanation about this algorithm can be found in [10]. The envelope process and the sifting process are the key points of the algorithm in Figure 1. The sifting process is a recursive procedure which ensures that the estimated modes can satisfy the characteristic properties of the IMF; the envelope process, instead, is the evaluation of envelopes of maxima and minima of the signal.

The main drawbacks of the EMD are the mode mixing and the end effect. The mode mixing concerns the combination of signals with widely different scales, while the end effect is the signal distortion at the extremity of the signal itself. These shortcomings can undermine the physical meaning of the estimated IMFs. In order to enhance the results of the EMD, several improved versions of the EMD algorithm have been developed in the last 20 years [13–15].

**2.3. The Ensemble Empirical Mode Decomposition.** The EEMD (Ensemble Empirical Mode Decomposition) [30] is an improved version of the EMD and its algorithm is summarized in Figure 2. Unlike the EMD, which could estimate IMFs affected by severe mode mixing, the EEMD calculates the so-called true modes or IMF\* and represents a more reliable decomposition of the signal.

Departing from original signal  $x(t)$ , a new set of  $N$  signals (where  $N$  represents the number of trials or realizations) is created by adding different zero-mean white noise  $w(t)$  of finite variance  $\sigma$ . Then, the EMD is performed for each signal  $x_n$  obtaining  $N$  mode sets composed of  $K$  modes each. At the end, the true IMF set composed of a number  $K$  of true modes IMF\* is evaluated by ensemble averaging each  $k$ th IMF set previously obtained.

Different from the EMD, the EEMD depends on two arbitrary parameters: the number of trials and the variance of the added white noise. The relationship between these parameters is as follows:

$$\varepsilon = \frac{\sigma}{\sqrt{N}}, \quad (2)$$

where  $N$  is the number of trials,  $\sigma$  is the variance of the added noise, and  $\varepsilon$  is the error standard deviation defined as the difference between the original signal and the corresponding IMFs. The proper selection of these parameters is needed in order to obtain negligible errors. Commonly [10, 31], a few hundreds of averages and  $\sigma \approx 0.02$  are usually enough in

order to obtain satisfactory results. However, the selection of  $\sigma$  depends on the application since high values of  $\sigma$  are suitable for data dominated by low-frequency signals and vice versa [10].

**2.4. The Complete Ensemble Empirical Mode Decomposition with Adaptive Noise.** The Complete Ensemble Empirical Mode Decomposition with Adaptive Noise (CEEMDAN) represents a step further with respect to EEMD and it has been proposed for the first time by Torres et al. [15]. As shown in Figure 2, the EEMD calculates the true modes averaging a certain number of noisy IMF sets evaluated independently of each other and each IMF $_{n,k}$  is determined considering the residue of corresponding previous mode IMF $_{n,k-1}$ .

On the contrary, the CEEMDAN algorithm (Figure 3) does not estimate the true modes in a single step as in the EEMD but such true modes are calculated sequentially. Specifically, for the estimation of each true mode, the CEEMDAN algorithm takes into account the contribution of the residue evaluated from the previous true mode. Therefore, the CEEMDAN guarantees the exact correspondence between the original signal and the set of decomposed signals, which is not ensured by the EEMD [32]:

$$x(t) = \sum_{n=k}^K \text{IMF}_k^*(t) + r(t). \quad (3)$$

Referring to Figure 3, at each iteration, the  $k$ th true mode is estimated from the previous residue calculated by the  $(k - 1)$ th mode perturbed by the white noise. Otherwise, in this algorithm the added white noise for the estimation of the  $k$ th IMF actually is the  $k$ th mode obtained performing the EMD on the white noise. A more exhaustive explanation of the CEEMDAN algorithm can be found in [32, 33]. The main advantages of this method are the exact reconstruction of the signal and the possibility of changing the noise level at each stage.

**2.5. Gear Fault Identification by Condition Indicators.** The presence of gear faults leads to changes in the vibration signature measured on the gearboxes. A number of researches can be found in the literature about the development of parameters for the quantification of the vibration signature modification [4, 9]. These parameters are generally called condition indicators (CIs).

In this study, the following standard CIs have been considered: kurtosis, Crest Factor (CF), and FM0. The kurtosis is the standardized moment of a probability distribution, the CF is the ratio between the peak value and the RMS (Root Mean Square) value and the FM0 is the ratio between the peak-to-peak value and the sum of the gear mesh harmonics. These parameters are particularly effective for the identification of local changes in the vibration signature, as in the case of localized gear faults.

Furthermore, two new CIs are proposed based on the vibration signal RMS values evaluated for each tooth: Crest Pitch Factor (CPF) and the Normalized Skewness Variance Product (NSVP). In other words, the angle domain vibration

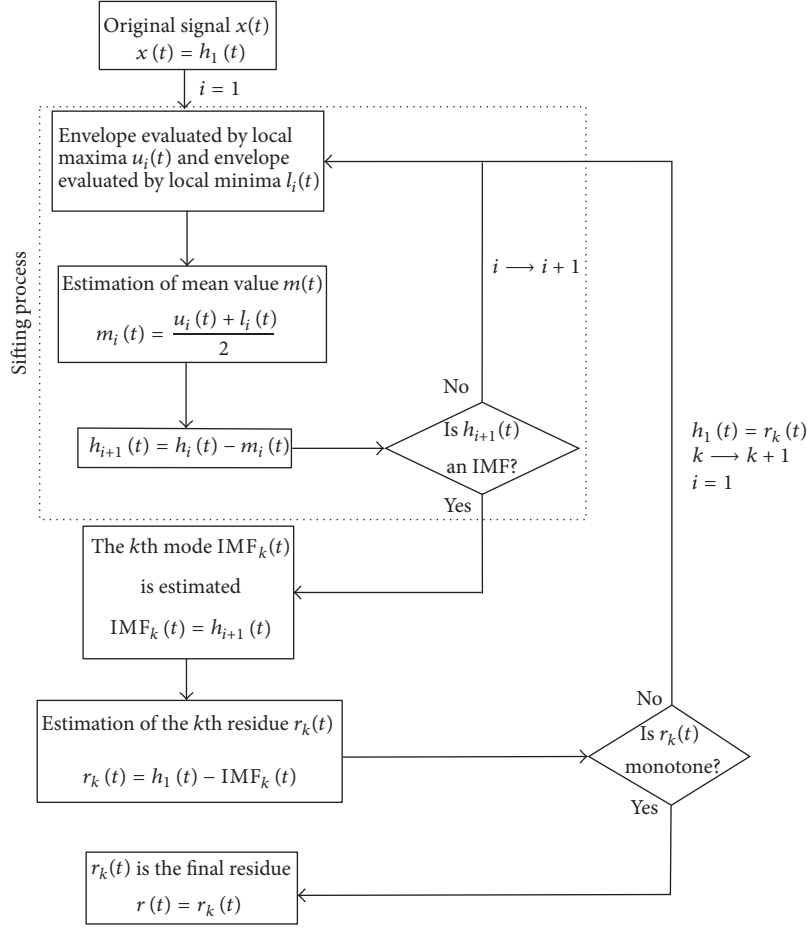


FIGURE 1: Flow-chart of the EMD algorithm.

signal referred to a single revolution (namely,  $x(\theta)$ ) is split into a number of parts equal to the number of teeth; then, the RMS value is estimated for each part. Let  $\text{RMS}_p^i$  be the RMS value of the  $i$ th tooth, and  $\text{RMS}_p^i$  is defined as follows:

$$\text{RMS}_p^i = \text{RMS} \left[ x \left( \theta_p + \frac{z}{2\pi} (i-1) \right) \right] \quad (4)$$

with  $0 \leq \theta_p < \frac{z}{2\pi}$ ,

where  $\theta_p$  is the angular pitch,  $z$  is the number of teeth, and RMS is the Root Mean Square operator. The whole set of  $\text{RMS}_p^i$  is

$$\{\text{RMS}_p\} = \begin{Bmatrix} \text{RMS}_p^1 \\ \vdots \\ \text{RMS}_p^i \\ \vdots \\ \text{RMS}_p^z \end{Bmatrix}. \quad (5)$$

For a gear having localized faults, a local deviation from the mean value of  $\text{RMS}_p$  is expected. The first CI, called CPF,

is defined as the ratio of the maximum value of  $\text{RMS}_p$  with respect to the  $\text{RMS}_p$  ensemble mean value:

$$\text{CPF} = \frac{\max[\text{RMS}_p]}{E[\text{RMS}_p]}, \quad (6)$$

where  $E$  is the ensemble mean operator. Now, let us consider the difference among adjacent  $\text{RMS}_p^i$  values:

$$\{\text{RMS}_{pd}\} = \begin{Bmatrix} \text{RMS}_p^2 - \text{RMS}_p^1 \\ \vdots \\ \text{RMS}_p^i - \text{RMS}_p^{i-1} \\ \vdots \\ \text{RMS}_p^z - \text{RMS}_p^{z-1} \end{Bmatrix}. \quad (7)$$

Intuitively,  $\text{RMS}_{pd}$  values should be close to zero for healthy gears since the variation between two consecutive RMS pitch values is slight. On the other hand,  $\text{RMS}_{pd}$  exhibits nonzero values when local changes of the vibration signature occur, since the vibration signature of a healthy meshing tooth is different from a faulty one. On the basis of these

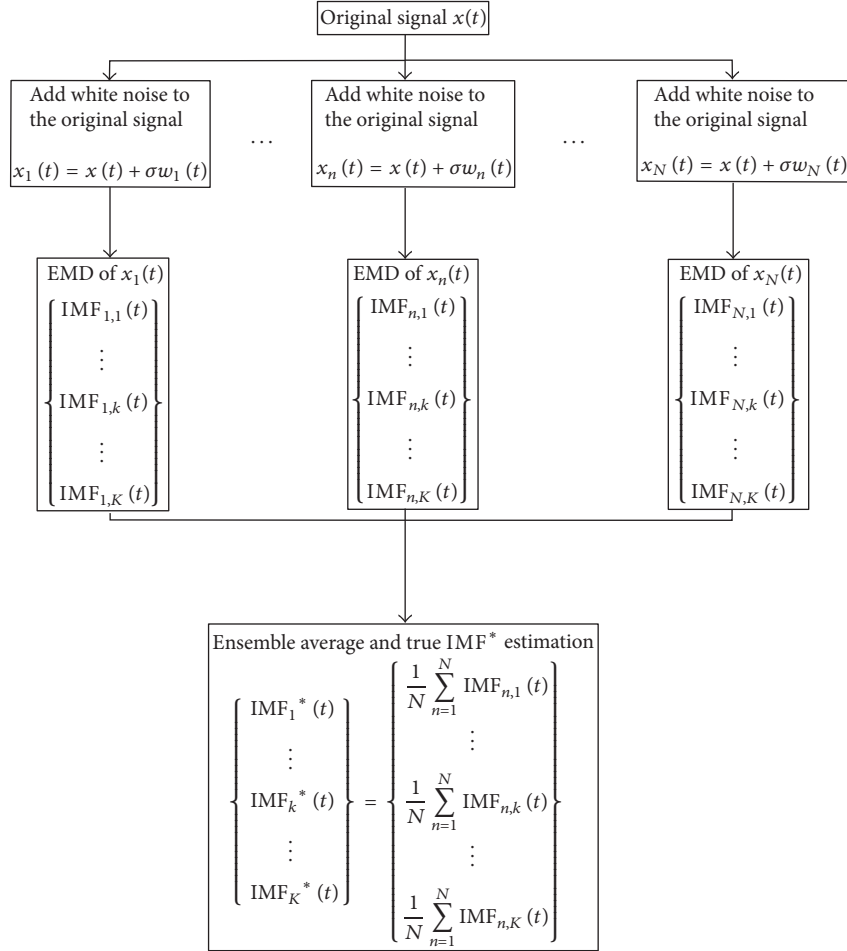


FIGURE 2: Flow-chart of the EEMD algorithm with  $N$  trials and  $K$  modes per trial.

considerations, the second proposed CI, called NSVP, is defined as the product between skewness and variance of the  $RMS_{pd}$  normalized by the peak-to-peak value of  $RMS_{pd}$ :

$$NSVP = \frac{\text{var} [RMS_{pd}] \text{skew} [RMS_{pd}]}{\text{pp} [RMS_{pd}]}, \quad (8)$$

where  $\text{var}$  is the variance operator,  $\text{skew}$  is the skewness operator, and  $\text{pp}$  is the peak-to-peak value.

### 3. Problem Statement and the Proposed Method

In theory, the vibration signal of a gearbox operating at steady-state condition appears as a composition of harmonics having as fundamental frequencies the meshing frequencies. The localized gear faults can appear in the vibration signals as impulsive components and local modulation of amplitude and/or phase [34]. These local components are visible on the spectrum as side-bands centred on the meshing frequencies. The pure impulsive component depends on the period of the

occurrence (the shaft period) and on the impulse response function of the system, and thus it depends on parameters that are not strictly related to gear II or gear III. The local modulation of amplitude and phase is a function of the gear mesh frequency of the faulty wheel. Thus, considering two gears with different (and not multiple) number of teeth, the analysis of the local modulation period due to the localized defect should lead to the identification of the faulty gear. Indeed, the modulation depends on the gear mesh frequency that is different for the considered gears.

When the TSA is performed according to a certain shaft period, it is possible to set apart only the tones that are synchronous with the shaft of interest. However, the TSA cannot separate those gear mesh harmonics belonging to two or more gears which are rotating in the same shaft (which is a very common case in multistage gearbox). Hence, in order to identify the faulty gear, the basic idea of this work is to exploit the local change of the meshing vibration due to the amplitude and phase modulation rather than the impulsive component. A signal separation method based on EMD algorithm is described hereafter in order to overcome this problem, which is fairly common in practical applications

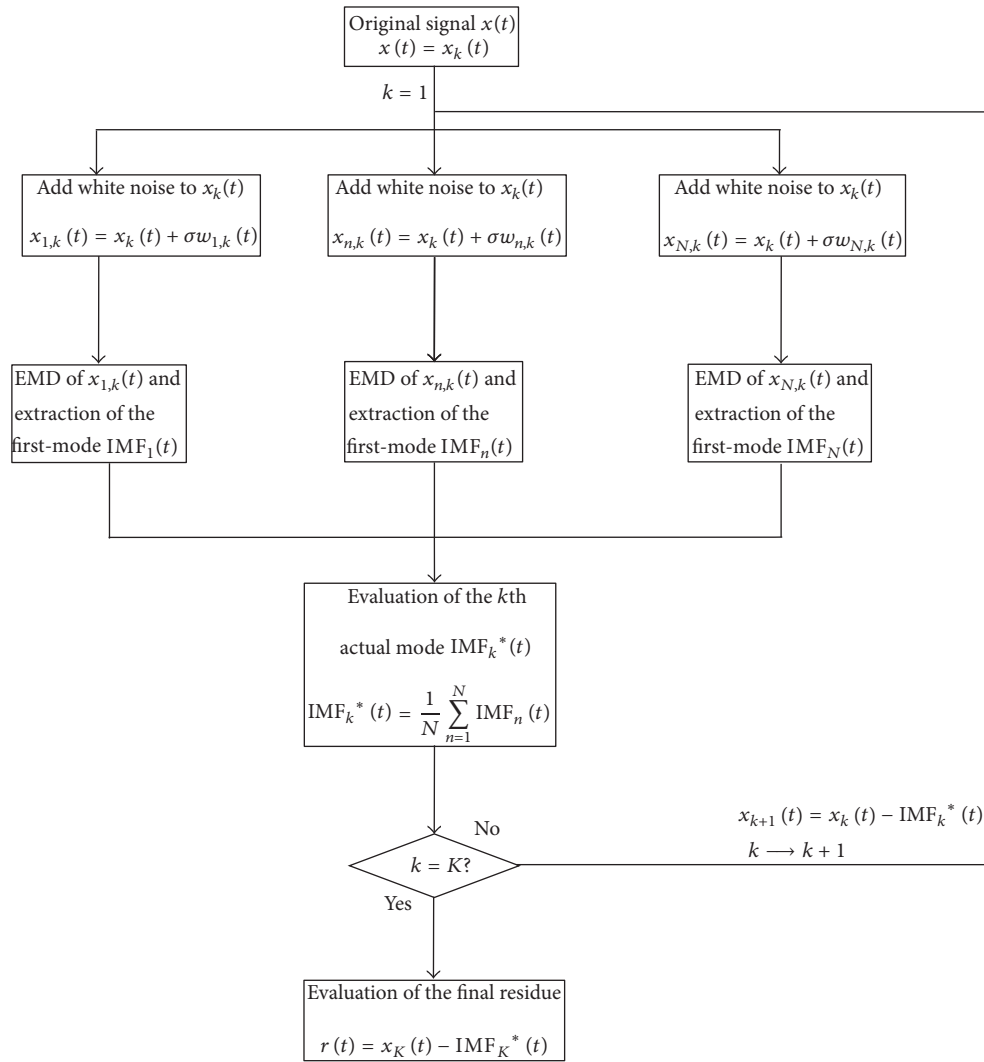


FIGURE 3: Flow-chart of the CEEMDAN algorithm.

with a significant implication concerning the reduction of maintenance costs and time.

Let us consider the two-stage gearbox shown in Figure 4, composed of four spur gears (namely, I, II, III, and IV) operating at steady-state conditions. Furthermore, let us suppose the presence of a localized fault on wheel II.

Thus, taking advantage from the EMD-based decomposition, two representative vibration signatures characterizing the meshing vibration of gear II and gear III, respectively, can be built taking into account the physically meaningful IMFs. The physically meaningful IMFs are intended as those IMFs that describe the gear mesh vibration signature of the gear of interest. Therefore, the representing signal of the gear will be the sum of these modes (if they are more than one). Figure 5 describes the proposed methodology (summarized in 4 fundamental steps) for the generic two-stage gearbox in Figure 4.

Under the assumption that the gear fault on the intermediate shaft is evident on the TSA, the first step involves the low-pass filtering since several high frequency signal

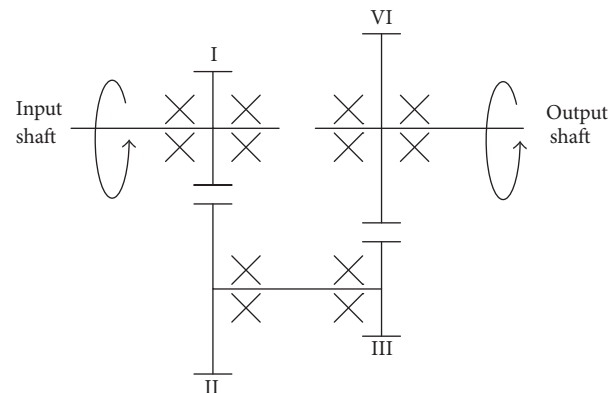


FIGURE 4: Schematic of a two-stage gearbox.

components unrelated to the gear mesh vibration signature can persist also after the TSA. In addition, the proposed signal processing procedure focuses on the local modulation

of amplitude and phase; hence a low-pass filter is desirable in order to cut off the high frequency signal components that should belong to the impulsive events. Therefore, the signal is conditioned with a low-pass filter with a cut-off order (the signal belongs to the angle domain) equal to 3 times the gear mesh order of the greater gear. Bearing in mind that the filtering process could reduce also some significant components, it is anyway reasonable to assume that the gear mesh vibration signature is properly described taking into account the first 3 meshing gear harmonics (and their sidebands).

The second step consists in the decomposition of the signal and the estimation of the regular signals of gears II and III. EMD, EEMD, and CEEMDAN have been considered, in order to investigate the effects on the use of different EMD algorithms for the signal decomposition. In this work, 500 trials and a fixed white noise standard deviation of 0.2 have been adopted, as suggested in [30, 32]. Furthermore, it has to be remarked that the procedure has been developed in MATLAB environment exploiting the EMD algorithms available at <http://perso.ens-lyon.fr/patrick.flandrin/emd.html> and [http://bioingenieria.edu.ar/grupos/ldnlys/meteorres/re\\_inter.htm](http://bioingenieria.edu.ar/grupos/ldnlys/meteorres/re_inter.htm). Instead, the regular signal is defined as the sum of the gear mesh harmonics from the TSA signal. In this application the fundamental gear mesh order and the first two harmonics are taken into account. The meaning of the estimation of the regular signals will be clarified hereafter.

The third step is the core of the proposed methodology. A major issue on the use of the Empirical Mode Decomposition is the physical interpretation of the IMFs. In fact, there are no established procedures for the identification of the meaningful modes for gear applications. Otherwise, the aim of this work is to generate, from the calculated IMF set, two signals representing the gear mesh vibration signals of gear II and gear III, distinctly. Therefore, it is important not just to identify the physically meaningful modes but also to determine if the mode describes the gear mesh vibration signature of gear II, gear III, or neither of these. The selection criterion of the physically meaningful modes developed in this work is based on the Pearson's Correlation Coefficient (PCC) between the regular signals and the IMFs. The PCC is an indicator of the linear correlation between two variables (signals) and conceptually is similar to the normalized cross-correlation between two signals with zero lag [35]. PCC value  $c$  evaluated for discrete dataset  $x$  and  $y$  of  $n$  samples (e.g., the discrete signals in the angle domain) is defined as follows:

$$c = \frac{\sum_{i=1}^n (x_i - \bar{x})(y_i - \bar{y})}{\sqrt{\sum_{i=1}^n (x_i - \bar{x})^2 \sum_{i=1}^n (y_i - \bar{y})^2}}, \quad (9)$$

where  $\bar{x}$  and  $\bar{y}$  are the mean value of  $x$  and  $y$ , respectively. The PCC can take values between  $-1$  and  $1$ , where positive values mean a direct correlation while negative ones mean inverse correlation. For our purpose,  $\text{PCC} \geq 0.7$  means a strong linear correlation,  $0.3 \leq \text{PCC} < 0.7$  means moderate correlation,  $0.1 \leq \text{PCC} < 0.3$  means weak correlation, and  $\text{PCC} = 0$  means no correlation. In this work, the PCC has been exploited as the merit index for the mode selection in order to

allocate each IMF to gear II, gear III, or neither of these. Referring to Figure 5, the assignment process regards the mode selection procedure for building the representative signals of gear II and gear III, namely,  $M^{\text{II}}(\theta)$  and  $M^{\text{III}}(\theta)$ , respectively. The selection criterion that evaluates the physical significance of the modes is based on these properties:

- (1) If  $\text{PCC} \geq 0.3$  (which means at least moderate correlation), the mode is assigned to the representative signal set.
- (2) If no IMF satisfies the previous properties, the mode having the maximum value of PCC is representative of the gear.

Therefore, referring to Figure 5, the representative vibration signal of gear II,  $M^{\text{II}}(\theta)$ , is composed of all the modes (called  $m_j^{\text{II}}(\theta)$ ) satisfying one of these properties and the same occurs for  $M^{\text{III}}(\theta)$ . The PCCs are evaluated by the regular signal (e.g., an ideal healthy mesh gear vibration) and the IMFs. Since the modes are estimated from the faulty gear vibration signal, a moderate correlation with the regular signal is expected. Thus, property 1 aims to include all the modes showing a moderate correlation with the regular signal having, however, a significant relationship with the gear vibration signature from the physical standpoint. The second property is introduced in order to include at least one IMF also if property 1 is not met.

Lastly, in the fourth step the estimation of  $M^{\text{II}}(\theta)$  and  $M^{\text{III}}(\theta)$  of gear II and gear III, respectively, is carried out by means of the sum of the selected modes  $m_j^{\text{II}}(\theta)$  and  $m_j^{\text{III}}(\theta)$  evaluated in the third step. After a visual inspection of the representative signals, the objective comparison between  $M^{\text{II}}(\theta)$  and  $M^{\text{III}}(\theta)$  is achieved by means of different CIs. For this purpose, in order to identify localized gear faults, several CIs can be used for the evaluation of the vibration signal peakiness, which is correlated with the severity of the localized fault. In this study, the following standard CIs have been considered: kurtosis and Crest Factor (CF) [9, 36]. Furthermore, the effectiveness of the proposed CIs, that is, CPF and NSVP, has been tested for the simulated vibration signals and the real case studies.

## 4. Application to Simulated Vibration Signals

In this section, the first subsection regards the mathematical formulation of the meshing vibration signal model with localized fault in the angle domain; in the second subsection, the effectiveness of the proposed methodology will be verified by means of the simulated signals.

**4.1. Signal Model Formulation.** Several works [34, 37, 38] regarding the time domain vibration signal modeling of gear faults can be found in the literature. Since the proposed method departs from an averaged angle domain vibration signal (TSA), an angle domain model of the meshing vibration signal of a spur gear with  $z$  teeth is proposed hereafter. In healthy gearboxes, meshing gear vibration  $x$  with respect to angle  $\theta$  is mainly composed of harmonics with fundamental

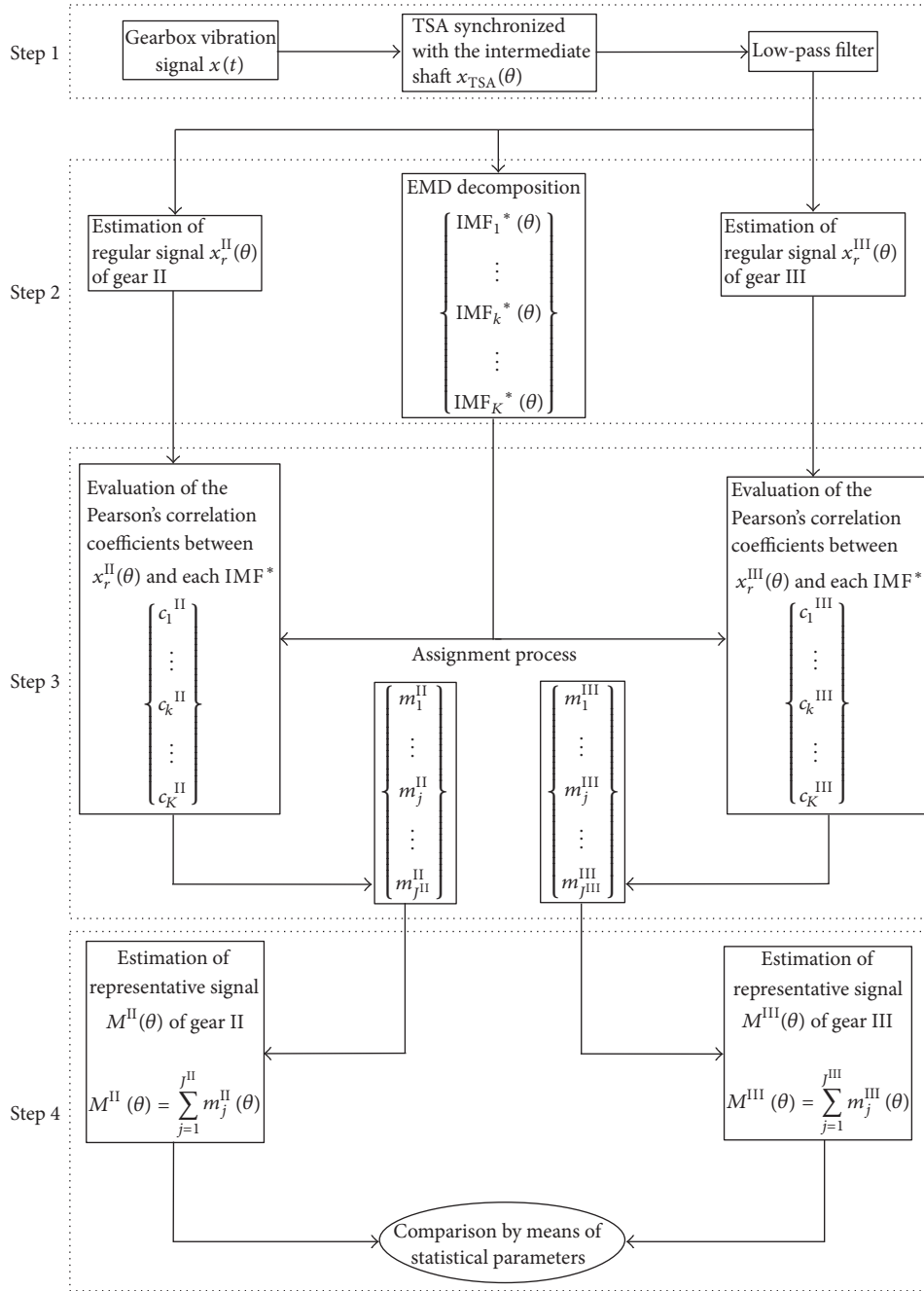


FIGURE 5: Flow-chart of the proposed methodology.

order corresponding to the number of teeth of the gear of interest. For a complete revolution,  $x(\theta)$  can be expressed as follows:

$$x(\theta) = \sum_{n=1}^N X_n \cos(nz\theta + \phi_n), \quad (10)$$

where  $N$  is the number of harmonics,  $X_n$  is the amplitude of the  $n$ th harmonics,  $\phi_n$  is the phase of the  $n$ th harmonics, and  $z$  is the number of teeth of the gear.

Let us consider the two-stage healthy gearbox shown in Figure 4. In a complete revolution, the angle domain meshing vibration  $x(\theta)$  related to the intermediate shaft may be expressed as follows:

$$x(\theta) = \sum_{n=1}^N X_{II,n} \cos(nz_{II}\theta + \phi_{II,n}) + \sum_{n=1}^N X_{III,n} \cos(nz_{III}\theta + \phi_{III,n}), \quad (11)$$

where  $N$  is the number of harmonics,  $X_{II,n}$  is the amplitude of the  $n$ th harmonics of gear II,  $\phi_{II,n}$  is the phase of the  $n$ th harmonics of gear II,  $z_{II}$  is the number of teeth of gear II,  $X_{III,n}$  is the amplitude of the  $n$ th harmonics of gear III,  $\phi_{III,n}$  is the phase of the  $n$ th harmonics of gear III, and  $z_{III}$  is the number of teeth of gear III. Equation (11) states that the meshing vibration signal  $x(\theta)$  is composed of the meshing vibration related to gear II and the gear mesh vibration related to gear III since both gears II and III rotate synchronously.

The presence of a localized gear fault causes a change in the vibration signal model that involves a local amplitude modulation, a local phase modulation, and an impulsive component. Hence assuming localized faults in gear II, (11) can be rewritten as

$$\begin{aligned} x_{\text{sim,II}}(\theta) &= x^{\text{II}}(\theta) + x^{\text{III}}(\theta) + \delta(\theta) \\ &= \sum_{n=1}^N X_{II,n} [1 + a_{II,n}(\theta)] \cos[nz_{II}\theta + \phi_{II,n} + b_n(\theta)] \\ &\quad + \sum_{n=1}^N X_{III,n} \cos(nz_{III}\theta + \phi_{III,n}) + \delta(\theta), \end{aligned} \quad (12)$$

where  $a_{II,n}$  is the local amplitude modulation function due to localized fault in gear II,  $b_{II,n}$  is the local phase modulation function due to localized fault in gear II, and  $\delta$  is the impulsive component due to localized fault in gear II. The local amplitude function  $a_{II,n}$  and phase modulation function  $b_{II,n}$  used in (13) are described as a Gaussian shape window centred at angle  $\theta_0$  as follows:

$$a_n(\theta) = A_n e^{-(\theta-\theta_0)/\sigma_a^2} \quad (13)$$

$$b_n(\theta) = B_n e^{-(\theta-\theta_0)/\sigma_b^2}, \quad (14)$$

where  $A_n$  and  $B_n$  are the amplitude of the local modulation and  $\sigma$  is the window width. In addition,  $\delta(\theta)$  (see (13)) is the damped impulse response that takes into account the impulsive component due to the engagement of the faulted tooth. This component is defined as a train of Dirac impulses having unitary amplitude convoluted by an arbitrary impulse response function (in the form of a 3rd FIR filter):

$$\delta(\theta) = s(\theta) * h, \quad (15)$$

where  $s$  is the train of unitary impulses corresponding to the fault occurrence and  $h$  is the impulse response function. Note that (15) is valid only in steady-state conditions. In fact, this formulation keeps its physical meaning only when the frequency domain is equivalent to the order domain up to a proportional constant (the fundamental rotation frequency). Hence, this is true only if the rotation frequency of the system is, to a good approximation, constant.

TABLE 1: Simulated signal parameters.

	$x_{\text{sim,II}}(\theta)$	$x_{\text{sim,III}}(\theta)$
$z$	93	12
$N$	3	3
$X$	[6.000 3.639 2.207]	[6.000 3.639 2.207]
$A$	[1.075 3.668 -4.518]	[1.075 3.668 -4.518]
$B$	[0.862 0.319 -1.308]	[0.862 0.319 -1.308]
$\sigma_a$	0.011	0.087
$\sigma_b$	0.011	0.087
$\theta_0$	174.179	180.000
$h$	[1.000 -0.300 0.910]	[1.000 -0.300 0.910]

Analogously, the gear mesh vibration model can be written in the case of a localized fault in gear III:

$$\begin{aligned} x_{\text{sim,III}}(\theta) &= x^{\text{II}}(\theta) + x^{\text{III}}(\theta) + d(\theta) + \delta(\theta) \\ &= \sum_{n=1}^N X_{II,n} \cos(nz_{II}\theta + \phi_{II,n}) \\ &\quad + \sum_{n=1}^N X_{III,n} [1 + a_{III,n}(\theta)] \\ &\quad \cdot \cos[nz_{III}\theta + \phi_{III,n} + b_n(\theta)] + \delta(\theta). \end{aligned} \quad (16)$$

Referring to the gearbox depicted in Figure 4, (13) and (16) represent the gear mesh vibration models used for the preliminary verification of the methodology.

**4.2. Results and Discussion.** Two different simulated signals called  $x_{\text{sim,II}}(\theta)$  and  $x_{\text{sim,III}}(\theta)$  have been considered: the first simulated signal is described in (12) and refers to the case of a localized defect in gear II; the second one is described in (16) and refers to the case of a localized defect in gear III. The parameters used for the MATLAB implementation of  $x_{\text{sim,II}}(\theta)$  and  $x_{\text{sim,III}}(\theta)$  are reported in detail in Table 1, while Figure 6 shows the simulated signals. In the first case the localized fault has been simulated on the 45th tooth of gear II whereas in the second case the localized fault has been simulated on the 6th tooth of gear III, which correspond to an angle rotation of about 174 deg and 180 deg, respectively.

As mentioned in Section 4.1, the overall simulated signal is a superposition of the vibration signature in the angle domain of the two gears, where the healthy gear is represented by pure tones and the faulty gear is composed of pure tones having local amplitude and phase modulation with the contribution of an impulsive component. De facto, such signals represent a synthesized version of the TSA computed with respect to the intermediate shaft and, according to the properties of the TSA, the contribution of the background noise has been neglected. Considering the proposed diagnostic protocol, Step 1 can be skipped with this vibration signal model since the starting signal is already the TSA of the signal.

The method has been performed using EMD, EEMD, and CEEMDAN in order to investigate the effect of different EMD

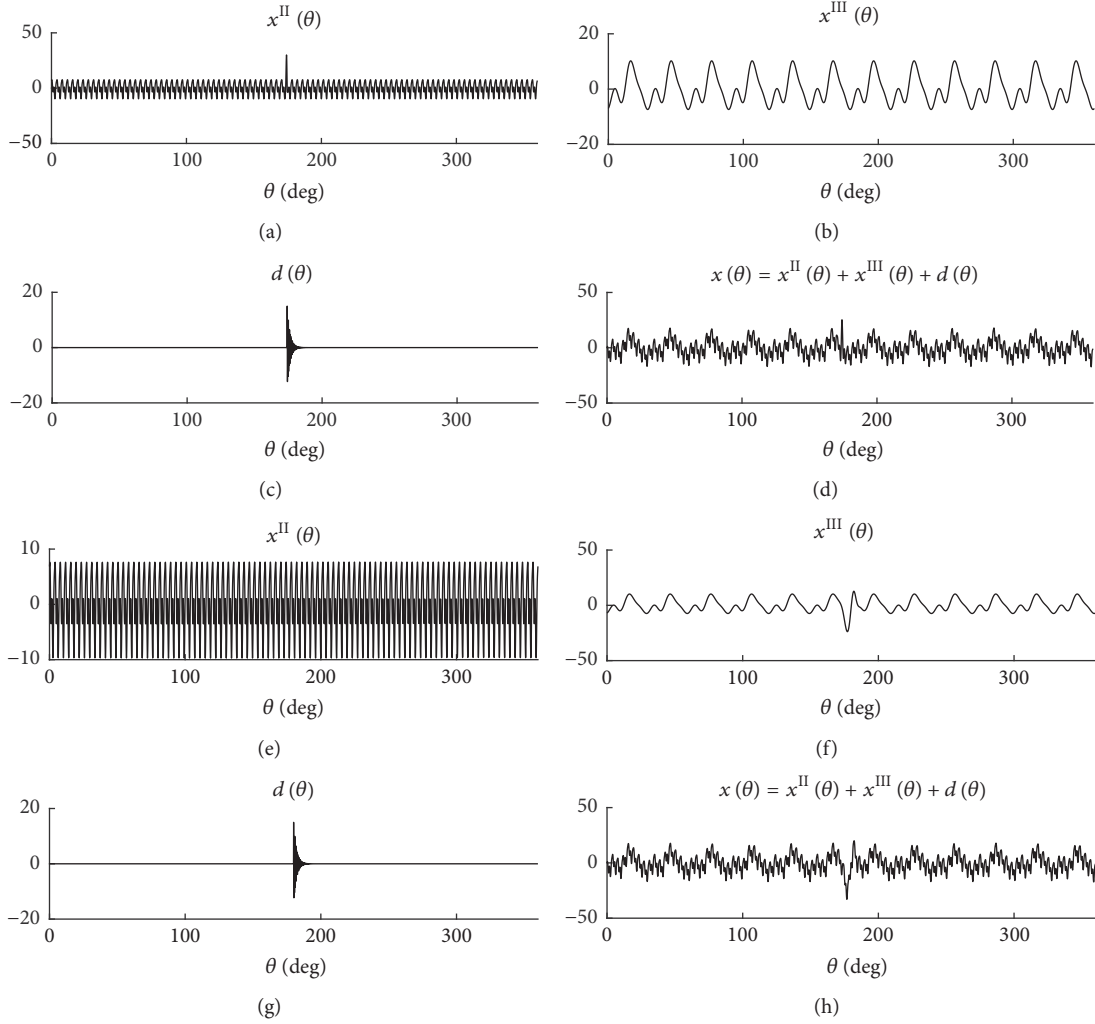


FIGURE 6: Simulated signals in the angle domain: (d)  $x_{\text{sim,II}}$  and (a–c) its components and (h)  $x_{\text{sim,III}}$  and (e–g) its components.

algorithms on the effectiveness of the signal decomposition. In agreement with the settings suggested in the literature, 500 averages and white noise standard deviation of 0.02 have been used for the EEMD and CEEMDAN. The results of the signal decomposition of  $x_{\text{sim,II}}(\theta)$  and  $x_{\text{sim,III}}(\theta)$  are reported in Figures 7 and 8, respectively. The residue signal, which is a monotonic function, is not displayed since it is not useful for the goal of this work. It should be noted that EMD returns a limited number of modes (5 excluding the residue, i.e., the monotonic mode) whereas the total number of tones present on the simulated signal is 6 since it is equal to the total number of gear mesh harmonics accounted. This behavior can be interpreted as poor quality of the signal decomposition using EMD with respect to EEMD and CEEMDAN.

For the sake of completeness, the estimated PCC values are collected in Figure 9 where the square symbol refers to  $c_i^{\text{II}}$  and the star symbol refers to  $c_i^{\text{III}}$ . In each diagram, the gray horizontal line refers to the threshold corresponding to  $\text{PCC} = 3$ . According to the proposed criterion, the representative signals of gear II and gear III are showed in Figures 10 and 11.

The visual inspection of the representative signals shown in Figure 10 highlights that all the considered EMD algorithms have led to satisfying results. In this case, as expected, representative signal  $M^{\text{II}}$  related to the 93-teeth gear exhibits a localized signal distortion at about 170 deg due to the simulated defect (in agreement to the input data in Table 1) whereas the waveform  $M^{\text{III}}$  does not show irregularities. It should be remarked that  $M^{\text{III}}$  estimated by the EMD (Figure 10(d)) is less regular than the others just in correspondence to the angle where  $M^{\text{II}}$  has the local amplitude/phase modulation. Table 2 collects the statistical indicators estimated by  $M^{\text{II}}$  and  $M^{\text{III}}$ . All the indicators return a positive deviation between the faulty gear and the healthy one, with the only exception of the kurtosis when the EMD is performed; this behavior is in agreement with the observations previously made by the visual inspection of the signal.

Similar remarks can be mentioned by observing Figure 11. Indeed,  $M^{\text{III}}$  shows a sudden change of the signal amplitude at about 180 deg that corresponds to the position of the simulated fault (see Table 1). Again, the waveform of  $M^{\text{II}}$  does

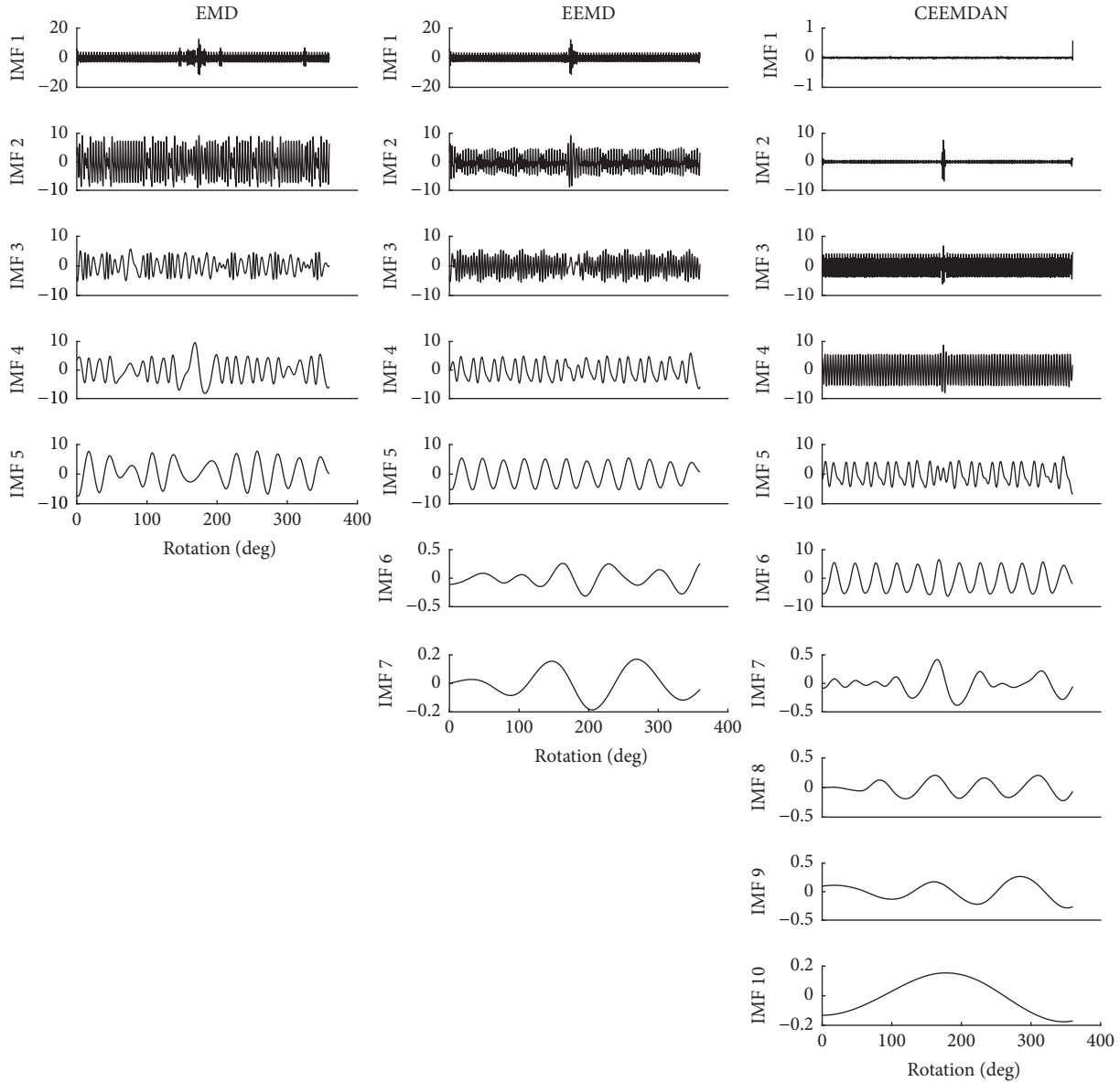


FIGURE 7: IMF sets of  $x_{sim,II}$  obtained by using EMD, EEMD, and CEEMDAN.

not exhibit any abrupt change, although the EMD returns a quiet irregular waveform with respect to the other EMD algorithms. In fact, the indicators collected in Table 3 highlight that negative percentage differences are present only for the EMD, as expected. However, the method performed using the EEMD and the CEEMDAN has allowed clearly identifying the faulty gear both by visual inspection and by comparing condition indicators.

Finally, the validation of the method by simulated signals has pointed out the following aspects:

- (i) The signal decomposition by means of the EMD is the worst one among the other EMD algorithms.
- (ii) The faulty gear has been correctly identified in both the simulated cases.
- (iii) NSVP is the most sensitive indicator.

## 5. Application to Real Vibration Signals in the Case of Localized Gear Faults

In the current section, the proposed methodology has been performed in 2 different cases' studies, discussing the main results. Section 5.1 concerns the investigation of the method using a dedicated gear test bench whereas Section 5.2 regards a more complex transmission mounted on a test rig. The main results have been discussed, focusing on the effectiveness of the proposed methodology performed using actual vibration signals.

*5.1. Case 1.* The first case study is a two-stage gearbox mounted on a dedicated test rig shown in Figure 12(a) located at the Engineering Department of the University of Ferrara. Detailed information about this test rig can be found in

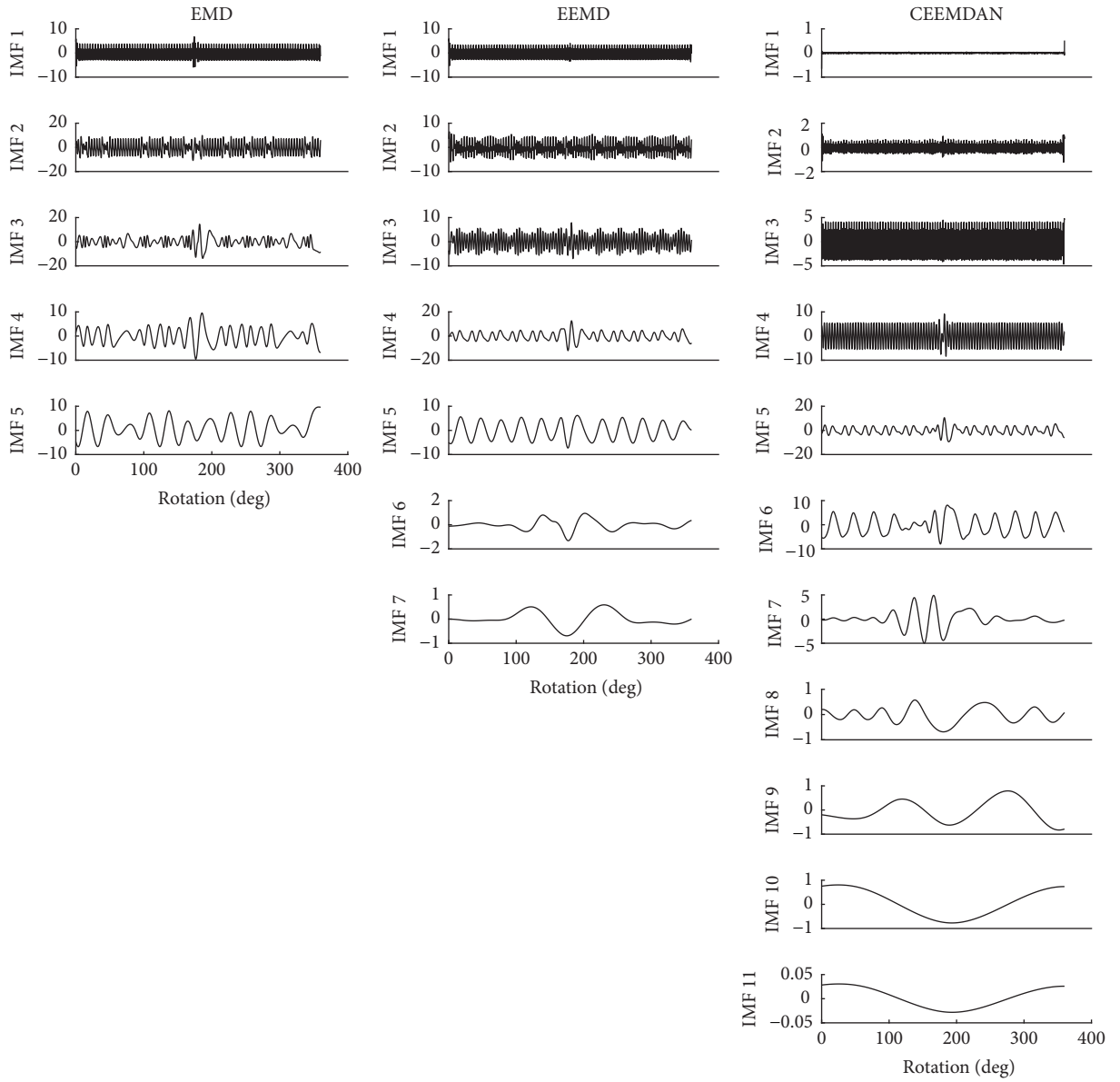


FIGURE 8: IMF sets of  $x_{sim,III}$  obtained by using EMD, EEMD, and CEEMDAN.

TABLE 2: CIs for the simulated signal with localized fault in gear II.

		Kurtosis	CF	CPF	NSVP
EMD	Gear II (faulty)	2.395	4.017	1.854	0.310
	Gear III (healthy)	2.742	2.673	1.083	0.0796
	Gear II versus gear III [%]	-12.671	50.269	71.244	291.452
EEMD	Gear II (faulty)	2.484	4.494	1.872	0.173
	Gear III (healthy)	2.165	2.014	1.036	0.022
	Gear II versus gear III [%]	14.713	123.180	80.722	667.777
CEEMDAN	Gear II (faulty)	2.340	4.284	1.857	0.205
	Gear III (healthy)	2.177	1.992	1.027	0.016
	Gear II versus gear III [%]	7.487	115.058	80.777	1156.891

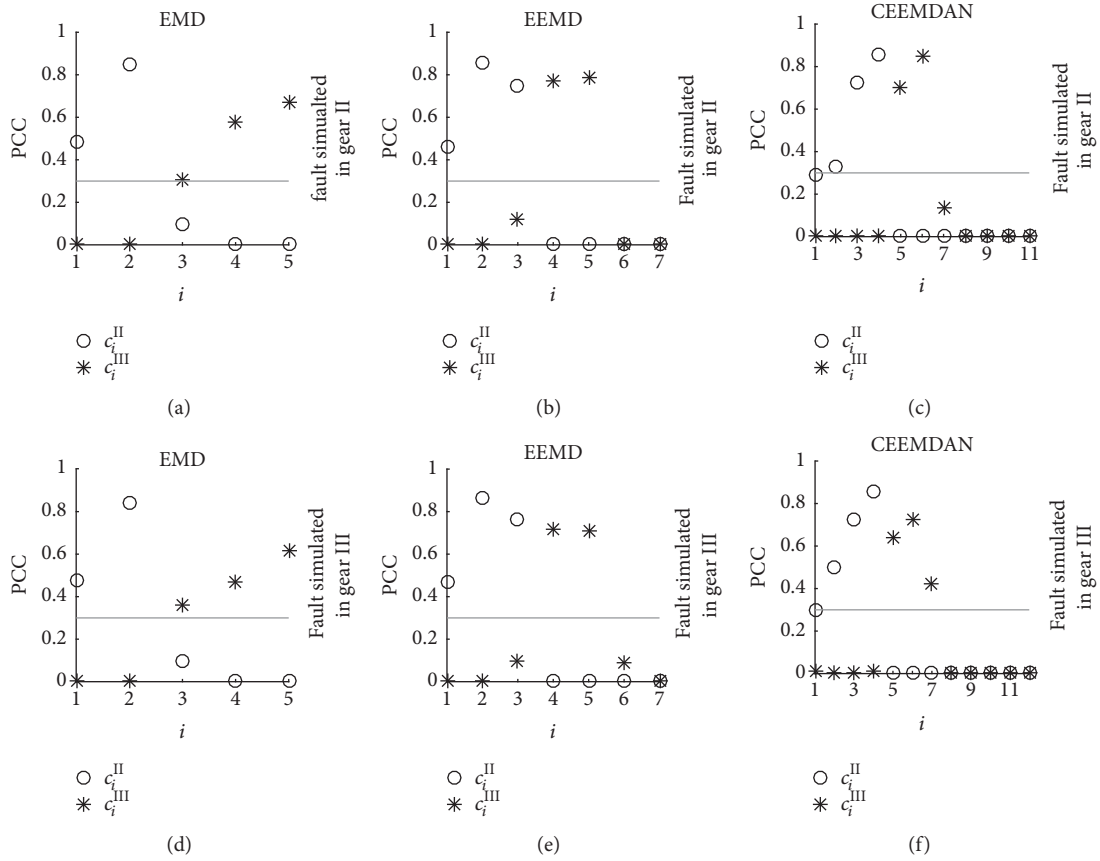


FIGURE 9: PCC values (a–c) in the case of the simulated signal with localized fault in gear II and (d–e) in the case of the simulated signal with localized fault in gear III.

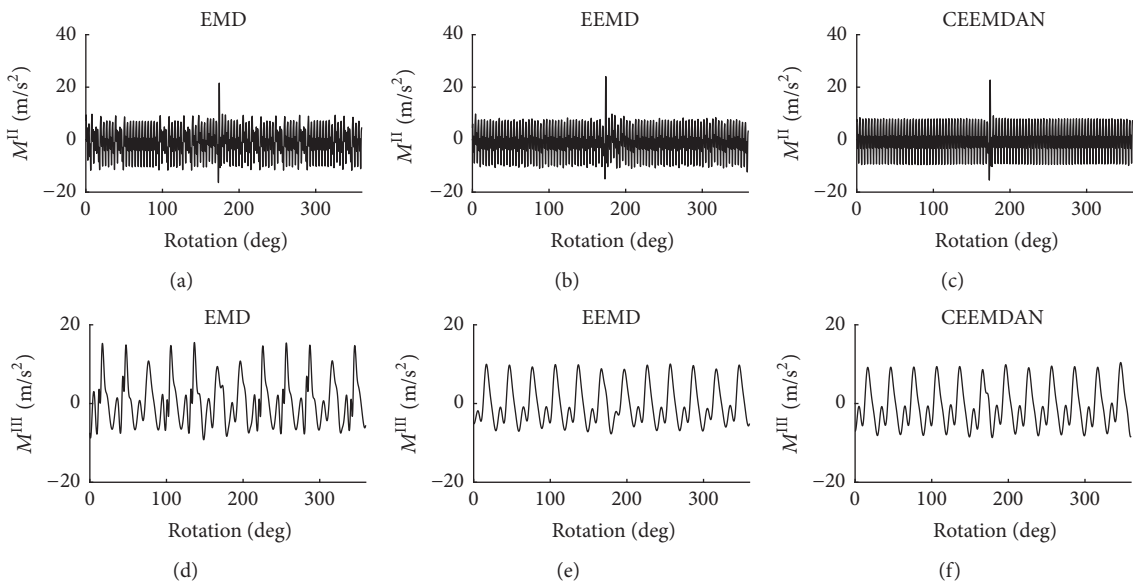


FIGURE 10: Representative signals for (a–c) gear II and (d–f) gear III in the case of the simulated signal with localized fault in gear II.

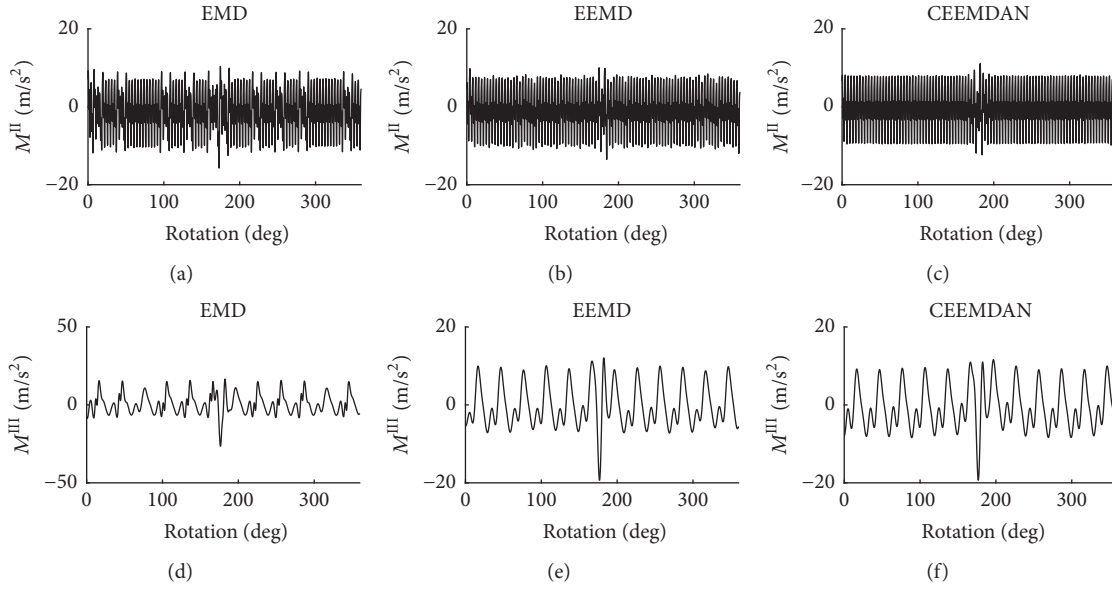


FIGURE 11: Representative signals for (a–c) gear II and (d–f) gear III in the case of the simulated signal with localized fault in gear III.

TABLE 3: CIs for the simulated signal with localized fault in gear III.

		Kurtosis	CF	CPF	NSVP
EMD	Gear II (healthy)	2.167	2.989	1.625	0.288
	Gear III (faulty)	3.980	4.146	1.579	0.261
	Gear III versus gear II [%]	83.697	38.733	-2.756	-9.628
EEMD	Gear II (healthy)	2.062	2.569	1.329	0.007
	Gear III (faulty)	2.855	3.578	1.562	0.334
	Gear III versus gear II [%]	38.482	39.266	17.488	4958.513
CEEMDAN	Gear II (healthy)	2.039	2.357	1.309	0.013
	Gear III (faulty)	2.647	3.428	1.469	0.351
	Gear III versus gear II [%]	29.847	45.404	12.228	2528.605

[39]. The investigated gearbox is composed of two stages of helical gears: the first one having 18 and 71 teeth whereas the second one has 12 and 55 teeth. Hence, referring to the gearbox scheme in Figure 4, gear II and gear III have 71 teeth and 12 teeth, respectively. The localized fault, namely a gear tooth spall, has been artificially seeded on the 71-teeth gear, as shown in Figure 12(b). The test has been carried out in steady-state condition at 3600 rpm using a nominal load of 48.8 Nm.

The vibration signals in the radial direction have been collected by means of B&K piezoelectric accelerometer type 4943 placed on the bearing support of the first stage pinion with sampling frequency 12.4 kHz for a total time length of 4 s while the input shaft speed has been measured by a tachometer sensor.

Figure 13 collects the TSA of the measured vibration signal as well as its spectrogram. The TSA has been performed in the angular domain taking into account 4260 points per revolution. The localized fault is easy to recognize on both the diagrams since it appears as a sudden increase of the signal amplitude in a slight rotation range. Thus, even if the presence of the gear tooth spall is obvious, these approaches are not able to identify which gear owns the fault.

As done before, three different EMD algorithms have been considered in order to verify the sensitivity of the final results with respect to the adopted EMD method. The signal decomposition has been performed using the same settings reported in Section 4.2 and the results are collected in Figure 14. According to the PCC values collected in Figure 15, the representative signals of gear II and gear III have been computed, as reported in Figure 16. From the visual inspection of the representative signals in Figure 16 it is not hard to identify the faulty gear. Indeed, the waveform related to the 71-teeth wheel exhibits a large amplitude increase at 170 deg that is the effect of the engagement of the faulty tooth. However, Figures 16(d) and 16(e) show a sudden change of the signal amplitude at about 170 deg that corresponds exactly to the angle position of the defect in gear II (clearly visible in Figures 16(a)–16(c) and in the TSA in Figure 13(a)). The diagram related to the CEEMDAN in Figure 16(e) actually displays a local change of amplitude too. However it should be noted that such a change occurs at about 250 deg, which is not in agreement with the fault position shown on the TSA of the signal.

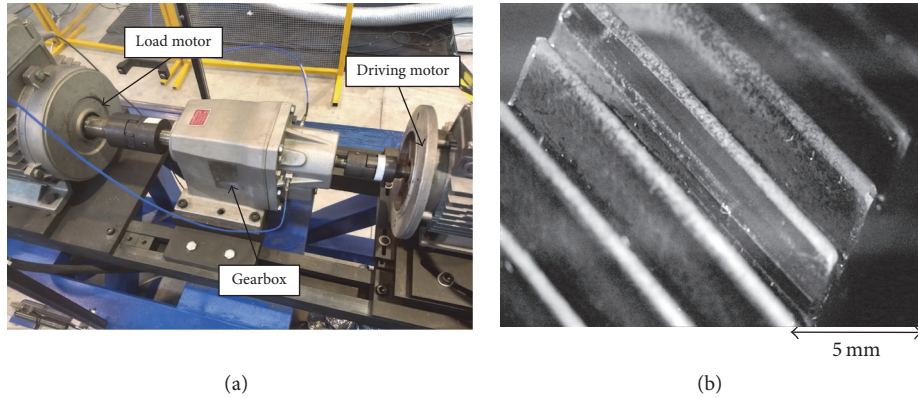


FIGURE 12: (a) Experimental setup of Case 1 and (b) gear with a spalled tooth.

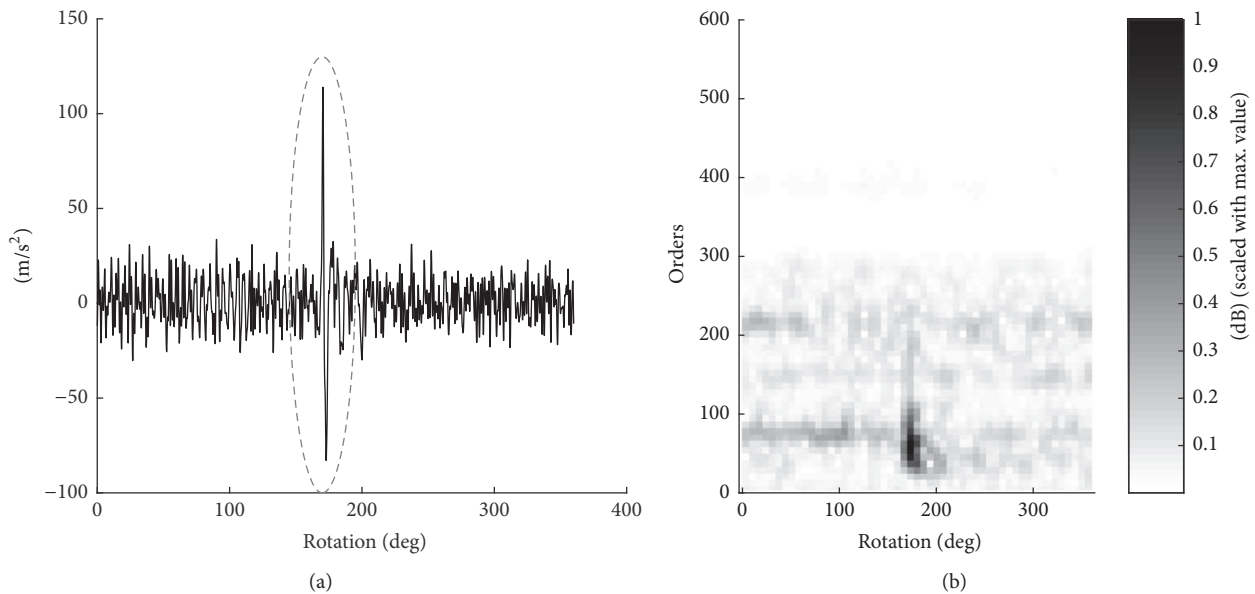


FIGURE 13: (a) Time Synchronous Average related to the intermediate shaft of Case 1 (the dashed circle highlights the impulsive signal component due to the damaged tooth engagement) and (b) the related spectrogram (300 samples of window length and 75% overlap).

Unfortunately, the visual inspection of the signal can be open to different interpretations; thus the fault identification is determined by the comparison of condition indicators. Table 4 highlights a significant difference between gear II and gear III, with a minimum percentage difference of 93.872. The proposed CIs (i.e., CPF and NSVP) are the most sensitive to the presence of an impulsive component in the vibration signature as demonstrated by the larger percentage difference with respect to the other traditional CIs.

Finally, in this first experimental case the proposed method is effective in the identification of the faulty gear. Moreover, CEEMDAN is the EMD algorithm that returns the best result taking into account the CIs values as well as the waveform of the representative signals.

**5.2. Case 2.** The second case study concerns a more complex gearbox driven by an asynchronous motor. Figure 17 shows the experimental setup: the time domain vibration signal

in the radial direction has been acquired by a monoaxial piezoelectric accelerometer (PCB 353B18) with a sampling frequency of 25.6 kHz, while the tachometer signal has been simultaneously collected using a tachometer probe with zebra tape. The transmission exhibits abnormal loudness due to a localized gear fault on the two-stage gearbox just after the input cardan shaft (see Figure 17(b)). The steady-state operational test has been carried out at 600 rpm at the input cardan shaft. Considering the gearbox layout in Figure 4, gear II has 92 teeth whereas gear III has 10 teeth.

Gear II presents a bump on a tooth flank caused by the handling during the surface hardening process. Such a faulty tooth flank engages only in the reverse motion and it has been verified by visual inspection. Furthermore, such a natural defect is clearly visible in the TSA signal performed on the intermediate shaft using 3680 samples per revolution, as reported in Figure 18(a). The presence of the fault is clear also on the spectrogram as well in Figure 18(b). As in Case 1,

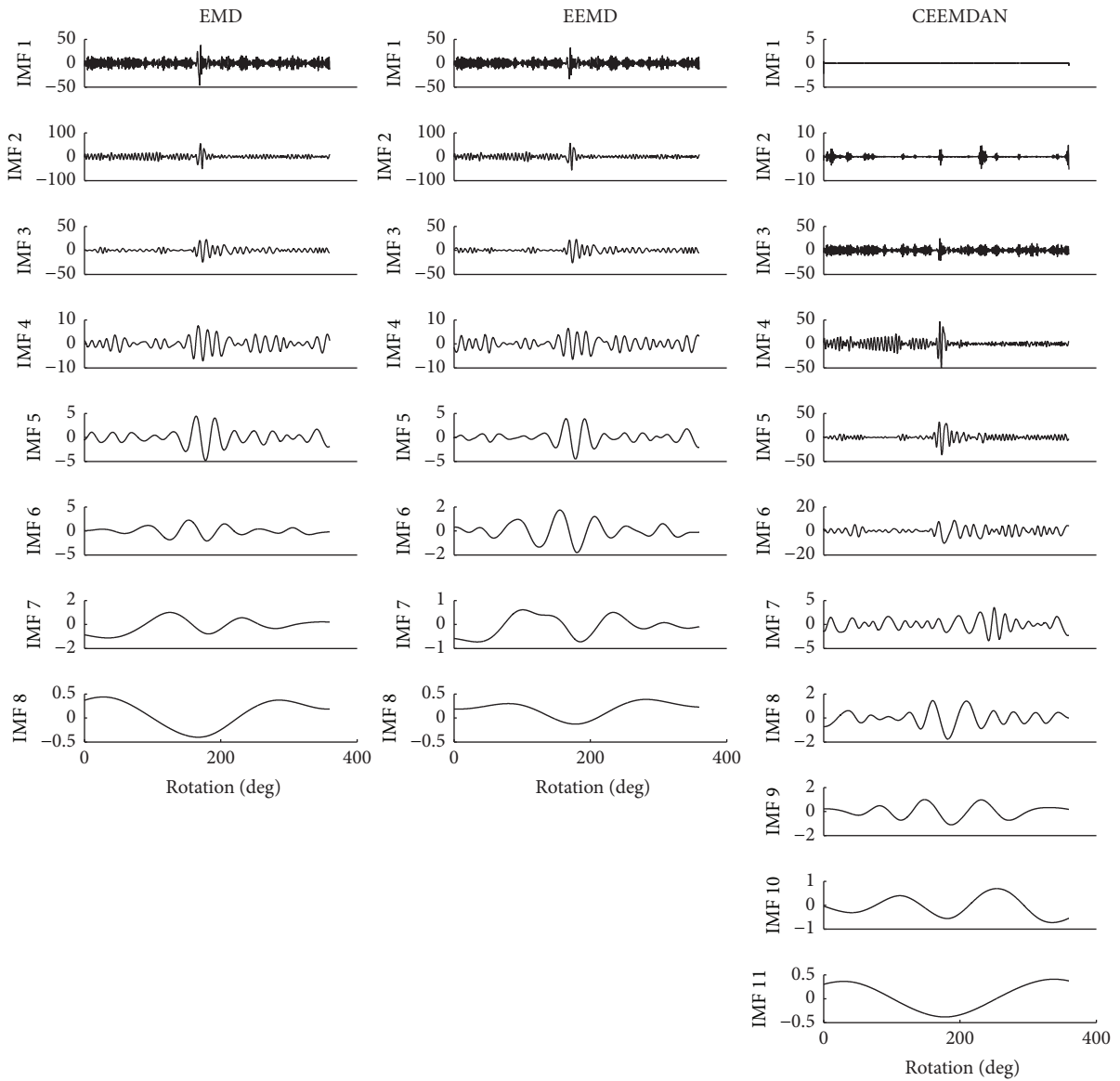


FIGURE 14: IMF sets of Case 1 obtained by using EMD, EEMD, and CEEMDAN.

TABLE 4: CIs for the vibration signal of Case 1, with localized fault in gear II.

		Kurtosis	CF	CPF	NSVP
EMD	Gear II (faulty)	10.220	8.785	4.437	1.395
	Gear III (healthy)	3.785	8.021	2.288	0.251
	Gear II versus gear III [%]	170.043	142.209	93.872	457.089
EEMD	Gear II (faulty)	9.945	7.806	4.444	1.205
	Gear III (healthy)	2.962	2.931	1.942	0.309
	Gear II versus gear III [%]	235.745	166.309	128.859	290.713
CEEMDAN	Gear II (faulty)	8.031	7.177	4.332	1.139
	Gear III (healthy)	3.141	3.036	2.141	0.112
	Gear II versus gear III [%]	155.666	136.382	102.324	917.173

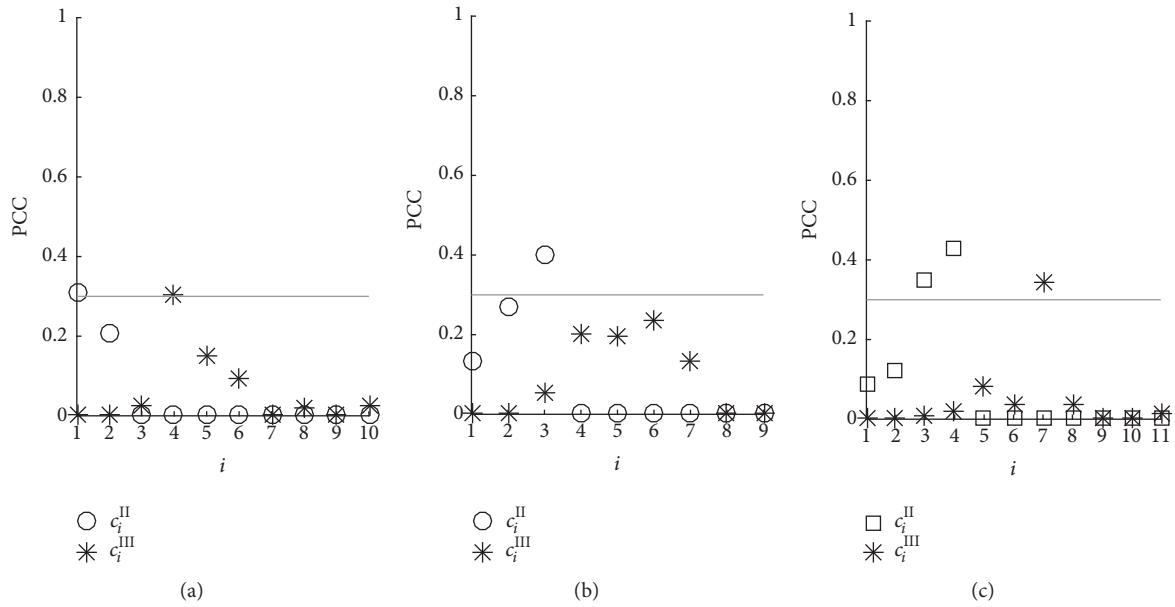


FIGURE 15: PCC values of Case 1 estimated taking into account (a) EMD, (b) EEMD, and (c) CEEMDAN.

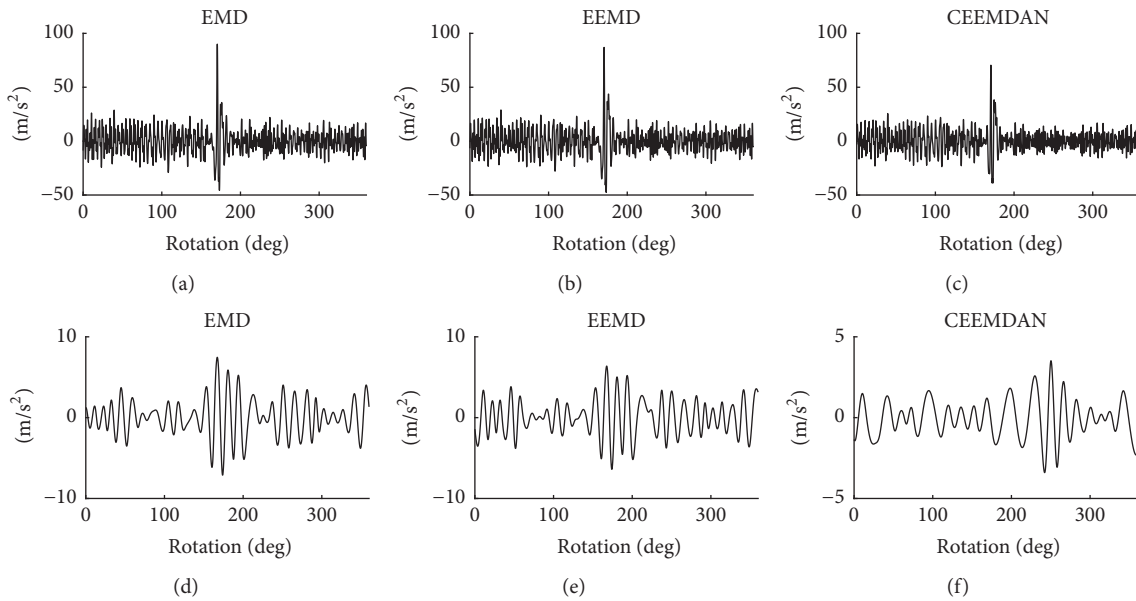


FIGURE 16: Representative signals of (a–c) gear II and (d–f) gear III for Case 1.

these signal processing techniques are not able to identify if the defect is related to the gear of 92 or 10 teeth.

Again, this experimental case study has been investigated by using the same modus operandi of Case 1. For the sake of completeness, signal decomposition results and the PCC values for the estimation of the representative signals are reported in Figures 19 and 20, respectively. By going directly to the visual inspection of the representative signals (Figure 21), it can be noted that in this case the different EMD algorithms have a significant impact on the final results of the

methods. From the physical standpoint, the representative signal related to gear II (see Figures 21(a)–21(c)) correctly reflects the presence of the fault at about 170 deg due to the localized increase of the signal amplitude. However, this behavior is also present on the representative signal related to gear III computed with the EMD and the EEMD (see Figures 21(d) and 21(e)). On the other hand, the representative signals estimated with the CEEMDAN are easy to interpret since the signal related to gear III (Figure 21(f)) does not contain any remarkable local change of amplitude that can be attributed

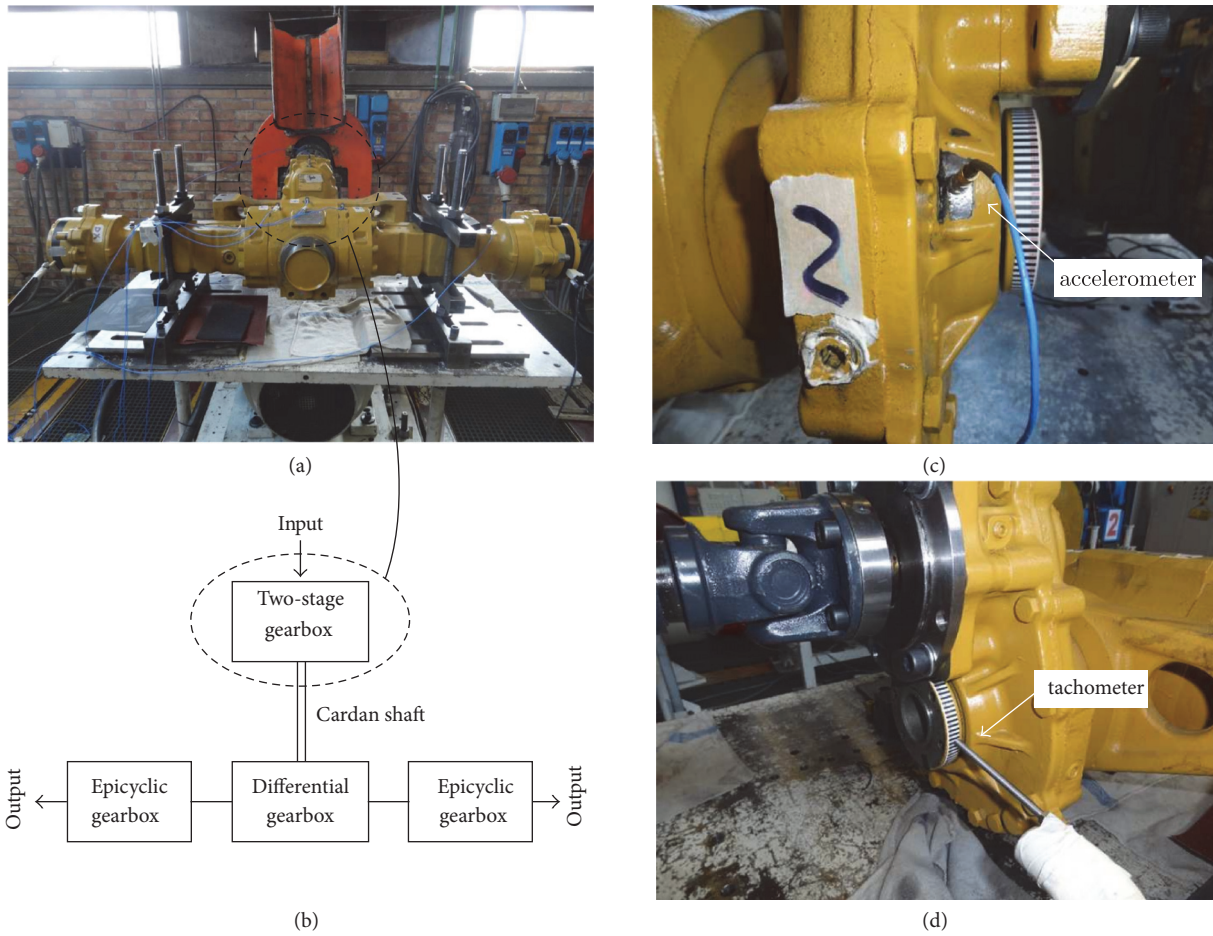


FIGURE 17: Experimental setup of Case 1: (a) transmission system on the test bench, (b) schematic of the transmission, (c) accelerometer, and (d) tacho probe with zebra tape.

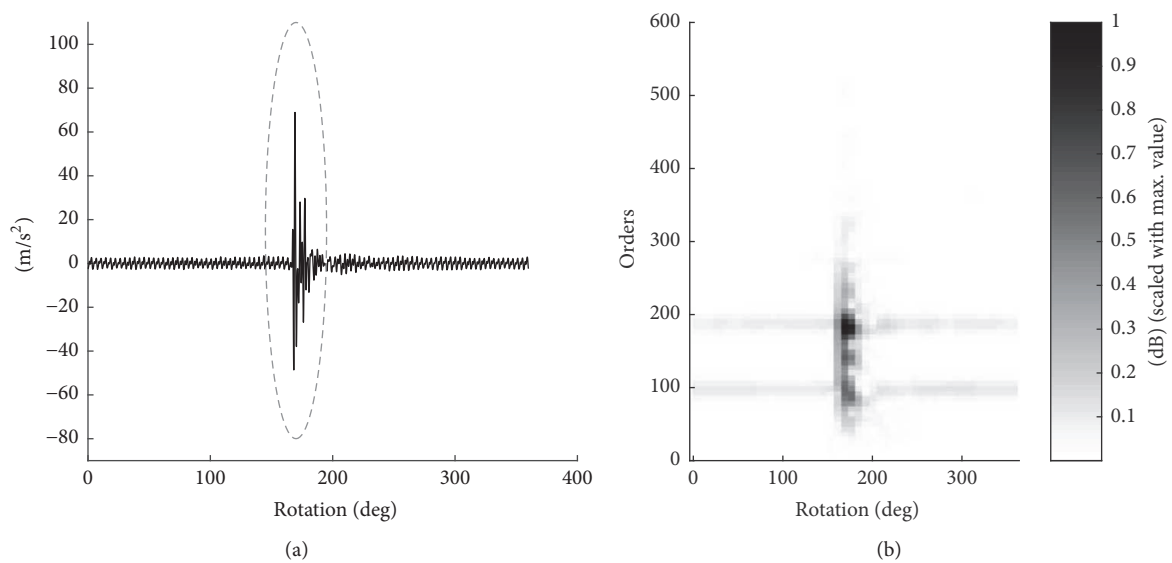


FIGURE 18: (a) Time Synchronous Average related to the intermediate shaft of Case 2 (the dashed circle highlights the impulsive signal component due to the damaged tooth engagement) and (b) the related spectrogram (225 samples of window length and 75% overlap).

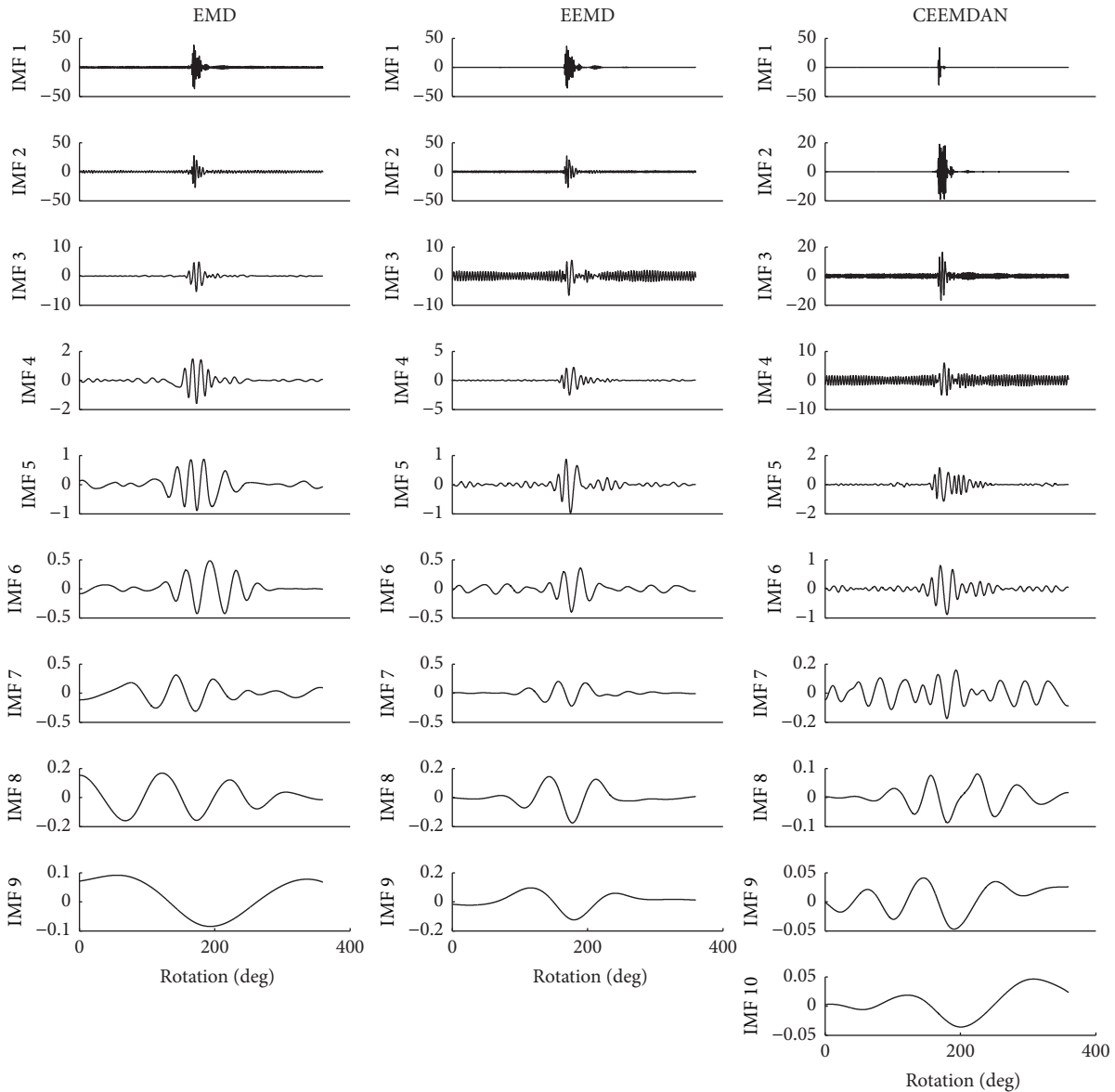


FIGURE 19: IMF sets of Case 2 obtained by using EMD, EEMD, and CEEMDAN.

to a localized gear fault. Therefore, the only EMD algorithm that allows a clear visual interpretation of the signals is the CEEMDAN.

The remarks gathered by the visual inspection of the signal can be confirmed by analyzing the CIs collected in Table 5. In fact, the higher percentage differences between the faulty gear and the healthy one are achieved considering the CEEMDAN. Furthermore, it should be noted that the results obtained with the EEMD are not satisfying since the percentage difference is low for the CF and CPF while the kurtosis completely fails on the identification of the faulty gear.

Although this experimental case has been more difficult to handle than the first one, the methodology has provided a correct result when the CEEMDAN is performed. The use of several CIs allows defining an objective criterion in order to

define which gear is faulty, reducing the error due to the user interpretation.

## 6. Conclusions

Commonly, the gear fault detection is restricted to the identification of the stage containing the faulty gear rather than the faulty gear itself. However, the exact knowledge of the faulty gear is of prime importance in industrial applications. The goal is to propose a methodology being able to overcome the limit of traditional signal processing techniques that detect just the stage of the faulty gear. For this purpose, an EMD-based methodology has been presented for the local gear fault diagnosis, proposing also two new condition indicators based on the RMS values estimated on the angular pitch rather than the entire vibration signal.

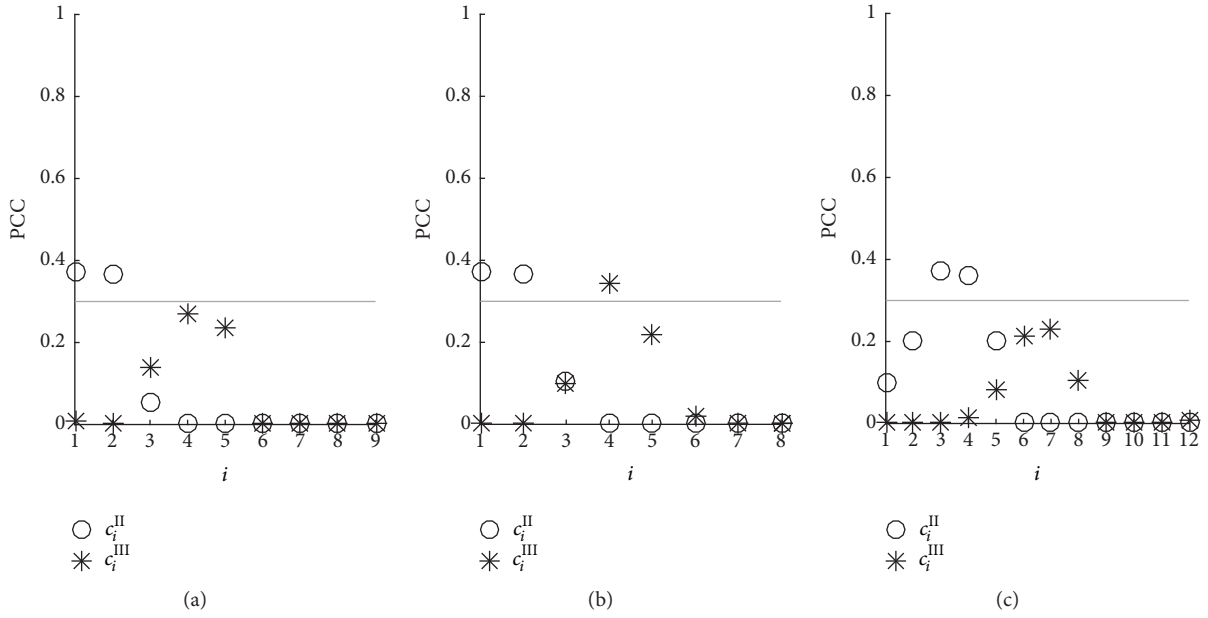


FIGURE 20: PCC values of Case 2 estimated taking into account (a) EMD, (b) EEMD, and (c) CEEMDAN.

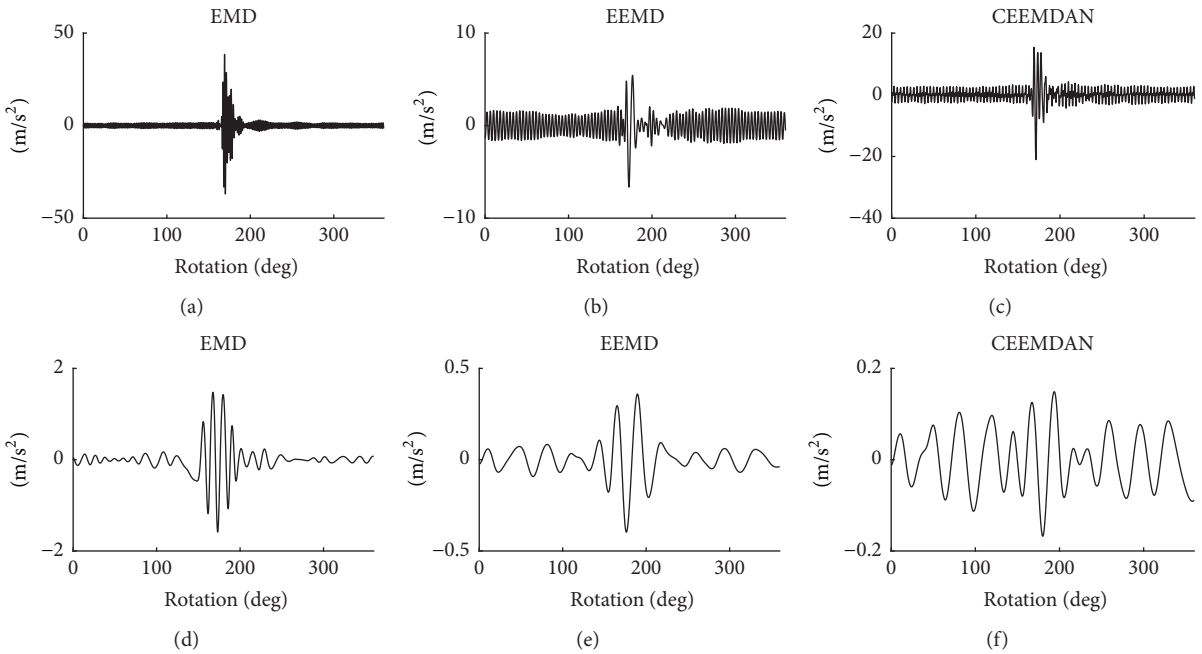


FIGURE 21: Representative signals of (a-c) gear II and (d-f) gear III for Case 2.

In order to test the reliability and the robustness of the methodology, simulated signals and two different real case studies have been analyzed by means of three different EMD algorithms. The first experimental case addresses a two-stage gearbox having an artificial gear tooth fault whereas the second one concerns a transmission system with a natural defect. The methodology successfully identifies the faulty gear in both the experimental tests, especially when the CEEMDAN is performed. On the basis of these results, the CEEMDAN is the most effective signal decomposition

technique, since it returns the clearest results from both the qualitative and quantitative standpoints. Moreover, the proposed CIs—especially the NSVP—are very sensitive to the presence of a localized change of the vibration signature, simplifying the detection of the faulty gear.

On these grounds, the presented method can be considered reliable for the identification of a faulty gear when the fault occurs in a shaft with multiple gears. Eventually, this diagnosis method is particularly suitable for industrial applications since it is completely automatic.

TABLE 5: CIs for the vibration signal of Case 2, with localized fault in gear II.

		Kurtosis	CF	CPF	NSVP
EMD	Gear II (faulty)	48.803	10.910	13.704	0.085
	Gear III (healthy)	12.182	4.979	4.317	0.089
	Gear II versus gear III [%]	300.604	119.140	217.457	-5.017
EEMD	Gear II (faulty)	6.100	5.304	3.694	0.064
	Gear III (healthy)	7.526	4.072	2.805	0.010
	Gear II versus gear III [%]	-18.950	30.240	31.677	541.743
CEEMDAN	Gear II (faulty)	19.974	8.444	7.079	0.476
	Gear III (healthy)	2.455	2.712	1.549	0.013
	Gear II versus gear III [%]	713.512	210.441	357.026	3696.969

## Conflicts of Interest

The authors declare that there are no conflicts of interest regarding the publication of this paper.

## References

- [1] R. B. Randall, *Vibration-Based Condition Monitoring*, John Wiley & Sons Ltd, 2011.
- [2] J. Antoni and R. B. Randall, "Differential diagnosis of gear and bearing faults," *Journal of Vibration and Acoustics*, vol. 124, no. 2, pp. 165–171, 2002.
- [3] J. Antoni, "Cyclostationarity by examples," *Mechanical Systems and Signal Processing*, vol. 23, no. 4, pp. 987–1036, 2009.
- [4] A. Raad, J. Antoni, and M. Sidahmed, "Indicators of cyclostationarity: theory and application to gear fault monitoring," *Mechanical Systems and Signal Processing*, vol. 22, no. 3, pp. 574–587, 2008.
- [5] T. Barszcz and R. B. Randall, "Application of spectral kurtosis for detection of a tooth crack in the planetary gear of a wind turbine," *Mechanical Systems and Signal Processing*, vol. 23, no. 4, pp. 1352–1365, 2009.
- [6] G. Dalpiaz, A. Rivola, and R. Rubini, "Effectiveness and sensitivity of vibration processing techniques for local fault detection in gears," *Mechanical Systems and Signal Processing*, vol. 14, no. 3, pp. 387–412, 2000.
- [7] G. L. McDonald, Q. Zhao, and M. J. Zuo, "Maximum correlated Kurtosis deconvolution and application on gear tooth chip fault detection," *Mechanical Systems and Signal Processing*, vol. 33, pp. 237–255, 2012.
- [8] G. L. McDonald and Q. Zhao, "Multipoint Optimal Minimum Entropy Deconvolution and Convolution Fix: Application to vibration fault detection," *Mechanical Systems and Signal Processing*, vol. 82, pp. 461–477, 2017.
- [9] V. Sharma and A. Parey, "Gear crack detection using modified TSA and proposed fault indicators for fluctuating speed conditions," *Measurement*, vol. 90, pp. 560–575, 2016.
- [10] N. E. Huang, Z. Shen, S. R. Long et al., "The empirical mode decomposition and the Hilbert spectrum for nonlinear and non-stationary time series analysis," *Proceedings A*, vol. 454, no. 1971, pp. 903–995, 1998.
- [11] Z. He, Y. Shen, and Q. Wang, "Boundary extension for HilbertHuang transform inspired by gray prediction model," *Signal Processing*, vol. 92, no. 3, pp. 685–697, 2012.
- [12] X. Hu, S. Peng, and W.-L. Hwang, "EMD revisited: a new understanding of the envelope and resolving the mode-mixing problem in AM-FM signals," *IEEE Transactions on Signal Processing*, vol. 60, no. 3, pp. 1075–1086, 2012.
- [13] N. E. Huang and Z. Wu, "Ensemble empirical mode decomposition: a noise-assisted data analysis method," *Advances in Adaptive Data Analysis (AADA)*, vol. 1, no. 1, pp. 1–41, 2009.
- [14] J.-R. Yeh, J.-S. Shieh, and N. E. Huang, "Complementary ensemble empirical mode decomposition: a novel noise enhanced data analysis method," *Advances in Adaptive Data Analysis: Theory and Applications*, vol. 2, no. 2, pp. 135–156, 2010.
- [15] M. E. Torres, M. A. Colominas, G. Schlotthauer, and P. Flandrin, "A complete ensemble empirical mode decomposition with adaptive noise," in *Proceedings of the 36th IEEE International Conference on Acoustics, Speech, and Signal Processing*, pp. 4144–4147, Prague, Czech Republic, May 2011.
- [16] S. J. Loutridis, "Damage detection in gear systems using empirical mode decomposition," *Engineering Structures*, vol. 26, no. 12, pp. 1833–1841, 2004.
- [17] S. J. Loutridis, "Instantaneous energy density as a feature for gear fault detection," *Mechanical Systems and Signal Processing*, vol. 20, no. 5, pp. 1239–1253, 2006.
- [18] J. Cheng, D. Yu, J. Tang, and Y. Yang, "Application of frequency family separation method based upon EMD and local Hilbert energy spectrum method to gear fault diagnosis," *Mechanism and Machine Theory*, vol. 43, no. 6, pp. 712–723, 2008.
- [19] L. Hui, Y. Zhang, and H. Zheng, "Wear detection in gear system using Hilbert-Huang transform," *Journal of Mechanical Science and Technology*, vol. 20, no. 11, pp. 1781–1789, 2006.
- [20] J. Lin and Q. Chen, "Application of the EEMD method to multiple faults diagnosis of gearbox," in *Proceedings of the 2010 IEEE International Conference on Advanced Computer Control, ICACC 2010*, pp. 395–399, March 2010.
- [21] Z. P. Feng, M. Liang, Y. Zhang, and S. M. Hou, "Fault diagnosis for wind turbine planetary gearboxes via demodulation analysis based on ensemble empirical mode decomposition and energy separation," *Journal of Renewable Energy*, vol. 47, pp. 112–126, 2012.
- [22] L. Zhao, W. Yu, and R. Yan, "Gearbox fault diagnosis using complementary ensemble empirical mode decomposition and permutation entropy," *Shock and Vibration*, vol. 2016, Article ID 3891429, 8 pages, 2016.
- [23] Y. Lei, Z. Liu, J. Ouazri, and J. Lin, "A fault diagnosis method of rolling element bearings based on CEEMDAN," *Proceedings of the Institution of Mechanical Engineers, Part C: Journal of Mechanical Engineering Science*, vol. 231, no. 10, pp. 1804–1815, 2015.
- [24] S. Mohanty, K. K. Gupta, and K. S. Raju, "Vibro-acoustic fault analysis of bearing using FFT, EMD, EEMD and CEEMDAN

- and their implications,” *Lecture Notes in Electrical Engineering*, vol. 387, pp. 281–292, 2016.
- [25] Y. Lei, J. Lin, Z. He, and M. J. Zuo, “A review on empirical mode decomposition in fault diagnosis of rotating machinery,” *Mechanical Systems and Signal Processing*, vol. 35, no. 1-2, pp. 108–126, 2013.
- [26] J. Antoni, F. Bonnardot, A. Raad, and M. El Badaoui, “Cyclostationary modelling of rotating machine vibration signals,” *Mechanical Systems and Signal Processing*, vol. 18, no. 6, pp. 1285–1314, 2004.
- [27] S. Braun, “The synchronous (time domain) average revisited,” *Mechanical Systems and Signal Processing*, vol. 25, no. 4, pp. 1087–1102, 2011.
- [28] G. Rilling and P. Flandrin, “One or two frequencies? The empirical mode decomposition answers,” *IEEE Transactions on Signal Processing*, vol. 56, no. 1, pp. 85–95, 2008.
- [29] P. Flandrin, G. Rilling, and P. Gonçalves, “Empirical mode decomposition as a filter bank,” *IEEE Signal Processing Letters*, vol. 11, no. 2, pp. 112–114, 2004.
- [30] Z. H. Wu and N. E. Huang, “Ensemble empirical mode decomposition: a noise-assisted data analysis method,” *Advances in Adaptive Data Analysis (AADA)*, vol. 1, no. 1, pp. 1–41, 2009.
- [31] Y. Lei, Z. He, and Y. Zi, “Application of the EEMD method to rotor fault diagnosis of rotating machinery,” *Mechanical Systems and Signal Processing*, vol. 23, no. 4, pp. 1327–1338, 2009.
- [32] M. A. Colominas, G. Schlotthauer, and M. E. Torres, “Improved complete ensemble EMD: a suitable tool for biomedical signal processing,” *Biomedical Signal Processing and Control*, vol. 14, no. 1, pp. 19–29, 2014.
- [33] M. A. Colominas, G. Schlotthauer, M. a. Torres, and P. Flandrin, “Noise-assisted EMD methods in action,” *Advances in Adaptive Data Analysis: Theory and Applications*, vol. 4, no. 4, 1250025, 11 pages, 2012.
- [34] R. B. Randall, “A new method of modeling gear faults,” *Journal of Mechanical Design*, vol. 104, no. 2, pp. 259–267, 1982.
- [35] J. Dybała and R. Zimroz, “Rolling bearing diagnosing method based on empirical mode decomposition of machine vibration signal,” *Applied Acoustics*, vol. 77, pp. 195–203, 2014.
- [36] B. Assaad, M. Eltabach, and J. Antoni, “Vibration based condition monitoring of a multistage epicyclic gearbox in lifting cranes,” *Mechanical Systems and Signal Processing*, vol. 42, no. 1-2, pp. 351–367, 2014.
- [37] W. Wang, “Early detection of gear tooth cracking using the resonance demodulation technique,” *Mechanical Systems and Signal Processing*, vol. 15, no. 5, pp. 887–903, 2001.
- [38] G. DElia, *Fault detection in rotating machines by vibration signal processing techniques [PhD Thesis]*, Università degli Studi di Bologna, 2008.
- [39] G. Dalpiaz, G. DElia, and S. Delvecchio, “Design of a test bench for the vibro-acoustical analysis and diagnostics of rotating machines,” in *in proceedings of The Second World Congress on Engineering Asset Management & The Fourth International Conference on Condition Monitoring*, pp. 777–792, Harrogate, UK, 2007.

## Research Article

# Data-Driven Iterative Vibration Signal Enhancement Strategy Using Alpha Stable Distribution

Grzegorz Żak,<sup>1</sup> Agnieszka Wyłomańska,<sup>2</sup> and Radosław Zimroz<sup>1</sup>

<sup>1</sup>*Diagnosics and Vibro-Acoustics Science Laboratory, Wrocław University of Science and Technology, Na Grobli 15, 50-421 Wrocław, Poland*

<sup>2</sup>*KGHM Cuprum Research & Development Center, Ul. Sikorskiego 2-8, 53-659 Wrocław, Poland*

Correspondence should be addressed to Grzegorz Żak; [grzegorz.zak@pwr.edu.pl](mailto:grzegorz.zak@pwr.edu.pl)

Received 12 June 2017; Accepted 26 July 2017; Published 12 September 2017

Academic Editor: Andrzej Katunin

Copyright © 2017 Grzegorz Żak et al. This is an open access article distributed under the Creative Commons Attribution License, which permits unrestricted use, distribution, and reproduction in any medium, provided the original work is properly cited.

The authors propose a novel procedure for enhancement of the signal to noise ratio in vibration data acquired from machines working in mining industry environment. Proposed method allows performing data-driven reduction of the deterministic, high energy, and low frequency components. Furthermore, it provides a way to enhance signal of interest. Procedure incorporates application of the time-frequency decomposition,  $\alpha$ -stable distribution based signal modeling, and stability parameter in the time domain as a stoppage criterion for iterative part of the procedure. An advantage of the proposed algorithm is data-driven, automatic detection of the informative frequency band as well as band with high energy due to the properties of the used distribution. Furthermore, there is no need to have knowledge regarding kinematics, speed, and so on. The proposed algorithm is applied towards real data acquired from the belt conveyor pulley drive's gearbox.

## 1. Introduction

Local damage detection in rotating machines is one of the most frequent topics in condition monitoring literature. Generation of such signal is well recognized ([1–4]). Basically, the problem is related to detection of cyclic impulsive disturbances in noisy observation. Different approaches have been used for signal modeling (cyclostationary [5], stochastic [6], autoregressive [7]), enhancement (SOI extraction [8–10], denoising including adaptive noise cancellation [11] and spatial wavelet denoising [12], averaging: time domain [13, 14], time-frequency domain), sources separation (discrete-random [15]), damage detection criteria (kurtosis, cyclostationary indicators, and statistical measures) [4, 10, 16–18], and so on. Special attention was paid to damage detection at early stage of development, in nonstationary speed/load condition, and so on. In the literature one can find several interesting reviews concerning mentioned problem to get holistic, more detailed view [19–22].

One might conclude that almost everything was done to be able to diagnose damage. However, in the practical applications there are plenty of challenging cases that prove

difficult for the classical methods. In this paper we will present an interesting case related to heavy duty gearbox operating in harsh environment. Based on this example, we propose novel, data-driven procedure for damage detection. An important fact is that there are two damage types (with different nature and localization). One of them is easy to notice directly from raw signal. However, the second one produces weak signature and is hardly detectable. We have started with most popular tools as spectral kurtosis-based filter and envelope analysis. Unfortunately, the results are not satisfactory. So it motivates us to search for alternative solutions. As mentioned, it is expected that signal of interest (SOI) will be impulsive. There are plenty of techniques in time series analysis that are focused on data with such behavior. One can easily notice increasing number of publications concerning application of heavy-tailed distributions towards vibration and sound signals [23–27]. Such interest is especially aimed towards  $\alpha$ -stable distribution which is a generalization of Gaussian one. In [23] one can find a thorough description on how to model and apply such distribution towards data. Modifications and extensions of existing methods towards

heavy-tailed distribution can be found in the literature with promising results ([24–27]).

It motivates us to test our recently developed tools related for  $\alpha$ -stable distribution based filtering procedure. Again it was slightly better (improvement noticeable at spectrogram) but still requires advanced interpretation. We have identified that the problem is related to signal structure and high energy concentration in low frequency range of spectrum. Filtering is just simply multiplication of complex spectrum of signal with filter characteristics in frequency domain. Even small values of filter coefficients at low frequencies might result in still poor signal to noise ratio (SNR) in output signal. Our strategy is instead of direct extraction of SOI, we propose attenuating noninformative high energy signal components and then use  $\alpha$ -stable distribution based filter to extract SOI. Such strategy appeared to be very effective as presented in [28]. A key question is how to design filter to attenuate noninformative part. We propose using  $\alpha$ -stable distribution approach (we already use it for SOI extraction based on  $\alpha$  parameter); however, in first stage we will use scale parameter  $\sigma$ . We mention that the  $\alpha$  parameter gives information on how heavy the distribution tail is and  $\sigma$  is responsible for the scale of the distribution. During experiments it has appeared that  $\sigma$ -based filtering performed several times provides much better results than just one filtration. Obviously, we immediately tested iterative  $\alpha$ -based filtering for SOI extraction but without spectacular success. Finally, we propose a two-stage procedure for signal preprocessing:

- (i) Iterative  $\sigma$ -based filtering with stability parameter in the time domain as stoppage criterion for high energy noninformative part attenuation.
- (ii)  $\alpha$ -based filtering for further SOI signal enhancement.

In the end, this paper combines method of data-driven filtering together with heavy-tailed distribution modeling. Such connection provides new insight towards modeling of subsignals from time-frequency decomposed signal.

The paper is organized as follows: Section 1 contains introduction about the topic of paper together with short summary of work done in the field. In Section 2 we present methodology associated with our procedure and in Section 3 we apply our procedure towards real vibration data from the gearbox of drive pulley of belt conveyor. In Section 4 we summarize results and provide conclusions.

## 2. Methodology

In this section we present the methodology useful in the problem of local damage detection based on the analysis of the vibration signal. We propose the approach based on the analysis of subsignals obtained in time-frequency representation (spectrogram) of given signal. Mentioned subsignals are analyzed using appropriate statistics (called selectors). Till now, the most popular statistic was kurtosis, one of the measures that can point out these frequency bins on time-frequency map that reveals the most impulsive nature. When the kurtosis is applied to the appropriate subsignals, then it is called the spectral kurtosis (SK), [10]. We recall that the spectrogram  $\text{spec}(t, f)$  for given time point  $t \in T$  and

frequency  $f \in F$  is defined through the short time Fourier transform (STFT) in the following way [29]:

$$\text{spec}(t, f) = |\text{STFT}(t, f)|^2 = \sum_{k=0}^{n-1} x_k w(t-k) e^{2j\pi f k/n}, \quad (1)$$

where  $w(t-k)$  is the shifting window and  $x_k$  is the input signal ( $k = 0, 1, \dots, n-1$ ). Parameters for the spectrogram should be chosen with user preferences for best visibility of the impulsive behavior in the visual representation of the spectrogram. Parameters to be chosen are window length, number of samples overlapping, and number of samples used for fast Fourier transform (nfft). In case of the vibration signals acquired from pulley drive gearbox for belt conveyor analyzed in Section 3 we found them to be optimal at the following levels: window length equal to 256 samples, number of samples overlapping equal to 240 samples, and number of samples used for the FFT equal to 512 samples.

Thus the spectral kurtosis (SK) statistic for input signal  $x_k (k = 0, 1, \dots, n-1)$  is defined in the following way [10]:

$$\text{SK}(f) = \#T \frac{\sum_{t \in T} |\text{STFT}(t, f)|^4}{\left(\sum_{t \in T} |\text{STFT}(t, f)|^2\right)^2} - 2, \quad (2)$$

where  $\#T$  denotes the number of elements of the set  $T$ , that is, number of time points at which STFT is calculated.

However for some real signals the spectral kurtosis does not give expected results because it can be sensitive for impulses not related to damage (i.e., artifacts). Therefore, as it was mentioned, there are other statistics considered that can be applied instead of the kurtosis; see [16].

In this paper we propose not to calculate simple statistic for set of subsignals obtained by decomposition of raw data by spectrogram but to describe each subsignal by stochastic model that has similar properties as appropriate time series. One of the easiest stochastic models is based on the assumption that the vector of observations contains realizations of independent identically distributed random variables. The most known distribution is the Gaussian one. However, the Gaussian distribution is not appropriate to modeling data with impulses, like for instance subsignals from time-frequency representation (spectrogram) related to damage. It is more convenient to take under consideration more general distribution, that is, such that it can be appropriate to describe subsignals corresponding to informative frequency band (IFB) and from noninformative frequency bands. Of course for those regions the parameters of the chosen distribution will be different. One of the possibilities is the  $\alpha$ -stable distribution [30], which is a generalization of the Gaussian one. The random variable  $X$  has  $\alpha$ -stable distribution if its characteristic function is given by

$$\begin{aligned} \phi_X(t) &= E \exp(itX) \\ &= \begin{cases} \exp \left\{ -\sigma^\alpha |t|^\alpha \left( 1 - i\beta \text{sign}(t) \tan\left(\frac{\pi\alpha}{2}\right) \right) + i\mu t \right\}, & \alpha \neq 1, \\ \exp \left\{ -\sigma |t| \left( 1 + i\beta \frac{2}{\pi} \text{sign}(t) \ln(|t|) \right) + i\mu t \right\}, & \alpha = 1. \end{cases} \end{aligned} \quad (3)$$

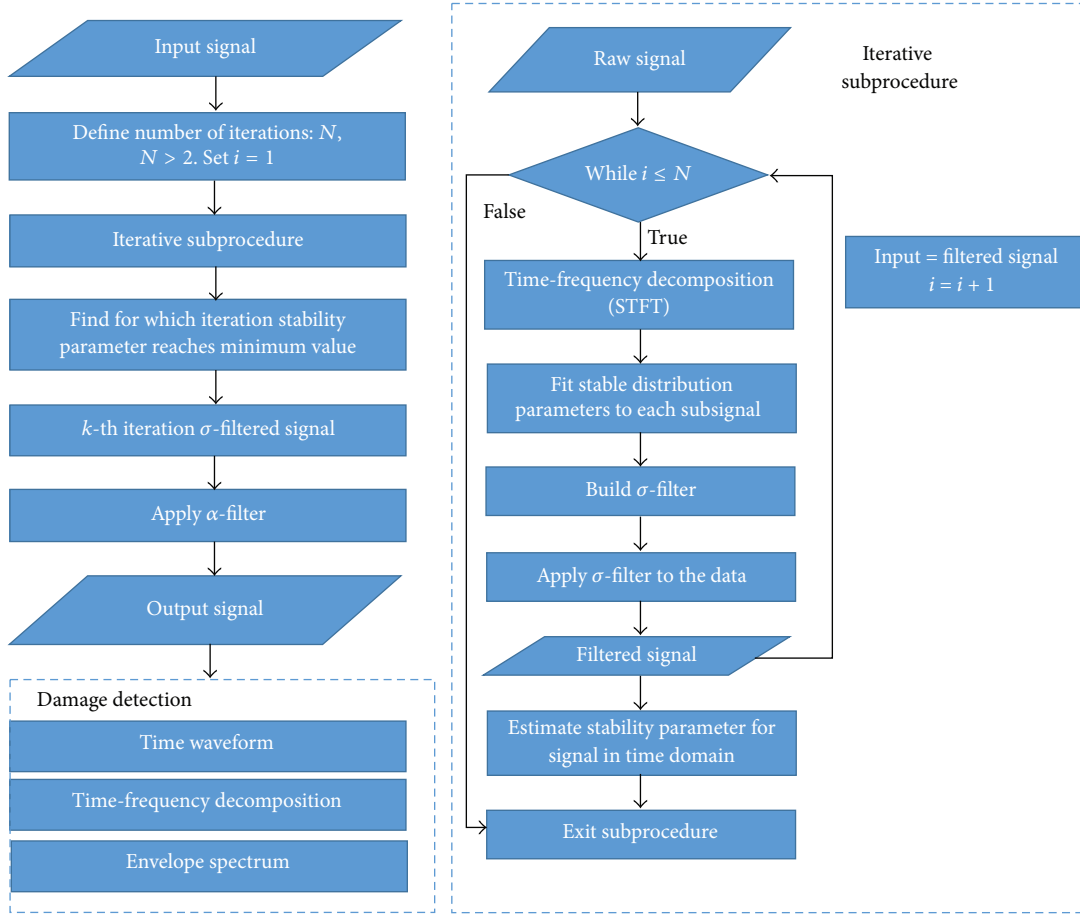


FIGURE 1: Flowchart of the procedure.

We provide short description of distribution parameters. Stability parameter  $\alpha \in (0, 2]$  defines how impulsive the realizations of the distribution are. There is a relation between  $\alpha$  value and impulsiveness of the signal, with lower values we observe more impulsive behavior. The parameter  $\sigma > 0$  is responsible for the scale (or energy) of the distribution. It behaves in a similar way to the variance of the Gaussian case (i.e., for  $\alpha = 2$ ). The parameter  $\beta \in [-1, 1]$  is responsible for the distribution skewness and  $\mu \in \mathbb{R}$  represents distribution shift. It corresponds to the mean for  $1 < \alpha \leq 2$  and the median for  $0 < \alpha \leq 1$ . It is worth mentioning that, in general, the probability density function, as well as the cumulative distribution function for  $\alpha$ -stable distributed random variable, is not given in explicit form. There are only three exceptions: Gaussian, Levy, and Cauchy distributions. Moreover, finite  $p$ th moments exist only for  $p < \alpha$ . The  $\alpha$ -stable distribution and processes have found many interesting applications, also in technical diagnostics [24]. In our approach, instead of kurtosis calculation for each subsignal from time-frequency representation, we propose examining the  $\alpha$  and  $\sigma$  parameters calculated on the basis of appropriate subsignals. We estimate those parameters by using the regression method [31], where it is widely discussed. Whole idea is based on the regression of the characteristic function of the sample.

Here, we use parameters  $\alpha$  and  $\sigma$  as indicators of impulsivity and energy, respectively.

Subsignals coming from bands with high energy should have significantly higher scale parameter. High energy in the spectrogram of the vibration signal from gearbox is connected with the deterministic component of the signal. Combining such information one can construct filter characteristic which will allow for deterministic component attenuation. Filter construction is as follows. Let us assume that estimated parameters  $\sigma$  of  $\alpha$ -stable distribution for set of subsignals extracted from the time-frequency decomposition are denoted as  $\hat{\sigma} = \{\hat{\sigma}(f_1), \hat{\sigma}(f_2), \dots, \hat{\sigma}(f_M)\}$ , where  $M = \lfloor \text{nfft}/2 \rfloor + 1$ . We define filter characteristic as follows:

$$\sigma_{\text{filter}}(f) = 1 - \frac{\hat{\sigma}(f)}{\max(\hat{\sigma})}. \quad (4)$$

We define stoppage criterion as minimum value of the stability parameter of the signal in the time domain. This parameter indicates impulsivity of the data. The lower the value of this parameter, the higher the impulsivity. One of the other approaches would be to use kurtosis as indicator. However, it is not suggested as it can be easily affected by single impulses that are not related to the fault.

Filtered signal is now assumed to be input signal for the spectrogram and whole procedure restarts at calculation of

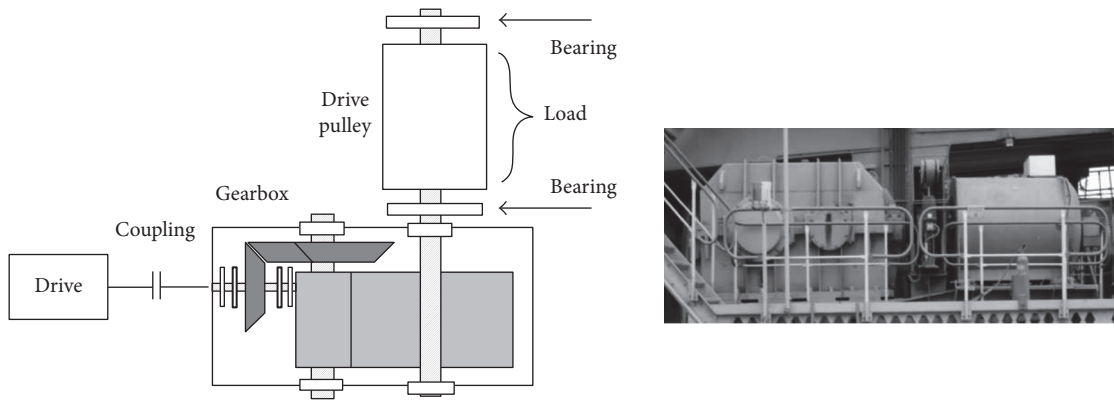


FIGURE 2: Investigated machine.

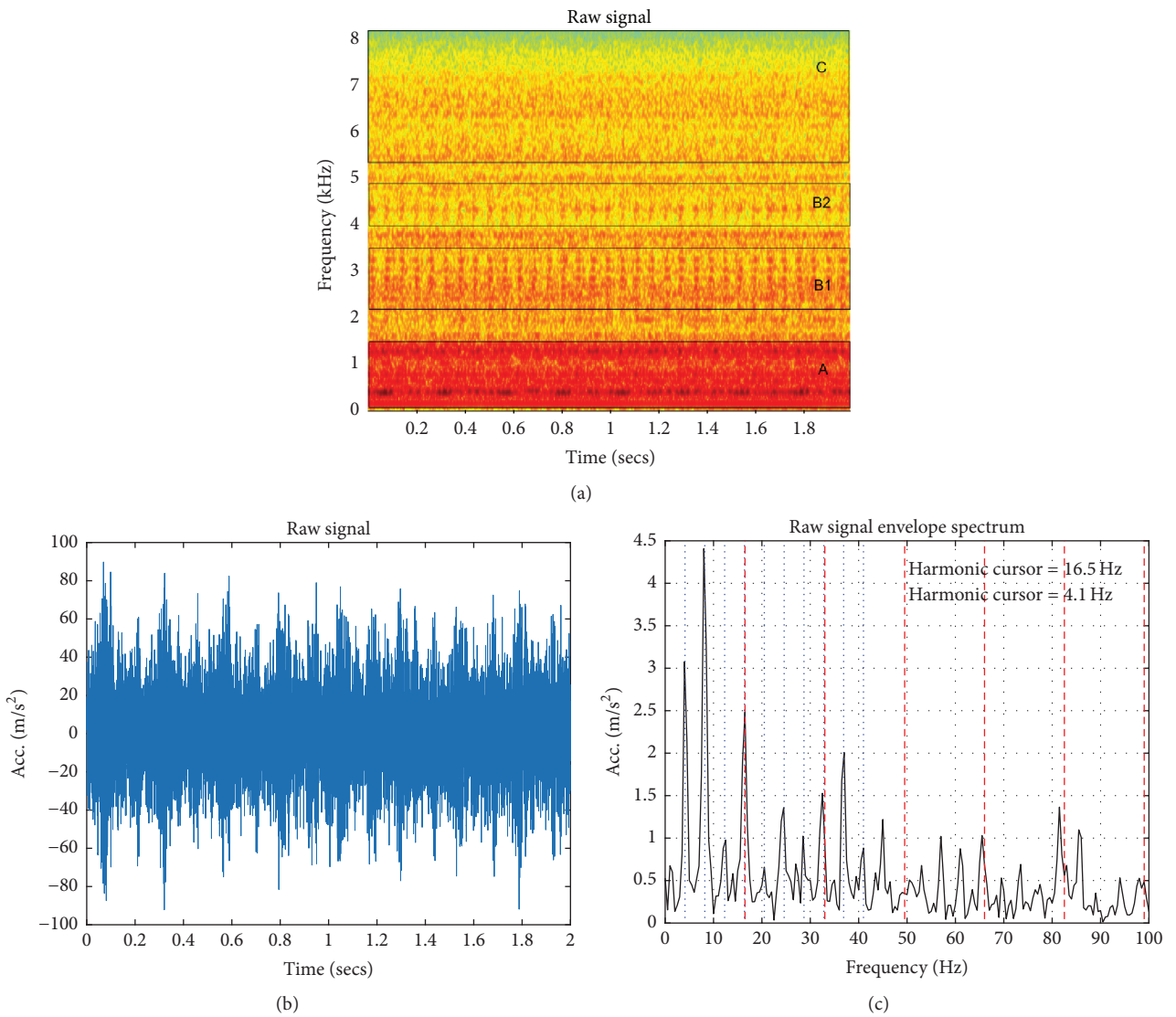


FIGURE 3: Spectrogram of the signal (a), time waveform of the signal (b), and its envelope spectrum (c).

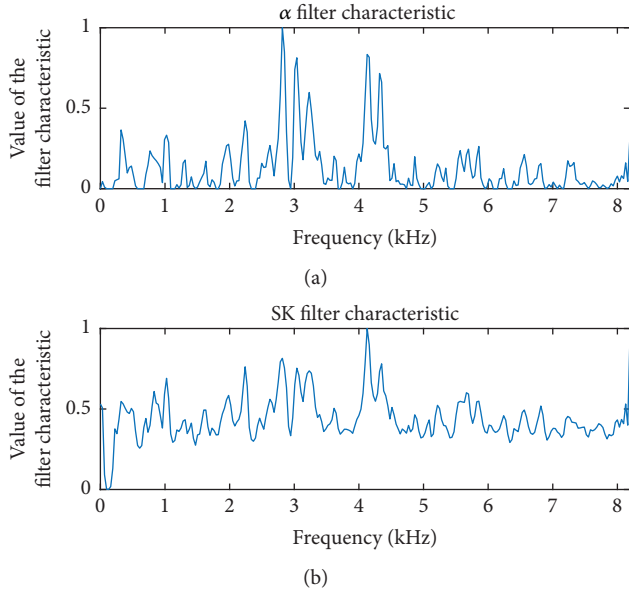


FIGURE 4: Filter characteristics based on the  $\alpha$ -stable distribution (a) and spectral kurtosis (b).

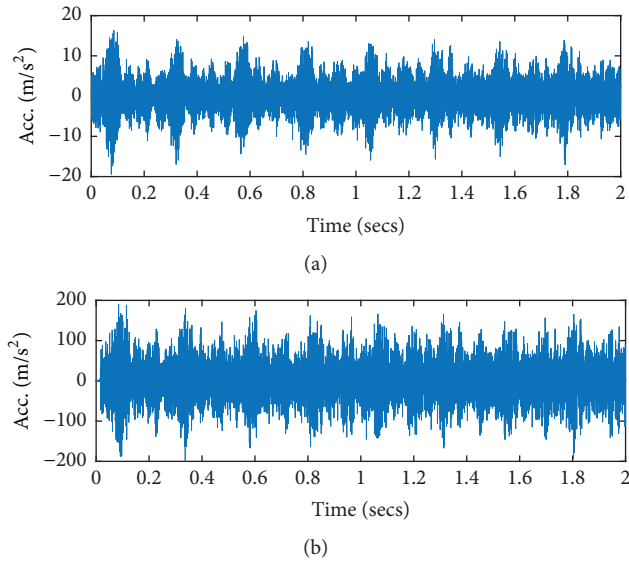


FIGURE 5: Time waveforms of  $\alpha$ -filtered signal (a) and SK-filtered signal (b).

the spectrogram with repeated filtrations until  $N$  iterations. After performing all iterations one needs to find in which iteration the stability parameter of the signal in time domain reaches the minimum value for the filtered signal. This allows us to determine where deterministic component has been attenuated best. Filtered signal from that iteration has now highly attenuated deterministic component. In addition, we can use  $\alpha$ -filtration [24] to easily enhance impulsive component of the signal. Let us assume that estimated vector of  $\alpha$  parameters for subsignals from time-frequency

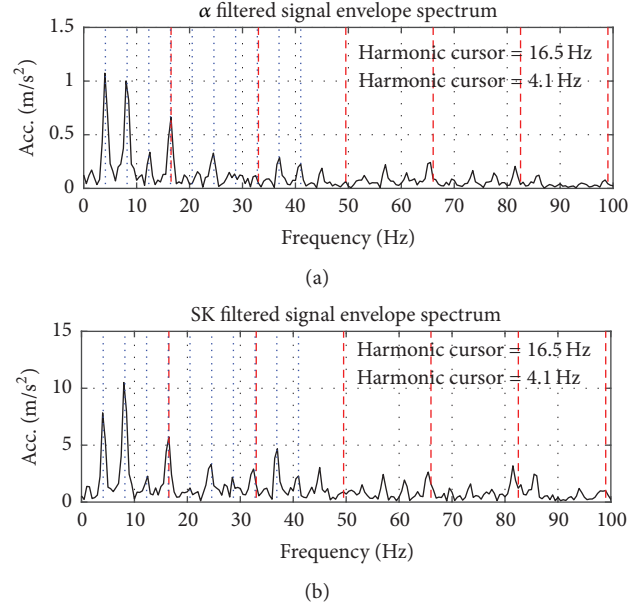


FIGURE 6: Envelope spectra of  $\alpha$ -filtered signal (a) and SK-filtered signal (b).

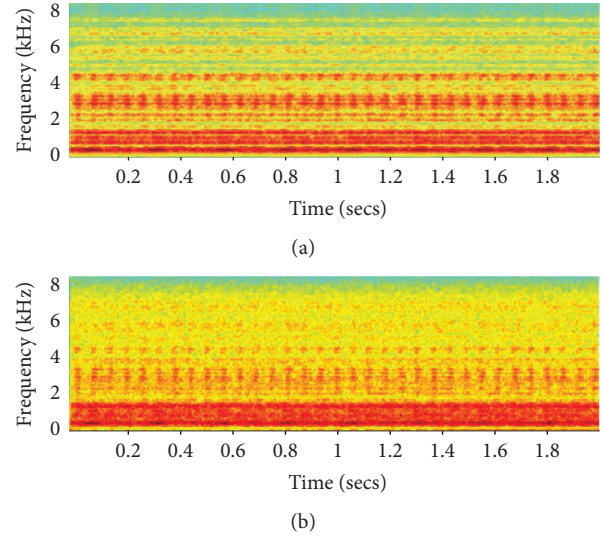


FIGURE 7: Spectrograms of  $\alpha$ -filtered signal (a) and SK-filtered signal (b).

representation is given by  $\hat{\alpha} = \{\hat{\alpha}(f_1), \hat{\alpha}(f_2), \dots, \hat{\alpha}(f_M)\}$ . Then  $\alpha$  filter characteristic would be defined as

$$\alpha_{\text{filter}}(f) = \frac{\max(\hat{\alpha}(f)) - \hat{\alpha}(f)}{\max(\hat{\alpha}(f)) - \min(\hat{\alpha}(f))}. \quad (5)$$

Output signal has now significantly reduced deterministic component, enhanced impulsive component, and can be easily analyzed in time, frequency, and time-frequency domains. In Figure 1 we present the flowchart of the described procedure.

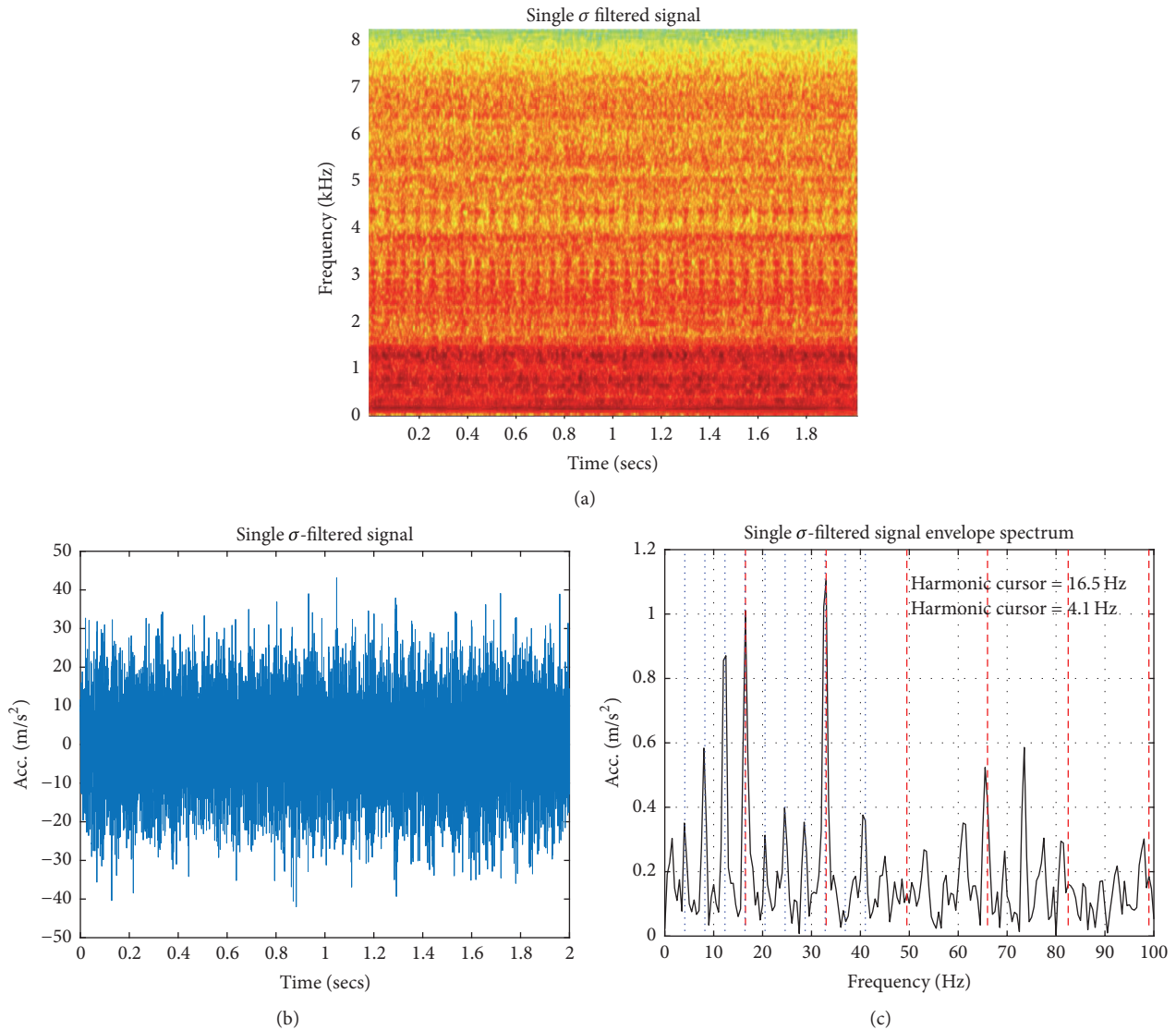


FIGURE 8: Spectrogram of the signal (a), time waveform of the signal (b), and its envelope spectrum (c).

### 3. Real Data Analysis

To prove efficiency of the proposed methodology we will show results of application of data-driven filtration to real vibration data from complex mechanical system operating in mining industry (Figure 2). Moreover, gearbox comes from driving system used in belt conveyor, a very popular technology, commonly used in mining industry for material transportation. Measurements have been performed using Bruel Kjaer Pulse system. Parameters of data acquisition depend on the investigated object. In this case, they are as follows: duration 2 s, sampling frequency 16384 Hz, and the expected faults frequencies are 4.1 Hz and 16.5 Hz. This section is divided into two subsections. First subsection contains results of applying spectral kurtosis method for enhancement of the impulsive component in the signal and applying  $\alpha$ -filter. Second subsection contains novel procedure, namely, data-driven filtration described in Section 2.

In Figure 3 one can observe time waveform of the signal, its envelope spectrum, and its time-frequency decomposition, namely, spectrogram. There are presently 3 main type frequency bands in the spectrogram: first containing low frequency high energy component responsible for the shape of the signal (marked with A), second being informative frequency bands (IFB) placed at 2.5–3.5 kHz and 4–4.5 kHz (marked with B1 and B2, resp.), and noninformative high frequency band (marked with C). Furthermore, it can be easily seen that it is correct placement of IFBs when observing values of  $\alpha$ -stable distribution parameter estimated for each frequency bin (Figure 4(a)). In Figure 3(c) one can see envelope spectrum of the signal with marked frequencies of both faults with its harmonics. First fault with frequency equal to 4.1 Hz (blue vertical lines) overlaps second fault with frequency equal to 16.5 Hz (red vertical lines). Due to the operation regime of the machine it was not possible to perform visual inspection. Parameters of the machine are

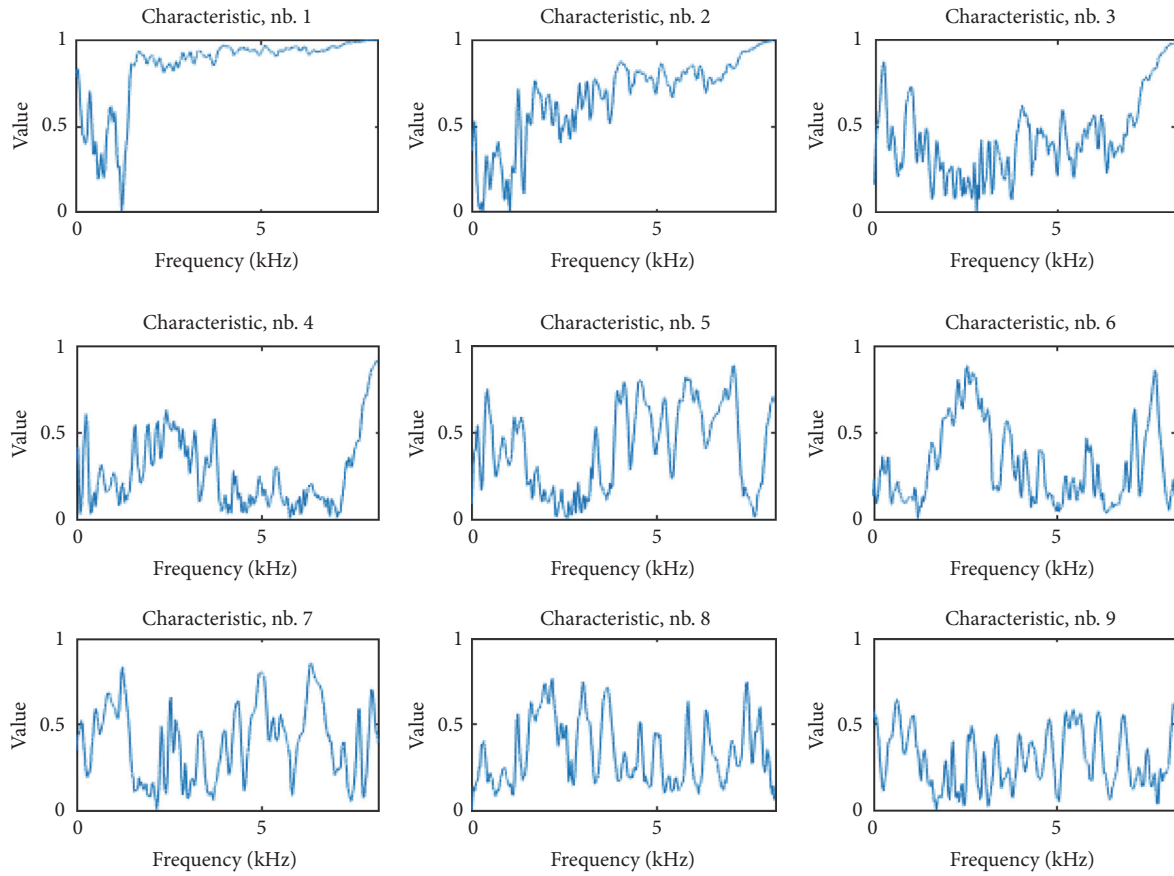


FIGURE 9:  $\sigma$ -filter characteristics for each iteration.

known including shaft and mesh characteristic frequencies. It allows for the rough fault detection in time domain. However, second fault is not visible in any domain.

**3.1. Spectral Kurtosis and  $\alpha$  Filtration Comparison.** This subsection contains results of application of spectral kurtosis to the vibration data measured on the gearbox casing and moreover it contains authors' procedure of  $\alpha$ -stable distribution based filtration. Both spectral kurtosis and  $\alpha$  act in the literature as measures of impulsivity of the subsignals from the spectrogram.

In Figure 4 one can observe filter characteristics for filtration methods based on the  $\alpha$ -stable distribution (a) and spectral kurtosis (b). One can denote more precise informative band selection in the method using  $\alpha$ -stable distribution.

Using obtained filter characteristics one can perform filtration of the raw signal. The following figures contain filtered signals in different domains. In Figure 5 one can observe result of the filtration in the time domain. In comparison to the raw signal time waveform it can be denoted that impulsive component has been slightly enhanced.

However, comparing envelope spectra (Figure 6) one cannot easily determine existence of both faults in the frequency domain due to the visible fault overlapping hidden fault. Such situation happened due to the second fault frequency being

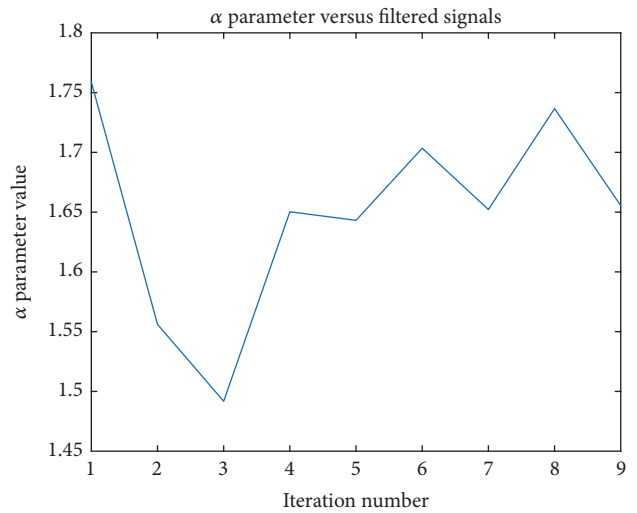


FIGURE 10: Stability parameter for each  $\sigma$ -filtered signal.

multiplicative of the first one, the same as in unprocessed signal envelope spectrum.

It can be seen here in Figure 7 that  $\alpha$  filter heavily enhanced impulsive component in its bands while SK results are poor in this case.

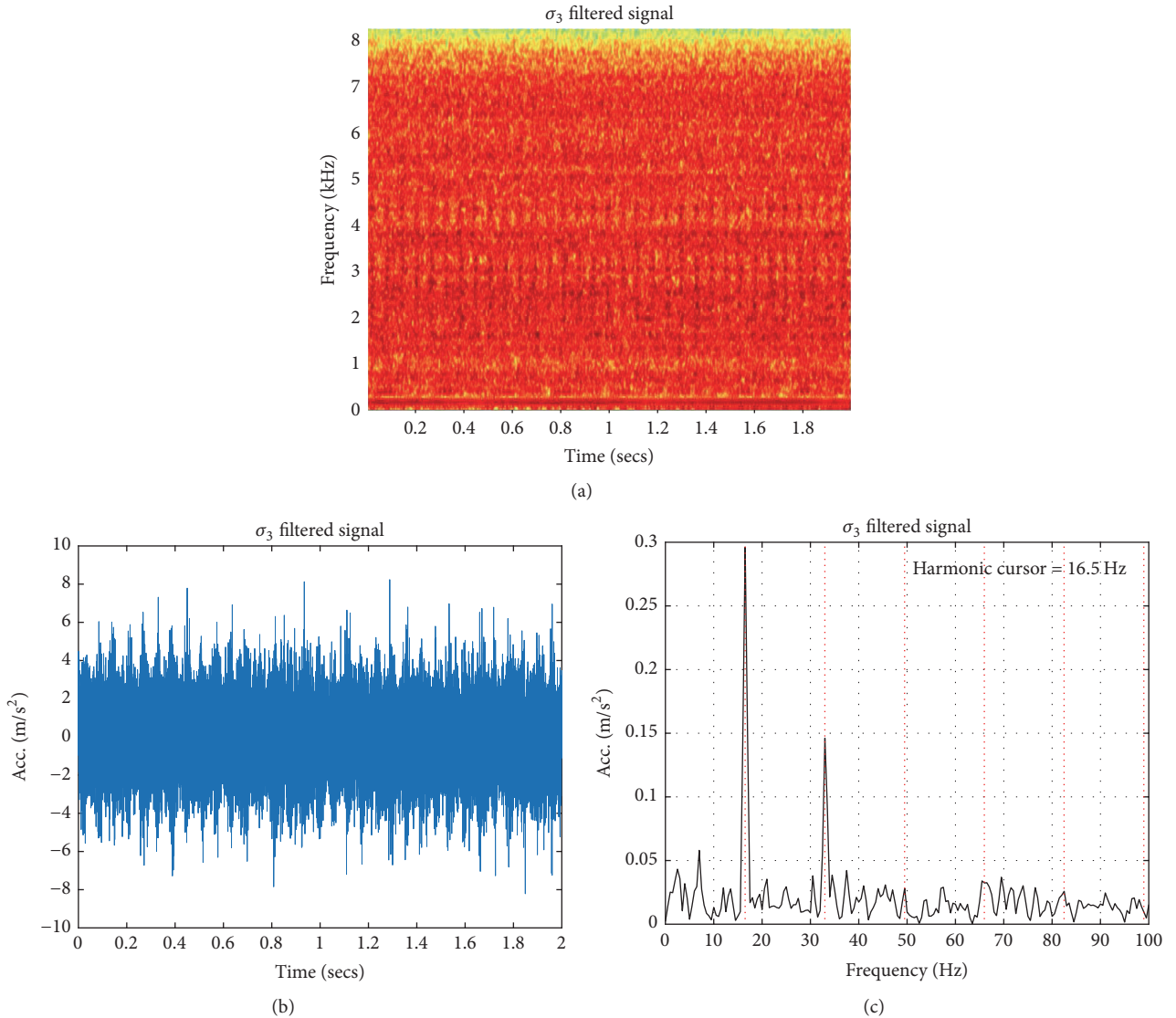


FIGURE 11: Spectrogram of the signal (a), time waveform of the signal (b), and its envelope spectrum (c).

Further iterations of  $\alpha$ -filter do not improve SNR due to the behavior of the model. Fitting  $\alpha$ -stable distribution to the signal filtered with  $\alpha$ -filter will result in similar distribution of the  $\alpha$  parameters.

**3.2. Novel Method Results.** In this subsection one can denote that it contains results for the single  $\sigma$ -filtration which will provide reference point together with  $\alpha$ -filtration described in previous section, consecutive filter characteristics for each of the iterative  $\sigma$ -filtrations, and finally result of applying  $\alpha$ -filter to the  $\sigma$ -filtered signal with minimum value of the stability parameter for the signals in the time domain.

As for the comparison to the  $\alpha$ -filtration we performed  $\sigma$ -filtration by fitting  $\alpha$ -stable distribution towards subsignals extracted from the time-frequency decomposition of the raw vibration signal. Combining information visible in Figure 8 one can see that deterministic component of the signal has been attenuated (Figures 8(a) and 8(c)) providing even

distribution of the energy on the spectrogram. Furthermore, envelope spectrum allows one to see fundamental frequency of the hidden fault along with its harmonics. However, time waveform does not yet provide important result about the fault.

Based on results from  $\alpha$ -filtration (Figures 5–7) and  $\sigma$ -filtration (Figure 8) we can say that neither  $\alpha$  nor  $\sigma$  filtration provide satisfactory results. Both improve slightly SNR but results are not perfect. Given properties of both parameters one can apply procedure from Figure 1 iteratively. Given raw vibration signal it is necessary to decompose it via STFT. Further, one establishes  $\sigma$ -filter characteristics (Figure 9) and filters signal and the procedure is repeated.

Each of the filtrations is based on the  $\alpha$ -stable distribution and its scale parameter, namely,  $\sigma$ . Filtering iteratively demands fitting mentioned distribution to the subsignals extracted from the time-frequency decomposed signal and further filtered signals. It allows for the creation of the  $\sigma$ -filter

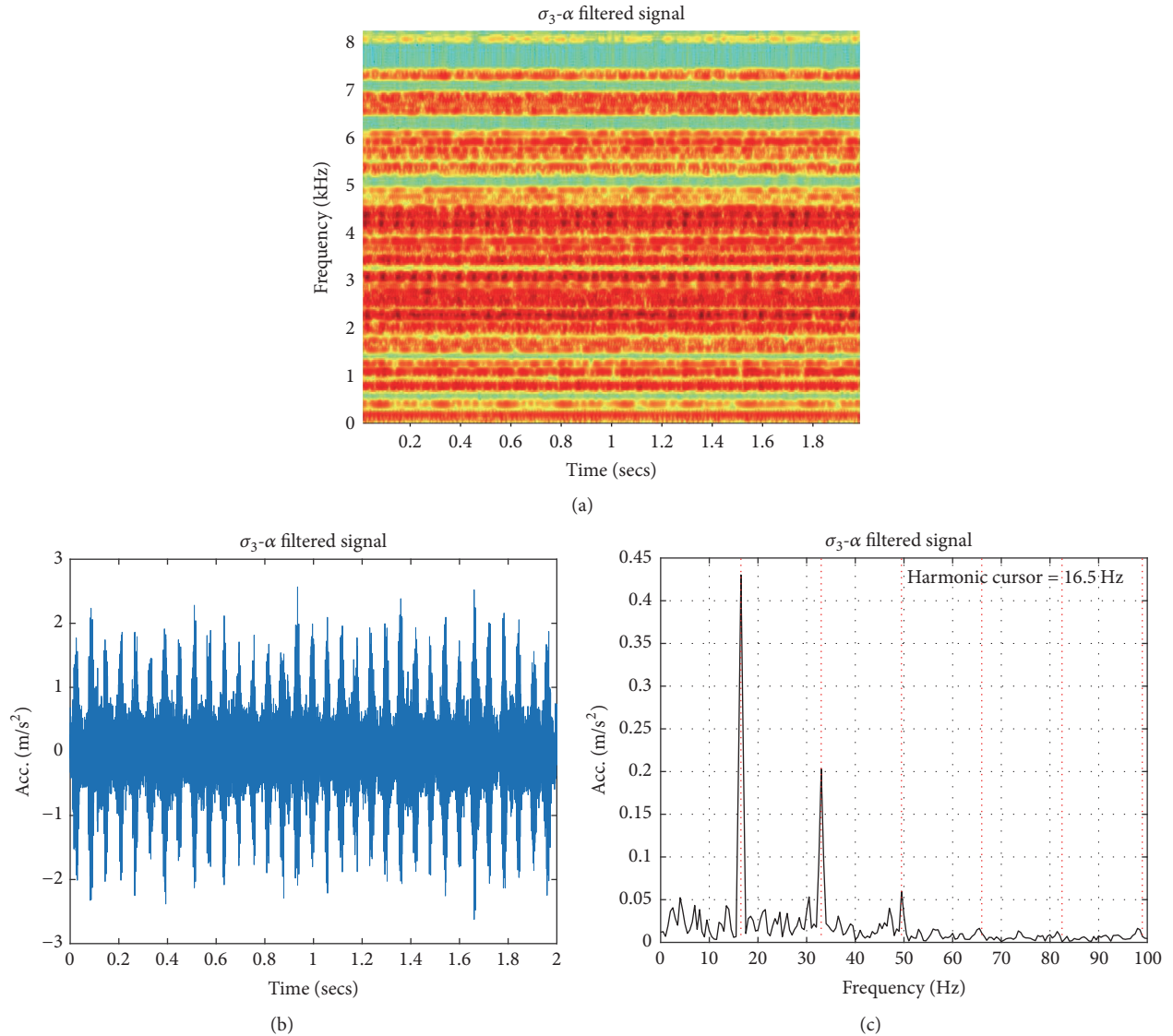


FIGURE 12: Spectrogram of the signal (a), time waveform of the signal (b), and its envelope spectrum (c).

characteristics which are presented in Figure 9. It can be seen that first three iterations put emphasis on the attenuation of the deterministic component of the signal. Further iterations will result in attenuation of the different components of the signal. In Figure 10 one can see stability parameter value after each filtration. It can be observed that the lowest value of this parameter was estimated for the third filtration. Additionally, we tested iterative procedure for parameter  $\alpha$  as SOI enhancement method. However, results after iterative procedure using this parameter were similar to the results after single  $\alpha$ -filtration.

In Figure 11 one can see results of the iterative filtration using  $\sigma$ -filter. Procedure has been applied three times resulting in lowest value of stability parameter for the sample. First, one can notice equalization of amplitudes through most of the frequency bands in the spectrogram in Figure 11(a). Furthermore, it can be seen that attenuation of the deterministic components allowed us to obtain frequency of the fault and its

harmonic on the envelope spectrum. Detected frequency of the fault is equal to 16.5 Hz. However, still one can not distinct impulsive behavior in the time domain and as such one needs to consider methods allowing for improving SNR. In our case, we have used previously developed  $\alpha$ -stable distribution stability parameter procedure for enhancement of the IFB.

Combining results obtained using iterative application of  $\sigma$ -filter with  $\alpha$ -filter which enhances impulsive components one can observe that result allows one for the detection of the hidden fault. In Figure 12(a) it can be seen that bands containing impulsive component connected to the fault have been strongly emphasized. Observing Figures 12(b) and 12(c) it can be seen that hidden fault is now easily observable in both time and frequency domain.

#### 4. Conclusions

In the paper a novel procedure for SOI denoising is proposed. It is  $\alpha$ -stable distribution based data-driven filters set that

iteratively attenuates high energy low frequency components by  $\sigma$ -filtering and finally enhances impulsive components by  $\alpha$ -filtering. As stoppage criterion for iterative  $\sigma$ -filtering, stability parameter of the signal in time domain was applied as a measure of impulsivity in the signal. Applying  $\alpha$ -filtering iteratively does not result in improving signal to noise ratio. Application of the procedure was performed on the real data from the complex mechanical system. Measured data was acquired from the gearbox of the belt conveyor's pulley drive. There were two existing faults in the system, first located at 4.1 Hz frequency and second at 16.5 Hz frequency. Due to the second being close multiplicative of the first one it was not possible to determine its existence in any domain. Applying novel procedure it was possible to attenuate certain parts of the signal and enhance visibility of the second fault. In other words, we were able to detect both damage types.

### Conflicts of Interest

The authors declare that there are no conflicts of interest regarding the publication of this paper.

### Acknowledgments

This work is partially (A. Wyłomańska) supported by the Framework Programme for Research and Innovation Horizon 2020 under Grant Agreement no. 636834 (DISIRE, Integrated Process Control based on Distributed In Situ Sensors into Raw Material and Energy Feedstock).

### References

- [1] P. D. McFadden and J. D. Smith, "Vibration monitoring of rolling element bearings by the high-frequency resonance technique—a review," *Tribology International*, vol. 17, no. 1, pp. 3–10, 1984.
- [2] R. B. Randall and J. Antoni, "Rolling element bearing diagnostics—a tutorial," *Mechanical Systems and Signal Processing*, vol. 25, no. 2, pp. 485–520, 2011.
- [3] P. D. Samuel and D. J. Pines, "A review of vibration-based techniques for helicopter transmission diagnostics," *Journal of Sound and Vibration*, vol. 282, no. 1-2, pp. 475–508, 2005.
- [4] J. Antoni, F. Bonnardot, A. Raad, and M. El Badaoui, "Cyclostationary modelling of rotating machine vibration signals," *Mechanical Systems and Signal Processing*, vol. 18, no. 6, pp. 1285–1314, 2004.
- [5] R. B. Randall, J. Antoni, and S. Chobsaard, "A comparison of cyclostationary and envelope analysis in the diagnostics of rolling element bearings," in *Proceedings of the IEEE International Conference on Acoustics, Speech, and Signal Processing (ICASSP '00)*, pp. 3882–3885, Istanbul, Turkey, June 2000.
- [6] J. Obuchowski, A. Wyłomańska, and R. Zimroz, "Stochastic modeling of time series with application to local damage detection in rotating machinery," *Key Engineering Materials*, vol. 569-570, pp. 441–448, 2013.
- [7] J. Obuchowski, A. Wyłomańska, and R. Zimroz, "Two-stage data driven filtering for local damage detection in presence of time varying signal to noise ratio," *Vibration Engineering and Technology of Machinery*, vol. 23, pp. 401–410, 2014.
- [8] J. Antoni, "Fast computation of the kurtogram for the detection of transient faults," *Mechanical Systems and Signal Processing*, vol. 21, no. 1, pp. 108–124, 2007.
- [9] T. Barszcz and A. Jabłoński, "A novel method for the optimal band selection for vibration signal demodulation and comparison with the Kurtogram," *Mechanical Systems and Signal Processing*, vol. 25, no. 1, pp. 431–451, 2011.
- [10] J. Antoni and R. B. Randall, "The spectral kurtosis: application to the vibratory surveillance and diagnostics of rotating machines," *Mechanical Systems and Signal Processing*, vol. 20, no. 2, pp. 308–331, 2006.
- [11] G. K. Chaturved and D. W. Thomas, "Adaptive noise cancelling and condition monitoring," *Journal of Sound and Vibration*, vol. 76, no. 3, pp. 391–405, 1981.
- [12] J. Lin, M. J. Zuo, and K. R. Fyfe, "Mechanical fault detection based on the wavelet de-noising technique," *Journal of Vibration and Acoustics*, vol. 126, no. 1, pp. 9–16, 2004.
- [13] S. Braun, "The synchronous (time domain) average revisited," *Mechanical Systems and Signal Processing*, vol. 25, no. 4, pp. 1087–1102, 2011.
- [14] J. Obuchowski, R. Zimroz, and A. Wyłomańska, "Blind equalization using combined skewness-kurtosis criterion for gearbox vibration enhancement," *Measurement*, vol. 88, pp. 34–44, 2016.
- [15] R. B. Randall and N. Sawalhi, "A new method for separating discrete components from a signal," *The Sound and Vibration*, vol. 45, no. 5, pp. 6–9, 2011.
- [16] J. Obuchowski, A. Wyłomańska, and R. Zimroz, "Selection of informative frequency band in local damage detection in rotating machinery," *Mechanical Systems and Signal Processing*, vol. 48, no. 1-2, pp. 138–152, 2014.
- [17] G. Żak, J. Obuchowski, A. Wyłomańska, and R. Zimroz, "Novel 2D representation of vibration for local damage detection," *Mining Science*, vol. 21, pp. 105–113, 2014.
- [18] R. Makowski and R. Zimroz, "New techniques of local damage detection in machinery based on stochastic modelling using adaptive Schur filter," *Applied Acoustics*, vol. 77, pp. 130–137, 2014.
- [19] Y. Lei, J. Lin, Z. He, and M. J. Zuo, "A review on empirical mode decomposition in fault diagnosis of rotating machinery," *Mechanical Systems and Signal Processing*, vol. 35, no. 1-2, pp. 108–126, 2013.
- [20] Z. Feng, M. Liang, and F. Chu, "Recent advances in time-frequency analysis methods for machinery fault diagnosis: a review with application examples," *Mechanical Systems and Signal Processing*, vol. 38, no. 1, pp. 165–205, 2013.
- [21] Z. K. Peng and F. L. Chu, "Application of the wavelet transform in machine condition monitoring and fault diagnostics: a review with bibliography," *Mechanical Systems and Signal Processing*, vol. 18, no. 2, pp. 199–221, 2004.
- [22] R. Yan, R. X. Gao, and X. Chen, "Wavelets for fault diagnosis of rotary machines: a review with applications," *Signal Processing*, vol. 96, pp. 1–15, 2013.
- [23] M. Shao and C. L. Nikias, *Signal Processing with Alpha-Stable Distribution and Applications*, John Wiley and Sons Inc, New York, NY, USA, 1995.
- [24] G. Żak, A. Wyłomańska, and R. Zimroz, "Data-driven vibration signal filtering procedure based on the alpha-stable distribution," *Journal of Vibroengineering*, vol. 18, no. 2, pp. 826–837, 2016.
- [25] G. Żak, A. Wyłomańska, and R. Zimroz, "Application of alpha-stable distribution approach for local damage detection in

- rotating machines,” *Journal of Vibroengineering*, vol. 17, no. 6, pp. 2987–3002, 2015.
- [26] P. G. Georgiou, “Alpha-stable modeling of noise and robust timedelay estimation in the presence of impulsive noise,” *IEEE Transactions on Multimedia*, vol. 1, no. 3, pp. 291–301, 1999.
- [27] G. Yu, C. N. Li, and J. F. Zhang, “A new statistical modeling and detection method for rolling element bearing faults based on alpha-stable distribution,” *Mechanical Systems and Signal Processing*, vol. 41, no. 1-2, pp. 155–175, 2013.
- [28] G. Żak, A. Wylomańska, and R. Zimroz, “Local damage detection methods based on the stochastic modeling techniques,” in *Proceedings of the 24th Mediterranean Conference on Control and Automation (MED ’16)*, pp. 355–360, Athens, Greece, June 2016.
- [29] J. B. Allen, “Short term spectral analysis, synthesis, and modification by discrete Fourier transform,” *IEEE Transactions on Acoustics, Speech, and Signal Processing*, vol. 25, no. 3, pp. 235–238, 1977.
- [30] G. Samorodnitsky and M. Taqqu, *Stable Non-Gaussian Random Variables*, Chapman and Hall, London, UK, 1994.
- [31] I. A. Koutrouvelis, “Regression-type estimation of the parameters of stable laws,” *Journal of the American Statistical Association*, vol. 75, no. 372, pp. 918–928, 1980.

## Research Article

# Measures of Dependence for $\alpha$ -Stable Distributed Processes and Its Application to Diagnostics of Local Damage in Presence of Impulsive Noise

Grzegorz Żak,<sup>1</sup> Marek Teuerle,<sup>2</sup> Agnieszka Wyłomańska,<sup>3</sup> and Radosław Zimroz<sup>1</sup>

<sup>1</sup>*Diagnostics and Vibro-Acoustics Science Laboratory, Wrocław University of Science and Technology, Na Grobli 15, 50-421 Wrocław, Poland*

<sup>2</sup>*Faculty of Pure and Applied Mathematics, Hugo Steinhaus Center, Wrocław University of Science and Technology, Wrocław, Poland*

<sup>3</sup>*KGHM Cuprum Research & Development Center, Wrocław, Poland*

Correspondence should be addressed to Grzegorz Żak; [grzegorz.zak@pwr.edu.pl](mailto:grzegorz.zak@pwr.edu.pl)

Received 12 June 2017; Accepted 1 August 2017; Published 6 September 2017

Academic Editor: Andrzej Katunin

Copyright © 2017 Grzegorz Żak et al. This is an open access article distributed under the Creative Commons Attribution License, which permits unrestricted use, distribution, and reproduction in any medium, provided the original work is properly cited.

Local damage detection in rotating machinery is simply searching for cyclic impulsive signal in noisy observation. Such raw signal is mixture of various components with specific properties (deterministic, random, cyclic, impulsive, etc.). The problem appears when the investigated process is based on one of the heavy-tailed distributions. In this case the classical measure can not be considered. Therefore, alternative measures of dependence adequate for such processes should be considered. In this paper we examine the structure of dependence of alpha-stable based systems expressed by means of two measures, namely, codifference and covariation. The reason for using alpha-stable distribution is simple and intuitive: signal of interest is impulsive so its distribution is heavy-tailed. The main goal is to introduce a new technique for estimation of covariation. Due to the complex nature of such vibration signals applying novel methods instead of classical ones is recommended. Classical algorithms usually are based on the assumption that theoretical second moment is finite, which is not true in case of the data acquired on the faulty components. Main advantage of our proposed algorithm is independence from second moment assumption.

## 1. Introduction

Local damage detection is crucial task in the modern condition monitoring. Most of the methods are based on detection of cyclic impulsive signal in noisy observation. Many authors explore new possibilities for more efficient fault detection. Difficulty of this problem is found in the properties of the vibration data acquired from the industrial machines. Such signals are often affected by the non-Gaussian noise. This noise is a result of the vibration contamination from nearby working machines. During signal processing, it highly affects the chance of the fault detection. Main reason behind the interest in this task has serious economical background. In early stages, local damage is usually masked by the high energy of other signal components. It results in low signal-to-noise ratio and thus such fault often remains undetected.

Main problem in local damage detection based on vibration signal analysis is type of the background noise. In many fields noise is non-Gaussian. In such case, methods used as a standard ones are not sufficient enough [1–6]. Impulsive behavior of noise enforces application of methods adequate for this type of signal. In this paper, we provide technique that is based on the one of the most known impulsive-type models,  $\alpha$ -stable distribution-based one.

The  $\alpha$ -stable distribution and processes belong to the so-called heavy-tailed family, which indicates the extreme values of a corresponding random variable (or process) are more probable than in the Gaussian case. Since Mandelbrot introduced the  $\alpha$ -stable distribution in modeling of financial asset returns [7, 8], numerous empirical studies have been done in different applications. Indeed, this distribution can be applied in finance [9–11], biology and microbiology

[12, 13], plasma fluctuations in fusion devices [14–18], physics [19], and electrical engineering [20]. The  $\alpha$ -stable distributions have found also applications in technical diagnostics [21, 22].

As was mentioned, the local damage of rotating machine is demonstrated by cyclic behavior of vibration signal. The cyclic nature of given data can be recognized by analyzing of statistics which indicate the dependence inside the process. Clearly, the classical measure is autocovariance (or autocorrelation). However, as mentioned, when the signal has impulsive nature, the classical measure should not be considered. Indeed, the second moment does not exist; thus covariance is infinite. In this case, the alternative measures of dependence are examined. The most known measures adequate for heavy-tailed processes are codifference and covariation [23]. The codifference is considered for infinitely divisible processes and is defined through the characteristic function of given process. Therefore the empirical equivalent of codifference is based on the empirical characteristic function [24]. The second measure defined only for  $\alpha$ -stable distributed processes is based on the spectral measure; then the problem of its estimation is much more complicated. The main goal of this paper is to introduce a new estimation method for covariation which follows directly from its definition. This approach complements the gap in the problem of covariation estimation, rarely discussed in the literature.

As the application, we show how the empirical codifference and covariation can be useful in the problem of local damage detection based on the vibration signal analysis.

The rest of the paper is organized as follows: in Section 2 we present main properties of  $\alpha$ -stable distributed random variables in one-dimensional and multidimensional case. In Section 3 we present the alternative measures of dependence adequate for processes with infinite variance, namely, covariation and codifference. Next section is devoted to the empirical counterparts of mentioned measures. The main goal is the introduction of a new technique of estimation of covariation which is based on the spectral measure estimation. In Section 5 we present how the proposed techniques can be useful in the problem of local damage detection in rotating machines. Last section concludes the paper.

## 2. The $\alpha$ -Stable Distribution

In this section we introduce the  $\alpha$ -stable distribution and present main properties of  $\alpha$ -stable distributed random variables. We consider separately one-dimensional and multidimensional cases.

*2.1. One-Dimensional Case.* There are few equivalent definitions of  $\alpha$ -stable distributed random variables. One of the definition is in terms of its characteristic function.

Namely, a random variable  $X$  is said to have  $\alpha$ -stable distribution if there are parameters  $0 < \alpha \leq 2$ ,  $\sigma > 0$ ,

$-1 \leq \beta \leq 1$ , and  $\mu \in \mathbb{R}$  such that the characteristic function of  $X$  has the following form [23]:

$$\begin{aligned} \phi_X(t) &= E \exp(itX) \\ &= \begin{cases} \exp \left\{ -\sigma^\alpha |t|^\alpha \left( 1 - i\beta \operatorname{sign}(t) \tan\left(\frac{\pi\alpha}{2}\right) \right) + i\mu t \right\} & \alpha \neq 1, \\ \exp \left\{ -\sigma |t| \left( 1 + i\beta \frac{2}{\pi} \operatorname{sign}(t) \ln(|t|) \right) + i\mu t \right\} & \alpha = 1. \end{cases} \end{aligned} \quad (1)$$

In the above function the  $\alpha$  parameter is called stability index,  $\sigma$  is the scale parameter, and  $\beta$  is the skewness parameter while  $\mu$  is the shift parameter. It is worth mentioning that for  $\beta = 0$  and  $\mu = 0$  the random variable  $X$  with characteristic function given in (1) is called symmetric  $\alpha$ -stable.

Although the  $\alpha$ -stable distribution and processes have found many practical applications, they possess some drawbacks. One of them is that the probability density function (as well as cumulative distribution function) for  $\alpha$ -stable distribution does not have useful analytical form. However, there are three exceptions, the Gaussian distribution (for  $\alpha = 2$ ), Lévy distribution (for  $\alpha = 1/2$ ), and Cauchy distribution (for  $\alpha = 1$ ).

One of the main properties of  $\alpha$ -stable distributed random variables is the so-called heavy-tailed behavior. In probability theory, heavy-tailed distributions are probability distributions whose tails are not exponentially bounded; that is, they have heavier tails than the exponential distribution. For  $\alpha < 2$  the  $p$ th moment exists only for  $p < \alpha$  while for  $p \geq \alpha$  it is infinite. Therefore, in case  $\alpha < 2$  the second moment of  $\alpha$ -stable distributed random variable  $X$  does not exist which indicates that many of the techniques valid for Gaussian case can not be applied.

*2.2. Multidimensional Case.* A  $d$ -dimensional  $\alpha$ -stable random vector  $\mathbf{X}$  can be defined by means of its characteristic function. Namely,  $\mathbf{X}$  is  $d$ -dimensional  $\alpha$ -stable random vector if there exists a finite measure  $\Gamma$  on  $(d-1)$ -dimensional unit sphere  $\mathbb{S}^{d-1}$  (called spectral measure) and shift vector  $\boldsymbol{\mu}^0 \in \mathbb{R}^d$  such that its characteristic function has the following form [23]:

$$\begin{aligned} \Phi(\mathbf{t}) &= E \exp(-i \langle \mathbf{X}, \mathbf{t} \rangle) = \exp(-\mathbf{I}(\mathbf{t})) \\ &= \exp \left( - \int_{\mathbb{S}^{d-1}} \psi_\alpha(\langle \mathbf{t}, \mathbf{s} \rangle) \Gamma(d\mathbf{s}) + i \langle \mathbf{t}, \boldsymbol{\mu}^0 \rangle \right), \\ \psi_\alpha(u) &= \begin{cases} |u|^\alpha \left( 1 - i \operatorname{sgn}(u) \tan \frac{\pi\alpha}{2} \right) & \text{if } \alpha \neq 1, \\ |u| \left( 1 + i \frac{2}{\pi} \operatorname{sgn}(u) \ln |u| \right) & \text{if } \alpha = 1, \end{cases} \end{aligned} \quad (2)$$

and  $\langle \mathbf{t}, \mathbf{s} \rangle = t_1 s_1 + t_2 s_2 + \dots + t_d s_d$  denotes inner product of  $\mathbf{t}, \mathbf{s} \in \mathbb{R}^d$ .

Let us observe that  $\mathbf{I}(\mathbf{t}) = -\ln \Phi(\mathbf{t})$  and therefore  $\mathbf{I}$  is the exponent of the characteristic function  $\Phi(\mathbf{t})$  of random vector  $\mathbf{X}$ . It is obvious that  $\alpha$ -stable random vectors inherit properties from one-dimensional case, for instance, the heavy-tailed behavior of vectors' marginal distributions. It is also interesting that any linear combination of the marginal

distributions of  $\mathbf{X}$  of the form  $Y = \sum_{k=1}^d a_k X_k$  have  $\alpha$ -stable one-dimensional distribution; see theorem 2.1.2 [23]. The contrary is only true if all linear combinations  $Y = \sum_{k=1}^d a_k X_k$  are symmetric or have stability index greater than or equal to one or are strictly stable.

As it was mentioned, despite many interesting properties of  $\alpha$ -stable distributions and interesting applications, there are many disadvantages. One of them is related to the fact that for  $\alpha$ -stable distribution the main measure of dependence, such as correlation (or covariance), can not be used for  $\alpha < 2$ , since in this case, as was indicated above, the theoretical second moment is infinite. Therefore, there is a need to consider alternative measures of dependence that can be adequate for infinite variance processes. In the next section we introduce two of them and indicate their interesting properties.

### 3. Alternative Measures of Dependence for Infinite Variance Processes

One of the measures that is often considered as a tool for measuring interdependence is the codifference. This measure is defined for general class of processes, namely, infinitely divisible. For the stationary infinite divisible process  $\{X(t)\}$  the codifference is defined as follows [23]:

$$\begin{aligned} \text{CD}(X(t), X(0)) &= \log(\mathbf{E} \exp(i(X(t) - X(0)))) \\ &\quad - \log(\mathbf{E} \exp(iX(t))) \\ &\quad - \log(\mathbf{E} \exp(-iX(0))). \end{aligned} \quad (3)$$

The main properties of the codifference one can be found, for example, in [23]; we only mention here that this measure can be considered as an extension of the autocovariance. In case the  $\{X(t)\}$  process is Gaussian the codifference reduces simply to the autocovariance [25]. The codifference carries enough information to detect ergodic properties of the process  $\{X(t)\}$  [26]. It is also closely related to another measure, namely, dynamical functional, discussed, for example, in [27–32], in the context of chaotic behavior recognition. The codifference is also used to examine the so-called long range dependence (or long memory) in case the correlation function is not defined [33].

Another alternative measure of dependence is the covariation. This measure is defined only for symmetric  $\alpha$ -stable random variables with  $\alpha > 1$ . If  $T_1$  and  $T_2$  are jointly symmetric  $\alpha$ -stable with  $\alpha > 1$  and  $\Gamma$  is the spectral measure of a random vector  $(T_1, T_2)$ , then the covariation of  $T_1$  on  $T_2$  is the real number defined as [23]

$$\text{CV}(T_1, T_2) = \int_{\mathbb{S}_2} s_1 s_2^{(\alpha-1)} \Gamma(ds), \quad (4)$$

where  $\mathbb{S}_2$  is the unit sphere in  $\mathbb{R}^2$  and the signed power  $z^{(p)}$  is given by  $z^{(p)} = |z|^p \text{sign}(z)$ . The main properties of the covariation can be found in [23]. We only mention, in contrast to codifference, that the covariation is not symmetric measure when  $\alpha < 2$  and when  $\alpha = 2$  it is equal to half of the covariance of  $T_1$  on  $T_2$ . Moreover, for  $\alpha > 1$ , the covariation

induces a norm on the linear space of jointly symmetric  $\alpha$ -stable random variables. Namely, if  $T_1$  is a symmetric  $\alpha$ -stable random variable with  $\alpha > 1$ , then

$$\|T_1\|_\alpha = (\text{CV}(T_1, T_1))^{1/\alpha}. \quad (5)$$

The covariation norm of given random variable is equal to its scale parameter. If we assume  $T_1$  and  $T_2$  are symmetric  $\alpha$ -stable with  $\alpha > 1$ , then the codifference of  $T_1$  on  $T_2$  can be expressed by means of the covariation norm; namely [23, 34],

$$\text{CD}(T_1, T_2) = \|T_1\|_\alpha^\alpha + \|T_2\|_\alpha^\alpha - \|T_1 - T_2\|_\alpha^\alpha. \quad (6)$$

### 4. Empirical Measures of Dependence for Infinite Variance Processes

In this section we introduce the methods of estimating of the alternative measures of dependence, adequate for infinite variance processes, considered in the previous section. We mention that the estimator of codifference was introduced previously in the literature; therefore we only show here the idea of estimating method. The main result of the paper is presented in Section 4.2, where we introduce a new tool of covariation estimating.

*4.1. Codifference.* For the stationary process  $\{X(t)\}$  we define an estimator of codifference in the following way [25]:

$$\begin{aligned} \widehat{\text{CD}}(X(t), X(s)) &= \ln(\widehat{\phi}(1, -1, X(t), X(s))) \\ &\quad - \ln(\widehat{\phi}(1, 0, X(t), X(s))) \\ &\quad - \ln(\widehat{\phi}(0, -1, X(t), X(s))), \end{aligned} \quad (7)$$

where  $\widehat{\phi}(u, v, X(t), X(s))$  is an estimator of the characteristic function:

$$\widehat{\phi}(u, v, X(t), X(s)) = \mathbf{E} \exp\{i(uX(t) + vX(s))\}. \quad (8)$$

In [24] an efficient methodology is introduced for estimating the codifference from a single trajectory of stationary process. Namely, if  $\{x_k, k = 1, \dots, N\}$  is realization of a stationary process  $\{X(t)\}$ , then the estimator of the characteristic function takes the form

$$\begin{aligned} \widehat{\phi}(u, v, X(t), X(s)) &= \frac{1}{N} \sum_{k=1}^{N-|t-s|} \exp(i(ux_{k+|t-s|} + vx_k)). \end{aligned} \quad (9)$$

At the end we should mention that the estimator of codifference for linear  $\alpha$ -stable process has very good properties [24, 35, 36] and has been successfully used, for instance, in the problem of proper model recognition [25] as well as to detect impulsive behavior of real data [21].

*4.2. Covariation.* We estimate the covariation using formula (4); therefore a spectral measure  $\Gamma$  should be estimated first. In general, the spectral measure of  $d$ -dimensional stable

random vector is a measure over  $d$ -dimensional unit sphere. It can be continuous, as well as discrete. In practice, we use a fact proved by Byczkowski et al. [37] that every spectral measure can be approximated by its discrete approximation. From this reason formula (4) can be estimated in the following way:

$$\widehat{CV}(X, Y) = \sum_{i=1}^n s_{1,i} s_{2,i}^{(\alpha-1)} \Gamma^* (\{\mathbf{s}_i\}), \quad (10)$$

where  $\Gamma^*$  is the discrete approximation of spectral measure  $\Gamma$  and  $\mathbf{s}_i = (s_{1,i}, s_{2,i})$  for  $i = 1, 2, \dots, n$  are locations on unit circle of  $\Gamma^*$  masses.

In the literature one can find several approaches to spectral measure's estimation, starting from methods based on empirical characteristic functions of bivariate SaS vectors [38, 39], through spherical harmonic analysis [40] and quantile lines [41], to generalized empirical likelihood method [42]. In this work, for the illustration purposes, we use the method of estimating of the discrete spectral measure proposed by Nolan et al. [38], which is based on one-dimensional projections of bivariate SaS vectors and the empirical characteristic functions. The method is presented in the following part.

Let us consider an independent identically distributed (i.i.d.) sample  $\mathbf{X}_1, \mathbf{X}_2, \dots, \mathbf{X}_k$  from bivariate SaS vector  $\mathbf{X} = (X, Y)$ . First we construct a set of one-dimensional projections  $\langle \mathbf{X}_1, \mathbf{t}_i \rangle, \langle \mathbf{X}_2, \mathbf{t}_i \rangle, \dots, \langle \mathbf{X}_k, \mathbf{t}_i \rangle$  for every point  $\mathbf{t}_i$  of a grid  $\mathbf{t}_1, \mathbf{t}_2, \dots, \mathbf{t}_n$  that is equally distributed over  $\mathbb{S}^1$ .

In the next step, for all samples  $\langle \mathbf{X}_1, \mathbf{t}_i \rangle, \langle \mathbf{X}_2, \mathbf{t}_i \rangle, \dots, \langle \mathbf{X}_k, \mathbf{t}_i \rangle$  we estimate one-dimensional parameters of univariate  $\alpha$ -stable random variables  $\alpha(\mathbf{t}_i), \sigma(\mathbf{t}_i), \beta(\mathbf{t}_i), \mu(\mathbf{t}_i)$  using McCulloch empirical quantile method [43]. Then we derive the empirical estimator of characteristic function's exponent:

$$\widehat{\mathbf{I}}(\mathbf{t}_i) = \begin{cases} \widehat{\sigma}^{\widehat{\alpha}(\mathbf{t}_i)}(\mathbf{t}_i) \left( 1 - i\widehat{\beta}(\mathbf{t}_i) \tan \frac{\pi\widehat{\alpha}(\mathbf{t}_i)}{2} \right) & \text{if } \widehat{\alpha}(\mathbf{t}_i) \neq 1, \\ \widehat{\sigma}(\mathbf{t}_i) (1 - i\widehat{\mu}(\mathbf{t}_i)) & \text{if } \widehat{\alpha}(\mathbf{t}_i) = 1. \end{cases} \quad (11)$$

Obtained vector  $\widehat{\mathbf{I}} = [\widehat{\mathbf{I}}(\mathbf{t}_1), \dots, \widehat{\mathbf{I}}(\mathbf{t}_n)]$  is the projection estimator of  $\mathbf{I}$ . Since we estimate a discrete approximation of spectral measures, we assume that all its mass is concentrated in points of unit circle  $\mathbb{S}^1: \mathbf{s}_1, \mathbf{s}_2, \dots, \mathbf{s}_n$ . Therefore, we have

$$\mathbf{I}(\cdot) = \sum_{i=1}^n \psi_\alpha(\langle \cdot, \mathbf{s}_i \rangle) \Gamma^* (\{\mathbf{s}_i\}), \quad (12)$$

where  $\Gamma^*$  is the discrete approximation of the true spectral measure  $\Gamma$  and function  $\psi_\alpha$  is defined in (2).

Nolan et al. in [38] suggest taking  $\mathbf{s}_j = \mathbf{t}_j$  for  $j = 1, \dots, n$  and assume that  $n = 2m$ ,  $m \in \mathbb{N}$ ; then empirical version of equation (12) can be rewritten in the following matrix equation form:

$$\widehat{\mathbf{c}} = \widehat{\mathbf{A}}\Gamma^*, \quad (13)$$

where  $\widehat{\mathbf{c}} = [c_1, c_2, \dots, c_n]$  is a row vector with elements:

$$c_i = \begin{cases} \Re \widehat{\mathbf{I}}(\mathbf{t}_i) & i = 1, 2, \dots, m, \\ \Im \widehat{\mathbf{I}}(\mathbf{t}_i) & i = m, m+1, \dots, n, \end{cases} \quad (14)$$

and  $\widehat{\mathbf{A}} = [a_{i,j}]_{i,j}^n$  is a square matrix with the following entries:

$$a_{i,j} = \begin{cases} \Re \psi_\alpha(\langle \mathbf{t}_i, \mathbf{t}_j \rangle) & i = 1, 2, \dots, m, \\ \Im \psi_\alpha(\langle \mathbf{t}_i, \mathbf{t}_j \rangle) & i = m, m+1, \dots, n. \end{cases} \quad (15)$$

In above formulas  $\Re$  and  $\Im$  denote real and imaginary part of complex number, respectively.

To avoid further numerical problems with inverting formula (13) such as obtaining the spectral measure masses of negative sign, we can obtain  $\Gamma^*$  by minimizing some functional:

$$\widehat{\Gamma}^* = \min_{\Gamma^* > \mathbf{0}} \|\widehat{\mathbf{c}} - \widehat{\mathbf{A}}\Gamma^*\|. \quad (16)$$

In our further numerical experiments of estimating the covariance measure we implemented the above presented algorithms in MATLAB package including `fmincon` routine.

We also note that another method of estimating covariation measure was suggested previously in the literature [44]. This method leads to estimation of normalized covariation and is based on the  $p$ th moment approach. In order to obtain the empirical covariation adequate to definition (4) by using the method introduced in [44] there is a need to know the theoretical stability index and the scale parameter of appropriate random variable. From the practical point of view, this means there is a need to estimate both of them. However, we have compared that method to the one proposed in this paper and result suggests that methodology proposed in this paper leads to even better estimates of the true values for theoretical models examined in the next section. One can find also other approaches of calculating the covariation from financial data [45].

## 5. Application for Local Damage Detection in Rotating Machines

Local damage (crack, pitting, spall, breakage, etc.) in mechanical components produces events, short in time (impulsive) and wideband in frequency, disturbance which occurred in measured vibration. Undetected local damage could develop into more severe one and lead to the breakdown of the whole machine. Thus, local damage detection is one of the most widely explored problems in modern condition monitoring. Detection of such damage in industrial reality might be practically difficult due to poor signal-to-noise ratio and specific properties of informative signal. Localized damage causes significant, local increase of interaction of surfaces being in contact. It means that at these time moments forces/moments are several (or more) times bigger than during normal operation. It accelerates degradation and might rapidly (much quicker than distributed damage) cause catastrophic failure.

Vibration analysis seems to be the most effective approach for this problem. Mechanism of generation of informative signals is well recognized [1–4, 46]. Local change of stiffness associated with crack or loss of surface causes impulsive disturbance in the signal. Due to rotation of elements, these disturbances should be cyclic [5]. These two features impulsiveness and periodicity are a basis for damage detection. However, detection of impulsive behavior or period of such behavior is often difficult. Thus, many different decomposition techniques of raw signal could be used. In this paper we used one of the most known decomposition methods, namely, time-frequency decomposition via Short-Time Fourier Transform (spectrogram).

The time series from the spectrogram corresponding to given frequency are called the subsignals. They are analyzed using appropriate statistics (called selectors). Undoubtedly, the most popular statistic was kurtosis [6], one of the measures that can point out these frequency bins on time-frequency map revealing the most impulsive nature. However, for many real signals the kurtosis-based approach does not give expected results because it can be sensitive for impulses not associated with damage (related to artifacts, non-Gaussian noise, or even regular operation of other parts of machines, i.e., valves).

The idea of spectral kurtosis was extended and other selectors were proposed for local damage detection [5, 47–49]. Generally, the mentioned selectors are constructed under the assumption that distribution of subsignal corresponding to healthy condition should resemble Gaussian one in comparison to distribution of subsignal corresponding to damage condition. The idea of modeling of the subsignals from time-frequency representation was also extended to more general class of distribution, namely,  $\alpha$ -stable, [21, 50]. As it was mentioned in the previous sections, the  $\alpha$ -stable distributions are especially important in the context of modeling of data with visible jumps; therefore they can be appropriate for describing of subsignals related to damage. In this case the value of  $\alpha$  parameter is significantly smaller than 2. On the other hand, for  $\alpha$  close to 2, the stable distribution is close to Gaussian one; therefore the class of  $\alpha$ -stable distributions can be also used for modeling of subsignals for healthy case. Because of that reason the  $\alpha$ -stable distribution approach seems to be appropriate in the problem of local damage detection.

To get information about hidden periodicity in the signal, so-called Spectral Correlation Density map and spectral coherence were calculated as bifrequency maps. One of the most popular algorithms was simple: decompose signal into set of df frequency bins using spectrogram and next for each bin calculate spectrum. Unfortunately, signal is nonstationary and highly impulsive for set of frequency bins so at least from theoretical point of view using classical techniques is not appropriate. Then we propose using  $\alpha$ -stable distribution perspective and consequently measures adequate for infinite variance processes, namely, codifference and covariation, described in the previous sections.

Visualization of such measures for each subsignal results in new form of lag-frequency map that presents diagnostic information in very clear way [21]. Similar approach without

TABLE I: Characteristic frequencies.

Component	Frequency (Hz)	Result
$f_{01}$ (Hz)	$f_{01} = \frac{n_1}{60}$	16.58 Hz
$f_{02}$ (Hz)	$f_{02} = \frac{n_2}{60} = \frac{n_1}{60 \cdot u_1}$	4.1 Hz
$f_{03}$ (Hz)	$f_{03} = \frac{n_3}{60} = \frac{n_1}{60 \cdot u_1 \cdot u_2}$	1.31 Hz
$f_{z12}$	$f_{z12} = \frac{n_1 \cdot z_1}{60}$	381.42 Hz
$f_{z34}$	$f_{z34} = \frac{n_2 \cdot z_3}{60}$	147.6 Hz
$U_p$	$U_p = \frac{z_2 \cdot z_4}{z_1 \cdot z_3}$	12.69

the assumption of  $\alpha$ -stable distribution of appropriate subsignals was presented in [51].

Mining machines seem to be one of the most complex machines in industry with complex structure, high-power, time-varying load, and so on. In this paper we will concentrate on the belt conveyor system, commonly used for continuous transport of bulk material (coal, overburden, copper ore, etc.) in both opencast and underground mines. Depending on the design (power required by the machine to move) belt conveyor driving station might consist of one up to four drive units with 630 or 1000 kW power each. In our research 630 kW two-stage gearbox was considered. Real data analysis was performed on the vibration signal of a two-stage gearbox that operates in an open-pit mine and transfer torque from an engine to a belt conveyor pulley. Measurements were made using Bruel-Kjaer Pulse system with following acquisition parameters: length of the signal equal to the 2.5 s and sampling frequency 16384 Hz. Sensors were mounted on the housing of the gearbox.

Gearbox has been operating under regular conditions. Load has not been measured directly; however it was assumed based on the visual inspection of material stream transported on the belt that gearbox has been properly loaded. Frequency sampling used in the data acquisition is one of the typical values for this measurement system (power of 2). It is worth denoting that mining machines are those of high-power and their characteristic frequencies are relatively low. In the further analysis it can be seen that for higher frequencies (above couple of kHz) there is no information contained in these bands. Scheme of the gearbox is presented in Figure 1 with frequencies of the shafts presented in Table I. As one can see, frequencies of the shafts ( $f_{01}$  of shaft  $w1$ ,  $f_{02}$  of shaft  $w2$ , and  $f_{03}$  of shaft  $w3$ ), gear mesh frequencies ( $f_{z12}$  for first stage,  $f_{z34}$  for second stage), and ratio ( $U_p$ ) can be easily estimated. We have also given the calculated frequencies for the investigated gearbox. Investigated gearbox has shaft speed equal to 995 RPM. Speed of second and third shaft are equal to 246 RPM and 78 RPM, respectively. Ratios of first and second stage are equal to  $u_1 = 4.04$  and  $u_2 = 3.14$ , respectively. Numbers of teeth on the gears are as follows:  $z_1 = 23$ ,  $z_2 = 93$ ,  $z_3 = 36$ , and  $z_4 = 113$ . However, we were not able to investigate visually condition of the gears. On the other hand, according to the state of the start and our own experience, we know that cyclic impulsive

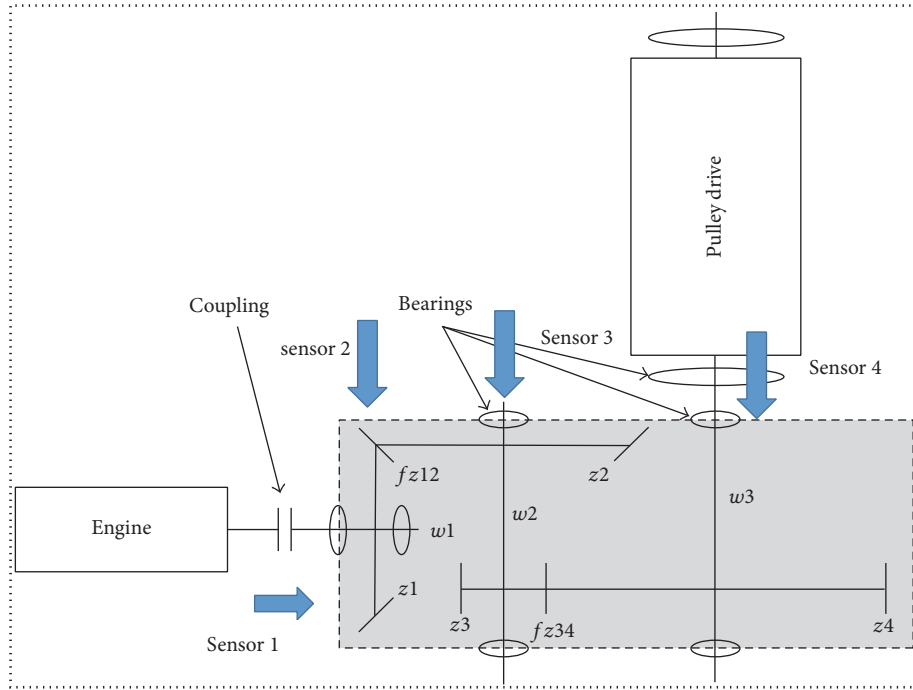


FIGURE 1: Scheme of the gearbox.

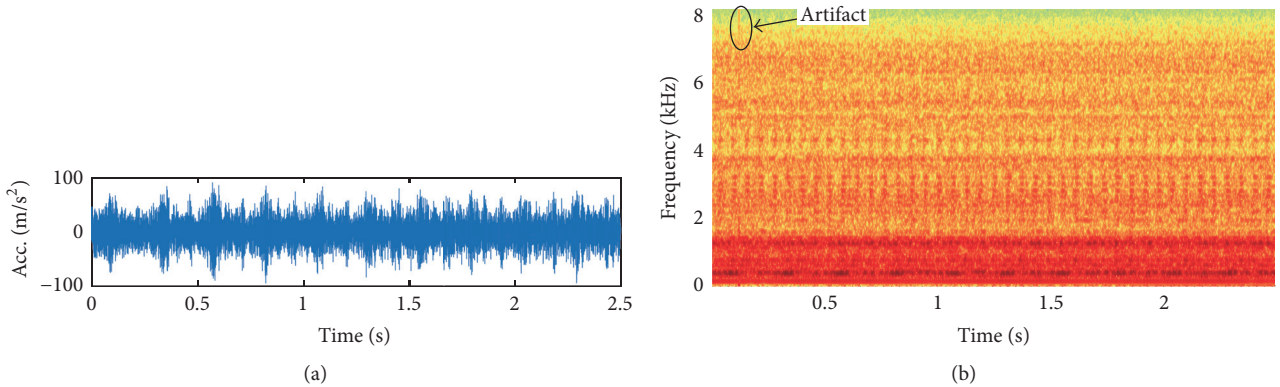


FIGURE 2: The raw vibration signal (a) and its spectrogram (b).

behavior at fault characteristic frequency means that there is a local damage on gear mounted on shaft rotating with that frequency.

Knowing design factors of the machine, one can calculate the fault frequencies for each component. In this vibration signal two fault frequencies were detected: 4.1 Hz and 16.5 Hz. After the technical survey they were confirmed to be placed on the first shaft (local damage at 16.5 Hz) and on the second shaft (distributed fault with strong amplitude modulation at 4.1 Hz).

In Figure 2 we present both time waveform of the acquired signal and its time-frequency decomposition, namely, spectrogram. We remind the reader that the spectrogram is a square of absolute value of the Short-Time Fourier Transform defined for time point  $t$  and frequency  $f$  as follows [5]:

$$\text{STFT}(t, f) = \sum_{k=0}^{n-1} x_k w(t-k) e^{2j\pi f k/N}, \quad (17)$$

where  $w(t-\tau)$  is the shifted window and  $x_0, \dots, x_{n-1}$  is the input signal.

It can not be easily observed that in the time domain the analyzed signal exhibits impulsive behavior. Cyclic changes of the amplitude are present due to the high energy in the low-frequency band responsible for the deterministic component of the signal.

Observing spectrogram (see Figure 2(b)) one can point out three main types of frequency bands. First type has high energy (red band on the spectrogram) and is placed at low frequencies (below 1 kHz). It carries strong energy and thus it is responsible for the amplitude modulation of the signal, as it can be seen in Figure 2(a). One can see

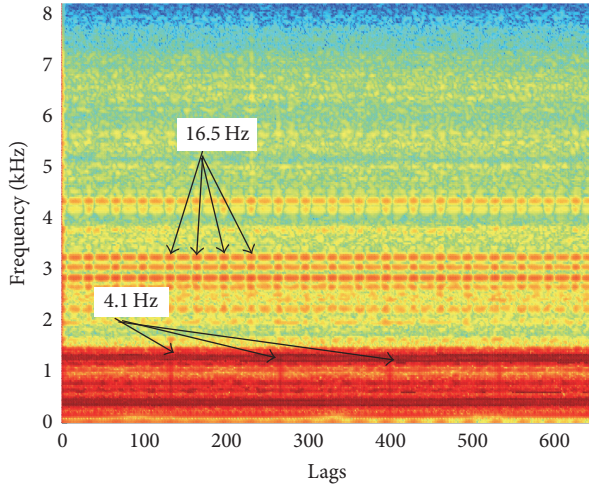


FIGURE 3: Codifference map of the investigated signal.

impulsive behavior repeating 4 times per second. However, second fault (16.5 Hz) is not visible due to the lower energy in comparison to the first one. Second type of the frequency bands is with low energy and it is connected with high-frequency additive noise in the signal ( $>7$  kHz). In this band we can observe abnormal behavior at 0.2 s. It is related to the artifact, impulsive event which is not connected with the fault. Third type of the band containing information about the fault is usually called an informative frequency band. In this band we can observe mainly impulsive behavior. In our case we can see that impulses are present at bands 2–3.5 kHz and 4–5 kHz. Energy of the impulses significantly exceeds energy of the background noise.

As the next step of our analysis we performed estimation of the codifference measure on each of the extracted subsignals from time-frequency decomposition, each related to certain frequency bin. Combining estimates together, one obtains codifference measure for each of the observed subsignals. In Figure 3 one can see results of the application towards investigated signal.

It can be observed that lag-frequency representation has been improved over spectrogram. Both informative frequency bands have increased ratio of fault visibility. In this bands one can easily observe impulsive behavior at peaks with distance between them equal to 33 lags which translates to 0.0606 s and corresponds to 16.5 Hz. Uncertainty of the location of impulses is related to the resolution of the spectrogram. Increasing the resolution allows for more precise location of the fault in the new lag-frequency representation but results in the drawback of the increased computational time. One can observe that low-frequency band which contained no information in the spectrogram now holds important information about the second fault. We observe recurring impulses at peaks with distance between them equal to 132 lags which translates to 0.243 s and is equal to 4.11 Hz, close to the real fault frequency.

Summing up, new lag-frequency representation provides superior overall information in comparison to the spectrogram.

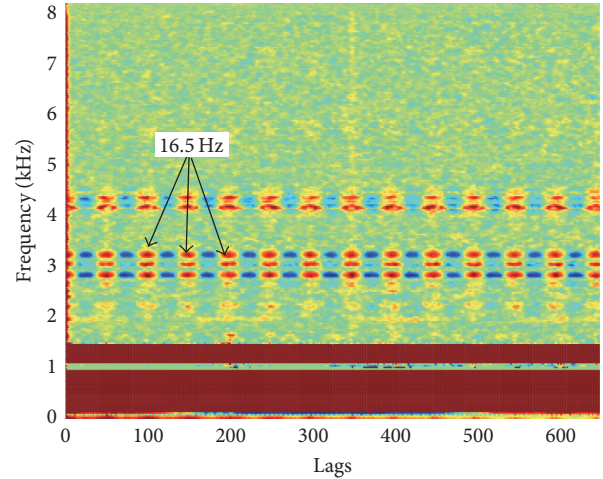


FIGURE 4: Covariation map of the investigated signal.

In Figure 4 we present the result of the estimated covariation map. This map is constructed similarly to the previous one; however for each subsignal from the spectrogram we calculate the empirical covariation applying the new algorithm. It can be denoted that two frequency bands at which repeating sequences are present are similar to informative frequency bands from the spectrogram (except the low-frequency band containing information about 4.1 Hz fault).

It can be concluded that this representation provides more clear look at selection of the informative frequency band. Furthermore, repeating sequences allow us to detect the fault. Each dot at informative frequency bands is placed at peaks which have distance between them equal to 33 lags and translates to 0.0606 s which corresponds to 16.5 Hz which is frequency of the fault.

As it was said earlier kurtosis-based approach does not give expected results. It is due to the kurtosis being sensitive towards singular impulses (e.g., artifacts). In Figure 5 we present kurtogram of the investigated signal. The artifact has wideband frequency signature.

However, it is more visible in the low-energy high-frequency band. Thus, kurtosis in this band is significantly higher than for the impulsive behavior in the informative frequency bands. Highest value of the kurtosis is reached at dyad [8106.6667 Hz; 170.6667 Hz] which results in the frequency band [7936 Hz; 8277.3334 Hz] which is not the correct one.

Summing up, provided new lag-frequency representations when combined together provide substantial information about the fault and its location in carrier frequency. Furthermore, using both of them allows for easier, more precise detection of the fault frequency. One can see more transparently features on the new lag-frequency representations than on the basis of the spectrogram.

## 6. Conclusions

In this paper the problem of local damage detection based on the vibration signal analysis is discussed. Real signals

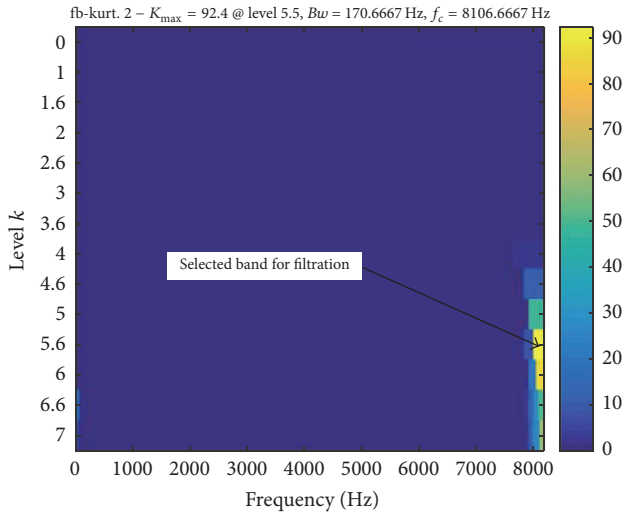


FIGURE 5: Kurtogram of the investigated signal.

often acquired in the noisy environment possess impulsive behavior which is not related to the fault. Therefore the classical methods of fault detection seem to be inappropriate in this case. The main point of our methodology is the assumption that the examined signals exhibit heavy-tailed behavior and are modeled by  $\alpha$ -stable distribution. In general, the local damage is demonstrated by periodic behavior of given signal. However this periodicity very often is not visible in the raw signal but can be recognized by statistics that measure dependence between data. By the assumption of  $\alpha$ -stable distribution we propose considering empirical measures of dependence adequate for such distribution-based models, namely, codifference and covariation. Because in the literature one can find research articles devoted to the problem of codifference estimation, the main attention of this paper is paid to the covariation estimation method. We gave complete description of the new estimation technique and show the application to local damage detection based on real signal of mining machine working in harsh environment. The proposed techniques are compared with the classical kurtosis-based approach.

## Conflicts of Interest

The authors declare that there are no conflicts of interest regarding the publication of this paper.

## Acknowledgments

This work is partially (A. Wyłomańska) supported by the Framework Programme for Research and Innovation Horizon 2020 under Grant Agreement no. 636834 (DISIRE-Integrated Process Control Based on Distributed In-Situ Sensors into Raw Material and Energy Feedstock).

## References

- [1] P. D. McFadden and J. D. Smith, "Vibration monitoring of rolling element bearings by the high-frequency resonance

- technique—a review," *Tribology International*, vol. 17, no. 1, pp. 3–10, 1984.
- [2] R. B. Randall and J. Antoni, "Rolling element bearing diagnostics—a tutorial," *Mechanical Systems and Signal Processing*, vol. 25, no. 2, pp. 485–520, 2011.
- [3] P. D. Samuel and D. J. Pines, "A review of vibration-based techniques for helicopter transmission diagnostics," *Journal of Sound and Vibration*, vol. 282, no. 1-2, pp. 475–508, 2005.
- [4] J. Antoni, F. Bonnardot, A. Raad, and M. El Badaoui, "Cyclostationary modelling of rotating machine vibration signals," *Mechanical Systems and Signal Processing*, vol. 18, no. 6, pp. 1285–1314, 2004.
- [5] J. Obuchowski, A. Wyłomańska, and R. Zimroz, "Selection of informative frequency band in local damage detection in rotating machinery," *Mechanical Systems and Signal Processing*, vol. 48, no. 1-2, pp. 138–152, 2014.
- [6] J. Antoni, "Cyclostationarity by examples," *Mechanical Systems and Signal Processing*, vol. 23, no. 4, pp. 987–1036, 2009.
- [7] B. t. Mandelbrot, "Stable paretian random functions and the multiplicative variation of income," *Econometrica*, vol. 29, pp. 517–543, 1961.
- [8] B. Mandelbrot, "New methods in statistical economics," *Journal of Political Economy*, vol. 71, no. 5, pp. 421–440, 1963.
- [9] S. Rachev and S. Mittnik, *Stable Paretian Models in Finance*, Wiley, 2000.
- [10] J.-P. Bouchaud and M. Potters, *Theory of Financial Risks*, Cambridge University Press, Cambridge, UK, 2000.
- [11] P. Carr, H. Geman, D. B. Madan, and M. Vor, "The fine structure of asset returns: an empirical investigation," *Journal of Business*, vol. 75, no. 2, pp. 305–332, 2002.
- [12] M. F. Shlesinger, J. Klafter, and Y. M. Wong, "Random walks with infinite spatial and temporal moments," *Journal of Statistical Physics*, vol. 27, no. 3, pp. 499–512, 1982.
- [13] V. Ziburdaev, S. Denisov, and J. Klafter, "Levy walks," *Reviews of Modern Physics*, vol. 87, no. 2, pp. 483–530, 2015.
- [14] V. Y. Gonchar, A. V. Chechkin, E. L. Sorokovoĭ, V. V. Chechkin, L. I. Grigor'eva, and E. D. Volkov, "Stable Lévy distributions of the density and potential fluctuations in the edge plasma of the U-3M torsatron," *Plasma Physics Reports*, vol. 29, no. 5, pp. 380–390, 2003.
- [15] R. Jha, P. K. Kaw, D. R. Kulkarni, and J. C. Parikh, "Evidence of Lévy stable process in tokamak edge turbulence," *Physics of Plasmas*, vol. 10, no. 3, pp. 699–704, 2003.
- [16] T. Mizuuchi, V. V. Chechkin, K. Ohashi et al., "Edge fluctuation studies in Heliotron J," *Journal of Nuclear Materials*, vol. 337-339, no. 1-3, pp. 332–336, 2005.
- [17] K. Burnecki, A. Wyłomańska, A. Beletskii, V. Gonchar, and A. Chechkin, "Recognition of stable distribution with Lévy index  $\alpha$  close to 2," *Physical Review E*, vol. 85, no. 5, 2012.
- [18] K. Burnecki, A. Wylomanska, and A. Chechkin, "Discriminating between Light- And heavy-tailed distributions with limit theorem," *PLoS ONE*, vol. 10, no. 12, 2015.
- [19] A. Janicki and A. Weron, "Can one see  $\alpha$ -stable variables and processes," *Statistical Science*, vol. 9, no. 1, pp. 109–126, 1994.
- [20] B. W. Stuck and B. Kleiner, "A statistical analysis of telephone noise," *Bell System Technical Journal*, vol. 53, no. 7, pp. 1263–1320, 1974.
- [21] G. Żak, A. Wyłomańska, and R. Zimroz, "Application of alpha-stable distribution approach for local damage detection in rotating machines," *Journal of Vibroengineering*, vol. 17, no. 6, pp. 2987–3002, 2015.

- [22] G. Yu, C. N. Li, and J. F. Zhang, "A new statistical modeling and detection method for rolling element bearing faults based on alpha-stable distribution," *Mechanical Systems and Signal Processing*, vol. 41, no. 1-2, pp. 155–175, 2013.
- [23] G. Samorodnitsky and M. Taqqu, *Stable Non-Gaussian Random Processes*, Chapman & Hall, New York, NY, USA, 1994.
- [24] D. Rosadi, "Testing for independence in heavy-tailed time series using the codifference function," *Computational Statistics & Data Analysis*, vol. 53, no. 12, pp. 4516–4529, 2009.
- [25] A. Wyłomańska, A. Chechkin, J. Gajda, and I. M. Sokolov, "Codifference as a practical tool to measure interdependence," *Physica A*, vol. 421, pp. 412–429, 2015.
- [26] M. Magdziarz, "Correlation cascades, ergodic properties and long memory of infinitely divisible processes," *Stochastic Processes and Their Applications*, vol. 119, no. 10, pp. 3416–3434, 2009.
- [27] J. Janczura and A. Weron, "Ergodicity testing for anomalous diffusion: small sample statistics," *Journal of Chemical Physics*, vol. 142, no. 14, 2015.
- [28] S. Cambanis, J. Hardin, and A. Weron, "Ergodic properties of stationary stable processes," *Stochastic Processes and Their Applications*, vol. 24, no. 1, pp. 1–18, 1987.
- [29] S. Cambanis, K. Podgórski, and A. Weron, "Chaotic behavior of infinitely divisible processes," *Studia Mathematica*, vol. 115, no. 2, pp. 109–127, 1995.
- [30] A. Janicki and A. Weron, *Simulation and Chaotic Behaviour of alpha-Stable Stochastic Processes*, Marcel Dekker, New York, NY, USA, 1994.
- [31] K. Burnecki and A. Weron, "Algorithms for testing of fractional dynamics: A practical guide to ARFIMA modelling," *Journal of Statistical Mechanics: Theory and Experiment*, no. 10, 2014.
- [32] M. Magdziarz and A. Weron, "Anomalous diffusion: testing ergodicity breaking in experimental data," *Physical Review E*, vol. 84, no. 5, 2011.
- [33] P. Embrechts and M. Maejima, *Selfsimilar Processes*, Princeton University Press, Princeton, NJ, USA, 2002.
- [34] J. Nowicka-Zagrajek and A. Wyłomańska, "Measures of dependence for stable ar(1) models with time-varying coefficients," *Stochastic Models*, vol. 24, no. 1, pp. 58–70, 2008.
- [35] D. Rosadi and M. Deistler, "Estimating the codifference function of linear time series models with infinite variance," *Metrika*, vol. 73, no. 3, pp. 395–429, 2011.
- [36] D. Rosadi, "Order identification for Gaussian moving averages using the codifference function," *Journal of Statistical Computation and Simulation*, vol. 76, no. 6, pp. 553–559, 2006.
- [37] T. Byczkowski, J. P. Nolan, and B. Rajput, "Approximation of multidimensional stable densities," *Journal of Multivariate Analysis*, vol. 46, no. 1, pp. 13–31, 1993.
- [38] J. P. Nolan, A. K. Panorska, and J. H. McCulloch, "Estimation of stable spectral measures," *Mathematical and Computer Modelling*, vol. 34, no. 9-11, pp. 1113–1122, 2001.
- [39] M. Mohammadi, A. Mohammadpour, and H. Ogata, "On estimating the tail index and the spectral measure of multivariate  $\alpha$ -stable distributions," *Metrika*, vol. 78, no. 5, pp. 549–561, 2015.
- [40] M. Pivato and L. Seco, "Estimating the spectral measure of a multivariate stable distribution via spherical harmonic analysis," *Journal of Multivariate Analysis*, vol. 87, no. 2, pp. 219–240, 2003.
- [41] Y. Dominicy and D. Veredas, "The method of simulated quantiles," *Journal of Econometrics*, vol. 172, no. 2, pp. 235–247, 2013.
- [42] H. Ogata, "Estimation for multivariate stable distributions with generalized empirical likelihood," *Journal of Econometrics*, vol. 172, no. 2, pp. 248–254, 2013.
- [43] J. H. McCulloch, "Simple consistent estimators of stable distribution parameters," *Communications in Statistics. B. Simulation and Computation*, vol. 15, no. 4, pp. 1109–1136, 1986.
- [44] C. M. Gallagher, "A method for fitting stable autoregressive models using the autocovariation function," *Statistics & Probability Letters*, vol. 53, no. 4, pp. 381–390, 2001.
- [45] O. E. Barndorff-Nielsen, P. R. Hansen, A. Lunde, and N. Shephard, "Multivariate realised kernels: consistent positive semi-definite estimators of the covariation of equity prices with noise and non-synchronous trading," *Journal of Econometrics*, vol. 162, no. 2, pp. 149–169, 2011.
- [46] J. Wodecki, R. Zdunek, A. Wyłomańska, and R. Zimroz, "Local fault detection of rolling element bearing components by spectrogram clustering with semi-binary nmf," *Diagnostyka*, vol. 18, no. 1, pp. 3–8, 2017.
- [47] I. Obuchowski, A. Wyłomańska, and R. Zimroz, "The local maxima method for enhancement of time-frequency map and its application to local damage detection in rotating machines," *Mechanical Systems and Signal Processing*, vol. 46, no. 2, pp. 389–405, 2014.
- [48] J. Obuchowski, A. Wyłomańska, and R. Zimroz, "Recent developments in vibration based diagnostics of gear and bearings used in belt conveyors," *Applied Mechanics and Materials*, vol. 683, pp. 171–176, 2014.
- [49] J. Obuchowski, A. Wyłomańska, and R. Zimroz, "Stochastic modeling of time series with application to local damage detection in rotating machinery," *Key Engineering Materials*, vol. 569-570, pp. 441–448, 2013.
- [50] G. Żak, J. Obuchowski, A. Wyłomańska, and R. Zimroz, "Application of ARMA modelling and alpha-stable distribution for local damage detection in bearings," *Diagnostyka*, vol. 15, no. 3, pp. 3–10, 2014.
- [51] G. Żak, J. Obuchowski, A. Wyłomańska, and R. Zimroz, "Novel 2d representation of vibration for local damage detection," *Mining Science*, vol. 21, pp. 105–113, 2014.